

Chapter 2. Accelerator

2.1 Accelerator Design

2.1.1 Overview

A. 4GSR

One of features of 4th generation storage rings is that it reduces natural emittance by a factor of 10-100 compared to that of 3rd generation storage rings by using more bending magnets per each cell. Typical 3rd generation storage rings use 2-3 bending magnets (DBA or TBA) per cell while 4th generation storage rings use 5-9 bending magnets per cell. This concept was first reported in 1993, and attempted for design of Swiss Light Source. After 2000, successful operation of 3rd generation of storage rings has ripe the technology, and first application of the compact vacuum chamber and the small aperture magnets to MAX-IV (Sweden) announced era of 4th generation storage rings.

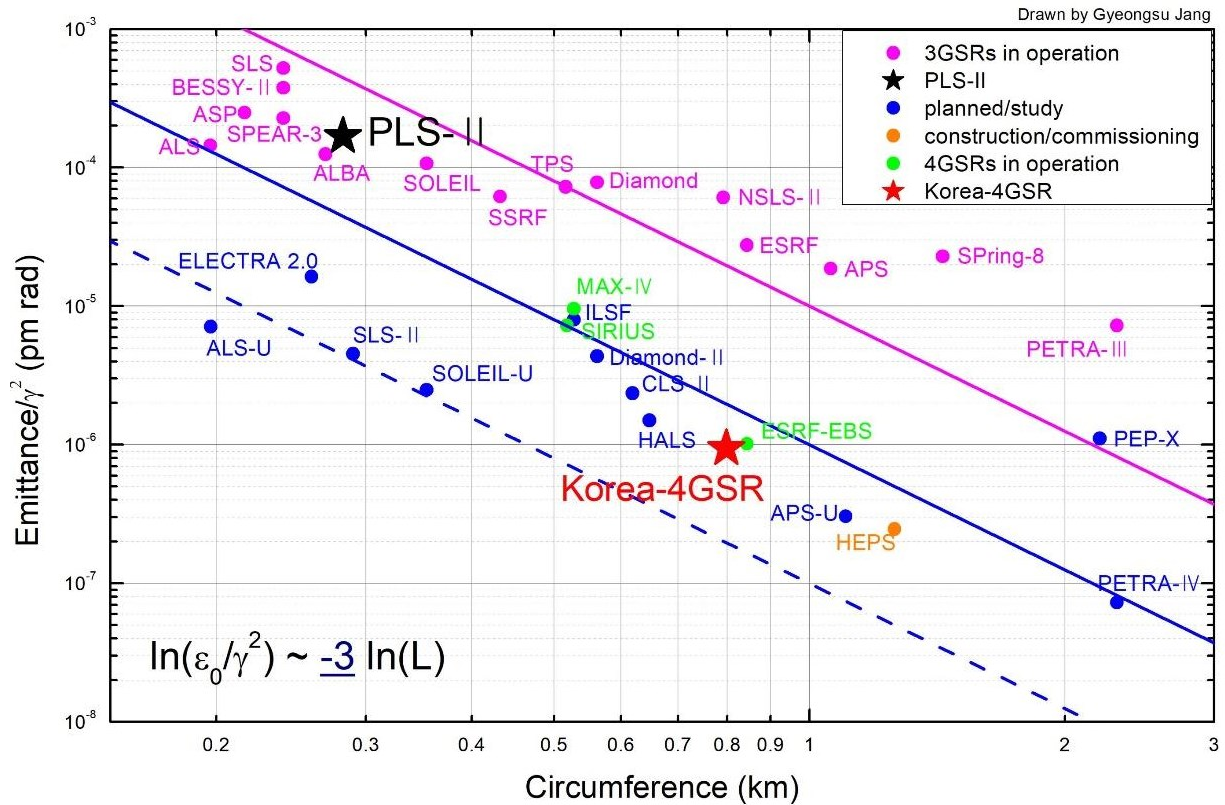
Following successful commissioning and operation of MAX-IV, SIRIUS stored the electron beam and started user operation recently. ESRF-EBS, an upgrade project of ESRF storage ring, had completed its machine commissioning in a short time and started user operation in August, 2020. Other 4GSR projects include APS-U (USA) and ALS-U (USA) which are another upgrade project, and HEPS (China) is a greenfield machine which is under commissioning. In addition, many existing storage rings plan to upgrade to 4GSR, and research for new 4GSR projects is actively underway.

In <Figure 2.1.1.1>, the performance distribution according to the storage ring circumference for third-generation synchrotron accelerators and 4GSR is shown. As indicated in (Equation 2.1.1.1), the emittance of the storage ring is proportional to the square of the electron beam energy and inversely proportional to the cube of the storage ring circumference (the number of dipole magnets in the storage ring).

$$\varepsilon \propto F(lattice) \frac{E^2}{C^3} \quad (\text{Eq. 2.1.1.1})$$

As shown in <Figure 2.1.1.1>, the performance of the storage ring (emittance) naturally improves with a larger circumference. However, through the successful operation of a multi-bend lattice incorporating a greater number of dipole magnets—first attempted by MAX IV—the storage ring emittance was reduced by more than tenfold compared to existing third-generation synchrotron accelerators. Following this, ESRF-EBS (the upgraded machine of France's ESRF) introduced longitudinal variations in the magnetic field within dipole magnets 2.1.7(longitudinal gradient dipoles). Additionally, APS-U added the concept of reverse bending, which was introduced by PSI, to the ESRF-EBS type lattice. SLS-II also considered both longitudinal gradient dipoles and reverse bending. Applying these concepts into the lattice design enabled to achieve an emittance reduction of more than 50 times compared to existing third-generation storage rings.

In Korea, preliminary studies at the Pohang Accelerator Laboratory examined the realization of minimum emittance from a beam physics perspective, despite many challenging aspects of the device. This achieved performance corresponding to the blue dotted line in <Figure 2.1.1.1> However, due to potential risks and challenges associated with the device design, it was decided to aim for the performance indicated by the blue line to ensure a more stable implementation. Compared to PLS-II, which has a storage ring circumference of 281 meters, the new Korea-4GSR has expanded to 800 meters, allowing us to expect performance improvements exceeding 100 times.



<Figure 2.1.1.1> Performance distribution of 3GSRs and 4GSRs according to circumference.

B. Major Parameters

In the initial design of the storage ring, selecting the key parameters is extremely important. However, major variables like beam energy are intricately linked with various factors, making it challenging to set target values in a straightforward manner. Therefore, it is necessary to make reasonable choices by considering as many aspects as possible, including the surrounding environment (role-sharing with PLS-II) and the anticipated budget.

(1) Selection of Electron Beam Energy

First, the beam physics parameters related to the electron beam can be summarized as follows, where E is the electron beam energy, B is the magnetic field strength of the dipole magnets, n represents the higher harmonics of the undulator, and λ_u is the undulator period.

- Emittance: $\propto E^2$
- Required RF power: $\propto E^4$

- Magnetic field gradient: $\propto E$
- Instability, IBS, and Touschek lifetime: Higher energy is advantageous
- Photon beam energy from dipole magnet source [keV]: $\propto BE^2$
- Photon beam energy from undulator source [keV]: $\propto \frac{nE^2}{\lambda_u}$

At a given storage ring circumference, using a lower energy allows for achieving lower emittance, requires significantly less RF power, and reduces the magnetic field strength linearly, which is advantageous in terms of operating costs. However, higher energy is beneficial for beam instability, intra-beam scattering (IBS) (IBS growth rate $\propto \frac{1}{E^4}$), and Touschek lifetime (Touschek lifetime $\propto E^3$). Considering these factors, a direction can be set. For example, APS-U reduced its energy from 7 GeV to 6 GeV, resulting in a 36% increase in brilliance due to improvements in emittance and beam current.

Generally, the electron beam energy should be carefully considered based on the usable energy range of the photon beam; increasing the electron beam energy is advantageous for achieving higher photon beam energies. However, experiences with recent third-generation synchrotron accelerators show that using super-bends (shortening the length of dipole magnets and increasing the magnetic field to generate higher-energy photon beams) can produce photon beams of 20 to 30 keV even at an electron beam energy of 3 GeV in dipole magnets. In undulators, by reducing the undulator period and using higher harmonics, high-brilliance photon beams up to 30 keV are being generated.

Calculations considering a storage ring circumference of 800 m indicate that up to 30 keV, a storage ring energy of 4 GeV can offer higher brilliance than 6 GeV. Of course, by using high-field wigglers, photon beams up to 100 keV can be utilized even at 4 GeV. If there were no limitations on the storage ring size, a facility with a larger circumference and higher electron beam energy (e.g., 6 GeV) could deliver better performance, but this would require a larger budget for construction and operation.

(2) Selection of Electron Beam Current

Higher beam current is advantageous for photon beam characteristics (flux and brilliance).

However, the increased photon beam power must be stably handled by the storage ring's chamber and the beamline optics. Additionally, sufficient RF power must be available. Considering brilliance of photon beam at energy of interest, beam current of 400 mA is set as the target beam current for the brightness mode. This can be achieved with 10 to 12 modules of NRF system occupying three straight sections and harmonic cavities mitigating collective effects.

(3) Selection of RF Operating Frequency

In the 4GSR, as emittance decreases, it is necessary to secure sufficient beam lifetime, which is achieved by increasing the bunch length using a lower storage ring RF frequency. However, this approach limits the number of bunches that can be filled, requiring a higher charge per bunch, so a more effective frequency should be selected considering this. Additionally, the ability to increase the bunch length to some extent using a harmonic cavity is considered when selecting the storage ring RF frequency.

The RF frequency of the main RF cavity of the 4GSR is 500 MHz, which is the same as PLS-II, making it easy for the 4GSR to procure related power sources and equipment. Moreover, sharing major equipment between the 4GSR and PLS-II would enable more stable facility operation. In addition, by implementing a 1.5 GHz bunch lengthening cavity, we plan to increase the bunch length to by a factor of 4 as needed to secure the desired beam lifetime.

Accordingly, the booster will use the same 500 MHz RF system, and the injector linac will select 3 GHz, an integer multiple, to allow for multi-bunch injection.

(4) Selection of Injector (Linear Accelerator vs. Booster)

To inject electron beams into the storage ring, the energy must be increased as much as nominal energy of the storage ring, and the options for this are a linear accelerator or a booster. Facilities like PLS-II, MAX IV, NanoTerasu are utilizing a full-energy linac as an injector. SPring-8 completed an upgrade that utilizes the SACLA facility as a full-energy injector for the storage ring. Others use boosters to reduce construction and operating costs, use injection beams with lower emittance (especially the vertical beam size is much smaller with a booster), and ensure energy stability of the injection beam.

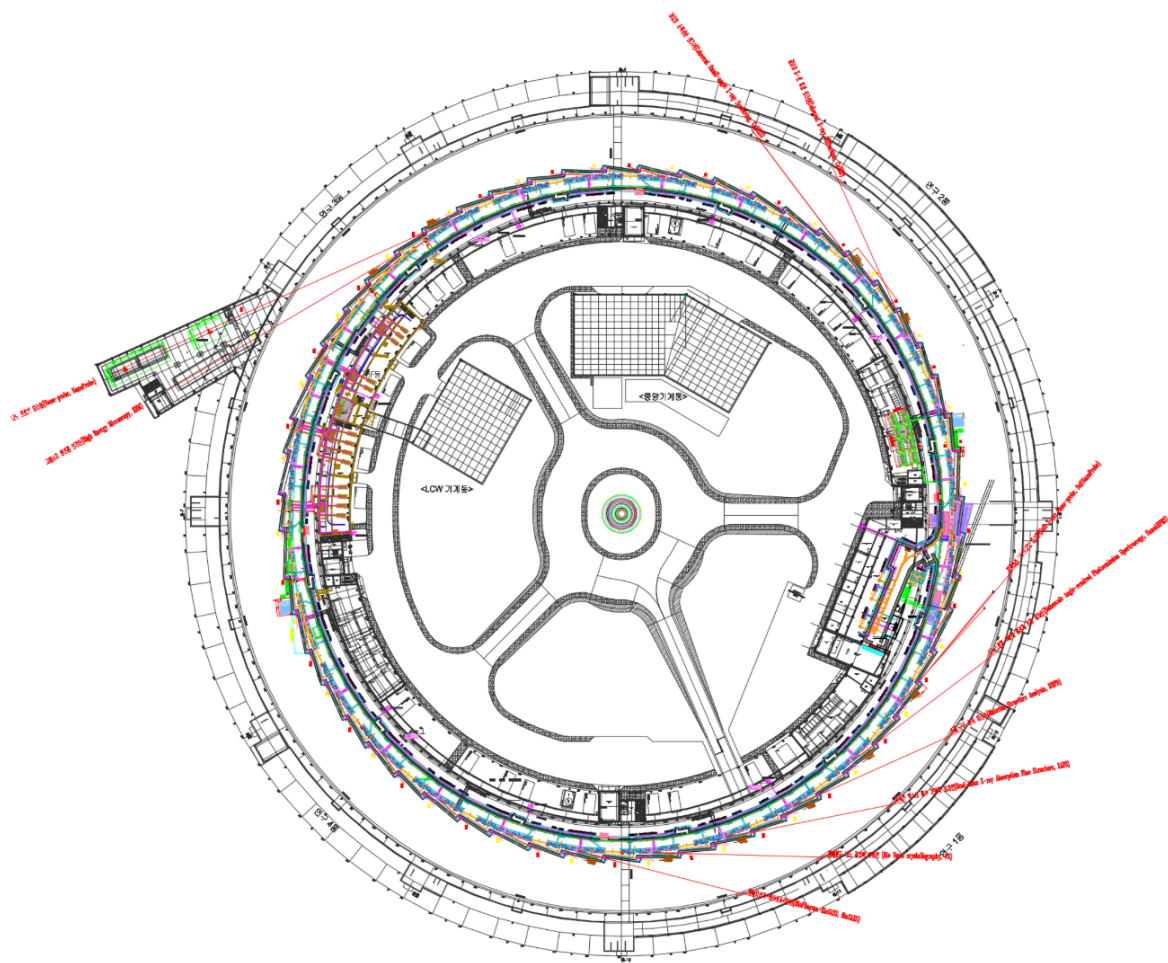
The 4GSR has chosen the booster option, taking advantage of these benefits and because PAL-XFEL is already operating independently and effectively. Furthermore, if the storage ring is upgraded to lower emittance in the future, the booster can also be upgraded accordingly and still serve as an effective injector

C. 4GSR Parameters

Based on the summarized content above, we have organized the target parameters and the overall outline. <Figure 2.1.1.2> shows the overall layout of the 4GSR. It consists of a 200 MeV injector linear accelerator, a 4 GeV booster, and a 4 GeV, 800 m storage ring, with the booster and storage ring installed in the same tunnel.

A total of 52 beamlines can be installed, and up to 60 beamlines are possible using canted insertion devices (IDs) if necessary. Out of 28 cells, one is designated for the injection area, and three are for RF installation. Excluding these four straight sections, 24 straight sections are available for the installation of insertion devices. The main parameters are presented in <Table 2.1.1.1>

An emittance of 62 pm has been achieved, and in round beam mode, the emittance can be reduced to 40 pm. The target beam current is 400 mA operation. For the injection method, we will use the conventional four-kicker system. However, to prepare for future upgrades, we will also consider the nonlinear injection kicker, which has proven its advantages at SIRIUS, through R&D.



<Figure 2.1.1.2> Layout of 4GSR, which consists of 200 MeV injector linac, 4 GeV booster and 800 m storage ring.

<Table 2.1.1.1> 4GSR general parameters

Parameters	Values
Energy / GeV	4
Number of cells	28
Straight sections: Number & length / m (ID straight sections, high-beta straight sections)	26 / 6.06, 2 / 5.40
Ring circumference / m	799.297
Natural emittance / pm rad	62
Regular hor/ver @ coupling	58 / 6 @ 10%
IBS (400 mA) hor/ver @ coupling	80 / 8 @ 10%
Energy spread / %	0.126
Bunch length mm	3.6 (without HC) / 14.4 (with HC)

<Table 2.1.1.2> Parameters on RF cavity, injection scheme, vacuum, and magnets

Parameters	Values
RF frequency / MHz	499.593
# cavities / total voltage	10 / 3.5 MV
# buckets: total / gap	1,332 / 308
Harmonic RF system	3 rd , active, NC
Average current / mA	400
Lifetime / h (ideal lattice, w/o bunch lengthening)	7.30 (flat) / 29.22 (round)
Top up operation	Yes
Injection scheme	4 kicker bump
Beam pipe (in achrom.) / mm ²	D: 24(H)*18(V) @ ID straight section
Max. bending magnet field / T	2
Max. quadrupole grad. T/m	55
Max. sextupole strength T/m ²	1,737
Max. octupole strength T/m ³	120,083

2.1.2 Storage Ring Design

A. Major Design Consideration

Currently, third-generation storage rings (3GSR) with beam emittances on the order of nanometers employ a double-bend achromat (DBA) structure, which has two bending magnets per cell, or a triple-bend achromat (TBA) structure with three bending magnets per cell. In contrast, fourth-generation storage rings (4GSR) with low emittances in the tens of picometers utilize a multi-bend achromat (MBA) structure that arranges multiple dipole magnets to reduce emittance. To achieve low emittance in the MBA structure, arranging strong quadrupole magnets between dipole magnets is needed since low emittance is achieved around certain amount of phase advance in the bending magnet. This large phase advance in the ring eventually leads to strong nonlinearity in the dynamics of the storage ring.

The strength of an individual quadrupole magnet is given by the normalized strength K_1 , where $K_1 = \frac{1}{B\rho} \frac{\partial B_y}{\partial x}$. Here, $B\rho$ is the beam rigidity, and $\frac{\partial B_y}{\partial x}$ is the gradient of the vertical magnetic field along the horizontal direction in a curvilinear coordinate system. When the beam energy deviates by $\delta = \frac{dp}{p}$, the effective strength of the quadrupole magnets becomes $K = \frac{K_1}{1+\delta}$. The natural chromaticity, which is induced by chromatic aberrations in focusing elements, is given by (Equation 2.1.2.1).

$$\xi_0 \sim -\frac{1}{4\pi} \oint K\beta ds \quad (\text{Eq. 2.1.2.1})$$

To achieve optimal lifetime and avoid beam instabilities such as microwave instability, the chromaticity must be adjusted using chromatic sextupoles. For storage rings with a positive momentum compaction factor, the chromaticity is set to zero or slightly above zero to combat collective effects.

The use of strong quadrupole magnets significantly increases the natural chromaticity, necessitating strong sextupole magnets for chromaticity correction. After chromaticity correction, the relationship between the strength of chromatic sextupoles of equal length l and the dispersion is given by (Equation 2.1.2.2) and (Equation 2.1.2.3) below. These equations are calculated under the assumption that the target chromaticity is zero.

$$m_1 = -\frac{1}{\eta_{x1}} \frac{4\pi}{l_s} \frac{\xi_{x0}\beta_{y2} + \xi_{y0}\beta_{x2}}{\beta_{x1}\beta_{y2} - \beta_{x2}\beta_{y1}} \quad (\text{Eq. 2.1.2.2})$$

$$m_2 = +\frac{1}{\eta_{x2}} \frac{4\pi}{l_s} \frac{\xi_{x0}\beta_{y1} + \xi_{y0}\beta_{x1}}{\beta_{x1}\beta_{y2} - \beta_{x2}\beta_{y1}} \quad (\text{Eq. 2.1.2.3})$$

Here, m_1 and m_2 denote strengths of the two chromatic sextupoles, η_x is the dispersion, ξ_{x0} and ξ_{y0} are the horizontal and vertical natural chromaticities, and β_x and β_y are the horizontal and vertical beta functions, respectively. As seen from (Equation 2.1.2.2) and (Equation 2.1.2.3), the strength of the chromatic sextupoles after chromaticity correction has linear dependence to the natural chromaticity and inversely proportional to the dispersion at the sextupole magnet locations. The use of strong quadrupoles increases natural chromaticity (Equation 2.1.2.1), requiring strong sextupoles which deteriorate the nonlinear dynamics.

From the perspective of single-particle dynamics, a characteristic of the MBA structure is that one cell consists of multiple unit cells. The beta function values within the unit cell are set close to those satisfying the theoretical minimum emittance (TME), allowing the design of a lattice with minimal emittance within a given geometry when utilizing the MBA structure. An MBA unit cell includes at least one dipole magnet and quadrupole magnet. The nonlinear driving terms representing the nonlinearity of the storage ring propagate through identical unit cells and are canceled out at the end of a cell through high-order achromat characteristics. The unit cell has a small value of dispersion, requiring strong chromatic sextupoles. To cancel out significant nonlinear driving terms caused by strong chromatic sextupoles, geometric sextupoles are typically used at zero-dispersion regions.

The Hybrid MBA (HMBA) structure is a modified version based on the MBA structure. It has two dispersion bumps per cell and places chromatic sextupole magnets at these bumps to reduce the strength of the chromatic sextupoles. Geometric sextupole magnets are generally not used. Due to the presence of dispersion bumps, the emittance becomes larger compared to the MBA structure, but since weaker sextupole magnets are used, it exhibits weaker nonlinear characteristics than the MBA structure, allowing the storage ring to have a larger dynamic aperture. The major nonlinear driving terms are canceled within the cell through the $-I$ transformation condition between the two dispersion bumps.

Generally, the MBA structure has a larger momentum aperture compared to the HMBA structure, while the HMBA structure has a larger dynamic aperture than the MBA structure.

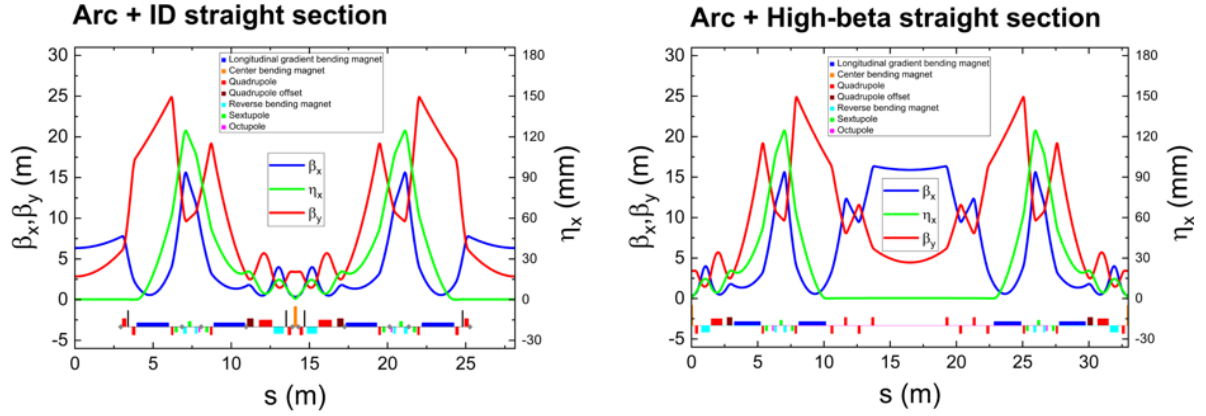
The momentum aperture is an input required for calculating the Touschek lifetime, which is proportional to the cube of the momentum aperture width and the cube of the storage ring beam energy. If optimization can increase the momentum aperture to a level similar to that of the MBA structure, then in the medium to high energy range (4–6 GeV), the 4GSR using the HMBA structure can have a larger dynamic aperture than the MBA structure and a sufficiently long Touschek lifetime suitable for operation.

In determining the lattice structure of the Korea-4GSR storage ring, comprehensive studies between the MBA and HMBA structures have been conducted since before the Conceptual Design Report (CDR) stage. These studies considered linear optics design, vacuum chamber radius and collective effects, nonlinear dynamics optimization, dynamic aperture, Touschek lifetime, and other factors. It has been confirmed that the HMBA structure is the most suitable design for an 800 m circumference and a 4 GeV electron beam energy.

B. Linear Optics

The storage ring consists of 28 cells and has a two-fold geometric symmetry. All 28 arc regions are identical, and the straight sections connecting adjacent arcs are of two types: ID straight sections and high-beta straight sections. Out of the total 28 straight sections, 26 are insertion device (ID) straight sections, and 2 are high-beta straight sections. One of the two high-beta straight sections is used for off-axis injection, where the injection septum (thick septum and thin septum) and kicker magnets are located. The other high-beta straight section is occupied by 4 of 10 main rf cavities.

<Figure 2.1.2.1> shows the arrangement of magnets in the storage ring lattice and the Twiss functions. Observing the dispersion (green line), it remains in a dispersion-free state until encountering the first bending magnet. After passing through the bending magnet, the beam's dispersion increases sharply. This region of rapid dispersion increase is called a dispersion bump, and as seen in <Figure 2.1.2.1>, sextupole magnets are placed within the dispersion bump.



<Figure 2.1.2.1> Storage ring magnet arrangement and Twiss functions. Arc + ID straight section (left) and arc + high-beta straight section (right).

In <Figure 2.1.2.1>, one can find that the dispersion decreases sharply as it passes through two bending magnets with a dipole field sign of minus. Magnets with a negative bending field bend the beam in the opposite direction to normal bending magnets and are called anti-bends. It contributes to minimize the dispersion invariant function which helps lowering natural emittance. Additionally, the anti-bends have quadrupole-gradient components with a positive sign, and these quadrupole components also serve to further reduce the dispersion. Moreover, if the signs of the dipole field and the quadrupole-gradient in a bending magnet are opposite, the damping partition number increases, reducing the emittance. In <Figure 2.1.2.1>, one can see that in all bending magnets with quadrupole-gradient components, the signs of the dipole field and quadrupole component are opposite. By using these quadrupole components, we reduce the emittance while simultaneously controlling the linear beam dynamics by adjusting the strength of the quadrupole components.

The beam emittance in the storage ring is given by (Equation 2.1.2.4).

$$\varepsilon_x = \frac{C_q \gamma^2}{J_x} \frac{\int \frac{(\gamma_x \eta_x^2 + 2\alpha_x \eta_x \eta'_x + \beta_x \eta'^2_x)}{|\rho|^3} ds}{\int \frac{1}{\rho^2} ds} \quad (\text{Eq. 2.1.2.4})$$

Here, J_x is the damping partition number, η_x, η'_x are horizontal dispersion, and horizontal dispersion derivative, respectively, $\alpha_x = -\frac{\beta_x}{2}$, $\gamma_x = -\frac{1+\alpha_x^2}{\beta_x}$, ρ is the bending radius, and C_q is a constant given by (Equation 2.1.2.5).

$$C_q = \frac{55}{32\sqrt{3}} \frac{\hbar}{mc} \approx 3.83 \times 10^{-13} \text{ m} \quad (\text{Eq. 2.1.2.5})$$

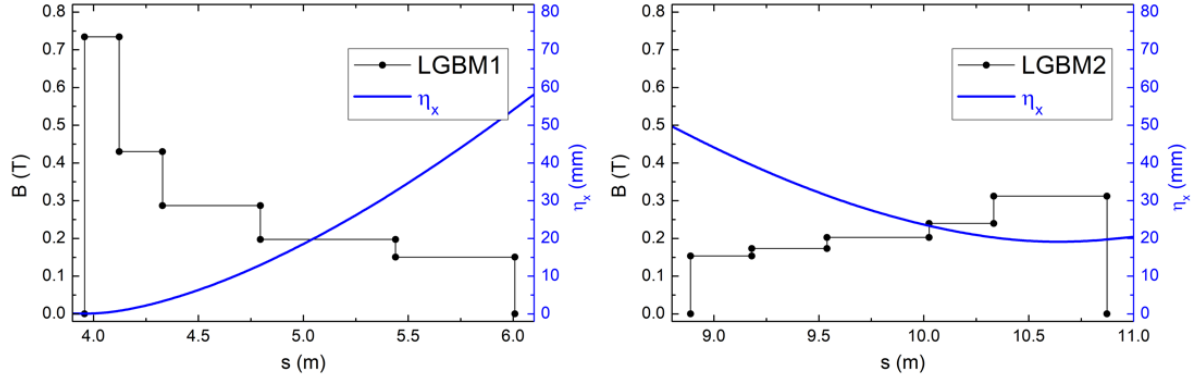
Here, \hbar is the Planck constant, m is the mass of the particle constituting the beam (i.e., the electron), and c is the speed of light.

From (Equation 2.1.2.4), we can deduce that increasing the damping partition number J_x reduces the emittance, and that smaller dispersion in the bending magnets leads to smaller emittance. This is the reason for creating a dispersion bump and then rapidly reducing the dispersion using anti-bends. As the electron beam passes through the third dipole magnet in a state of reduced dispersion, and then passes through another anti-bend, the dispersion decreases further before passing through the bending magnet located at the center of the arc region. The centrally located bending magnet, called the center-bend, has a field strength of about 2 Tesla. Due to the strong dipole field of the center bend, the synchrotron radiation emitted by the electron beam has higher peak energy. By placing the center-bend, we can configure beamlines originating from this position. Also, because of the strong dipole field of the center-bend, even a small increase in dispersion when the electron beam passes through the super bend causes a significant increase in the beam's emittance. Therefore, anti-bends are placed upstream to minimize the dispersion when passing through the center bend.

To create the dispersion bump, it is inevitable that the dispersion is relatively large in the first and second dipoles. To reduce the emittance increase caused by these two dipoles, they are arranged as longitudinal gradient bend magnets (LGBM), where the field strength varies along the longitudinal position. The emittance in (Equation 2.1.2.4) can be approximately expressed as:

$$\varepsilon_x = \frac{C_q \gamma^2}{J_x} \frac{\int \frac{(\gamma_x \eta_x^2 + 2\alpha_x \eta_x \eta'_x + \beta_x \eta'^2_x)}{|\rho|^3} ds}{\int \frac{1}{\rho^2} ds} \propto \int \eta_x^2 B ds \quad (\text{Eq. 2.1.2.6})$$

Here, B is the dipole field strength. From (Equation 2.1.2.6), we can expect that in a dipole with the same average dipole field and average length, the emittance will be reduced if the dispersion and the magnetic field have similar distributions. Therefore, we create a field distribution where the dipole field decreases when the dispersion increases, and the dipole field increases when the dispersion decreases. <Figure 2.1.2.2> shows the dispersion and bending field distributions in the first and second longitudinal gradient dipoles, respectively.



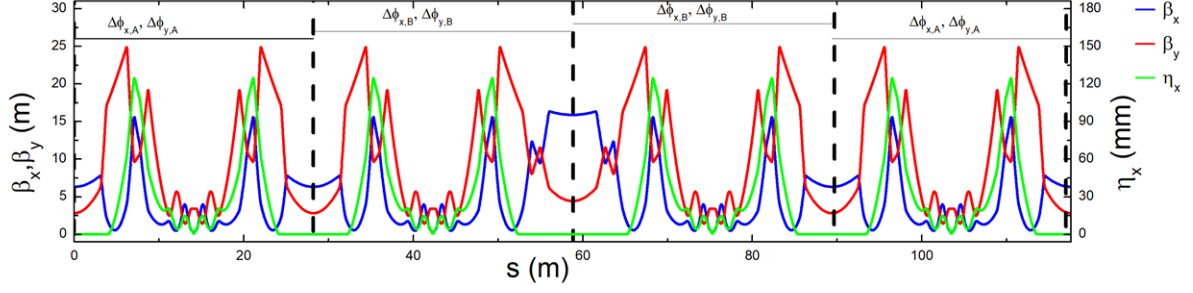
<Figure 2.1.2.2> Dispersion and B field distribution at the first LGBM (left) and the second LGBM (right).

Within an arc, the phase advance between the two dispersion bumps is up to approximately 3π in the horizontal direction and up to π in the vertical direction, satisfying the $-I$ transformation condition in the linear matrix. Under these linear optics conditions, the strength of the resonance driving terms excited by the chromatic sextupole magnets in the first dispersion bump can be effectively canceled out by those in the second dispersion bump.

The high-beta straight sections of the storage ring are designed to secure a sufficiently large dynamic aperture for off-axis injection. If the acceptance A is the area in the horizontal or vertical phase space of the storage ring where a single particle is not lost, and the beta function at any longitudinal position of the storage ring is β , then the dynamic aperture x_{max} at that position is given by the relation, $x_{max} = \sqrt{\beta A}$ (at the position where α is zero). Since the acceptance A of the storage ring is constant regardless of the longitudinal position, the dynamic aperture is proportional to the square root of the beta function β .

To increase the dynamic aperture at the injection point, both the acceptance and the beta function β at the injection location need to be increased. While acceptance can be increased through nonlinear dynamics optimization, it is difficult to enhance it beyond a certain converging value. Therefore, by increasing the beta function at the injection location, the dynamic aperture required for off-axis injection can be secured.

Breaking the symmetry of the storage ring negatively affects its nonlinear dynamics properties. If we keep the lengths of all 28 straight sections of the storage ring identical but increase the beta function in a specific straight section, the periodic symmetry of the linear optics is broken, resulting in a decrease in acceptance.



<Figure 2.1.2.3> High-beta straight section and ID straight section. $\Delta\phi_{x,A} = \Delta\phi_{x,B}$ and $\Delta\phi_{y,A} = \Delta\phi_{y,B}$

Even if the geometric symmetry is broken, we can restore the nonlinear dynamics properties of the storage ring to some extent by tuning the phase advance in the region where the geometric symmetry is broken. That is, by increasing the beta function at a specific location while maintaining the acceptance of the storage ring, we can significantly increase the dynamic aperture. The beta function and phase advance in the beam dynamics of the storage ring have the following relationship, as given by (Equation 2.1.2.7):

$$\phi = \int \frac{1}{\beta} ds \quad (\text{Eq. 2.1.2.7})$$

Due to the inverse relationship between the beta function and the phase advance, we can match the linear optics to have the same phase advance as the ID straight sections by making the high-beta straight sections longer.

As shown in <Figure 2.1.2.3>, the cells that include the high-beta straights and those that include ID straight sections have the same phase advance, thus maintaining the 28-fold symmetry for on-momentum particles. The impact of the high-beta straight sections on acceptance is minimized, and the beta function at the center of the high-beta straight section is approximately 2.5 times larger than at the center of the ID straight sections, resulting in a dynamic aperture that is about 1.6 times larger.

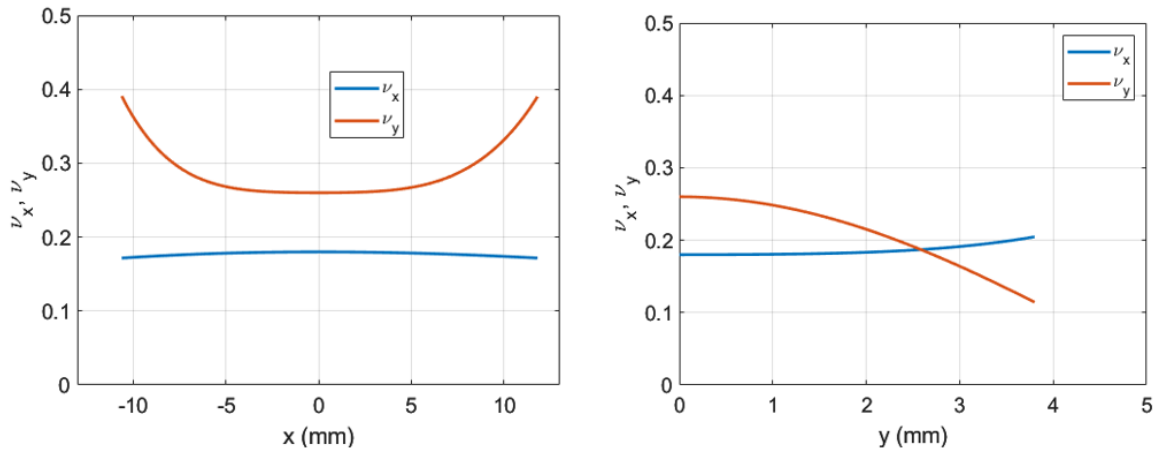
The main parameters of storage ring is given as <Table 2.1.2.1>.

<Table 2.1.2.1> Storage ring main parameters

Parameter	Value (w/o IDs)	Value (w/ 9 IDs)
Natural emittance	61.57 pm	52.55 pm
Circumference	799.297 m	
Beam energy	4 GeV	
Working point ν_x, ν_y	68.179 / 23.260	
Natural chromaticity ξ_x, ξ_y	-112.1 / -85.3	
Chromaticity ξ_x, ξ_y (corrected)	5.8, 3.5	
Horizontal damping partition J_x	1.84	1.64
Momentum compaction α	7.8×10^{-5}	
Energy loss per turn U_0	1.098 MeV	1.449 MeV
Energy spread	0.126%	0.104%
Main RF voltage	3.080 MV	3.500 MV
Main RF frequency	499.593 MHz	499.593 MHz
Main RF synchronous phase (w/o harmonic cavity, w/ harmonic cavity)	159.13 deg, 156.36 deg	155.55 deg, 152.24 deg
Harmonic number	1332	
Damping times (H / V / L)	10.55 ms/ 19.43 ms / 16.79 ms	8.98 ms/ 14.72 ms / 10.81 ms
Harmonic cavity voltage	0.950 MV	1.048 MV
Harmonic cavity frequency	1,498.78041 MHz	1,498.78041 MHz
Harmonic cavity phase	351.70 deg	350.49 deg
Bunch length (w/o harmonic cavity, w/ harmonic cavity)	3.6 mm, 14.4 mm	2.8 mm, 11.4 mm
Beta function at center of ID straight β_x, β_y	6.33 m / 2.84 m	
Beta function at center of high- beta straight β_x, β_y	15.90 m / 4.45 m	

C. Nonlinear Beam Dynamics

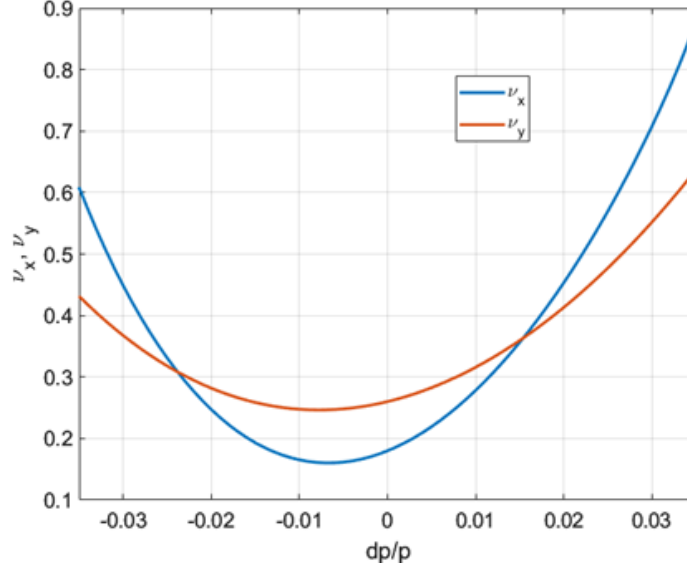
After chromaticity correction, nonlinear effects caused by chromatic sextupoles can occur. These effects may lead to two side effects: difficulty in off-axis injection due to a small on-momentum dynamic aperture (DA) and rapid beam loss due to a short beam lifetime. To suppress these effects and achieve stable accelerator operation, nonlinear beam dynamics must be optimized.



<Figure 2.1.2.4> Amplitude dependent tune shift.

Result for x-offset (left) and y-offset (right).

The optimization of nonlinear beam dynamics was carried out by iteratively adjusting the horizontal and vertical phase advances between dispersion bumps in the arc region, as well as the strengths of sextupoles and octupoles. Through this optimization, the amplitude-dependent tune shift and momentum-dependent tune shift, which directly affect the width of the dynamic aperture and momentum aperture, were reduced. <Figure 2.1.2.4> shows the amplitude-dependent tune shift at the center of the high-beta straight, and <Figure 2.1.2.5> displays the momentum-dependent tune shift. The horizontal and vertical tunes do not cross integer or half-integer tunes with changes in x or y amplitude, nor do they show areas indicating strong resonances, such as resonance islands.

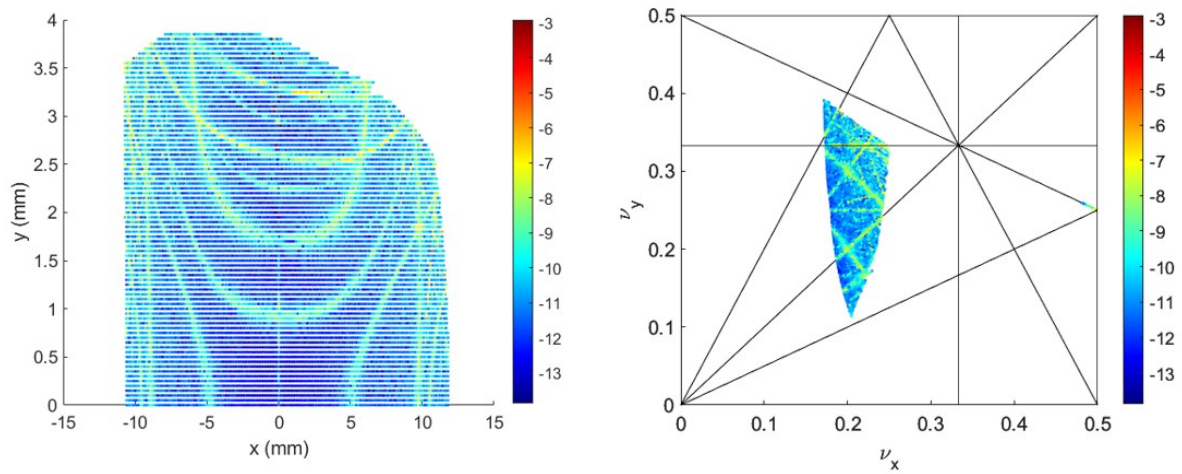


<Figure 2.1.2.5> Momentum dependent tune shift.

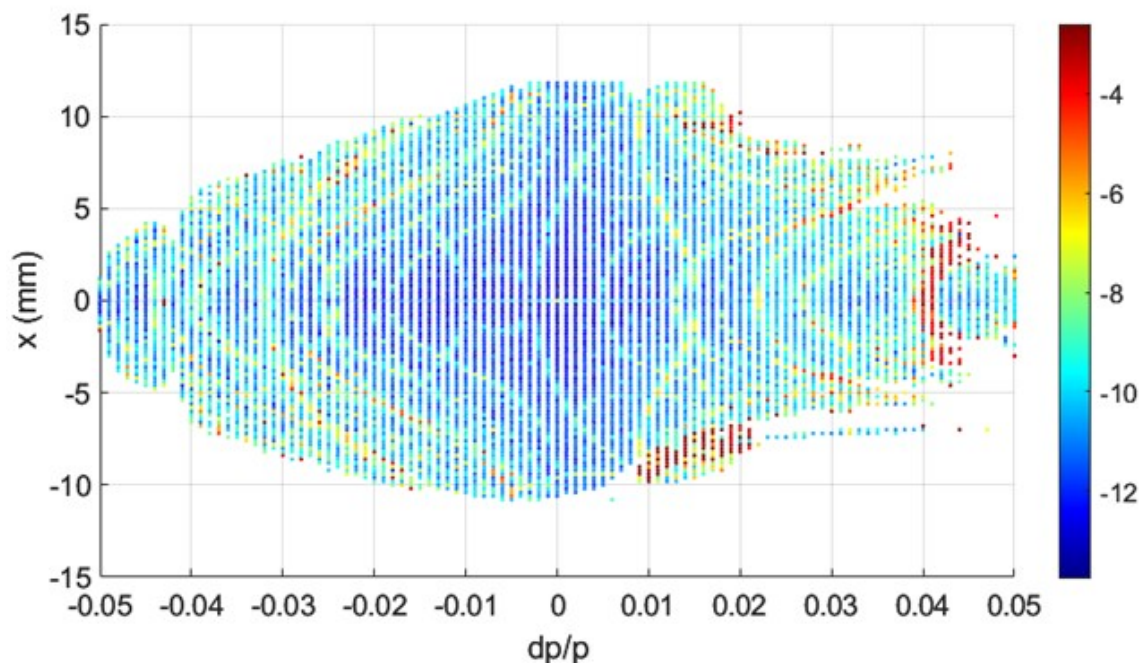
The results of investigating the stable regions and instabilities due to high-order resonances in the x-y space, tune space, and x-dp/p space through frequency map analysis are shown in <Figure 2.1.2.6>. These results were obtained under conditions without the effects of the RF cavity and radiation damping. The left figure in <Figure 2.1.2.6> corresponds to the dynamic aperture from 4D tracking. The color code in <Figure 2.1.2.6> corresponds to the diffusion rate. The diffusion rate is defined as in (Equation 2.1.2.8). It represents the difference between the tune calculated from the first 512 turns' turn-by-turn coordinate information and the tune calculated from the second 512 turns (when $N = 1,024$). The smaller the value, the more stable the particle motion at that location, and it is important to note that if a thick, sharp resonance line is observed, beam loss may occur at that location.

$$d_r = \left(\frac{\sqrt{\Delta v_x^2 + \Delta v_y^2}}{N} \right) \quad (\text{Eq. 2.1.2.8})$$

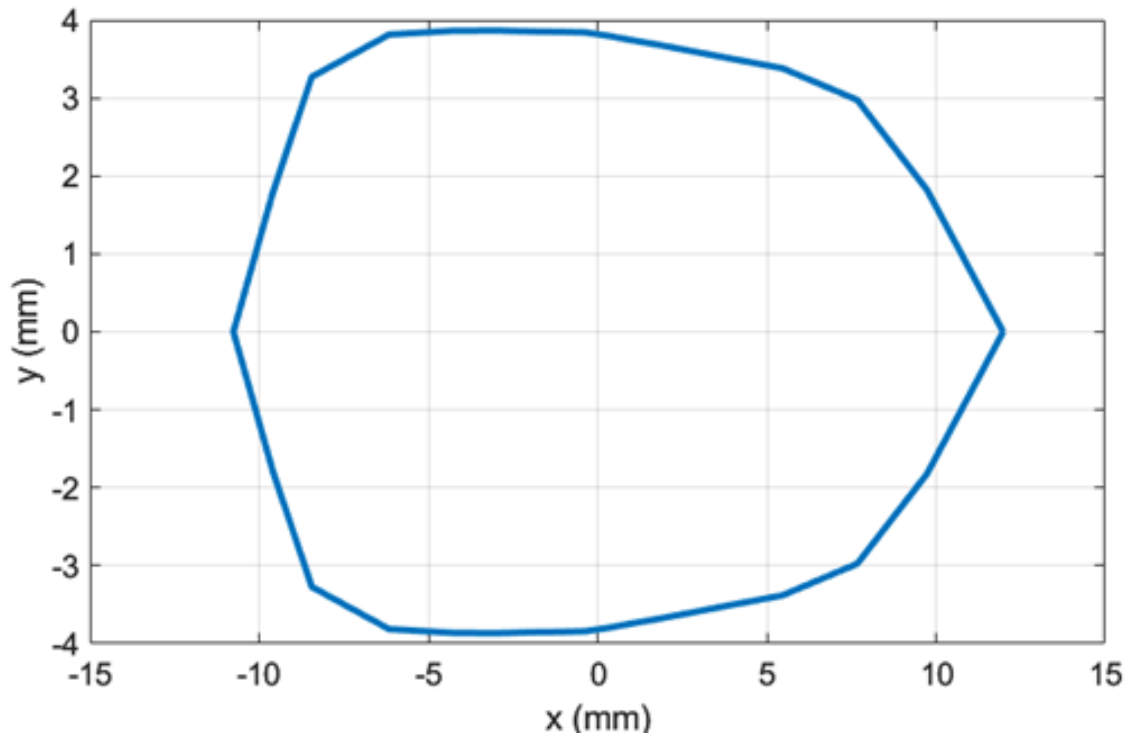
The distribution of the diffusion rate compared to the nominal tune from the frequency map analysis appears stable, and it does not pass through the half-integer resonance line, which could be a critical resonance line. The strength of the third-order resonance line also appears to be relatively small. The results of the frequency map analysis, obtained by varying the energy offset (dp/p) and the x-direction offset, are shown in <Figure 2.1.2.7>. The x-direction dynamic aperture does not decrease sharply with changes in dp/p, and the region with a high diffusion rate at the edge does not seem to have a critical impact on achieving a stable dynamic aperture and Touschek lifetime.



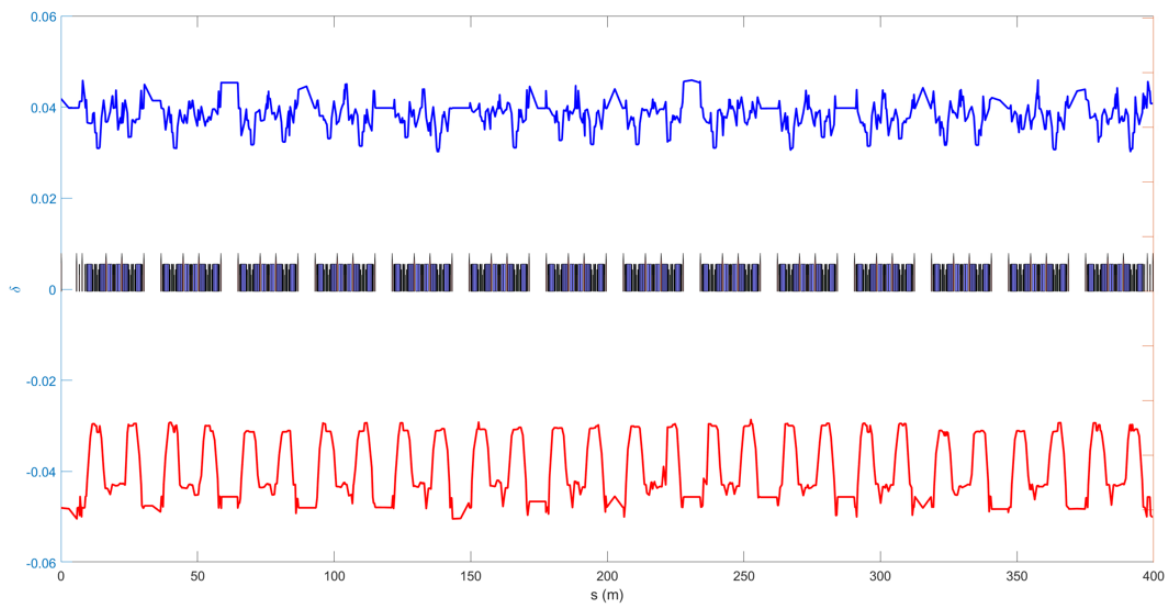
<Figure 2.1.2.6> Results of frequency map analysis for x-y offset. Diffusion rate distribution on the x-y space (left) and tune space (right).



<Figure 2.1.2.7> Results of frequency map analysis for x-dp/p offset.



<Figure 2.1.2.8> Dynamic aperture at the middle of the high-beta straight section. 6D tracking results for ideal lattice. The tracking simulation includes physical apertures of the storage ring lattice.



<Figure 2.1.2.9> Local momentum aperture for the half of the storage ring.

<Figure 2.1.2.8> and <Figure 2.1.2.9> show the dynamic aperture and momentum aperture results for an ideal lattice without errors, respectively. The tracking was performed for 2,048 turns, and the effects of the RF cavity and damping due to synchrotron radiation were included in the 6D tracking. The impact on the dynamic aperture and momentum aperture when realistic error factors, such as magnet alignment errors and strength errors, are included is described in section 2.1.3.H, "Commissioning Simulations."

D. Tune Setting

The integer part of the tune in the storage ring was set to values that avoid high-order resonances. Due to the periodicity of the storage ring and specific resonance driving terms, high-order resonance effects can appear in addition to integer and half-integer resonances. In the HMBA structure, the $-I$ transformation between dispersion bumps is effective in canceling out the strength of resonance driving terms, but for high-order resonance driving terms, the strength may remain significant.

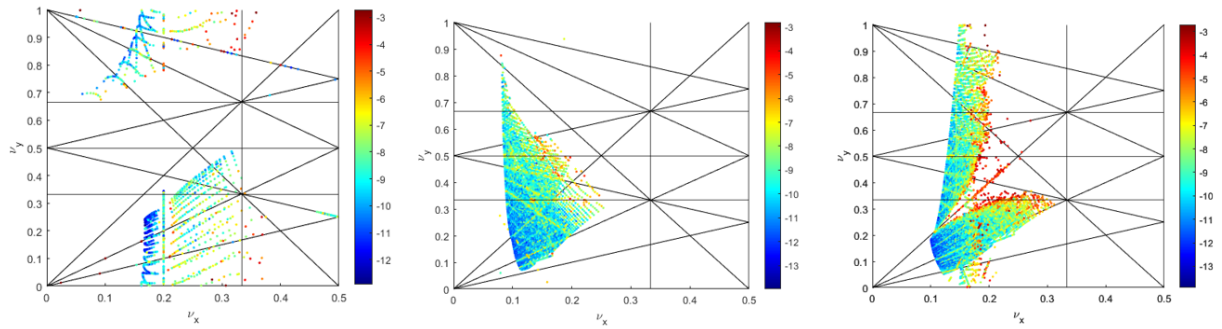
Through frequency map analysis, it was confirmed whether specific resonance effects grow when the storage ring has integer tunes other than (68, 23) (<Figure 2.1.2.10>). When the integer tune is lower by 1 in the horizontal direction, a resonance line appears at the fractional horizontal tune of 0.2. This line corresponds to a 5th-order resonance, and it is understood that the 5th-order resonance driving term has a large magnitude, and the resonance line of $5\nu_x = 28N$ is excited. Since the period of the ring for on-momentum particles is 28, the resonance line equation has a right-hand side integer value of $28N$, i.e., $67.20 \times 5 = 336 = 28 \times 12$.

When the integer tune is increased by 1 in the vertical direction, a strong resonance appears on one of the 3rd-order resonance lines, $2\nu_x - \nu_y = 28N$.

This is specifically expressed as $68.10 \times 2 - 24.20 = 112 = 28 \times 4$.

In terms of photon beam brightness, higher tunes or lower beta function values in the ID straight section are advantageous, but when the horizontal integer tune is increased by more than 1, the beta function in the ID straight section decreases significantly. In the H7BA structure, this leads to a sharp increase in second-order chromaticity, which in turn results in a shorter Touschek lifetime. Therefore, when the horizontal integer tune is increased by more than 1 (horizontal integer tune 69), it was excluded from the candidate working points.

Considering the frequency map analysis results described above and the optical characteristics of the H7BA, the integer tune working point of the storage ring was set to (68, 23).



<Figure 2.1.2.10> Results of frequency map analysis for x-y offset. Integer tune of (67, 23) (left), (68, 23) (middle), and (68, 24) (right).

References

- [1] SLS 2.0 Storage Ring Technical Design Report.
- [2] EBS Storage Ring Technical Report.
- [3] Diamond-II Technical Design Report.
- [4] Jang, Gyeongsu, et al., "Low emittance lattice design for Korea-4GSR, Nuclear Inst. And Methods in Physics Research, A 1034 (2022).
- [5] Wiedemann, H. (1993). Particle Accelerator Physics I. Berlin: Springer.
- [6] Beam-based Correction and Optimization for Accelerators, Xiaobiao Huang, CRC Press, 2022.
- [7] Terebilo, in Proceedings of the 19th Particle Accelerator Conference, Chicago, IL, 2001 (IEEE, Piscataway, NJ, 2001), pp. 3203-3205.

2.1.3 Beam Dynamics Topics

A. RF Voltage Optimization

Increasing the RF voltage increases the RF momentum acceptance (MA), which helps to increase the Touschek lifetime. At the same time, increasing the RF voltage increases the slope of the voltage at the synchronous phase, which decreases the bunch length of the beam and thus decreases the lifetime. Therefore, to maximize the Touschek lifetime, a scan of Touschek beam lifetime according to RF voltage was performed. The beam lifetime is greatly affected by the charge per bunch and whether the beam is a flat beam or a round beam. The maximum beam current target for Korea-4GSR is 400 mA, and in multi-bunch operation mode, the charge per bunch is about 1 nC.

The results of the RF voltage scan for a charge of 1 nC per bunch, in multi-bunch operation mode, are given in <Figure 2.1.3.1>. For both flat and round beams, the lifetime increases up to 2.6 MV. Then up to 3.0 MV, the lifetime slightly decreases and increases. Above 3.0 MV, the lifetime decreases again. Lattice momentum acceptance is shown in <Figure 2.1.3.2>. As you can see in the figure, the lattice positive acceptance (LPA) is about 4%, and the lattice negative acceptance (LNA) is about 5%. When the RF voltage reaches 2.6 MV, the RF acceptance becomes about 4%, similar to the LPA. Therefore, up to 2.6 MV, the effect of increasing MA dominates, increasing the lifetime.

However, if the RF voltage exceeds 2.6 MV, the effect of increasing MA is not seen in the positive direction and is only seen in the negative direction. At the same time, the bunch length decreases, so the effects of increasing and decreasing the lifetime are seen simultaneously. When the RF voltage exceeds 3.0 MV, the RF acceptance exceeds the value of LNA, so the effect of increasing MA disappears. Instead, the bunch length decreases (<Figure 2.1.3.3>), resulting in a decrease in lifetime. At this time, the optimal RF value is between 2.6 MV and 3.0 MV. Among them the optimal RF voltage was determined to be 3.0 MV based on the point where the RF acceptance is the largest.

However, the results in <Figure 2.1.3.1> and <Figure 2.1.3.2> are based on the condition where no Insertion device (ID) is placed in the storage ring. The ID placed in the straight section of the storage ring significantly affects the characteristics of the synchrotron radiation as the beam passes through the ID. Therefore, the ID model must consider the requirements of the users and can only be decided in the future. Thus, we first performed RF optimization without the ID and obtained the results shown in <Figure 2.1.3.1>. When

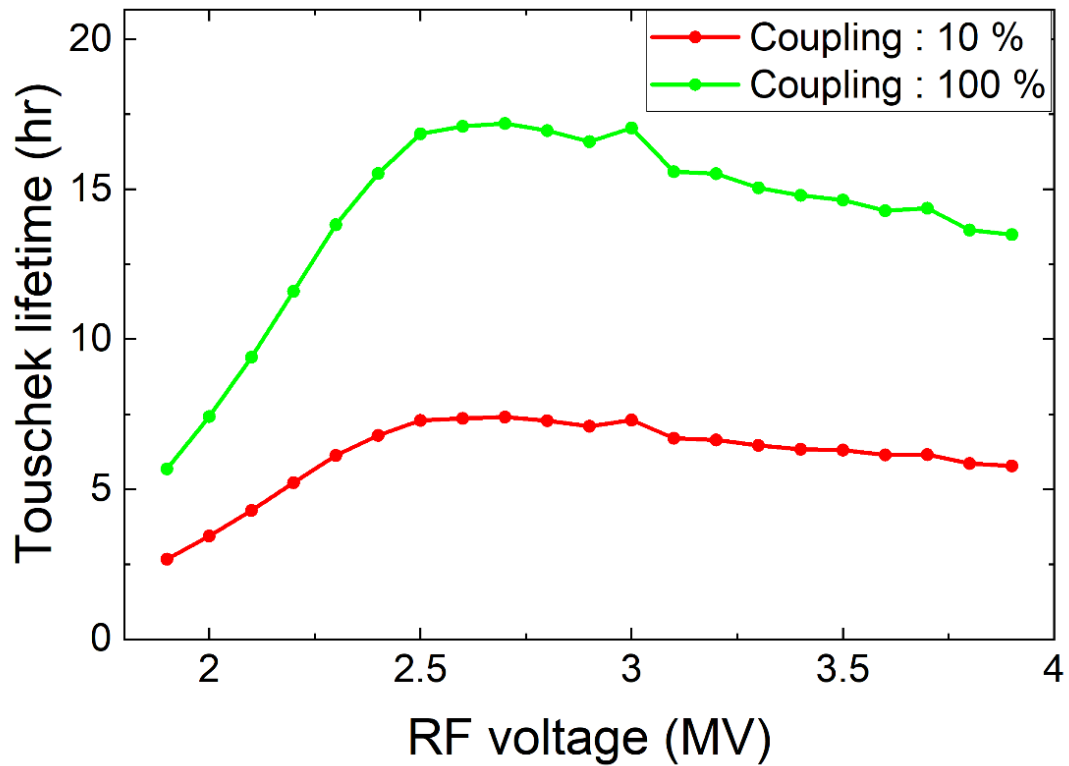
the ID is installed, additional energy loss of the electron beam occurs due to the ID. Currently, nine initial ID beamlines are planned, and the additional energy loss caused by these ID beamlines is approximately 352 keV. As the energy loss of the beam increases due to the ID, the RF voltage and synchronous phase are adjusted accordingly. To optimize the beam lifetime, the RF MA value indicated in <Figure 2.1.3.2> should be maintained. From <Figure 2.1.3.2>, it can be seen that the RF MA is 4.8%. To restore the additional energy loss of 352 keV with an RF MA of 4.8.

$$\psi_s = \pi - \sin^{-1} \left(\frac{U_0 + U_{ID} + U_{wall}}{V_0} \right) \quad (\text{Eq. 2.1.3.1})$$

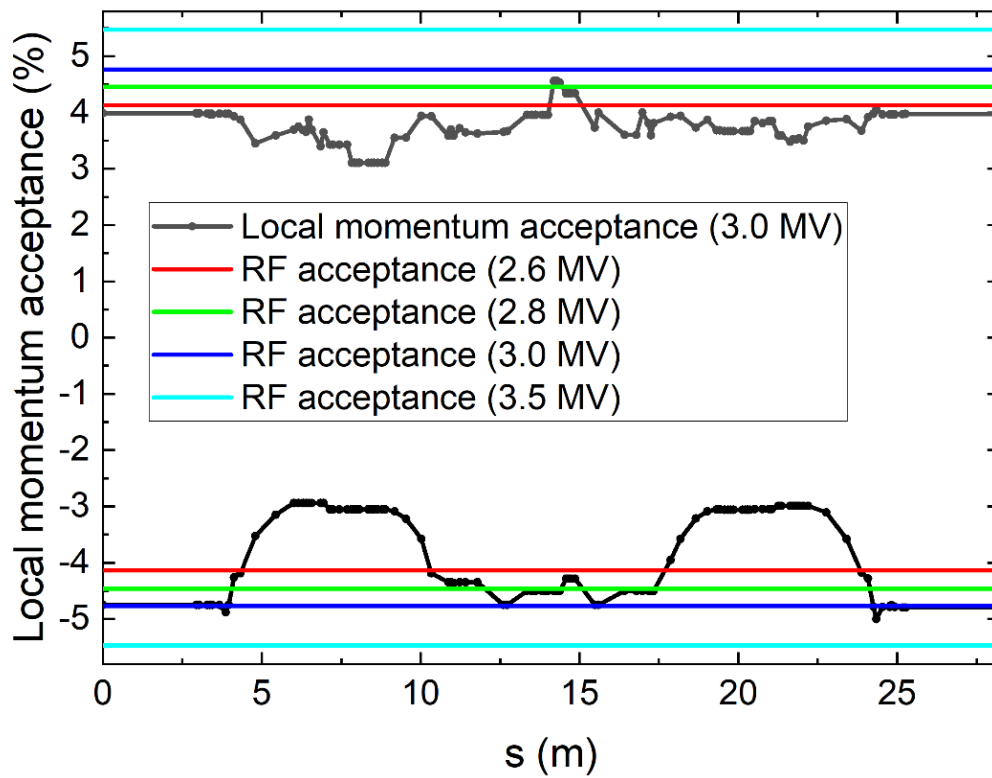
Here, ψ_s is the synchronous phase of the RF, U_0 is the energy loss due to bending, U_{ID} is the energy loss due to the ID, and U_{wall} is the energy loss due to resistive wall. The synchronous phase of the RF is determined by the RF voltage and energy loss. When solving for V_0 considering the energy loss due to bending U_0 along with the energy losses due to the ID and resistive wall ($U_{ID} + U_{wall}$), we can get an equation written in ψ_s . Substituting this equation back into (Equation 2.1.3.2) and solving for V_0 , we can derive the equation written in RF acceptance.

$$\delta_B = \sqrt{-\frac{2eV_0}{\pi E_0 h \alpha} \left[\cos \psi_s + \left(\psi_s - \frac{\pi}{2} \right) \sin \psi_s \right]} \quad (\text{Eq. 2.1.3.2})$$

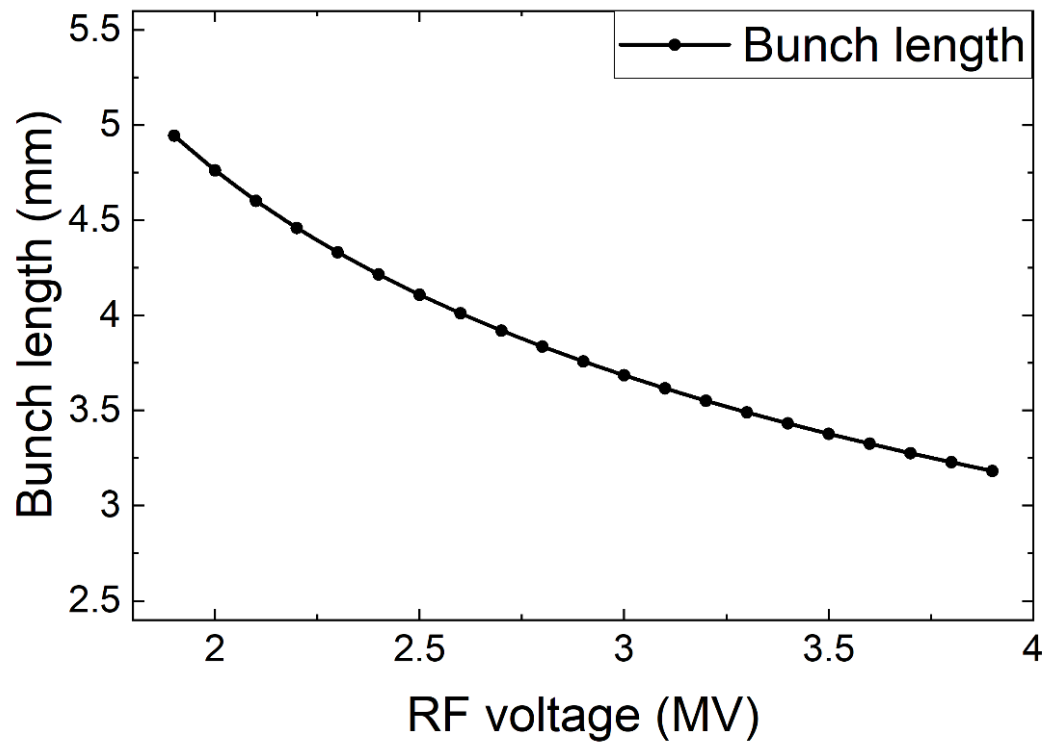
Here, e is the electron charge, E_0 is the energy of the electron, h is the harmonic number, α is the momentum compaction factor, and δ_B is the RF acceptance.



<Figure 2.1.3.1> Results of Touschek beam lifetime vs RF voltage scan in multi-bunch mode.



<Figure 2.1.3.2> MA and RF acceptance at 3.0 MV RF voltage.



<Figure 2.1.3.3> Bunch length along with RF voltage.

Reference

- [1] M. Sands, The physics of electron-positron storage rings, SLAC-121, 1970.

B. ID Effects

In synchrotron radiation facilities, electrons are stored in a storage ring and used as a light source by utilizing the characteristic that they emit electromagnetic waves when accelerated. Especially from the third-generation storage ring, IDs have been added to produce light that is more useful for experiments. When these IDs are added, the parameters of the storage ring also change. Therefore, for the 4GSR, we examined how the parameters of the storage ring change due to the IDs.

○ ID specifications

To investigate the changes in storage ring parameters by the ID, we first need to identify the specifications of the ID. Currently, 4GSR initially plans to have nine ID beamlines and one bending beamline, with specific details provided in <Table 2.1.3.1>. The nine ID beamlines will include undulators, which come in two types: in-vacuum undulators and elliptically polarized undulators. Depending on the desired experiment and purpose, the undulators will have different lengths, magnetic field strengths, and periods. To achieve such a strong field, the minimum gap must be 5 mm, and this small gap also determines the vertical beam stay clear, which is a crucial factor for injection efficiency.

○ Ring parameters with synchrotron radiation integrals

The parameters of the storage ring can be expressed in terms of the synchrotron radiation integrals. Synchrotron radiation integrals are defined by (Equation 2.1.3.3).

<Table 2.1.3.1> Initial beamline plan of Korea-4GSR

Beam port	Light source	Length [m]	Peak Field [T]	Period [mm]	Minimum gap [mm]
ID21	In-vacuum undulator	3.0000	1.2250	24.00	5.00
ID24	In-vacuum undulator	3.0000	0.7850	16.00	5.00
ID26-1	In-vacuum undulator	1.5000	1.2250	24.00	5.00
ID26-2	Elliptical polarized EPU78	2.0000	0.9540	78.00	15.00
	Circular polarized EPU78		0.6020		
	Max horizontal polarized EPU78		0.7760		
ID25	Elliptical polarized EPU98	3.6260	1.0100	98.00	15.00
	Circular polarized EPU98		0.6633		
	Max horizontal polarized EPU98		0.8799		
ID03	In-vacuum undulator	3.0000	1.2270	22.00	5.00
ID04	In-vacuum undulator	3.0000	1.0211	20.00	5.00
ID23	In-vacuum undulator	3.0000	1.2250	24.00	5.00
ID22	In-vacuum undulator	3.0000	1.0210	20.00	5.00
BM10	Center bend	Already considered			
ID10	In-vacuum undulator	3.0000	1.2253	20.00	5.00

$$I_1 = \oint ds \left\{ \frac{\eta}{\rho} \right\},$$

$$I_2 = \oint ds \left\{ \frac{1}{\rho^2} \right\},$$

$$I_3 = \oint ds \left\{ \frac{1}{|\rho|^3} \right\}, \quad (\text{Eq. 2.1.3.3})$$

$$I_4 = \oint ds \left\{ \frac{\eta}{\rho} \left(\frac{1}{\rho^2} + 2k_1 \right) \right\},$$

$$I_5 = \oint ds \left\{ \frac{\gamma\eta^2 + 2\alpha\eta\eta' + \beta\eta'^2}{|\rho|^3} \right\},$$

Here, η is the dispersion, α, β, γ is the Twiss functions, and ρ is the curvature radius of the reference particle. k_1 is defined as the normalized quadrupole strength.

$$k_1 = \left(\frac{1}{B\rho}\right)\left(\frac{\partial B_y}{\partial x}\right) \quad (\text{Eq. 2.1.3.4})$$

By using (Equation 2.1.3.4) to express the storage ring parameters, we can obtain the results shown in (Equation 2.1.3.5).

$$\varepsilon_x = C_q \gamma^2 \frac{I_5}{I_2 - I_4},$$

$$\sigma_\delta^2 = C_q \gamma^2 \frac{I_3}{2I_2 + I_4},$$

$$U_0 = \frac{C_\gamma}{2\pi} E^4 I_2,$$

$$\tau_x = \frac{4\pi T_0}{C_\gamma E^3 (I_2 - I_4)}, \quad (\text{Eq. 2.1.3.5})$$

$$\tau_y = \frac{4\pi T_0}{C_\gamma E^3 I_2},$$

$$\tau_\delta = \frac{4\pi T_0}{C_\gamma E^3 (2I_2 + I_4)},$$

$$\alpha_c = \frac{I_1}{C}$$

Changes in storage ring parameters can be understood through variations in synchrotron radiation integrals.

○ Ring parameters change from IDs

To understand the changes in the storage ring parameters due to the ID, it is necessary to know the impact of the synchrotron radiation integrals caused by the ID. The additional synchrotron radiation integrals generated by the ID can be calculated as shown in (Equation 2.1.3.6), assuming the magnetic field of the undulator is a simple sine function.

$$I_{1,ID} = -\frac{\lambda_{ID}^2 B_{ID}^2 L_{ID}}{8\pi^2 \times (B\rho)^2},$$

$$I_{2,ID} = -\frac{B_{ID}^2 L_{ID}}{2 \times (B\rho)^2},$$

$$I_{3,ID} = -\frac{4B_{ID}^3 L_{ID}}{3\pi \times (B\rho)^3}, \quad (\text{Eq. 2.1.3.6})$$

$$I_{4,ID} = -\frac{3\lambda_{ID}^2 B_{ID}^4 L_{ID}}{32\pi^2 \times (B\rho)^4},$$

$$I_{5,ID} = -\frac{\langle \beta_x \rangle \lambda_{ID}^2 B_{ID}^5 L_{ID}}{15\pi^2 \times (B\rho)^5},$$

Here, λ_w is the undulator's period B_{ID} is the undulator's maximum magnetic field strength, L_{ID} is the undulator's length, $B\rho$ is the magnetic rigidity, and $\langle \beta_x \rangle$ is the average value of the beta function at the undulator's location. The changes in ring parameters due to the undulator can be easily obtained using (Equation 2.1.3.5) and (Equation 2.1.3.6). First, the ratio of the emittance with the undulator added to the ring, ε_{all} and the emittance without the undulator, ε_{ring} is given by (Equation 2.1.3.7).

$$\frac{\varepsilon_{all}}{\varepsilon_{ring}} = \frac{C_q \gamma^2 \frac{I_{5,all}}{I_{2,all} - I_{4,all}}}{C_q \gamma^2 \frac{I_{5,ring}}{I_{2,ring} - I_{4,ring}}} = \frac{\frac{I_{5,ring} + I_{5,ID}}{I_{2,ring} + I_{2,ID} - I_{4,ring} - I_{4,ID}}}{\frac{I_{5,ring}}{I_{2,ring} - I_{4,ring}}} = \frac{1 + \frac{I_{5,ID}}{I_{5,ring}}}{1 + \frac{I_{2,ID} - I_{4,ID}}{I_{2,ring} - I_{4,ring}}} \quad (\text{Eq. 2.1.3.7})$$

2.1.3.7)

In (Equation 2.1.3.7), the magnitude of $I_{2,ID}$ is generally smaller compared to $I_{4,ID}$. Therefore, by neglecting $I_{4,ID}$ in (Equation 2.1.3.7), (Equation 2.1.3.8) can be obtained.

$$\frac{\varepsilon_{all}}{\varepsilon_{ring}} = \frac{1 + b L_{ID}}{1 + a L_{ID}}$$

$$\text{where } a = \frac{B_{ID}^2}{2(I_{2,ring} - I_{4,ring})(B\rho)^2} \text{ and } b = \frac{\langle \beta_x \rangle \lambda_{ID}^2 B_{ID}^5}{15\pi^2 I_{5,ring} \times (B\rho)^5} \quad (\text{Eq. 2.1.3.8})$$

In a similar way, the effect of the undulator on energy spread can also be investigated. The change in energy spread, caused by the installation of the undulator, follows the same functional form as that of emittance.

$$\frac{\sigma_{\delta, all}^2}{\sigma_{\delta, ring}^2} = \frac{1 + d L_{ID}}{1 + c L_{ID}}$$

$$\text{where } c = \frac{B_{ID}^2}{(2I_{2,ring} + I_{4,ring})(B\rho)^2} \text{ and } d = \frac{4B_{ID}^3}{3\pi I_{3,ring}(B\rho)^3} \quad (\text{Eq. 2.1.3.9})$$

In other words, whether the energy spread increases, remains the same, or decreases is

determined by the ratio of d/c , and the degree of change depends on the length of the undulator. Notably, d/c is independent of the undulator's λ_w . The damping time follows the shape of a rational function.

$$\frac{\tau_{all}}{\tau_{ring}} = \frac{1}{1+eL_{ID}} \text{ where } e_x = \frac{B_{ID}^2}{(2I_{2,ring} - I_{4,ring})(B\rho)^2},$$

$$e_y = \frac{B_{ID}^2}{(2I_{2,ring})(B\rho)^2}, e_\delta = \frac{B_{ID}^2}{(2I_{2,ring} + I_{4,ring})(B\rho)^2} \quad (\text{Eq. 2.1.3.10})$$

Momentum compaction factor follows the shape of a simple linear function.

$$\frac{\alpha_{c,all}}{\alpha_{c,ring}} = 1 - fL_w \text{ where } f = \frac{\lambda_{ID}^2 B_{ID}^2}{8\pi^2 \alpha_{c,ring} C (B\rho)^2} \quad (\text{Eq. 2.1.3.11})$$

○ Applying ID Effect Study on 4GSR

Previously, we established theoretically that it is challenging to reduce emittance in storage rings with small emittance using an undulator. Therefore, we investigated whether the same conclusion applies to the 4GSR. First, the synchrotron radiation integrals for the 4GSR are shown in <Table 2.1.3.2>.

<Table 2.1.3.2> Synchrotron radiation integrals of Korea-4GSR

Synchrotron radiation integrals	Values
I_1	$6.2147 \times 10^{-2} \text{ m}$
I_2	$3.0454 \times 10^{-1} \text{ m}^{-1}$
I_3	$2.3972 \times 10^{-2} \text{ m}^{-2}$
I_4	$-2.5666 \times 10^{-1} \text{ m}^{-1}$
I_5	$1.4715 \times 10^{-6} \text{ m}^{-1}$

Additionally, the synchrotron radiation integrals for the configuration with nine undulators, as shown in <Table 2.1.3.1>, are presented in <Table 2.1.3.3>.

<Table 2.1.3.3> Synchrotron radiation integrals with the initial nine beamlines of Korea-4GSR

Synchrotron radiation integrals	Values
$I_{1,ID}$	$-4.24739 \times 10^{-6} \text{ m}$
$I_{2,ID}$	$9.32240 \times 10^{-2} \text{ m}^{-1}$
$I_{3,ID}$	$6.59512 \times 10^{-3} \text{ m}^{-2}$
$I_{4,ID}$	$-1.91798 \times 10^{-8} \text{ m}^{-1}$
$I_{5,ID}$	$2.38397 \times 10^{-9} \text{ m}^{-1}$

Using the results from <Table 2.1.3.3> the changes in the storage ring parameters can be calculated, as shown in <Table 2.1.3.4>.

<Table 2.1.3.4> Changes in storage ring parameters from ID

Ring parameters	Without IDs	With 9 IDs	With 24 IDs
Energy loss per turn [keV]	1,098	1,449	2,035
Emittance [pm]	61.57	52.88	42.85
Energy spread [%]	0.1264	0.1054	0.0909
Horizontal damping time [ms]	10.54	9.04	7.31
Vertical damping time [ms]	19.43	14.88	10.70
Longitudinal damping time [ms]	16.79	10.98	6.97

In addition to the changes in storage ring parameters due to the nine IDs, calculations were also made for the case where IDs are fully installed throughout the storage ring. The values of the synchrotron radiation integrals for the nine IDs (in <Table 2.1.3.3>) can be scaled to compute the values for 24 IDs. The reason for choosing 24 IDs is that this is the maximum number of straight sections available in the 4GSR. The 4GSR consists of two high-beta straight sections and 26 ID straight sections. Each of the two high-beta straight sections is filled with an injection systems and RF cavities.

Additionally, at least two of the remaining 26 straight sections must accommodate RF cavities, allowing for a maximum installation of 24 IDs. Under certain conditions, if the straight sections need to be utilized, the number of IDs may be less than 24. However, for the current calculations, we consider the changes when the maximum possible number of IDs is installed. As seen in <Table 2.1.3.4>, the energy loss per turn increases due to the presence of the IDs, which in turn requires adjustments in RF voltage and power. As

described in Section 2.1.3.A “RF Voltage Optimization ” , when RF voltage corrections are made to maintain the same RF acceptance with the installation of IDs, the results are presented in <Table 2.1.3.5>.

<Table 2.1.3.5> Required RF voltage according to the number of IDs

	Without IDs	With 9 IDs	With 24 IDs
RF voltage [MV]	3.00	3.50	4.19
RF acceptance [%]	4.767	4.765	4.766

At this time, the energy loss per turn due to the resistive wall effect throughout the storage ring is assumed to be 60 keV. Additionally, the required RF power was calculated as a function of the operating beam current, and the results are presented in <Table 2.1.3.6>.

<Table 2.1.3.6> Required RF power according to the number of IDs

Current [mA]	Required RF power [kW]		
	Without IDs	With 9 IDs	With 24 IDs
100.0	109.765	149.381	205.407
200.0	219.530	298.761	410.814
300.0	329.295	448.142	616.221
400.0	439.060	597.523	821.628
500.0	548.825	746.904	1,027.035

Referring to <Table 2.1.3.6>, when the target beam operating current is 400 mA, the required RF power is 598 kW with the initial installation of nine beamlines, and it increases to 822 kW when all 24 IDs are installed throughout the storage ring.

References

- [1] Wiedemann, H. (1993). Particle Accelerator Physics I. Berlin: Springer.
- [2] Helm, R. H., Lee, M. J., Mortorn, P. L. & Sands, M. (1973). IEEE Trans. Nucl. Sci. 20, 900-901.
- [3] Wiedemann, H. (1998). Nucl. Instrum. Methods Phys. Res. A, 266, 24-31
- [4] Walker, R. P. (1995). CAS-CERN Accelerator School: 5th Advanced Accelerator Physics Course, 20 September-1 October 1993, Rhodes, Greece, pp. 807-835.
- [5] Jang, Gyeongsu, et al. "Investigation of the damping wiggler effect and application on the PAL fourth-generation storage ring." Journal of Synchrotron Radiation 27.6 (2020): 1510-1517.

C. Coupling Study

In an ideal lattice, horizontal motion and vertical motion are independent of each other. However, if there are rotation errors in the quadrupole magnets or alignment errors in the sextupole magnets, these two motions become coupled. Alternatively, skew quadrupole magnets can be intentionally employed to create a correlation between horizontal and vertical motion. When these two motions are coupled, the ratio of horizontal emittance to vertical emittance is defined as coupling, which can be expressed using (Equation 2.1.3.12).

$$\chi = \frac{\varepsilon_y}{\varepsilon_x} \quad (\text{Eq. 2.1.3.12})$$

Here, χ represents coupling, ε_x denotes horizontal emittance, and ε_y signifies vertical emittance. When the coupling within the storage ring is determined, the equilibrium emittance can be calculated using (Equation 2.1.3.13).

$$\frac{d\varepsilon_x}{dt} + \frac{d\varepsilon_y}{dt} = -\frac{2}{\tau_x}\varepsilon_x - \frac{2}{\tau_y}\varepsilon_y + \frac{2}{j_x\tau_x}C_q\gamma^2\frac{I_5}{I_2} \quad (\text{Eq. 2.1.3.13})$$

Here, τ_x, τ_y represent the horizontal and vertical damping times, respectively, while j_x denotes the horizontal damping partition number. In the above equation, the magnitude of the vertical excitation term is negligible, allowing us to use the relationship between damping times and damping partition numbers. Consequently, the equilibrium emittance in the storage ring can be obtained as shown in (Equation 2.1.3.14) and (Equation 2.1.3.15).

$$\varepsilon_x = \varepsilon_{x0} \left(\frac{j_x}{j_x + \kappa j_y} \right) \quad (\text{Eq. 2.1.3.14})$$

$$\varepsilon_y = \varepsilon_{x0} \left(\frac{\kappa j_x}{j_x + \kappa j_y} \right) \quad (\text{Eq. 2.1.3.15})$$

Here, ε_{x0} represents the natural emittance, which is obtained through (Equation 2.1.2.4), and j_y denotes the vertical damping partition number.

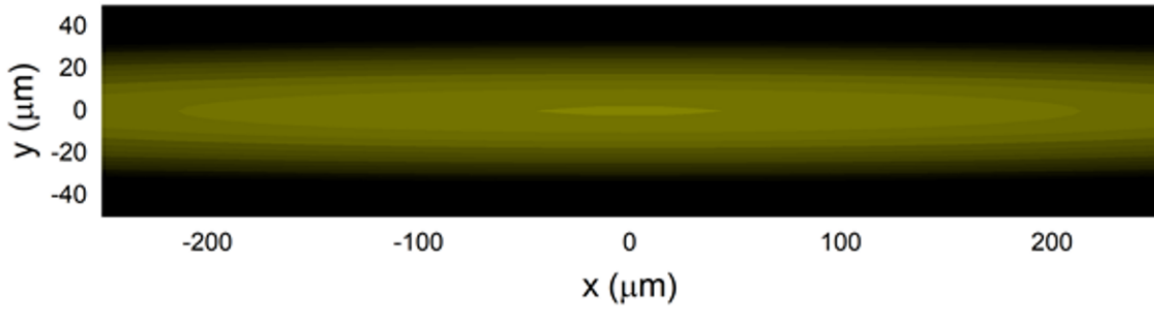
Typically, the quality of synchrotron radiation in the 3GSR is evaluated in terms of brilliance. Brilliance is proportional to the product of horizontal and vertical emittance. Generally, vertical emittance tends to be less than horizontal emittance. By reducing the already small vertical emittance further and increasing the higher horizontal emittance, we can enhance the product of the two, thereby increasing brilliance. Theoretically, vertical dispersion in the ring is expected to be zero at all positions, suggesting that vertical emittance

should also be zero. However, as the beam emits synchrotron radiation at an angle of approximately $1/\gamma$, a very small level of vertical emittance is always present. The primary factors contributing to vertical emittance arise from unavoidable errors within the storage ring, such as tilt errors in the dipole magnets, alignment errors in the quadrupole magnets, and alignment errors in the sextupole magnets. These errors that generate vertical emittance are referred to as coupling errors.

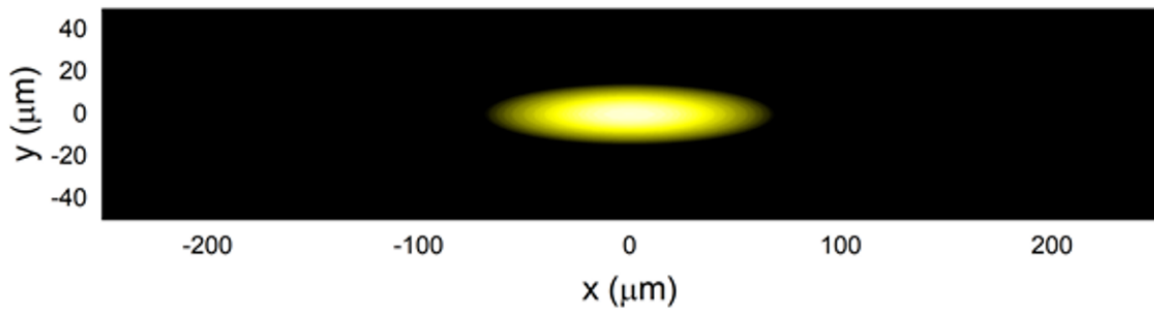
In 3GSRs, skew quadrupoles are placed to eliminate these coupling errors, maximizing the brilliance of the synchrotron radiation. However, in 4GSRs with horizontal emittance below 100 pm, the photon beam emitted by the electron beam exhibits diffraction-limited characteristics across a wide photon energy range. Consequently, the quality of synchrotron radiation becomes more critical in terms of matching the phase space of the beam and the synchrotron radiation rather than just brilliance. To achieve this matching, operating a round beam with equal horizontal and vertical emittance can be advantageous. When a round beam is created, the increase in vertical emittance is balanced by a decrease in horizontal emittance, which helps mitigate the emittance increase caused by Intra beam Scattering (IBS), as explained in the Intra beam Scattering section.

However, to create a round beam, the fractional parts of the horizontal and vertical tunes must be similar to establish a coupling resonance state. When the beam is in coupling resonance, oscillating the beam in the horizontal direction causes the horizontal amplitude to decrease while the vertical amplitude increases, resulting in a coupled oscillation phenomenon. Therefore, if the coupling beam is injected off-axis, it will oscillate with a large amplitude in the vertical direction before sufficiently damping and stabilizing.

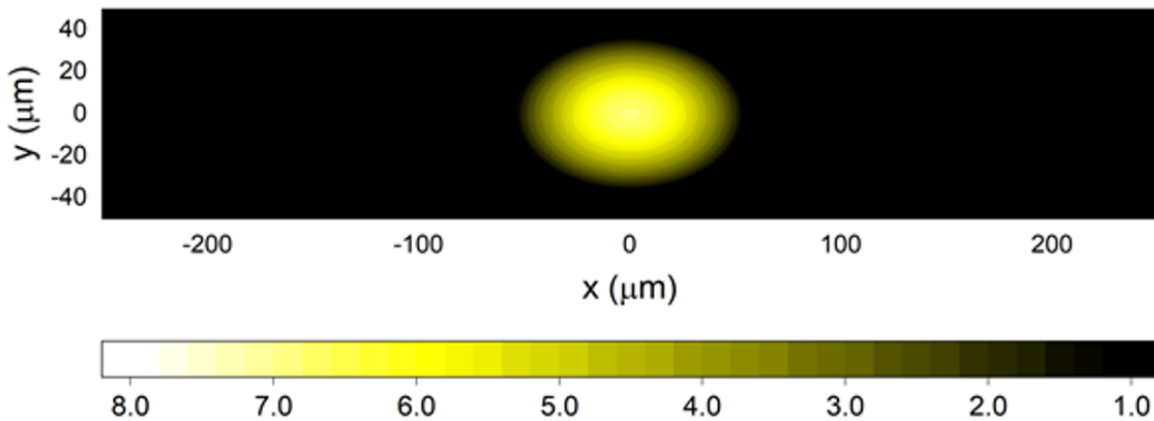
A) PLS-II electron beam with 1% coupling at ID



B) Korea-4GSR electron beam with 10% coupling at ID



C) Korea-4GSR electron beam with 100% coupling at ID



<Figure 2.1.3.4> Beam size comparison for PLS-II and 4GSR.

At locations where insertion devices are placed, which have a narrow vertical aperture, the risk of beam loss significantly increases. Consequently, using off-axis injection becomes challenging for round beams. We compared the simulation results of flat beams and round beams through tune adjustments with those from the 3GSR, specifically the PLS-II, and displayed the findings in <Figure 2.1.3.4>. In the figure, the electron density is represented

using a logarithmic scale with color coding. Higher densities are indicated by white, while lower densities transition from yellow to black. Densities greater than 8 are shown in white, and densities below 1 are represented in black. The 4GSR exhibits a small emittance, resulting in a very small beam size for the flat beam case. In the case of coupling beams, both horizontal and vertical emittances are equal, yielding a shape that is close to circular. In the 4GSR, even for flat beams, the ratio of vertical to horizontal emittance is kept at approximately 10%, which is about 100 times that of the 3GSR, considering the effects of IBS. This ratio can be adjusted using skew quadrupoles.

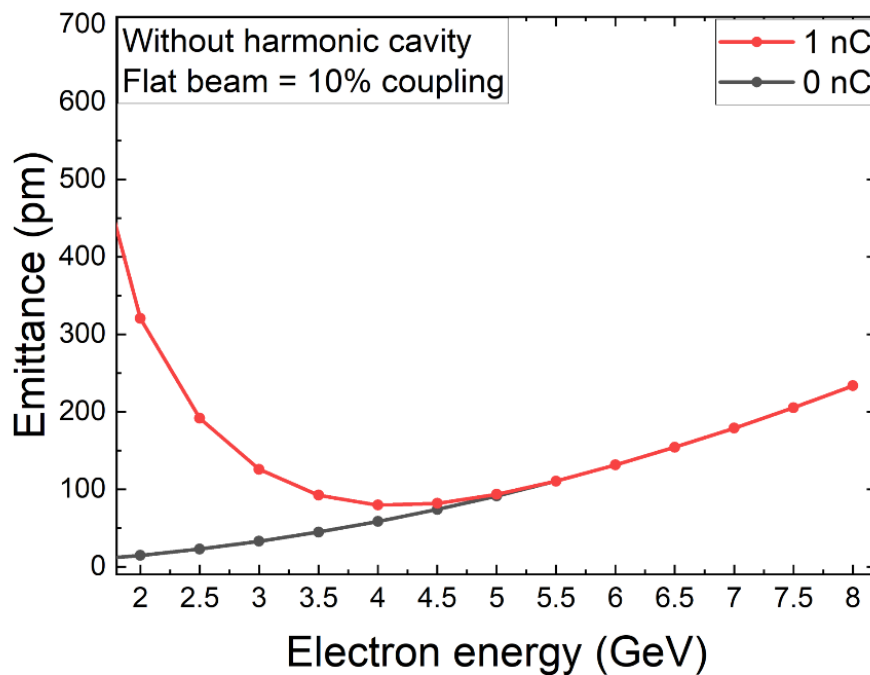
References

- [1] Oh, Bonghoon, et al. "Characteristics of Photon Beam and Preservation of Coherence in Fourth-Generation Light Sources." *Applied Sciences* 11.24 (2021): 11896.
- [2] Ko, Jinjoo, et al. "Characteristics of the Synchrotron Radiation of Fourth-Generation Storage Rings." *Journal of the Korean Physical Society* 77 (2020): 363-367.
- [3] Lee, J., et al. "Concurrent operation of round beam and flat beam in a low-emittance storage ring." *Nuclear Engineering and Technology* (2023).

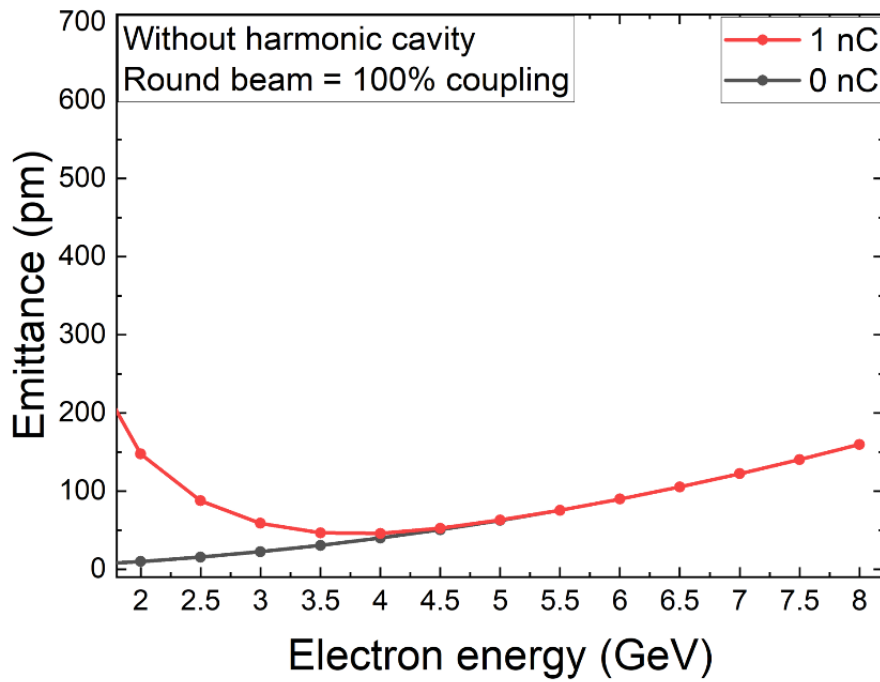
D. Intrabeam Scattering (IBS)

Intrabeam Scattering (IBS) refers to the phenomenon where particles within a beam collide randomly, leading to an increase in emittance. While the IBS effect does not significantly impact the emittance increase in 3GSRs with nm-order emittance, it becomes considerably more pronounced in 4GSRs, which have much smaller emittance in the range of hundreds to tens of pm. IBS is primarily influenced by factors such as bunch length, bunch charge, and beam energy. An increase in bunch length not only reduces the IBS effect but also positively affects the beam lifetime, which is why there are plans to install a third harmonic cavity to increase the bunch length by a factor of four. Considering IBS, beam emittance was calculated based on beam energy. For a flat beam with a coupling of 10%, the results are shown in <Figure 2.1.3.5>, while for a round beam with a coupling of 100%, the results are in <Figure 2.1.3.6>.

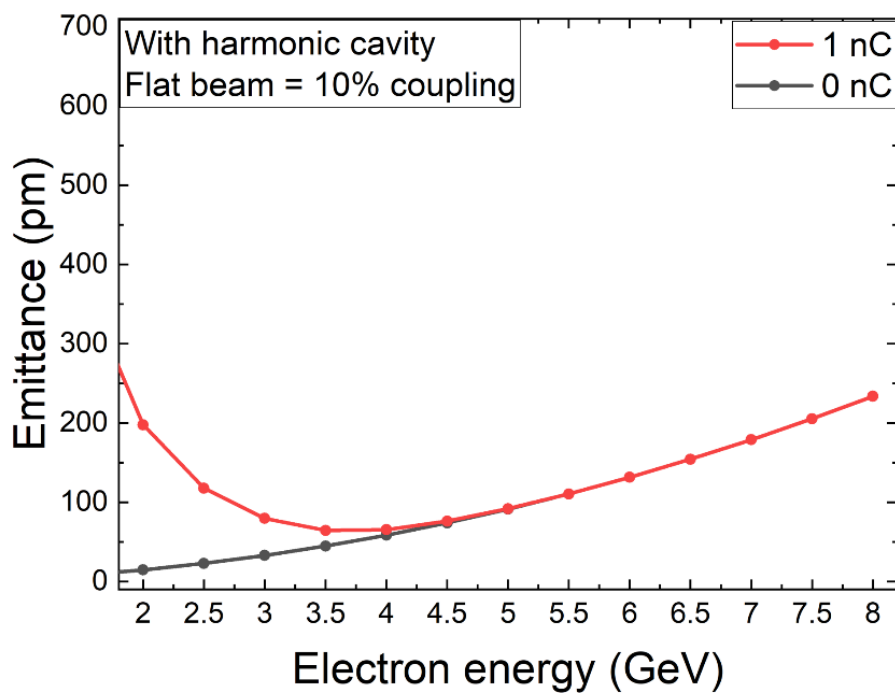
The IBS-considered beam emittance is minimized at a beam energy of 4.0 GeV for both flat and round beams. In multi-bunch operation mode with a bunch charge of 1 nC, the emittance of the flat beam increases by 36.2%, from 58.40 pm to 79.57 pm, whereas the round beam's emittance increases by 14.7%, from 39.91 pm to 45.79 pm. When using a harmonic cavity, the longer bunch length reduces the emittance increase due to IBS. In the case of the flat beam, the emittance rises to 65.32 pm, representing an 11.8% increase, while the round beam's emittance increases to 41.56 pm, which is a 4.1% rise.



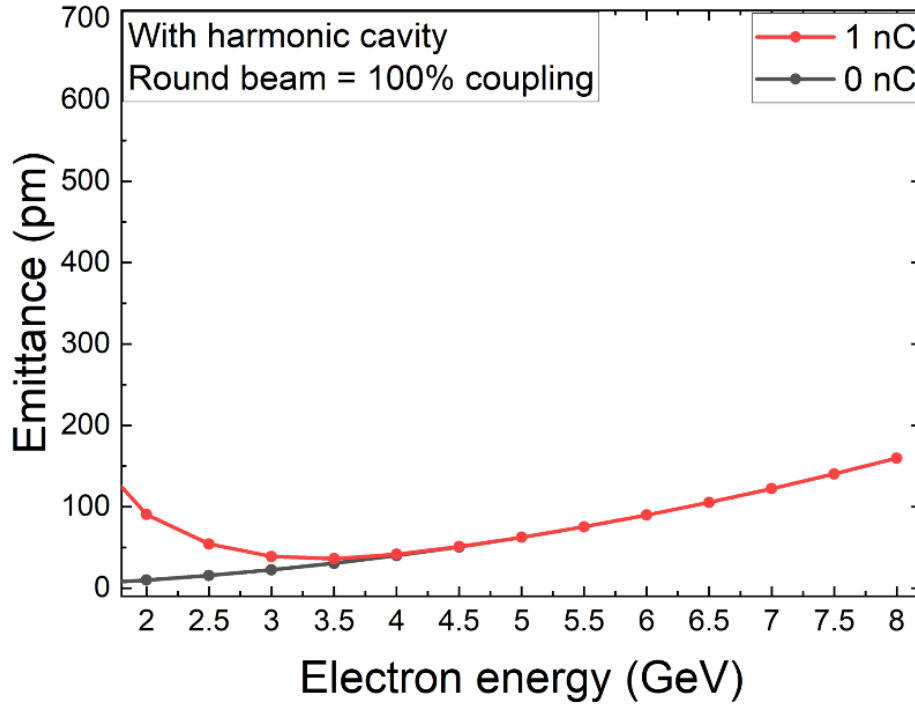
<Figure 2.1.3.5> Changes in emittance of a flat beam due to IBS as a function of energy.



<Figure 2.1.3.6> Changes in emittance of a round beam due to IBS as a function of energy.



<Figure 2.1.3.7> Changes in emittance of a flat beam due to IBS as a function of energy with a harmonic cavity.



<Figure 2.1.3.8> Changes in emittance of a round beam due to IBS as a function of energy with a harmonic cavity.

In the 4GSR, there are plans to use a harmonic cavity to increase the beam lifetime. By utilizing a harmonic cavity, the length of the electron bunch increases, which results in a lower charge density and subsequently reduces the effects of IBS. <Figures 3.1.3.7> and <Figure 2.1.3.8> demonstrate that using a harmonic cavity leads to a smaller increase in emittance due to IBS compared to when it is not used.

References

- [1] Bjorken, J. D. & Mtingwa, S. K. (1983). Part. Accel. 13, 115-143.

E. Beam Lifetime

Electrons stored in the storage ring do not remain indefinitely; they have a finite lifetime. The four most important factors influencing this lifetime are quantum lifetime, elastic scattering lifetime, Bremsstrahlung lifetime, and Touschek lifetime. Each of these factors has been calculated for the 4GSR as well.

○ Quantum lifetime

When electrons in the storage ring are accelerated, they emit synchrotron radiation, which is quantized. The quantized energy changes of the electrons cause variations in their oscillation amplitudes. If these amplitude variations exceed the acceptance limit of the storage ring, the electrons are lost. The beam lifetime determined by this mechanism is called quantum lifetime. Quantum lifetime can be calculated using (Equation 2.1.3.16).

$$\tau_{q_{\epsilon,x}} = \frac{\tau_{\epsilon,x} e^{\xi_{\epsilon,x}}}{2\xi_{\epsilon,x}}, \quad \frac{1}{\tau_q} = \frac{1}{\tau_{q_{\epsilon}}} + \frac{1}{\tau_{q_x}} \quad (\text{Eq. 2.1.3.16})$$

In this context, $\tau_{q_{\epsilon}}$ refers to the longitudinal quantum lifetime, and τ_{q_x} to the transverse quantum lifetime, while τ_q represents the overall quantum lifetime. τ_{ϵ} is the longitudinal damping time, and τ_x is the transverse damping time. ξ_{ϵ} corresponds to $\frac{1}{2} \left(\frac{\Delta E_{RF}}{\sigma_{\epsilon}} \right)^2$, and ξ_x to $\frac{1}{2} N_v^2$. Here, ΔE_{RF} stands for the RF acceptance, σ_{ϵ} is the rms energy spread, and N_v is the ratio of the dynamic aperture to the beam size. For 4GSR, τ_x is 10.5 ms, τ_y is 19.4 ms, τ_{ϵ} is 16.8 ms, and the relative energy spread is 0.126%. Since the RF acceptance is always greater than 1.3%, $\frac{\sigma_{\epsilon}}{E_0}$ is always greater than 10. The beam size in the storage ring is much smaller than 100 μm , and the dynamic aperture is always larger than 1 mm in both horizontal and vertical directions. Therefore, N_v is also always greater than 10. When calculated using (Equation 2.1.3.16), the quantum lifetime always exceeds 10^{14} hours, which means the quantum lifetime is effectively infinite.

○ Elastic scattering lifetime

The electrons stored in the storage ring move within it and eventually collide with the remaining gas. As a result of the collision, the electrons undergo changes in their angular momentum, causing betatron oscillations. If these betatron oscillations exceed the vacuum chamber, the electrons are lost. The lifetime determined by this mechanism is called the elastic scattering lifetime, or alternatively, the gas scattering lifetime. The elastic scattering lifetime can be calculated using (Equation 2.1.3.17).

$$\sigma_g = \frac{4\pi Z(Z+1)r_e^2}{\gamma^2} \frac{\beta_m \langle \beta \rangle}{h_m^2}, \quad n_g = n \frac{P}{RT} N_A, \quad \frac{1}{\tau_g} = c n_g \sigma_g \quad (\text{Eq. 2.1.3.17})$$

Here, σ_g is the differential scattering cross-section between the electron and nucleus, r_e is the classical electron radius, γ is the Lorentz factor, β_m is the beta value at the minimum half aperture, h_m is the minimum half aperture, $\langle \beta \rangle$ is the average beta value, n_g is the number of atoms per residual gas molecule, Z is the atomic number of the residual gas, n is the number of atoms per residual gas molecule, P is the vacuum pressure, R is the universal gas constant, T is the temperature, N_A is Avogadro's constant, τ_g is the elastic scattering lifetime, and c is the speed of light. When calculated for the case of 4GSR with a pressure of 10^{-9} mbar, the results are shown in <Table 2.1.3.7>.

<Table 2.1.3.7> Elastic scattering lifetime at a vacuum pressure of 10^{-9} mbar in 4GSR

Gas	Lifetime [h]
H ₂	1025.4
CO	36.0
CO ₂	22.1
N ₂	36.6

Given that the average pressure inside the storage ring is below 10^{-9} mbar, the elastic scattering lifetime is considered sufficient for stable operation.

○ Bremsstrahlung lifetime

Stored electrons in the storage ring collide with residual gas as they move within the ring, leading to changes in their angular momentum, as previously described. However, not only does angular momentum change, but there is also a change in energy. If the change in energy exceeds the energy acceptance, the electrons will be lost. The lifetime determined by this mechanism is referred to as the Bremsstrahlung lifetime or the inelastic gas scattering lifetime. The Bremsstrahlung lifetime can be calculated using (Equation 2.1.3.18).

$$\sigma_b = \frac{4r_e^2}{137} Z(Z + \eta) \left(\frac{4}{3} \ln \ln \frac{E_0}{\Delta E_{RF}} - \frac{5}{6} \right) \ln \ln \frac{183}{Z^{\frac{1}{3}}},$$

$$n_g = n \frac{P}{RT} N_A, \quad \frac{1}{\tau_b} = c n_g \sigma_b \quad (\text{Eq. 2.1.3.18})$$

Here, σ_b is the differential scattering cross-section for Bremsstrahlung, r_e is the classical electron radius, η is $\frac{\ln \ln (530/Z^{2/3})}{\ln \ln (183/Z^{1/3}) + 1/8}$, $\frac{\Delta E_{RF}}{E_0}$ is the RF acceptance, n_g is the number of atoms per residual gas molecule, Z is the atomic number of residual gas, n is the number of moles, P is the vacuum pressure, R is the universal gas constant, T is the temperature, N_A is Avogadro's constant, τ_b is the Bremsstrahlung lifetime, and c is the speed of light. For the case of 4GSR, Bremsstrahlung lifetime at a pressure of 10^{-9} mbar, can be found in <Table 2.1.3.8>.

<Table 2.1.3.8> Bremsstrahlung lifetime at a vacuum pressure of 10^{-9} mbar in 4GSR

Gas	Lifetime [h]
H ₂	2273.3
CO	98.6
CO ₂	60.6
N ₂	10.0

Considering that the pressure within the storage ring is typically below 10^{-9} mbar, the Bremsstrahlung lifetime is deemed sufficient for operation.

○ Touschek lifetime

The Touschek lifetime is determined by a mechanism similar to that of the Bremsstrahlung lifetime, where electrons are lost when their energy exceeds the energy acceptance. The difference lies in the fact that the cause of the energy change is due to collisions among the electrons, rather than collisions with residual gas. The Touschek lifetime for the 4GSR was obtained through elegant simulation in the section 2.1.3.A “RF voltage optimization” . At the optimal RF voltage, a Touschek lifetime of 7.3 hours was achieved, which is the most significant factor in determining the overall lifetime. Therefore, we investigated methods to increase the Touschek lifetime by operating with a round beam and utilizing a harmonic cavity, with the results presented in <Table 2.1.3.9>.

<Table 2.1.3.9> Touschek lifetime in 4GSR

Flat beam : coupling 10%			Round beam : coupling 100%		
Without HC	Without IBS	With IBS	Without HC	Without IBS	With IBS
Emittance (H/V)	58.40/5.84 pm	79.57/7.96 pm	Emittance (H/V)	39.91/39.91 pm	45.79/45.79 pm
Touschek lifetime	7.30 h	8.52 h	Touschek lifetime	17.04 h	17.38 h
With HC	Without IBS	With IBS	With HC	Without IBS	With IBS
Emittance (H/V)	58.40/5.84 pm	65.32/6.53 pm	Emittance (H/V)	39.91/39.91 pm	41.56/41.56 pm
Touschek lifetime	29.22 h	34.09 h	Touschek lifetime	68.18 h	66.39 h

Looking at <Table 2.1.3.9>, it can be seen that even when using only one of the two methods without combining them, a lifetime of over 17 hours can be achieved.

References

- [1] M. Sands, The Physics of Electron Storage Rings, SLAC-121, Nov. 1970.
- [2] Borland, Michael, et al. "Simulation of Gas-Scattering Lifetime using Position-and Species-Dependent Pressure and Aperture Profiles." Proceedings of the 2015 International Particle Accelerator Conference. 2015.
- [3] Piwinski, CERN Accelerator School General Acc. Phys., CERN 85-19.
- [4] H. W. Koch and J. W. Motz, Rev. of Modern Phys., Vol.31, No.4, Oct. 1959.

F. Error and Tolerance

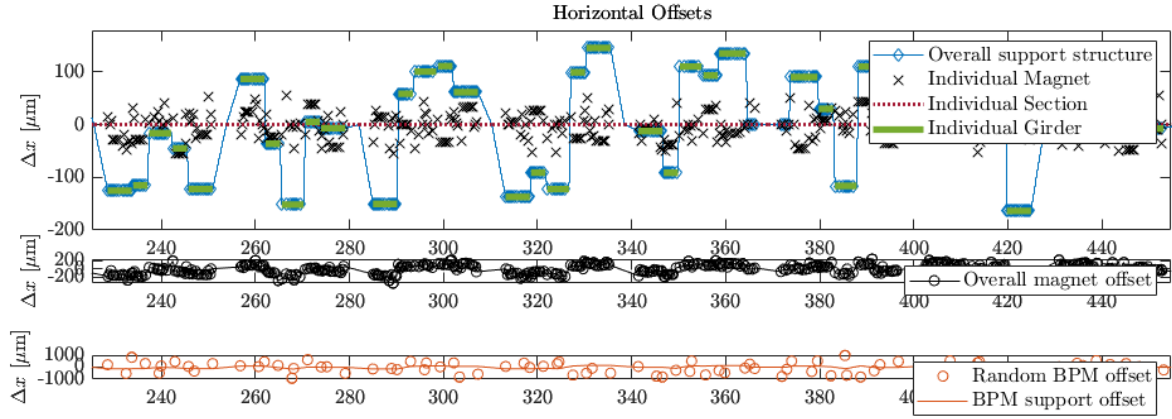
For all magnets and girders in the storage ring, required misalignment error, rotation error, and strength error are set as <Table 2.1.3.10>. BPM errors; offset before beam-based alignment, noise for closed orbit mode and turn-by-turn mode, roll and calibration error are given as <Table 2.1.3.11>. These are rms values and it is assumed that each magnet error follows Gaussian distribution and the distribution is cut in the two-sigma boundary.

<Table 2.1.3.10> Storage ring magnet & girder tolerance (rms value)

Magnet	Misalignment (μm) (X/Y/Z)	Rotation (μrad) (Roll/Pitch/Yaw)	Strength error (%)
LGBM	30 / 30 / 250	400 / 100 / 100	0.05
Combined-function magnet	30 / 30 / 250	400 / 100 / 100	0.05
Quadrupole	30 / 30 / 250	400 / 700 / 700	0.05
Center bend	30 / 30 / 250	400 / 100 / 100	0.05
Sextupole	30 / 30 / 250	400 / 700 / 700	0.05
Octupole	30 / 30 / 250	400 / 700 / 700	0.05
Girder	100 / 100 / 100	400 / - / -	-

<Table 2.1.3.11> Storage ring BPM error (rms value)

Offset (μm) (X/Y)	Noise (Closed orbit) (μm) (X/Y)	Noise (Turn-by-turn) (μm) (X/Y)	Roll (μrad)	Calibration error (%) (X/Y)
500 / 500	1 / 1	100 / 100	100	5 / 5



<Figure 2.1.3.9> Horizontal magnet offset along longitudinal position for an arbitrary random error seed.

The magnet misalignment values in <Table 2.1.3.10> are based on the alignment relative to the girder. As shown in <Figure 2.1.3.9>, the overall magnet offset of a specific magnet is given as the sum of the misalignment of the girder and the misalignment of the magnet relative to the girder. The description of the commissioning simulation process using the error tolerances in <Table 2.1.3.10> and <Table 2.1.3.11>, as well as the evaluation of lattice performance, continues in section 2.1.3.H, "Commissioning Simulations."

G. Amplification Factor

When constructing a storage ring, the actual lattice will deviate from the ideal design. Various factors contribute to these discrepancies, which in turn affect many characteristics of the storage ring compared to the ideal lattice. To correct for these deviations, corrector magnets are added, and the strengths of the individual magnets are optimized. The first step in this process is to use the corrector magnets to determine the closed orbit. To achieve this, it is necessary to decide where to position the correctors. To investigate this, the amplification factor of 4GSR was analyzed. The amplification factor is defined as shown in (Equation 2.1.3.19).

$$x_{COD}^2 = \beta(z)A_{\Delta x}^2\sigma_{\Delta x}^2 + \beta(z)A_{\Delta B/B}^2\sigma_{\Delta B/B}^2 + \beta(z)A_{\Delta\theta}^2\sigma_{\Delta\theta}^2 \quad (\text{Eq. 2.1.3.19})$$

Here, x_{COD} is the closed orbit distortion, $\beta(z)$ is the beta function value at the measurement location, $\sigma_{\Delta x}^2$ is the RMS misalignment error, $\sigma_{\Delta B/B}^2$ is the RMS field strength error, $\sigma_{\Delta \theta}^2$ is the RMS kick angle, and $A_{\Delta x}^2, A_{\Delta B/B}^2$, and $A_{\Delta \theta}^2$ are defined as shown in (Equation 2.1.3.20).

$$A_{\Delta x}^2 = \frac{N\beta_i}{8\pi\nu} (k_i L_i)^2, \quad A_{\Delta B/B}^2 = \frac{N\beta_i}{8\pi\nu} (\theta_i)^2, \quad A_{\Delta \theta}^2 = \frac{N\beta_i}{8\pi\nu} \quad (\text{Eq. 2.1.3.20})$$

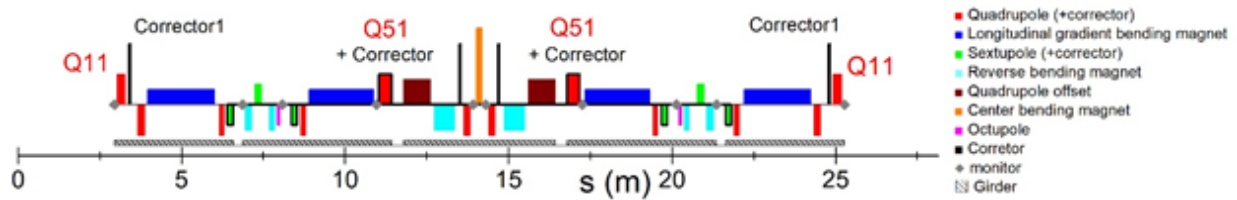
Here, N is the number of magnets, β_i is the beta function value at the location of the magnets, ν is the tune, k_i is the quadrupole component of the magnets, L_i is the length of the magnets, and θ_i is the bending angle of the magnets. $A_{\Delta x}^2$ represents the impact on the closed orbit due to the alignment errors of the quadrupole magnets, while $A_{\Delta B/B}^2$ indicates the influence on the closed orbit caused by the field strength errors of the dipole magnets. To identify the magnets that have the greatest impact due to errors, the amplification factor was calculated and is presented in <Table 2.1.3.12>.

<Table 2.1.3.12> The values of amplification factor

Amplification factor type	Magnet name	A_x	A_y	$A = \sqrt{A_x^2 + A_y^2}$
Quadrupole $A_{\Delta x}$ with $\sigma_{\Delta x}^2 = 100\mu m$	QH1	0.12	0.05	0.13
	QH2	0.15	0.12	0.20
	QH3	0.27	0.17	0.32
	QH4	0.06	0.10	0.11
	Q11	1.09	0.76	1.33
	Q12	0.42	0.81	0.91
	Q31	0.56	1.00	1.14
	Q32	0.49	0.88	1.01
	Q51	0.93	0.80	1.22
	Q52	0.34	0.52	0.62
Dipole $A_{\Delta B/B}$ with $\sigma_{\Delta B/B}^2 = 0.1\%$	LGBM1	0.16	0.68	0.70
	LGBM2	0.20	0.35	0.40
	DQ51	0.20	0.25	0.32
	CENT	0.06	0.13	0.14

Here, to compare the amplification factor, the alignment error was calculated with a standard of 100 μm , while the field strength error was set at 0.1%. This benchmark is based on error tolerance considerations. Looking at <Table 2.1.3.12>, the magnets that produce

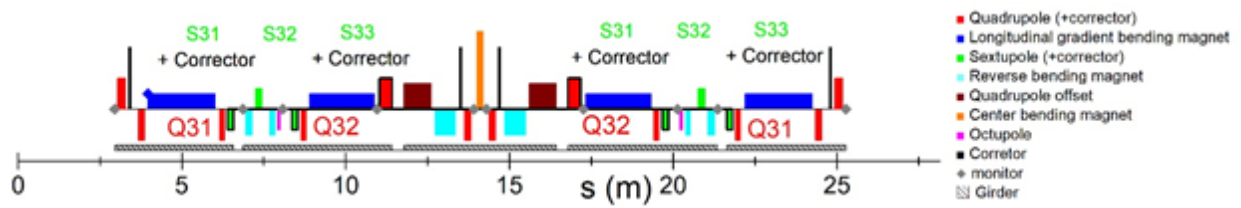
the strongest orbit distortion due to errors are Q11 and Q51. To correct this, an independent corrector was placed near Q11, as shown in <Figure 2.1.3.10>, and the Q51 magnet was designed to incorporate a built-in corrector.



<Figure 2.1.3.10> Schematic diagram of magnet arrangement for 4GSR, highlighting the Q11 and Q51 magnets.

While it would be ideal to have an independent corrector in place, there was no space around Q51 to position a corrector, so it was decided to integrate it into the design. Next, to determine how effectively the closed orbit changes when the corrector is placed, the calculations of $A_{\Delta\theta}^2$ were performed. The options for placing the corrector included integrating it into the quadrupole or sextupole magnets, as well as positioning an independent corrector, and the corresponding amplification factors were investigated. The results are shown in <Table 2.1.3.13>.

For comparison of the amplification factors, the kick intensity was set at $500 \mu rad$. The most effective magnets were found to be the quadrupole magnets Q31 and Q32, as well as the sextupole magnets. Among these, the sextupole magnets were slightly more effective, leading to the decision to integrate the corrector into one of them. However, since the three sextupole magnets are nearly in the same phase during betatron oscillation, using all three might be inefficient. Therefore, it was decided to integrate the corrector into the S31 and S33 magnets, as they have the same length, making it easier to design the integrated corrector compared to the differently sized S32. The final arrangement is shown in <Figure 2.1.3.11>.

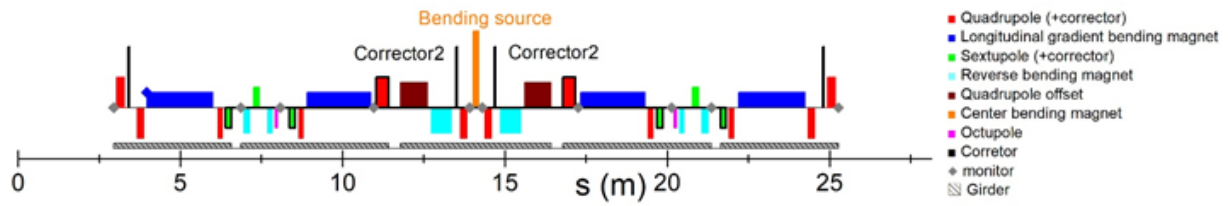


<Figure 2.1.3.11> Schematic diagram of the magnet arrangement for 4GSR, highlighting the S31 and S33 magnets.

<Table 2.1.3.13> The values of amplification factor

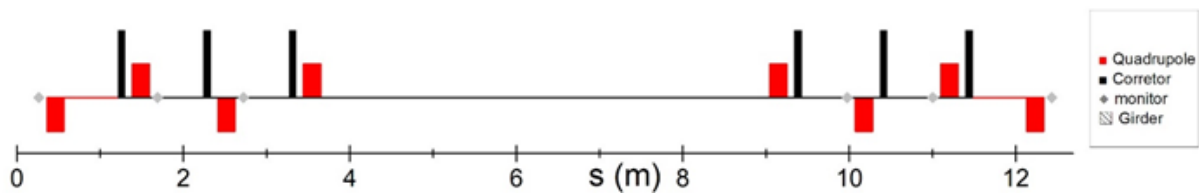
Amplification factor type	Magnet name	A_x	A_y	$A = \sqrt{A_x^2 + A_y^2}$
Embedded corrector $A_{\Delta\theta}$ with $\sigma_{\Delta\theta}^2 = 500 \mu m$	QH1	27.54	11.46	29.83
	QH2	20.03	16.35	25.85
	QH3	22.34	13.73	26.22
	QH4	12.29	19.39	22.95
	Q11	64.88	45.15	79.04
	Q12	37.18	70.92	80.07
	Q31	50.39	89.75	102.93
	Q32	44.04	79.20	90.62
	Q51	33.02	28.58	43.67
	Q52	21.88	33.16	39.73
	S31	64.50	79.82	102.62
	S32	91.70	57.17	108.06
	S33	54.82	74.02	92.11
Independent corrector $A_{\Delta\theta}$ with $\sigma_{\Delta\theta}^2 = 500 \mu m$	Corrector1	54.11	55.38	77.43
	Corrector2	33.81	27.69	43.71

Additionally, as shown in <Figure 2.1.3.12>, the 4GSR is designed to utilize the center bending magnet for the bending beamline. To ensure stable photon beam for users in this configuration, a corrector magnet is needed near the center bending magnet. Therefore, an independent corrector magnet, designated as “corrector2”, was added near the center bending magnet.



<Figure 2.1.3.12> Schematic diagram of the magnet arrangement for 4GSR, highlighting the bending source and corrector 2 magnets.

The independent corrector was employed not only as a static corrector but also as a fast corrector, allowing it to be used for fast orbit feedback to provide the most stable beam delivery to the beamline. Additionally, anticipating the need for extra correction during injection into the high-beta straight section, six more correctors were added, as shown in <Figure 2.1.3.13>.



<Figure 2.1.3.13> Schematic diagram of the magnet arrangement in the high-beta straight section of 4GSR.

The BPMs were paired with correctors, and wherever possible, they were placed close to their corresponding correctors. As a result, the number of BPMs and correctors in 4GSR is the same. Each cell contains 10 pairs, and the entire storage ring is equipped with a total of 288 BPMs and correctors.

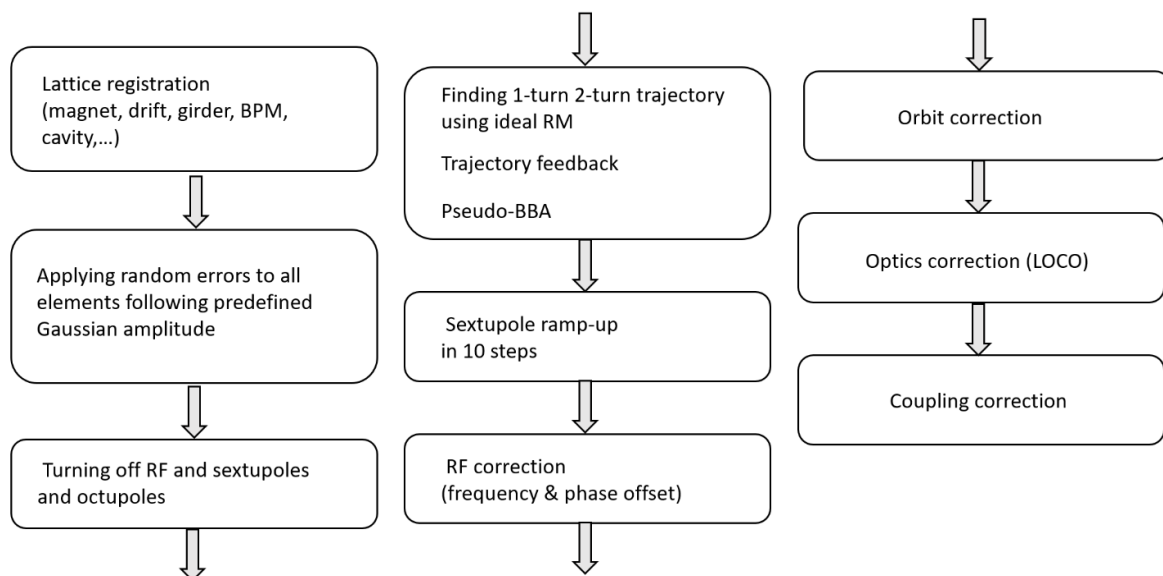
Reference

- [1] Miles, John F. Concerning the strength of closed orbit correction dipoles in the arcs of LHC V4. 2. No. LHC-Project-Note-43. CERN-LHC-Project-Note- 43, 1996.

H. Commissioning Simulations

The accumulation of understanding and experience in storage ring beam dynamics, along with advancements in simulation tools, has enabled the commissioning simulation of the 4GSR storage ring. Compared to the 3GSR, the 4GSR has stronger quadrupole and sextupole fields, and orbit, beta functions, and other parameters are more sensitive to error sources. Therefore, to reliably achieve the desired performance of the storage ring, a more systematic lattice correction strategy is required at each stage of commissioning. The objectives of the commissioning simulation and the benefits that can be obtained through simulation can be summarized as follows:

1. The suitability of the error tolerance range, including magnet misalignment errors, field errors, and tilt errors, can be evaluated from a beam physics perspective.
2. The optimal locations for correctors and BPMs that enable effective corrections can be identified.
3. A lattice ensemble can be created, and using this ensemble, the performance of the storage ring, such as dynamic aperture and Touschek lifetime, can be predicted within a statistical range.
4. Script files necessary for the commissioning process can be prepared, and potential trial-and-error issues that may arise during commissioning can be preemptively learned, allowing for faster commissioning.



<Figure 2.1.3.14> Correction chain of commissioning simulations for the Korea-4GSR storage ring.

For the commissioning simulation of 4GSR, the Toolkit for Simulated Commissioning (SC) tool was used. This tool, developed by T. Hellert and others at LBNL, is based on Accelerator Toolbox (AT) and the MATLAB Middle Layer (MML). It is currently being utilized for the commissioning simulations of most 4GSR facilities under construction. The tool provides functions and scripts necessary for corrections, such as trajectory correction, RF correction, orbit correction, and Linear Optics from Closed Orbits (LOCO), and it is expected to be useful during the actual commissioning process as well.

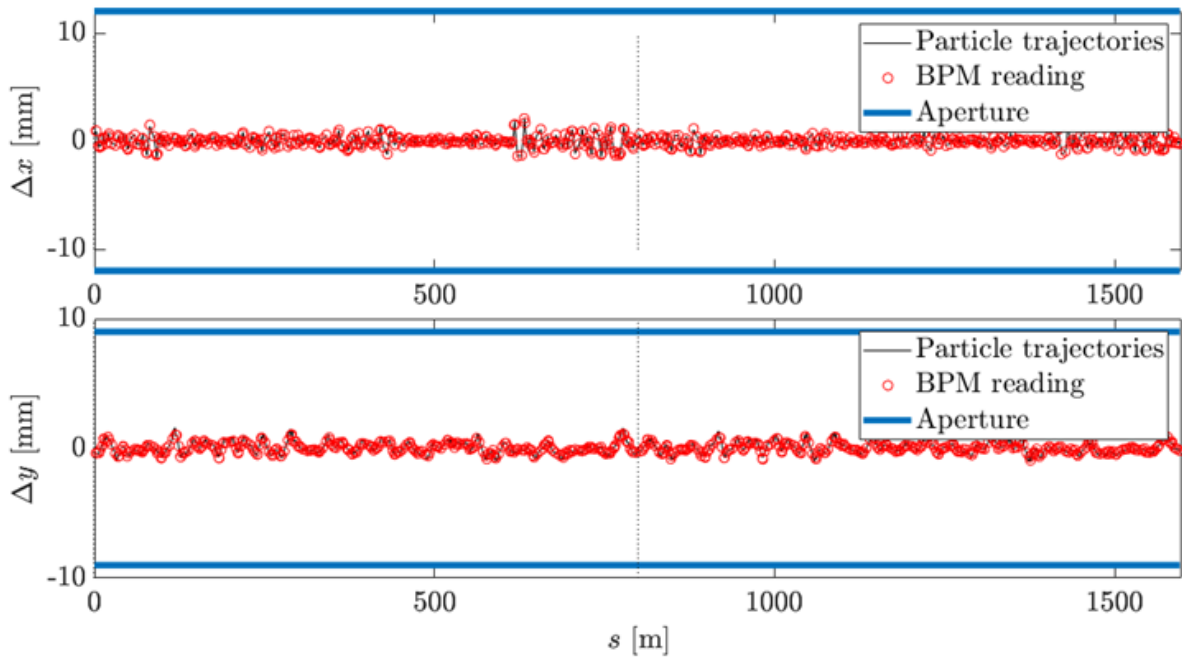
A schematic representation of the commissioning simulation process through SC is shown in <Figure 2.1.3.14>. In the AT environment, lattice information, including magnets, drifts, girders, and BPMs, is input, and error tolerance ranges, such as those provided in <Table 2.1.3.10> and <Table 2.1.3.11>, are assigned to each element (Lattice registration). Next, random errors with a Gaussian distribution are applied within the error tolerance range (Applying random errors). The correction process starts by turning off the main RF cavity, sextupoles, and octupoles (Turning off RF and sextupoles). By turning off the sextupoles, the strong orbit distortion effects caused by the sextupole magnets and their misalignment errors can be avoided, allowing for the stable identification of 1-turn and 2-turn trajectories.

The next step is to find the trajectory where the injected beam can survive after 1 or 2 turns in the storage ring (Finding 1-turn, 2-turn trajectory). During this process, the orbit response matrix (ORM) calculated from the ideal lattice and its inverse matrix are used. Beam-based alignment is then performed to reduce the offset between the BPM and the adjacent quadrupole magnets to approximately 50 μm RMS.

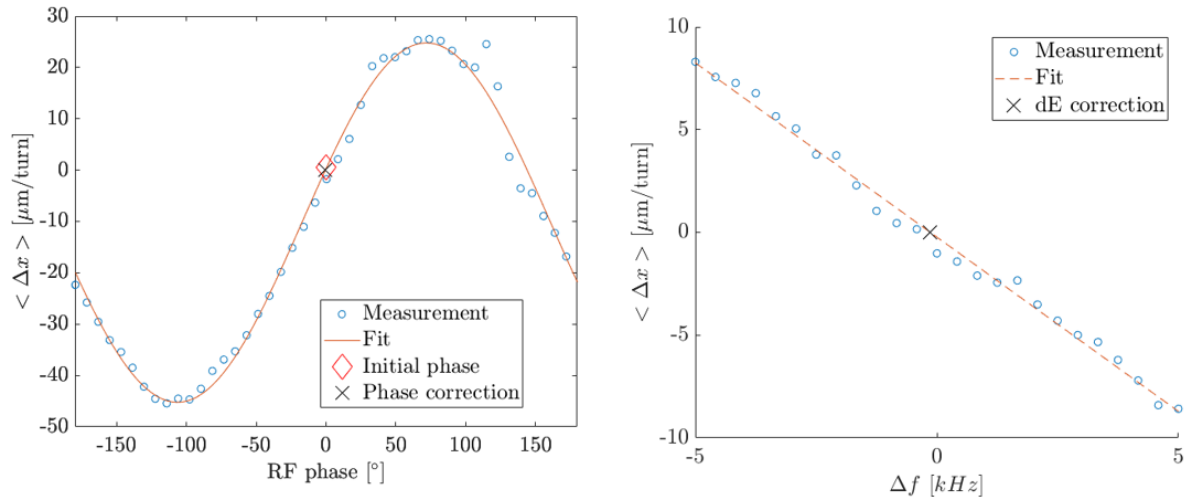
Following this, the strength of the sextupole and octupole magnets is gradually increased in 10 steps, each step increasing the strength by 1/10 of the design value. At each step, trajectory feedback is performed using the ORM of the ideal lattice, and the RF correction process is repeated several times to adjust the trajectory altered by the ramp-up of the sextupole and octupole magnets, ensuring the synchronous condition of the RF cavity. As the ramp-up proceeds, the tune may shift due to the quadrupole field created by the sextupole misalignment, potentially bringing the tune into contact with integer or half-integer resonances, making it difficult to find a stable trajectory. In such cases, trajectory feedback is performed using the inverse matrix of the ORM, or the tune is adjusted by modifying the strength of the matching quadrupoles in the HMBA cell. If there is no closed orbit and the tune cannot be calculated, tune adjustment is iteratively performed in the direction that increases beam transmission, assuming this moves away from bad resonances, until a stable

trajectory or orbit is found.

Next, the RF cavity is turned on, and beam-based RF correction is performed. Phase correction and frequency correction are iterated multiple times to ensure the beam is positioned at the synchronous phase in the longitudinal phase space. Phase correction involves scanning the phase within a range of $\pm 180^\circ$, assuming that the synchronous phase corresponds to the phase where the average value of all turn-by-turn BPM data per turn is 0. The effects of synchrotron motion are ignored by using the BPM data from the first 10 turns. For RF frequency correction, the frequency is scanned within a few kHz range, similarly assuming that the synchronous frequency corresponds to the frequency where the average value of all turn-by-turn BPM data per turn is 0. Using the first 12 turns of turn-by-turn BPM data, it was confirmed that the synchronous frequency could be reliably found.



<Figure 2.1.3.15> Example of trajectory correction.



<Figure 2.1.3.16> Example of RF correction: RF phase correction and RF frequency correction.

Once the sextupole ramp-up is completed and the closed orbit is found, key parameters of the storage ring, such as the periodic beta function values, tune, chromaticity, and emittance, can be obtained. Although the closed orbit can be found after the sextupole ramp-up, the closed orbit at this stage significantly deviates from the design orbit, so an orbit correction process is necessary to minimize the RMS orbit and achieve the desired storage ring parameters. In the orbit correction process, the orbit response matrix (ORM) is obtained by measuring the change in BPM readings in response to changes in correctors from the closed orbit obtained after the sextupole ramp-up. The inverse response matrix and the Singular Value Decomposition (SVD) method are then used to minimize the RMS BPM readings.

The orbit correction process is iterated within a loop that gradually decreases the Tikhonov regularization parameter from a large to a small value. The iteration continues until no further improvement in the RMS orbit is observed. If the strength of the correctors used in orbit correction approaches their mechanical limits during the loop, those correctors will be excluded from the next iteration, and the matrix columns corresponding to those correctors will no longer be used in the inverse matrix calculation. If the convergence of the RMS orbit is slow during the orbit correction process, the ORM can be remeasured to improve the efficiency of orbit correction at lower RMS orbits.

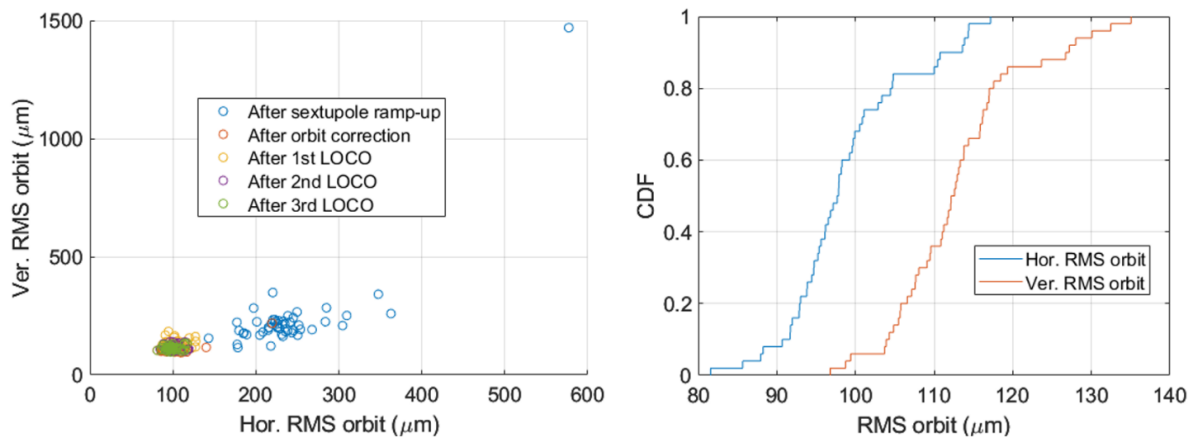
The next step is to perform Linear Optics from Closed Orbits (LOCO) to adjust key linear optics parameters such as tune, emittance, and beta-beat to be closer to the ideal lattice values. LOCO was performed three times. In the 1st LOCO, all pure quadrupoles (non-combined-

function magnets) were used, and in the 2nd and 3rd LOCO, all pure quadrupoles and skew magnets were used to adjust beta-beat and coupling.

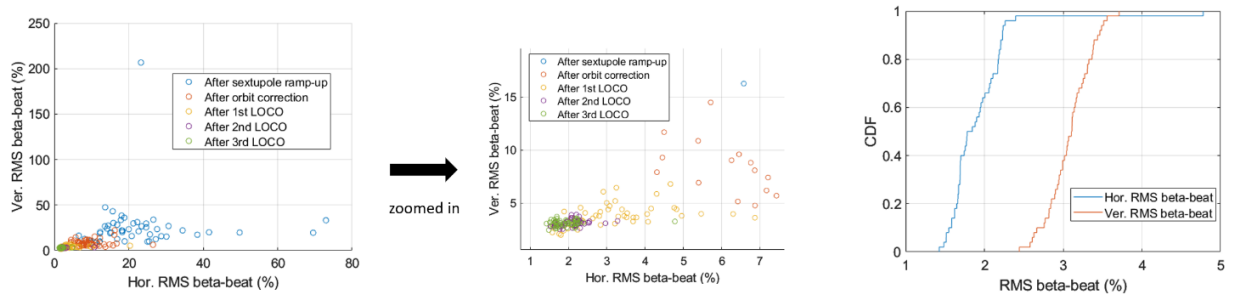
Finally, during the coupling correction process, the strength of the skew magnets is adjusted to set the coupling ratio to 10%. The change in beta-beat during this process is negligible, so there is no need to perform LOCO again. After the LOCO process, orbit correction is performed to restore the orbit that was disturbed by the LOCO process.

A lattice ensemble of 50 error lattices was generated using the error values provided in <Table 2.1.3.10>. The distribution and improvement of the RMS orbit, beta-beat, dispersion-beat, tune, chromaticity, emittance, dynamic aperture, and Touschek lifetime for each step of the correction chain are shown in <Figures 3.1.3.17-22>.

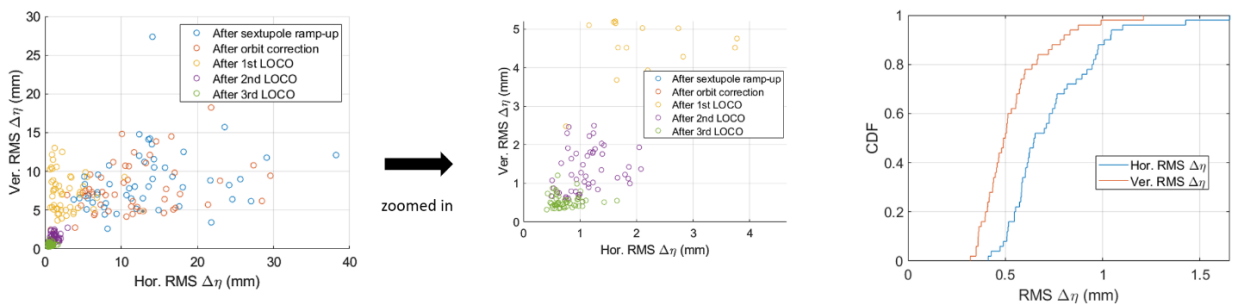
After the sextupole ramp-up, the RMS orbit is approximately 200–400 μm in both the horizontal and vertical directions, and after completing the entire correction chain, the RMS orbit is reduced to about 100 μm . The main improvement in the RMS orbit occurs during the orbit correction process (<Figure 2.1.3.17>).



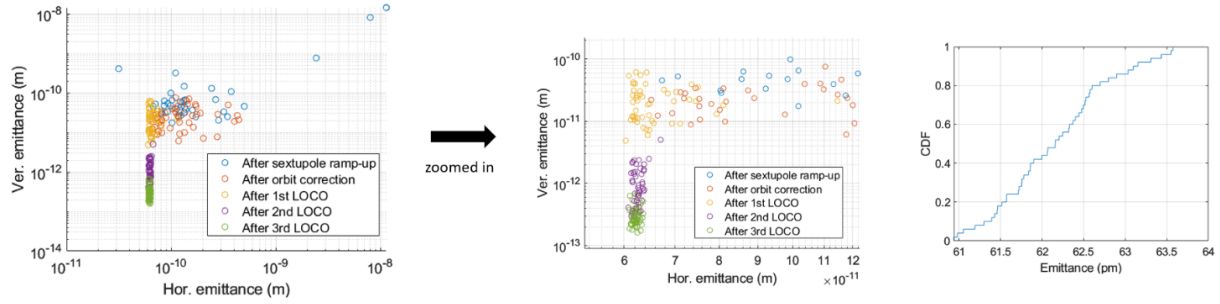
<Figure 2.1.3.17> RMS orbit of the lattice ensemble for each correction step (left) and cumulative distribution function of RMS orbit after correction is done (right).



<Figure 2.1.3.18> Beta-beat of the lattice ensemble for each correction step (left) and cumulative distribution function of beta-beat after correction is done.



<Figure 2.1.3.19> Dispersion-beat of the lattice ensemble for each correction step (left) and cumulative distribution function of dispersion-beat after correction is done.

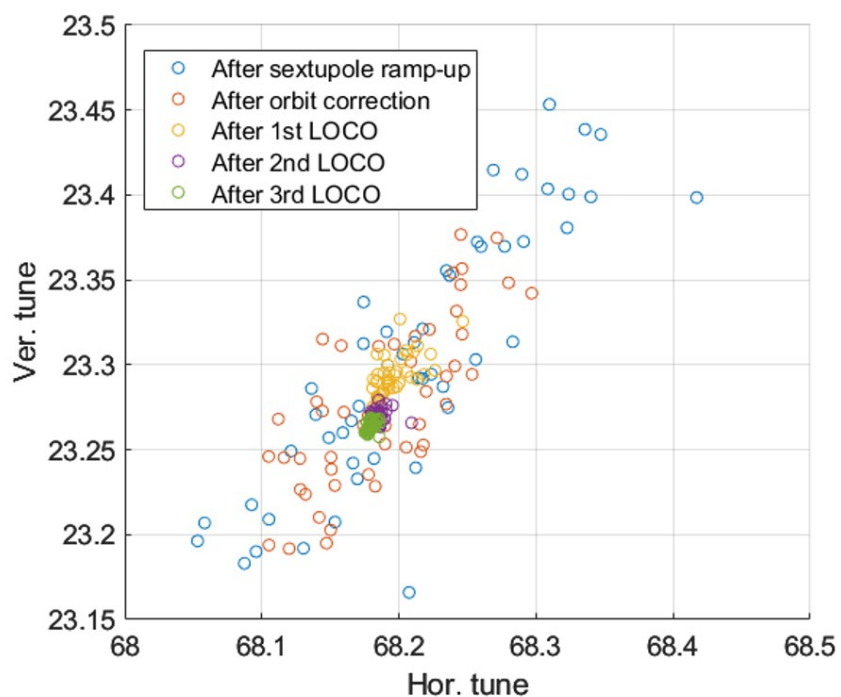


<Figure 2.1.3.20> Emittance of the lattice ensemble for each correction step (left) and cumulative distribution function of emittance after correction is done.

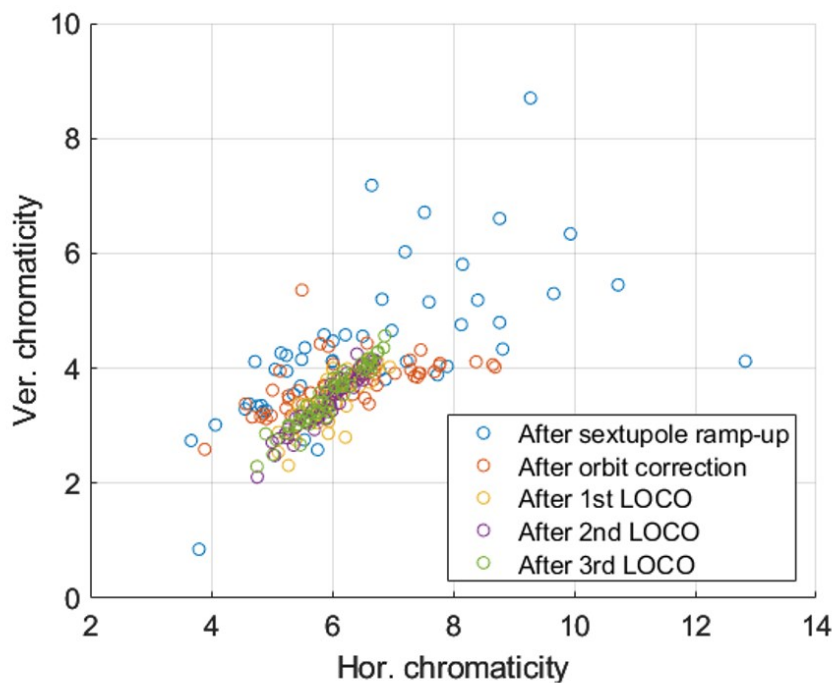
The beta-beat shows a wide distribution, reaching up to 200% after the sextupole ramp-up. After orbit correction, it improves to below 10%, and ultimately improves to about 2% in the horizontal direction and 3% in the vertical direction (<Figure 2.1.3.18>).

The dispersion-beat shows a distribution similar to that of the beta-beat. After correction, the results show a distribution ranging from 0.3 mm (best case) to 1.5 mm (worst case) (<Figure 2.1.3.19>).

In the case of emittance, its value changes significantly depending on the correction step. After the sextupole ramp-up, the horizontal emittance in the worst case was as large as 10 nm. After orbit correction, it improved significantly to 120 pm in the worst case. After the 3rd LOCO, the worst case emittance is about 2.5% larger than the design emittance. For vertical emittance, the value is about 10 pm after the 1st LOCO and below 1 pm after the 2nd LOCO (<Figure 2.1.3.20>).



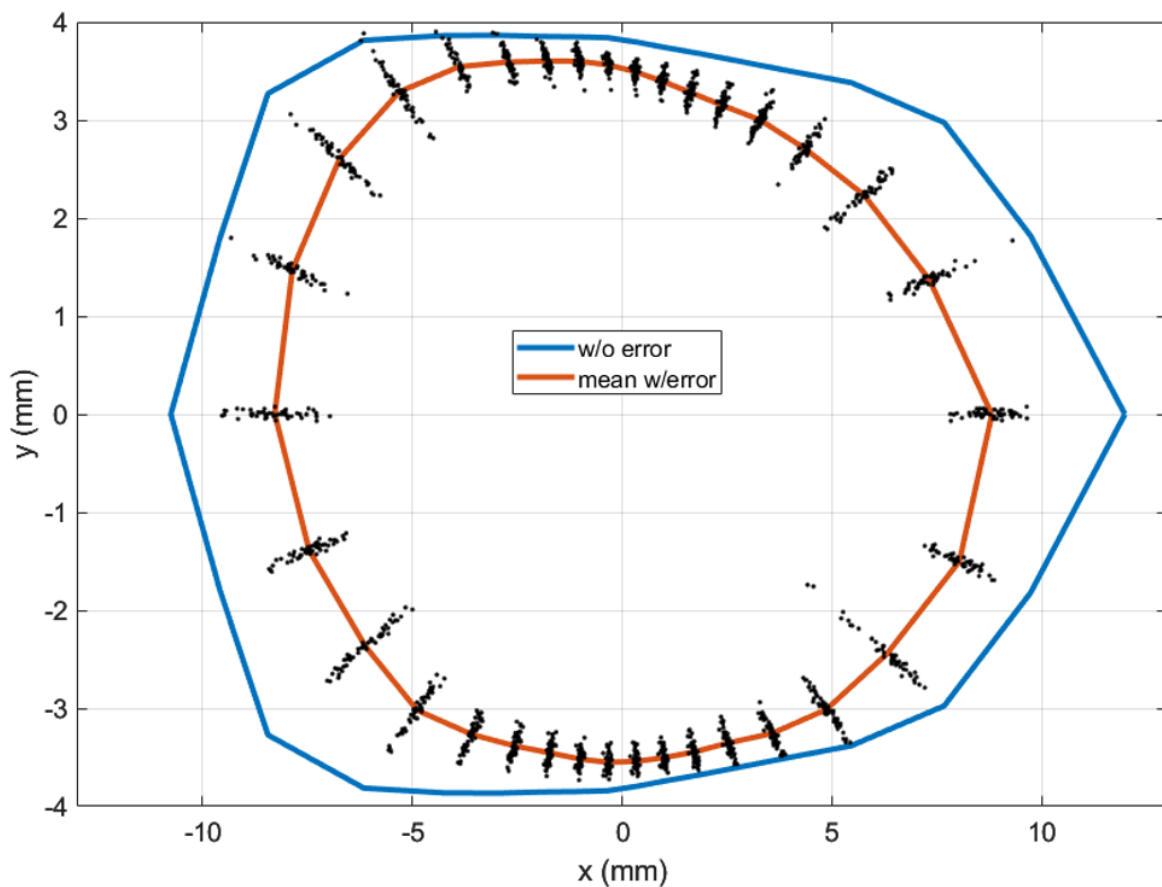
<Figure 2.1.3.21> Tune of the lattice ensemble for each correction step.
Design tune is (68.18, 23.26).



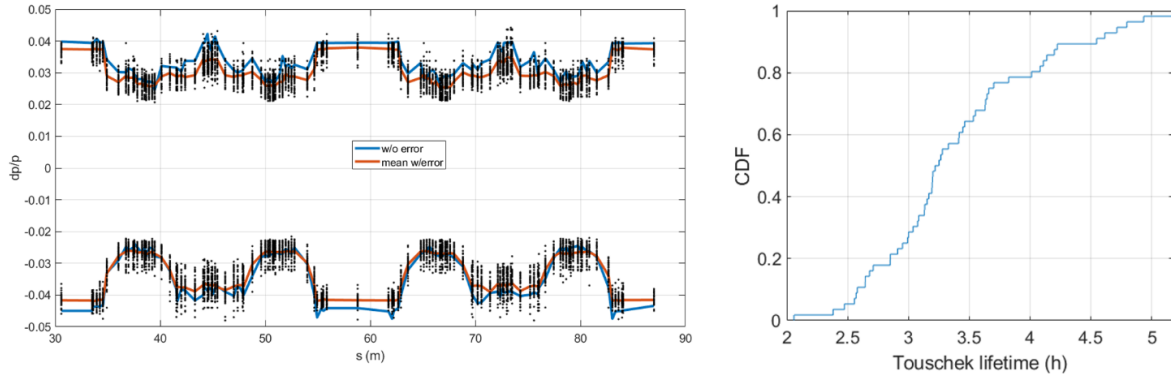
<Figure 2.1.3.22> Chromaticity of the lattice ensemble for each correction step.
Design chromaticity is (5.8, 3.5).

In the case of tune, after the sextupole ramp-up, it shows a wide distribution, ranging from 0.05 to 0.42 in the horizontal direction and from 0.15 to 0.46 in the vertical direction. After orbit correction, the tune distribution shows improvement. The result of tune improvement through orbit correction without changing the quadrupole strength indirectly reflects the sensitivity and impact on storage ring parameters when the closed orbit significantly deviates from the center of high-order magnets like sextupoles and octupoles (<Figure 2.1.3.21>). Once the corrections are completed, the tune converges to the design tune value.

Similarly, chromaticity shows significant improvement after orbit correction and continues to converge around the design chromaticity as the correction chain progresses. Although the distribution of chromaticity has a wider spread compared to the tune distribution after correction, this is understandable, as the sextupole strength was not used as a variable during the LOCO process (<Figure 2.1.3.22>). Afterward, the sextupole strength can be adjusted as needed to further fine-tune the chromaticity to match the design values.



<Figure 2.1.3.23> Dynamic aperture of the lattice ensemble after correction is done.



<Figure 2.1.3.24> Momentum aperture of the lattice ensemble (left) and cumulative distribution function of Touschek lifetime after correction is done

The results of the dynamic aperture calculation at the center of the high-beta straight section for 50 random error seeds after correction are shown in <Figure 2.1.3.23>. Tracking was performed for 2048 turns after assigning a physical aperture of 12 mm in the horizontal direction and 9 mm in the vertical direction to all drift spaces and magnets. The average dynamic aperture for the 50 random error seeds is -8.28 mm at the position where $y = 0$, with a standard deviation of 0.62 mm, a minimum of -6.96 mm, and a maximum of -9.53 mm. These results indicate that, after correction, the lattice has a dynamic aperture large enough to allow for off-axis injection.

The results of the momentum aperture and Touschek lifetime calculations for the 50 random error seeds after correction are shown in <Figure 2.1.3.24>. The Touschek lifetime was calculated under the condition of a single bunch with a charge of 1 nC and an RMS bunch length of 3.66 mm. The bunch lengthening effect due to the harmonic cavity was not considered. Under the 10% coupling condition, the Touschek lifetime for the ideal lattice is 7.30 hours. For the corrected lattice ensemble, the Touschek lifetime has an average of 5.18 hours with a standard deviation of 0.64. Since the Touschek lifetime is proportional to the cube of the momentum aperture width, it is highly sensitive to the reduced momentum aperture caused by errors, and the Touschek lifetime values for the lattice ensemble show a wide distribution.

References

- [1] Terebilo, in Proceedings of the 19th Particle Accelerator Conference, Chicago, IL, 2001 (IEEE, Piscataway, NJ, 2001), pp. 3203-3205.
- [2] T. Hellert et al., "Lattice correction and commissioning simulation of the Advanced Light Source upgrade storage ring", Phys. Rev. Accel. Beams 25/110701, 2022.
- [3] G. Penn et al., "Comparisons Between AT and Elegant Tracking", in Proc. of 12th Int. Particle Accelerator Conf. (IPAC'21): Campinas, Brazil, 2021.
- [4] T. Hellert et al., "Toolkit for simulated commissioning of storage-ring light sources and application to the advanced light source upgrade accumulator", Phys. Rev. Accel. Beams 22/100702, 2019.
- [5] V. Sajaev, "Commissioning simulations for the Argonne Advanced Photon Source upgrade lattice", Phys. Rev. Accel. Beams 22/040102, 2019.

I. Orbit stability

Orbit stability is a critical performance metric in low-emittance storage rings, directly impacting beam quality, experimental resolution, and overall facility reliability. In 4GSRs, the stringent requirements for beam stability demand careful evaluation and control of all perturbation sources. Even nanometer-scale orbit fluctuations can degrade photon beam coherence and compromise the performance of high-precision beamlines.

This study was undertaken to systematically identify and quantify the primary contributors to orbit instability in Korea-4GSR. The scope of the analysis includes transverse and longitudinal orbit disturbances arising from mechanical vibration, current ripple in magnet power supplies, and RF system errors. These sources were selected based on their relevance to low emittance rings and their potential to introduce time-dependent orbit deviations.

The study combines analytical modeling with tracking simulations to evaluate orbit jitter under realistic operating conditions, including the presence of harmonic RF cavities and quantum excitation effects. The target orbit stability for Korea-4GSR is set to 10% of the beam size which is 1,923 nm in horizontal plane, 408 nm in vertical plane. This benchmark reflects international standards for 4GSRs and ensures compatibility with advanced beamline instrumentation. The results presented in this chapter provide a foundation for future mitigation strategies and system optimization to meet this demanding specification.

○ Vibration

Ground vibration is one of the principal external disturbance sources that can compromise beam orbit stability in low-emittance storage rings. Even sub-micron displacements of magnetic elements can induce significant orbit distortions at beamline source points, thereby degrading the effective brightness and coherence of the photon beam.

In this study, orbit stability under ground vibration was evaluated using the relation

$$x_{orbit} = x_{ground} \times G_{girder} \times G_{orbit} \quad (\text{Eq. 2.1.3.21})$$

where x_{ground} is the measured ground displacement, G_{girder} is the girder amplification factor, and G_{orbit} is the orbit amplification factor derived from the lattice optics. For conservative estimation, the girder amplification factor was assumed to be unity across all frequencies.

The ground vibration spectrum was obtained via direct power spectral density (PSD) measurements at a representative site location. Only the vertical component was measured; the horizontal vibration spectrum was assumed to be identical, reflecting current limitations of the measurement apparatus. A new instrument capable of simultaneous three-dimensional vibration measurements is planned for future deployment, and horizontal vibration data will be updated accordingly.

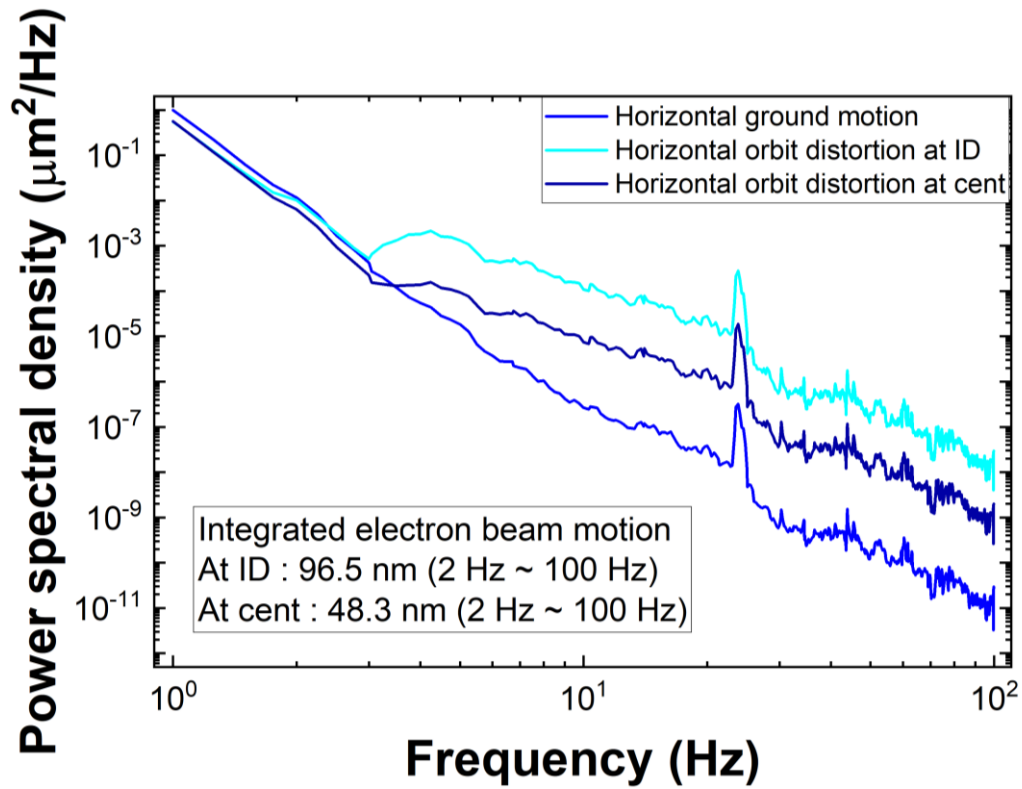
To extend the single-point PSD measurement into the entire storage ring, spatial coherence of ground motion was introduced [1,2,3]. Ideally coherence length should be derived from multi-point simultaneous measurements, which have not yet been conducted at the Korea-4GSR site. Therefore, coherence properties measured at APS were adopted as a reference [1]. The horizontal and vertical coherence lengths were modeled as

$$L_x(f) = \frac{100}{f^{1.1}}, \quad L_y(f) = \frac{125}{f^{1.4}} \quad (\text{Eq. 2.1.3.22})$$

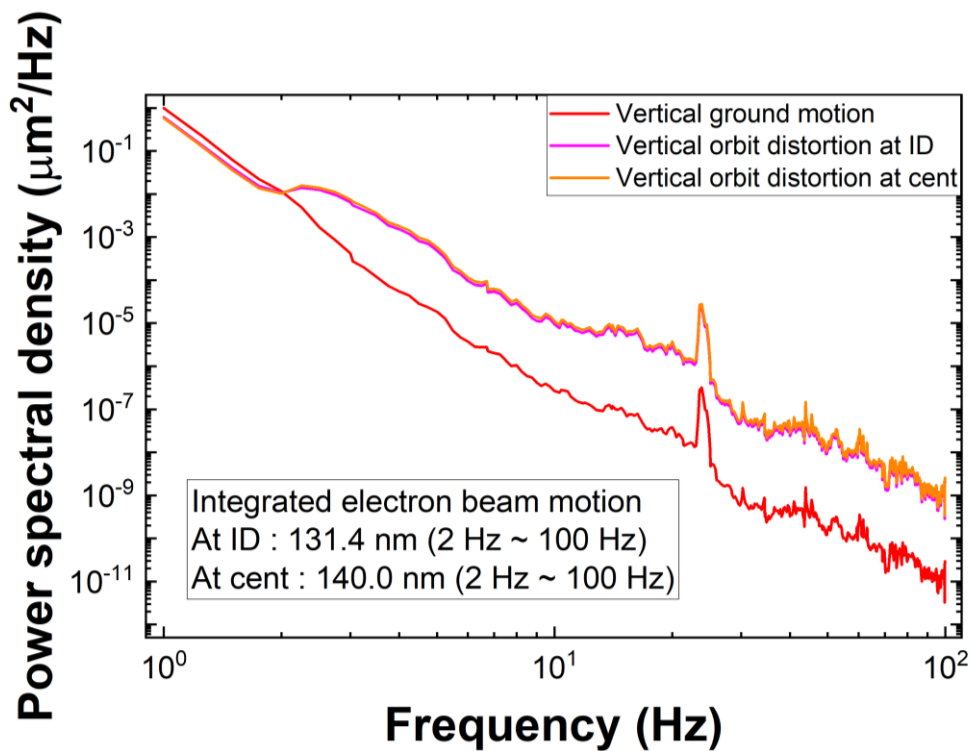
where f is the vibration frequency in Hz.

The simulation procedure began with the random initialization of a displacement field on a reference grid along the ring circumference, representing uncorrelated white noise. The field was transformed into frequency space using a discrete Fourier transform. In the spectral domain, a low-pass filter was applied to impose spatial coherence at each vibration frequency. The cutoff wavenumber was determined from the frequency-dependent coherence lengths, which define the correlation scale of ground motion in both planes. Spectral components above the cutoff were attenuated, yielding a filtered field with appropriate spatial correlation. An inverse Fourier transform was then applied to return the displacement field to real space.

The resulting displacement field was interpolated from the reference grid to the exact longitudinal positions of lattice elements. Each interpolated displacement was subsequently rotated into the local coordinate system of the element, ensuring proper orientation of misalignment. These element-specific displacements were then applied as misalignment errors in the lattice model, and the corresponding closed-orbit distortion was estimated as a function of frequency. By repeating this process across the relevant frequency range and integrating the results, the RMS orbit jitter was obtained.



<Figure 2.1.3.25> Power spectral density of horizontal ground motion and orbit distortion at different locations.



<Figure 2.1.3.26> Power spectral density of vertical ground motion and orbit distortion at different locations.

The integrated orbit distortion from ground vibration, evaluated over the 2-100 Hz frequency range, was found to be 96.5 nm at the IDs and 48.3 nm at the center bending

magnets in the horizontal plane, while the corresponding values in the vertical plane were 131.4 nm at the IDs and 140.0 nm at the center bending magnets. The lower cutoff at 2 Hz was selected because the current measurement device shows poor resolution at very low frequencies, making it difficult to distinguish true ground motion from background noise, while contributions above 100 Hz are negligible due to the intrinsically small vibration amplitudes. In this study, the girder amplification factor was conservatively assumed to be unity; however, in practice the amplification factor is typically less than one in the low-frequency region. Since the low-frequency contribution dominates the integrated vibration, the actual RMS orbit jitter is expected to be smaller than the values demonstrated here.

○ Current ripple

Current ripple in magnet power supplies is a notable source of beam orbit stability in low-emittance storage rings. These fluctuations introduce perturbation to the closed orbit of the stored beam. To evaluate this effect at Korea-4GSR, the orbit displacement was modeled using the relation

$$x_{orbit} = I_{ripple} \times A_{attenuation} \times G_{orbit} \quad (\text{Eq. 2.1.3.23})$$

where I_{ripple} is the relative current ripple, $A_{attenuation}$ is the attenuation factor as a function of ripple frequency, and G_{orbit} is the orbit amplification factor derived from the lattice optics.

In this study, the definition of ripple was tailored to reflect the operational characteristics of different magnet types. For main magnets such as dipoles and quadrupoles, ripple was defined as the deviation relative to the nominal operating current. However, for corrector magnets—whose operating currents vary and lack a clearly defined nominal value—the ripple was defined as the deviation relative to the maximum rated current. This approach ensures a consistent and conservative basis for analysis. Representative ripple levels were adopted based on surveys of similar facilities [3]: 50 ppm for corrector magnets and 10 ppm for main magnets.

<Table 2.1.3.14> Current ripple according to magnet types

Magnet type	Current ripple [ppm]
Corrector	50
Quadrupole	10
Sextupole	-
Combined magnet (DQ51)	10
Reverse bending magnet	10
Longitudinal gradient bending magnet	10
Center bending magnet	10

The attenuation factor accounts for the suppression of high-frequency ripple components due to the electromagnetic response of the magnet system. It comprises two distinct contributions: one from the vacuum chamber and the other from the magnet yoke. Chamber attenuation arises primarily from eddy currents induced in the conductive chamber walls and is modeled analytically using the expression [4]

$$B_{int}(t) = \frac{B_0}{\sqrt{1+(w\tau)^2}} \sin(wt - \tan^{-1}(w\tau)), \quad \tau = \frac{1}{2}\mu_0\sigma_c b d \quad (\text{Eq. 2.1.3.24})$$

where is $B_{int}(t)$ is the attenuated field inside the chamber, w is the ripple frequency, μ_0 is the permeability of free space, σ_c is the conductivity of the chamber material, b is the beam pipe radius, and d is the wall thickness. For Korea-4GSR, the chamber parameters are: $\sigma_c = 2.5 \times 10^7 \frac{1}{\Omega \cdot m}$, $b = 9.0 \text{ mm}$, and $d = 2.5 \text{ mm}$.

Attenuation due to the magnet yoke is more complex and cannot be readily described by analytical expressions. Accurate estimation requires detailed electromagnetic simulations using finite-element tools such as OPERA. As such simulations have not yet been conducted for Korea-4GSR, a constant yoke attenuation factor of 0.35 was conservatively assumed across all frequencies. This assumption reflects typical values observed in similar magnet systems and provides a practical basis for preliminary orbit jitter estimation.

The orbit amplification factor was calculated using the lattice optics and accounts for both geometric misalignment and field errors induced by current ripple. The dominant sources of orbit distortion are quadrupole misalignments and dipole field deviations. In the context of current ripple, these manifest as time-dependent variations in magnetic field strength: ripple in quadrupole magnets alters the focusing strength, leading to differential kicks that distort

the closed orbit, while ripple in dipole magnets directly modifies the bending field, shifting the beam trajectory. These effects are amplified by the lattice optics, particularly in regions of high beta function or dispersion, and are captured quantitatively through the orbit amplification formalism.

<Table 2.1.3.15> Operating angle for various type of magnets (or maximum angle for correctors).

Magnet type	Horizontal angle [mrad]	Vertical angle [μrad]
Corrector	0.400	0.400
Combined magnet (DQ51)	34.728	34.728
Reverse bending magnet (DQ31)	-2.4	-2.4
Reverse bending magnet (DQ32)	-1.49	-1.49
Reverse bending magnet (DQ52)	-7.8	-7.8
LGBM1	41.690	41.690
LGBM2	33.564	33.564
Center bending magnet	27.800	27.800

<Table 2.1.3.16> Assumed rms orbit for calculating the orbit distortion from quadrupole misalignment

Plane	RMS orbit [μm]
Horizontal	110
Vertical	130

The rms orbit distortion can be calculated using

$$x_{rms}^2 = A_{\Delta x}^2 \sigma_{\Delta x}^2 + A_{\Delta B/B}^2 \sigma_{\Delta B/B}^2 \theta^2 \quad (\text{Eq. 2.1.3.25})$$

where $A_{\Delta x}^2$ is the orbit amplification factor from quadrupole misalignment, $A_{\Delta B/B}^2$ is the amplification factor from dipole field strength error, $\sigma_{\Delta x}^2$ is the rms misalignment, $\sigma_{\Delta B/B}^2$ is the field strength error and θ is the operational kick angle. For corrector magnets, θ is the maximum kick angle. The field strength error induced by current ripple can be decomposed into its constituent components: the relative current ripple and the attenuation effects of both the vacuum chamber and the magnet yoke. This relationship is expressed as

$$\sigma_{\Delta B/B}^2 = \sigma_{\Delta I/I}^2 \times A_{chamber} \times A_{yoke} \quad (\text{Eq. 2.1.3.26})$$

Substituting this into the general expression for orbit distortion, the rms orbit displacement becomes

$$x_{rms}^2 = \left(\frac{N\beta_i}{8 \sin^2 \pi v} k_{operation}^2 L^2 \sigma_{\Delta x}^2 + \frac{N\beta_i}{8 \sin^2 \pi v} \times A_{chamber} \times A_{yoke} \theta^2 \right) \sigma_{\Delta I/I}^2 \quad (\text{Eq. 2.1.3.27})$$

where $\sigma_{\Delta x}^2$, θ , $\sigma_{\Delta I/I}^2$ represent the rms misalignment, the operational kick angle, and the rms current ripple, respectively. These values are tabulated in <Tables 2.1.3.16>, <Table 2.1.3.17>, and <Table 2.1.3.14>. The resulting orbit jitter, calculated using these parameters, is summarized in Table <2.1.3.17>.

<Table 2.1.3.17> Orbit stability from current ripple

Magnet type	x at ID [nm]	y at ID [nm]	x at cent [nm]	y at cent [nm]
Corrector	370.8	239.4	87.8	262.4
Quadrupole	12.1	11.0	2.9	12.0
Reverse bending magnet	591.1	7.9	140.0	8.7
Combined magnet	870.7	7.4	206.3	8.1
Center bending magnet	509.3	0.8	120.7	0.9
Longitudinal gradient bending magnet	2022.9	3.3	479.2	3.7
Total with LGBM	2365.7	239.9	560.5	262.9
Total without LGBM	1226.7	239.9	290.6	262.9

Among the various magnet types, the LGBM was identified as the primary contributor to horizontal orbit distortion. This is due to its large bending angle, which amplifies the effect of a given relative field error. Even a small ripple-induced deviation in the LGBM's field strength results in a substantial horizontal kick, making it the most sensitive element in the horizontal plane. In contrast, the vertical orbit distortion is dominated by the corrector magnets. While vertical kicks can arise from dipole tilting, quadrupole misalignment, and corrector field errors, the latter was found to be the most significant contributor. This is because the vertical steering function is highly sensitive to variations in corrector strength, and the assumed 50 ppm ripple in these magnets leads to relatively large vertical orbit excursions.

Despite this, the overall vertical orbit disturbance remains sufficiently small to satisfy the design requirements of Korea-4GSR. For horizontal stability, however, further improvements may be considered. Employing more sensitive and stable MPS for the LGBM would directly reduce horizontal orbit jitter. Alternatively, replacing the LGBM with a permanent magnet version could eliminate current ripple altogether, though this would require careful thermal and field tuning to maintain operational flexibility. These mitigation strategies, combined with future ripple measurements and electromagnetic simulations, will be essential for achieving the stringent orbit stability goals of the storage ring.

○ Energy oscillation

Energy oscillation in storage rings arises primarily from perturbations in the RF system, specifically RF phase errors and RF voltage fluctuations. These errors act as external driving forces on the longitudinal beam dynamics, which can be modeled as a damped harmonic oscillator. The longitudinal motion of particles in the phase space resembles a damped oscillation, and RF errors introduce periodic driving forces that excite energy oscillations.

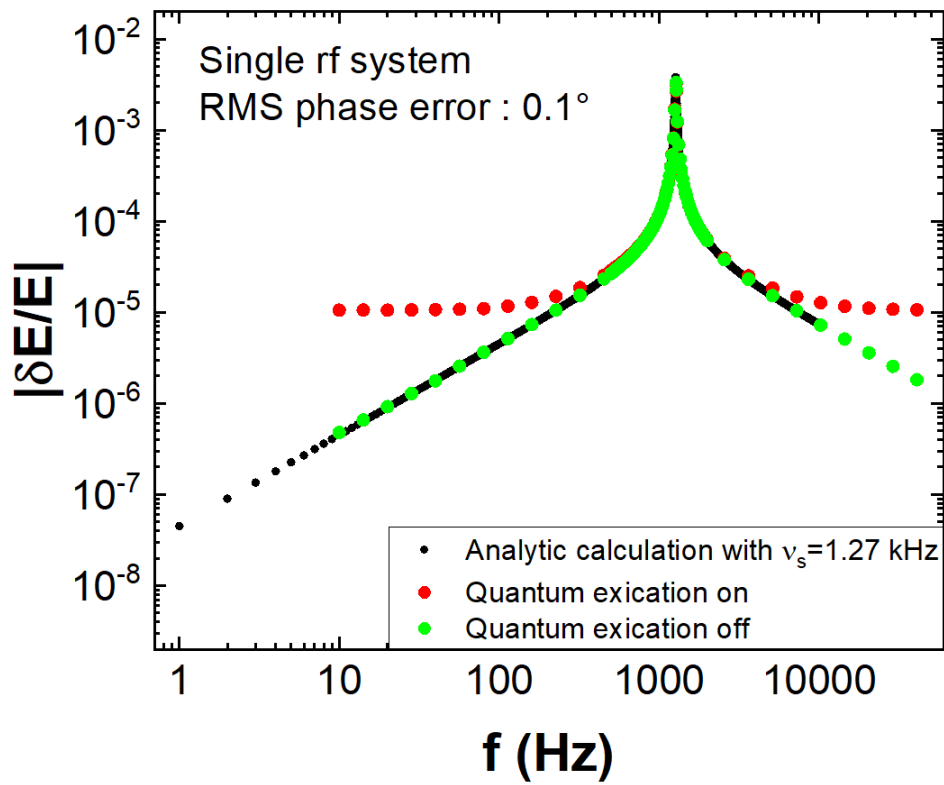
The general solution for a driven damped harmonic oscillator is well known and given by

$$\frac{A}{F_0/m} = \frac{1}{\sqrt{(w_0^2 - w^2)^2 + (\frac{ww_0}{Q})^2}}, Q = \frac{mw_0}{b} \quad (\text{Eq. 2.1.3.28})$$

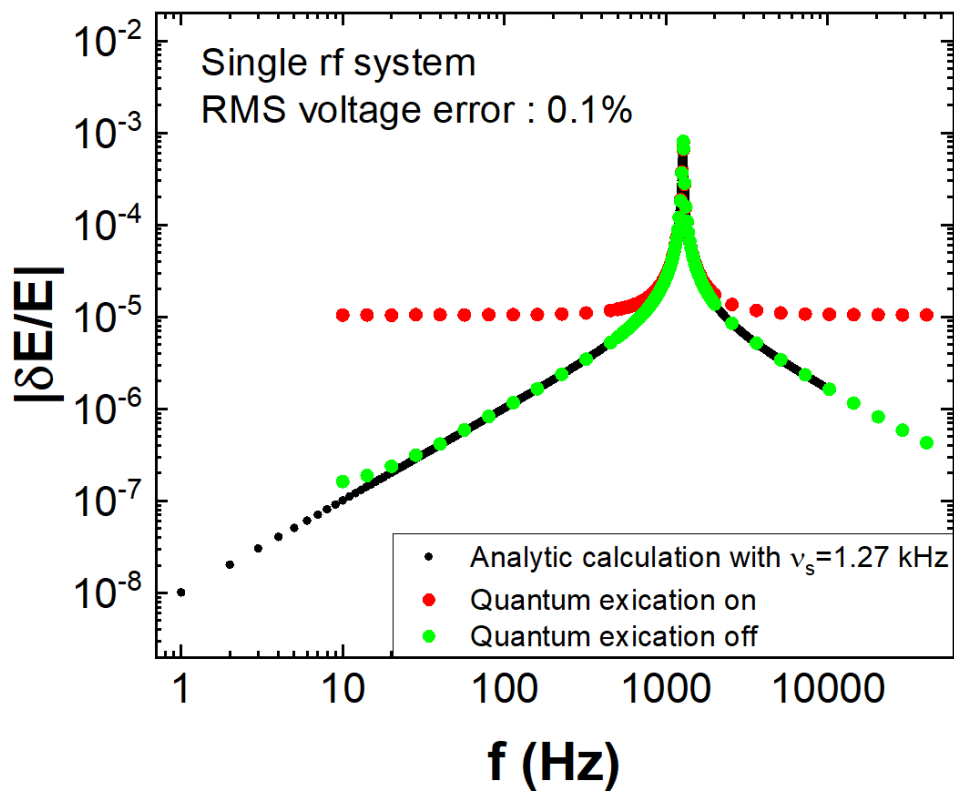
where A is the oscillation amplitude, F_0 is the driving force amplitude, m is the effective mass, w_0 is the natural frequency (synchrotron frequency), w is the driving frequency, Q is the quality factor representing damping, and b is the damping coefficient. Analogously, the beam's response to RF excitation can be described by [5,6].

$$x_{rms} = \left| \frac{\delta E}{E} \right| \eta_x = \frac{w_s^2}{\sqrt{(w_s^2 - w_{mod}^2)^2 + \left(\frac{2w_{mod}}{\tau_\delta} \right)^2}} \frac{w_{mod} \eta_x}{\alpha_c w_{rf}} |\Delta \phi_{RF, noise}| \quad (\text{Eq. 2.1.3.29})$$

where $\left| \frac{\delta E}{E} \right|$ is the energy oscillation, η_x is the dispersion, w_s is the synchrotron oscillation, w_{mod} is the RF error modulation frequency, w_{rf} is the main RF frequency, α_c is the momentum compaction factor, τ_δ is the longitudinal damping time, and $|\Delta \phi_{RF, noise}|$ is the amplitude of rf phase error. Since RF phase and voltage errors affect the beam similarly, voltage-induced energy oscillation was analyzed using the same framework, with the exception of a scaling factor involving $\tan \varphi_{synch}$.



<Figure 2.1.3.27> Energy oscillation amplitude as a function of RF phase error frequency with rms 0.1° phase error amplitude.

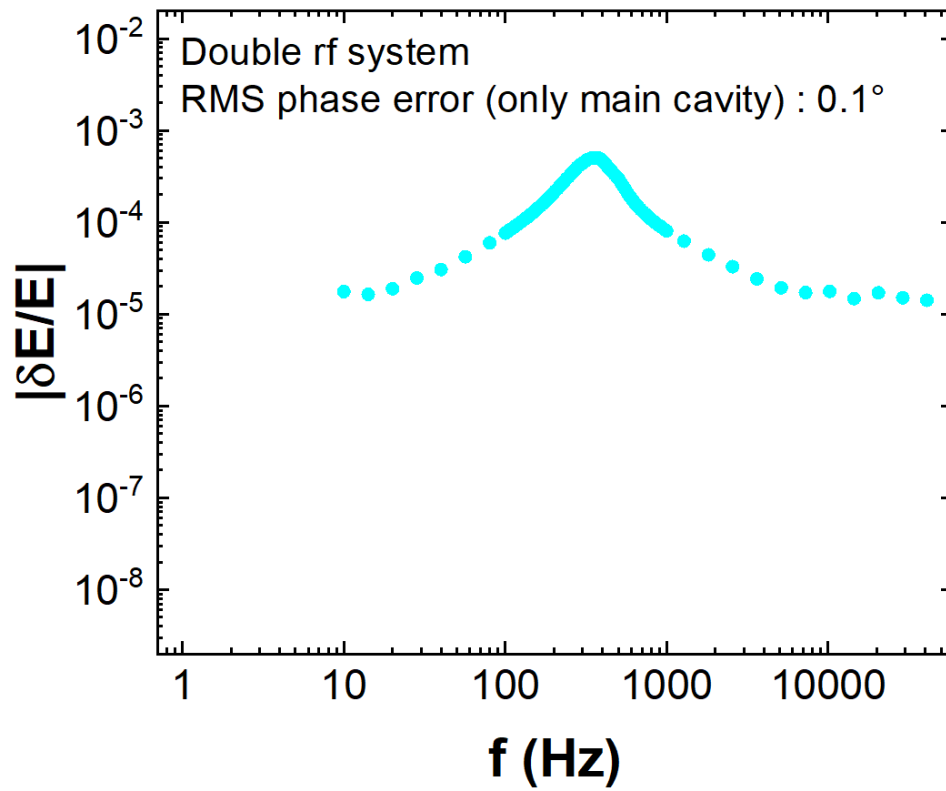


<Figure 2.1.3.28> Energy oscillation amplitude as a function of RF voltage error frequency with rms 0.1% voltage error amplitude.

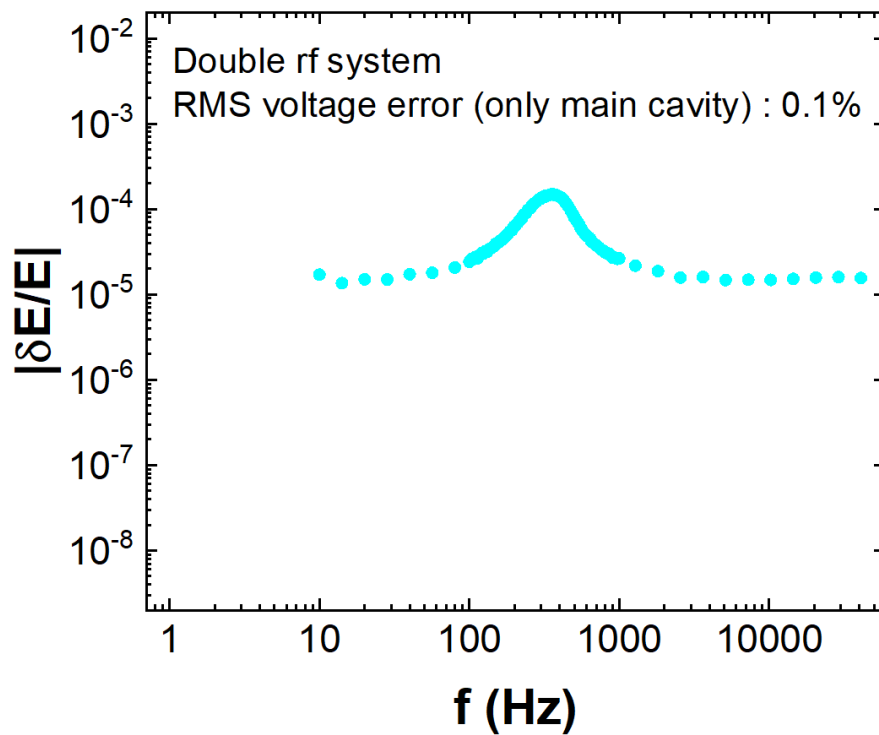
<Figure 2.1.3.27> and <Figure 2.1.3.28> illustrate the energy oscillation amplitude as a function of RF phase and voltage error frequency, respectively, assuming RMS error amplitudes of 0.1° and 0.1%. Three cases were compared: analytical calculation, simulation with quantum excitation off, and simulation with quantum excitation on. The analytical model, which excludes quantum excitation, closely matches the simulation results when quantum excitation is disabled. In contrast, simulations with quantum excitation enabled show larger oscillation amplitudes, especially at modulation frequencies far from the synchrotron frequency. This comparison confirms the analytical model's validity under idealized conditions and underscores the importance of including quantum effects in realistic simulations.

When multiple RF cavities are used—such as a main RF cavity combined with a harmonic cavity—the longitudinal dynamics become significantly more complex. The presence of two RF systems modifies and broadens the synchrotron frequency spectrum. Moreover, in a dual-RF configuration, the synchrotron frequency becomes amplitude-dependent (i.e., it varies with longitudinal action), rendering the linear harmonic approximation invalid.

As a result, tracking simulations are essential for accurately evaluating orbit stability under RF error conditions in two-cavity systems. These simulations were conducted across a range of driving frequencies to assess beam sensitivity to RF noise. In realistic harmonic cavity configurations, additional factors such as cavity impedance, beam loading, and RF feedback loops further complicate the dynamics—especially when the harmonic cavity operates in passive mode, making it difficult to define RF error tolerances. However, for the purpose of analyzing energy oscillation, only the RF potential was considered, excluding these effects. This simplification is justified not only because impedance-related effects are not expected to be dominant contributors to longitudinal oscillation amplitude, but also because the harmonic cavity lowers the synchrotron frequency, bringing it closer to the frequency range where RF noise tends to be most pronounced. This shift increases the system's sensitivity to phase and voltage errors, making the harmonic cavity configuration more vulnerable to noise-induced energy oscillation. Therefore, the analysis focused on the main RF cavity error, providing a conservative and representative estimate of orbit disturbance under realistic conditions.



<Figure 2.1.3.29> Energy oscillation amplitude as a function of RF phase error frequency with rms 0.1° phase error amplitude with harmonic cavity.



<Figure 2.1.3.30> Energy oscillation amplitude as a function of RF voltage error frequency with rms 0.1% voltage error amplitude with harmonic cavity.

Although direct measurements of RF noise spectra are not yet available for Korea-4GSR, the RF group has recently begun measuring the PSD. Due to time constraints, this data could not be incorporated into the current report. Preliminary findings indicate that the dominant RF noise components lie below 200 Hz, and within this range, 200 Hz is the closest to the synchrotron frequency. Based on this observation, a 200 Hz single-frequency condition was selected for conservative calculation. In the absence of full PSD data, the RF group's target tolerance values—0.1° phase error and 0.1% voltage error—were used to estimate the orbit disturbance under realistic operating conditions. Under this assumption, the orbit disturbance was calculated for both phase and voltage errors. The results are summarized in <Table 2.1.3.18>.

<Table 2.1.3.18> Orbit stability from energy oscillation

Parameters	Without harmonic cavity		With harmonic cavity	
	0.1° phase error	0.1% voltage error	0.1° phase error	0.1% voltage error
$\left \frac{\delta E}{E} \right $	9.21×10^{-6}	2.07×10^{-6}	2.05×10^{-4}	6.23×10^{-5}
x_{rms}	18.42 nm	4.15 nm	410.95 nm	124.59 nm
y_{rms}	9.21 nm	2.07 nm	205.48 nm	62.30 nm

○ Total orbit stability

To evaluate the overall orbit stability of Korea-4GSR, the contributions from vibration, current ripple, and energy oscillation were combined using rms summation

$$x_{rms,total} = \sqrt{x_{rms,vibration}^2 + x_{rms,ripple}^2 + x_{rms,energy\ oscillation}^2} \quad (\text{Eq. 2.1.3.30})$$

where $x_{rms,vibration}$ is the rms orbit stability from vibration, $x_{rms,ripple}$ is that from current ripple, $x_{rms,vibration}$ that from energy oscillation. This method assumes that each error source is statistically independent, which is a reasonable approximation given their distinct physical origins and temporal characteristics.

<Table 2.1.3.19> Total orbit stability

Error source	x_{rms} at ID	y_{rms} at ID	x_{rms} at cent	y_{rms} at cent
Vibration	96.5 nm	131.4 nm	87.8 nm	140.0 nm
Current ripple	1226.7 nm	239.9 nm	290.6 nm	262.9 nm
Energy oscillation without HC	18.88 nm	9.44 nm	18.88 nm	9.44 nm
Energy oscillation with HC	429.42 nm	214.72 nm	429.42 nm	214.72 nm
Total without HC	1231 nm	274 nm	304 nm	298 nm
Total with HC	1303 nm	348 nm	526 nm	367 nm
Stability requirement	1923.0 nm	408.2 nm	463.1 nm	453.9 nm

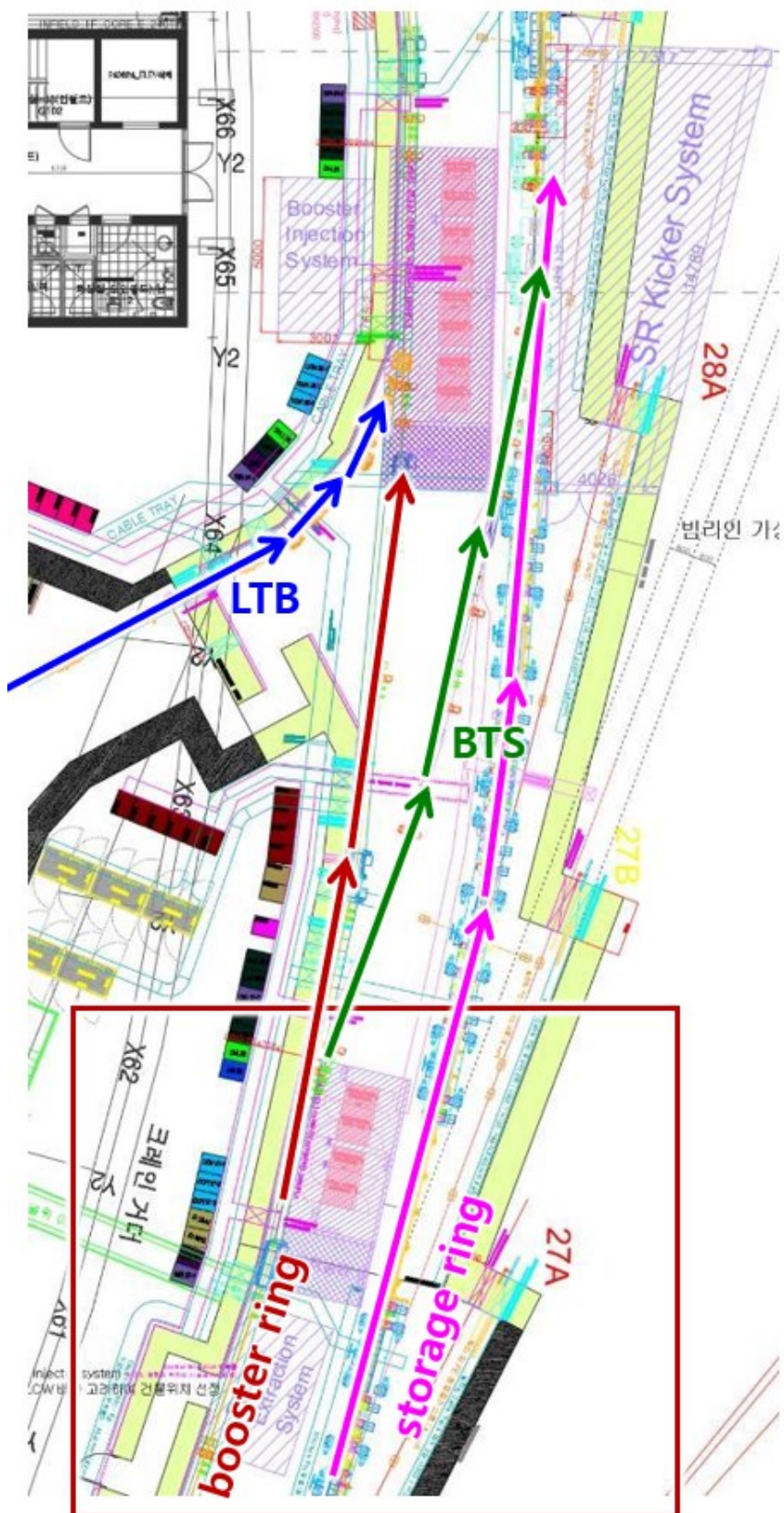
<Table 2.1.3.19> presents the total orbit distortion at ID and center bend magnet from three major sources: vibration, current ripple, and energy oscillation. Current ripple is the dominant contributor to horizontal jitter, especially at ID locations, while vibration primarily affects the vertical plane. Energy oscillation has minimal impact without the harmonic cavity but becomes significant when the cavity is present due to increased sensitivity to RF noise. Despite these effects, both configurations—without and with harmonic cavity—meet the orbit stability requirements of Korea-4GSR, confirming the robustness of the baseline design.

While the current analysis confirms that the Korea-4GSR orbit stability meets design requirements under passive conditions, future work will focus on evaluating the impact of active orbit feedback systems. Such systems are expected to suppress orbit distortions, particularly those arising from low-frequency noises. By incorporating fast orbit feedback and slow orbit feedback loops, the effective rms orbit deviation can be reduced, potentially allowing for relaxed specifications on noise sources. A quantitative assessment of orbit stability with feedback will be conducted to establish revised tolerance margins and optimize system-level design trade-offs.

2.1.4 Injection System

A. Introduction

Accelerator elements that generate electron beam bunches injected into the storage ring are collectively called the injector. The injector of the 4GSR can be broadly divided into a linear accelerator (linac) and a booster. The linac generates electron bunches using an electron gun and accelerates them to an energy of up to 200 MeV. The booster receives the 200 MeV electron bunches from the linac and accelerates them up to 4 GeV. The booster is concentric with the storage ring and shares the tunnel with it. The linac is located inside the storage ring tunnel. The beam transfer section connecting the linac and the booster is named LTB (linac to booster), and the section connecting the booster to the storage ring is named BTS (booster to storage ring).



<Figure 2.1.4.1> Injector layout.

B. Booster Beam Dynamics

The booster receives a 200 MeV electron beam from the linear accelerator and accelerates it to 4 GeV before delivering it to the storage ring. Boosters can generally be categorized into two types: one that shares the tunnel with the storage ring, and one that uses a separate tunnel. As shown in <Table 2.1.4.1>, each option has its advantages, but we have chosen the method that shares the tunnel with the storage ring. The main reason is that sharing the tunnel with the storage ring increases the circumference, making it easier to lower the beam emittance. This also allows us to better prepare for future upgrades to the storage ring in case more stringent injection conditions are required.

<Table 2.1.4.1> Comparison of booster types; sharing the tunnel with the storage ring and use separate tunnel

Advantages of sharing tunnel with storage ring	Advantages of using separate tunnel
Cost	Commissioning & install
Emittance	Low noise
Magnet & Power supply capacity	-
Space	-
Sharing the tunnel is relatively advantageous	

The parameters of the 4 GeV booster are shown in <Table 2.1.4.2>. The repetition rate is set to 2 Hz, with an injection energy of 200 MeV and an extraction energy of 4 GeV, resulting in an energy ramping factor of 20. The ramping-up time to increase the electron beam energy from 200 MeV to 4 GeV is set to 250 ms. The total time for ramping down, injection, extraction, and the hysteresis loop is also set to 250 ms. <Figure 2.1.4.2> illustrates the ramping cycle of the booster operating at 2 Hz. The booster injection uses one injection kicker for on-axis injection. Similarly, booster extraction uses one extraction kicker, and the kicker magnet and power supply share the same specifications as those of the storage ring's injection kicker magnet and power supply. The circumference of the booster is 772.893 m, which ensures a distance of 4.1 m between the electron beams in the storage ring and the booster.

The maximum beam current is set to 1 mA, allowing for an injection rate of up to 2 mA/s. Under these conditions, it takes 200 seconds to fill the storage ring from 0 mA to 400 mA (with the assumption of 100% efficiency). The betatron tune has been positioned to avoid resonances, and the horizontal and vertical values have been set close to each other to enable

a round beam if needed. The RF frequency has been adjusted to differ by less than 1 kHz from the storage ring's RF frequency, enabling operation at the same RF frequency in practice. The selected RF frequency is 499.593975 MHz, with a harmonic number of 1288.

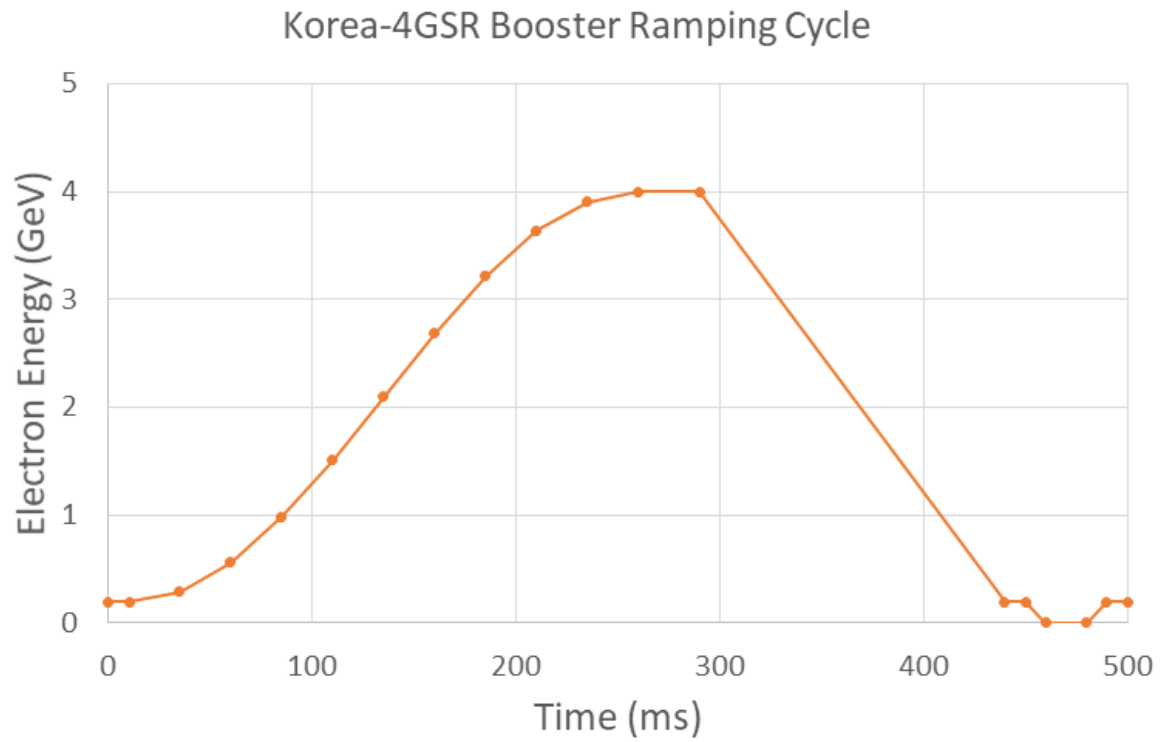
The natural emittance is 10 nm, which is sufficient for storage ring injection. The damping time is around 8 ms, adequate for 2 Hz operation. One turn radiation loss is 1.67 MeV; thus, three normal conducting RF cavities will be installed to operate with a 3 MV gap voltage. Even if one RF cavity fails, the system is designed to secure a gap voltage of over 2 MV using the remaining two cavities, allowing for some degree of ramping and storage ring injection.

The booster lattice adopts a FODO cell structure, with bending magnets functioning as combined function magnets, which also serve as horizontally defocusing quadrupole magnets. The booster consists of 60 FODO cells, with a sextupole pair placed every two FODO cells, so that two FODO cells form one periodic cell, resulting in a total of 30 periodic cells for the booster. To maintain a consistent distance with the racetrack-shaped storage ring, the length of the booster's FODO cells and the dipole magnet angles were adjusted. As a result, 56 FODO cells have a length of 25.7231 m, while 4 cells have a length of 26.3231 m. Among the 60 dipole magnets, 56 have a rotation angle of 6.07° , and 4 have a rotation angle of 5.02° . The one-cell lattice function for a dipole magnet with a 6.07° rotation angle is illustrated in <Figure 2.1.4.4>. The maximum straight section length is 5.52 m, and the 60 straight sections are allocated for injection, extraction, diagnostics, human access, and instrument access areas.

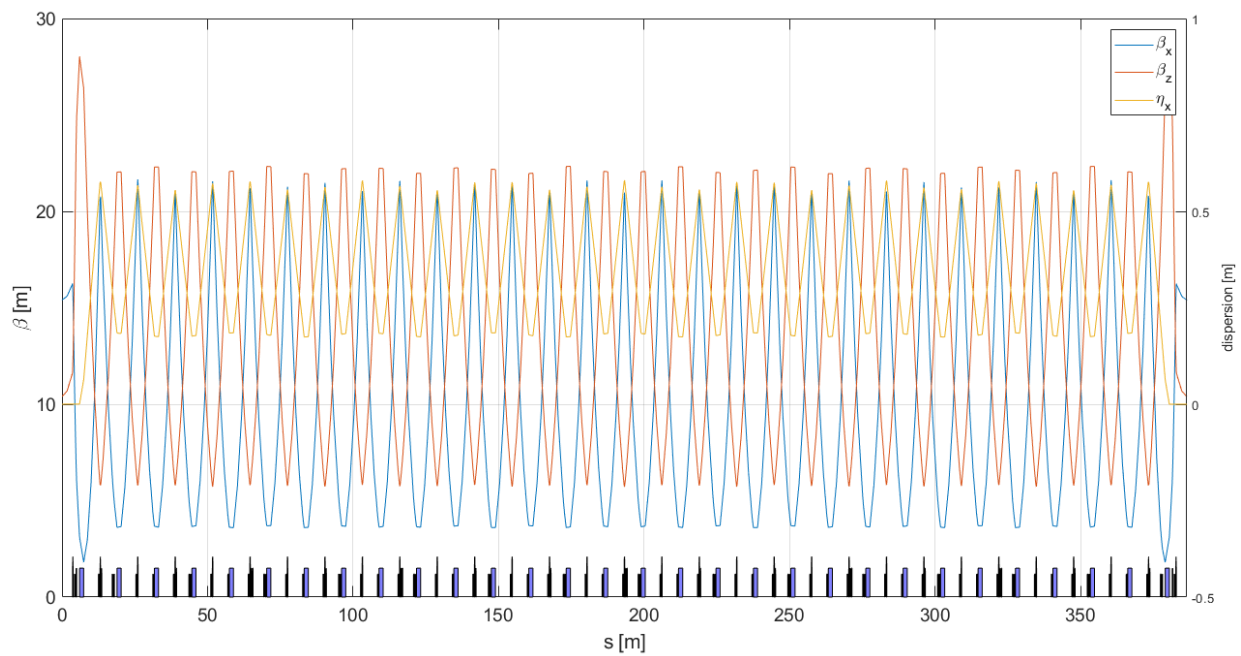
Chromaticity correction is achieved using total 60 sextupole magnets, yielding sufficient dynamic aperture as shown in <Figure 2.1.4.5>. Considering cases where the beam from the linear accelerator is off-energy, the off-energy dynamic aperture was also confirmed in <Figures 3.1.4.5> and <3.1.4.6>. The results show sufficient dynamic aperture at $\pm 1\%$ off-energy without errors included.

<Table 2.1.4.2> Booster parameters

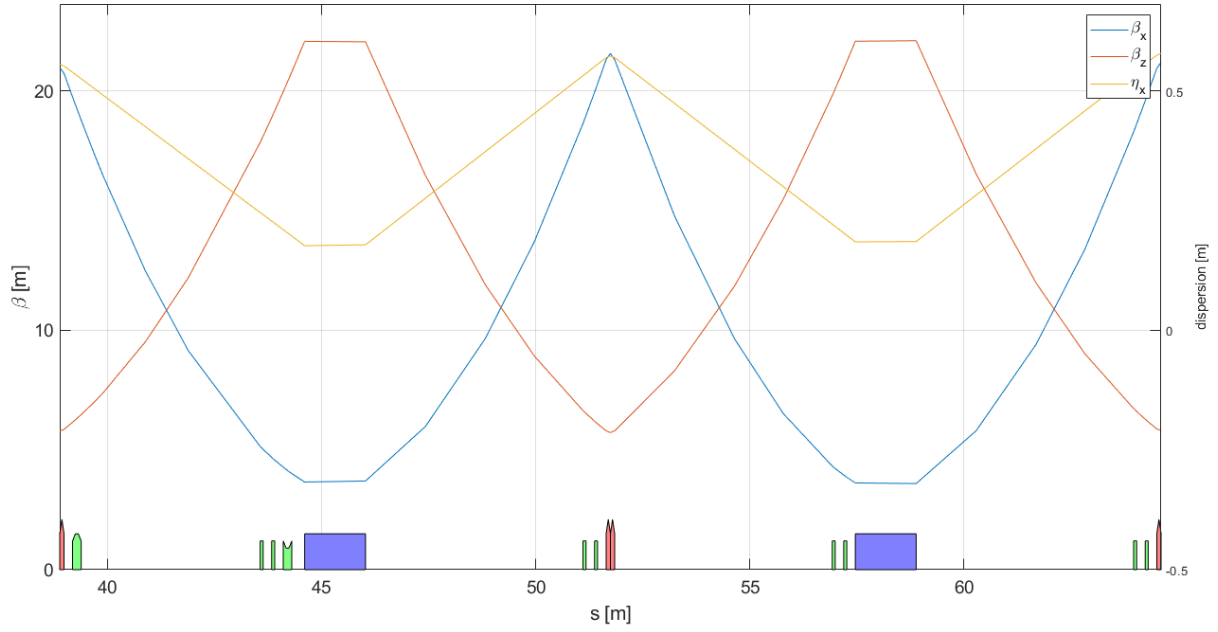
773 m Booster		Values	Unit
Design Parameters	Circumference	772.893	m
	Beam Energy (Inj. - Ext.)	0.2 to 4	GeV
	Cell number	60	–
	Natural Emittance at 4 GeV	10.90	nm rad
	Natural Emittance at 200 MeV	27.25	pm rad
	Momentum Compaction	0.0013	–
Tune and Chromaticity	Horizontal Tune	17.77	-
	Vertical Tune	10.70	-
	Natural Horizontal Chromaticity	-22.26	-
	Natural Vertical Chromaticity	-15.05	-
	Horizontal Chromaticity	2	(Target)
	Vertical Chromaticity	2	(Target)
Radiation related quantities at 4 GeV	Energy Loss per Turn	1671.3	keV
	Energy Spread	0.110	%
	Horizontal Damping Time	7.9	ms
	Vertical Damping Time	12.3	ms
	Longitudinal Damping Time	12.7	ms
	Synchrotron Frequency	4935	Hz
	Synchrotron Tune	0.0127	
	Bunch Length	13.4	mm
Radiation related quantities at 200 MeV	Energy Loss per Turn	0	keV
	Energy Spread	5.48e-03	%
	Horizontal Damping Time	63.39	s
	Vertical Damping Time	98.72	s
	Longitudinal Damping Time	68.43	s
	Synchrotron Frequency	6970	Hz
	Synchrotron Tune	0.01797	–
	Bunch Length	0.47	mm



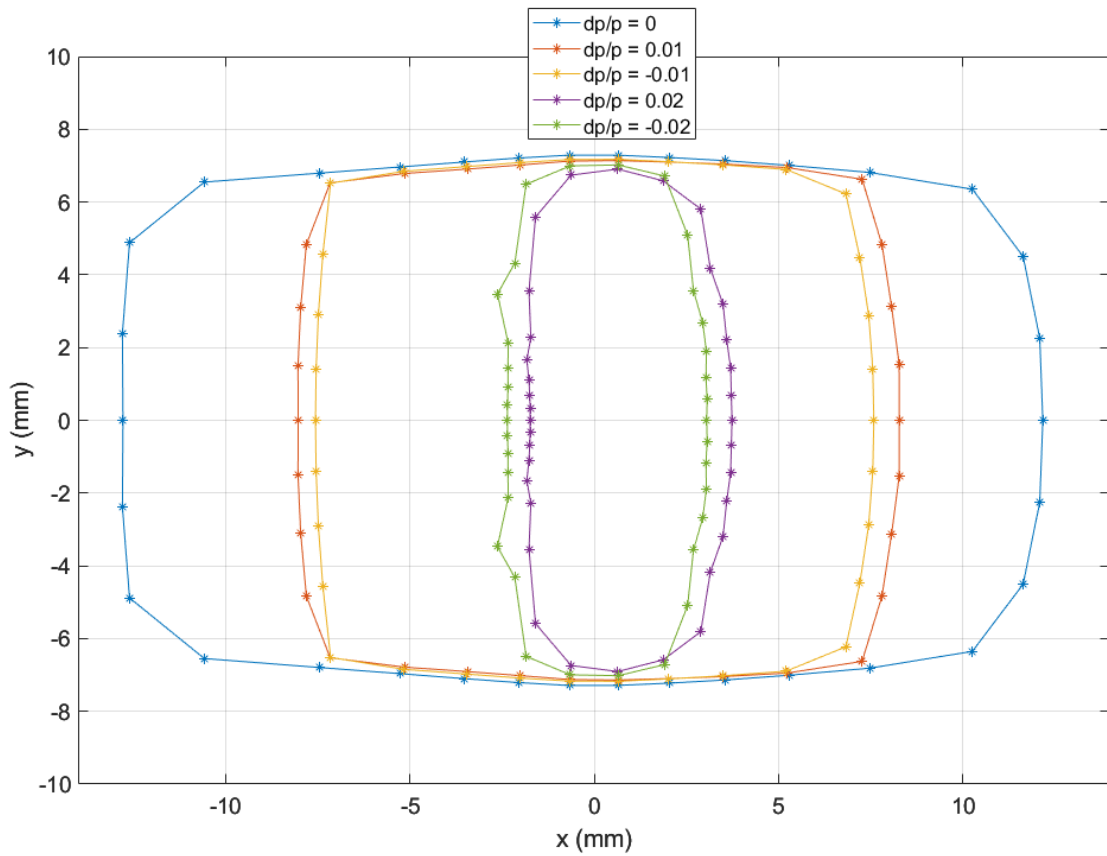
<Figure 2.1.4.2> Booster energy ramping cycle.



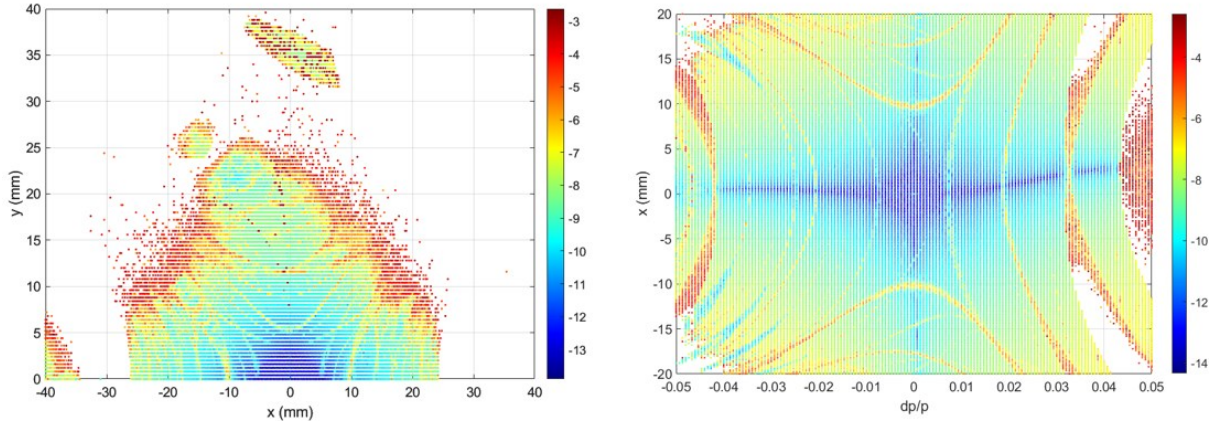
<Figure 2.1.4.3> Booster lattice and Twiss functions. Half ring is shown.



<Figure 2.1.4.4> Booster one cell lattice and Twiss functions.

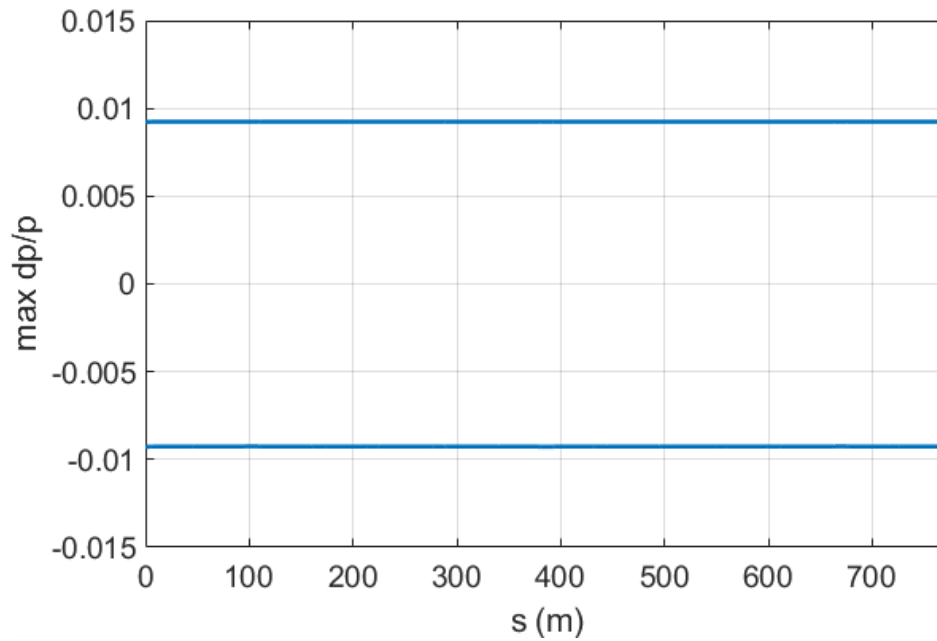


<Figure 2.1.4.5> Booster dynamic apertures at the injection point for varied energy offset.
Physical aperture information included for particle tracking simulation.

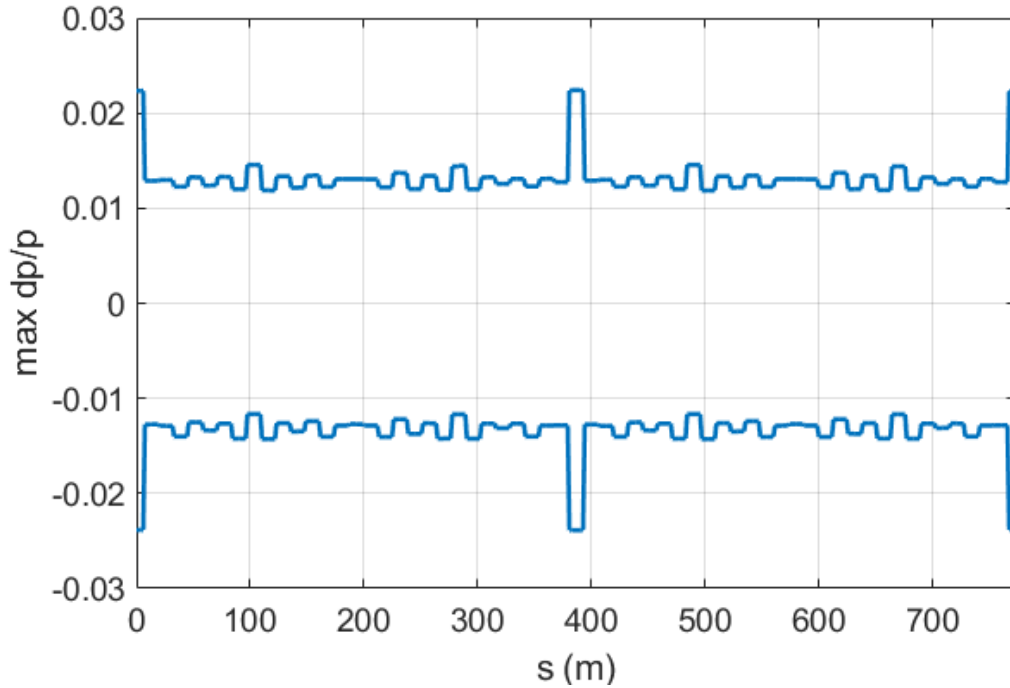


<Figure 2.1.4.6> Booster frequency map analysis at the injection point (left: x-y offset, right: x- dp/p offset). Physical aperture information not included.

<Figures 2.1.4.27> and <Figure 2.1.4.28> show the local momentum acceptance in the booster when the electron beam energy is 4 GeV and 200 MeV, respectively. The gap voltage is 3 MV at 4 GeV and 0.25 MV at 200 MeV. The ramping curve of the RF gap voltage in the booster ring follows the same shape as the energy ramping curve in <Figure 2.1.4.2>, with only the start and end values set differently, and omitting the hysteresis loop.



<Figure 2.1.4.7> Booster local momentum aperture at 4 GeV energy. Physical aperture information included for particle tracking simulation.

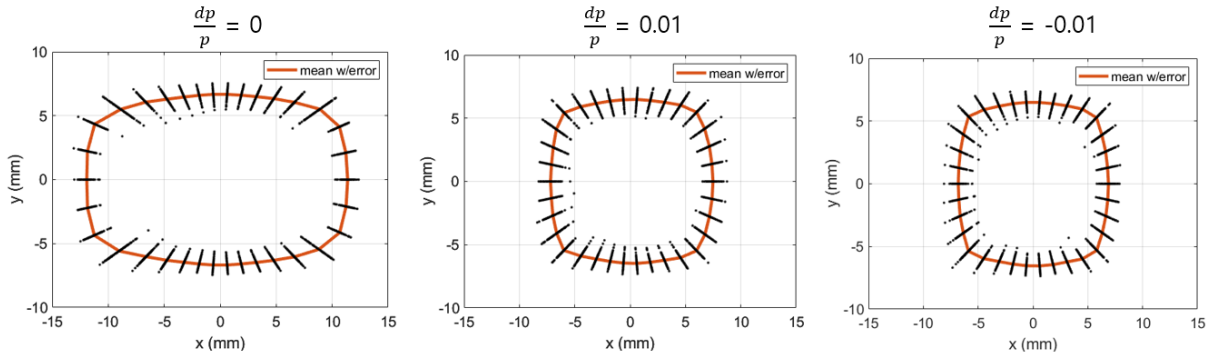


<Figure 2.1.4.8> Booster local momentum aperture at 200 MeV energy. Physical aperture information included for particle tracking simulation.

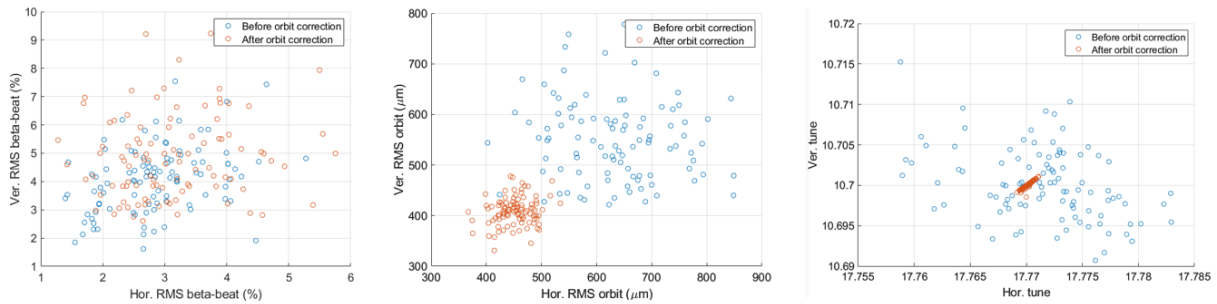
The magnet error tolerance for the booster magnets is shown in <Table 2.1.4.3>. Based on this error tolerance, a commissioning simulation was performed with 100 random error seeds to compare the dynamic aperture <Figure 2.1.4.9>. The booster commissioning simulation is simpler than the storage ring commissioning simulation. Since the booster sextupole strength is not strong, a sextupole ramp-up process was not required to find the closed orbit. The magnets are connected in series by type, and each magnet lacks a trim coil, so it is expected that BBA and LOCO will be challenging to perform. After orbit correction, the rms beta-beat is approximately 3% horizontally and 4% vertically, and the rms orbit is about 400-500 μm , similar to the intrinsic BPM position offset <Figure 2.1.4.10>.

<Table 2.1.4.3> Booster magnet tolerance (rms value)

Magnet	Misalignment (μm) (X/Y/Z)	Rotation (μrad) (Roll/Pitch/Yaw)	Strength error (%)
Dipole	100 / 100 / 200	400 / 100 / 100	0.10
Quadrupole	100 / 100 / 200	400 / 700 / 700	0.10
Sextupole	100 / 100 / 200	400 / 700 / 700	0.10



<Figure 2.1.4.9> Dynamic apertures for an error lattice ensemble of 100 random error seeds.



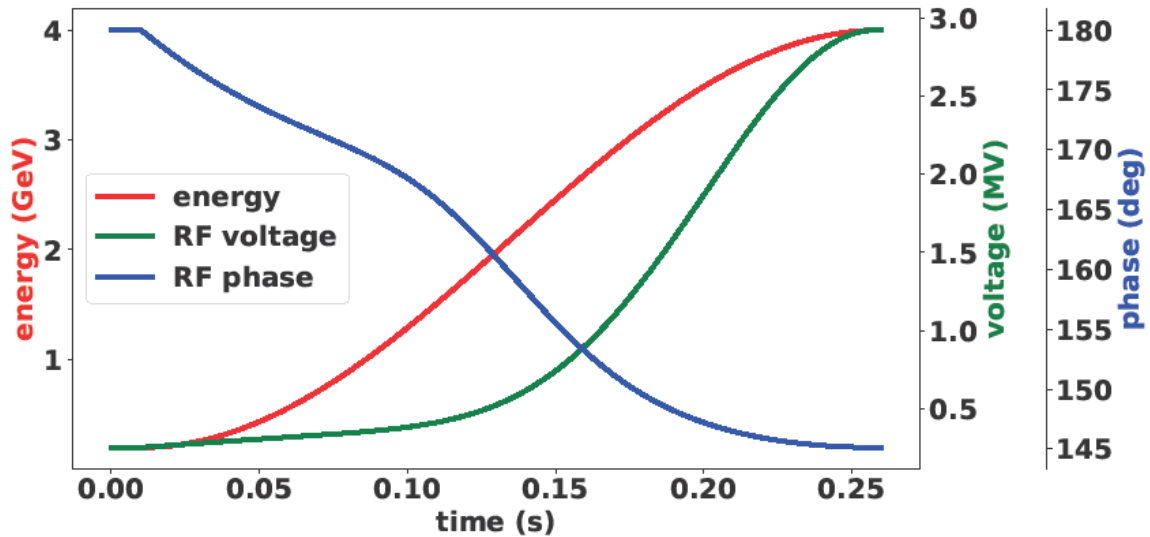
<Figure 2.1.4.10> Distribution of lattice properties before and after orbit correction for a error lattice ensemble of 100 random error seeds.

C. Booster Ramping Study

Unlike the electron storage ring, where the emittance during the ramping process of the booster is determined by the effects of radiation damping and quantum excitation, it is mainly determined by the effect of adiabatic damping caused by acceleration. The effect of adiabatic damping is generally determined by the degree of electron beam acceleration, which in turn is determined by the voltage and phase within the accelerating cavity. In the 4GSR booster, the energy change is defined in the form of a sine wave, and once the initial and final voltages are set, the profile in the ramping section can be determined.

In the design plan, the initial voltage within the accelerating cavity is set at 0.25 MV to prevent the synchronous frequency from becoming too large at the energy of the initial electron beam, which is 200 MeV. The voltage at the extraction point is set slightly lower than 3.0 MV, which is about 1.8 times the radiation loss per turn of the electron beam in

order to ensure the stable operation of the booster ring. During ramping, to secure stability at both the injection from the linac into the booster and the extraction, there are flat-top regions where neither the voltage nor energy changes, lasting 10 ms for injection and 30 ms for extraction. The ramping profile is shown in <Figure 2.1.4.11>.



<Figure 2.1.4.11> Voltage and phase variation in a sine wave-shaped energy ramping profile with an initial voltage of 0.25 MV and an extraction voltage of 3.0 MV [1].

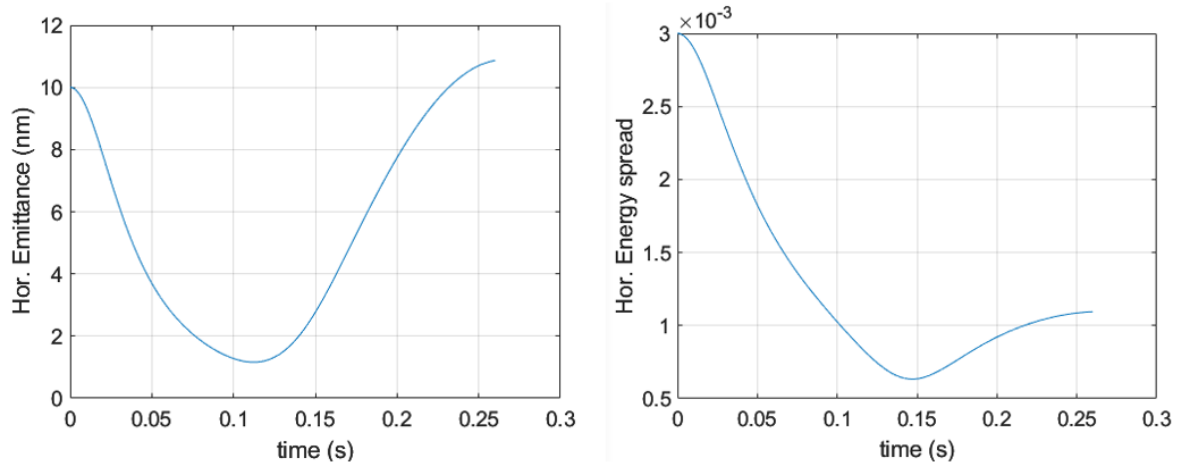
When considering radiation damping, quantum excitation, and adiabatic damping, the horizontal emittance and relative energy spread can be expressed as (Equation 2.1.4.1) and (Equation 2.1.4.2), respectively.

$$\frac{d\varepsilon_x(t)}{dt} = -\frac{\varepsilon_x(t)}{E} \left(\frac{\partial E(t)}{\partial t} + J_x P_Y(t) \right) + C_q \left(\frac{P_Y(t) E(t)}{m_0^2 c^4} \right) \frac{I_5}{I_2} \quad (\text{Eq. 2.1.4.1})$$

$$\frac{d\delta_E^2(t)}{dt} = -\frac{\delta_E^2(t)}{E} \left(\frac{\partial E(t)}{\partial t} + J_z P_Y(t) \right) + C_q \left(\frac{P_Y(t) E(t)}{m_0^2 c^4} \right) \frac{I_3}{I_2} \quad (\text{Eq. 2.1.4.2})$$

In the above equations, $\delta_E = \frac{\sigma_E}{E}$, $C_q = 3.84 \times 10^{-13} \text{ m}$, P_Y is radiation loss power, J_x and J_z are horizontal damping partitions, and longitudinal damping partition, respectively. I_2, I_3, I_5 are the radiation integrals. The first term in the above equation represents the effect of adiabatic damping, the second term reflects the effect of radiation damping, and the final term shows the increase in emittance and relative energy spread due to quantum excitation. In the equation, the effect of adiabatic damping becomes stronger when the energy is lower and the energy change is greater, so it is expected to occur more

prominently at the beginning of the ramping process. While this equation allows the prediction of changes in each parameter, since the electron beam moves in six dimensions and coupling between dimensions can occur, a tracking simulation based on 10,000 macro particles was conducted to accurately assess the effects of ramping in the booster. Initial beam parameters are set to $\varepsilon_x = 10$ nm, $\delta_E = 0.3\%$, which corresponds to simulation results of the injector linac.



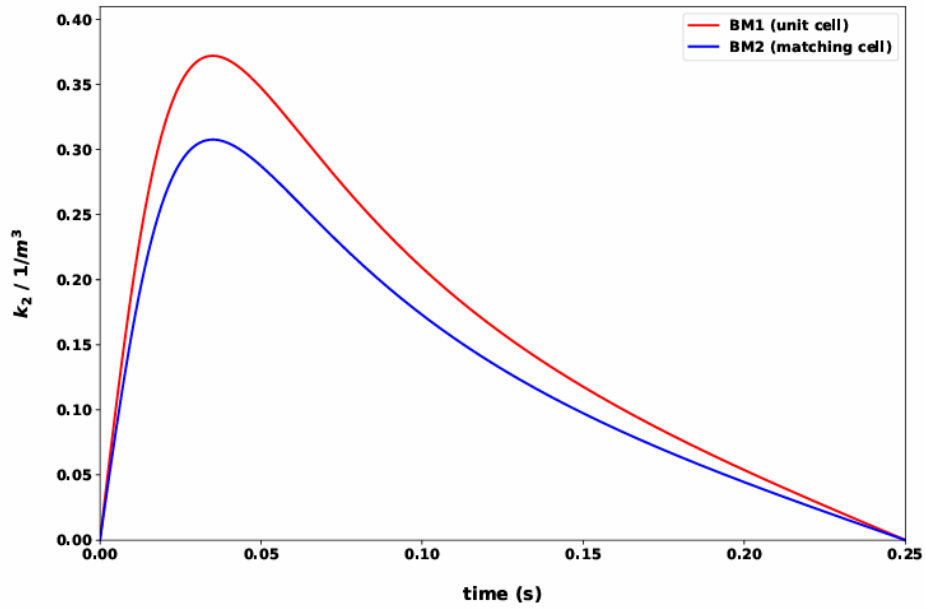
<Figure 2.1.4.12> Evolution of emittance, relative energy spread, in the booster when applying a sine-shaped energy ramping profile.

During energy ramping in the booster, the electron beam experiences a change in energy, which in turn requires adjustments to the strength of the dipole magnets to maintain the reference orbit of the electron beam. To counterbalance the magnetic flux density changes inside the chamber installed within the dipole magnets, eddy currents are generated in the opposite direction. The magnetic field generated by these eddy currents is proportional to the square of the distance, which can be expressed as a sextupole magnet component. The sextupole magnet component generated in the chamber due to the magnetic field changes is represented by (Equation 2.1.4.3).

$$K_2 = 2\mu_0\sigma F \frac{t_k}{h} \frac{1}{\rho B(t)} \frac{\partial B(t)}{\partial t}, \text{ where } F = 2 \int_0^1 [x^2 + (\frac{g}{w})^2 (1 - x^2)]^{1/2} dx \quad (\text{Eq. 2.1.4.3})$$

In (Equation 2.1.4.3), μ_0 is the permeability in a vacuum, σ is the electrical conductivity of the chamber material, t_k is the thickness of the chamber, w is the distance between the poles of the dipole magnet, ρ is the curvature radius of the dipole magnet, and

w and g represent the horizontal and vertical radii of the chamber, respectively. F is a function representing the shape of the chamber, approximated for an elliptical shape. When the chamber shape is close to circular, F converges to 2, and when the horizontal radius increases, it approaches 1. The chamber material for the 4GSR is SUS 316L, with an electrical conductivity of approximately 1.35 MS/s, and the shape is a circular pipe with equal horizontal and vertical radii. Considering these properties and the above ramping profile, the sextupole magnet component is calculated and shown in <Figure 2.1.4.13>.



<Figure 2.1.4.13> Shape of sextupole field strength induced by Eddy current in the bending magnet vacuum chamber [2].

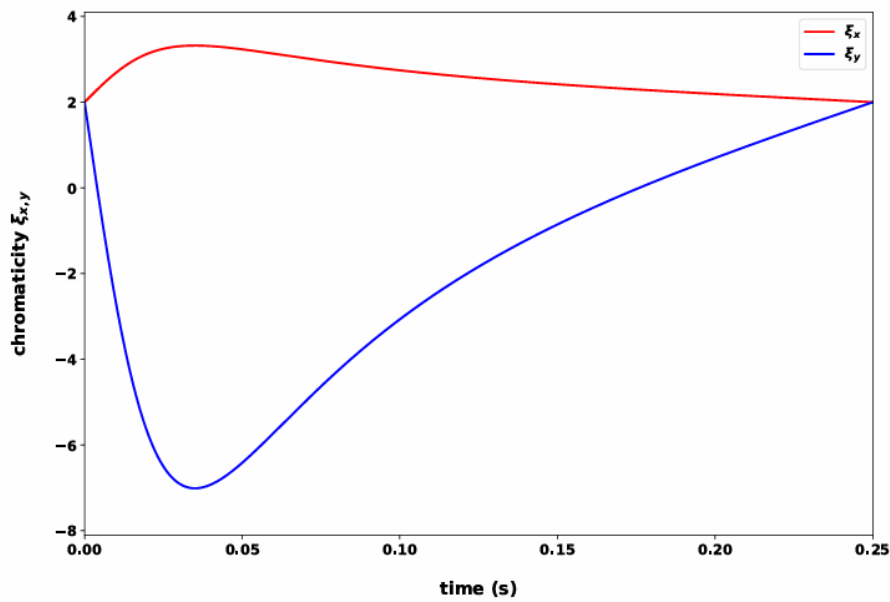
The calculated sextupole strength is small compared to the original sextupole magnet strength. However, since the dipole magnet is longer than the sextupole magnet, the integrated field may result in a significant change that cannot be ignored. To evaluate this, it is necessary to assess the change in chromaticity caused by the sextupole magnet component obtained from the above calculation. This can be calculated using (Equation 2.1.4.4) below.

$$\xi_x = \frac{1}{4\pi} \oint ds \beta_x(s) D_x(s) K_2(s) L_{K2},$$

$$\xi_y = \frac{-1}{4\pi} \oint ds \beta_y(s) D_x(s) K_2(s) L_{K2} \quad (\text{Eq. 2.1.4.4})$$

In the equation, β_x and β_y represent the horizontal and vertical beta functions where

the sextupole component is present, D_x is the dispersion function, and L_{K2} is the length of the sextupole component. Typically, at locations where the dipole magnets are installed, the horizontal betatron function is minimized, so the horizontal effect is expected to be negligible. However, in the FODO-type booster ring design, the vertical betatron function inevitably becomes large, so the vertical chromaticity could increase significantly. Based on the above equation, chromaticity calculations were performed. At this point, it was assumed that the initial chromaticity was corrected to +2 in both the horizontal and vertical directions using two sextupole magnets to mitigate head-tail instabilities and microwave instabilities that occur during high-current operation.



<Figure 2.1.4.14> Chromaticity changes due to Eddy current in the bending magnet vacuum chamber [2].

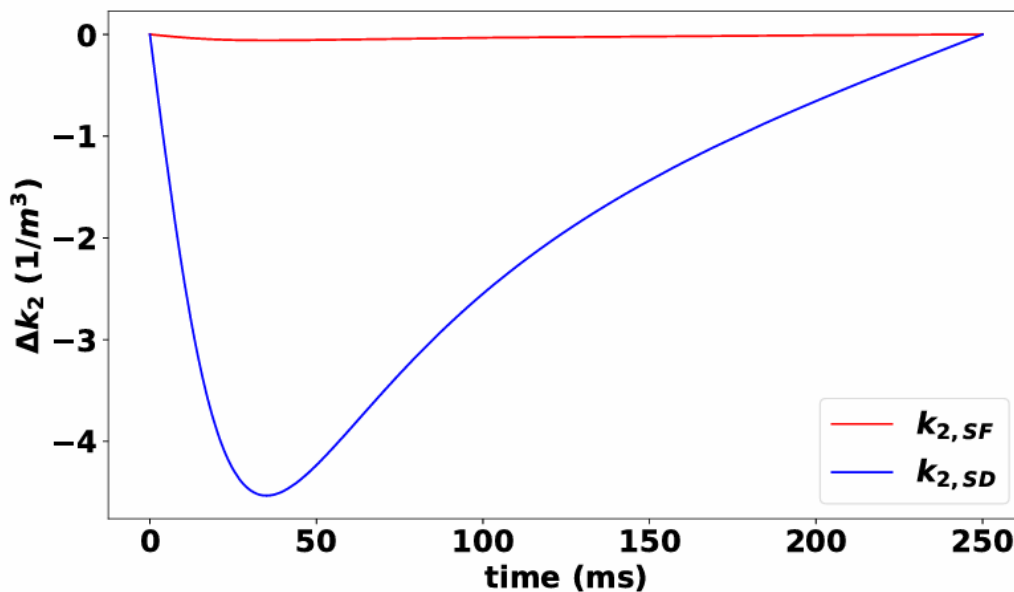
As shown in <Figure 2.1.4.14>, in the horizontal direction, there is an increasing trend of approximately 50% from the initial value of +2. However, in the vertical direction, despite the sextupole magnet component being small, the long length of the dipole magnet and the large vertical betatron function within the magnet lead to a chromaticity change of about -6. This can be corrected by adjusting the strength of the two sextupole magnets installed in each cell of the booster ring. In the booster ring design, each cell is equipped with two sextupole magnets, and they are placed near the locations where the horizontal and vertical

betatron functions reach their maximum values to minimize the required strength of the magnets. Therefore, the change in the strength of the sextupole magnets required for correction is expected to be minimal.

The chromaticity values corrected by the strength of the two sextupole magnet families ($K_{2,SD}$, $K_{2,SF}$) in the booster can be expressed using the matrix shown in (Equation 2.1.4.5) below.

$$\begin{pmatrix} \xi_x \\ \xi_y \end{pmatrix} = \frac{1}{4\pi} \begin{pmatrix} \sum_i \beta_{xi} D_{xi} L_i & -\sum_i \beta_{yi} D_{xi} L_i \\ -\sum_k \beta_{xk} D_{xk} L_k & \sum_k \beta_{yk} D_{xk} L_k \end{pmatrix} \begin{pmatrix} K_{2,SF} \\ K_{2,SD} \end{pmatrix} = M \begin{pmatrix} K_{2,SF} \\ K_{2,SD} \end{pmatrix} \quad (\text{Eq. 2.1.4.5})$$

In the above equation, β_{xi} and β_{yi} represent the horizontal and vertical beta functions at the i-th SF sextupole magnet, and β_{xk} and β_{yk} represent the horizontal and vertical betatron functions at the k-th SD sextupole magnet. D_{xi} and D_{xk} are the dispersion functions at the i-th and k-th sextupole magnets, respectively. By calculating the inverse of the matrix in the equation and taking the dot product with the desired chromaticity values, the required sextupole magnet strength can be determined. Applying this method, the additional sextupole magnet strengths for the two families required to correct the chromaticity caused by the eddy currents during the ramping process in the booster ring are shown in <Figure 2.1.4.15>.

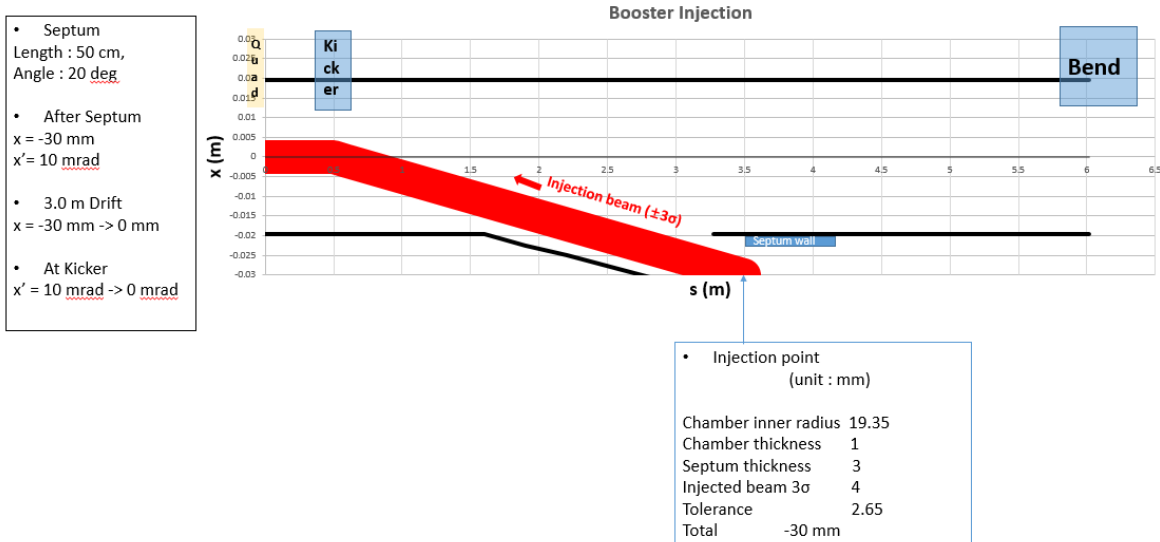


<Figure 2.1.4.15> Sextupole magnet strengths required to correct chromaticity changes due to Eddy current [2].

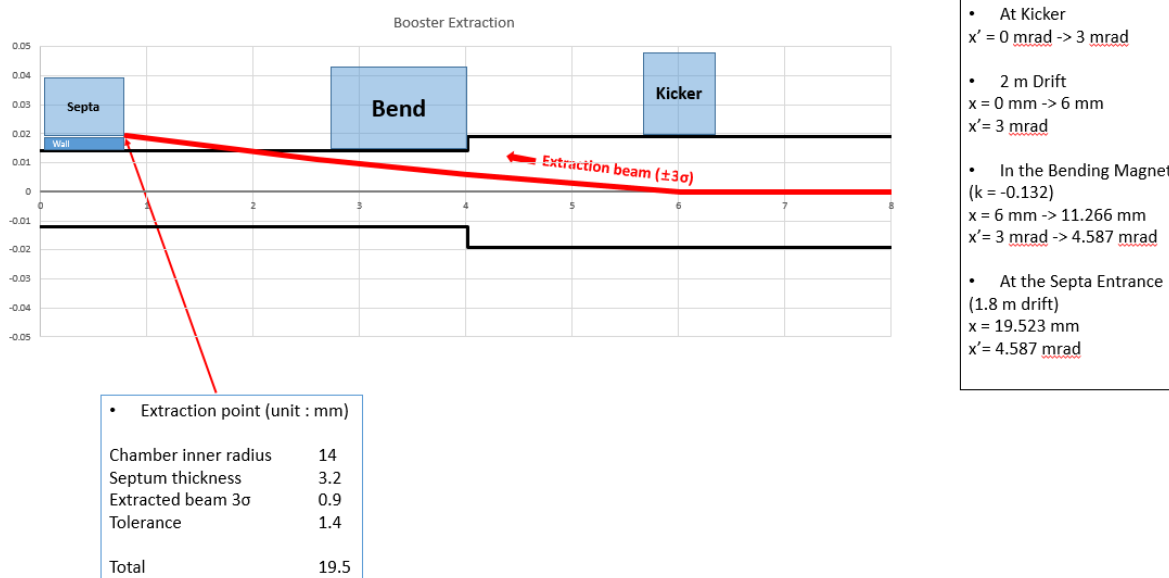
D. Booster Injection and Booster Extraction

The electron beam accelerated in the linear accelerator passes through the LTB and is injected into the booster using an on-axis injection method. The electron beam, coming out at an angle from the end of the septum magnet, passes through the drift section and is positioned on-axis at the kicker location. One kicker is used to align the electron beam on-axis and on-angle, allowing it to be injected into the booster. Below, <Figure 2.1.4.16> shows the booster injection layout. The septum magnet is located at the end of the LTB, bending the electron beam by 20° , and the beam is positioned at -30 mm, leaving a 10 mrad angle relative to the booster chamber. This position accounts for the vacuum chamber's radius, thickness, septum wall thickness, three times the size of the injected beam, and tolerance. The electron beam coming out of the septum passes through a 3-meter drift section and reaches the kicker position on-axis, where it receives a 10 mrad kick, completing the injection. Since the kicker's magnetic field must drop to zero before the injected beam makes one turn in the booster, the kicker pulse length requirement is that the falling time must be within $2.6 \mu\text{s}$. Additionally, since a 200 ns multi-bunch needs to receive kicks of the same strength, field flatness is required during the 200 ns period.

The 200 MeV electron beam injected into the booster is accelerated to 4 GeV and it is first extracted from the booster before being injected into the storage ring. The extraction from the booster is done using a single kicker, similar to the booster injection, but since the energy is 20 times higher, a stronger magnetic field is required. The booster extraction kicker uses the same magnet and power supply as the storage ring injection kicker. To reduce the current required for the kicker, the defocusing quadrupole component of the booster dipole magnet is utilized. First, the kicker provides a 3 mrad kick, and after passing through a 2-meter drift space, the electron beam enters the booster dipole magnet with a 6 mm offset, taking advantage of the defocusing quadrupole effect, which causes the dipole magnet to also kick the beam outward. As a result, when the electron beam exits the dipole magnet, it has an offset of 10.4 mm and an angle of 4.5 mrad. This increased angle is then used to guide the beam through a 2-meter drift space and into the septum. At the starting point of the septum, the extraction position is set to 19.4 mm, taking into account the vacuum chamber radius, vacuum chamber thickness, septum wall thickness, three times the size of the electron beam, and tolerance.

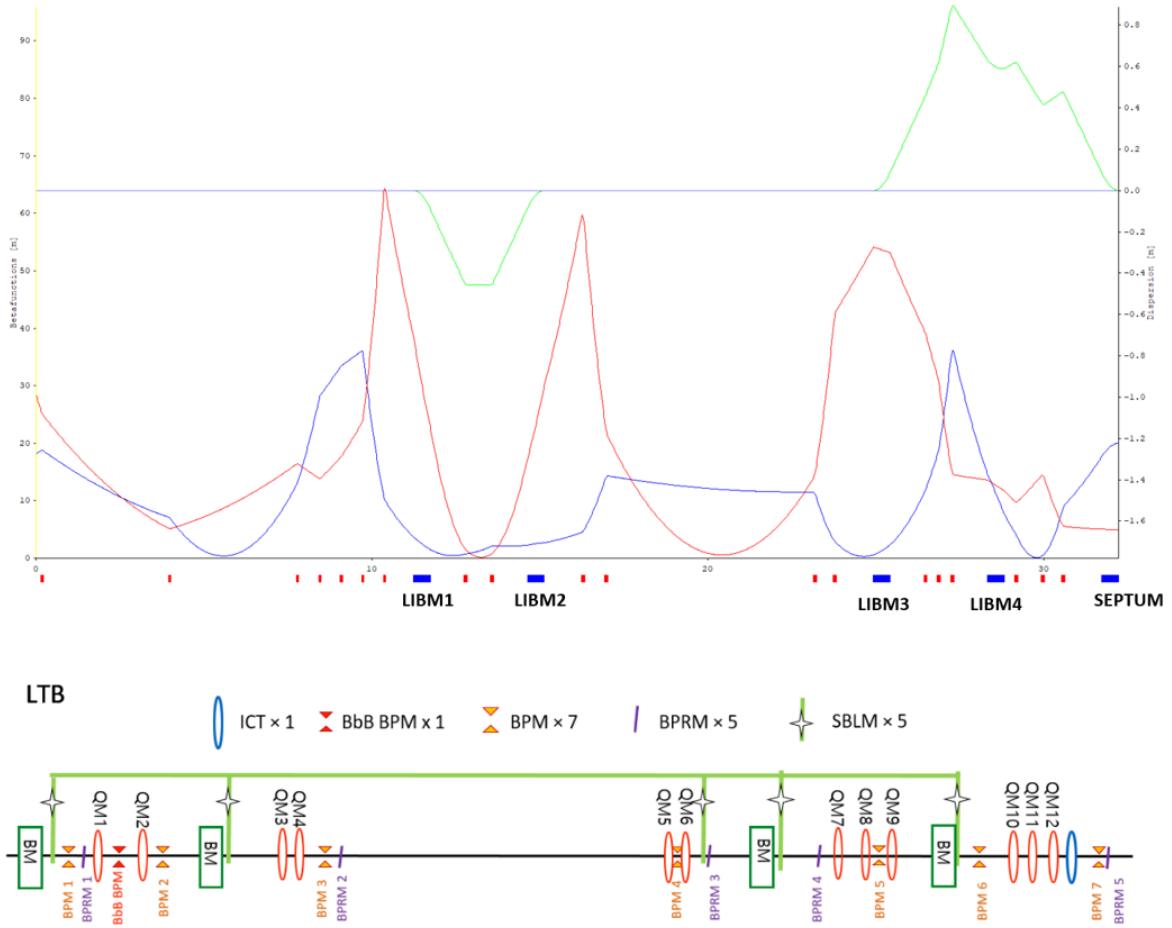


<Figure 2.1.4.16> Booster injection layout.



<Figure 2.1.4.17> Booster extraction layout.

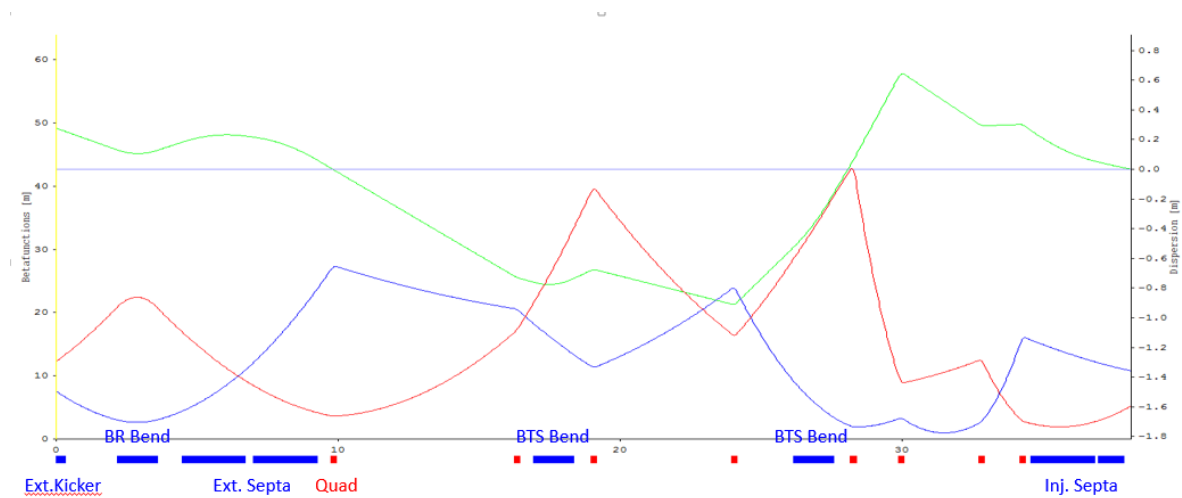
E. Linac-to-Booster (LTB) and Booster-to-Storage ring (BTS) Beam Transport Line



<Figure 2.1.4.18> LTB lattice and Twiss functions, and configuration of diagnostics devices.

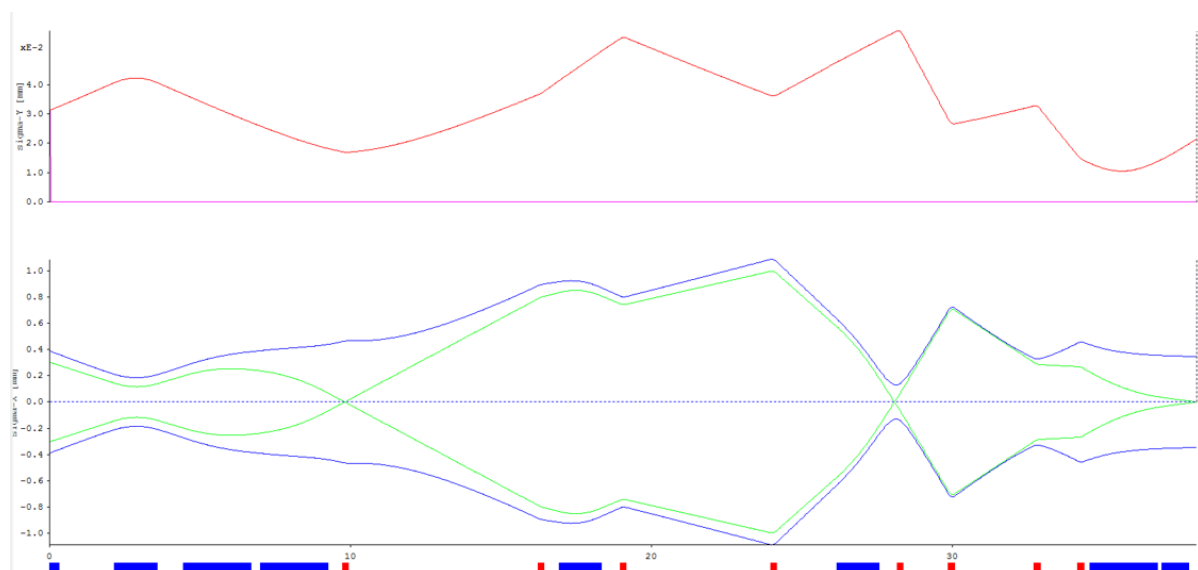
<Figure 2.1.4.18> shows the lattice and the beta function and dispersion at different positions of the Linac-to-Booster (LTB) beam transfer line. The LTB consists of four LTB bends and 12 quadrupole magnets. It is equipped with five BRPMs and five SBLMs, which are used to measure and analyze the beta function, allowing verification of the Twiss parameters of the beam injected into the LTB. The LTB is matched so that the dispersion, which increases after LIBM1, becomes zero after LIBM2, and the dispersion that increases after LIBM3 becomes zero after the septum. In the first dispersion bump, the beam pulse's energy distribution is measured using BPRMs, and a BPM capable of resolving bunches is installed to measure the center energy of each bunch in multi-bunch injection mode. The beta function at the end of the LTB has a value similar to that of the booster at the booster

injection point.



<Figure 2.1.4.19> BTS lattice and Twiss functions. Blue line: horizontal beta function, Red line: vertical beta function, Green line: horizontal dispersion.

The Booster to Storage Ring (BTS) beam transfer line consists of two dipole magnets and eight quadrupole magnets. The BTS beam transfer line is designed so that the Twiss functions at the end of the BTS, i.e., at the storage ring injection point, closely match the Twiss functions of the beam in the storage ring at that position. <Figure 2.1.4.20> shows the beam envelope along the BTS beam transfer line. From this, the calculated beam stay clear in the BTS is 4 mm horizontally and 1.2 mm vertically, and at the thin septum exit, it is 2 mm horizontally and 1.1 mm vertically. Based on this, the orbit bump height, thin septum thickness, and offset between the stored beam and the injected beam at the injection point are set to 7 mm, 1 mm, and 5 mm, respectively.



<Figure 2.1.4.20> BTS lattice and beam envelope function. Blue line: horizontal envelope, Red line: vertical envelope, Green line: envelope from dispersion function.

F. 200 MeV Linear Accelerator

(1) Specification and layout

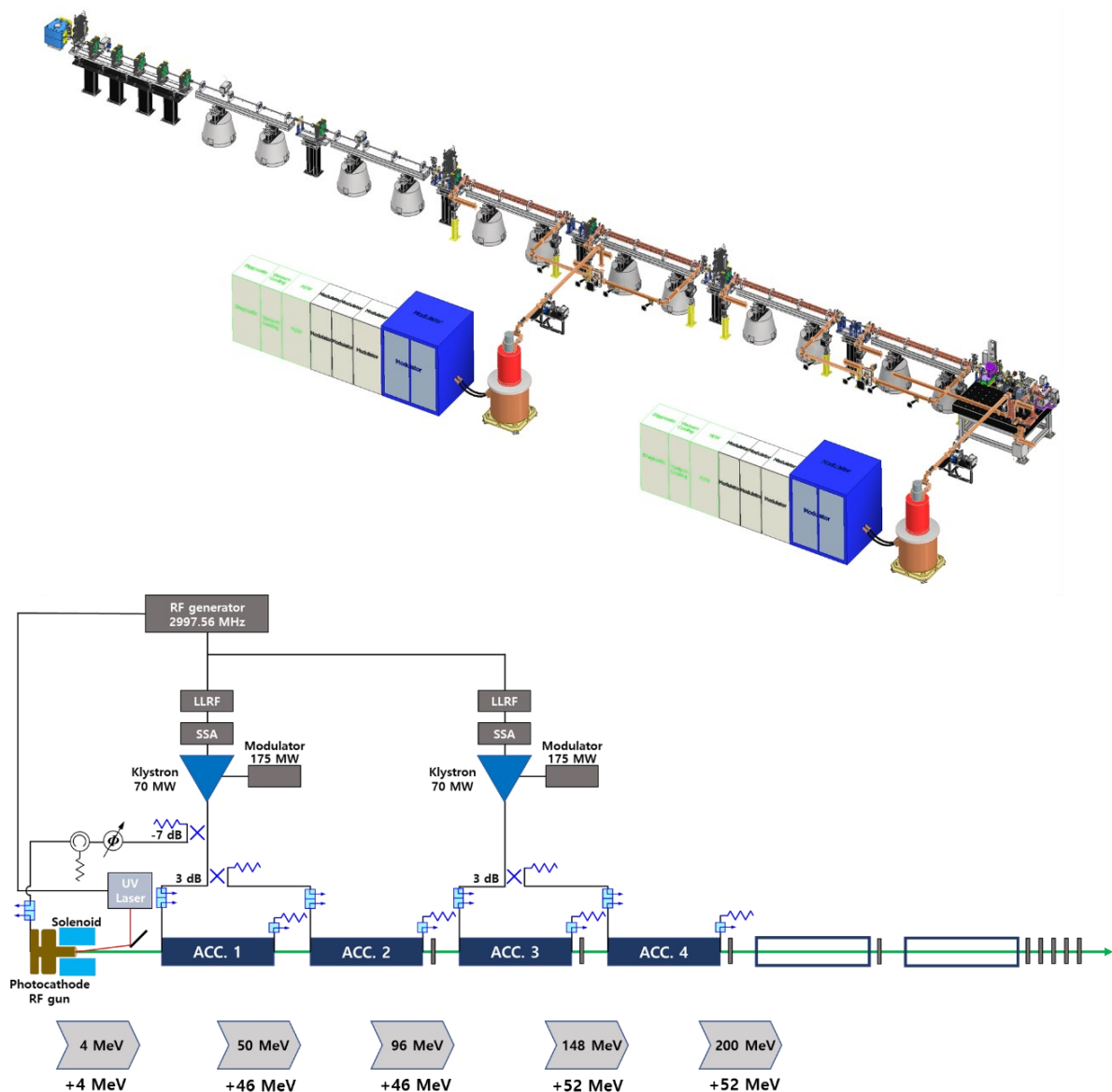
The linac generates a 200 MeV electron beam. Instead of a thermionic electron gun, it employs a photo-cathode RF gun with characteristically low emittance and low energy spread. The relevant key parameters are listed in <Table 2.1.4.4>. It supports two operation modes: single-bunch mode and multi-bunch mode, both with a RF repetition rate of 2 Hz. The mode switching time, including stabilization, is within 5 minutes.

<Table 2.1.4.4> Linear accelerator parameters

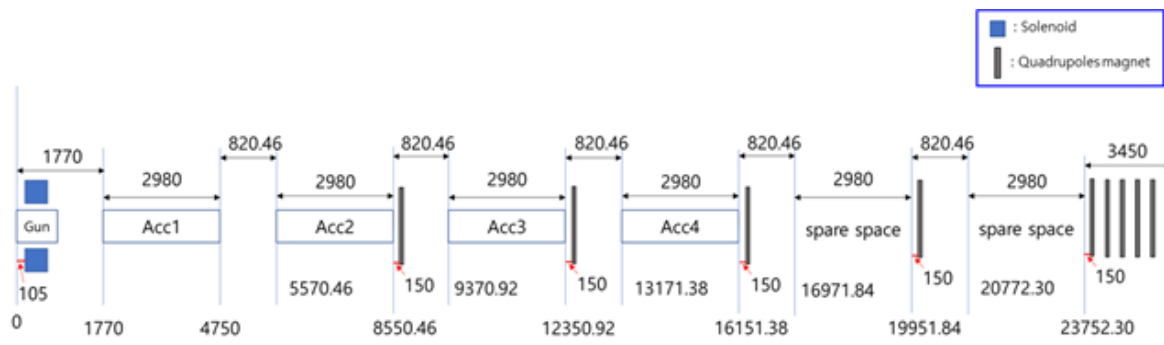
Classification	Single-bunch mode	Multi-bunch mode
Energy	200 MeV	200 MeV
Frequency	2,997.56 \pm 0.1 MHz	2,997.56 \pm 0.1 MHz
Emittance (at 200 MeV)	\leq 10 nm	\leq 10 nm
Relative energy spread (rms)	\leq 0.5 %	\leq 0.5 %
Pulse to Pulse energy jitter(rms)	\leq 0.2 %	\leq 0.2 %
Bunch charge (charge stability)	0.01 to 1 nC (2%)	1 to 3 nC (5%)
Pulse duration	6 to 8 ps FWHM	\approx 128 ns (64 bunches)
Repetition rate	2 Hz	2 Hz

The linac block diagram and layout are shown in <Figure 2.1.4.21> and <Figure 2.1.4.22>, respectively. The electron bunches generated by the UV laser in the RF photo-cathode gun are accelerated to 4 MeV within the gun. The electrons are further accelerated to 200 MeV, passing through the accelerating columns as in the PAL-XFEL. The gun energy is set lower than the XFEL's 6 MeV to reduce dark current and enhance operational stability. A solenoid magnet is installed between the electron gun and the first accelerating column to focus the initially accelerated electrons, and four accelerating columns are employed. Additional space has been secured for the future installation of two additional accelerating columns to allow for possible energy upgrades. Nine quadrupole magnets are installed after the second accelerating column to focus the electron beam and match it to the LTB (Linac to Booster).

The energy supplied to the electron gun and the first and second accelerating columns is provided by the first klystron modulator system, while the energy supplied to the third and fourth accelerating columns is provided by the second klystron modulator system. A 70 MW-class (about 55 MW is used) klystron modulator system is required to ensure stable energy supply. Each system is independently adjusted by a dedicated LLRF-SSA system. The high-power RF supplied to the gun is adjusted using a waveguide-type mechanical phase shifter and is fixed during operation. An isolator is installed to prevent RF power reflection and to ensure unidirectional propagation of the RF signal.



<Figure 2.1.4.21> Block diagram of the linear accelerator.



<Figure 2.1.4.22> Linear accelerator layout.

(2) RF System

The temperature and humidity of the klystron modulator gallery are controlled by the air conditioning system and maintained at 25 ± 1 °C and 45 ± 10 %, respectively. The linac tunnel is designed to adopt a Type 3 ventilation system; its temperature is maintained by the radiant heat of the accelerating columns and waveguides without a separate air conditioning system. The Low Conductive Water (LCW) supply temperatures for the accelerating columns and the electron gun are set to 27–33 °C and 30–60 °C, respectively. The reason for using these LCW supply temperatures is to accommodate frequency changes required during operation. Accelerating columns designed to have a resonant frequency of 2997.56 MHz at 30 °C are capable of frequency tuning of ± 150 kHz using the temperature change of ± 3 °C. A wider range of temperature tuning is specified for the electron gun, considering manufacturing tolerances.

○ Electron gun system

During the conceptual design phase, a thermionic electron gun was considered based on the experience of constructing and operating the PLS-II (a third-generation synchrotron radiation source). However, the design specifications were changed to a photo-cathode electron gun, which has superiority in terms of performance, manufacturing, and operation. The designed photo-cathode gun adopted a Cu-cathode, and its frequency is 2997.56 MHz. It was designed, referring to the photo-cathode electron gun developed for PAL-XFEL. The design parameters of the electron gun system are shown in <Table 2.1.4.5> below, and it will operate in both single-bunch mode and multi-bunch mode.

<Table 2.1.4.5> Design parameters of the electron gun system

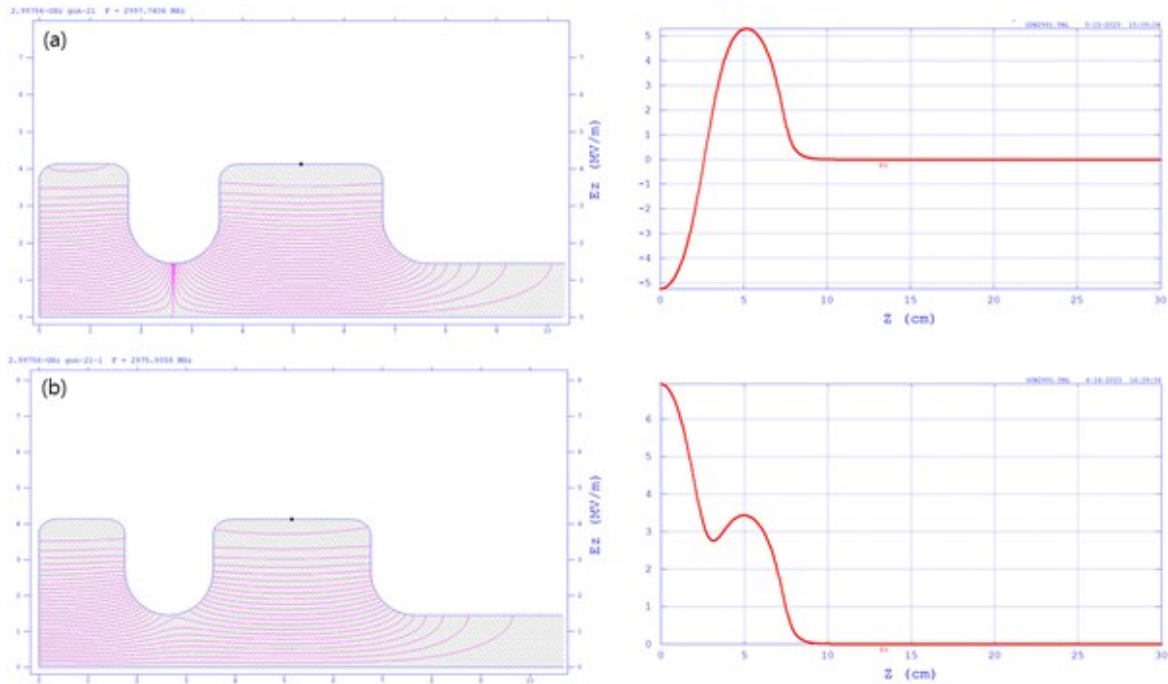
	Single bunch mode	Multi-bunch mode
Beam energy	4 MeV	4 MeV
Charge	0.01 to 1 nC	1 to 3 nC
Pulse length	≤ 20 ps	≈ 128 ns (64 bunches)
Repetition rate	2 Hz	2 Hz

The gun design used the SUPERFISH program developed by the Los Alamos National Laboratory (LANL) in the USA. The RF gun cavity consists of a full-cell and a half-cell and was designed as shown in <Figure 2.1.4.23> due to its cylindrical symmetry. The full-cell has a length of $\frac{\lambda}{2}$, while the half-cell length is approximately 0.5 times that of the full-cell.

To achieve field balance, the half-cell length was adjusted. Finally, a photo-cathode gun of approximately 1.52 cells was designed. The frequency difference between the π -mode and 0-mode is about 20 MHz, and the electric field lines and the strength of the longitudinal electric field of the designed RF cavity's π -mode and 0-mode were calculated using SUPERFISH and presented in <Figure 2.1.4.24>.



<Figure 2.1.4.23> RF gun cavity designed by SUPERFISH.



<Figure 2.1.4.24> The electric field lines and the strength of the longitudinal electric field computed by SUPERFISH for π -mode (a) and 0-mode (b)

○ Accelerating column

Through the domestic technology development process, the accelerating column for 4GSR was developed. The design is modified from PAL-XFEL at 2.856 GHz. The operating frequency was updated, and the coupler was redesigned to reduce beam oscillations in the coupler. The accelerating column material, excluding the flange, is oxygen-free, high-conductivity copper, and the column consists of 84 standard cells and two coupler cavities. The accelerating column is tuned to the reference frequency of 2997.56 MHz at 30 °C. It adopts the same $2\pi/3$ mode constant-gradient traveling wave structure as the XFEL.

(3) Beam Dynamics Simulation

To determine the operating conditions in which the electron beam generated from the electron gun meets the requirements after being accelerated while passing through the accelerating columns, including the last one, a beam dynamics simulation was performed by using the ASTRA program. A parameter sweep was conducted on the field gradient and input phase of the electron gun's accelerating column and the traveling wave accelerating columns, which accelerate the electron beam, as well as on the strength of the solenoids and quadrupole magnets that focus the electron beam.

As a result, the operating specifications were optimized by considering changes in the horizontal/vertical beam emittance, beam size, longitudinal bunch length, and energy spread. As the input field used in this process, the electric field data of each accelerating column and the solenoid's magnetic field data were calculated using the Poisson/Superfish codes. ASTRA's internal calculation method was used to compute the strength of quadrupole magnets. To consider the space charge effect in the low-energy region due to particle interactions within the electron beam, the code used over 10,000 macro particles. The electrons' equations of motion were used, and a variable Runge-Kutta step was utilized for effective computation. Additionally, to consider local minima/maxima that might be missed during the optimization of operating variables through parameter sweep, a Multi-Objective Genetic Algorithm (MOGA) was used.

○ Optimization of Operating Specifications Using Multi-Objective Genetic Algorithm (MOGA)

The design of a linear accelerator corresponds to optimizing the operating specifications of key components. To achieve the desired beam parameters, various conditions should be considered, and multiple objective functions need to satisfy requirements simultaneously. A multi-objective genetic algorithm (MOGA) was used to optimize beam dynamics simulation. With the input phase of the accelerating columns composing the linear accelerator and the strength of magnets taken as variables, minimization of the rms energy spread and transverse normalized rms emittance at the linac end proceeded. In this process, beam size, divergence, average energy, and bunch length were taken as constraint functions, and the optimization proceeded, satisfying the requirements. <Table 2.1.4.6> shows the optimization functions and structural parameters used for optimizing the operating specifications.

<Table 2.1.4.6> Linac optimization functions and structural parameters

Optimization functions	Variables	Note
Objective Functions	rms Energy Spread	Minimization
	Horizontal Normalized rms Emittance	Minimization
	Vertical Normalized rms Emittance	Minimization
Constraint Functions	Horizontal rms Beam Size	< 0.3 mm
	Vertical rms Beam Size	< 0.3 mm
	Horizontal rms Divergence	< 0.2663 mrad
	Vertical rms Divergence	< 0.2663 mrad
	Bunch length	< 1.0 mm
	Transmission rate	> 99.99 %
	Average energy	> 200 MeV
Parameters	RF gun Input Phase	-20 to 20 degree
	Acc1&2 Input Phase	-20 to 20 degree
	Acc3&4 Input Phase	-20 to 20 degree
	Solenoid Strength	0.15 to 0.21 T
	Focusing Quad Strength	1 to 3 T/m
	Defocusing Quad Strength	-4 to -1 T/m

The Python-based pymoo library was utilized to use MOGA, and the Non-Dominated Sorting Genetic Algorithm II (NSGA-II) was applied.

The initial beam parameters used in the beam dynamics simulation are shown in <Table 2.1.4.7> below. These conditions were applied identically to both the single-bunch mode and multi-bunch mode simulations, except for the difference in charge.

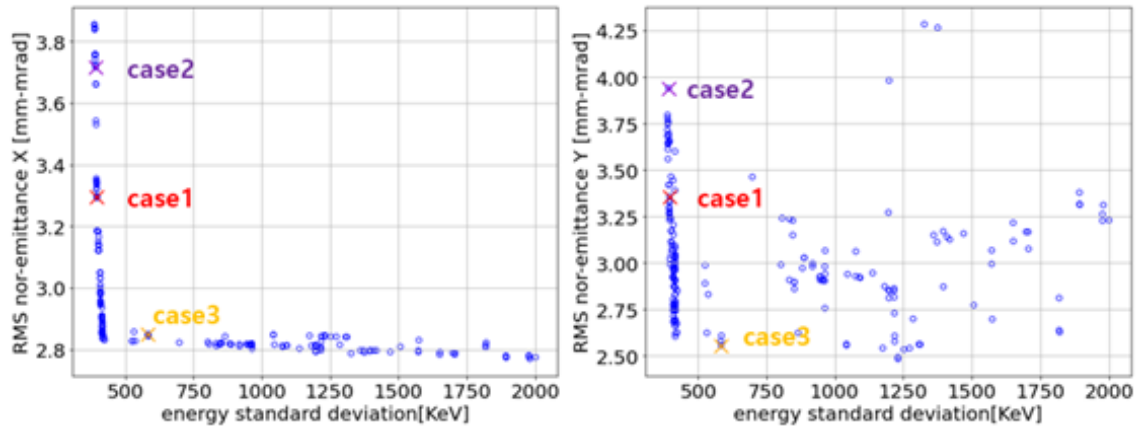
<Table 2.1.4.7> Initial beam parameters

	Initial beam parameters
Longitudinal Distribution	Gaussian
Transverse Distribution	Cut-Gaussian
Bunch Length (FWHM)	6 ps
Beam Diameters	2 mm

In the case of the accelerating columns, the input phase conditions where the energy of the accelerated electron beam is maximized and the energy spread is minimized for a given field gradient were identified. The input phases of accelerating columns 1 and 2, and 3 and 4 were synchronized in couples as they use the same RF power source. The optimal strength of the solenoid was identified to minimize the beam emittance and size, which increases due to the space charge effect. The two quadrupole magnets between accelerating columns 2 and 3, and between 3 and 4, were set to their optimal strengths based on the beam emittance and the horizontal and vertical size after the final accelerating column. If needed, the beam emittance and size can be further adjusted in the transfer section from the Linac to the booster ring.

○ Simulation of single-bunch operation

The operational specifications were optimized, assuming a maximum bunch charge of 1 nC in single-bunch operation. <Figure 2.1.4.25> shows the distribution of optimized solutions in the objective space over 300 generations. A clear Pareto front is observed in the distribution of optimized solutions for the horizontal normalized rms emittance with respect to the energy spread. In the distribution, there are solutions scattered in the emittance direction. This is because the vertical quadrupole magnet is located at the linac end, resulting in less vertical focusing than horizontal focusing. When the order of the quadrupole magnets was changed, it was confirmed that the solution distribution in the objective space also changed accordingly.



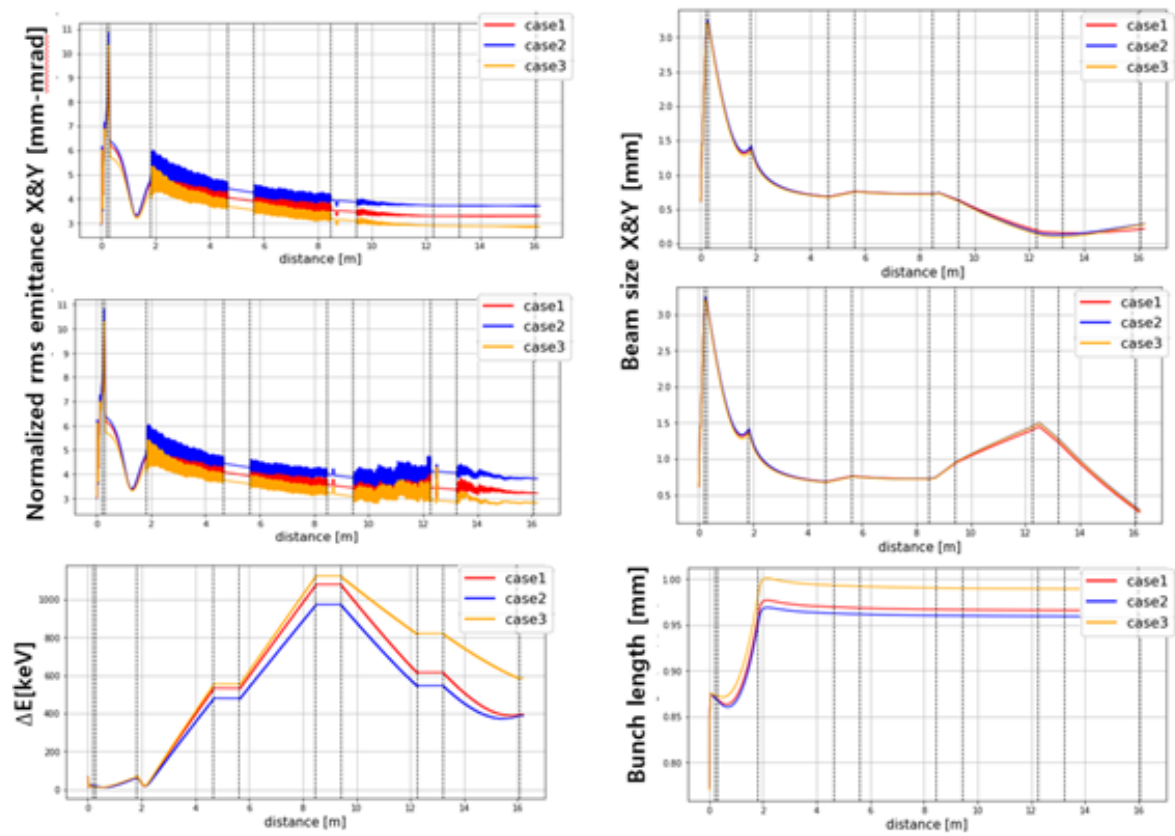
<Figure 2.1.4.25> Optimized solutions in the objective space (generation : 300).

Three cases were examined to compare the beam dynamics results in the distribution of non-dominated solutions obtained using MOGA. These cases had different weightings for energy spread out of objective functions, as shown in <Table 2.1.4.8>

<Table 2.1.4.8> Choice of cases depending on the objective's importance

Mode	Longitudinal	Transverse	
	Energy Spread	Emittance X	Emittance Y
Case 1	0.5	0.25	0.25
Case 2	0.8	0.1	0.1
Case 3	0.3	0.35	0.35

<Figure 2.1.4.26> shows linac's beam dynamics simulation results for these three cases. For all three cases, the transverse normalized rms emittance in the linac shows a stable variation and damping with respect to the optimized operation variables. The energy spread increases in the first and second accelerating columns but then decreases in the third and fourth columns, demonstrating that the RF input phase has been optimized to minimize it. Similarly, it satisfies the design requirements.



<Figure 2.1.4.26> Linac's beam dynamics simulation bn result based on the optimized case.

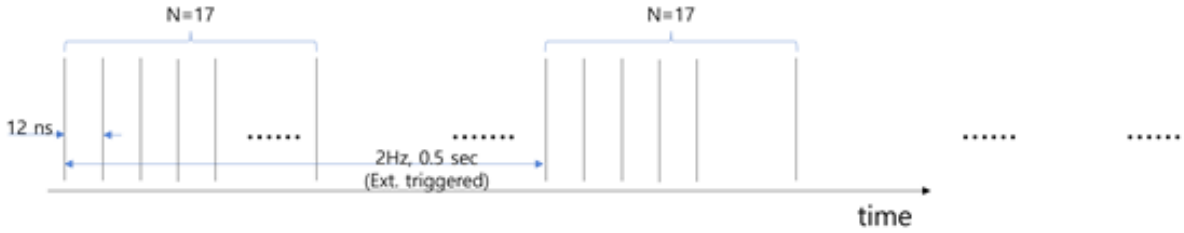
<Table 2.1.4.9> shows the beam parameters obtained by the linac's beam dynamics simulation for three cases. At the linac end, all meet the requirements of <Table 2.1.4.4> energy spread < 1 MeV (0.5%), transverse geometric emittance < 10 nm, and bunch length < 1 mm.

<Table 2.1.4.9> Beam tracking simulation result

	Case 1	Case 2	Case 3	Unit
Energy Spread	381.50	372.17	584.24	keV
Geometric Emittance X	8.44	9.52	7.37	mm-mrad
Geometric Emittance Y	8.18	9.71	7.21	mm-mrad
Beam Size X	0.21760	0.29162	0.28593	Mm
Beam Size Y	0.26149	0.29447	0.28566	Mm
Bunch Length	0.96584	0.95932	0.98924	Mm
Average Energy	200.16	200.61	200.92	MeV

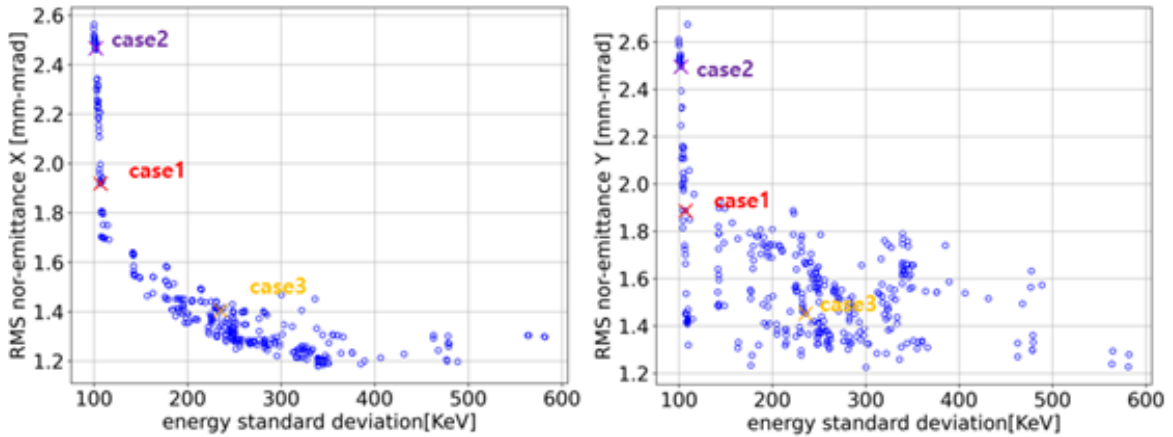
○ Simulation of multi-bunch operation

The multi-bunch operation is based on 64 bunches as the default, but the simulations were performed over a broader range. Simulations were conducted for two scenarios, one consisting of 17 bunches per bunch train and the other of 102 bunches. <Figure 2.1.4.27> shows the multi-bunch scenario composed of 17 bunches. In the case of multi-bunch operation, the charge per bunch and the bunch spacing are determined by the number of bunches included in the bunch train. Accordingly, simulations were performed to optimize the operating specifications of each device in the linac for multi-bunch acceleration.



<Figure 2.1.4.27> A multi-bunch scenario consisting of 17 bunches.

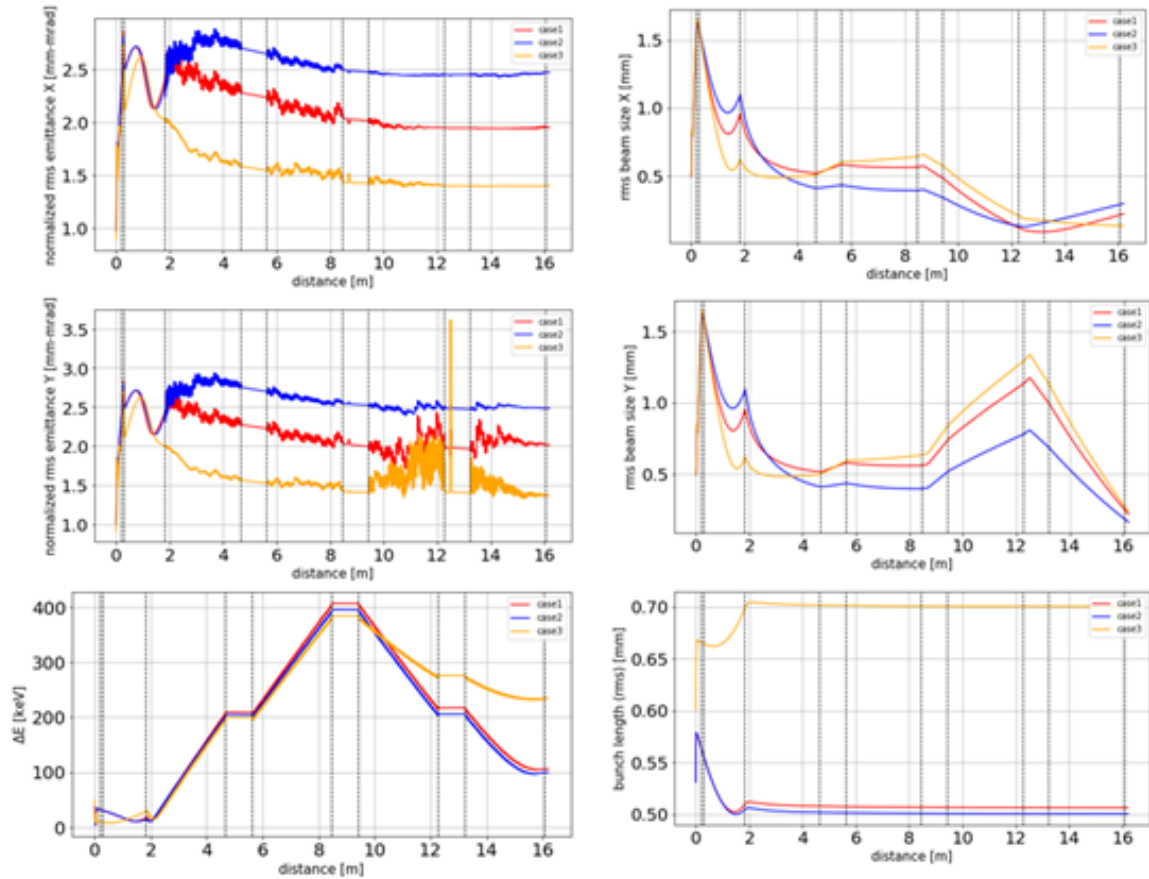
For the multi-bunch mode consisting of 17 bunches, the operational specifications were optimized for the case where the total charge is 3 nC, the highest allowed value, which means each bunch has 176 pC.



<Figure 2.1.4.28> The MOGA-based optimization results when the bunch charge is 176 pC.

Beam tracking simulations were performed after choosing the three cases from <Table 2.1.4.5>, as in single bunch mode, among various operational specifications optimized using MOGA, as shown in <Figure 2.1.4.28>. <Figure 2.1.4.29> and <Table 2.1.4.7> present the beam parameters obtained from beam dynamics simulations and confirm that there are

differences in values depending on the weighting of the objective function. At the linac end, all of them meet the requirements in <Table 2.1.4.4> energy spread < 1 MeV (0.5%), transverse geometric emittance < 10 nm, and bunch length < 1 mm.



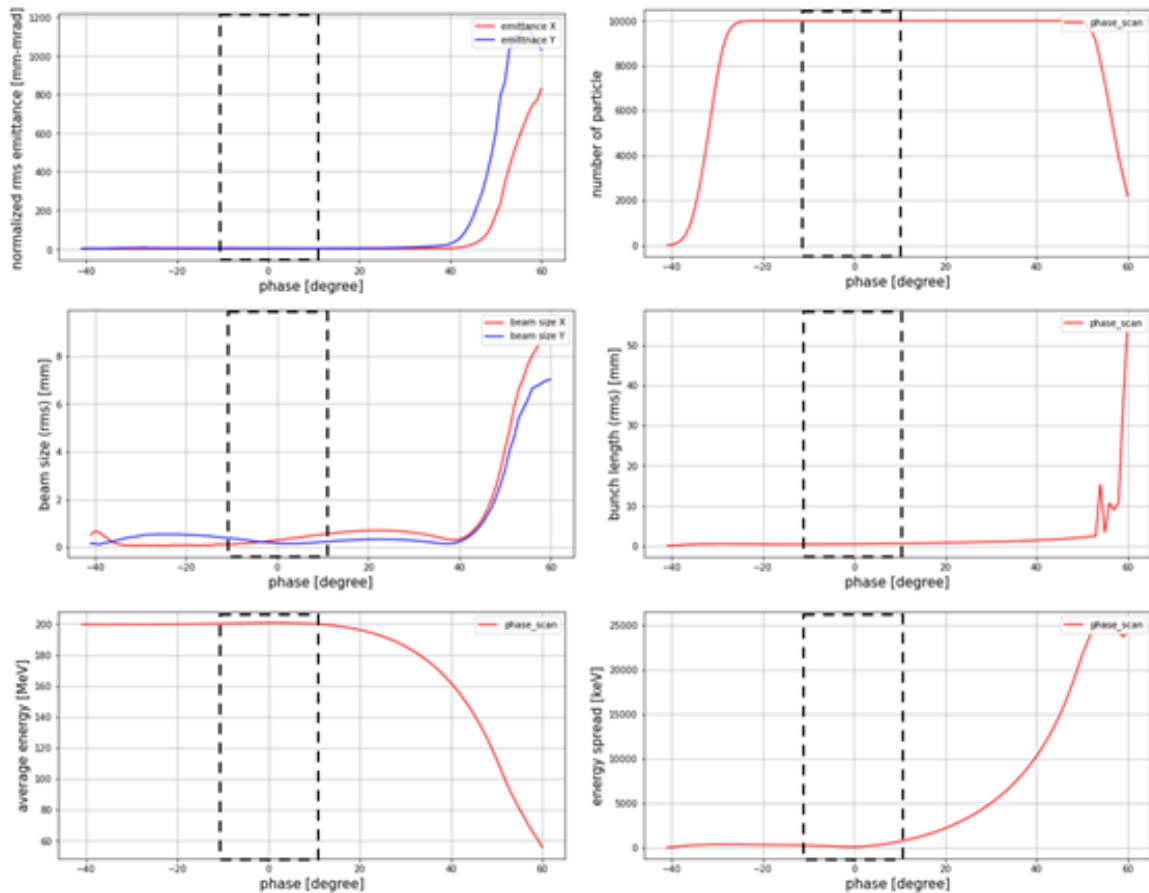
<Figure 2.1.4.29> Beam dynamics simulation result in the linac based on the optimized case.

<Table 2.1.4.10> Beam tracking simulation result for bunches of 176 pC charge

	Case 1	Case 2	Case 3	Unit
Energy Spread	106.40	99.888	234.61	keV
Emittance X	1.9534	2.4723	1.4045	mm-mrad
Emittance Y	2.0136	2.4842	1.3651	mm-mrad
Beam Size X	0.21993	0.29628	0.13241	Mm
Beam Size Y	0.21842	0.16310	0.23787	Mm
Bunch Length	0.50637	0.50047	0.70054	Mm
Average Energy	200.65	200.68	201.77	MeV

Based on Case 1, which had a charge of 176 pC, the allowable range of input phase when each bunch entered the accelerating column was obtained according to the spacing between bunches. As a result of the parameter sweep simulations for the input phase of the

accelerating column, the electron beam's accelerated energy and beam loss are shown in <Figure 2.1.4.10>. For beam loss, the available input phase of the accelerating column is from -50 degrees to +30 degrees relative to the input phase that yields the maximum energy. However, to obtain an average electron beam energy of 200 MeV in a linac, the available input energy was confirmed to be narrowed to approximately ± 10 degrees. Within this range, the beam emittance, bunch length, and energy spread meet the design requirements. With these, it is possible to determine the constraint on the laser beam timing of the electron gun system during multi-bunch operation.



<Figure 2.1.4.30> Beam loss and property change according to the accelerating column input phase.

In the multi-bunch operation mode, when there are 102 bunches in the bunch train, the charge per bunch is approximately 30 pC. Considering the operational ease of the multi-bunch operation mode, the same accelerating column input phase and quadrupole strength as in the 176 pC charge Case 1 were used, and only the solenoid strength was optimized using a parameter sweep. The optimized operational specifications for both multi-bunch modes are shown in <Table 2.1.4.11>.

<Table 2.1.4.11> Optimized operational specifications
for the two multi-bunch modes below

	Variable	Charge		Unit
Operational Specifications	Charge	176	30	pC
	Gun Cavity Phase	-19.9185	-19.9185	degree
	Phase of accelerating column 1 & 2	-16.6376	-16.6376	degree
	Phase of accelerating column 3 & 4	1.6094	1.6094	degree
	Solenoid strength	0.187256	0.175	T
	Strength of quadrupole magnet 1	1.558093	1.558093	T/m
	Strength of quadrupole magnet 2	-2.95162	-2.95162	T/m

○ Error and Tolerance

An error study simulation was conducted using the random error function provided by ASTRA to determine the allowable range of each device for each of the optimized linac operational specifications based on the results of single and multi-bunch simulations. The variable ranges used for the error study of each linac device are as shown in <Table 2.1.4.12>. For the Gaussian distribution with the error value in the table as 1-sigma, a 2-sigma cutoff was applied. One hundred random simulations were performed for each operation mode to determine the allowable range of operation specifications of the devices and the beam characteristics.

<Table 2.1.4.12> Variable ranges for the linac error study

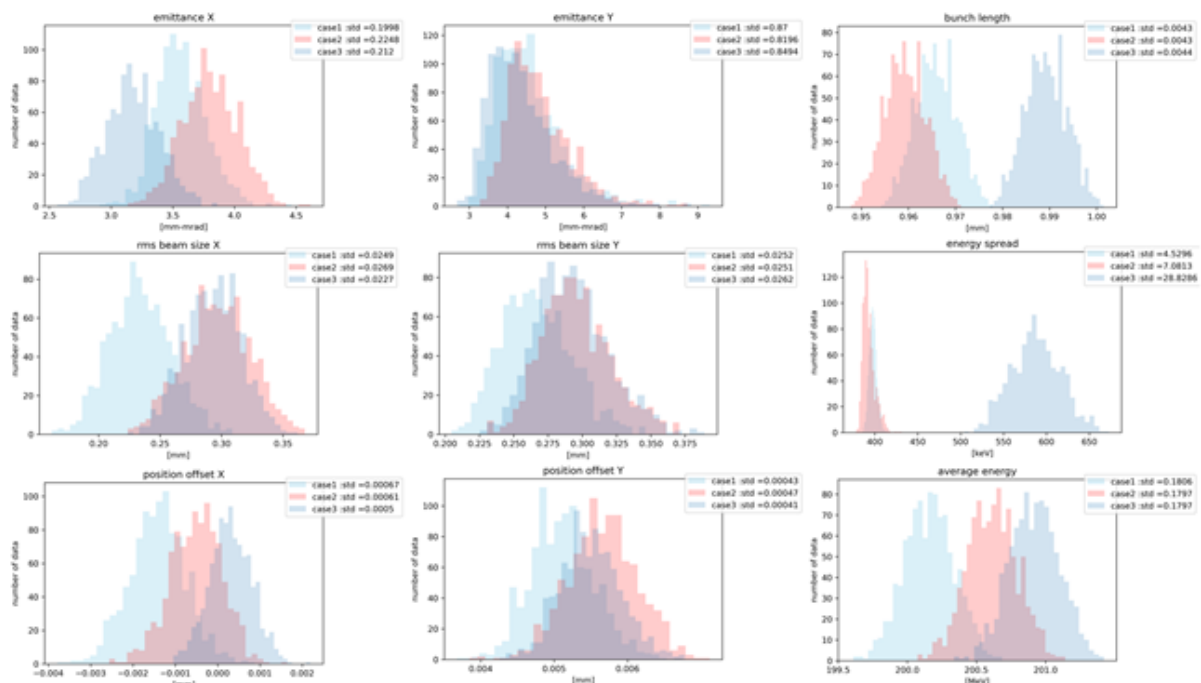
Categories	Parameters	Error Values	Units
RF Gun	Gradient	0.2	%
	Input Phase	0.2	Degree
Accelerating Cavity	Gradient	0.2	%
	Input Phase	0.2	Degree
Solenoid	Strength	0.1	%
Quadrupole	Strength	0.1	%

<Table 2.1.4.13> and <Figure 2.1.4.31> present the results of an error study for a single bunch mode with a charge of 1 nC. The standard deviation and distribution of the beam emittance X and Y, beam size X and Y, position offset X and Y, average beam energy, energy spread, and bunch length are shown. For the arbitrarily given errors, the degree to

which most beam parameters change is similar in all cases. However, the energy spread differs by up to 7 times depending on the case. Case 1, which has a value of less than 0.5% as required, is the most stable operation specification.

<Table 2.1.4.13> The error study results for a 1 nC bunch

	Case 1	Case 2	Case 3	Unit
Energy Spread	4.7003	7.2553	29.5605	keV
Emittance X	0.2091	0.2251	0.2105	mm-mrad
Emittance Y	0.8356	0.8033	0.8602	mm-mrad
Beam Size X	0.0253	0.0268	0.0227	Mm
Beam Size Y	0.0247	0.0248	0.0261	Mm
Position Offset X	0.00067	0.00062	0.00049	Mm
Position Offset Y	0.00043	0.00046	0.0004	Mm
Bunch Length	0.0044	0.0043	0.0045	Mm
Average Energy	0.1762	0.1749	0.1756	MeV



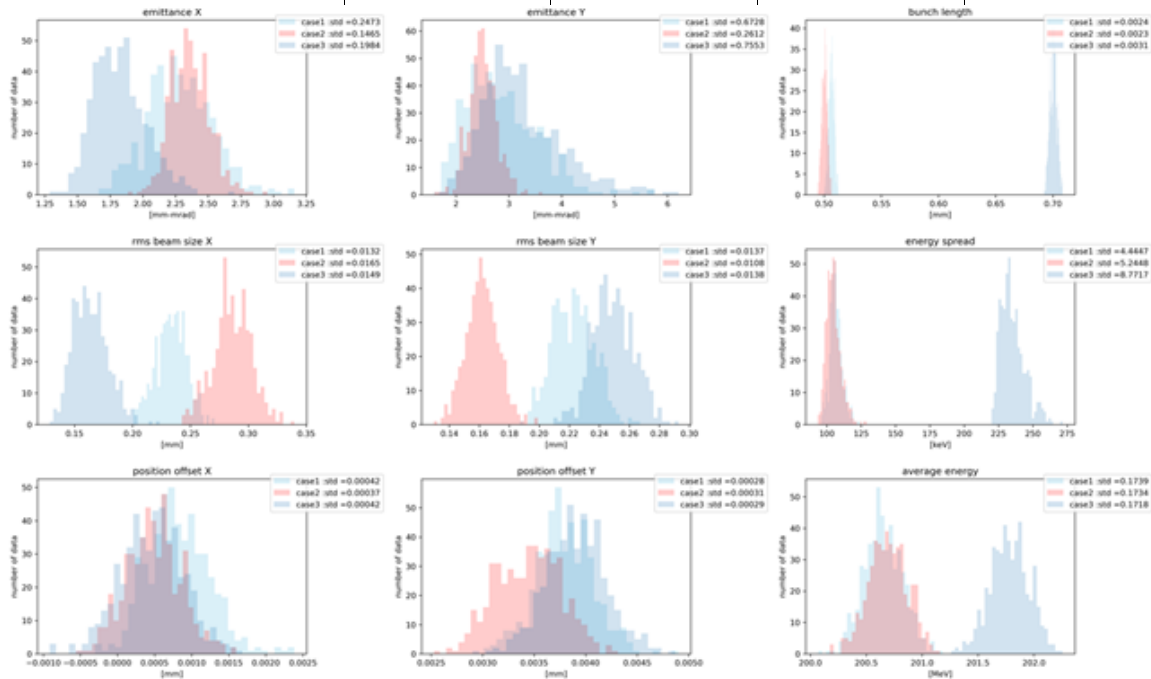
<Figure 2.1.4.31> The error study results for a 1 nC bunch.

<Table 2.1.4.14> and <Figure 2.1.4.32> present the results of an error study on a 176 pC bunch in the 17-bunch multi-bunch mode. The standard deviations and distributions of emittance X and Y, beam size X and Y, position offset X and Y, average energy, energy

spread, and bunch length are shown. For arbitrarily given errors, the degree to which most beam parameters change is similar in all cases. However, the energy spread varies significantly from case to case, indicating that Case 1, which has the smallest value, is the most stable operation specification.

<Table 2.1.4.14> The error study results for a 176 pC bunch

	Case 1	Case 2	Case 3	Unit
Energy Spread	4.4447	5.2448	8.7717	keV
Emittance X	0.2473	0.1465	0.1984	mm-mrad
Emittance Y	0.6728	0.2612	0.7553	mm-mrad
Beam Size X	0.0132	0.0165	0.0149	Mm
Beam Size Y	0.0137	0.0108	0.0138	Mm
Position Offset X	0.00042	0.00037	0.00042	Mm
Position Offset Y	0.00028	0.00037	0.00042	Mm
Bunch Length	0.0024	0.0023	0.0031	Mm
Average Energy	0.1739	0.1734	0.1718	MeV



<Figure 2.1.4.32> The error study results for a 176 pC bunch.

Among the three optimized operation specifications, selecting the case that allows for the most stable operation was possible when the error study results were reflected. <Table 2.1.4.15> shows the linac operation conditions and the beam parameters at the linac end for both single-bunch and multi-bunch modes.

<Table 2.1.4.15> Charge-dependent operational specifications and beam characteristics reflecting the error study results

	Variable	Charge			Unit
		Multi-bunch mode		Single-bunch mode	
Operational Specifications	Charge	0.176	0.030	1	nC
	Gun Cavity Phase	-19.9185	-19.9185	-15.8157	degree
	Phase of accelerating column 1 & 2	-16.6376	-16.6376	-19.0112	degree
	Phase of accelerating column 3 & 4	1.6094	1.6094	4.93055	degree
	Solenoid strength	0.187256	0.175	0.196828	T
	Strength of quadrupole magnet 1	1.558093	1.558093	1.399805	T/m
	Strength of quadrupole magnet 2	-2.95162	-2.95162	-2.87498	T/m
Beam Parameters	Horizontal emittance	1.9534	1.1334	3.2990	mm-mrad
	Vertical emittance	2.0136	1.3254	3.2145	mm-mrad
	Horizontal beam size (rms)	0.21993	0.28780	0.21760	mm
	Vertical beam size (rms)	0.21842	0.19896	0.26149	mm
	Bunch length	0.50637	0.34488	0.96584	mm
	Beam average energy	200.67	200.63	200.16	MeV

(4) Modulator and Klystron

○ Klystron

Klystrons are high-power microwave amplification devices that utilize pulse power supplied by a modulator to amplify RF waves. In the 4GSR, two S-band E37366 models manufactured by Canon will be used. Operating at a frequency of 2,997.6 MHz with approximately 500 W and 3 μ s pulses, they can deliver a maximum output of 70 MW to the accelerating columns, serving as the energy source for accelerating electrons.

The Canon E37366 klystron consists of six cavities, including an input cavity and an

output cavity, and an electron gun with a 1.9 micro perveance. It employs two RF windows, each capable of handling up to half of the maximum RF output. An RF window creates a vacuum seal between the inside and outside of the klystron. The RF outputs from the two klystrons are combined using a power combiner and transmitted to the accelerating columns through a waveguide. Magnets installed outside the klystron cavities focus the beam, with a maximum magnetic field strength of approximately 1.2 kG. The klystron's electron gun has an 8.9 cm diameter cathode and a maximum current density of about 8 A/cm². The electric field strength between the cathode and anode is approximately 200 kV/cm, and a pulse transformer is used to supply the pulses. The klystron body is immersed in an insulating oil tank. To shield against X-rays generated by the electron beam, the klystron collector and electron gun are surrounded by lead shielding. The Klystron output flange uses a PAL-type flange and gasket.



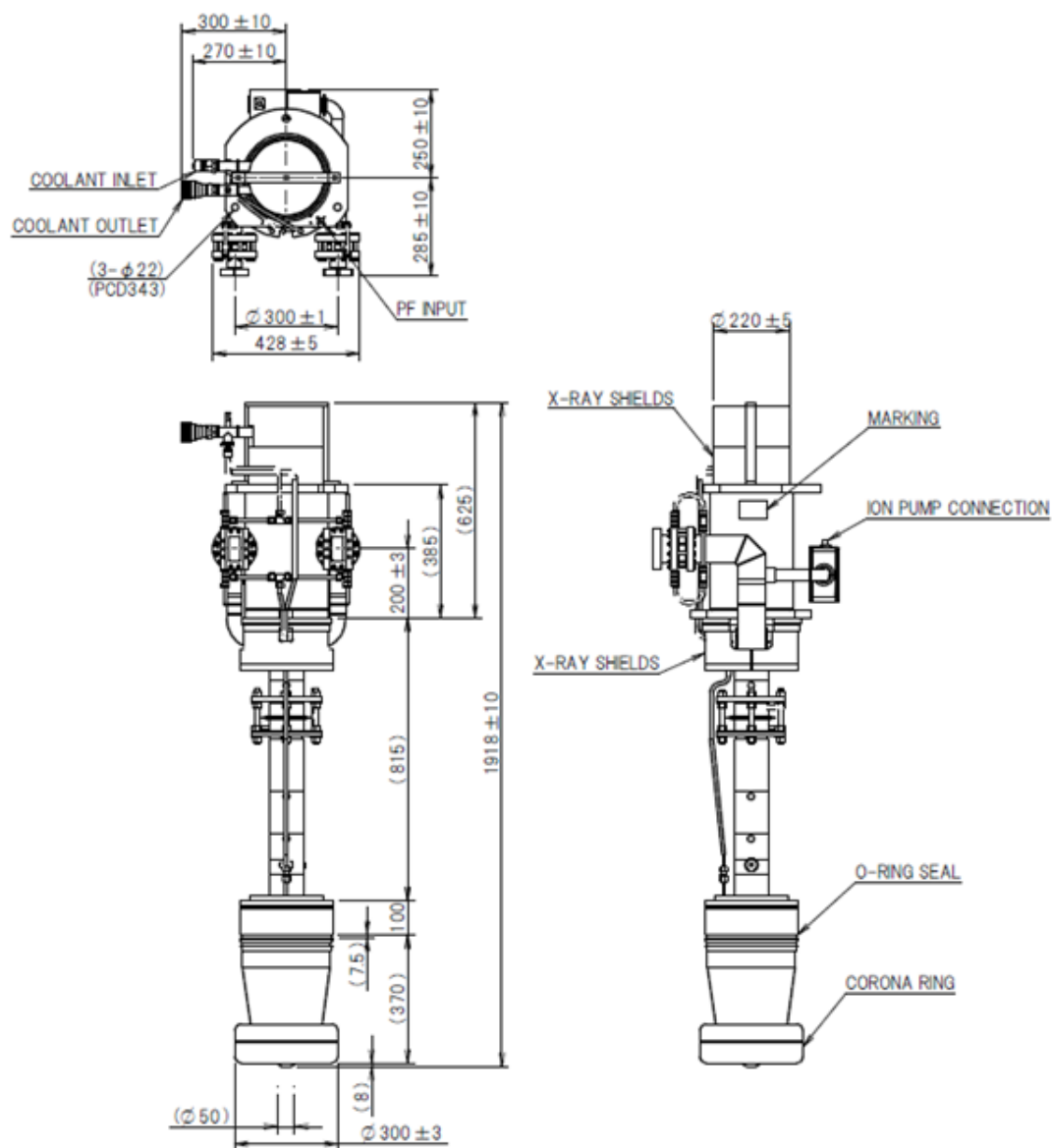
<Figure 2.1.4.33> Photo of a 70MW E37366 klystron.

<Table 2.1.4.16> shows the specifications for the E37366 klystron: frequency 2,997.6MHz, maximum output power 70MW, beam voltage 387kV, beam current 452A, and micro-perveance 1.9.

<Table 2.1.4.16> Specifications of an S-band klystron (E37366)

Description	Canon E37366	Unit
Frequency	2997.6	MHz
RF Pulse width	3.0	Ms
Beam voltage	387	kV
Beam current	452	A
Beam Voltage Pulse width	6.0	Ms
Repetition rate (max)	60	Hz
η -perveance	1.9	-
RF output power	≥ 70	MW
Average RF output power	5.0	kW
Drive power	500	W Max.
Gain	53	dB (max)
Efficiency	40	%
Focusing	VT-68915 Electron magnet	-
Filament voltage	90 to 110	Vac
Filament current	4.5 to 5.5	Aac
Water flow, min/klystron	55	l/min
Water flow, min/magnet	10	l/min
Cooling water inlet temperature, max	40	°C
Cooling water inlet pressure, max	10	kgf/cm ²

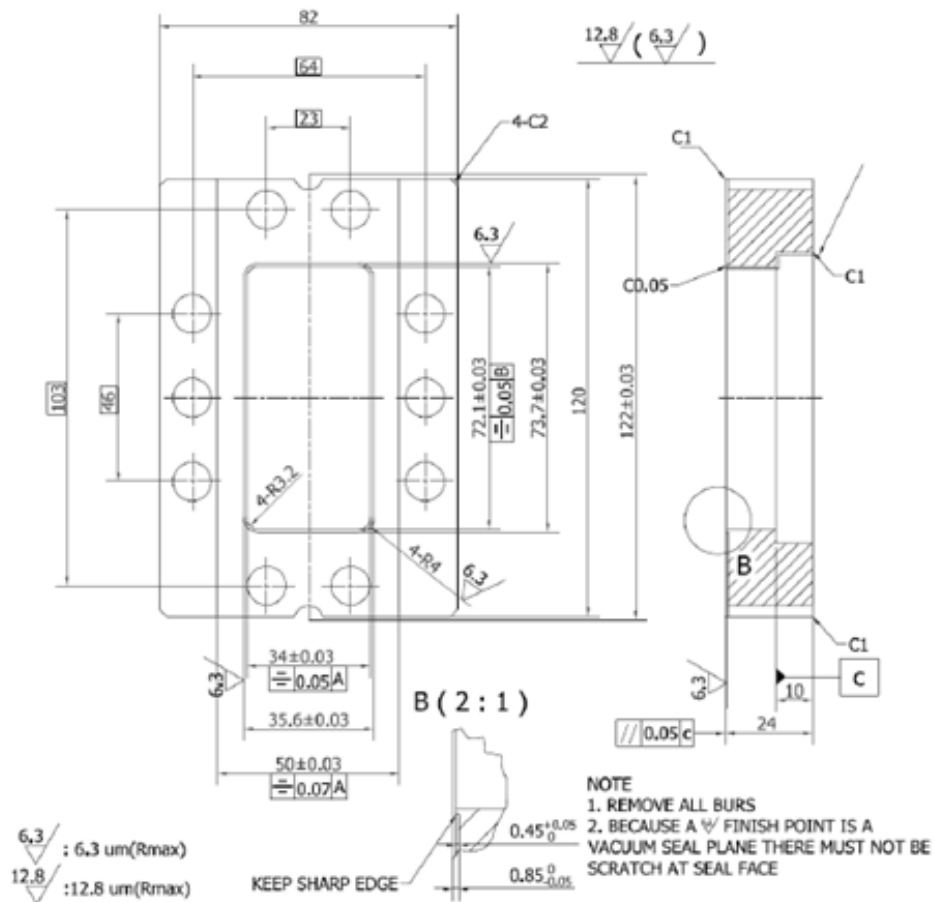
Unit: mm



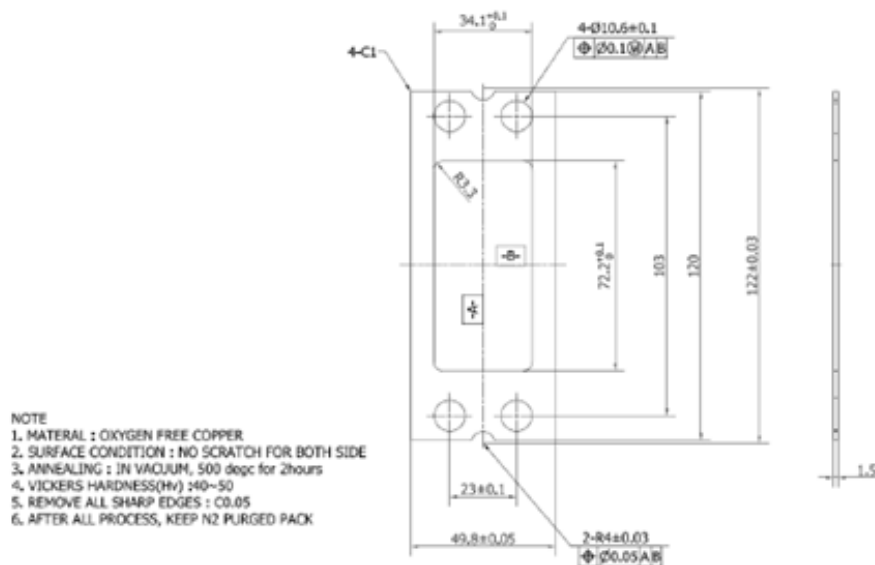
Outline Drawing E37366 (Tentative)

<Figure 2.1.4.34> Drawing of an E-37366 klystron.

Unit: mm



PAL Type Flange

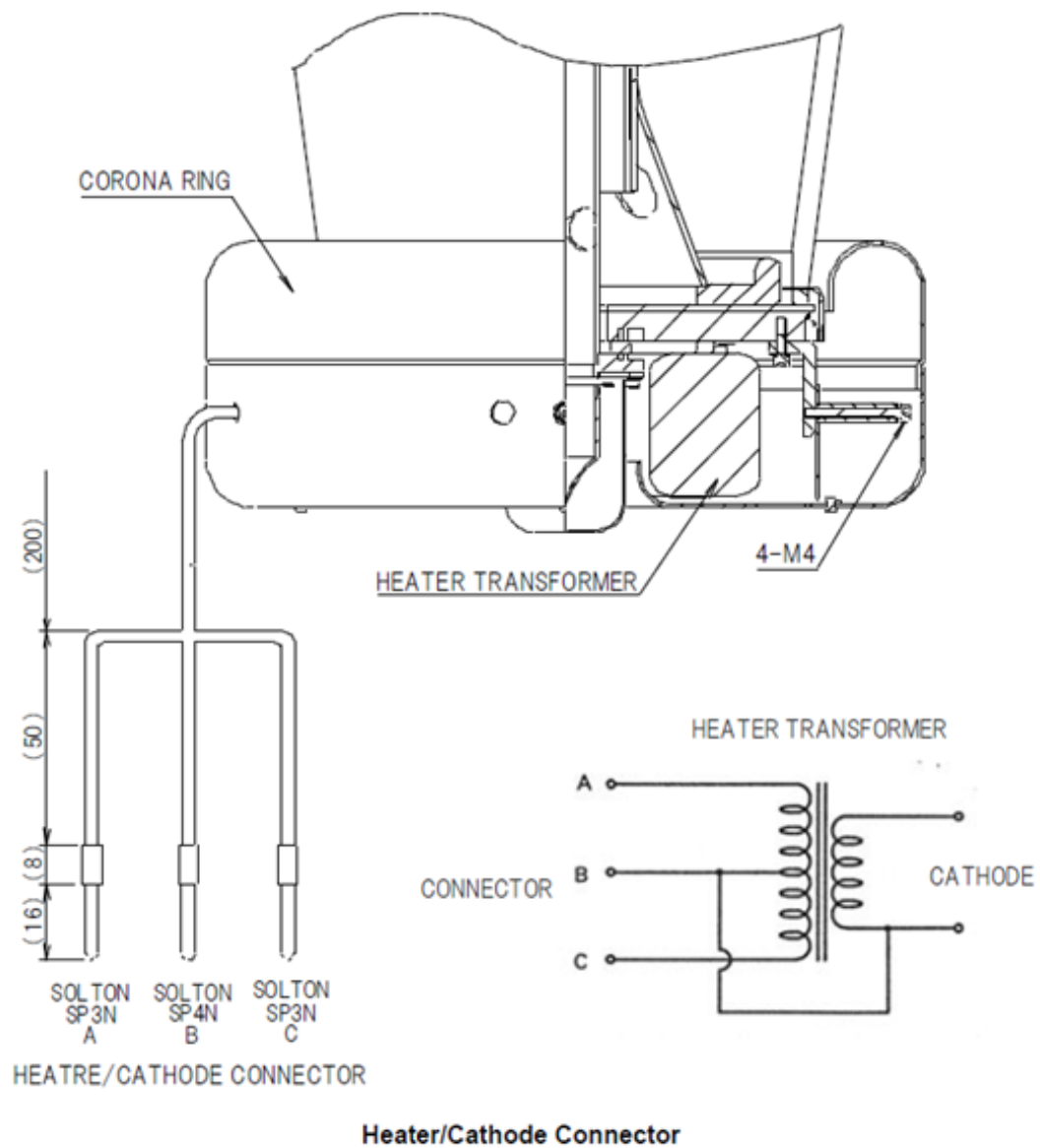


PAL Type Gasket (Excluded)

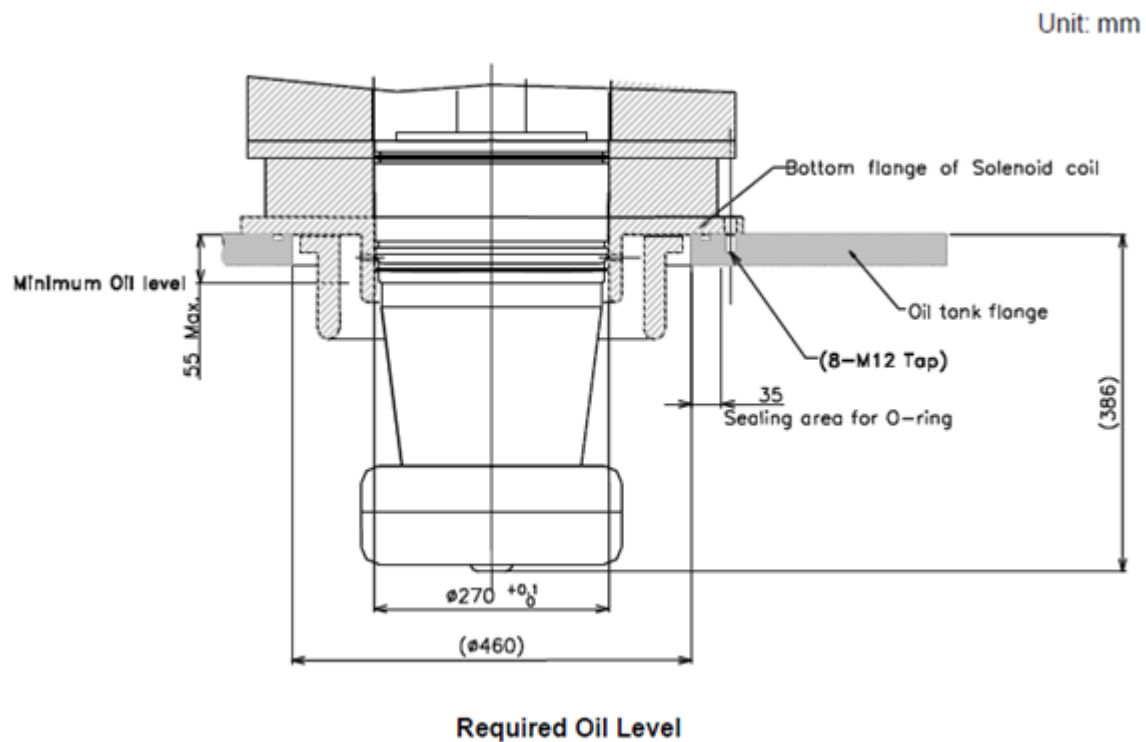
DIMENSIONAL DRAWING: PAL Type Flange

<Figure 2.1.4.35> The E-37366 klystron's output flange and gasket drawing.

Unit: mm



<Figure 2.1.4.36> The E-37366 klystron's Heater/Cathode connector drawing.



<Figure 2.1.4.37> The E-37366 klystron's Required Oil Level drawing.

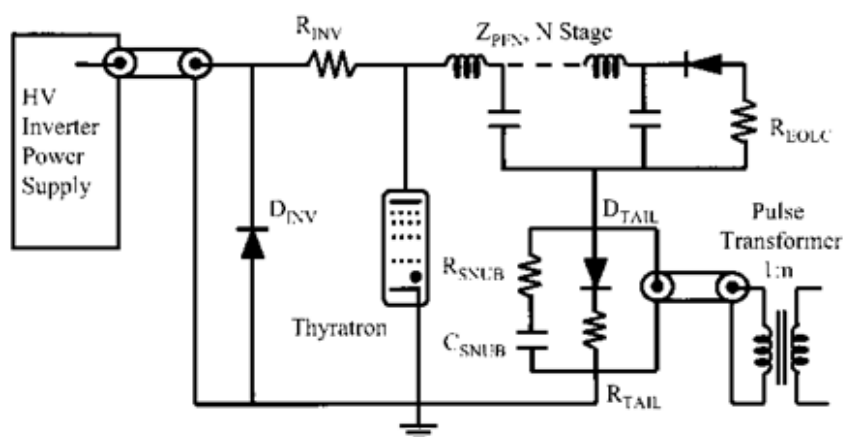
○ Modulator

In the 4GSR linac, a 70 MW klystron and two sets of 175 MW modulators using inverter-type high-voltage power supplies will be used as microwave sources to accelerate electrons up to 200 MeV. The specifications of each modulator are output 175 MW, beam voltage 387 kV, beam current 452 A, pulse width 6.2 μ s, repetition rate 60 Hz, and the load will be an S-band E37366 70 MW Klystron. The energy variation required for 4GSR is $\pm 0.2\%$ or less, and the voltage stability of the modulator's PFN is RMS 100 ppm or less. Introducing the inverter type high-precision high-voltage power supplies and DSP controllers makes it possible to meet these requirements and obtain high-voltage stability of the modulators. The high-voltage inverter power supply supplies at 60 kJ/s, and the charging time is about 15 ms. The modulator specifications are as shown in <Table 2.1.4.17>.

<Table 2.1.4.17> Modulator specifications

Description	Value	Unit
Peak Power	175	MW max
Inverter CC HVPS Average Power	90	kJ/sec
Repetition Rate	10	Hz max
Voltage Stability (rms)	> 0.01	%
Pulse Peak Output Voltage	387	kV
Pulse Peak Output Current	452	A
ESW	6.0	μ s
Flattop Width	3.0	μ s
Flattop Flatness	0.2	%
Charging Time	15	ms
Pulse Transformer Turn ratio	17	
Primary Impedance	3.0	ohm
PFN Total Capacitance	1.0	μ F
PFN Total Inductance	7.7	μ H

<Figure 2.1.4.38> is a circuit diagram of a modulator that generates pulses. The energy supplied from a high-voltage inverter power supply is directly charged to the PFN capacitor, and then the energy is transmitted to the load through a thyatron switch.

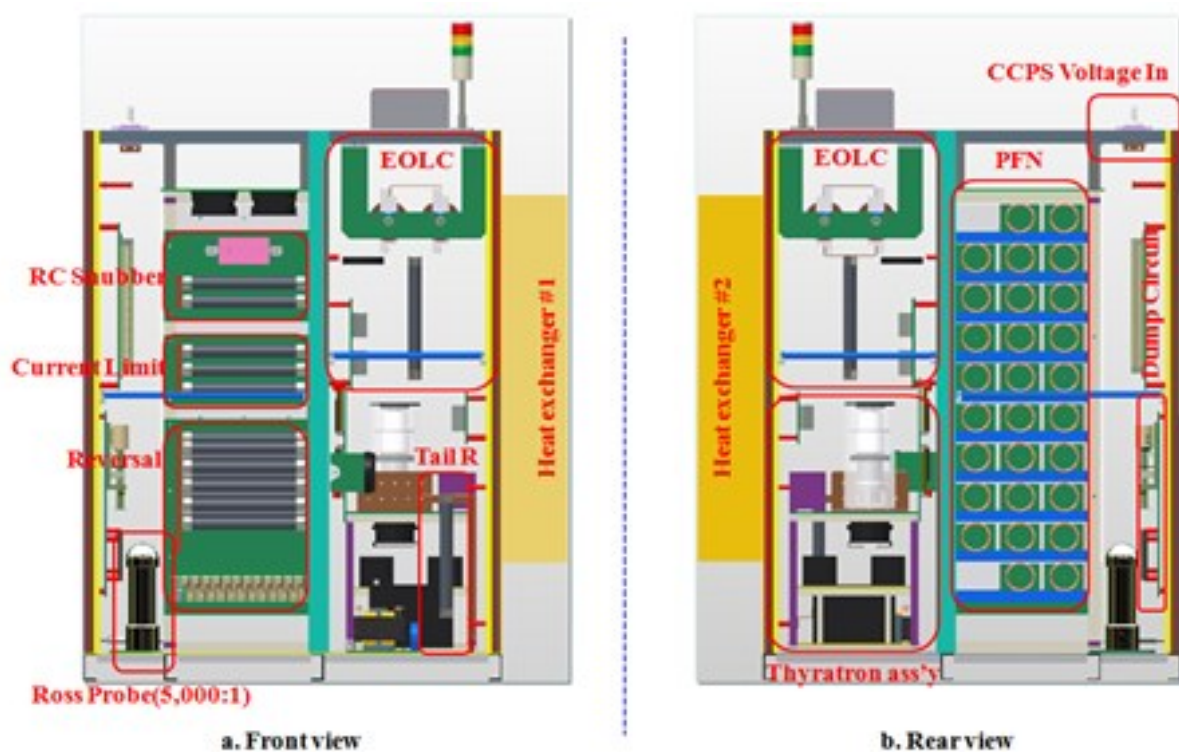


<Figure 2.1.4.38> The circuit diagram of a modulator using a high-voltage inverter power supply.

To meet the modulator's pulse flattop flatness specification of $\pm 0.2\%$ required for linac multi-bunch operation, the capacity and quantity of the PFN capacitor and PFN inductor

constituting the PFN were adjusted to design the pulse flatness within $\pm 0.2\%$.

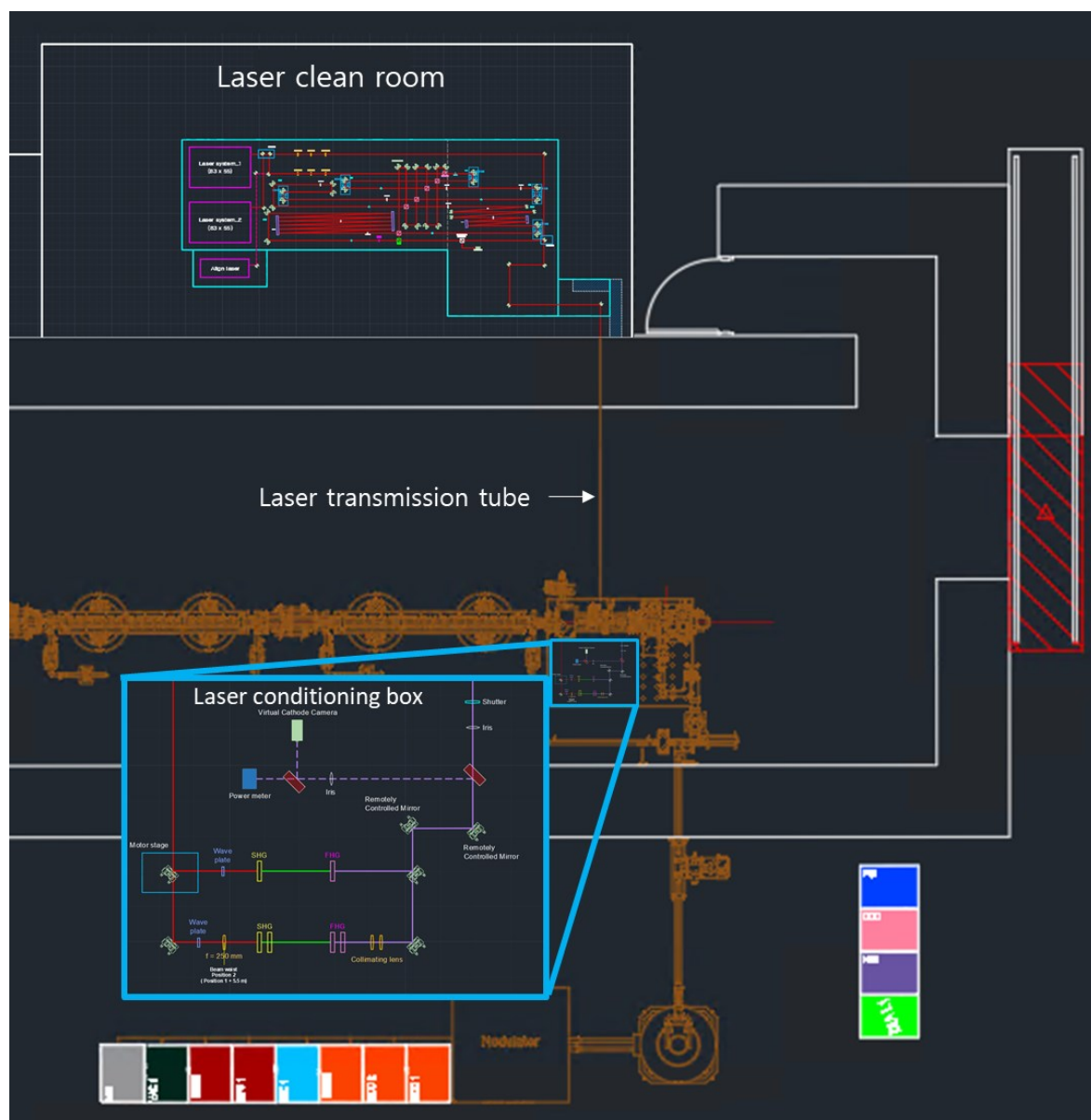
The modulator of the 4GSR linac will operate at 10 Hz, and much heat will be generated in the limiting resistor or protection circuit when charged by a thyatron switch and a high-voltage inverter power supply. Therefore, the design considered heat load measures for these conditions. In addition, since a high voltage will be applied, the design considered the internal space arrangement and measures against noise caused by the high current pulse. The heat source generated in the modulator consumes about 4-5 kW at the protection resistor during charging, and the consumption of other resistors will be designed to be within about 1-2 kW.



<Figure 2.1.4.39> Design of the modulator inside.

(5) Laser System

For the stable operation of the injector laser, a clean room will be constructed to control temperature and humidity (temperature stability within 0.5°C , humidity stability within 5%). To reduce EMI noise interference caused by the modulators, the laser room will be located on the opposite side of the gallery, similar to the PAL-XFEL setup. The laser is transmitted through a laser transmission tube, conditioned (e.g., size adjustment) on the gun table, and then injected into the gun. The laser specifications are based on a copper cathode. The basic repetition rate is 2 Hz, but it should be designed to operate at a higher repetition rate (>10 Hz) considering a feedback speed.

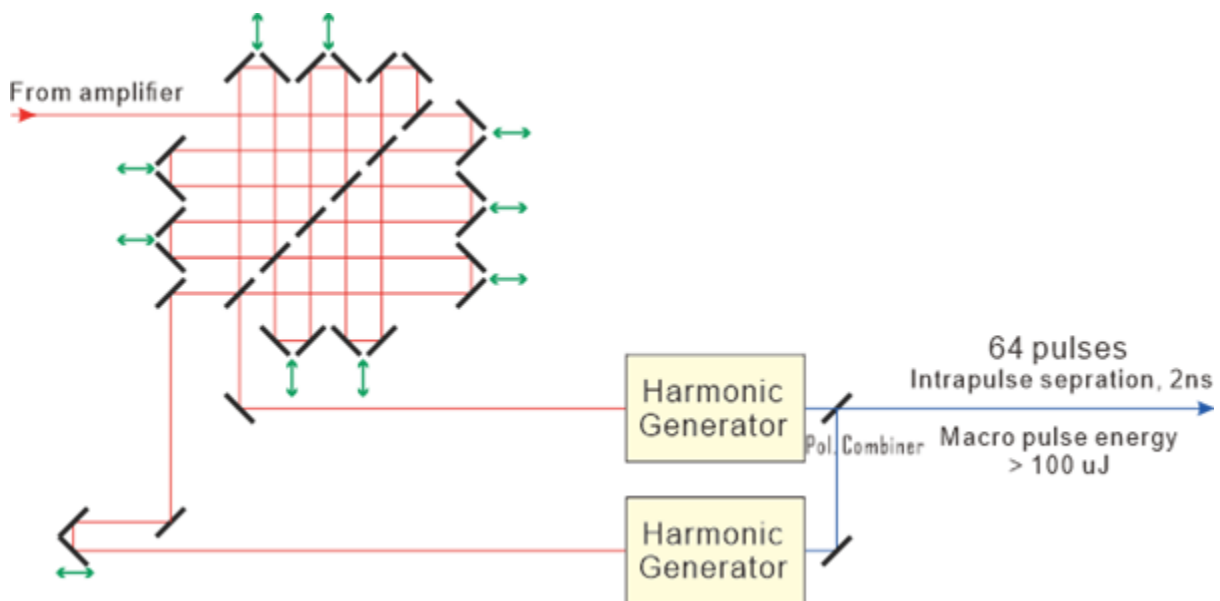


<Figure 2.1.4.40> Schematic layout of the laser transport system from the laser clean room to the photocathode.

<Table 2.1.4.18> Laser system specifications

Parameter	Single bunch mode	Multi-bunch mode
UV pulse length	6 to 8 ps FWHM	6 to 8 ps FWHM
UV pulse energy	> 100 μJ	> 100 μJ (64 pulses)
UV pulse energy stability	< 2%	< 5%
Timing sync. stability	< 200 fs rms	< 200 fs rms
Repetition rate	2 Hz, 10 Hz	2 Hz, 10 Hz

A split and delay is used to provide the 64 pulses (with an approximately 2-ns interval) required in the multi-bunch mode. The power and intervals of the pulses are consistently adjusted using the manual attenuator and mechanical time delay, which includes matching. After UV conversion at the split and delay device, the two outputs of 32 pulses are combined using a polarizing combiner to minimize energy loss. In particular, the time intervals can be finely tuned and monitored in real time to the level of 100 fs using a synchronized 499.593 MHz laser oscillator.



<Figure 2.1.4.41> 64 Laser multi bunch pattern generation.

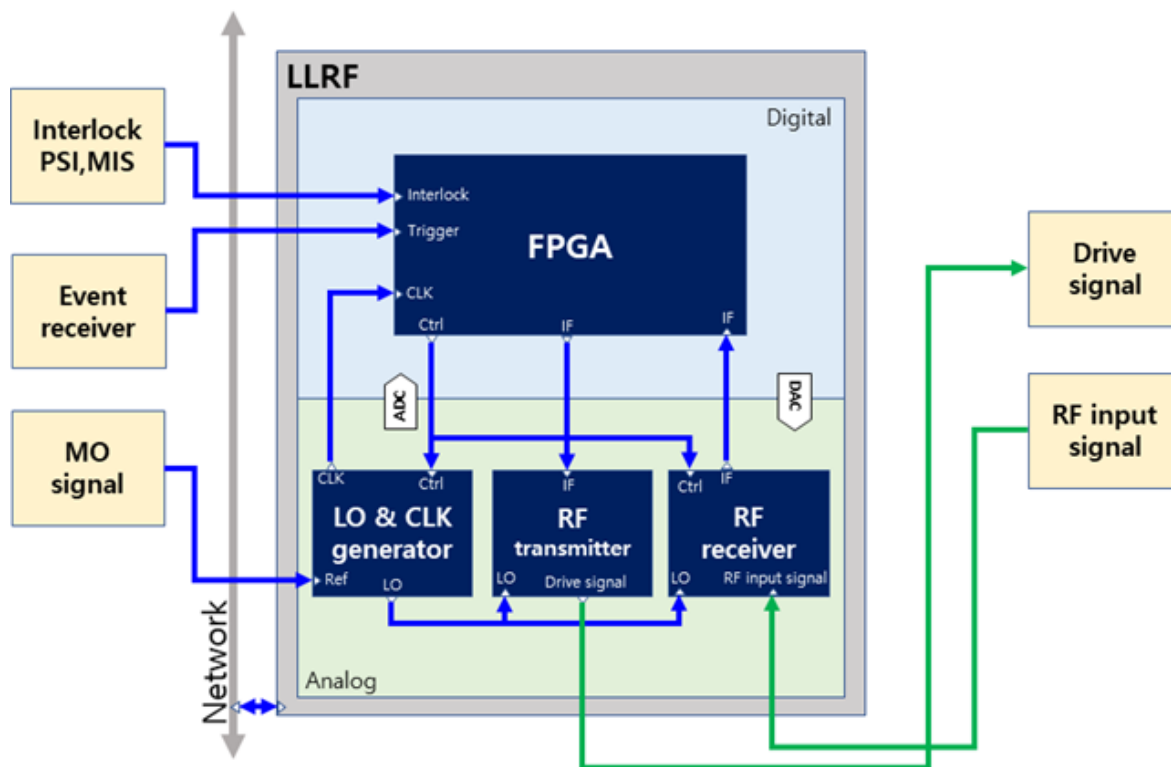
(6) Timing Control

○ Time Synchronization

The linac frequency has been decided to be 2997.56 MHz, an integer multiple of the storage ring frequency 499.593 MHz, for time synchronization with the storage ring. A time synchronization system will be built in three stages for perfect time synchronization. In the first stage, the linac commissioning and operation proceeds without time synchronization. In the second stage, the linac and storage ring operate in indirect time synchronization, similar to Japan's SACLA linac and SPring-8 storage ring. Finally, the entire accelerator operates in a fully time-synchronized state between the linac and the storage ring by sharing a single reference oscillator. The shot-by-shot injection timing is designed to be controlled through the event trigger and RF phase shifter. The DDS phase shifter with ~ 20 fs stability and ~ 5 fs resolution, developed and used in XFEL, will be applied.

○ LRF (Low-Level Radio Frequency)

The LLRF control system is a device that monitors and controls the state of the components of the RF system while electron beam is accelerated. It performs the following main functions: It continuously monitors the internal state of the RF system. Doing so, it monitors the operating status and takes necessary actions. Also, it can transmit and receive interlock signals with high-voltage modulator systems, PSI, MIS, and LCW systems for personnel and equipment protection. It provides protection functions such as automatically stopping the RF system in case of unexpected situations. Through these functions, the LLRF system maintains synchronization between the RF field and the electron beam and minimizes the external disturbing effects, enabling optimal acceleration. The system block diagram of the LLRF is shown in <Figure 3.1.4.24>, and the specifications are summarized in <Table 2.1.4.19>.



<Figure 2.1.4.42> LLRF system block diagram.

<Table 2.1.4.19> Specifications of the LLRF system

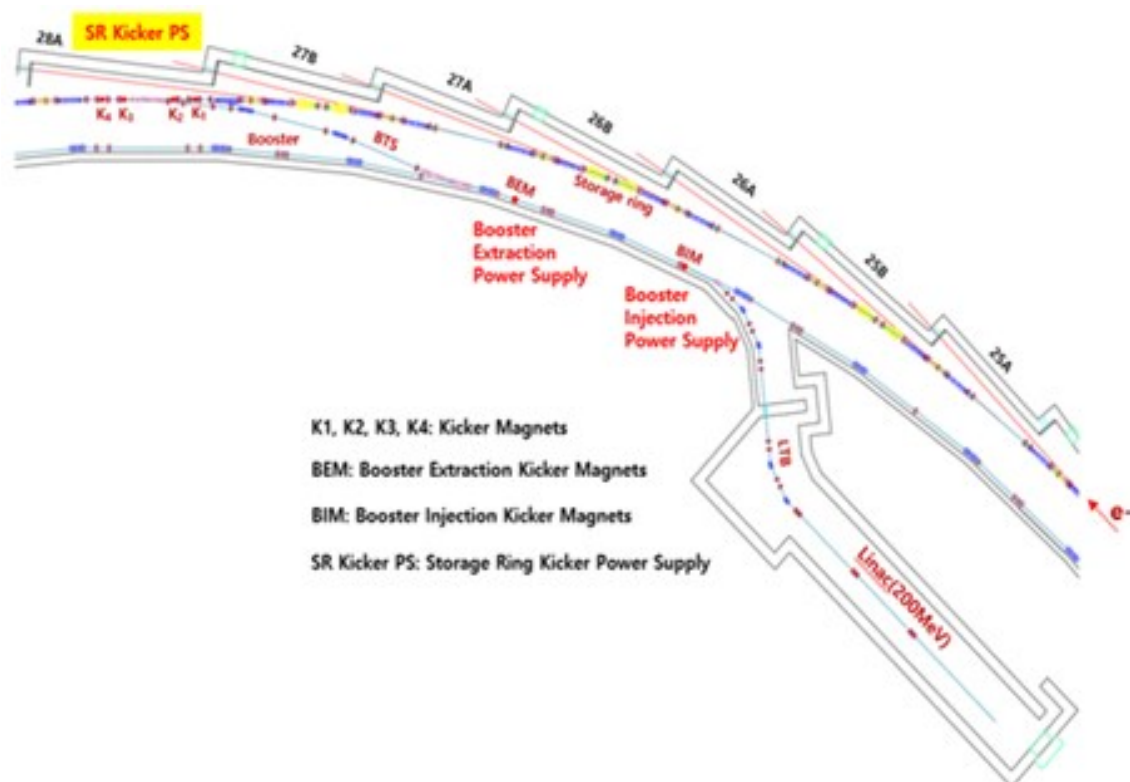
Parameter	Value
Operating frequency	2,997.56 MHz \pm 2 MHz
Number of channels (fast)	8
Channel-to-channel isolation	> 60 dB
Spurious-free dynamic range	> 60 dB
Amplitude dynamic range	\geq 25 dB
Power resolution	< 0.01%
Power stability	< 0.05% (upper 10 dB range)
Phase resolution	< 0.01°
Phase stability	< 0.05° (upper 10 dB range)
Output channel No.	1
Repetition rate	up to 10 Hz

G. Pulsed Power Supplies for Kicker Magnets

(1) Specifications and layout of the booster kicker

Pulse power supplies for kicker magnets are divided into power supplies for booster rings and power supplies for storage rings. The locations of the pulsed power supplies for the booster ring injection and extraction kicker magnets, along with the storage ring injection-kicker magnet, are shown in <Figure 2.1.4.43>. Electrons generated from an electron gun are accelerated to 200 MeV in the linac and then injected into the booster ring via the linac to booster (LTB) beam transport line. The energy of the injected electrons is ramped up in the booster ring to the final target energy of 4 GeV. The extraction kicker handles the extraction of the electron beam from the booster ring, and the extracted electron beam is injected into the storage ring by the storage ring injection kicker.

As shown in <Figure 2.1.4.43>, the power supplies for the booster ring kicker magnets will be placed in the shed area. To minimize inductance and reduce the length of the cables, the connection cables from the power supplies in the shed area to the magnets installed inside the booster ring tunnel goes through a separate trench.



<Figure 2.1.4.43> Location map of the booster kicker magnets and power supplies.

○ Injection system to the booster ring

The electron beam, accelerated to 200 MeV in the linac, enters the booster ring through the injection septum, and its trajectory is adjusted to be parallel to the central axis of the booster ring by the injection kicker. The design parameters of the booster ring injection magnet's pulsed power supply are shown in <Table 2.1.4.20>. To meet the requirements of the 4GSR storage ring, the 200 MeV linac considers two operating conditions. First, in the single-bunch mode, which generates two bunches per second, each bunch has a charge of about one nC. Second, for multi-bunch injection, 64 micro electron bunches with the total macro charge of 3 nC should be generated. To meet both conditions, the output pulse shape of the booster ring's injection power supply must be a flat-top type to allow multi-bunch injection. The flat-top width should be maintained for 200 ns. The pulse rise time may be ignored, but the pulse fall time should be designed to be within 2.0 μ s.

<Table 2.1.4.20> Parameters of the pulsed power supply for the booster ring's injection kicker magnet

Parameters	Injection
Pulse shape	half-sine
Switch type	IGBT
Pulse current [kA]	2
DC voltage [kV]	3
Flat-top width [μ s]	0.2
Rise time [μ s]	irrelevant
Fall time [μ s]	2.0
Magnet inductance [μ H]	0.45
Power supply system inductance [μ H]	< 1.9
Stability [%]	+/- 0.5
Repetition rate [Hz]	2

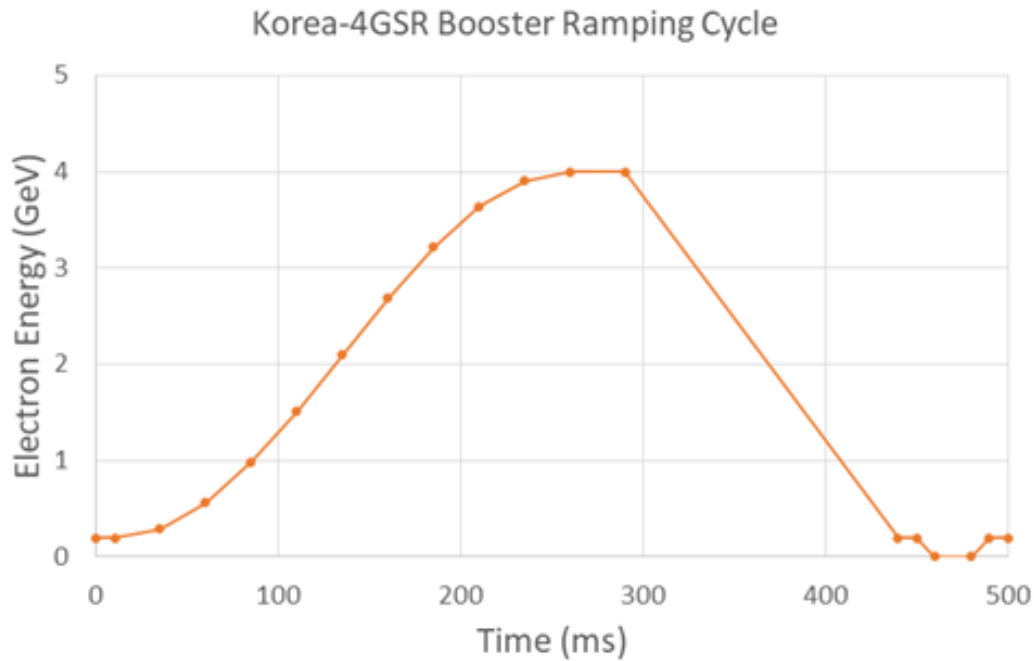
○ Booster ring extraction system

After being accelerated to 4 GeV in the booster ring, the extraction kicker in front of the injection septum deflects the electron beam circulating the booster ring out of its orbit. The design parameters of the booster ring's extraction power supply are shown in <Table 2.1.4.21>. Just as the booster ring's injection power supply, to meet both conditions (single and multi-bunch injection), the output pulse shape of the booster ring's extraction kicker pulsed power supply must also be a flat-top type to allow multi-bunch injection. The flat-top width should be maintained at 200 ns. The pulse rise time should be designed to be within 2.0 μ s, while the pulse fall time may be ignored.

<Table 2.1.4.21> Parameters of the pulsed power supply or the booster ring's extraction kicker magnet

Parameters	Extraction
Pulse shape	half-sine
Switch type	IGBT
Pulse current [kA]	7
DC voltage [kV]	14
Flat-top width [μ s]	0.2
Rise time [μ s]	2.0
Fall time [μ s]	irrelevant
Magnet inductance [μ H]	0.55
Power supply system inductance [μ H]	< 1.9
Stability [%]	+/- 0.5
Repetition rate [Hz]	2

The ramping cycle of the booster ring is as shown in <Figure 2.1.4.44> The electron beam with an energy of approximately 200 MeV from the linac has a dwell time of about 10 ms before the energy ramping in the booster. The ramping in the booster ring takes approximately 250 ms, and an electron beam of 4 GeV and 2 mA is obtained. After reaching the maximum energy, further stabilization takes about 30 ms, and then the electron beam is extracted from the booster ring and immediately sent to the storage ring injection system.



<Figure 2.1.4.44> Booster ring's ramping cycle.

(2) Specifications and layout of the storage ring kicker

The electron beam extracted from the booster ring should be bent horizontally to be injected into the storage ring. The final position of the beam in the booster ring should be the same height as the stored beam in the storage ring, and the injection septum magnet bends the electron beam at the booster ring end. The kicker magnet guides this bent electron beam to enter the dynamic range allowed by the storage ring. Initially, the injected beam and the already stored beam are separated by a thin wall of the injection septum. To merge the two beams into one beam, four kicker magnets are used to bring the part of the stored beam orbit at the injection area closer to the thin wall of the injection septum, allowing the injected beam to enter within the dynamic range of the storage ring. After orbiting the storage ring twice, the injected beam returns to nearly the same horizontal position with respect to the stored beam. Therefore, the current of the kicker magnet modulator should be zero after the electron beam has orbited the storage ring twice, or $2 \times 2.66 \mu\text{s}$ after the injection point, to avoid beam resonance and losses due to collisions with the injection magnet wall. If the kicker magnet power supplies are off, the beam transmitted through the beam transport line cannot enter the dynamic range of the storage ring.

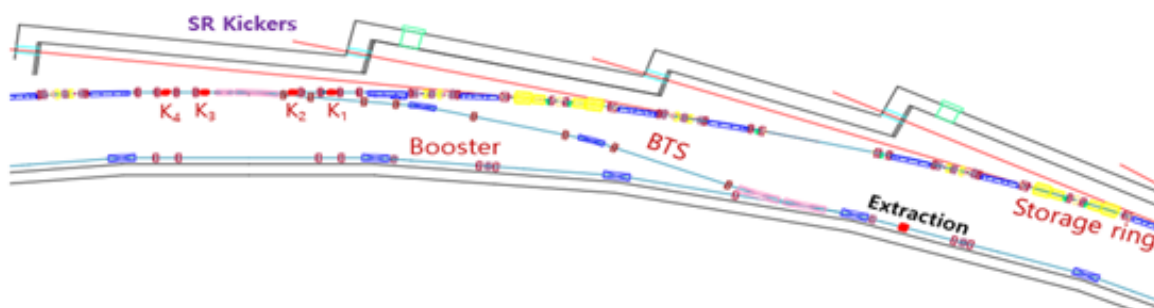
○ Storage ring kicker system

As shown in the location diagram of the storage ring magnets and kicker power supplies in <Figure 2.1.4.45> below, the storage ring kicker system consists of four magnets (K1, K2, K3, K4). Four power supplies (for storage ring kickers) are also configured to supply electric current to each magnet. However, the kicker power supply cabinets will be just two to reduce costs. The entire system is divided into three major parts.

The first is the control section. Integrated management and control, including the booster ring's kicker power supplies, will be located in the experimental hall building where the storage ring kicker system will be installed. The integrated management and control include the OPI that monitors the injection control interface and PLC devices that control the status and interlock of the power supplies.

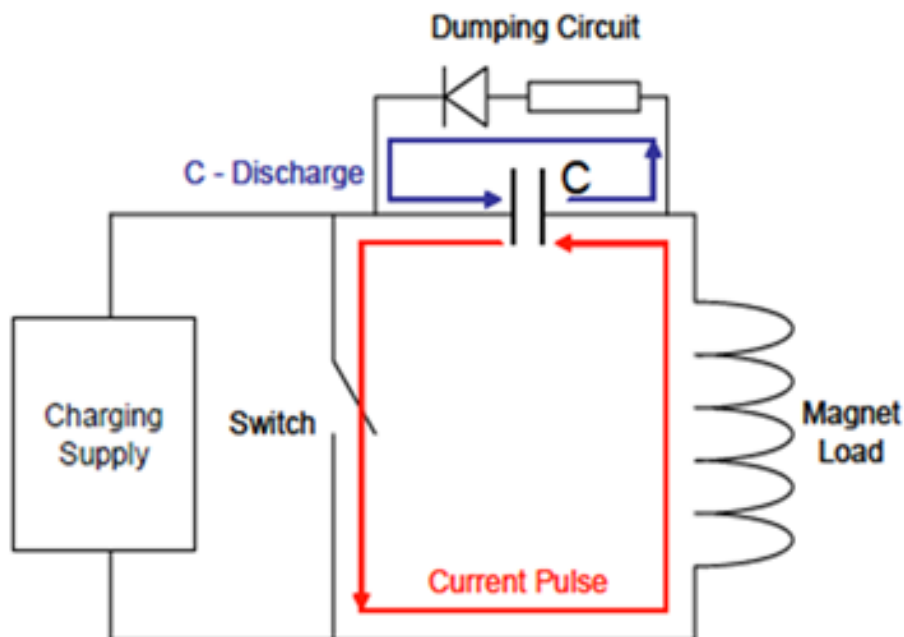
The second is the pulsed power supplies that provide a half-sine pulsed current to the kicker magnets. The most crucial point is that the error in the half-sine current supplied to the kicker magnets should be within $\pm 0.2\%$ to minimize the field error and reduce the orbit fluctuation. The circuit design of the 4GSR storage ring's injection power supplies already considered this point.

The third is the kicker magnets. The exact parameters have yet to be determined because they have yet to be designed and manufactured, but a four-bump magnet type, the PLS-II kicker magnet concept, will be adopted. As shown in the power supply location diagram, power supplies will be installed in the experimental hall, and the connection to the magnets to be installed inside the storage ring tunnel will use a separate trench to shorten the length of the connection cable (RG8U) to minimize the inductance effect.



<Figure 2.1.4.45> Location map of the booster ring and storage ring kicker magnets.

<Figure 2.1.4.45> is a simplified block diagram of the kicker power supplies. As shown in the figure, each kicker power supply is broadly composed of a charging supply, charging/discharging assembly, machine control, and magnet load. The main power to the kicker power supplies is a 3-phase 4-wire 380 V. Since 3-phase 208 V power supplies are required, 3-phase 208 V step-down transformers of 50 kVA are used, and inductors ($600 \mu\text{H}/50 \text{ A}$) are used to suppress the harmonics generated when the CCPS turns on. In the 3-phase 380 V power supply, it is possible to connect one of the three phases (R, S, T) and the neutral line (N) to use 220 V single-phase for various power supplies. The capacity of CCPS 1 set is $20 \text{ kV}/0.25 \text{ A} = 5 \text{ kW}$, and two sets of CCPS can supply the kicker power supplies for the K1, K2, K3, and K4 magnets. The 3-phase 208 V power supply is used as the input power for the CCPS, and one of the 3-phases (R, S, T) is connected to the neutral line (N) to use the 120 V single-phase for the thyatron power supply. The charging supply, which receives the 3-phase 208 V input, supplies the high voltage required for the charging/discharging assembly. The charging/discharging assembly charges this voltage into a capacitor and then supplies it to the load, the magnets, using a high-power Thyatron switch. The triggering signal of the switch is determined according to the timing signal from the main operation room. The machine control controls all system situations according to the command from the main operation room and informs the operation room of the current operating status. In addition, it allows the system to be locally controlled so that it can be inspected regularly or controlled in case of an abnormality.



<Figure 2.1.4.46> Schematic Diagram of the storage ring's kicker power supplies.

As shown in <Figure 2.1.4.46>, the pulsed power supplies that drive the 4GSR kicker magnets fundamentally use a series resonant circuit. The pulse shape of the output current is determined by the system's inductance L_t , capacitance C_t , and resistance R . When the charging voltage is V_0 , the current $i(t)$ has a value of (Eq. 2.1.4.6).

$$i(t) = \frac{V_0}{\omega L_t} e^{-\left(\frac{R}{2L_t}\right)t} \sin(\omega t) \quad (\text{Eq. 2.1.4.6})$$

Since the output current has a half-sine wave shape, assuming that the system's resistance is low, the pulse width is given by (Eq. 2.1.4.7), and the energy of a pulse is given by (Eq. 2.1.4.8).

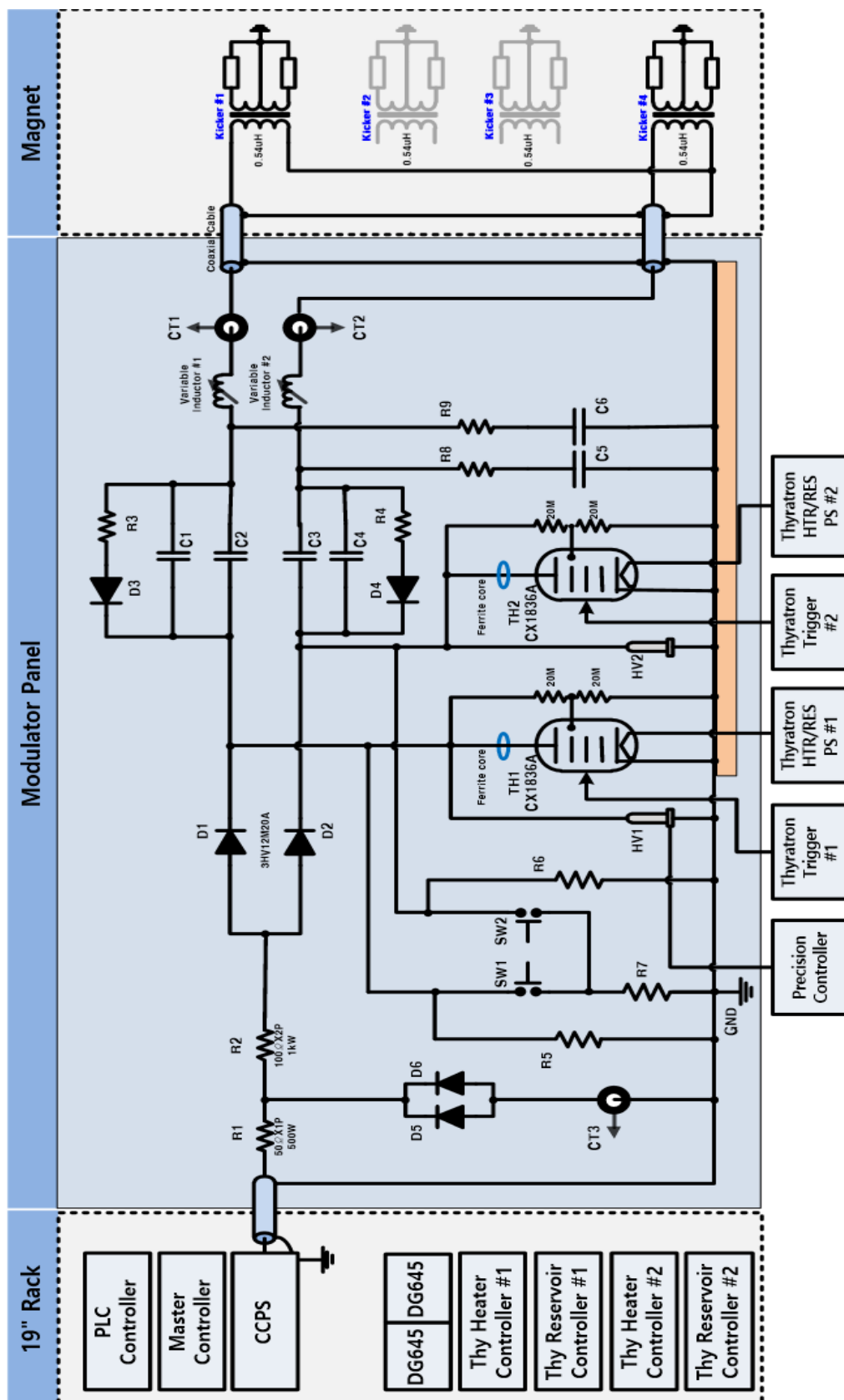
$$\text{Pulse width} \cong \pi \sqrt{L_t C_t} \quad (\text{Eq. 2.1.4.7}),$$

$$E_0 = \frac{1}{2} C_t V_0^2 \quad (\text{Eq. 2.1.4.8}).$$

The specifications of the pulsed power supplies for driving the kicker magnets are shown in <Table 2.1.4.22>.

<Table 2.1.4.22> Specifications of the storage ring's kicker power supplies

Parameters	Specification
Pulse shape	Half-sine
Pulse current	7 kA
Pulse-width	< 5 μ s
DC voltage	13 kV
Flat-top width	200 ns
Repetition Rate	2 Hz
Magnet inductance [μ H]	0.55
Power supply system inductance [μ H]	< 2.3
Pulse Current Difference	\pm 0.2%
Maximum Operable Beam Energy	4 GeV



<Figure 2.1.4.47> Circuit Diagram of the storage ring's kicker power supplies.

<Figure 2.1.4.47> shows the circuit diagram of the pulsed power supplies. The charging structure of the kicker consists of a charging resistor (protection resistor), a charging rectifier (protection diode), and a main capacitor. The main components of the kicker's discharging structure are Thyratrons (Th1, Th2), a reverse energy-dissipation structure (tail diode and tail resistor), and a transient suppression structure (RC snubber). After the power supply is charged, the two thyratrons conduct simultaneously to discharge the main capacitor energy rapidly into the load. The reverse energy-dissipation structure is connected in parallel with the main capacitor to maintain the energy charged in the forward direction and discharge the voltage charged in the reverse direction to the main capacitor. Rapid discharge of the reverse voltage restores a constant initial condition to the main capacitor before the next pulse, and it is also necessary to reduce the peak current of the high-voltage DC power supply generated during charging.

A series RC circuit is connected in parallel with the magnet load, thus maintaining the load current's continuity after the discharge. By retaining the load current, minimizing the sudden reverse voltage applied to the thyatron and capacitor is possible. Since the thyatron does not conduct in reverse, it controls the total reverse voltage. However, the maximum reverse voltage allowed by the circuit configuration (over 10 kV) cannot be withstood by the thyatron and significantly impacts on the capacitor lifetime. Therefore, reducing the reverse voltage of the thyatron and capacitor is very important in this type of resonant circuit. As mentioned earlier, the reduction of reverse voltage is implemented by a reverse energy-dissipation structure and a transient suppression structure.

Devices that assist the kicker modulator include a thyatron power supply, a thyatron trigger amplifier, a measurement and sensing device, and a system control device. The thyatron trigger amplifier receives a pulse signal generated from the main timing module as an optical signal pulse through an optical fiber and triggers the thyatron. The 4GSR kicker system should be able to measure the charging voltage, load current, magnetic field, and grid trigger pulse. The magnetic field sensor measures the magnetic field shape in the vertical directions of the electromagnet. The system control device controls the system using a PLC. The system control device displays the required voltage and current of all power supplies and the communication status with the protection device and the main operation room. The connection of the kicker power supplies and the pulse transformer installed on top of the kicker magnets will use RG-223 cables in parallel to reduce inductance. Since the load impedance is small, the impedance of the connection between the power supply and the load is also a significant value that cannot be ignored. Therefore, the output lines need to be

configured in parallel to reduce the impedance, which is calculated by the equation shown in <Table 2.1.4.23>.

<Table 2.1.4.23> Calculation of the RG8U coaxial cable inductance

RG8U Coaxial Cable Characteristics	
Cable Impedance	50 +/- 2 Ω
Cable Capacitance	101 pF/m
Cable Inductance	253nH/m, $Z = \sqrt{L/C}$; $L = Z^2 \times C$
Cable Inductance with 20 in parallel	with 20 in parallel = 0.125 μ H

The inductance of the RG8U coaxial cable calculated according to <Table 2.1.4.22> was applied to the PLS-II kicker power supply shown in <Figure 2.1.4.48>. When 20 strands were connected in parallel over a 10 m length, the calculated inductance was approximately 0.125 μ H, indicating a negligible impact on the overall inductance of the kicker power supply. Based on these results, we plan to use the PLS-II concept for the 4GSR kicker power supply when it is necessary to reduce the inductance of the coaxial cable.



<Figure 2.1.4.48> 20 coaxial cable strands in parallel connection.

2.1.5 Injection to the storage ring

This chapter introduces the injection of the beam into the storage ring. Due to the significant nonlinear effects in the 4GSR, the stable region for the beam (dynamic aperture) is not as large as that of 3GSR, making it a key issue to bring the injection beam and storage beam as close together as possible. This chapter demonstrates that the designed injection beam is injected into the storage ring without beam loss and introduces the conditions of the injection system required to achieve this.

A. Injected Beam Properties

The booster of the Korea-4GSR is installed in the same tunnel as the storage ring, allowing the booster circumference to be large enough to produce an injection beam with low emittance. While the injection beam's emittance could be further reduced depending on the booster design, a simple booster lattice structure is considered for easy installation and operation, generating a beam as shown in <Table 2.1.5.1>. The horizontal emittance is sufficiently low at 11 nm. One advantage of the booster is the very low vertical emittance, which facilitates the operation of insertion devices with a small aperture around the storage ring.

<Table 2.1.5.1> Parameters of storage ring injected beam

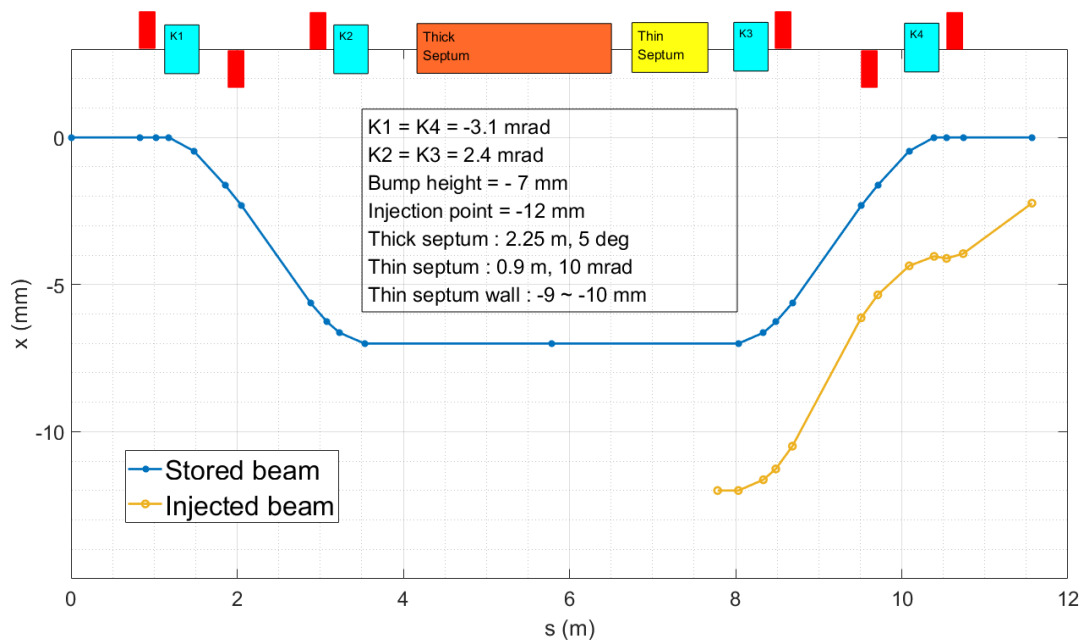
Parameters	Values	Unit
Horizontal emittance (H emittance)	10.9	nm
Vertical emittance (V emittance)	0.11	nm
rms energy spread	0.11	%
rms bunch length	13.4	mm

B. Injection System and Layout

With the advent of the 4th-generation storage ring light sources, many injection techniques have been introduced, and are being actively researched worldwide. Among these techniques is the well-established 4-bump injection method, which uses four kickers

and has been consistently used since the 1st generation, with its performance thoroughly verified. Among the various injection methods, the 4-bump injection technique, which uses four well-verified kickers, was chosen as the primary injection method for the 4GSR, in line with the direction of the conceptual design. This method requires a sufficiently wide stable region for the beam (dynamic aperture). Due to the nature of the 4GSR, which has a relatively smaller dynamic aperture compared to the 3GSR, the key feature of the 4GSR 4-bump injection method is minimizing the separation distance between the stored beam and the injected beam to overcome this limitation.

<Figure 2.1.5.1> shows the layout of the injection section in the conceptual design of the 4GSR. Four kicker magnets are installed in an 11.6-meter straight section where six quadrupole magnets are placed in the middle. After passing through the thick septum and thin septum magnets, the injected beam travels parallel to the stored beam with a separation of 5 mm and passes through kicker magnet 3. The horizontal position at the entrance of kicker 3 is offset by -12 mm from the center. As the injected beam passes through kickers 3 and 4, when the stored beam's horizontal position is at 0 mm, the injected beam oscillates around the stored beam with a 5 mm offset. The kicks applied at the kickers are 3.1 and 2.4 mrad, which are relatively small compared to the 9 mrad in PLS-II.



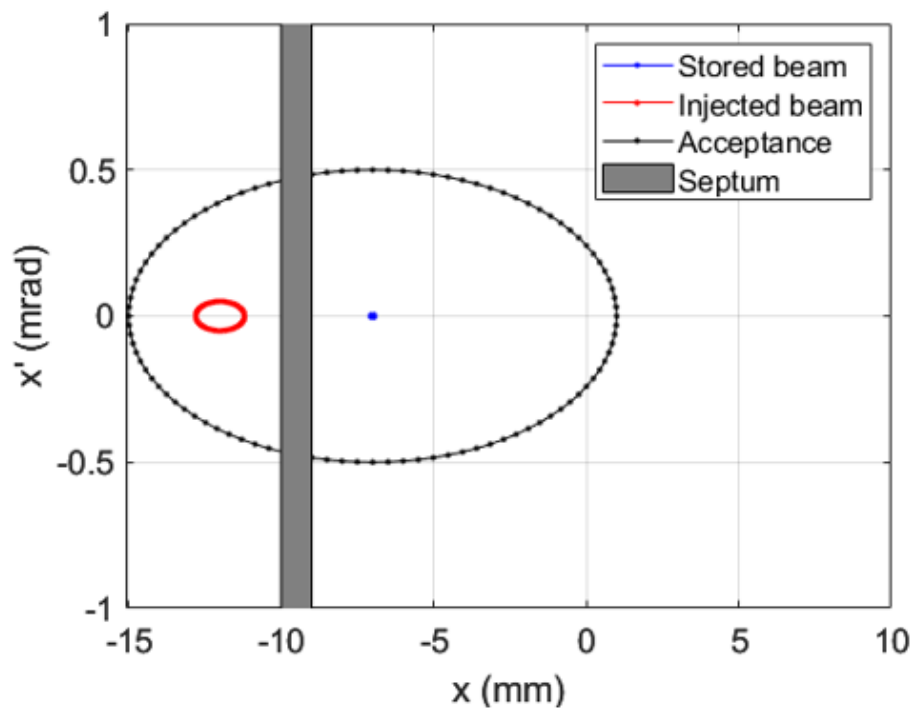
<Figure 2.1.5.1> Storage ring injection layout for Korea-4GSR.

The shape of the kicker pulse follows a typical model of a half-sine function, with a pulse duration of $5 \mu\text{s}$. Since it takes $2.67 \mu\text{s}$ for the electron beam to complete one turn around the storage ring, the injected beam will receive the kicker's magnetic field when the pulse

strength is at its peak. After completing one turn around the ring, on the next turn, the kicker's magnetic field strength will be zero. This means the system operates with a single-turn kick. A $5\ \mu\text{s}$ pulse duration is within a stable operating range, and compared to on-axis injection, where the kicker pulse duration is considered to be 10-50 ns, it is a much easier operating condition.

As for the septum magnets, one in-vacuum thin septum and one out-vacuum thick septum will be used. The wall thickness between the stored beam and the injected beam is 3 mm for the thick septum and 1 mm for the thin septum.

<Figure 2.1.5.2> conceptually shows the horizontal phase space positions of the injected and stored beams when the stored beam passes through the -7 mm bump orbit. As illustrated in <Figure 2.1.5.2>, the injected beam is injected with a -12 mm offset, while the stored beam has a -7 mm offset due to the bump orbit. The acceptance in the horizontal direction is assumed to be 8 mm, which is a reasonable estimate based on the results from section 2.1.3.H, "Commissioning Simulations.".

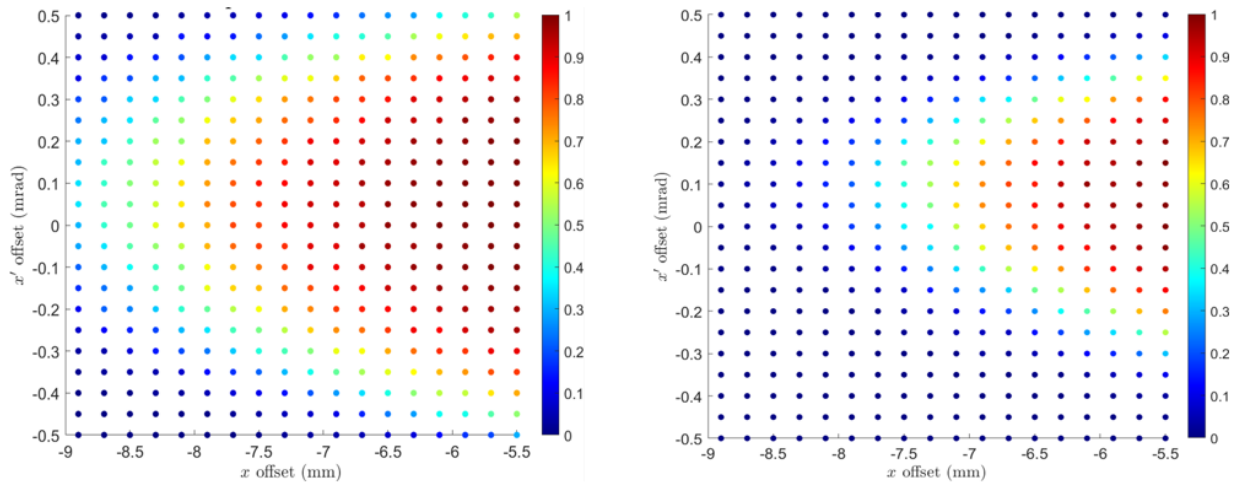


<Figure 2.1.5.2> Schematic view of stored beam and injected beam on the horizontal phase space.

C. Storage Ring Injection Simulation

Using the Accelerator Toolbox (AT), the injection efficiency was scanned by varying the x offset and x_p offset of the injected beam to identify the stable injection region in the x - x_p phase space. Among the 50 error lattices used in section 2.1.3.H, "Commissioning Simulations.", the seeds with the largest and smallest dynamic apertures are chosen. Then, multiparticles with a 3-sigma cut Gaussian distribution were generated following <Table 2.1.5.1> and tracking simulation was performed over 2000 turns to calculate the injection efficiency.

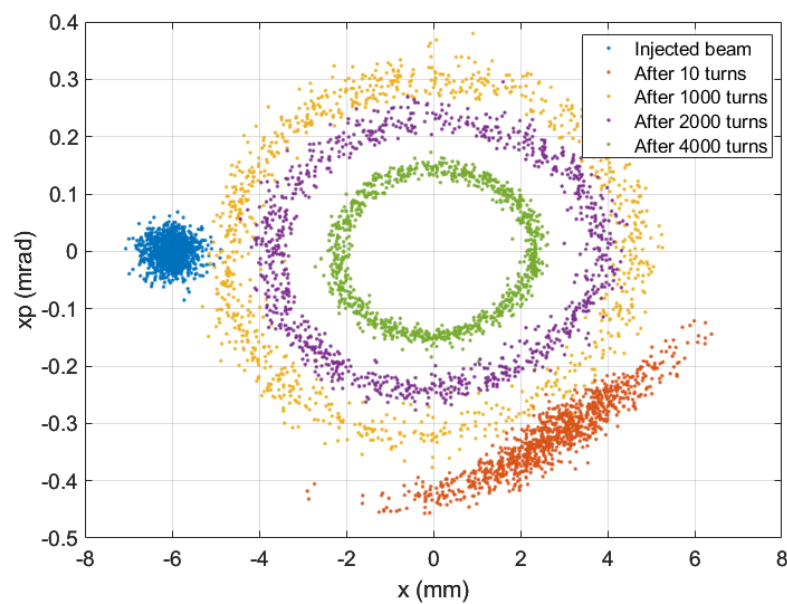
At the injection point, the injected beam is assumed to have the emittance, bunch length, and energy spread corresponding to the booster's 4 GeV energy. The beta function was matched to the storage ring's beta function at the injection point, and tracking simulations were carried out under these conditions <Figure 2.1.5.3>. The tracking includes effects from the RF cavity and radiation damping.



<Figure 2.1.5.3>Injection efficiency scan with x offset and x_p offset for the largest dynamic aperture error seed and the smallest dynamic aperture error seed. Color-code indicate injection efficiency; 1 means 100% injection efficiency.

The results show that even for the error seed with the smallest dynamic aperture, the injected beam can achieve nearly 100% injection efficiency at an x offset of -6 mm relative to the stored beam. For the error seed with the largest dynamic aperture, a nearly 100% injection efficiency is achievable up to an x offset of approximately -7 mm.

<Figure 2.1.5.4> shows the multiparticle distribution over turns in the x-xp phase space for the error seed with the largest dynamic aperture under the conditions of x offset = -6 mm and xp offset = 0.

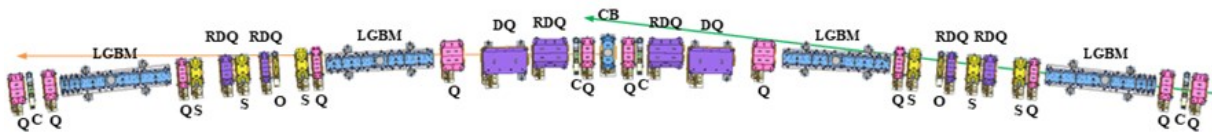


<Figure 2.1.5.4> Beam footprint for the seed of largest dynamic aperture. Initial x and xp offset are -6 mm and 0 mrad, respectively.

2.1.6 Magnet System

A. The Overview and Requirements of the Magnet System

4GSR consists of total 28 periodic sectors. As shown in <Figure 2.1.6.1>, each sector is equipped with 1 center bending (CB) magnet, 4 longitudinal gradient bending (LGBM) magnets, 2 transverse gradient bending (DQ51) magnets, 6 reverse-bending combined quadrupole magnets (RDQ), 12 quadrupole magnets, 6 sextuple magnets (S), 2 octupole magnets, and 4 fast correctors, totaling 37 main electromagnets. Difference from CDR is that the strengths of the quadrupole and sextuple magnets have been optimized, and octupole magnets have been added. Additionally, to improve the injection efficiency, the design has been modified to include racetrack sections in the lattice, requiring the installation of 12 additional quadrupole magnets and several H/V magnets.



<Figure 2.1.6.1> Layout of magnets for one sector.

Among these, four types of dipole bending magnets are used. These include LGBMs, transverse gradient bending magnets, reverse-bend dipole magnets, and 2 T CB magnets at the center of each sector. The LGBM has a magnetic field strength that changes stepwise in the beam motion direction, with LGBM1 varying from 0.7343 T to 0.1504 T and LGBM2 varying from 0.3121 T to 0.1536 T. Two of each type are installed per sector. However, each magnetic field profile of LGBM1 and LGBM2 should be deployed symmetrically around the CB magnet, and these two magnets should be classified as different, non-interchangeable magnets. Therefore, to avoid confusion, LGBMs are considered to have four types: LGBM1U, LGBM1D, LGBM2U, and LGBM2D.

Quadrupole bending (Quad bend) magnets, quadrupole reverse bending (Quad reverse-bend) magnets, and quadrupole magnets all share the same magnet shape. Quad bends offset the beam position in a typical quadrupole to bend the electron beam. Quad bends have four lengths and three apertures. For DQ51, the aperture radius (r_c) is 30.0 mm; for DQ32, the r_c is 20 mm; and for the rest, the r_c is 15.0 mm. The quadrupole strength is 26.4 T/m for DQ51, 26.1 T/m for DQ32, 58.1 T/m for DQ31, and 52.0 T/m for DQ52. In the case of quad

bends, if the quadrupole strength changes, the bending strength changes accordingly. Therefore, a trim coil is needed to maintain the bending strength even if the quadrupole strength varies. Some quad bends have the same length and aperture and can be considered the same type, but they all have different shapes due to the photon slot, and the yoke shape may vary depending on the position.

Each sector will be equipped with 12 quadrupole magnets. These magnets have four lengths, 145 mm, 200 mm, 250 mm, and 384 mm, and all have an aperture radius of 15.0 mm. The maximum strength of the gradient magnetic field is 56.2 T/m for Q32, which is slightly lower than in the CDR. The pole tip field is relatively low at around 0.85 T, so it can be achieved using a low-carbon steel core instead of expensive materials like Vanadium Permendur. Both quad bends and quadrupoles will be manufactured using solid cores and powered individually. To supplement the number of correctors, H/V corrector coils will be installed in Q51D and Q51U. The expected corrector strength is about a 0.4 mrad kick, but when exciting the corrector field, the degradation of multipole components should be accepted. As in quad bends, the core shape varies depending on the photon slot. However, within the same type of quadrupole magnets, coils of the same length can be used as compatible spares, and their electrical parameters are identical.

Each sector will have six sextupole magnets with an aperture radius of 20.0 mm. In the CDR, they are of the same length, 250 mm, but as the post-CDR lattice optimization progressed, additional lattice space was needed, so the lengths were optimized to two types, 180 mm and 200 mm. The maximum second derivative of the magnetic flux density is approximately 2,084 T/m² based on the 120% value of the lattice specification. It can be easily achieved with the existing low-carbon steel core. As in quadrupole magnets, there are differences in the photon exit slot depending on the position, but sextupole magnets with the same core length have identical electric and magnetic parameters. All sextupole magnets are multifunctional, including features such as H-corrector, V-corrector, and skew quad, just as in the PLS-II sextupole magnets. It is necessary to maintain a magnetic efficiency of over 98% to minimize the mutual interference between the trim function and the main sextupole magnet. Like other magnets, the design assumes the use of a solid core. As sextupole magnets will be set periodically in the period of 2 cells, the initial plan was to group them into 14 units and connect them to a single power supply. However, connecting each sextupole magnet to an individual power supply was decided to ensure maximum operational flexibility. Since a solid core is used, the corrector coil should be operated as a slow corrector at a low frequency.

All magnets, except the air coil corrector, are cooled with low-conductivity cooling water. The fundamental cooling water supply temperature is 25 °C, and a pressure difference of 6.0 bar (about 90 psi) is assumed between the supply and return cooling water. The maximum pressure on the return side is also limited to below 9.0 bar to reduce the pressure applied to the cooling water tubes. All magnets are designed so that the temperature rises will not exceed 20 K.

In addition to the 4GSR main ring, injector linac, linac to booster ring (LTB), booster ring, and booster ring to storage ring (BTS) require special magnets for injection purposes. For the injector linac, they are often included within the linac, and booster magnets are not technically challenging and can be easily procured commercially. The production of BTR magnets also does not have any technical difficulties.

Overall, the 4GSR requires 932 main magnets, including dipoles, quadrupoles, sextupoles, and octupoles. If more than 112 correctors are included, more than 1,044 magnets will be used. The "+" symbol indicates that a few H/V correctors will be added in the racetrack section. In addition to the main power supply, some magnets require trim windings. Since all magnets are operated with individual power supplies, there is no need for trim windings to support the main power supply. DQ requires trim windings to support the dipole field, and Q51 requires auxiliary power supplies for H/V correctors. For sextupoles, power supplies for H/V/SQ are needed in addition to the main power supply. Of course, correctors require two power supplies for H/V. Below, <Table 2.1.6.1> summarizes the requirements for all magnets used in each sector of the storage ring, where h_{gap} denotes the pole gap of the dipole magnets and GFR denotes the good field region.

<Table 2.1.6.1> Summary of requirements for all the magnets of the storage ring

Magnet Name	h_{gap} or r_c [mm]	GFR [mm]	Required Quantity	Strength [B, B', B'']	Effective Length [m]	Trim	Total PS	Remark
CB	7.0	±13.0	28	1.9942	0.186	-	28×A	-
LGBM1U	12.5	±13.0	28	From 0.7343	2.0505	-	-	
LGBM2U	12.5	±13.0	28	From 0.3051	1.9847	-	-	
LGBM2D	12.5	±13.0	28	From 0.3051	1.9847	-	-	
LGBM1D	12.5	±13.0	28	From 0.7343	2.0505	-	-	
DQ31U	15.0	7.0	28	58.1	0.200	V	28×A, 28×B	V trim is for maintaining B when B' changes.
DQ32U	20.0	10.0	28	26.1	0.145	V	28×A, 28×B	
DQ51U	30.0	15.0	28	-26.4	0.820	V	28×A, 28×B	
DQ52U	15.0	7.0	28	52.0	0.626	V	28×A, 28×B	
DQ52D	15.0	7.0	28	52.0	0.626	V	28×A, 28×B	
DQ51D	30.0	15.0	28	-26.4	0.820	V	28×A, 28×B	
DQ32D	20.0	10.0	28	26.1	0.145	V	28×A, 28×B	
DQ31D	15.0	7.0	28	58.1	0.200	V	28×A, 28×B	
QH1U	15.0	10.0	2	16.3	0.200	-	2×A	-
QH2U	15.0	10.0	2	28.0	0.200	-	2×A	-
QH3U	15.0	10.0	2	44.5	0.200	-	2×A	-
QH4U	15.0	10.0	2	18.0	0.200	-	2×A	-
Q11U	15.0	10.0	26	49.4	0.250	-	26×A	-
Q12U	15.0	10.0	26	-41.7	0.200	-	26×A	-
Q31U	15.0	10.0	28	-56.2	0.145	-	28×A	-
Q32U	15.0	10.0	28	-56.2	0.145	-	28×A	-
Q51U	15.0	10.0	28	53.6	0.384	H/V	28×A, 56×B	H/V corr
Q52U	15.0	10.0	28	-57.4	0.200	-	28×A	-
Q52D	15.0	10.0	28	-57.4	0.200	-	28×A	-
Q51D	15.0	10.0	28	53.6	0.384	H/V	28×A, 56×B	H/V corr
Q32D	15.0	10.0	28	-56.2	0.145	-	28×A	-
Q31D	15.0	10.0	28	-56.2	0.145	-	28×A	-
Q12D	15.0	10.0	26	-41.7	0.200	-	26×A	-
Q11D	15.0	10.0	26	49.4	0.250	-	26×A	-
QH4D	15.0	10.0	2	18.0	0.200	-	2×A	-
QH3D	15.0	10.0	2	44.5	0.200	-	2×A	-
QH2D	15.0	10.0	2	28.0	0.200	-	2×A	-
QH1D	15.0	10.0	2	16.3	0.200	-	2×A	-
S31U	16.0	10.0	28	1802	0.180	H/V/SQ	28×A, 84×B	-
S32U	16.0	10.0	28	2084	0.200	H/V/SQ	28×A, 84×B	-
S33U	16.0	10.0	28	1420	0.180	H/V/SQ	28×A, 84×B	-
S33D	16.0	10.0	28	1420	0.180	H/V/SQ	28×A, 84×B	-
S32D	16.0	10.0	28	2084	0.200	H/V/SQ	28×A, 84×B	-
S31D	16.0	10.0	28	1802	0.180	H/V/SQ	28×A, 84×B	-
O31U	15.0	10.0	28	2.4×10^5	0.080	-	28×B	-

O31D	15.0	10.0	28	2.4×10^5	0.080	-	$28 \times B$	-
C1U	12.5	10.0	28	0.37 mrad	0.121	H/V	$2 \times 28 \times B$	0.35 mm
C2U	12.5	10.0	28	0.37 mrad	0.121	H/V	$2 \times 28 \times B$	0.35 mm
C2D	12.5	10.0	28	0.37 mrad	0.121	H/V	$2 \times 28 \times B$	0.35 mm
C1D	12.5	10.0	28	0.37 mrad	0.121	H/V	$2 \times 28 \times B$	0.35 mm

The strength unit is T for a dipole magnet, T/m for a quadrupole magnet, T/m² for a sextupole magnet, and T/m³ for an octupole magnet. The uniformity requirement for a dipole is $\Delta B/B < 10^{-3}$, and the multipole component requirement is $< 1.0 \times 10^{-3}$. The DQ series means quad bends and quad reverse bends, with a field strength usage range of 95-105% of the nominal value. For a quadrupole, the usage range is 75-110% of the nominal value; for a sextupole, the usage range is 50-120%. Except for correctors, all magnets adopt a solid-type core. Regarding power supplies, type A is for the power supplies (PS) listed in the table; type B is for trim coils with 10 A and 30 W capacity, and type C means a PS with 2 A and 30 W capacity. Even if some magnets have the same aperture and length, they are labeled differently if photon slots are different. In the CDR, the LGBMs were planned as serially connected electromagnets, but they have been changed to permanent magnets.

B. Center Bend(CB) Magnet

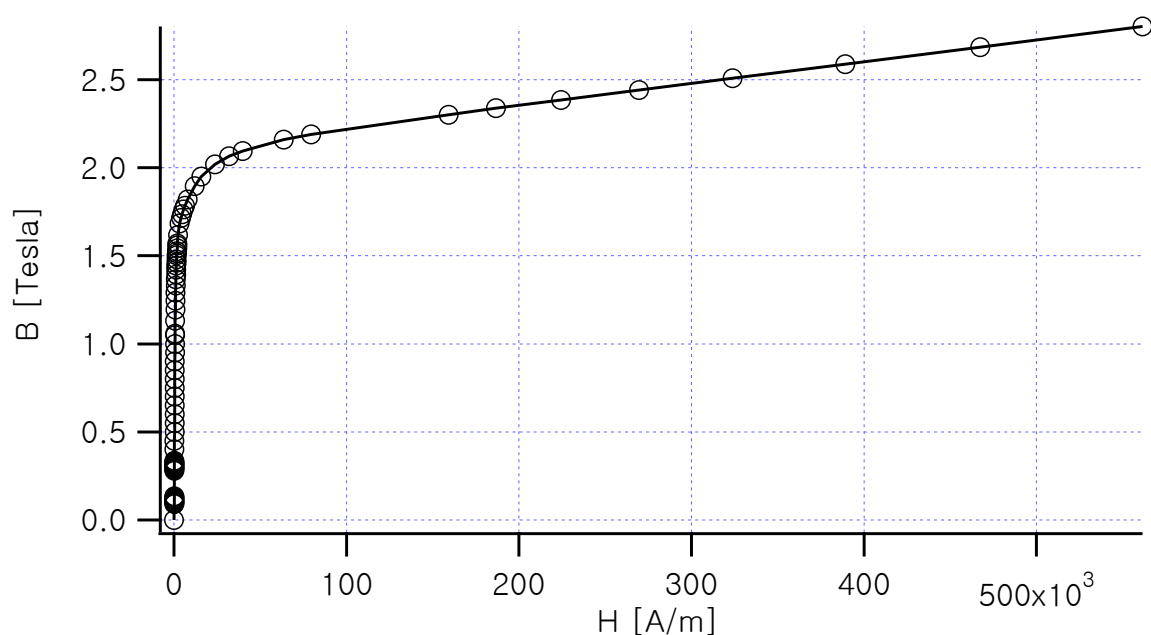
A periodic cell of the 4GSR electron storage ring (SR) requires 45 magnets. These include 4 longitudinal gradient bending magnets (LGBM), which are dipole magnets with a longitudinally changing magnetic field, 6 quad reverse-bends, where quadrupoles and dipoles are mixed, 2 quad bends, 12 quadrupole magnets, 6 sextupole magnets, 2 octupole magnets, 4 corrector magnets, and 1 high-field center bend (CB). In total, 28 CBs are required for the entire SR. The requirements for CB are a central magnetic field of 1.9942 T, an effective magnetic length of 0.186 m, and a uniformity of $\Delta B/B < 1.0 \times 10^{-3}$ within $|x| < 13.0$ mm. For maximum flexibility, individual power supplies were chosen for CBs. Considering the beam-stay-clear at the CB location and the vacuum chamber design, the minimum pole gap is specified by a 7.0 mm half-gap. Additionally, the two longitudinal faces of a CB are designed to be parallel.

The magnetic flux density requirement of 2 T is very high, approaching the saturated magnetic flux density of pure iron, which is the material limit at 2.1 T. Therefore, to meet this condition, the pole gap was determined to be the minimum required to satisfy the beam stay clearance, based on a 7.0 mm half-gap. Most magnets used in the 4GSR operate near

the limits of their magnetic material properties. Therefore, for analysis, the BH table must include data up to high flux densities. However, in many cases, data is sparse and only available up to lower flux densities (around 2 T). Here, for low-carbon steel, we used the BH table from the Poisson code, which includes data up to high magnetic fields. Since the required magnetic flux density is high, the final magnetic field can vary depending on the material's tolerance. Thus, precise control of the BH characteristics is necessary for manufacturing. The BH characteristics of a material used in the calculations are shown in <Figure 2.1.6.2> and are listed numerically in <Table 2.1.6.2> for future numerical comparisons.

Magnetic saturation should be avoided to achieve a high magnetic-flux density. Therefore, the pole was tapered in the x-direction and chamfered in the beam direction (z-direction) to minimize the magnetic saturation of the pole root. The uniformity of the magnetic flux density was optimized by installing a trapezoidal shim on the pole surface.

<Figure 2.1.6.3> shows the geometry and the flux shape of the 2D optimized core. In the three-dimensional analysis, a 60° chamfering was applied vertically to the beam direction to minimize magnetic saturation. Ultimately, as the uniformity requirement of the magnetic field integral must be satisfied, the uniformity of the magnetic field integral for various shim sizes is shown in <Figure 2.1.6.4>. <Figure 2.1.6.5> also shows the by distribution along the CB length. It shows that a maximum magnetic flux density of 2.0 T and an effective magnetic length of 186 mm are satisfied.

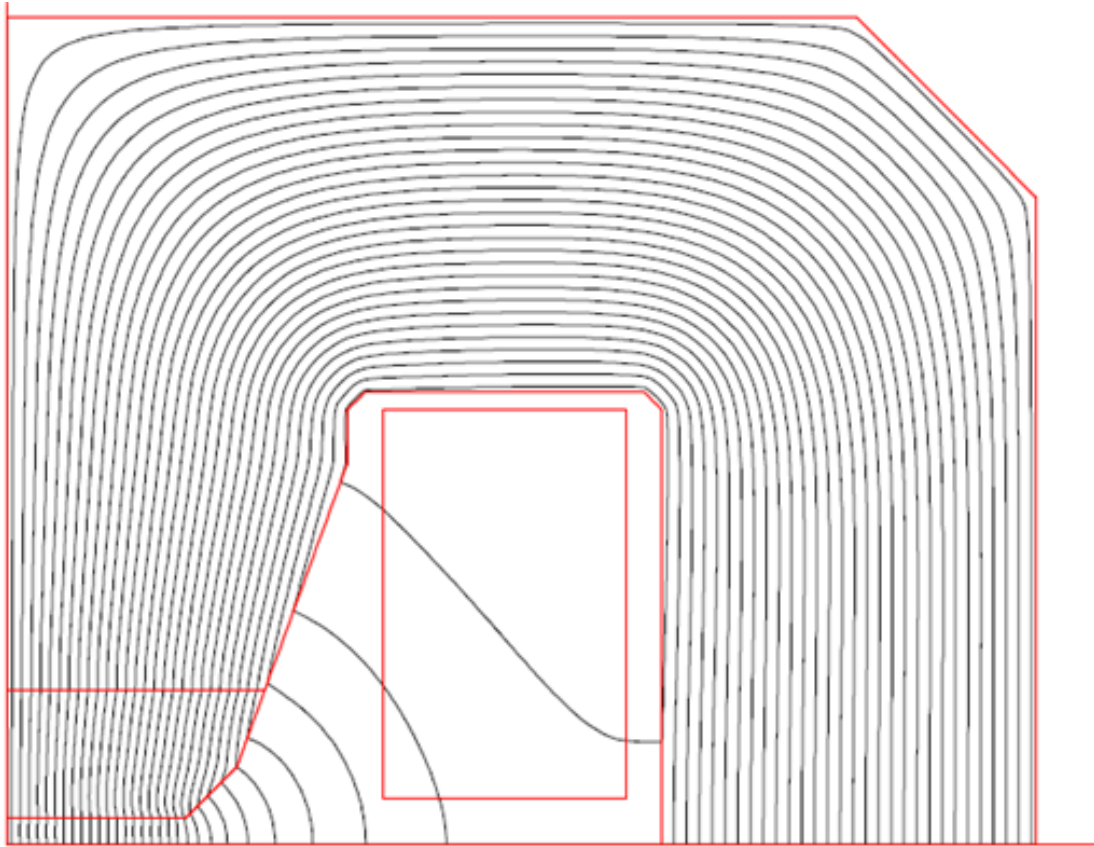


<Figure 2.1.6.2> The low carbon steel's BH curve used in the calculation.

<Table 2.1.6.2> BH table used in calculations
(expressed in numbers for comparison with future measurements)

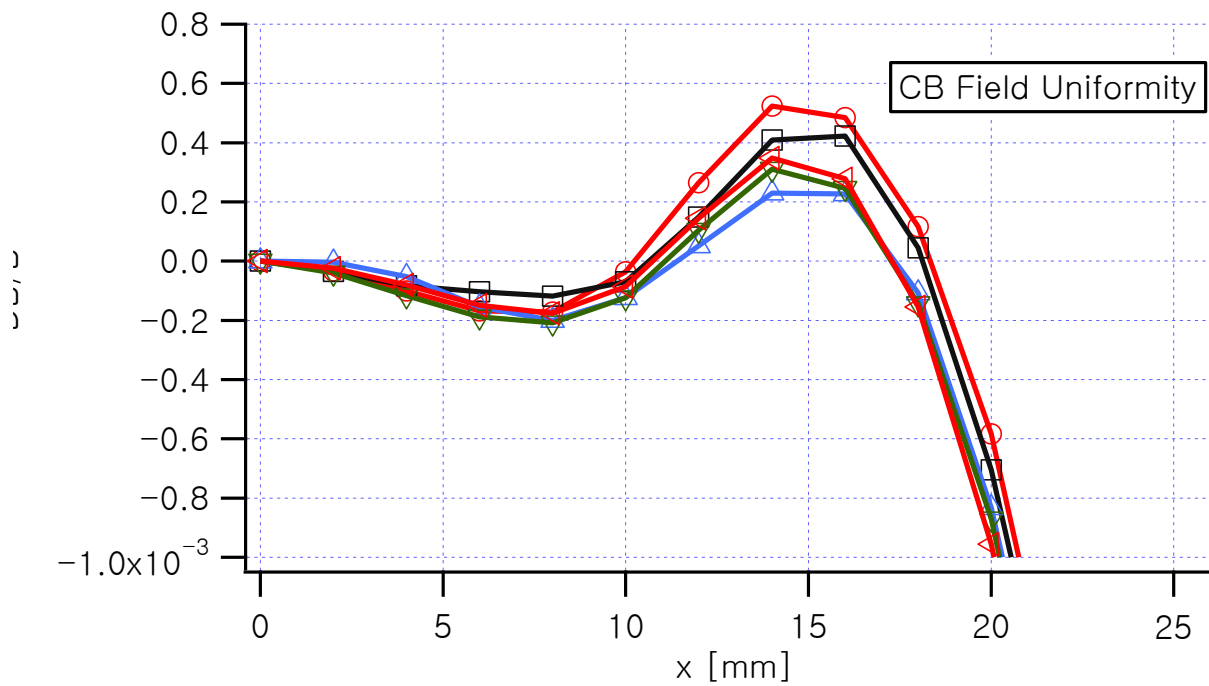
H [A/m]	B [Tesla]	H [A/m]	B [Tesla]	H [A/m]	B [Tesla]
0	0.0000	344.9	0.5500	1,909.7	1.5594
125.1	0.0900	364.9	0.6000	1,989.4	1.5705
131.7	0.0950	385.8	0.6500	2,387.5	1.6180
138.1	0.1000	408.0	0.7000	3,183.1	1.6840
144.4	0.1050	431.7	0.7500	3,978.9	1.7150
150.6	0.1100	457.2	0.8000	4,775.2	1.7360
156.6	0.1150	485.0	0.8500	5,570.7	1.7620
162.4	0.1200	515.5	0.9000	6,365.5	1.7830
168.1	0.1250	549.2	0.9500	7,957.7	1.8200
173.5	0.1300	586.7	1.0000	11,939.8	1.8950
178.7	0.1350	628.8	1.0500	15,915.5	1.9500
240.8	0.2800	636.6	1.0578	23,885.1	2.0200
242.2	0.2850	716.2	1.1319	31,846.4	2.0650
243.7	0.2900	795.8	1.1940	39,788.7	2.0950
245.3	0.2950	875.4	1.2451	63,662.0	2.1600
246.9	0.3000	954.9	1.2912	79,577.5	2.1900
248.6	0.3050	1034.5	1.3313	159,154.9	2.3000
250.3	0.3100	1114.1	1.3654	186,622.8	2.3386
252.1	0.3150	1193.7	1.3935	224,264.2	2.3850
254.0	0.3200	1273.2	1.4216	269,482.3	2.4408
255.8	0.3250	1352.9	1.4447	323,798.1	2.5079
257.8	0.3300	1432.4	1.4618	389,021.6	2.5885
259.7	0.3350	1511.9	1.4789	467,345.4	2.6854
288.1	0.4000	1591.5	1.5020	561,398.0	2.8019
306.8	0.4500	1671.2	1.5131	-	-
325.7	0.5000	1750.6	1.5252	-	-

Magnetic saturation should be avoided to achieve a high magnetic-flux density. Therefore, the pole was tapered in the x-direction and chamfered in the beam direction (z-direction) to minimize the magnetic saturation of the pole root. The uniformity of the magnetic flux density was optimized by installing a trapezoidal shim on the pole surface.

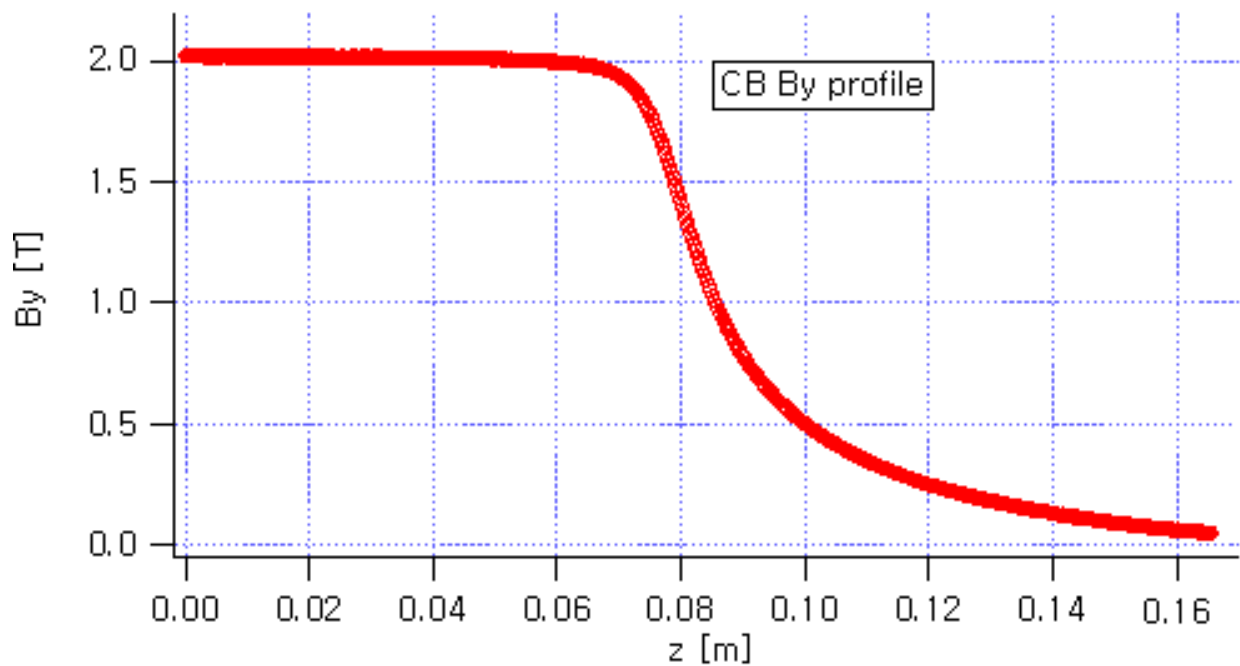


<Figure 2.1.6.3> 2D optimized shape and flux distribution of a pole and yoke.

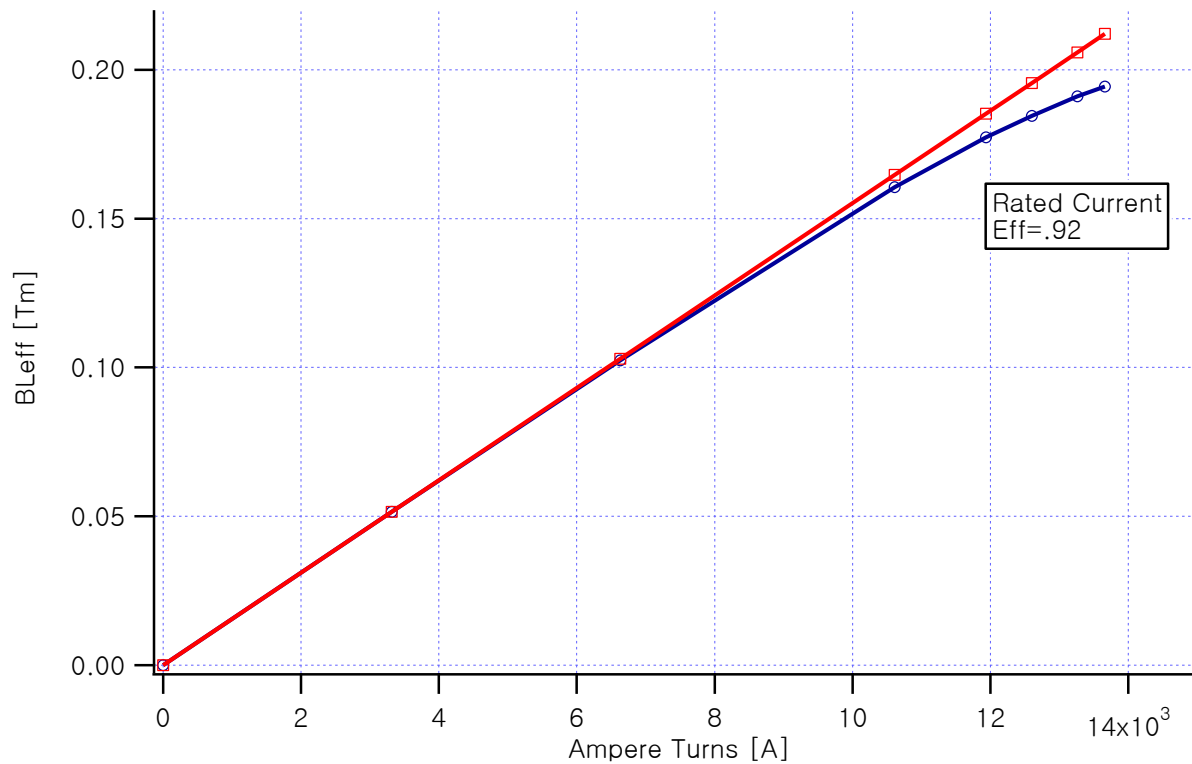
<Figure 2.1.6.3> shows the geometry and the flux shape of the 2D optimized core. In the three-dimensional analysis, a 60° chamfering was applied vertically to the beam direction to minimize magnetic saturation. Ultimately, as the uniformity requirement of the magnetic field integral must be satisfied, the uniformity of the magnetic field integral for various shim sizes is shown in <Figure 2.1.6.4>. <Figure 2.1.6.5> also shows the by distribution along the CB length. It shows that a maximum magnetic flux density of 2.0 T and an effective magnetic length of 186 mm are satisfied.



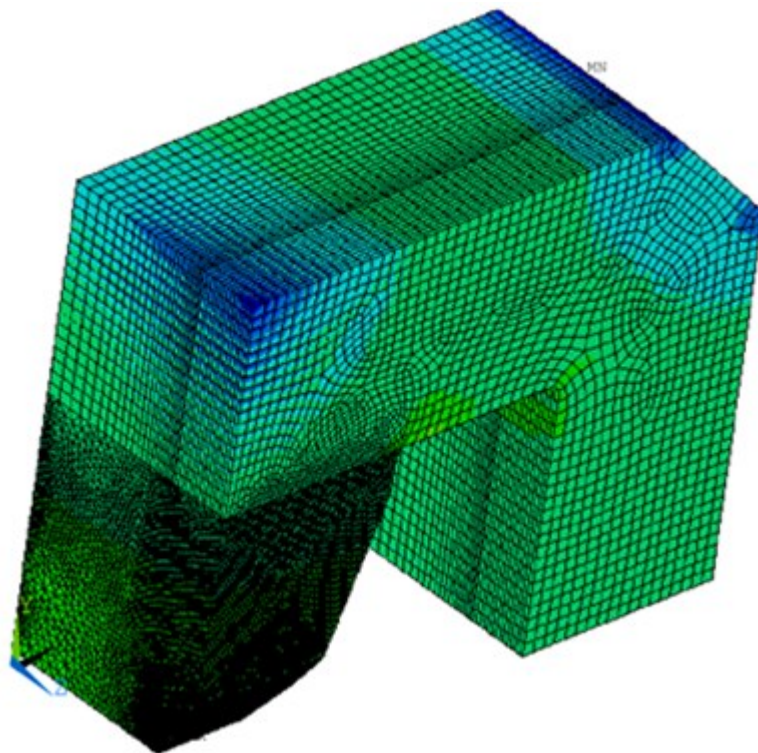
<Figure 2.1.6.4> Uniformity of magnetic field integral depending on several shim sizes.



<Figure 2.1.6.5> B_y distribution along the CB magnet length.



<Figure 2.1.6.6> Excitation curve of the field integral over the CB length depending on the current change. The magnetic efficiency at the rated current based on the ideal case is about 92%.



<Figure 2.1.6.7> A 3-dimensional FEM model figure.

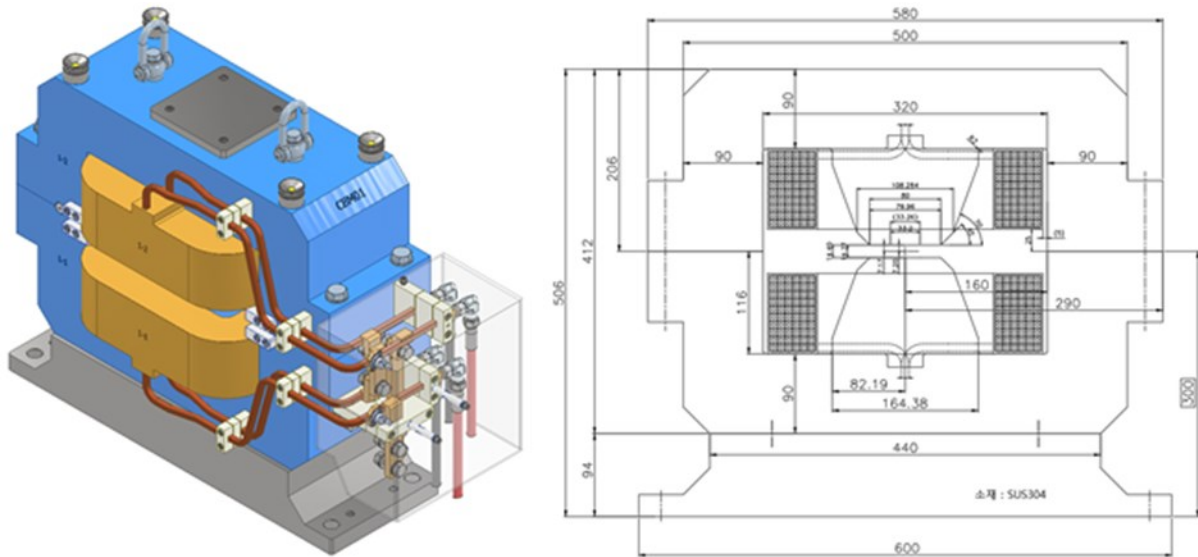
Excitation curves for the ideal case of infinite magnetic permeability and an actual material are shown in <Figure 2.1.6.6>. The expected magnetic efficiency at the rated current was calculated to be about 0.92, which was obtained by extrapolating the field

integral at a low current up to the rated current. <Figure 2.1.6.7> shows the 3D Finite Element Method (FEM) model. Only 1/8 of the whole magnet was modeled by using symmetry.

By combining the above results, the CB parameters are shown in <Table 2.1.6.3>, and the CB magnet after the final 3D design and the 2D cross-section at the center are shown in <Figure 2.1.6.8>.

<Table 2.1.6.3> Main parameters of the center bend

Parameters	Center Bend Magnet
Magnet shape	H-type / Solid
Bending angle at 4.0 GeV [deg]	1.5928
Pole gap at center [mm]	14.4
Nominal Magnetic field @I=221.3 A [T]	1.9942
Nominal Field integral @I=221.3 A [Tm]	0.3709
Effective magnetic length [mm]	186.0
Ampere turns per pole [kA]	12.84
Magnetic efficiency	0.89
Nominal current [A]	221.3
Resistance per magnet [Ω]	0.038
Voltage drop @I=221.3 A [V]	8.41
Rated power @I=221.3 A [kW]	1.86
Inductance [mH]	23
Coil cross-section [mm]	SQ8.0- \varnothing 4.0
Coil turns per pole	58
Cooling system	Water
LCW pressure drop [kgf/cm ²]	6.0
Total water flow rate [liters/min]	2.41
Cooling circuits per magnet	2
Temperature rise @I=221.3 A [K]	11.1
Mass (core/coil) [kg]	\leq 450
Application (Position)	4GSR SR



<Figure 2.1.6.8> CB magnet (right) and 2D cross section (left) after the final 3D design.

C. Longitudinal Gradient Bending Magnet (LGBM)

In each 4GSR sector, two LGBMs are deployed on each side of the CB. Since the longitudinal field profile of LGBMs should be mirror symmetric around CB, even if two LGBMs have the same field profile, one should be manufactured in the order of increasing magnetic field, and the other should be manufactured in the order of decreasing magnetic field. Therefore, treating each type as a separate magnet may eliminate any confusion. In an LGBM1, the magnetic flux density changes in the beam direction in 5 steps from 0.1504 T to 0.7343 T.

In an LGBM1 of each sector, the magnetic flux density increases in the beam direction, and in the other LGBM1, the magnetic flux density decreases (0.7343 T \rightarrow 0.1504 T) in the beam direction.

For an LGBM2, the magnetic flux density is reduced in five steps from 0.3121 T to 0.1535 T in the same way, and the remaining one is symmetric with respect to CB. An LGBM, like CB, has been designed as a C-type due to reasons such as photon beam extraction, easy vacuum design, and easy magnetic field measurement. In the case of LGBM2, the center full gap should be 24 mm or more, and the good field radius must meet the requirements of $\Delta B/B < 10.0 \times 10^{-4}$ at ± 13 mm.



<Figure 2.1.6.9> Finished prototype of Electric excited LGBM2

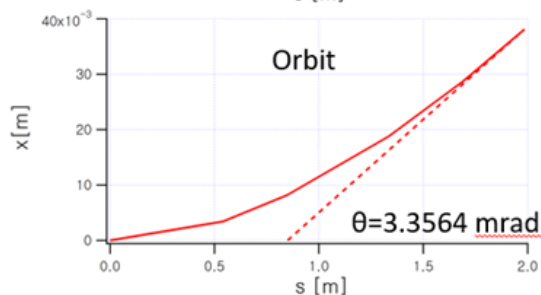
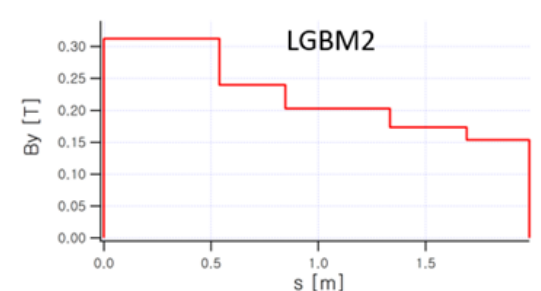
Initially, electromagnetic excitation of LGBM type magnets are assumed following APS-U case. A prototype of electric excited LGBM2 was designed and prototype was manufactured for the test. Detailed magnetic measurements showed that it meets all the 1st integral and 2nd integral, field uniformity requirements. The final assembled current excited LGBM2 prototype is shown in <Figure 2.1.6.9>.

One of the biggest reasons for choosing electromagnetic excitation was a possibility of PM degradation coming from the long-term radiation damage to the permanent magnets. However, during Machine Advisory Committee (MAC), and International Advisory Committee (IAC), the committee members advised that ESRF-EBS is experiencing no noticeable radiation damage for its 3 years operations and strongly recommended to consider options for PM based LGBM. Following the recommendations from the committee, LGBMs are redesigned using Sm₂Co₁₇ PM excitation. Sm₂Co₁₇ was chosen because it has a stronger resistance to the radiation damage although the remanence B_r is lower than the NdFeB type magnet.

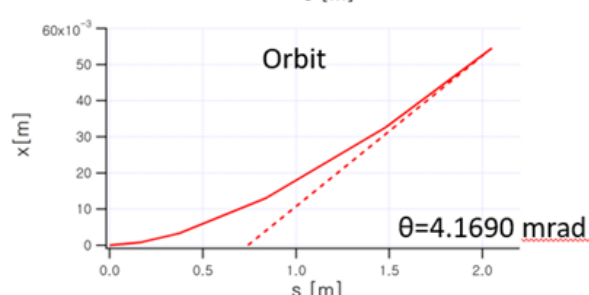
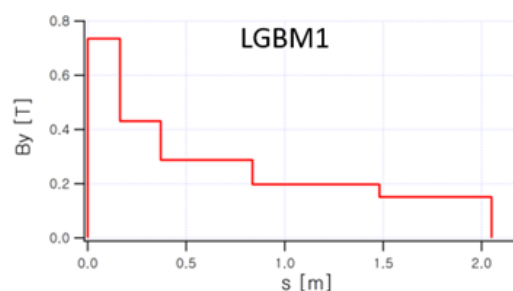
The key parameters LGBM1, LGBM2 are summarized in the Table <Table 2.1.6.4>. Key features include minimum pole gap of 25.0 mm, 5 steps in the field strength, about 2 m magnetic length. As with electrically excited version of LGBM, the field profile cannot follow the ideal profile by the beam dynamics because of the finite fringe fields but the impacts are minimal in beam emittances.

<Table 2.1.6.4> Main parameters of LGBM1 and LGBM2

Parameters	LGBM1	LGBM2	Remark
Magnet type	LGBM1U/LGBM1D	LGBM2U/LGBM2D	-
Required number	28/28	28/28	-
B1/B2/B3/B4/B5	0.7343/0.4302/0.2870 /0.1973/0.1504	0.3122/0.2397/0.2026 /0.1733/0.1535	Tesla -
Uniformity	< 1.0E-3	< 1.0E-3	$ x < \pm 13.0$ mm
Minimum pole gap	25.0	25.0	mm -
L1/L2/L3/L4/L5	0.1649/0.2061/0.4662 /0.6441/0.5690	0.5397/0.3076/0.4869 /0.3586/0.2919	m -
Total length	2.0505	1.9847	m Excluding field clamp
Bending angle	0.5201/0.3808/0.5746 /0.5456/0.3675	0.7235/0.3166/0.4237 /0.2668/0.1925	degrees
Total bending angle	2.388661 (41.690)	1.923062 (33.564)	degrees (mrad)
Field integral	0.556251	0.447827	Tm
Ideal apex point	0.7425	0.8500	m Starting from the high field side



Apex $s_0=0.850037$ m



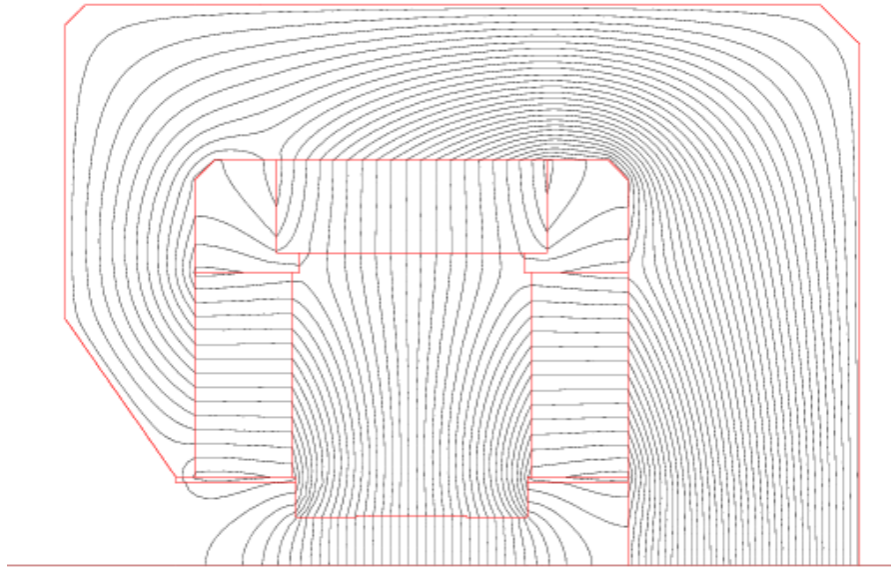
Apex $s_0=0.742563$ m

<Figure 2.1.6.10> Ideal field profile and apex points of LGBM1, LGBM2 magnets

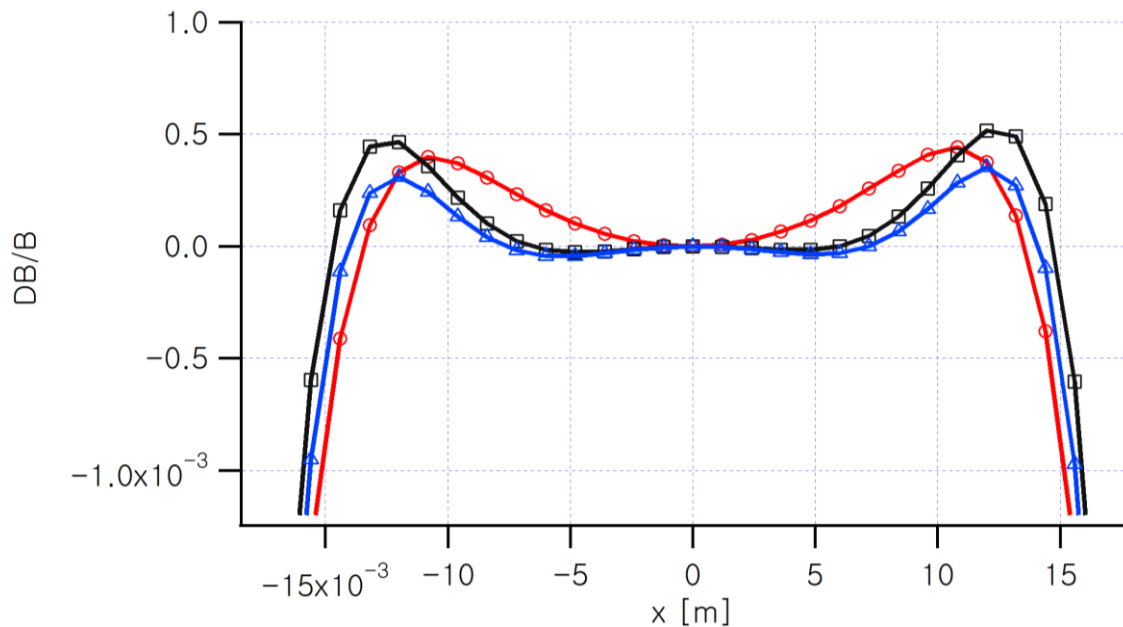
In <Figure 2.1.6.10> the ideal field profile of LGBM1, LGBM2 are shown. Also, ideal orbits based on the field profile is also shown with apex points. Apex points are defined as an intersection of tangent line of the orbit at the field free region with longitudinal axis. Apex points practically define the 2nd field integral of the magnet. If a dipole magnet meets the 1st field integral with correct apex points, the magnet is assumed to meet the beam dynamics specification. There could be small differences between the ideal orbit and actual orbit within the magnet which should be confirmed.

As stated in the previously, Samarium Cobalt based permanent magnet Sm₂Co₁₇ was chosen as a magnetic material. It has a remanence larger than $B_r > 1.13$ Tesla, coercivity $H_cB > 10.4$ kOe with $\mu_{||}=1.08$, $\mu_{\perp}=1.05$. This parameter is slightly conservative value to have some engineering margin. The magnet to magnet fluctuation of B_r should be less than 1%, and transverse angular error of the magnetization should be less than 1 degree. All magnets should be thermally stabilized at 140 °C for 3 hours for long term stability. The pole material is typical low carbon steel. Since the field strength is not high, application of Permendur is not considered. The low carbon steel pole should be annealed before final machining to guarantee maximum permeability.

The 2D structure of LGBM magnets and typical flux distributions are shown in <Figure 2.1.6.11>. It has a C-shape structure to facilitate a vacuum chamber installation and magnetic measurements. It has a central pole surrounded by side magnets and top magnets. The pole shape was optimized using traditional trapezoidal shims with small negative trapezoidal shim to maximize the good field region. The optimized 2-dimensional uniformity is shown in <Figure 2.1.6.12>. It meets the requirements of $\Delta B/B < 1.0E-3$ for $|x| < 13.0$ mm. The field profile is calculated for all excitation levels from 0.15 T to 0.73 Tesla which were low enough not affected by the magnetic saturation.

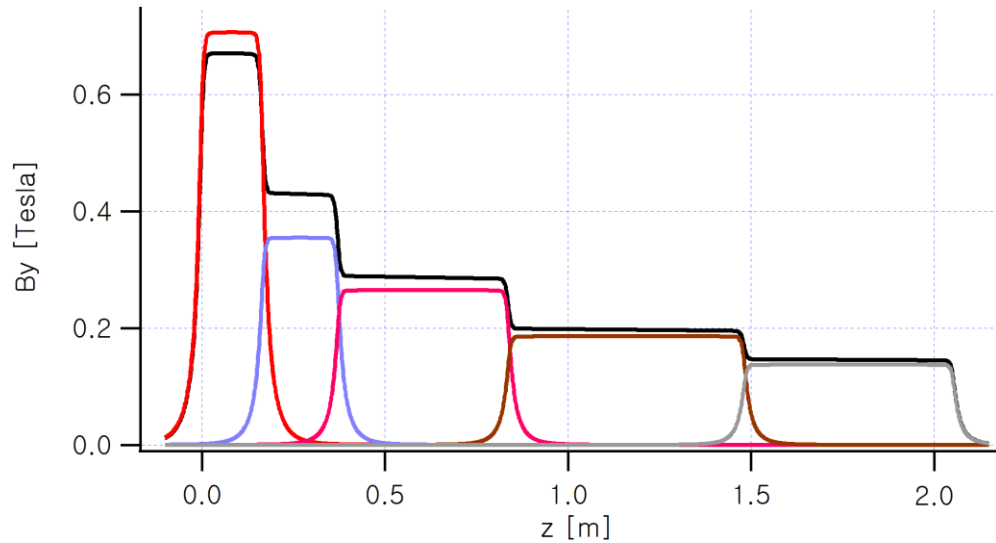


<Figure 2.1.6.11> 2D flux distribution shape of LGBM2.



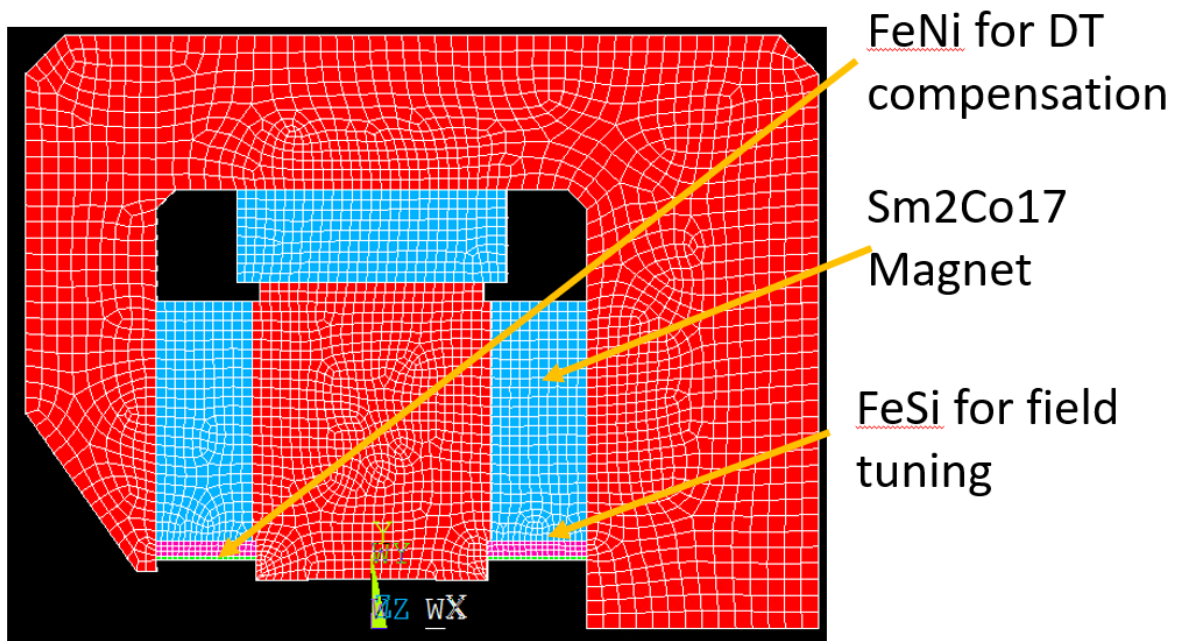
<Figure 2.1.6.12> Field uniformity of LGBM2 for various shims and field levels.

There are some technical challenges for full 3D design. The spacing between the each module is short (approximately 5mm), and the nearby modules interfere each other. The impact is shown in <Figure 2.1.6.13>. In this figure an ideal B profile for LGBM1 is shown with independent field profile for each modules. It can be seen that flux from higher pole leaks to the next pole which decreases the stronger field strength, while increasing the weaker pole. Therefore, each standalone module should be designed taking into account these cross talks between the modules. This cross-talk is most severe for LGBM M1 and M2 module as shown in the figure.



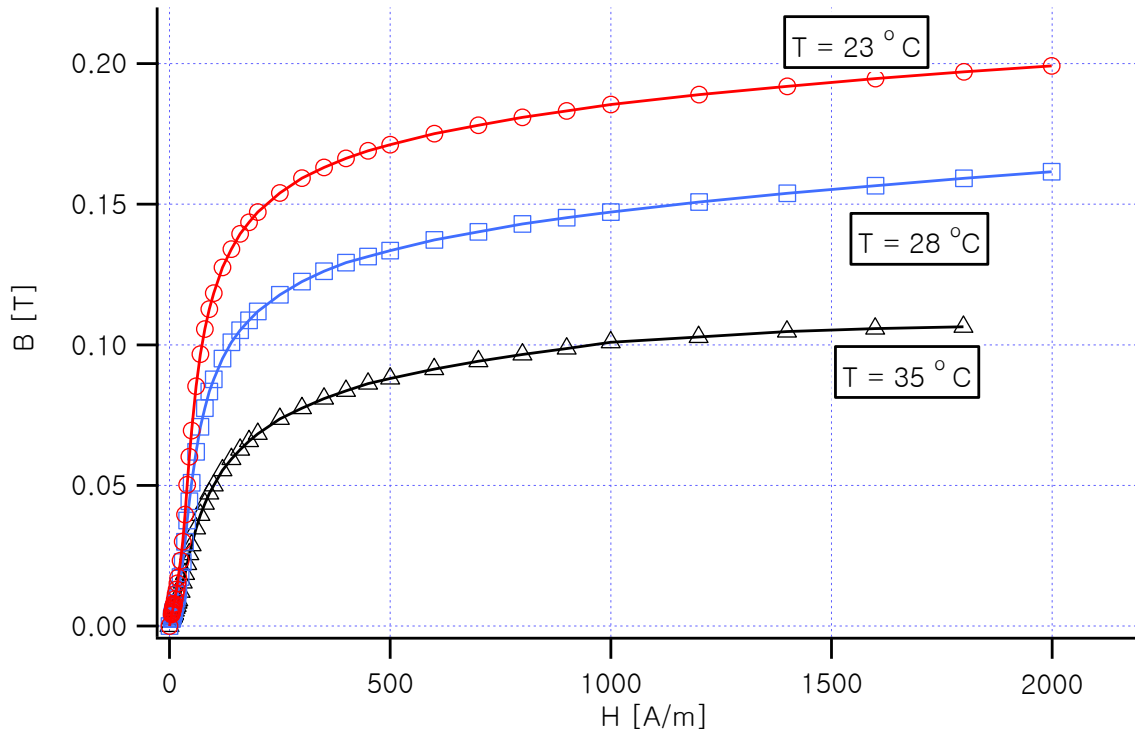
<Figure 2.1.6.13> Simulated field distribution of LGBM1 magnet. The spacing between the modules is 5 mm. The black graph shows the whole magnet while other color shows each single module. The crosstalk between the magnetic modules are clearly seen for stronger magnet module.

Another issue in PM based LGBM magnet is the field tuning problem. Since the permanent magnets are not perfect and have scatters in the strength, and angular errors, the assembled field profile is not always perfect and need fine tuning. Primary tuning scheme is using placing Silicon Steel (FeSi) plate on the magnets practically shortening some magnetic fluxes. Another scheme is using shunting bolts, which is a method applied for HEPS magnets. The working principle is same with FeSi but has another advantage in continuous tuning. A third tuning scheme is implementing movable flux shunts at both ends of the magnets. It can control the field strength about 0.5% for the 1st module (M1), and the last module (M5). In <Figure 2.1.6.14>, the location of FeSi plate and FeNi plate is shown.



<Figure 2.1.6.14> Location of FeSi plate for field tuning. Also FeNi plate for temperature tuning is also shown.

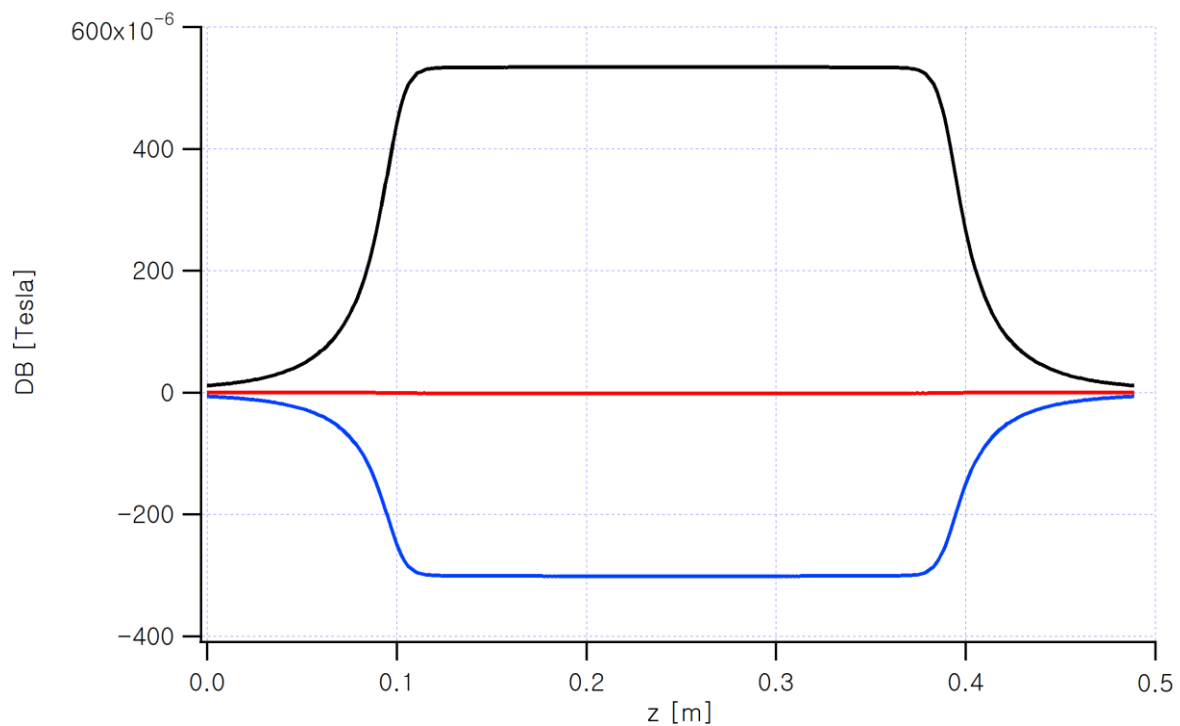
In addition, there is the issue of the temperature dependence of the magnets. Sm2Co17 magnet has a weaker temperature dependence than the NdFeB type magnet. But still it has a temperature dependence of 330 to 350 ppm/K. ESRF-EBS and HEPS applied FeNi plate to reduce the temperature dependence up to 50 ppm/K. FeNi plate has a temperature dependent saturation and passively controls the shunted flux decreasing the temperature dependence. In other words, it shunts slightly higher flux for lower temperature and less fluxes for higher temperature. To estimate the required thickness of FeNi plate, BH curves for 23°C, 28°C, 35°C are acquired from the manufacturer. The BH curve supplied from the manufacturer is shown in <Figure 2.1.6.15>.



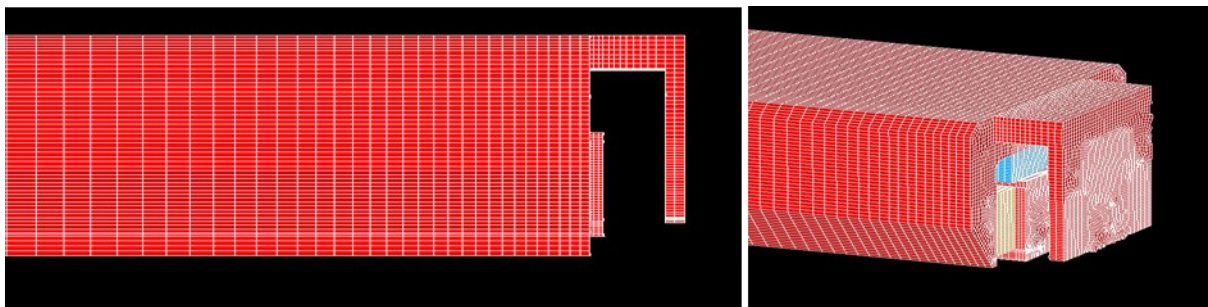
<Figure 2.1.6.15> BH characteristic curve of FeNi(Thermoflux55/100-G) sheet for various temperatures. Curie temperature is 55 °C and max saturation flux density at 20 °C=0.22 T.

To estimate the required FeNi thickness for a module, 3D simulation at two temperatures 23 °C, 28 °C are carried out. For different temperature, reduction in the PM remanance, and application of different BH table for FeNi are implemented. After several iterations, optimal thickness for the module is determined where the field change is minimal for two temperatures. <Figure 2.1.6.16> shows example of temperature compensation for a single LGBM1 module. The graph shows field changes at 23 °C and 28 °C. The black line is the non-compensated case, the blue line is the over-compensated case, and the red line is the optimally compensated case. In actual case, FeNi material property may have scattered, and the BH curve does not cover high field region. Therefore, it may need fine tuning with real experiments.

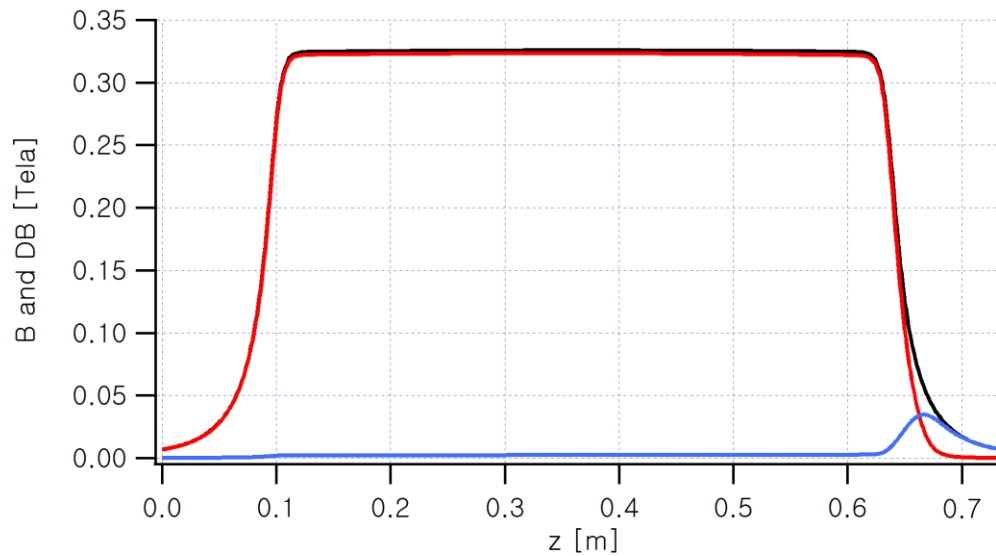
Furthermore, there is a fringe field issue. Nearby quadrupole cores are located between 106 mm to 168 mm. To minimize the interference between the LGBM and nearby magnets, it is needed to limit range of the fringe fields. For this purpose, field clamps are installed at both ends of LGBM magnets. <Figure 2.1.6.17> shows 3D FEM model to analyze the fringe fields. <Figure 2.1.6.18> shows measurement results of the field clamps. With field clamps, the range of the fringe field is reduced.



<Figure 2.1.6.16> Simulated ΔT compensation for a single module. The black line is the field difference for $\Delta T=5$ K without temperature compensated FeNi plate. The blue line is a field difference for two temperatures (23 °C, 28 °C) for FeNi thickness 2.5 mm, and it shows over-compensation. The red line is for FeNi thickness 1.6 mm which shows excellent temperature compensation for $\Delta T=5$ K. In this case the central field was 0.2862 T and the required FeNi thickness is mostly proportional to the central field strength.

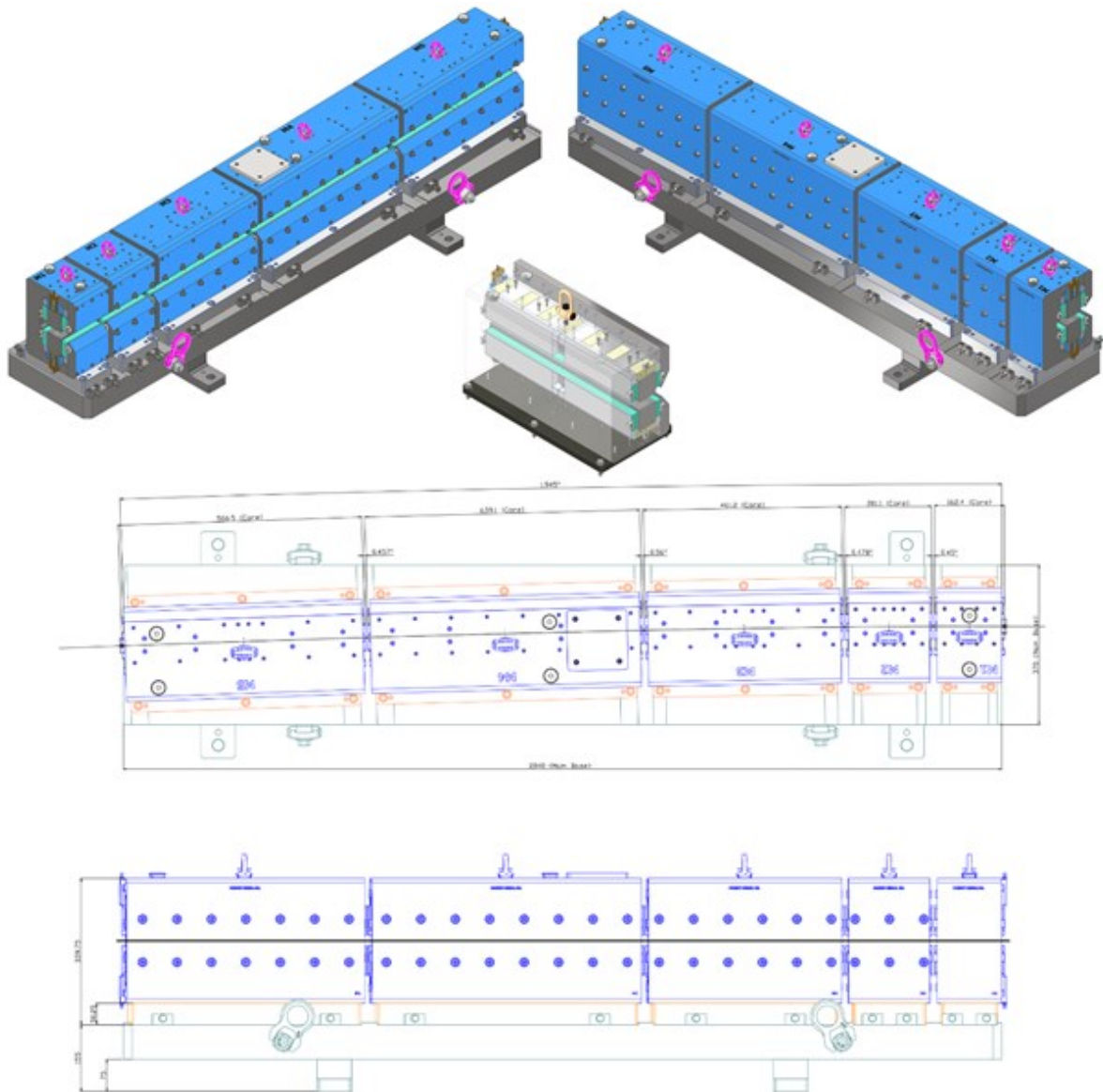


<Figure 2.1.6.17> Shape of the field clamp to limit the fringe field and interference with neighboring magnet.



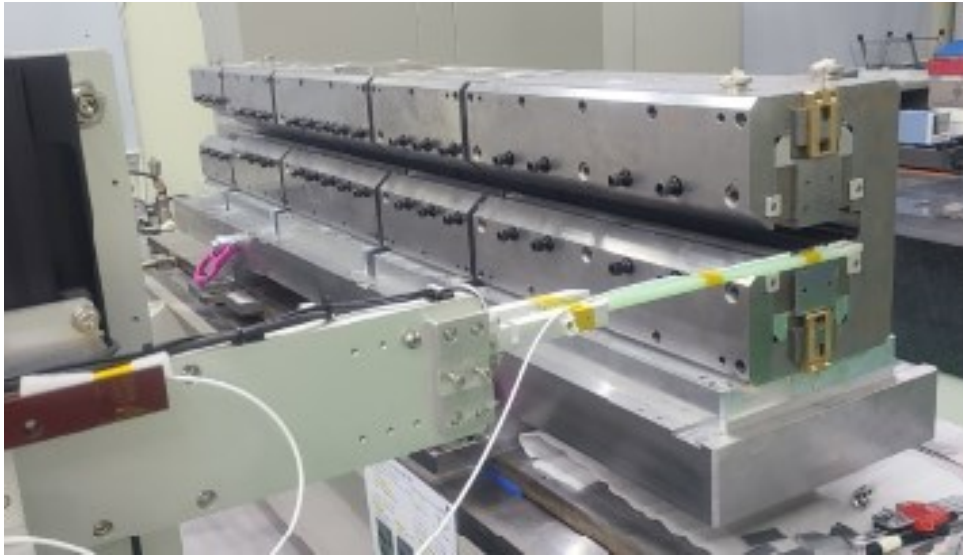
<Figure 2.1.6.18> Impact of the field clamp at the end of the magnet. The blue line shows the field difference with and without clamps. It is clearly shown that the fringe field range is limited due to the field clamp. The clamp vertical gap was 25 mm with 3.0 mm thickness transverse width was wide enough to cover the PM.

With these considerations, final 3D mechanical design is completed, and it's shown in <Figure 3.1.6.19>. On the right figure, the inner structure of magnet placement can be seen.

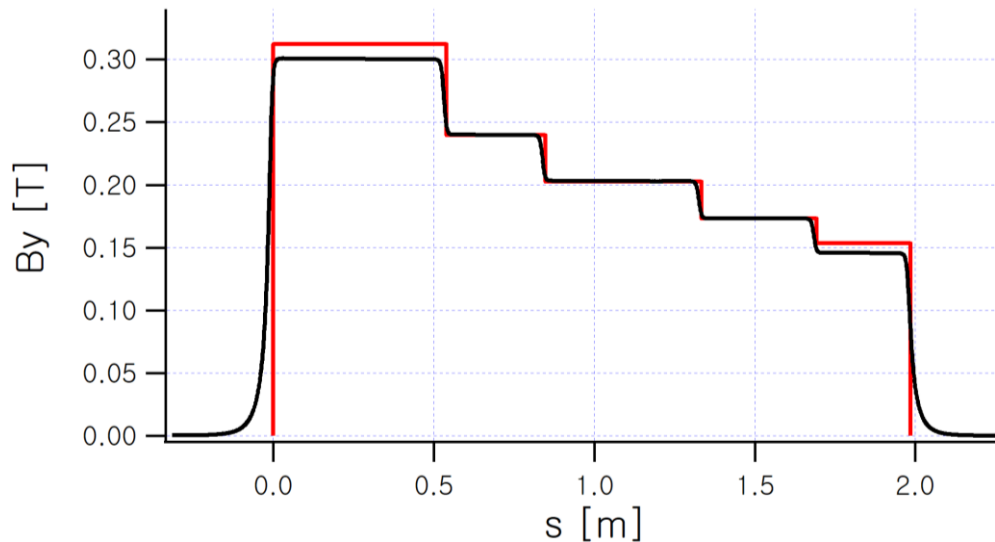


<Figure 2.1.6.19> 3D drawing of the LGBM1 assembly and one module 3D structure.

Based on the drawings, prototyping of LGBM2 has been done. Firstly, M1 was assembled and pole face parallelism, field uniformity, field tunability using FeSi plate, tuning bolt, tuning using end flux shunts, and application of field clamps to limit the fringe field range were tested. The results were mostly within the specification. <Figure 2.1.6.20> shows the final assembled shape of LGBM2 prototype on the measurement bench, and <Figure 2.1.6.21> shows the final magnetic measurement results compared with the lattice design field. It can be seen that the field is following the ideal field closely except M1, M5 modules. The fields from end modules are slightly lower than the ideal field due to the fringe field.



<Figure 2.1.6.20> LGBM2 prototype on the Hall probe measurement stage (without field clamp).



<Figure 2.1.6.21> Measured field profile along the LGBM2 compared with the ideal field.

For temperature compensation, FeNi plates are purchased and machined to several sizes. The final assembled LGBM2 will be transported to PAL for testing. The test will be done at the measurement room 1 at 23.5 °C, and 26.5 °C. The temperature cycling capability of the measurement room is already tested. The measurement will be done using stretched wire field integral measurement and central field measurement using NMR probe. The two results will be compared and the procedures for series production will be determined. Also using stretched wire roll error of each module will be tested and the procedure will be incorporated to the series production.

D. Quad Bend DQ31, DQ32, DQ51, DQ52

Quad bend achieves both bending and focusing of the electron beam simultaneously by guiding the electron beam offset from the center of the quadrupole magnet. In the 4GSR, there is also a reverse bend that bends the electron beam in the opposite direction of the dipole magnet to optimize the emittance. In the 4GSR, each sector contains four types of quad bends: one normal-bend quadrupole type and three reverse-bend quadrupole types. The beam physics requirements for these four types of quad bends are summarized in <Table 2.1.6.5>.

<Table 2.1.6.5> Main requirements for Quad Bends (NB, RB)

Magnet ID	DQ31	DQ32	DQ51	DQ52	Remark
Bend type	RB	RB	NB	RB	NB: Normal RB: Reverse
B [Tesla]	-0.160111	-0.137107	0.565074	-0.166079	-
B' [T/m]	55.371633	24.866186	-25.181377	48.533	-
Δx [mm]	2.891566	5.513803	22.440146	3.62	B/B'
L_{eff} [mm]	200.0	145.0	820.0	626.0	-
r_c [mm]	15.0	20.0	30.0	15.0	-

For quad bend magnets, the requirements are $B = 0.565$ T, and $B' = 22.44$ T/m, and the necessary offset is given as $x_c = B/B' = 22.44$ mm. Considering a GFR of approximately ± 7.0 mm in addition, the usable extent is up to $x = 29.44$ mm. Taking this into account, the aperture radius was decided to be 30.0 mm.

For quad reverse-bend magnets, the required x_c values are small as -2.89 mm (DQ31), -5.51 mm (DQ32), and -3.62 mm (DQ52). For DQ32, the aperture radius was set to 20 mm due to interference with the vacuum chamber, while a 15.0 mm aperture radius is used for DQ31 and DQ52 because of their large B' .

The multipole component requirements are limited to less than 10^{-3} of the main component at $r = 10$ mm. All quad bends will be connected to independent power supplies for maximum flexibility. To minimize long-term operational energy consumption, the current density was designed to be in the low range of 3.37–3.54 A/mm². The water cooling system constrains the temperature rise to 12.0 K or less, based on a pressure drop of 6.0 bar

in the LCW system. For example, the temperature rise of DQ51 is 10.5 K.

Quad reverse-bend magnets have the same layout as conventional quadrupole magnets, as in the APS-U design. Unlike conventional quadrupoles, however, quad reverse-bend magnets incorporate an x-axis offset in the beam trajectory and thus provide both bending and focusing. Consequently, a trim coil is required to generate a vertical magnetic field that maintains a constant dipole field—since the effective dipole component scales with the quadrupole gradient as $B_y = B'x_c$ —against variations arising from changes in the quadrupole strength. In determining the required dipole strength, the quadrupole strength is restricted to 95–105% of its nominal value. The trim coil is designed solely to maintain the dipole strength when the quadrupole strength is varied within this range.

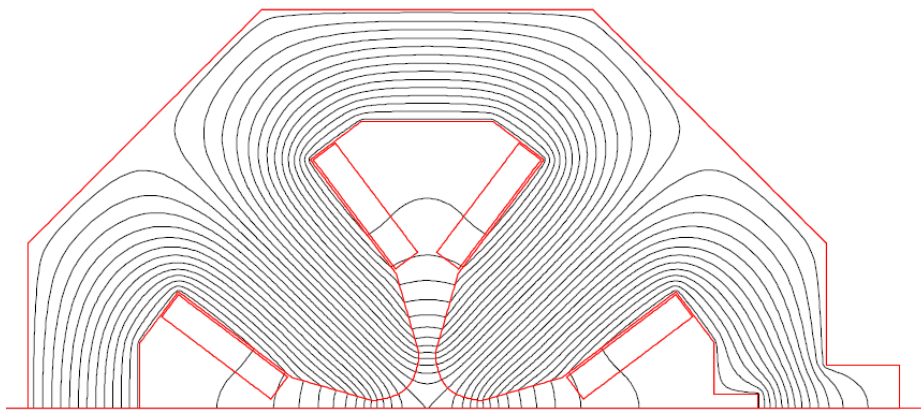
Also, like other quadrupoles or sextupoles, there is a slot for photon extraction. Even for the same DQ31, the position and size of the photon slot differ depending on whether it is placed after the ID section or after the CB. For the 4GSR quad bend, the necessary field strength can be achieved using only the conventional low-carbon steel, just like the quadrupole magnets. It simplifies manufacturing and reduces the budget. For DQ31 and DQ32, the sagitta due to bending is small, being 60 μm and 27 μm , respectively, so a straight core magnet shape is used. For DQ51 and DQ52, the sagitta is larger, being 3.562 mm and 0.610 mm, respectively, so the pole shape was decided to be curved following the orbit.

<Table 2.1.6.6> shows the main parameters of the normal bend DQ51 and the reverse bends (DQ31, DQ32, DQ52).

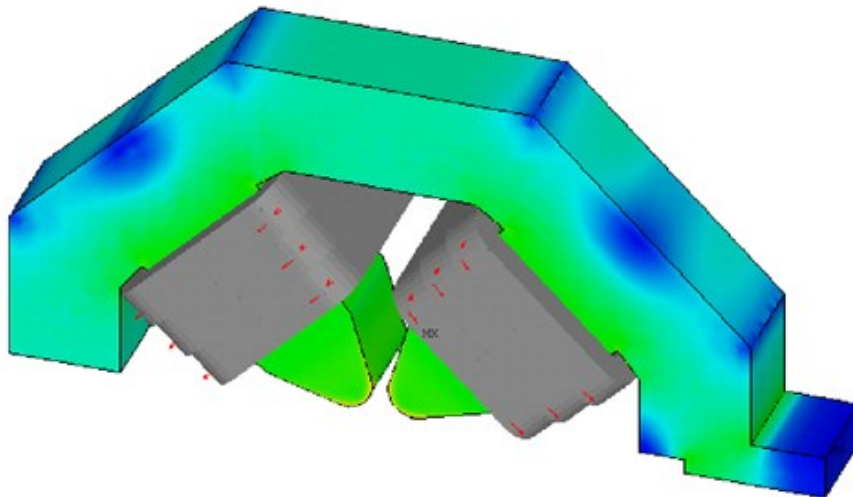
<Table 2.1.6.6> Main parameters of DQ31, DQ32, DQ51, and DQ52 Magnets

Magnet Type	DQ31	DQ32	DQ51	DQ52
Magnet shape	Solid, RB	Solid, RB	Solid, NB	Solid, RB
Required number	56	56	56	56
Feature	Parallel Face Straight	Parallel Face Straight	Parallel Face Curved Pole Straight Yoke	Parallel Face Straight
Aperture radius [mm]	15.0	20.0	30.0	15.0
Good field radius @ offset [mm]	5.0	5.0	7.0	5.0
Multipoles	$<1.0\text{E}^{-3}$	$<1.0\text{E}^{-3}$	$<1.0\text{E}^{-3}$	$<1.0\text{E}^{-3}$
Beam offset [mm]	2.89	5.51	22.44	3.62
Max. field gradient [T/m] 105% nominal	58.14	26.11	26.44	50.96
Nominal B [T]	-0.160111	-0.137107	0.565074	-0.727950
Effective magnetic length [mm]	200.0	145.0	820.0	626.0
Sagitta [mm]	0.060	0.027	3.562	0.610
Core length [mm]	189.3	138.0	809.5	620.8
Main coil size [mm]	SQ6.5-Ø3.5	SQ6.5-Ø3.5	SQ9.0-Ø5.0	SQ6.5-Ø3.5
Main coil turns per pole	46	36	42	44
Ampere-turns per pole [A]	5479	4312	9761	4404.0
Current [A]	119.1	119.8	232.4	100.1
Current density [A/mm ²]	3.75	3.77	3.84	3.11
Voltage per magnet [V]	8.1	5.26	22.5	16.9
Resistance [mΩ]	68.0	43.9	97.0	169.1
Power [kW]	0.97	0.63	5.23	2.141
Inductance [mH]	18.0			
Cooling system	Water	Water	Water	Water
Cooling circuit per magnet	2	2	4	4
LCW pressure drop [kgf/cm ²]	6.0	6.0	6.0	6.0
Total water flow rate [liter/min]	1.67	2.06	7.16	3.07
Temperature rise [K]	8.3	4.4	10.5	8.0
Trim coil cross-section [mm]	2.0×1.0	2.0×1.0	-	-
Trim turns per pole	32	32	-	-
Trim current [A]	3.42	3.02	-	-
Trim voltage [V]	2.574	1.873	-	-
Trim resistance [Ω]	0.752	0.620	-	-
Trim power [W]	8.8	5.65	-	-

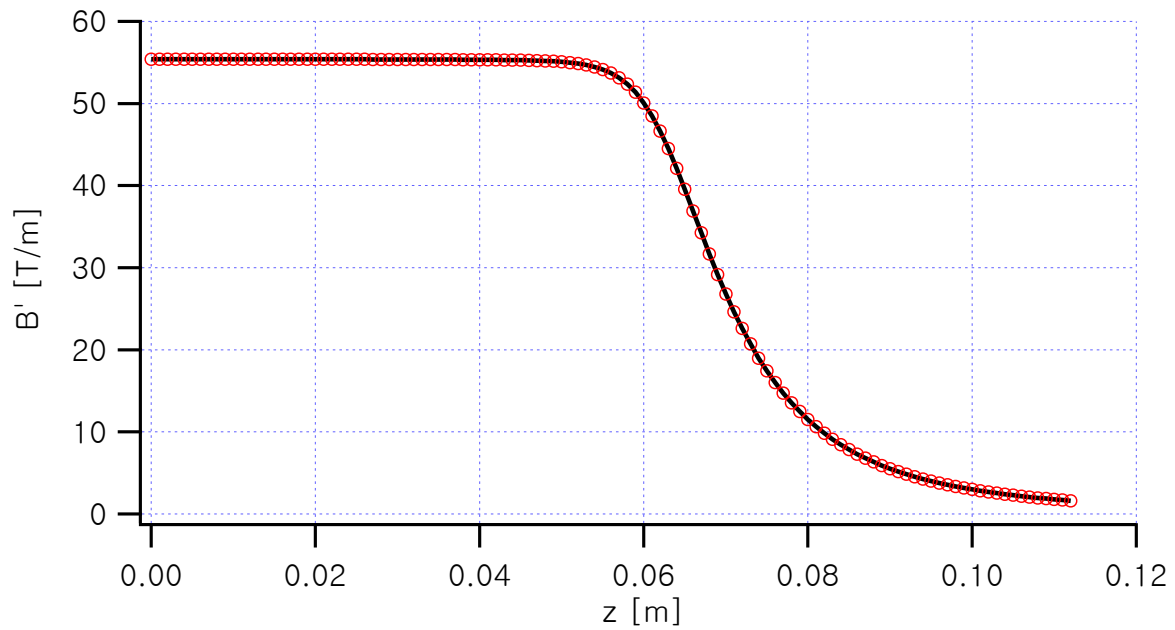
<Figure 2.1.6.22> shows the 2D flux distribution for DQ32 in the case of optimized pole and yoke shapes. <Figure 2.1.6.23> presents the 3D FEM analysis results for DQ32. End chamfering was determined to minimize the multipole component error caused by the edge effect, and 3D optimization design was performed based on the structure reflecting the final 2D cross-section and 3D edge chamfering. <Figure 2.1.6.24> shows the 3D analysis result and the calculated B' profile in the beam direction for DQ32. Based on this data, the 3D mechanical design was carried out, and the corresponding 2D manufacturing drawings were derived, with partial data shown in <Figure 2.1.6.25>.



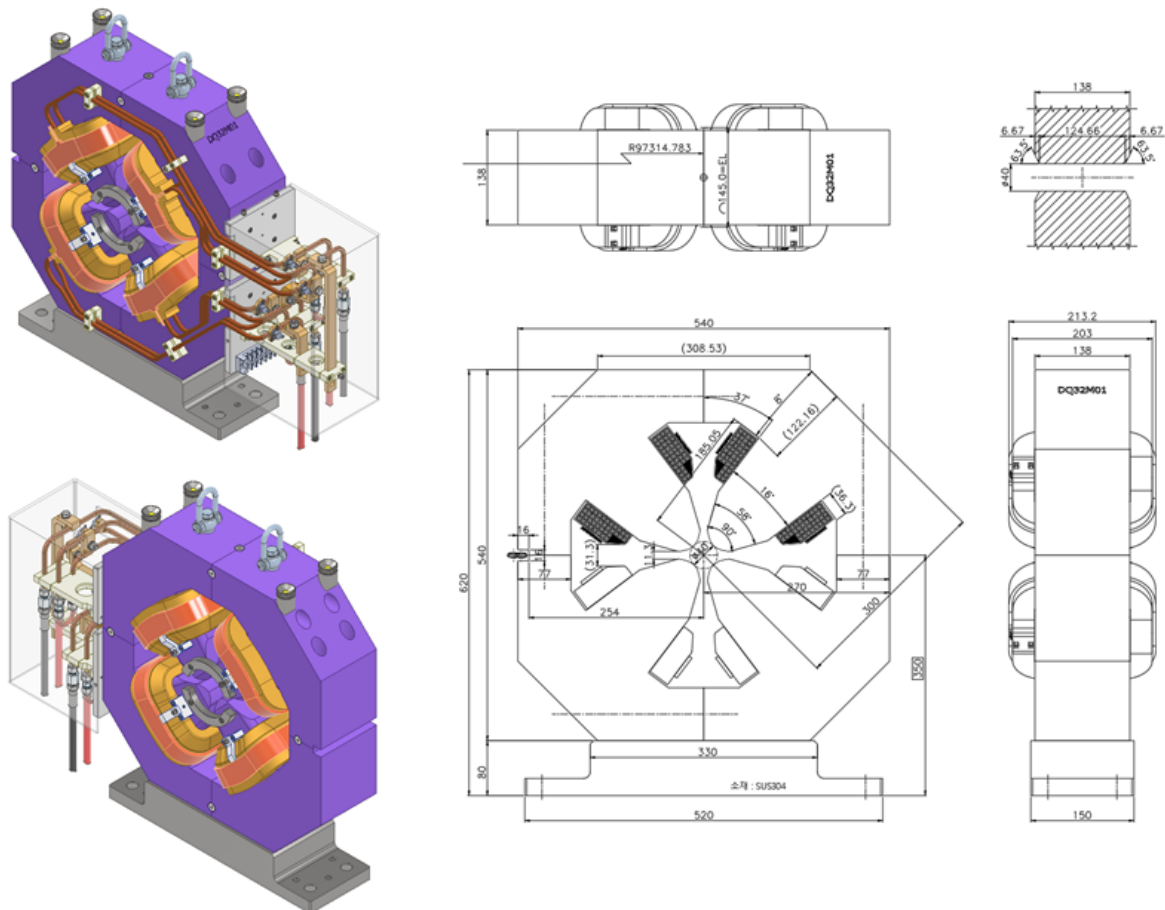
<Figure 2.1.6.22> Optimized 2D flux distribution of a DQ32 magnet.



<Figure 2.1.6.23> 3D FEM analysis result of a DQ32 magnet.



<Figure 2.1.6.24> Longitudinal B' profile of a DQ32 magnet (3D computation result).

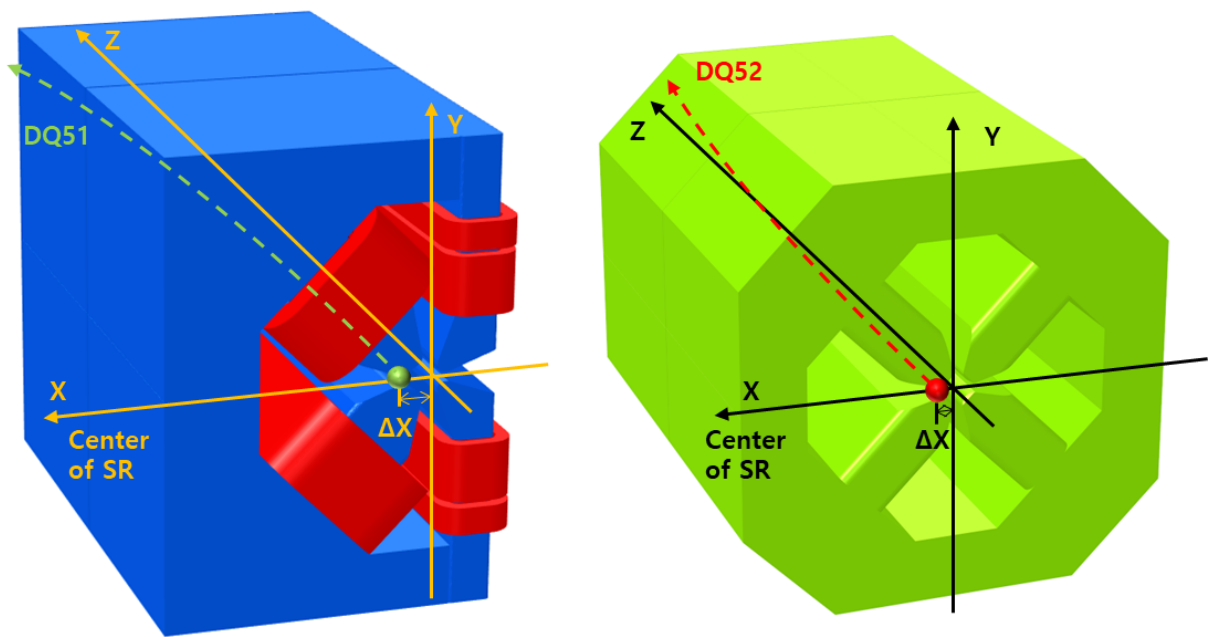


<Figure 2.1.6.25> DQ32's 3D CAD drawings and key 2D drawings of a DQ32 magnet.

DQ51 and DQ52 are used in the 4GSR storage ring with 2 units per cell, totaling 56 units each. Since the magnetic field strength of each Quad bend can be different, each magnet uses an independent power supply.

The quad bend magnet simultaneously serves the functions of both a quadrupole and a dipole magnet. It efficiently uses the storage ring space and has energy-saving benefits. In a typical quadrupole magnet, the electron beam passes through the magnet center and is not influenced by the dipole magnetic field. In contrast, the quad bend is designed so that the electron beam passes through a transversely offset point (Δx) and is affected by both the quadrupole and dipole magnetic fields. The magnet poles of the quad bend are curved, matching the electron beam's trajectory. The quadrupole magnetic fields of DQ51 and DQ52 have opposite signs, and the dipole magnetic fields also have opposite signs.

<Figure 2.1.6.26> illustrates the trajectories of the electron beam passing through DQ51 and DQ52. The left side of the figure shows the electron trajectory of DQ51 in green, and the right side of the figure shows the electron trajectory of DQ52 moving in the opposite direction in red.



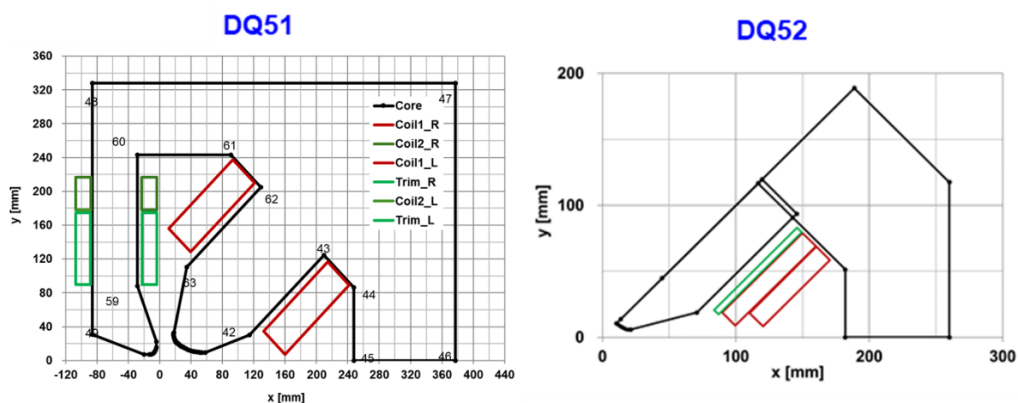
<Figure 2.1.6.26> Electron trajectories of quad bends (DQ51, DQ52).

<Table 2.1.6.7> Requirements of quad bends (DQ51, DQ52)

Parameters	DQ51	DQ52
Aperture radius [mm]	30.0	15.0
Good field radius ($x = \Delta x$) [mm]	15.0	7.0
Field gradient B' (@ Δx) [T/m]	-25.1814	48.533
Dipole field (@ Δx) [T]	0.5651	-0.1661
Magnetic effective length [m]	0.820	0.626
Bending angle [deg]	1.9898	0.4464
Offset Δx [mm]	22.440	3.62
Sagitta of poles [mm]	3.560	0.610
Multipole components (based on quadrupole component)	$< 1.0 \times 10^{-3}$	
B' change range [%]	95 to 105	
Core shape	Curved pole, straight return yoke, parallel planes	Straight

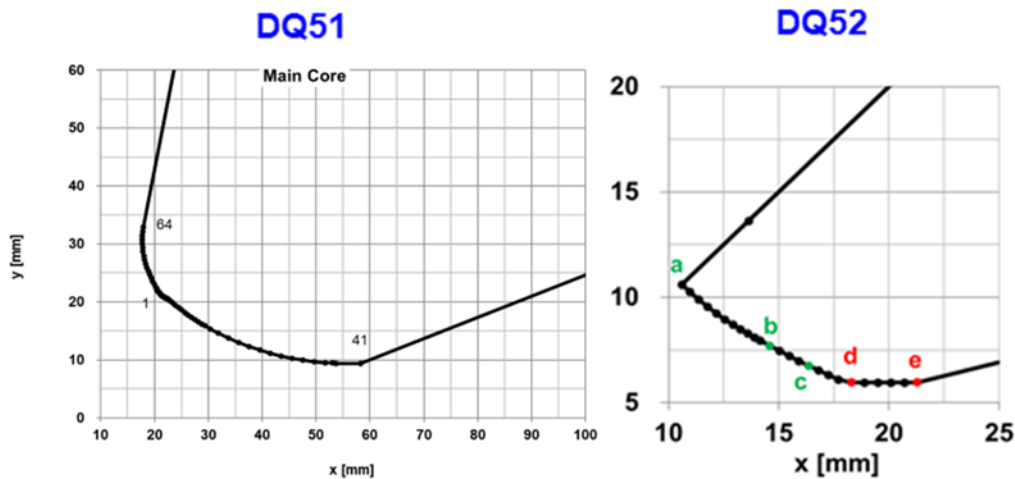
Beam physics requirements for DQ51 and DQ52 are listed in <Table 2.1.6.7>. Since the aperture radii of DQ51 and DQ52 are different, most of their parameters differ. Based on the quadrupole field, both magnets have the same relative multipole component condition as 1.0×10^{-3} or less. Since they are used in the storage ring, they have the same range of quadrupole field variation of 95 to 105% while maintaining a constant quadrupole strength.

As a computational simulation (FEM) code, OPERA 2D/3D/TOSCA was used, and the BH table of Iron (DT4), which is generally easy to obtain, was used for the core material. First, using OPERA 2D, the core cross-section was determined to satisfy the beam physics requirements, and then the pole chamfering was determined in OPERA 3D.



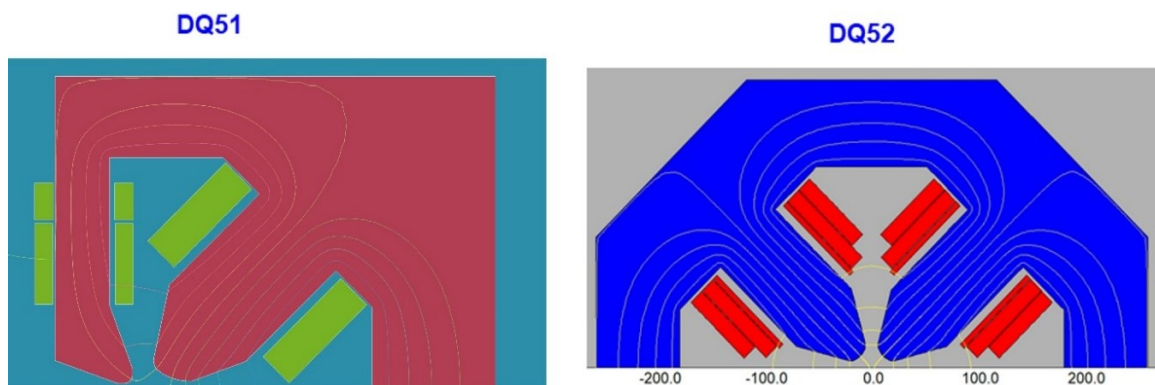
<Figure 2.1.6.27> Cross section of DQ51 and DQ52 core and 1/8 of coil.

<Figure 2.1.6.27> shows a 2D model cross-section of DQ51 and DQ52. The red and green line represents the coil, while the black line represents the core. Although irrelevant in 2D calculations, in a 3D model, the pole and yoke of the DQ52 are manufactured as straight lines. And while the pole line of the DQ51 follows the beam trajectory, but the return yoke is designed in a straight-line shape without curves, making production and management easier.



<Figure 2.1.6.28> Shape of Main Pole tip DQ51 and 1/2 in DQ52.

The electron beam position is not at the magnet center but offset by Δx in the transverse direction. Therefore, while the pole tip shape is fundamentally a hyperbola, the angles of the pole shape curves have been slightly adjusted to reduce the magnetic multipole components. In the right figure of <Figure 2.1.6.28>, segment ab is a hyperbola, and segments bc and cd have been altered in angle and segment length to reduce the multipole components. Segment de is a straight line parallel to the x-axis to help confirm and install the magnet. (The pole tip is close to a hyperbola, but the angles and lengths of the small segments that constitute the pole tip have been minutely changed to reduce the multipole components.)



<Figure 2.1.6.29> Magnetic flux lines of DQ51 and DQ52 computed by the OPERA 2D model.

In the OPERA 2D code, the magnet cross-section that meets the beam physics requirements is determined by analyzing the magnetic field changes depending on the pole tip shape and core size variations. <Figure 2.1.6.29> shows the magnetic flux lines calculated by OPERA 2D for the DQ51 and DQ52 models. The positions where the electron beam passes are offset by $\Delta x = 22.44$ mm for DQ51 and 3.62 mm for DQ52. Since the beam can pass through the yoke, the yoke is designed as a single-sided shape for the DQ51. The multipole components are calculated by determining the radial component of the magnetic field on the good field radius r_0 (15.0 mm for DQ51 and 7.0 mm for DQ52) with Δx as the origin. This magnetic field distribution is then Fourier-transformed to calculate the multipole components (B_n). The radial component B_r has the value given in the following equation (Eq. 2.1.6.1).

$$Br(r_0, \theta) = \sum (B_n \times \sin(n\theta)) \quad (\text{Eq. 2.1.6.1})$$

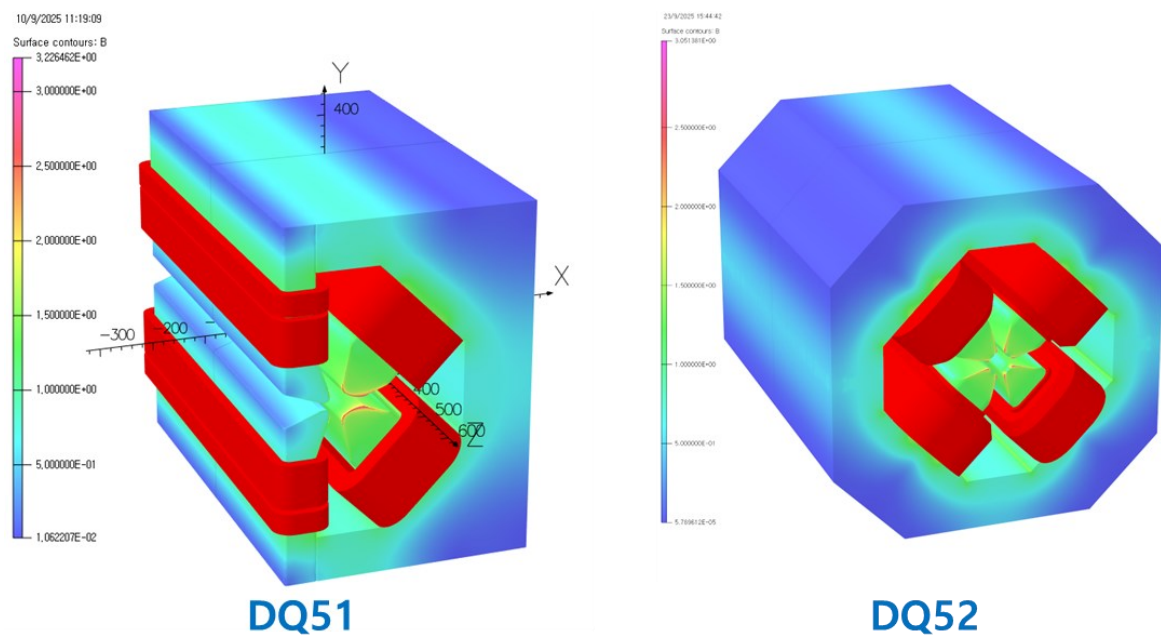
The results of multipole component calculation with OPERA 2D using (Eq. 2.1.6.1) are shown in <Table 2.1.6.8>.

<Table 2.1.6.8> Multipole components for DQ51 and DQ52, computed with OPERA 2D

2D (B_n/B_2)	DQ51	DQ52
B_3/B_2	-1.44×10^{-4}	1.88×10^{-5}
B_4/B_2	-1.80×10^{-5}	1.35×10^{-5}
B_5/B_2	3.23×10^{-4}	1.37×10^{-5}
B_6/B_2	-9.78×10^{-5}	-8.47×10^{-5}
B_7/B_2	-1.65×10^{-4}	-1.33×10^{-5}
B_8/B_2	2.01×10^{-6}	-9.83×10^{-5}
B_9/B_2	6.75×10^{-6}	-9.59×10^{-5}
B_{10}/B_2	-3.96×10^{-6}	-2.67×10^{-5}

Based on the core cross-section determined in 2D, the pole bends according to the electron beam trajectory, while the return yoke is made straight without bending. To reduce the multipole components calculated according to the electron beam trajectory in OPERA 3D, the chamfer size and angle on the pole pillar and pole tip were varied, and the magnetic field was analyzed to determine the chamfer. In the case of DQ51, the value was small, which was judged to be insignificant due to the influence of multipolar components, so polar cutting was omitted.

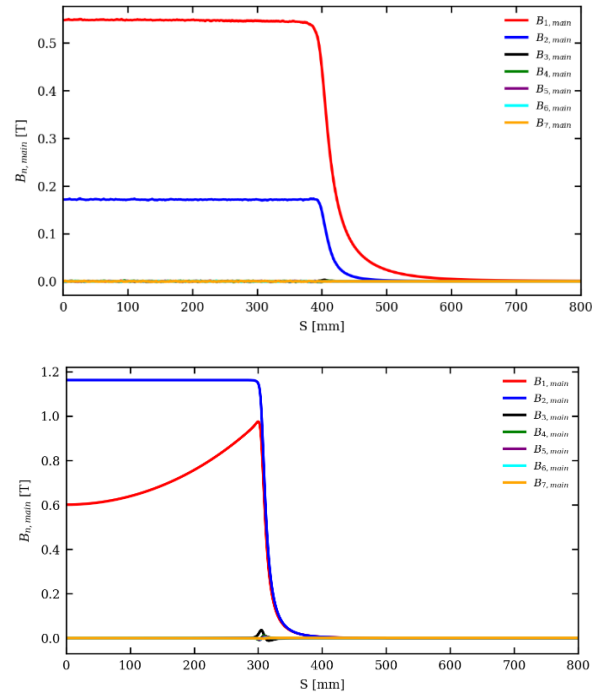
<Figure 2.1.6.30> shows the magnetic field distribution on the surfaces of DQ51 and DQ52. <Table 2.1.6.9> numerically presents the relative multipole components based on the quadrupole field. <Figure 2.1.6.31> illustrates the distribution of the multipole components according to the electron beam position (s-axis) for DQ51 and DQ52. The dipole field is indicated by the red line, the quadrupole field by the blue line, and the multipole field components other than these are observed only at the boundary of the magnets.



<Figure 2.1.6.30> Magnetic field distributions of the DQ51 and DQ52 magnets, calculated using OPERA 3D (TOSCA).

<Table 2.1.6.9> Multipole components for DQ51 and DQ52, computed with OPERA 3D according to the electron trajectory

3D (B_n/B_2)	DQ51	DQ52
B_3/B_2	7.31×10^{-4}	8.31×10^{-5}
B_4/B_2	1.06×10^{-3}	4.56×10^{-4}
B_5/B_2	4.33×10^{-4}	5.77×10^{-4}
B_6/B_2	5.77×10^{-5}	-3.10×10^{-5}
B_7/B_2	1.92×10^{-4}	-9.44×10^{-4}
B_8/B_2	1.73×10^{-4}	-1.25×10^{-3}
B_9/B_2	1.44×10^{-4}	-1.09×10^{-3}
B_{10}/B_2	-5.10×10^{-5}	-7.03×10^{-4}



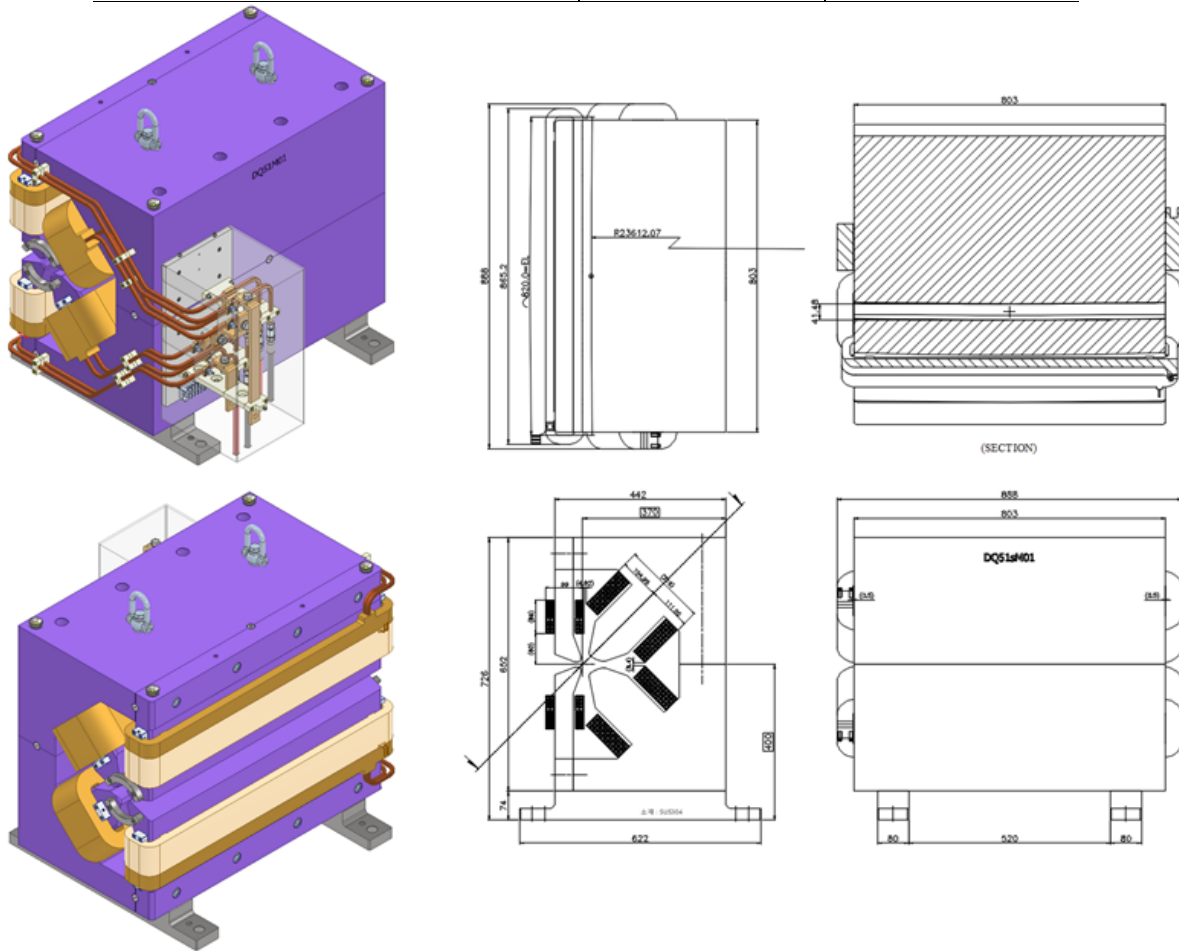
<Figure 2.1.6.31> Multipole components distribution of DQ51 and 52 depending on the electron.

The main parameters representing the design results are shown in <Table 2.1.6.10>. Based on these data, 3D machine design was performed, and 2D manufacturing drawings were derived accordingly. Some of the data are shown in <Figure 2.1.6.32> for DQ51 and <Figure 2.1.6.33> for DQ52. \

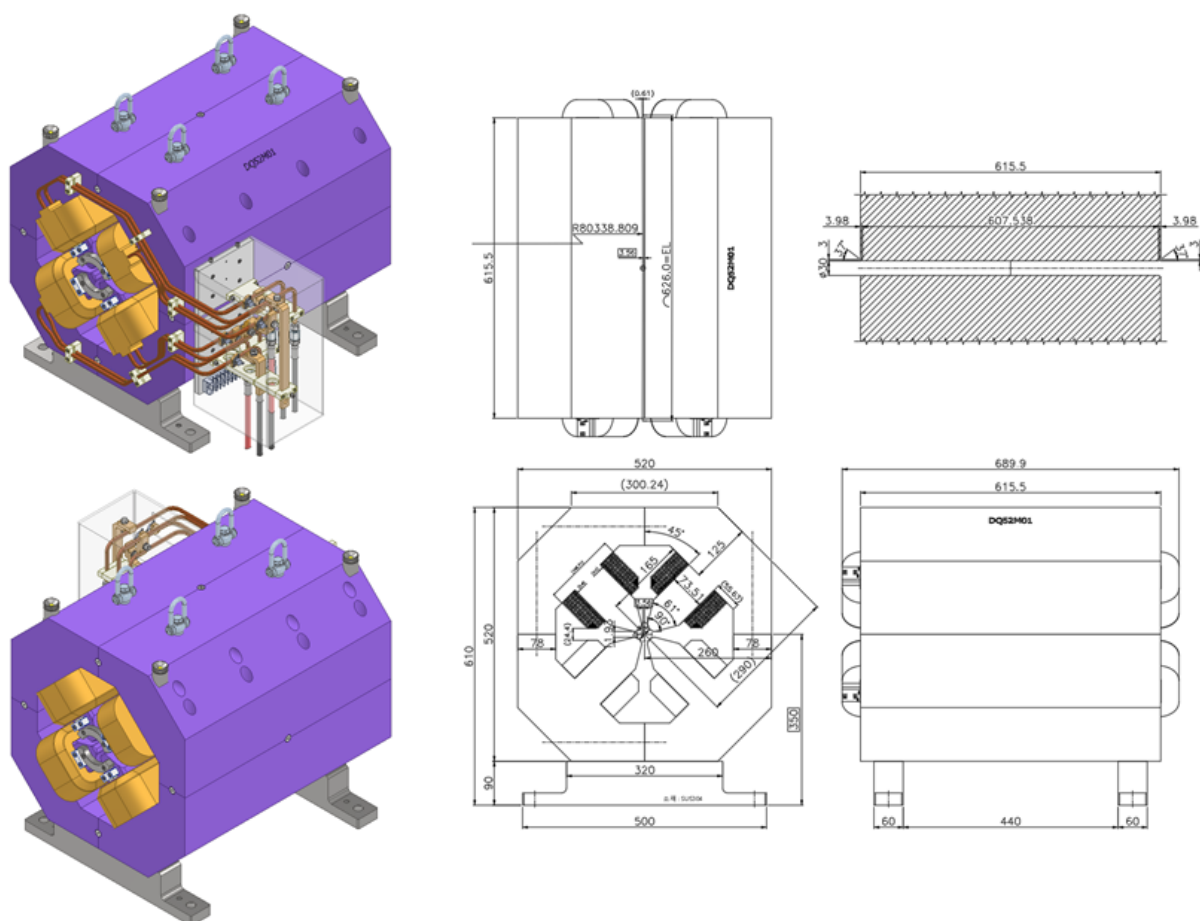
<Table 2.1.6.10> Main parameters of DQ51 and DQ52

Parameters	DQ51	DQ52
Aperture radius [mm]	30.0	15.0
Core length [mm]	803.0	615.5
Current [A]	200.48	100.09
Current density [A/mm ²]	2.48	3.15
Magnetic efficiency	0.95	0.98
Resistance [Ω]	0.13	0.17
Voltage [V]	26.06	16.92
Power [W]	5225	1694
Temperature rise [K]	15	8
Main coil cross-section [mm]	SQ9.0-Ø5.0	SQ6.5-Ø3.5
Main coil turns per pole	42	44
Mass [kg]	4937	1058

Trim coil cross-section [mm]	2.2×4.0	2.2×4.0
------------------------------	---------	---------



<Figure 2.1.6.32> DQ51 3D CAD drawings and key 2D drawings.



<Figure 2.1.6.33> DQ52 3D CAD drawings and key 2D drawings.

E. Quadrupole Magnets

Quadrupole magnets are used to focus electron beams, and in the case of the 4GSR, a high magnetic field gradient (B') must be achieved with a small aperture radius. Based on the dynamic aperture computed by beam physics and the vacuum chamber design, the aperture radius of quadrupole magnets was determined to be 15.0 mm. The required magnetic field gradient was set to be between 75% and 110% of the nominal value, with a maximum of approximately 60 T/m. There are four types of effective lengths: 145 mm (Q31/Q32), 200 mm (QH/Q12/Q52), 250 mm (Q11), and 384 mm (Q51). However, like quad bends or reverse bends, quadrupole magnets have different photon slots for extracting photons. So, even though the coil shape is the same, the core shape may differ. The multipole components are required to be less than 10^{-3} of the main component at $r = 10$ mm. As in quad bends, the pole tip field of quadrupole magnets is not high at about 0.90 T, so low-carbon steel was chosen as the core material. This simplifies production and can reduce the budget. One notable point is that a corrector coil is installed for Q51 to allow a kick of about 0.4 mrad in the H/V direction as per beam physics requirements.

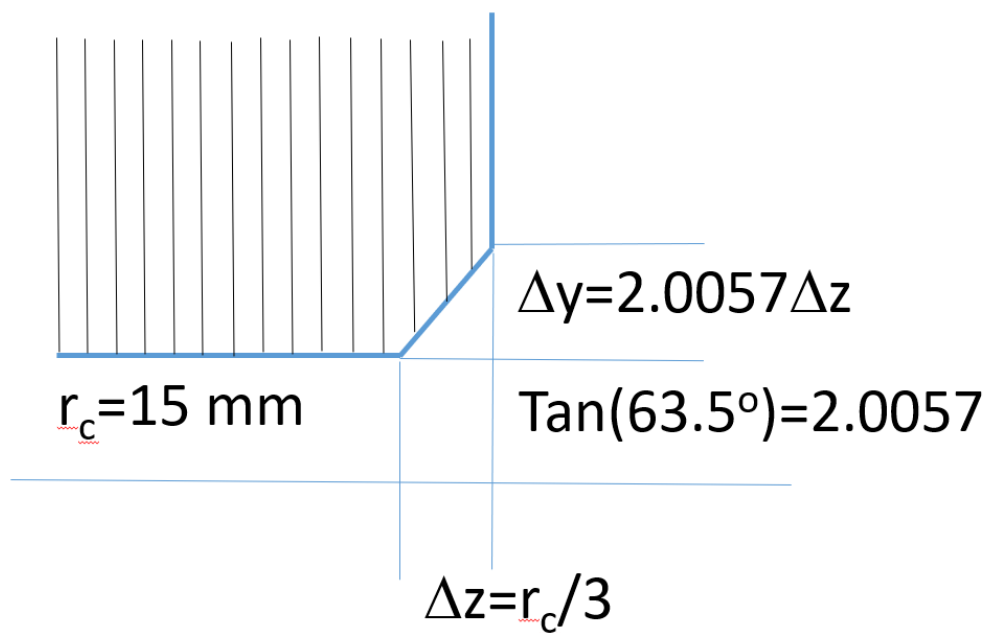
All quadrupole magnets will be connected to independent power supplies for maximum flexibility. As a design to minimize long-term operating energy consumption, the current density was determined to be low at 3.79 A/mm², and the cooling water temperature rise was determined not to exceed 8.1 K for $\Delta p = 6.0$ bar (QH/Q12/Q52). The position and size of the photon slot vary for the same Q11 depending on whether it is installed upstream or downstream. The parameters of the quadrupole magnets are listed in <Table 2.1.6.11>.

<Table 2.1.6.11> Main parameters of Q31, QH, Q12, Q52, Q11, and Q52 magnets

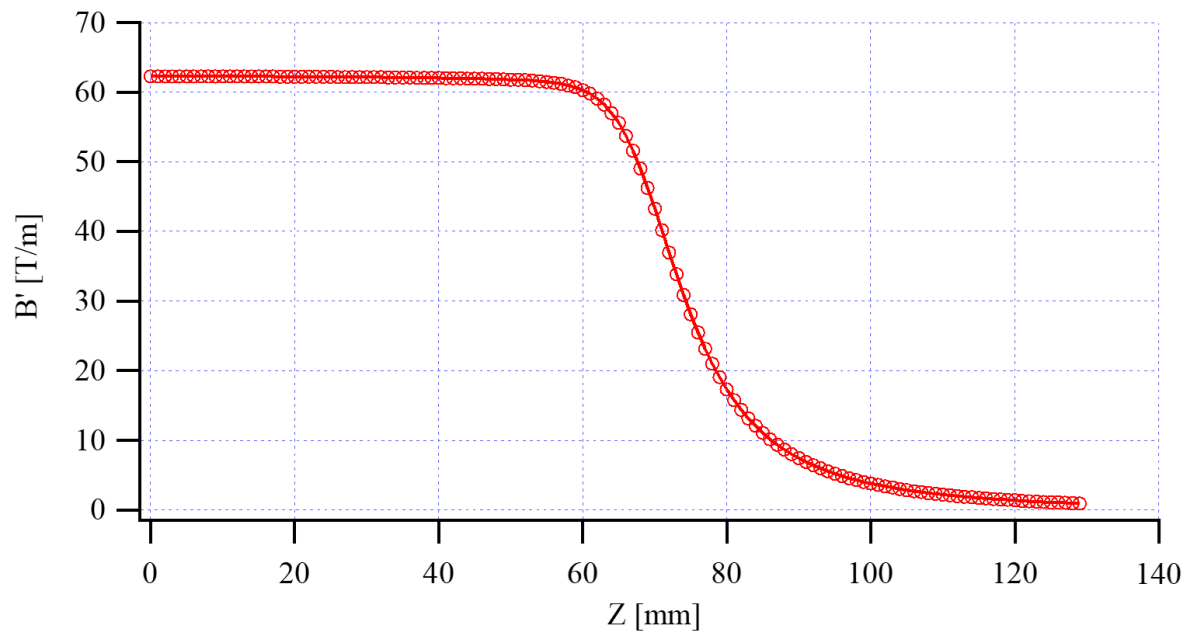
Parameters	Q31/Q32	QH/Q12/Q52	Q11	Q51
Magnet shape	H-type, Solid	H-type, Solid	H-type, Solid	H-type, Solid
Required number	112	124	52	56
Aperture radius [mm]	15.0	15.0	15.0	15.0
Good field radius [mm]	10.0	10.0	10.0	10.0
Max. field gradient [T/m]	56.2	57.4	49.4	53.6
Effective magnetic length [mm]	145.0	200.0	250.0	384.0
Core length [mm]	134.4	189.3	239.3	374.0
Main coil cross-section [mm]	SQ6.5-Ø3.5	SQ6.5-Ø3.5	SQ6.5-Ø3.5	SQ6.5- Ø3.5
Main coil turns per pole	44	46	44	44
Ampere-turns per pole [kA]	5.30	5.41	4.65	5.05
Current [A]	120.4	117.6	105.8	114.8
Current density [A/mm ²]	3.79	3.70	3.33	3.61
Voltage per magnet [V]	6.46	8.00	7.98	11.83
Resistance [mΩ]	53.7	68.0	75.4	103.1
Power [kW]	0.778	0.941	0.844	1.358
Inductance [mH]	26.0	37.0	40.0	62.0
Cooling system	Water	Water	Water	Water
Cooling circuit per magnet	2	2	2	4
LCW pressure drop [kgf/cm ²]	6	6	6	6
Total water flow rate [liter/min]	1.85	1.67	1.56	3.69
Temperature rise [K]	6.0	8.1	7.8	5.3
Trim strength for H/V corrector [mrad]				0.400
Trim coil cross-section [mm]				2.0×1.0
Trim coil turns per pole				46
Trim current [A]				3.43
Trim voltage [V]				5.88
Trim resistance [Ω]				1.71
Trim power [W]				20.1

The Quadrupole magnet essentially has the same shape as the Quad bend, so the flux distribution is similar to that of the Quad bend. 3D analyses were performed on various end

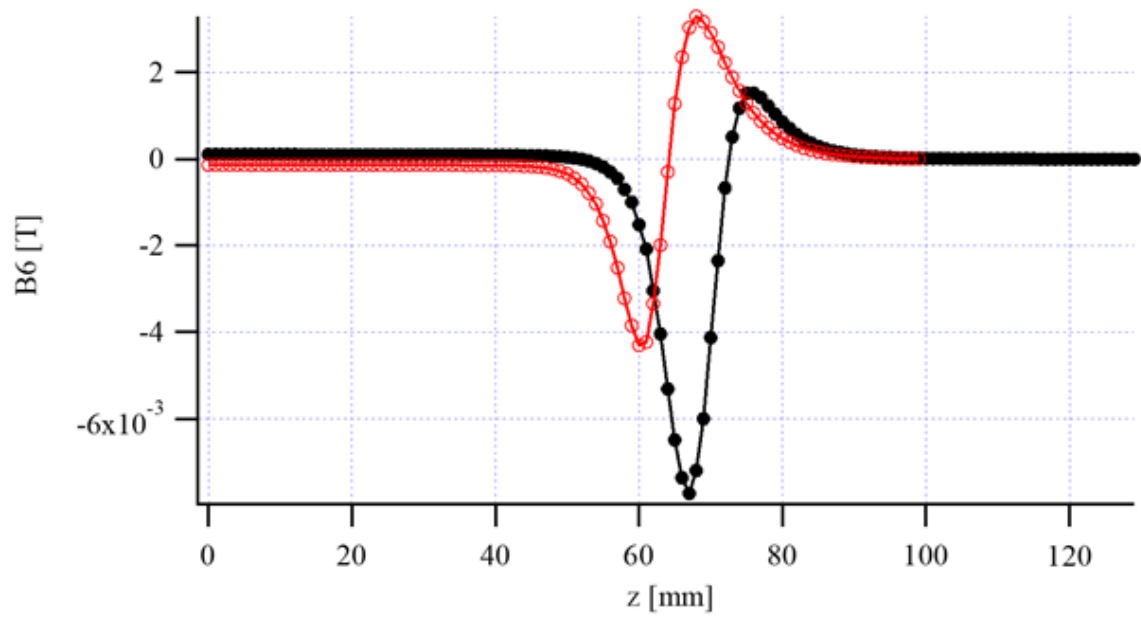
chamfering options to optimize the quadrupole end parts. The longitudinal distribution of the corresponding multipole components (particularly B_6 at $r = 10$ mm) was investigated. The final structure of the end chamfering is shown in <Figure 2.1.6.34>. Since the core saturation is low, the same chamfering can be applied to quadrupole magnets of different lengths. Based on the final 3D analysis, the longitudinal distribution of B' for Q31 is shown in <Figure 2.1.6.35>, and the end chamfering effect is illustrated in <Figure 2.1.6.36>. The red curve represents the optimized result, which makes the integral value approach zero and compensates for the B_6 contribution from the end through chamfering. The black curve represents the B_6 distribution before edge optimization. Before chamfering, the B_6 contribution from the end part is significant, whereas, after end chamfering, the B_6 contributions from the end part cancel each other out. Based on these design data, three-dimensional drawings were created. 3D CAD drawings and 2D key drawings are shown in <Figure 2.1.6.37>.



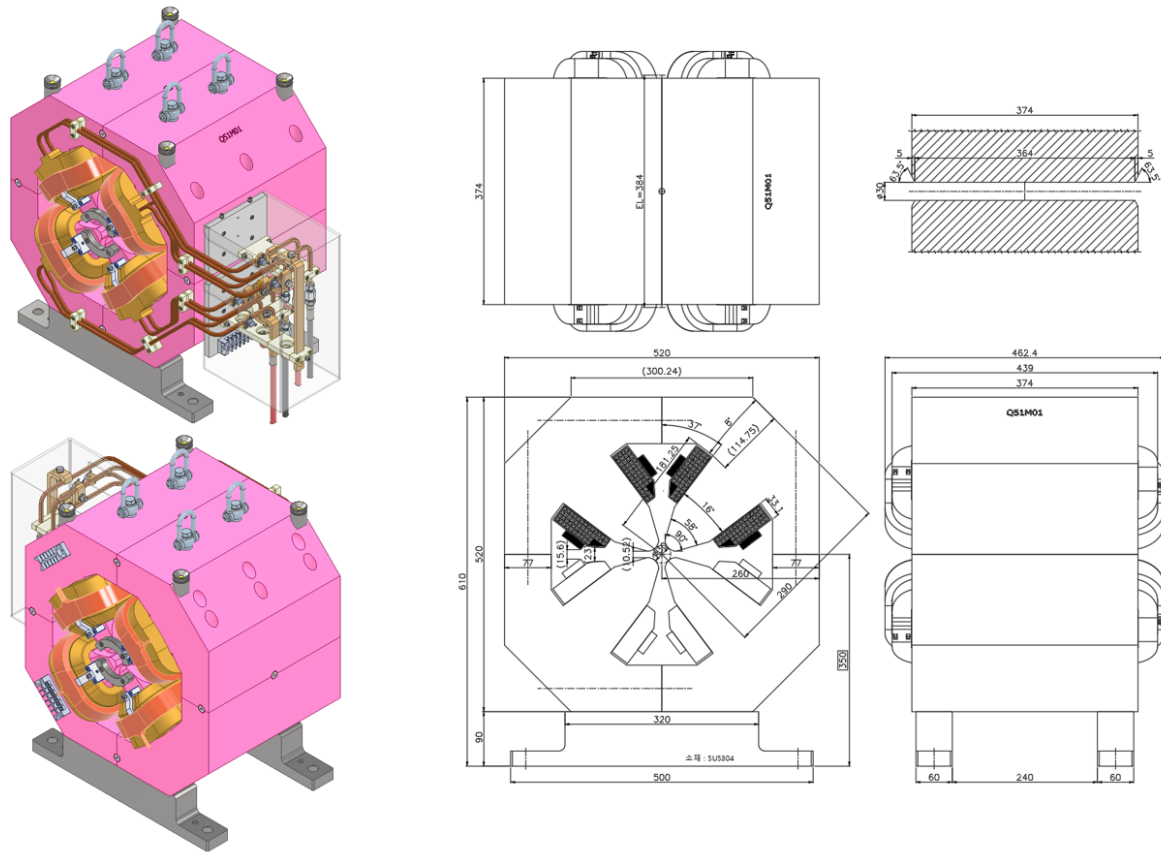
<Figure 2.1.6.34> Optimized end chamfering of a quadrupole magnet.



<Figure 2.1.6.35> Longitudinal profile of B' in Q31 and Q32 (3D computation result).



<Figure 2.1.6.36> B_6 optimization through end chamfering in Q31.



<Figure 2.1.6.37> 3D drawings and key 2D cross-section drawings in the Q51 quadrupole.

F. Sextupole Magnets

Each sector uses six sextupole magnets, for a total of 168. The aperture radius was increased from the previous design value of 16 mm to 20 mm to provide photon-extraction space and to satisfy the minimum pole-to-pole clearance of ± 6.5 mm, which must be reflected in the vacuum chamber design. With the addition of octupole magnets to the lattice, additional lattice space was required. Previously, all sextupole magnets had a length of 250 mm, but the new lattice has been optimized to have two types of sextupole magnets with lengths of 180 mm and 200 mm. The multipole components are required to be less than 10^{-3} compared to the main component at $r = 10.0$ mm, which is expected to be more easily achieved with the aperture increase. The operating range of the sextupole was set between 50% and 120% of the nominal value and designed based on the 120% of the nominal value. The maximum second derivative of the magnetic flux density (B'') is $2,084 \text{ T/m}^2$, 120% of the lattice nominal value.

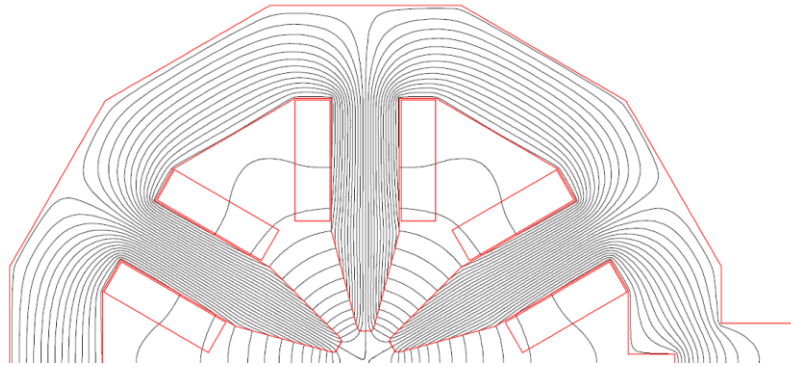
Even though all sextupole magnets have the same electrical and magnetic specifications, they may have different mechanical shapes due to the photon extraction slot, as in

quadrupole magnets. The B'' value of 2,084 T/m², corresponds to $B_{\text{tip}} = 0.5B''R_c^2 = 0.417$ T based on the pole tip field, and this can be sufficiently achieved using low-carbon steel. Sextupole magnets are multi-functional and will serve as H-correctors (H), V-correctors (V), and Skew Quadrupoles (SQ). Interference has been reported where the strength of H/V/SQ varies according to the excitation strength of the sextupole magnet due to the magnetic saturation of the magnet core (APS-U report). The magnetic efficiency of the sextupole must always be maintained at 96% or higher to minimize such interference. Since the excitation strength of the sextupole is that before magnetic saturation, maintaining an efficiency of 96% or higher is expected to be easy.

Another potential issue is that due to the photon slot problem in the vacuum chamber, there is a limit to the size poles can have, making it difficult to maintain all multipole components below 10^{-3} . Therefore, the Beam Physics Team needs to confirm that multipole components (especially $n = 9$) slightly exceeding the tolerance will not cause any problem in actual operation, as in APS-U. Another limitation comes from the assumption that the sextupole magnet core will use solid steel, and because of this, the response of the H/V corrector may not be sufficiently fast. Under these limitations, sextupoles should be used as slow orbit feedback (SOFB) correctors, so it is necessary to find out the exact response characteristics of the corrector after prototype production. In the CDR, sextupole magnets were planned to be deployed periodically with a period of 2 cells, and each of the 12 power supplies would connect 14 sextupoles in series. However, to secure maximum physical flexibility, the Beam Physics Team required the use of individual powering. Therefore, all sextupole magnets will be operated with individual power supplies.

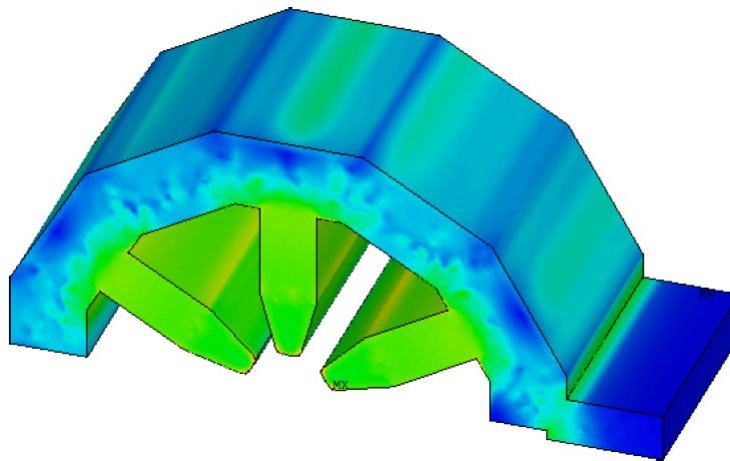
The total number of power supplies is estimated to be 168 main power supplies for the sextupoles and up to $3 \times 6 \times 28 = 504$ auxiliary power supplies. Since not all sextupoles may need SQs, the required number can be adjusted through precise simulation. Using individual power supplies for all sextupoles has the advantage of making it easier to control non-linearity. As a design to minimize long-term operational energy consumption, the current density was designed to be low at 3.70 A/mm², and the cooling water temperature rise was designed not to exceed a maximum of 3.0 K based on $\Delta p = 6.0$ bar. The 2D cross-sectional area of the sextupole was not based on an ideal profile but used a flat-pole face. As the vacuum chamber requires ± 6.5 mm pole-to-pole distance, tangential shimming should be done to an ideal profile with a very narrow pole tip, and the maximum shimming converges to a flat-pole surface. <Figure 2.1.6.38> shows the flux distribution based on the 2D FEM

(Finite Element Method) results for the sextupole cross-section.

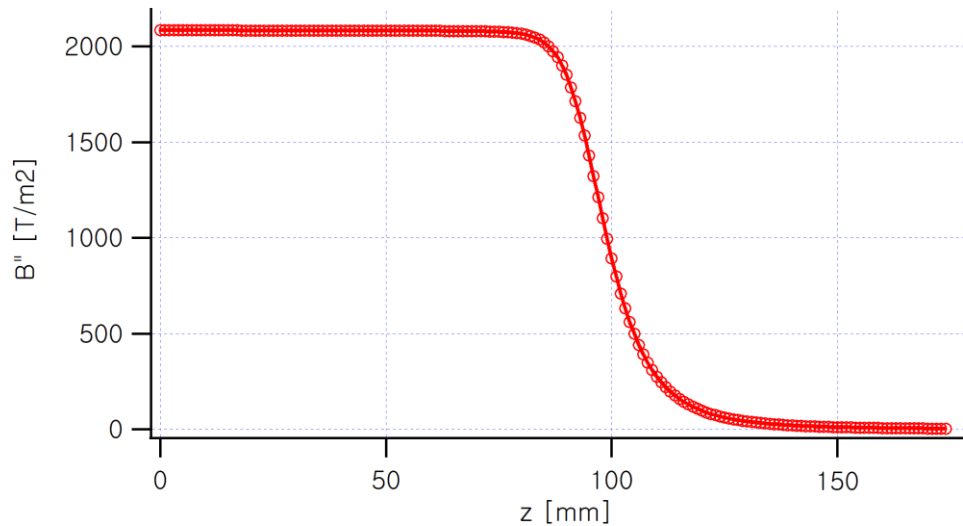


<Figure 2.1.6.38> Distribution of 2D flux in the S33 sextupole.

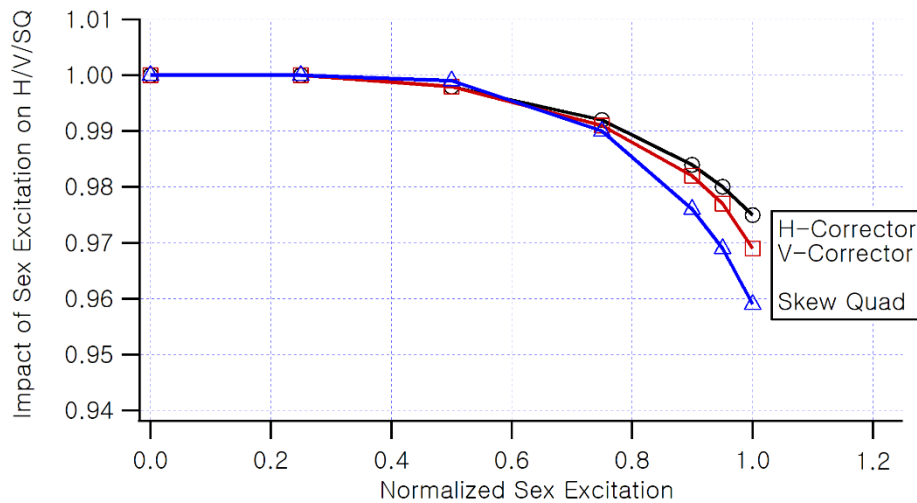
<Figure 2.1.6.39> and <Figure 2.1.6.40> show the three-dimensional analysis result of S33 and the calculated profile of B'' in the beam direction. As a result, the required core length was determined. Additionally, to understand how the effects of the H/V/SQ auxiliary magnets change as the excitation of the sextupole magnet changes, the variation in the trim magnet strengths (H/V/SQ) with changes in the sextupole excitation was calculated and presented in <Figure 2.1.6.41>.



<Figure 2.1.6.39> 3D analysis result of the S33 sextupole.



<Figure 2.1.6.40> Longitudinal B'' profile of the S33 Sextupole (3D calculation result).



<Figure 2.1.6.41> Reduction of auxiliary H/V/SQ depending on the sextupole excitation.

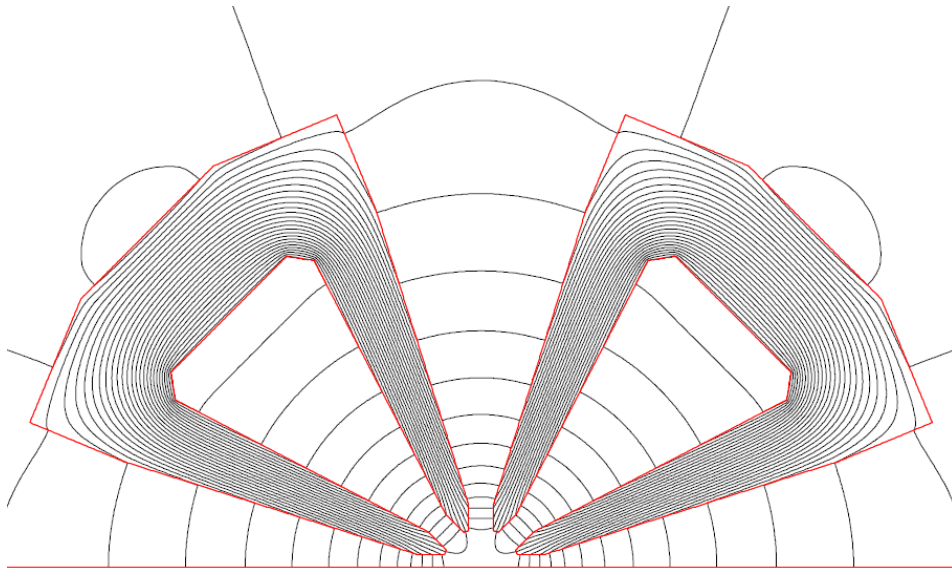
It is possible to know that even under the maximum sextupole excitation, more than 95% of the intensity is maintained compared to the zero excitation. Based on this data, a 3D mechanical design was performed, and the 3D drawings, along with other key 2D drawings, are shown in <Figure 2.1.6.42>. Finally, the final parameters of the S31/S33 and S32 magnets are summarized in <Table 2.1.6.12>.

Ampere-turns per pole [A]	2352.3	2352.3	-
Current [A]	117.6	117.6	-
Current density [A/mm ²]	3.70	3.70	-
Voltage per magnet [V]	3.89	4.22	Low voltage due to separate powering
Resistance [mΩ]	33.1	35.9	-
Power [kW]	0.46	0.50	-
Inductance [mH]	5.87	6.52	-
Cooling system	Water	Water	-
Cooling circuits per magnet	2	2	No overheating even with 1 cooling unit, but 2 unit is adopted because of production convenience
LCW pressure drop [kgf/cm ²]	6.0	6.0	-
Total water flow rate [liter/min]	2.31	2.37	
Temperature rise [K]	2.8	3.0	Very low level
Trim strength H/V/SQ [mrad, mrad, T/m]	0.6/0.6/1.0	0.6/0.6/1.0	0.6 mrad for H/V, 1.0 T/m for SQ
Trim coil cross-section [mm]	2.0×2.1	2.0×2.1	-
Trim coil turns per pole H/V/SQ	150/150/150	150/150/150	H: 50+100+50 turns V: 100+0+100 turns SQ: 0+50+0 turns
Trim B field H/V [T]	0.044	0.040	-
Trim current H/V/SQ	8.0/7.2/7.1	8.0/7.2/7.1	-
Trim voltage [V] H/V/SQ	6.7/5.9/1.5	7.2/6.4/1.6	-
Trim resistance [Ω] H/V/SQ	0.83/0.83/0.21	0.91/0.91/0.23	-
Trim inductance [mH] H/V/SQ	26/35/6.8	29/39/7.6	-
Trim power [W] H/V/SQ	53/41/10	58/45/11	-

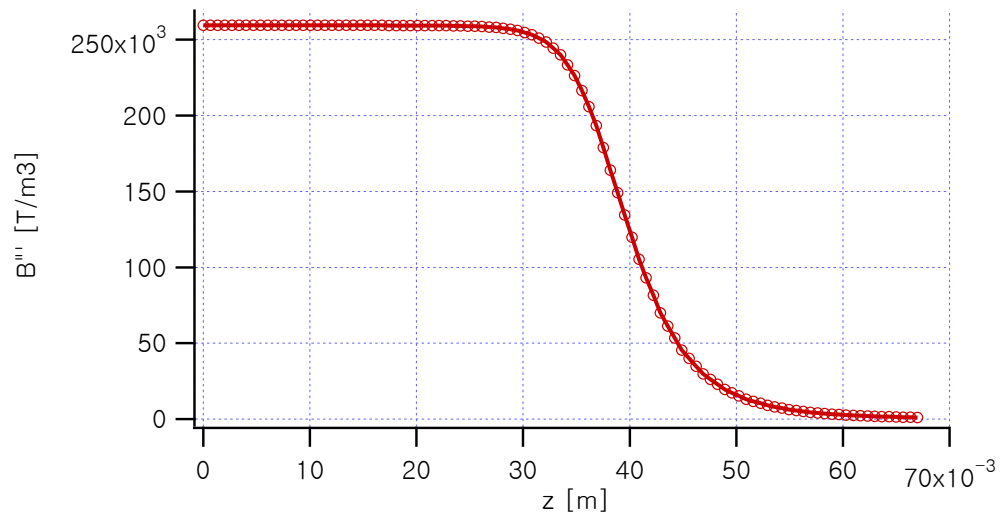
G. Octupole Magnet

As the 4GSR lattice was optimized, two additional octupole magnets were added per sector, and a total of 56 octupole magnets and the corresponding power supplies were additionally required. The requirements are an aperture radius of 15.0 mm, just like the

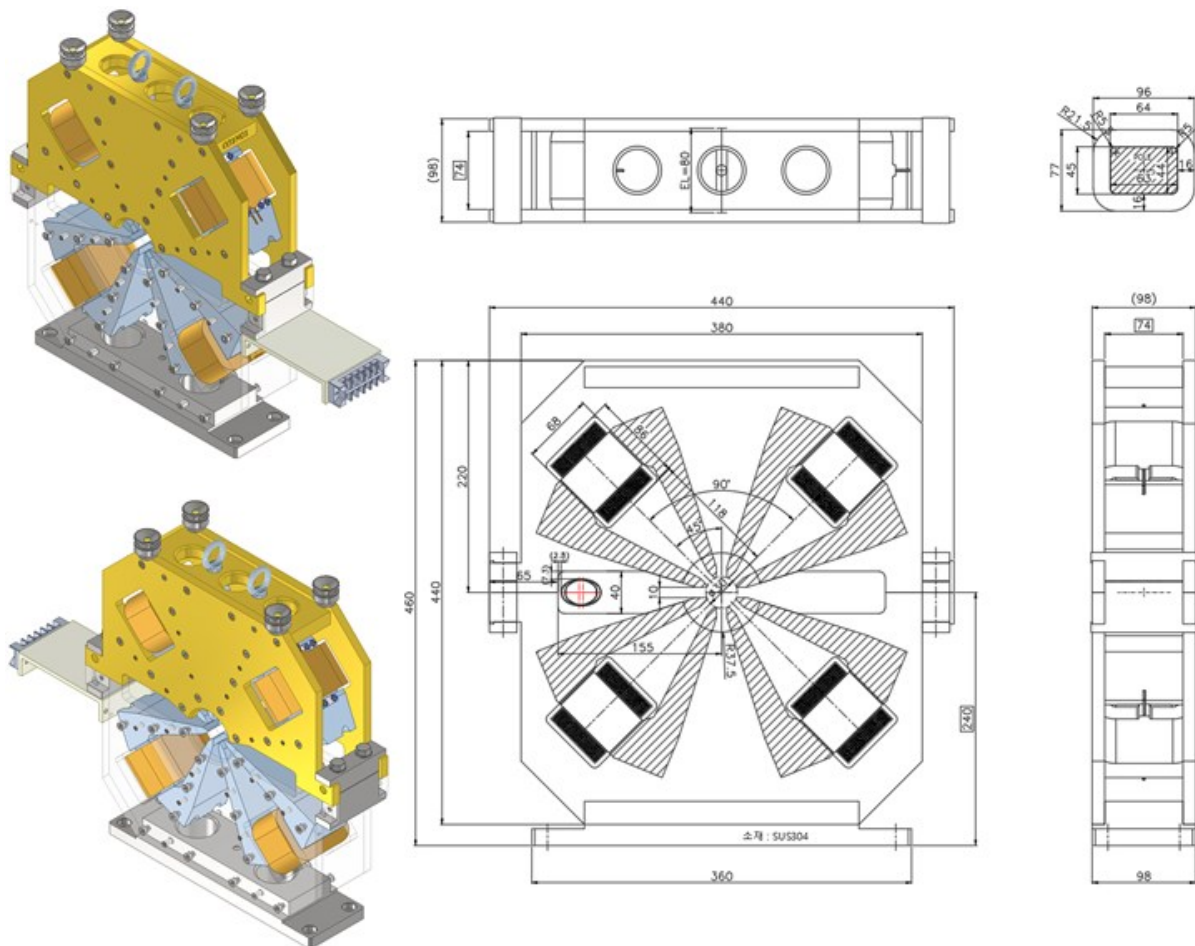
quadrupole, a magnetic length of 80 mm, and a maximum third derivative of 240,000 T/m³ or more. Based on the pole tip field, the magnetic field is not high as $B_{\text{tip}} = 1/6 B''' R_c^3 = 0.14$ T. However, the allowable pole tip field gets smaller with higher-order multipoles, so the magnetic saturation level should be judged by the quadrupole or sextupole components. Also, a pole-to-pole distance of ± 5.0 mm or more should be secured to accommodate the vacuum chamber. In this situation, winding coils on the poles are spatially impossible, so they are wound towards the return leg. Since the overall power was low, cooling with water appeared unnecessary, and the design used copper wires of 2.0 mm \times 1.0 mm for winding. It was decided to use four C-shaped steel cores for manufacturing and assemble the magnets with non-magnetic materials on both planes. The magnetic flux distribution from the two-dimensional analysis is shown in <Figure 2.1.6.43>. The distribution of B''' in the beam direction as calculated by 3D analysis is shown in <Figure 2.1.6.44>. The two-dimensional shape in <Figure 2.1.6.43> was extended to 3D to create 3D drawings and manufacturing drawings, with the 3D view and 2D central cross-section shown in <Figure 2.1.6.45>. The final parameters of the octupole magnets are summarized in <Table 2.1.6.13>.



<Figure 2.1.6.43> Two-dimensional magnetic flux distribution of an octupole magnet.
Coils are wound on the return yoke due to spatial limitation.



<Figure 2.1.6.44> Longitudinal B''' profile of an octupole magnet. Maximum strength is above 24×10^4 and the effective length is 80 mm.



<Figure 2.1.6.45> 3D drawings and 2D cross-section of an octupole magnet.

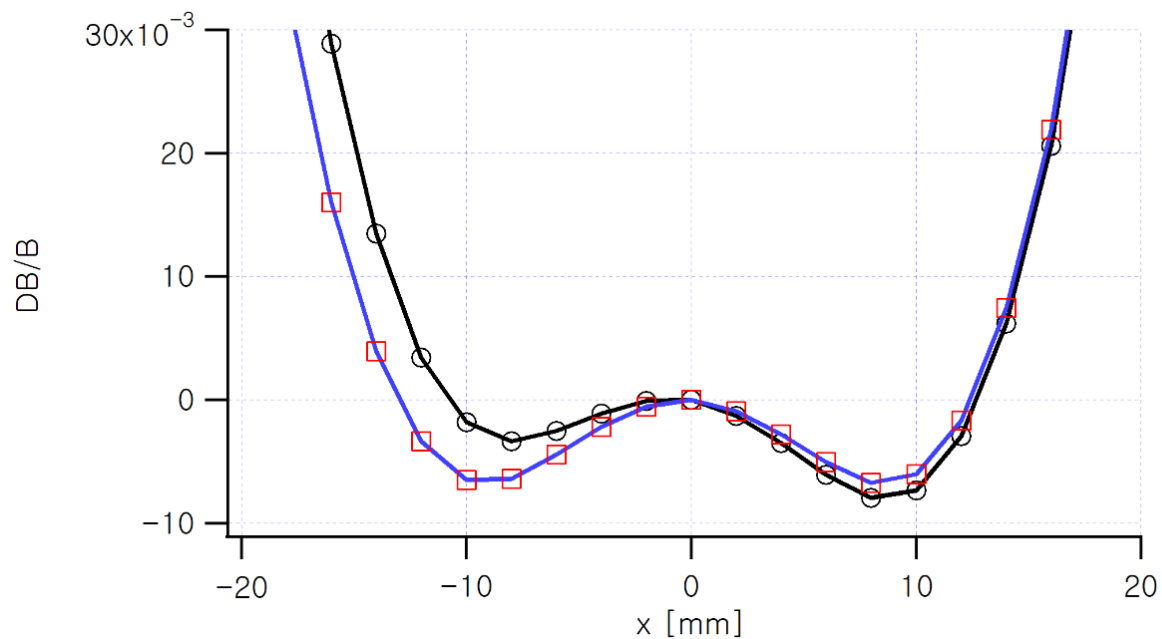
<Table 2.1.6.13> Main parameters of octopole magnet

Magnet Type	O31	Remark
Required number	56	2*28 (cell)
Aperture radius [mm]	15.0	-
Min. pole to pole distance [mm]	5.0	Pole to pole neck distance for Vacuum chamber
Good field radius [mm]	10.0	-
Max B''' [T/m ³]	240,000	About 2 times of the nominal value
Effective magnetic length [mm]	80.0	-
Core length [mm]	74.0	-
Coil turns per 2 poles	324	Back leg winding for 2 poles
Coil cross-section [mm]	2.0×1.0	-
Ampere-turns per 2 poles [A]	1,086	Ampere Turns in the back leg
Current [A]	3.35	-
Current density [A/mm ²]	1.68	-
Voltage per magnet [V]	12.1	-
Resistance [mΩ]	3.60	-
Power [W]	40.5	10 W per coil good for air cooling
Inductance [H]	0.58	-
Cooling system	Air cooling	-

H. Corrector Magnets

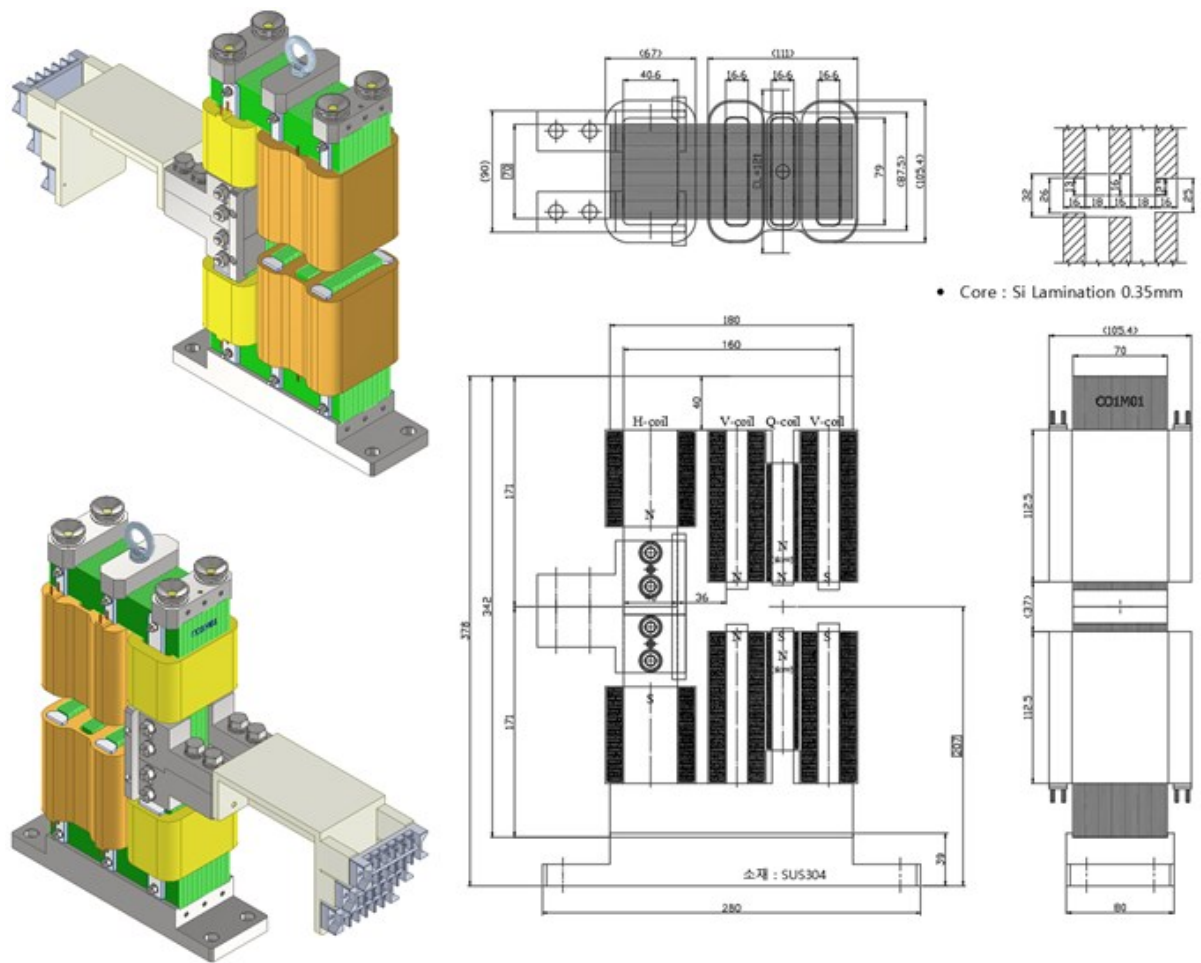
In the 4GSR, various magnets, including dipole, quadrupole, and sextupole magnets, are used. Each sector will be equipped with four corrector magnets (a total of 112, with 224 power supplies), and an additional four corrector magnets are planned for the high beta section. The required kick strength is based on error simulation, assuming a maximum kick of 0.6 mrad. The H and V correctors are installed in one magnet to minimize lattice space. The corrector shape benchmarked that of ESRF-EBS, with the H-corrector coils wound on the core's back leg and the V-corrector coils wound on the pole. Also skew quad (SQ) coil with ~1 T/m strength is also included in the corrector magnet reflecting MAC recommendation. Only a few SQ coils are expected to be used in the storage ring. They will

be used as fast correctors operating at high speed, so they are made with 0.35 mm lamination. To minimize the uniformity of the H-Field and V-Field, the pole was divided into three parts with different pole gaps. The center half-gap was set to 16 mm, the right half-gap to 12.5 mm, and the left half-gap to 13.0 mm. The uniformity of the field integral under these conditions is shown in <Figure 2.1.6.46>. It can be seen that the requirement of $|\Delta B/B| < 10^{-2}$ at $|x| < 10.0$ mm is satisfied. The two curves in the figure represent the conditions when the left and right half-gaps are the same and when there is a 0.5 mm difference. It is possible to see that the uniformity of the field integral improves and approaches symmetry when there is a 0.5 mm difference. For reference, the upper and lower parts are independently manufactured and assembled later after the vacuum chamber assembly.



<Figure 2.1.6.46> Uniformity of H-Corrector field integral (Data with a 0.5 mm difference in left and right half gaps to correct left and right asymmetry).

Based on these considerations, 3D drawings and manufacturing drawings were created, and the 3D view and 2D central cross-section are shown in <Figure 2.1.6.47>. As of August 2023, the prototype is being manufactured, and design values will be compared with future magnetic field measurements. The final parameters of the H/C corrector are summarized in <Table 2.1.6.14>.



<Figure 2.1.6.47> 3D CAD drawings and key 2D drawings of H/V corrector magnets.

<Table 2.1.6.14> Main parameters of H/V corrector magnets

Magnet Type	H-Corrector	V-Corrector	Remark
Magnet shape	Lamination H/V combined	Lamination H/V combined	Lamination thickness 0.35 mm
Required number	112 + 4	112 + 4	4*28 (cell) + 4 (high beta)
Half gap [mm]	13.0/16.0/12.5	13.0/16.0/12.5	left/center/right Optimized for uniformity
Good field region [mm]	$<\pm 10.0$	$<\pm 10.0$	-
Max. kick at 4 GeV [mrad]	0.600	0.600	-
Required BL [Tm]	8.0E-3	8.0E-3	for 0.6 mrad kick
Effective magnetic length [mm]	122.0	121.0	-
Core length [mm]	70.0	70.0	-
Coil area [mm ²]	8.55	8.55	Thick conductor to reduce
Coil turns per pole	65	105	H-corrector: Back-leg winding
Ampere-turns per pole [A]	931.3	1862.6	-
Current [A]	14.33	17.74	-
Current density [A/mm ²]	1.68	2.07	-
Voltage per magnet [V]	1.14	3.90	Low V because of using Thick conductor
Resistance [m Ω]	79.0	220	-
Power [W]	16.3	69.2	-
Inductance [mH]	16.0	23.0	Design Inductance is low to reduce time constant $\tau=L/R$
Cooling system	Air Cooling	Air Cooling	Being $j < 2.0$ A/mm ² level, air cooling is possible. After the prototype's production, the heat sink application will be reviewed.

I. Booster Magnets

(1) Dipole Magnets

For the finalized layout of the booster ring, the ramping/injection repetition will be 2 Hz, and the following magnets will be employed: 60 combined function dipole magnets (transverse gradient dipoles), 66 quadrupole magnets, 60 sextupole magnets, 10 skew quadrupole magnets, and 120 H and V corrector magnets each. Aside from the transverse gradient dipoles, most magnets are of lower strength, shorter length, and simpler structure, thus presenting no significant technical challenges compared to the storage ring magnets. This report will focus on the transverse gradient dipoles, which constitute the majority of the booster magnets and are more technically demanding.

Due to the 2 Hz operation, the booster magnets have two notable points: they should be made of low-carbon steel laminations of 0.5 mm thick or less, and many connections between magnets will be in series to minimize the excitation timing issues. The transverse gradient dipoles include four weak dipoles bending 5.02° and 56 strong dipoles bending 6.07° . For ease of manufacture and maintenance, the same magnets will be used for both weak and strong dipoles, with a lower current applied to the weak dipoles. The strong dipole's specifications are $B_0 = 0.9944$ T, $B' = 2.087$ T/m, $L_{\text{eff}} = 1.4215$ m, and $h_{\text{gap}} = 13.7$ mm. The four weak dipoles will be connected in two series pairs, while the 56 strong dipoles will be connected in series to four parallel power supplies. The reason for this connection scheme is to reduce the load on an MPS while minimizing the number of required individual power supplies to make commissioning easy. Consequently, six MPS units are needed, two for the weak dipoles and four for the parallel connections.

For the connection, each magnet needs to have four input and four output terminals, totaling four. Therefore, each coil on the up and down of the pole should have two pancake windings with their own input and output terminals. The number of coil turns was adjusted to 24 in the 4 parallel connections to reduce the overall MPS voltage. Simple resistive voltage drop and inductive voltage are estimated to be around 149 V and 458 V, respectively, in the case of linear ramping from 10% to 90% current over 0.25 seconds. For reference, the peak power of a strong dipole magnet is 4.95 kW. However, due to the ramping cycle operation, the duty cycle is approximately 0.32, and the effective power is about 1.59 kW.

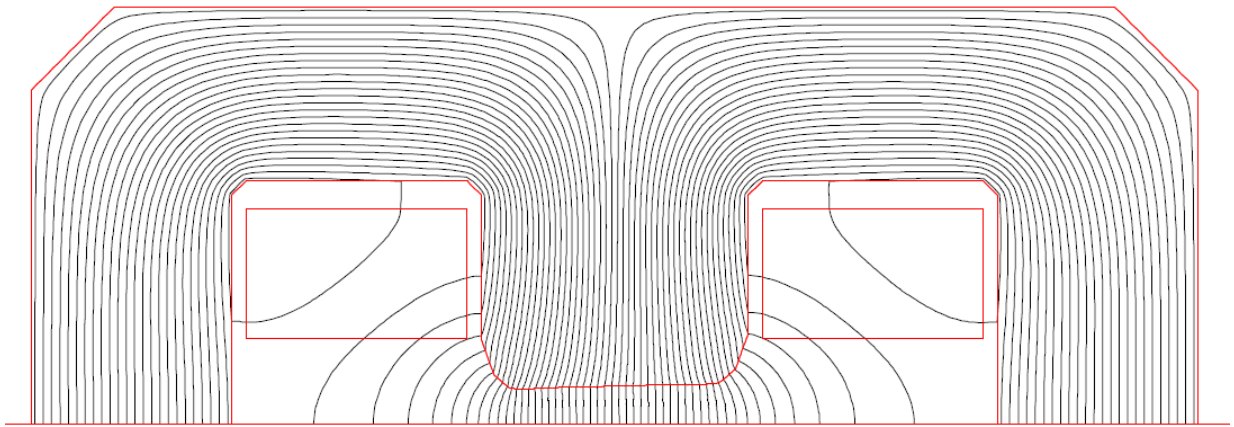
Optimizing a combined function dipole magnet, which uses both dipole and quadrupole components, is not easy. As a method to optimize the shape of a combined function dipole

magnet, the following conformal mapping was used to transform the combined dipole to the pure dipole shape from (x, y) to (u, v) . Here, (x, y) is the real coordinate system, while (u, v) is the conformal mapped geometry. The transformation is given by the following equation.

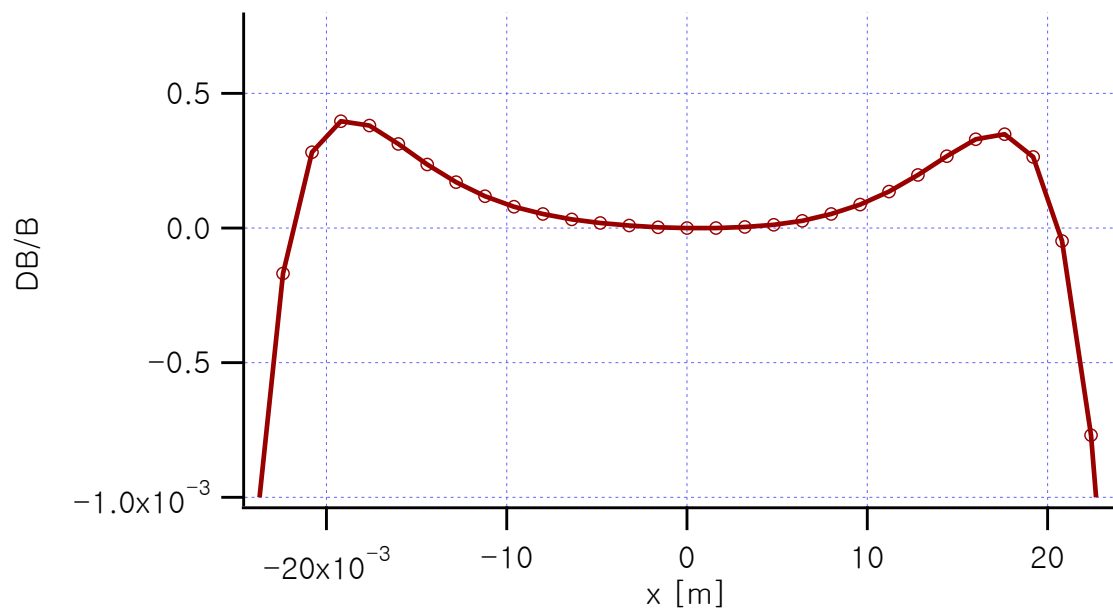
$$\omega = u + iv = \frac{Z^2}{H} = \frac{(X^2 - Y^2)}{H} + i \frac{2XY}{H},$$

$$\text{where } H = \sqrt{\frac{2B_0 h}{B'}}, Y = y, X = x + \frac{B_0}{B'} \quad (\text{Eq. 2.1.6.2})$$

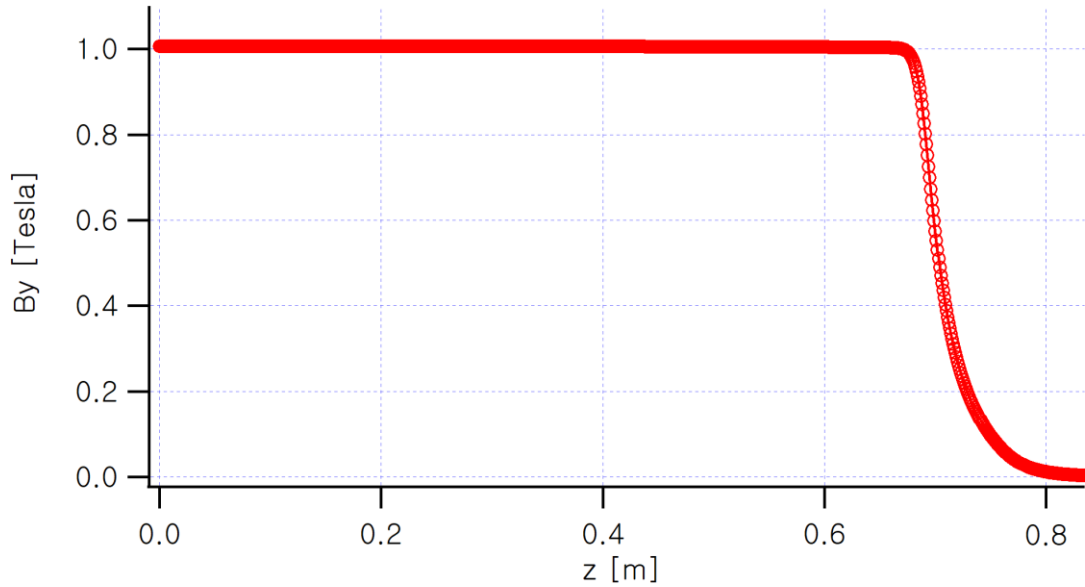
The u and v coordinates represent the pure dipole shape. In this plane, a trapezoid shim was installed on the pole surface. Then the coordinates were inversely transformed back to the original coordinates X, Y , after which a 2D FEM analysis was performed. After analyzing the calculation results to check the requirements for B, B' , and uniformity, the calculations were repeated using a new shim on the (u, v) plane again until the requirements were satisfied. For a strong combined function dipole, the sagitta is 18.8 mm, and for a weak combined function dipole, it is 15.6 mm. The good field region requirement here is $\Delta B/B < 4.0 \times 10^{-4}$ within ± 6.0 mm. When the sagitta spans both ends of $x = 0$, the good field region requirement is $\Delta B/B < 5.0 \times 10^{-4}$ at $|x| < 15.4$ mm. The magnetic flux distribution of the optimized 2D core shape is shown in <Figure 2.1.6.48>, and the uniformity after removing the gradient part from the combined magnetic field is shown in <Figure 2.1.6.49>. The result satisfies $\Delta B/B < 5.0 \times 10^{-4}$ at $|x| < 15.4$ mm. The 3D calculation results, including end chamfering, are shown in <Figure 2.1.6.50> for the longitudinal profile along the magnet axis, and in <Figure 2.1.6.51> for the distribution of $|B|$.



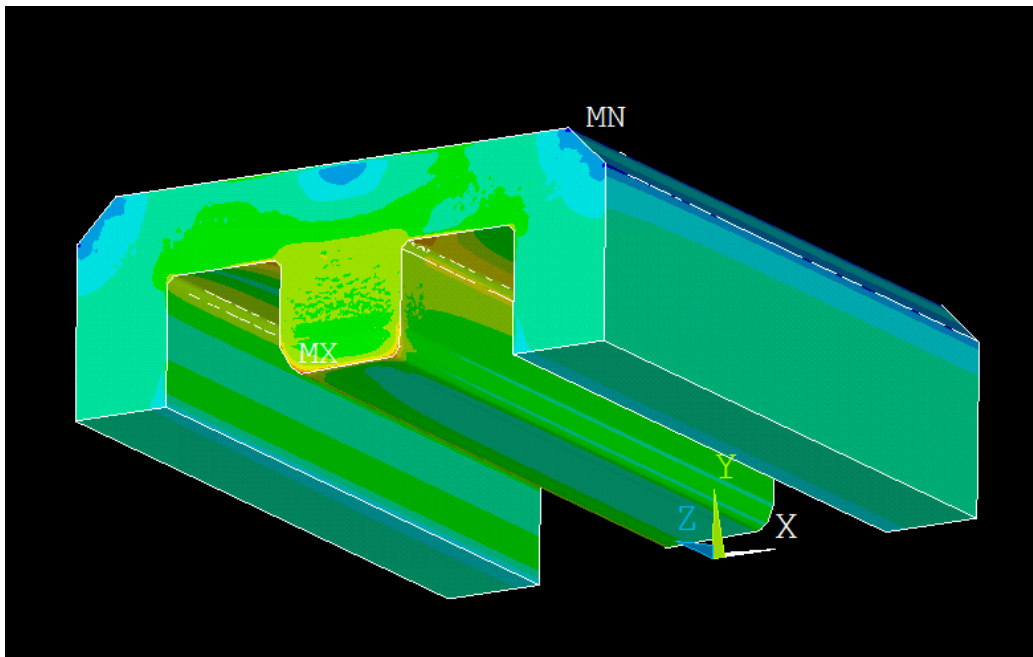
<Figure 2.1.6.48> Optimized 2D pole and yoke shape and the magnetic flux distribution.



<Figure 2.1.6.49> Uniformity of the booster dipole magnet.

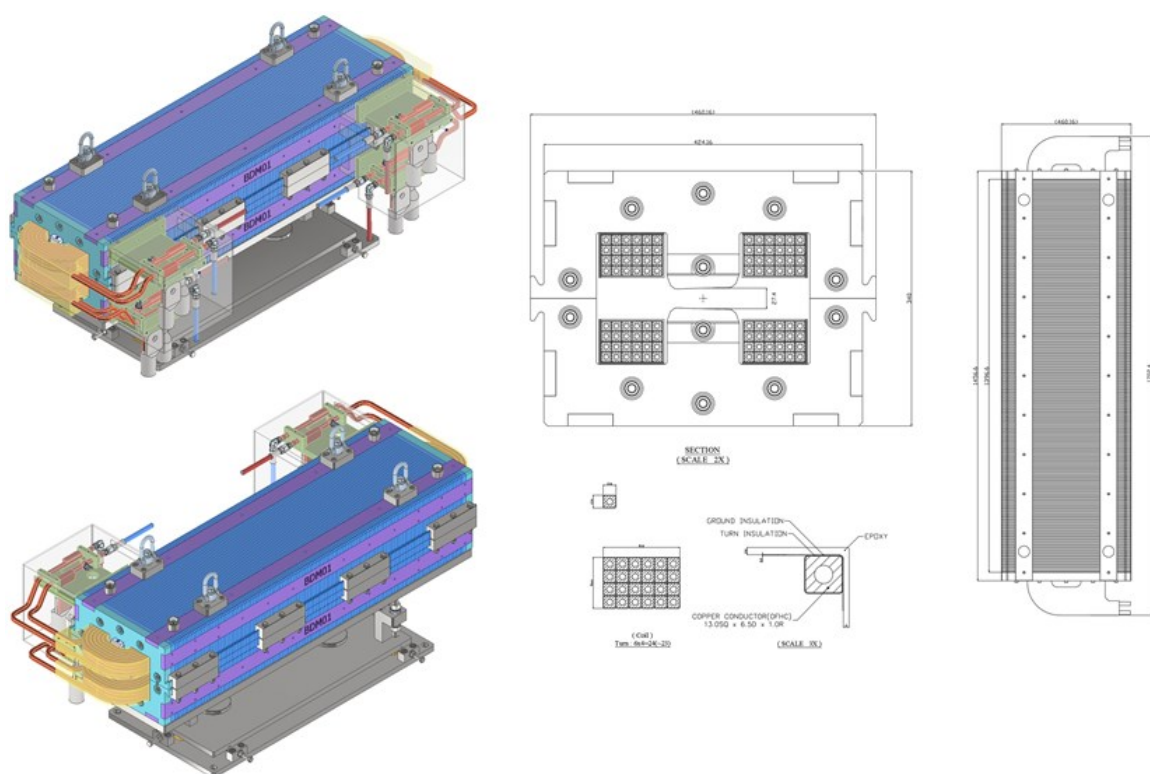


<Figure 2.1.6.50> Longitudinal field profile of the strong dipole magnet.



<Figure 2.1.6.51> 3D analysis example for the strong dipole. $|B|$ distribution.

Based on the optimization data so far, 3D mechanical design has been carried out. The 3D drawings and other key 2D cross-sectional drawings are shown in <Figure 2.1.6.52>. Finally, the ultimate parameters of the booster ring's strong and weak combined dipole magnets are summarized in <Table 2.1.6.15>.



<Figure 2.1.6.52> 3D drawings and 2D cross-section drawing of a booster dipole.

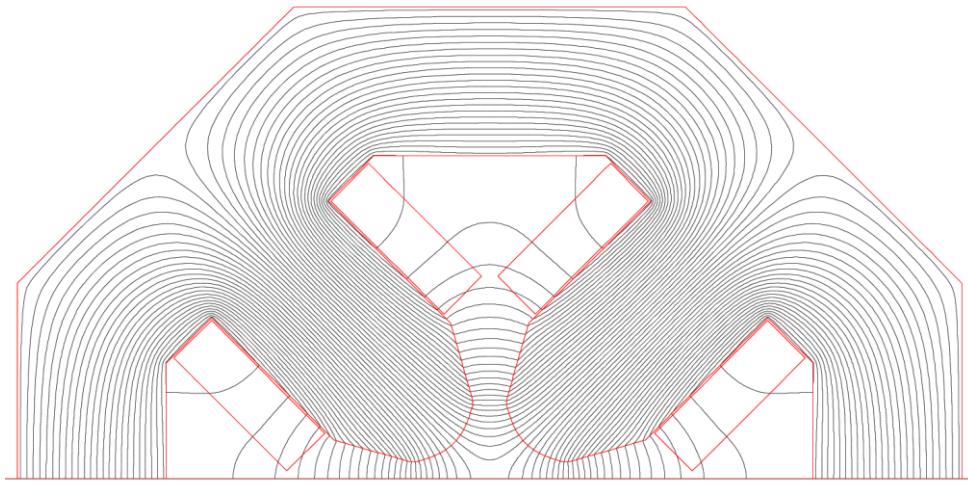
<Table 2.1.6.15> Main parameters of booster dipole magnets

Magnet Type	BD weak	BD strong	Remark
Magnet shape	H-type, Laminate	H-type, Laminate	-
Shape along the beam	straight	straight	-
Number of Magnets	4	56	4 weak magnets in the high beta section
Lamination thickness [mm]	0.5	0.5	Ramping cycle 2 Hz
Pole gap [mm]	27.40	27.40	at the gap center
Magnetic field [T]	0.8224	0.9944	Combined function dipole magnets
Max. field gradient [T/m]	1.456	1.760	-
bending angle [°]	5.02	6.07	-
Effective magnetic length [mm]	1,421.55	1,421.55	-
BL [Tm]	1.1690	1.4135	-
Sagitta [mm]	15.566	18.821	-
Uniformity	5.0×10^{-4}	5.0×10^{-4}	for $ x < 15.4$ mm

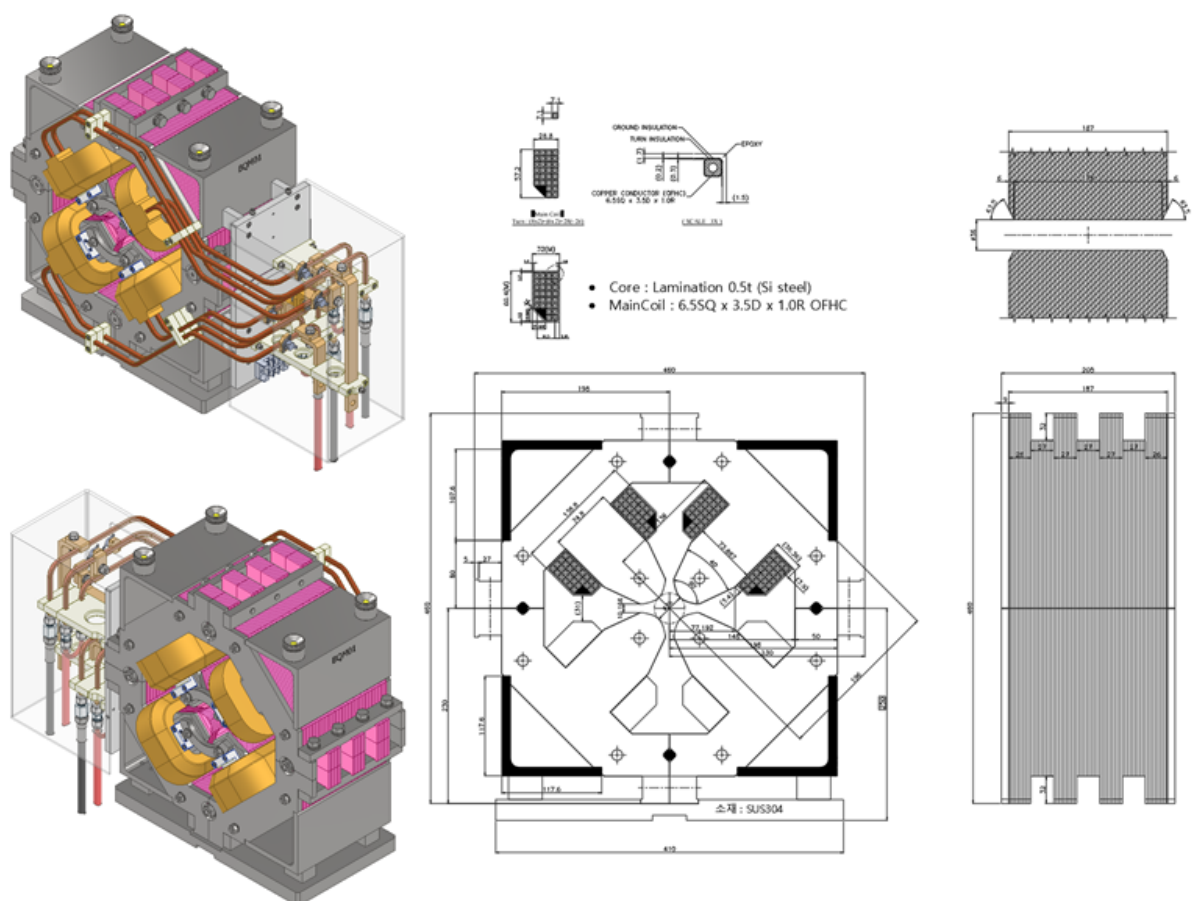
Core length [mm]	1396.6	1396.6	-
Number of turns per pole	6 (H)×4 (V)	6 (H)×4 (V)	Turns adjusted to limit the MPS voltage
Main Coil size [mm]	SQ13.0×Φ6.5	SQ13.0×Φ6.5	-
Ampere-turn [kA]	9.243	11.176	per pole
Efficiency	0.97	0.97	-
Current [A]	385.1	465.7	-
Current density [A/mm ²]	2.85	3.45	-
Voltage [V]	8.79	10.63	-
Resistance [mΩ]	22.8	22.8	-
Power [kW]/magnet	3.39	4.85	-
Inductance [H]	0.0185	0.0185	-
Cooling system	Water	Water	-
Cooling circuit number	2	2	-
LCW pressure drop [kgf/cm ²]	6	6	-
Total water flow rate [liter/min]	6.77	6.77	-
Duty	0.32	0.32	Ratio of effective power over full power due to cyclic excitation
Temperature rise [K]	2.3	3.4	As the effective power is lower compared to the maximum power, temperature rise is low.
Total Resistive Voltage Drop [V]	17.6	148.9	-
Inductive Voltage	54.0	457.4	Assuming 10% to 100% in 250 msec
Mass (core+coil) [kg]	≤1,344.46	≤1,344.46	-

(2) Quadrupole Magnet

The quadrupole magnets used in the booster were designed based on a bore radius of 17.7 mm to accommodate the elliptical vacuum chamber with a minor axis of 12.5 mm and a major axis of 24.0 mm. A total of 66 quadrupole magnets are required. As they need to operate at 2 Hz, like the combined-function dipole magnets, they should be fabricated by stacking 0.5 mm laminations. The maximum given magnetic field gradient is 29.0 T/m, and the effective magnet length must be 0.200 m. A total of 66 magnets are required. Due to the low magnetic flux density, the poles were designed without tapering for manufacturing convenience. The final 2D flux and core shape are shown in <Figure 2.1.6.53>, and a schematic 3D drawing illustrating only the electromagnet core and coil parts is presented in <Figure 2.1.6.54>. <Table 2.1.6.16> summarizes the main parameters of the booster quadrupole magnets. All magnets will be connected in series to reduce power supply costs and facilitate synchronization between magnets. When operated in series, the resistance, excluding the connecting conductors and lead parts, is approximately 2.22 Ω . Other magnets used in the booster, including the sextupoles, do not have fixed specifications or special requirements, so there are no difficulties in design and fabrication.



<Figure 2.1.6.53> 2D magnetic flux distribution of the booster quadrupole magnet.



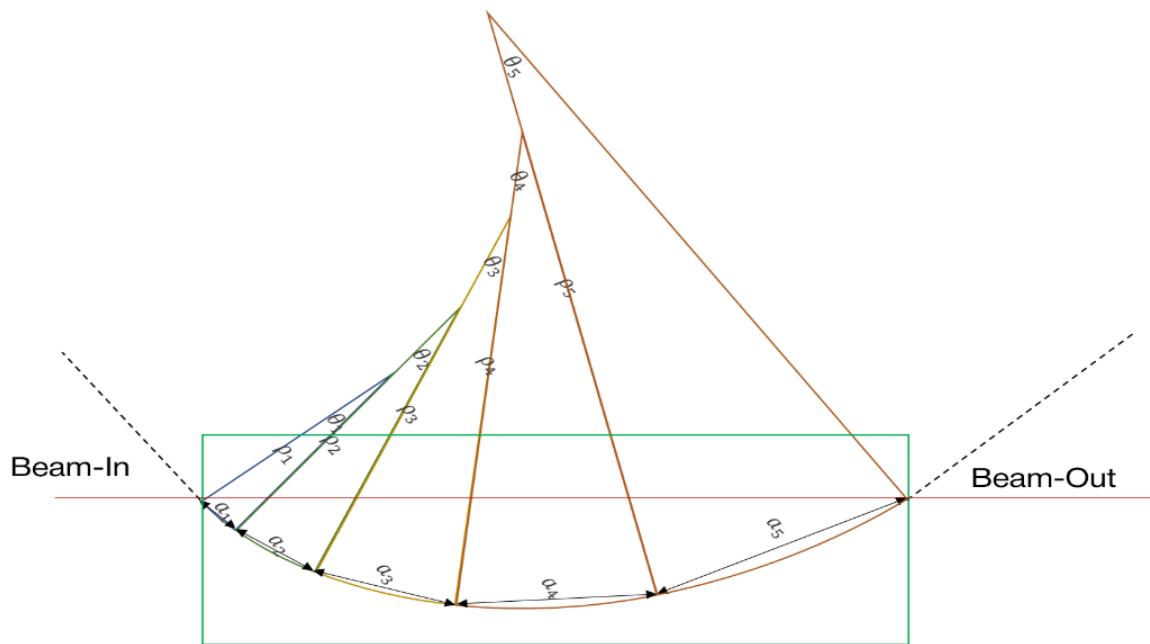
<Table 2.1.6.16> Main parameters of booster quadrupole magnets

Parameters	Value	Remark
Magnet Type	Booster Quadrupole	-
Required Number	66	-
Lamination [mm]	0.5	Ramping @2 Hz
B'max [T/m]	29.0	-
Bore Radius [mm]	17.7	-
Magnetic Length [m]	0.200	-
Magnetic Efficiency	0.98	-
Ampere Turns [kA]	3.68	per pole
Conductor	7×7×4φ	Unit: mm
Num. Turns	26	2*8
I _{max} [A]	141.5	-
J _s [A/mm ²]	3.98	-
V [V]	5/24	per magnet
Power [kW]	0.742	per magnet
Resistance [mΩ]	37.1	per magnet
Total Resistive Voltage Drop [V]	314	total 66 magnets
Number of cooling circuits	1	per magnet
ΔT [K]	3.5	duty 0.321 is considered
Coolant Velocity [m/sec]	1.30	-
Flow Rate [liter/min]	0.98	per magnet
Pressure Drop [kg/cm ²]	6.0	-
Inductance [mH]	11.2	per magnet

J. Magnetic Field Analysis of Dipole Magnets

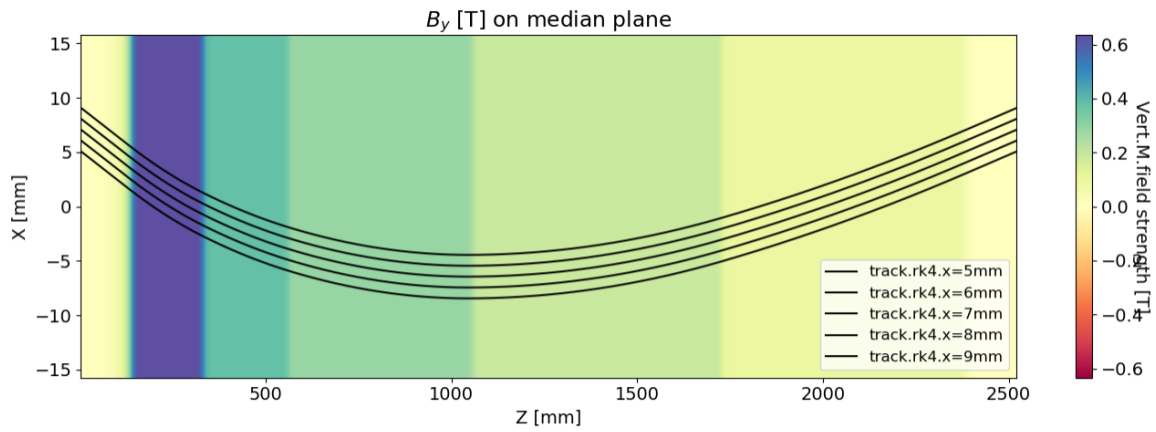
An evaluation was conducted for the 3D magnetic field distribution of the designed LGBM1. The optical design in beam physics calculates effects such as fringe field effect, edge angle effect, and multipole effect using a hard edge model based on thin lens approximation. While this model provides sufficiently accurate results for well-made magnets, differences, if any, between the actual magnetic field and the beam optics model can result in the storage ring beam being different from the design. LGBM is a special bending magnet that is made of several segments. Each segment has a different magnetic field, which is chosen carefully in combination with the dispersion D of the segment to minimize $\int DB'$ over the whole LGBM. Due to its complex structure, discrepancies with calculated values are likely, and it is important to verify it.

LGBM has stepwise bending angles, as shown in <Figure 2.1.6.55>, which are determined by magnetic rigidity (pB). Since the magnetic rigidity of a 4 GeV electron is approximately 13.34 Tm, knowing the B of the segment allows the determination of the corresponding radius of curvature, making it possible to create a diagram.



<Figure 2.1.6.55> Schematic figure of the stepwise bending angles and Beam-In and Beam-Out in an LGBM.

Using an explicit 4th order Runge-Kutta algorithm, we tracked the 4 GeV electrons to ensure that the beam always enters and exits at the same position, even if the incident and exit angles differ. The constant Δt used was 100 fs. The 3D B-field calculated from the FEM code was exported at intervals of 1 mm \times 1 mm \times 1 mm and used after 3D linear interpolation. <Figure 2.1.6.56> shows the tracking results. Tracking was performed at five locations at 1 mm intervals, all showing that the beam is extracted at the same x position. In this case, the incident angle of all five tracks was -1.53° , and the exit angle was 0.84° , consistently.



<Figure 2.1.6.56> Tracks with the same incident and exit locations.

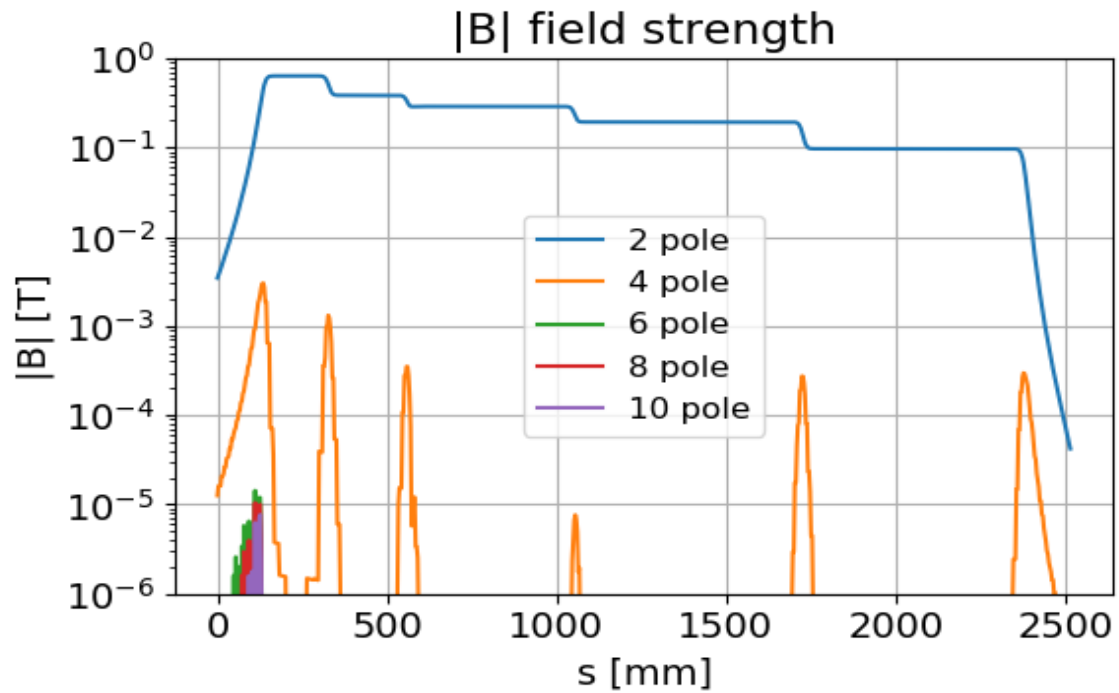
During the tracking process, at a specific stage, we called the magnetic field and extracted the multipole components while drawing a circle in the transverse plane of the momentum direction. For convenience (since the skew components are not required), the sine terms were removed, and only the cosine terms were used to calculate, as shown in (Eq. 2.1.6.3).

$$B_n = \frac{1}{\pi} \sum_{i=1}^M B_y(r_0 \theta) \cos(n\theta) \frac{2\pi}{M} \quad (\text{Eq. 2.1.6.3})$$

where n denotes the multipole order ($n = 1$: dipole, $n = 2$: quadrupole, \dots), M is the total number of sampling points ($M=100$), and r and θ are defined in the transverse plane with respect to the electron's momentum direction.

<Figure 2.1.6.57> shows the tracking result in terms of multipole field strength along the beam trajectory. It is possible to confirm that the quadrupole focusing and defocusing terms remain active through the edge effect for each longitudinal step. The high-order multipole terms, such as sextupole and octupole, and decapole, are identified as numerical noise

generated during the field interpolation process. Since their magnitude is at the level of 10^{-6} of B_0 , they can be regarded as negligible even if they exist.

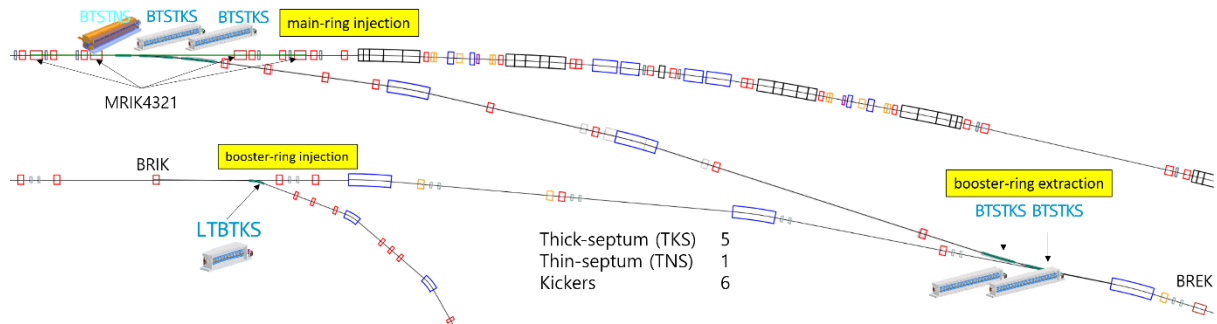


<Figure 2.1.6.57> Absolute value of multipole field strength along the beam trajectory.

K. Magnets for Beam Injection & Extraction

(1) Overview

Korea-4GSR consists of three injection and extraction sections: booster ring beam injection, booster ring beam extraction, and main ring beam injection (see <Figure 2.1.6.58>). To inject a 4 GeV electron beam into the main ring, four kicker magnets (main ring injection kicker, MRIK; two MRIK23 and two MRIK14) and three septum magnets (two booster to storage ring thick septa, BTSTKS, and one thin septum, BTSTNS) are utilized. For extracting a 4 GeV electron beam from the booster ring, one kicker magnet (booster ring extraction kicker, BREK) and two BTSTKS magnets are used. Lastly, to inject a 0.2 GeV electron beam into the booster ring, one septum magnet (linac thick septum, LITKS) and one kicker magnet (booster ring injection kicker, BRIK) are employed. In total, seven types and twelve specially structured pulsed magnets are required for the injection and extraction system (see <Table 2.1.6.17>).



<Figure 2.1.6.58> Layout of Korea-4GSR injection and extraction beamlines.

<Table 2.1.6.17> Key specifications of pulsed magnets for injection/extraction

4GSR Septums & Kickers	v20250215						
	LITKS	BTSTK S	BTSTN S	BRIK	BREK	MRIK2 3	MRIK1 4
Type	Thick-septum		Thin-septum	Ferrite Core Kicker			
Quantity	1	4	1	1	1	2	2
Bending angle [mrad]	349.1	56.7	25.0	10.0	3.0	2.6	3.1
Magnetic length [mm]	500	1100	500	200	400	347	400
Vertical gap [mm]	15	15	13	30	30	30	30
Width [mm]	30	26	16	50	50	50	50
Bending radius [m]	1.4	19.4	20.0	20.0	133.3	133.3	129.0
Peak field [T]	0.467	0.688	0.667	0.033	0.100	0.100	0.103
Peak current [kA]	5.6	8.3	7.0	0.81	2.41	2.41	2.49

Inductance [μ H]	1.23	2.35	0.76	0.41	0.82	0.71	0.82
Half-sine pulse width [μ s]	100.00	100.00	16.70	5.00	5.00	5.00	5.00
Hor. displacement [mm]	90.1	31.2	6.3	1.0	0.6	0.5	0.6
Yoke stacking shape	Curved	Curved	Straight	Straight	Straight	Straight	Straight

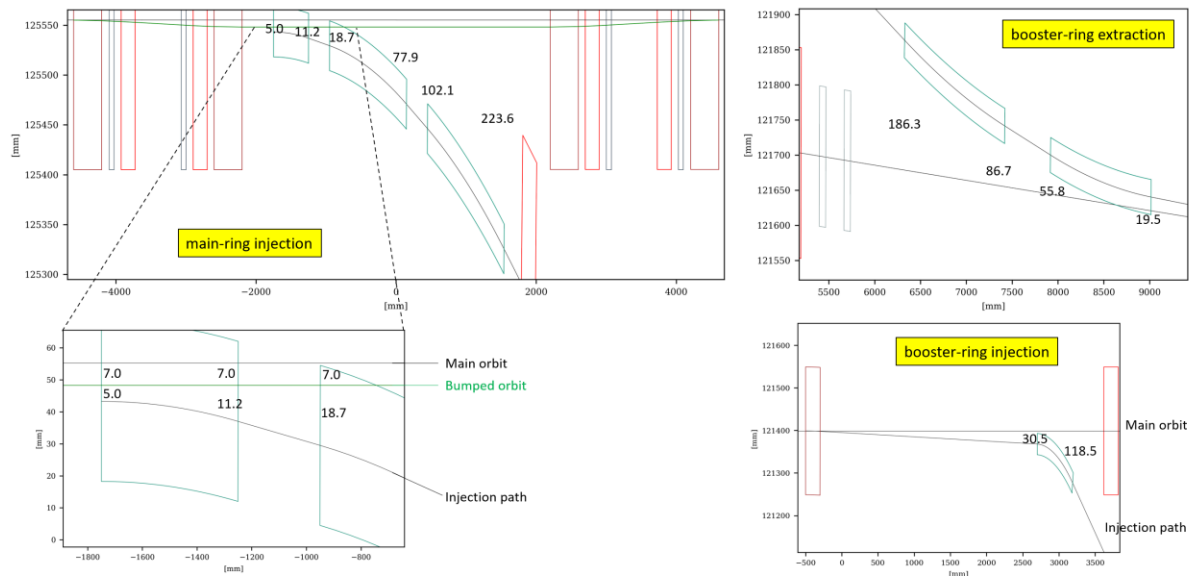
The four types of kicker magnets (BRIK, BREK, MRIK23, MRIK14) function to induce mrad-level orbit changes. The yoke material is ferrite, which has a low saturation field but excellent frequency response characteristics. The conductor is a single-turn winding, and a thin metal vacuum chamber (or titanium-coated ceramic chamber) is used.

Septum magnets are used to separate or combine different beam orbits within a confined space. One side of the septum blade generates a magnetic field to bend the trajectory, while the other side maintains a field-free region. If the minimum orbit distance is greater than 1 cm, an out-vacuum thick septum (-TKS) is used, while an in-vacuum thin septum (-TNS) is used for distances below 1 cm. The TNS utilizes eddy currents to shield the magnetic field, minimizing the septum blade thickness. The TKS employs a direct drive coil arrangement, which is more straightforward to manufacture due to fewer constraints on blade thickness (see <Table 2.1.6.18> and <Figure 2.1.6.59>).

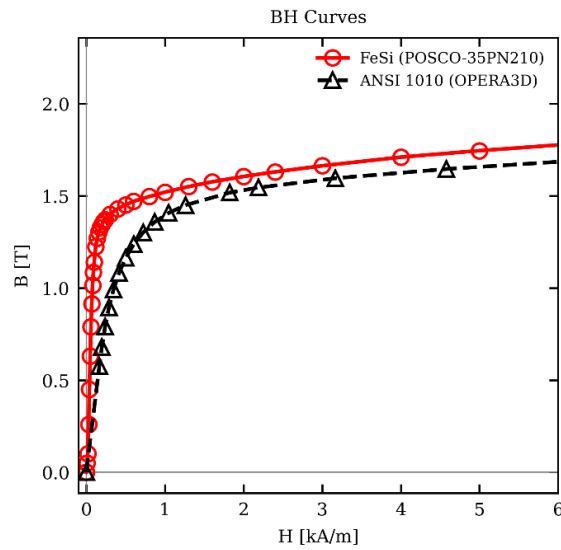
<Table 2.1.6.18> Orbit distance for each septum magnets

Septa (Location)	Orbit distance [mm]		Type
	Upstream	Downstream	
LITKS-1 (BR Injection)	123.9	30.2	Out-vacuum, direct drive
BTSTKS-1 (BR Extraction)	19.5	55.8	
BTSTKS-2 (BR Extraction)	86.7	186.3	
BTSTKS-3 (MR Injection)	223.6	102.1	
BTSTKS-4 (MR Injection)	77.9	18.7	
BTSTNS (MR Injection)	11.2	5.0	In-vacuum, indirect

The yoke for both types of septum magnets is made of laminated silicon steel sheets (0.35 mm thick). Compared to ferrite, this material has a lower broadband high-frequency response but a higher saturation capacity than low-carbon steel, making it suitable for septum magnet specifications (0.7 T maximum magnetic field, 100 μ s pulse width). All septum magnets were designed and simulated based on the BH curve data of POSCO-35PN210 non-oriented electrical steel (See <Figure 2.1.6.60>).



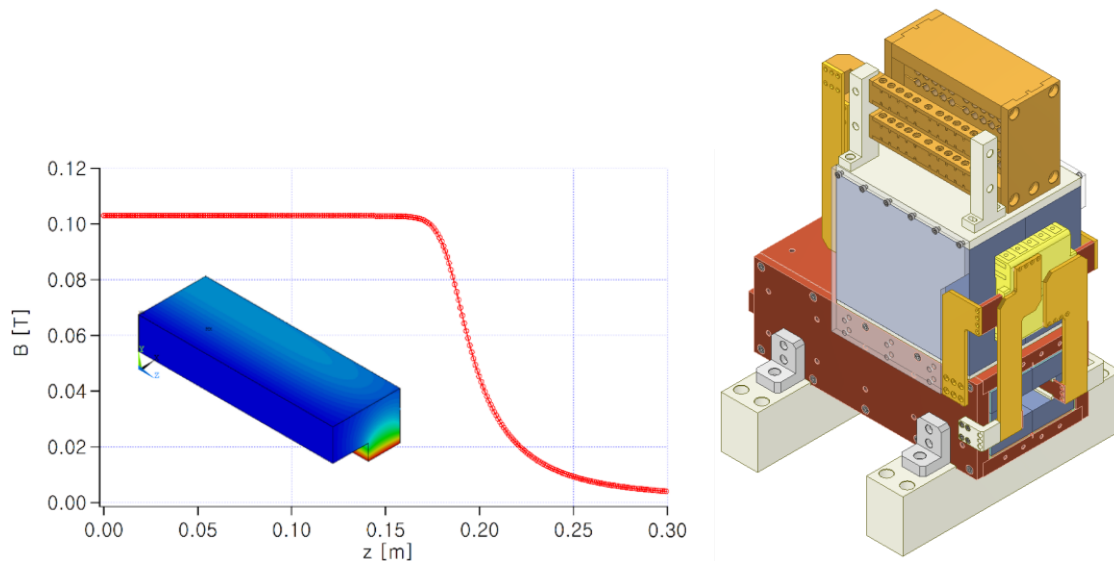
<Figure 2.1.6.59> Orbit distances of injected and extracted beams.



<Figure 2.1.6.60> BH Curve of the silicon steel used for calculation.

(2) Kicker (BRIK, BREK, MRIK23, MRIK14)

The designed kicker field profile and external drawings are shown in <Figure 2.1.6.61>. The conductor is single-turn wound on both sides of a window-type core and directly connected to a transformer at the top. The transformer is considered to minimize joule heating in the cables between the pulse power supply and the kicker. The power supply sends a pulse with twice the required voltage and half the current needed by the kicker, which is adjusted by the transformer just before the kicker magnet.



<Figure 2.1.6.61> Magnetic field profile and 3D model of the kicker magnet.

MRIK23 and MRIK14 kicker magnets have specifications as shown in <Table 2.1.6.19>. For a 4 GeV full-energy electron beam, they deflect the beam by 3.179 mrad over a length of approximately 40 cm. A thin metal chamber or a titanium-coated ceramic chamber is placed inside the ferrite core window frame, designed to generate a central magnetic field of 0.103 T. BRIK and BREK have the same structure and will be tuned to provide the appropriate kicking angle at 200 MeV and 4 GeV.

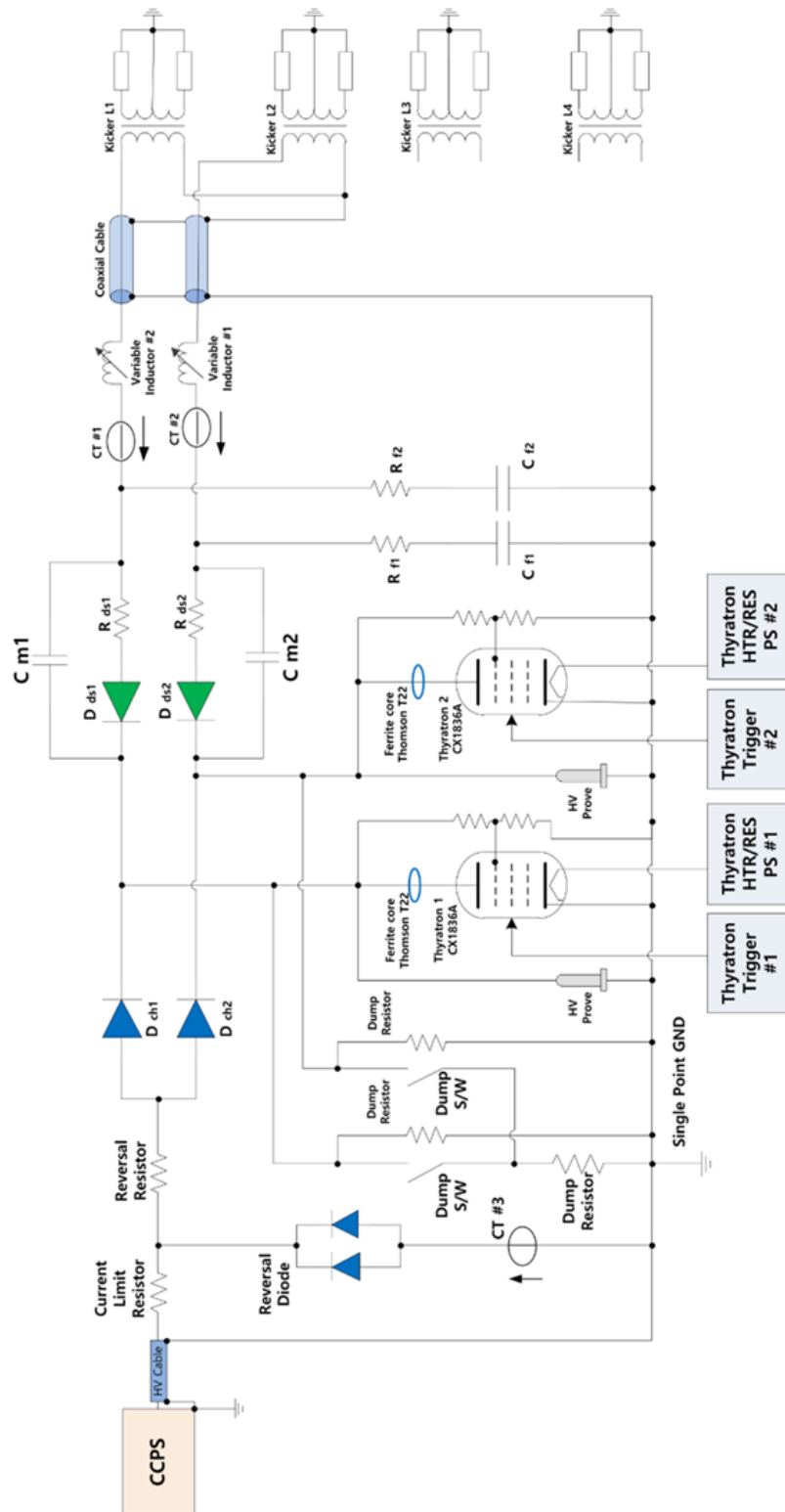
<Table 2.1.6.19> Technical parameters of kicker magnets

Parameters	Values	Unit
Max. kick angle @ 4 GeV	3.179	mrad
Field integral	4.24E-02	Tm
Vertical gap	30	mm
Horizontal clearance	64	mm
Core length	368	mm
Effective length	412	mm
Peak current	2.5	kA
Central field strength	0.103	T
Inductance before transformer	0.55	uH

The kicker power supply is a typical Pulse Forming Network (PFN)-based triggering circuit. The power drive unit consists of (1) a Capacitor Charging Power Supply (CCPS) for high-voltage charging, (2) a Current Limit Resistor & Reversal Resistor to restrict current and prevent reverse voltage, (3) a Reversal Diode to block reverse voltage, and (4) Dump Resistors to discharge stored charge after use (see <Figure 2.1.6.62>). For a half-sine pulse, the pulse width is designed to be less than 5 μ s, with a maximum pulse current of 7 kA and a repetition rate of 2 Hz (see <Table 2.1.6.20>).

<Table 2.1.6.20> Technical parameters of kicker power supplies.

Parameters	Values	Unit
Pulse current	7	kA
Pulse width	< 5	us
DC Volt. @ thyatron anode	14	kV
Flat-top width	200	ns
Rep. rate	2	Hz
Energy per pulse	70	J
Power supply system L	2.3	uH
Pulse current difference	+ - 0.2	T



<Figure 2.1.6.62> Kicker power supply circuit diagram.

(3) Thick Septum (LITKS, BTSTKS)

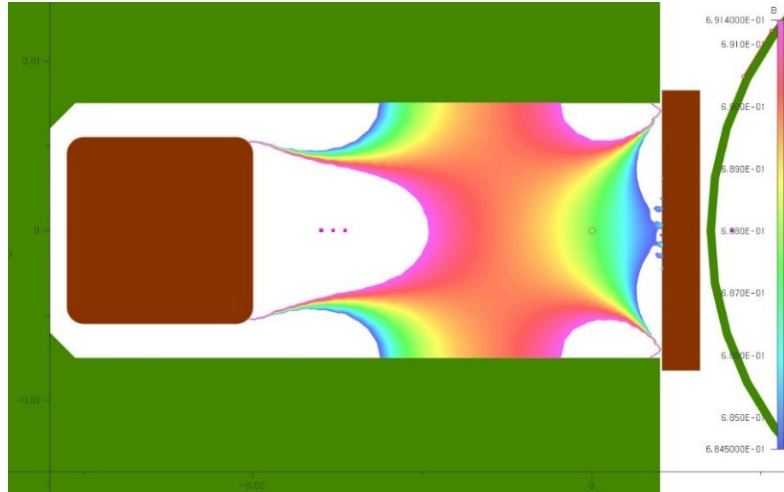
LITKS and BTSTKS have the same transverse geometrical cross-section, and pulse shape (half-sine 100 μ s). However, LITKS is manufactured by stacking laminated steel sheets in a curved shape to satisfy a magnetic length of 500 mm and a curvature radius of 1.4 m. BTSTKS has a magnetic length of 1100 mm and a curvature radius of 19.4 m, resulting in a smaller sagitta than LITKS (refer to <Table 2.1.6.21>). The minimum orbit distance is designed to be approximately 9 mm (2.5 mm septum blade, 1 mm vacuum chamber wall thickness, 0.5 mm μ -metal shield, and 2 mm beam clearance). This meets the minimum orbit distance requirement of 18.7 mm for thick septa.

<Table 2.1.6.21> Technical parameters of LITKS & BTSTKS

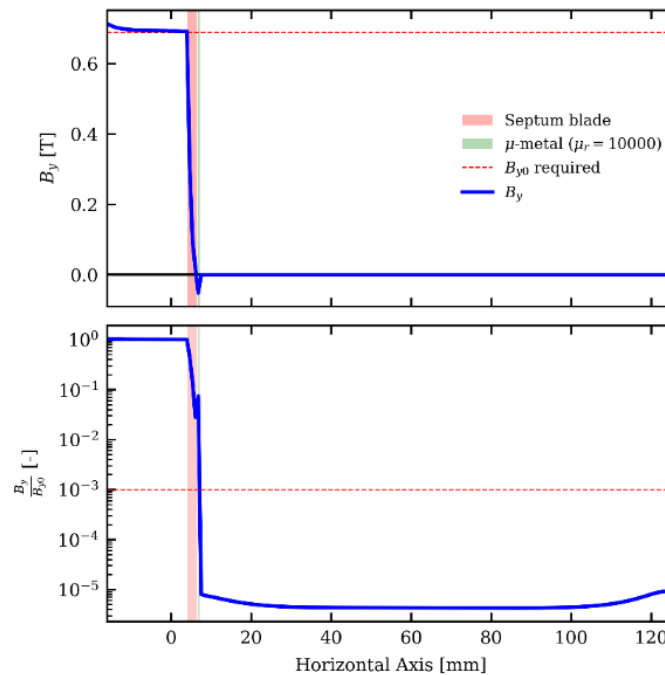
Parameters	BTSTKS	LITKS	Unit
Particle	e-		-
Kinetic energy	4	0.2	GeV
-Magnetic rigidity	13.34	0.67	Tm
Magnetic length	1.1	0.5	m
Bending angle	3.25	20	deg
-Central field	0.6881	0.4669	T
-Field integral	0.7569	0.2335	Tm
Septum type	Direct drive		-
Pulse type	Half-sine		-
Pulse width	100		μ s
Repetition rate	2		Hz
Peak current	8.296	5.600	kA
Full gap	15.0		mm
Full width	36.0		mm
Septum thickness	2.5		mm
μ -metal thickness	0.5		mm
Inductance	2.26	1.03	μ H
Resistance	1.85	0.84	m Ω
Ohmic heat per pulse	7.00	1.45	J

Field uniformity for the split beam section in BTSTKS, within $\pm 0.5\%$ range, is shown in <Figure 2.1.6.63>. Unlike iron-dominated DC magnets, the uniform region is not controlled by ferromagnetic core boundary conditions but is instead adjusted by peak current and magnet positioning. The leakage field distribution for a half-sine pulse width of 100 μ s is

shown in <Figure 2.1.6.64>. Due to the direct-drive structure, the leakage field outside the septum blade is opposite in direction, and its magnitude at the septum blade surface (2.5 mm thick) is reduced to approximately 1/100 of the internal field. By applying a 0.5 mm thick mu-metal sheet with a relative permeability of 100,000, the leakage field experienced by the external beam is further reduced to approximately 1/10,000 (see <Figure 2.1.6.64>).

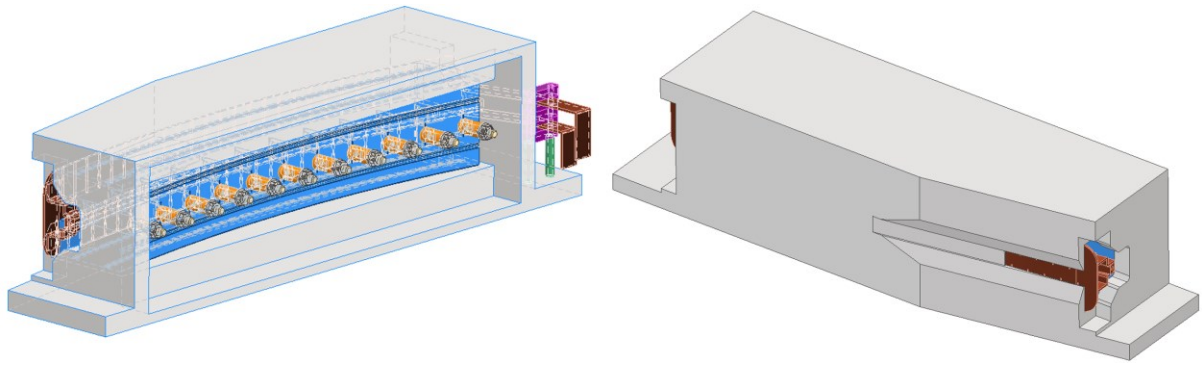


<Figure 2.1.6.63> Field uniformity of thick septum magnet ($\pm 0.5\%$).

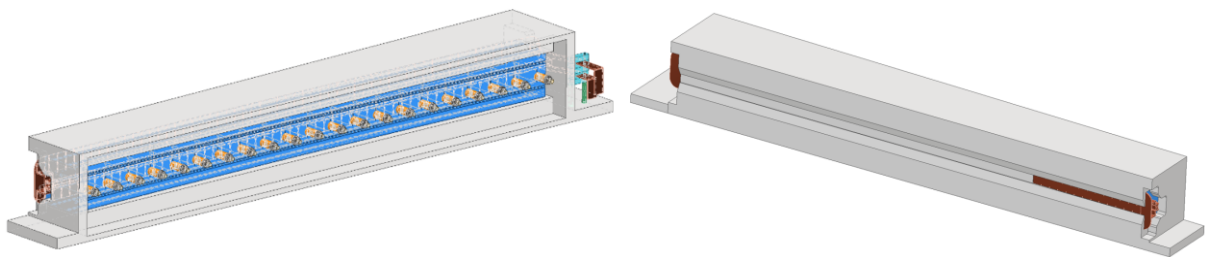


<Figure 2.1.6.64> Leakage field distribution of thick septum magnet.

<Figure 2.1.6.65> and <Figure 2.1.6.66> show the 3D CAD drawings of LITKS and BTSTKS for fabrication. Both magnets are of the out-vacuum type, and the vacuum chamber thickness will be determined by considering both the screening effect due to eddy currents and the mechanical rigidity of the vacuum chamber.



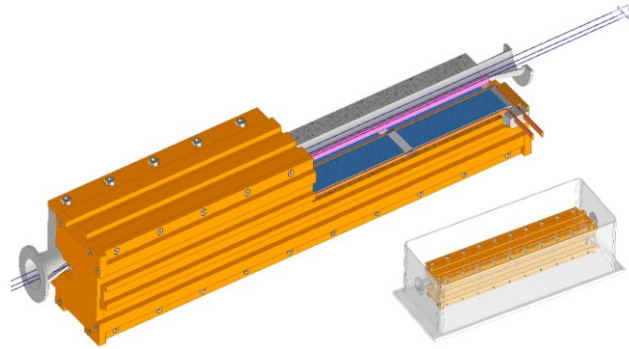
<Figure 2.1.6.65> 3D CAD model of LITKS.



<Figure 2.1.6.66> 3D CAD model of BTSTKS.

(4) Thin Septum (BTSTNS)

The stored beam orbit center in the main ring must be parallel to the injected beam orbit center within a 5 mm gap after the four kicker-induced bumps. This constraint necessitates the use of an in-vacuum septum magnet. A direct-drive method would require the insulated thick conductor itself to function as the septum blade. However, the eddy current septum design does not require the septum blade to be insulated, making it the optimal choice for achieving a 5 mm orbit distance.



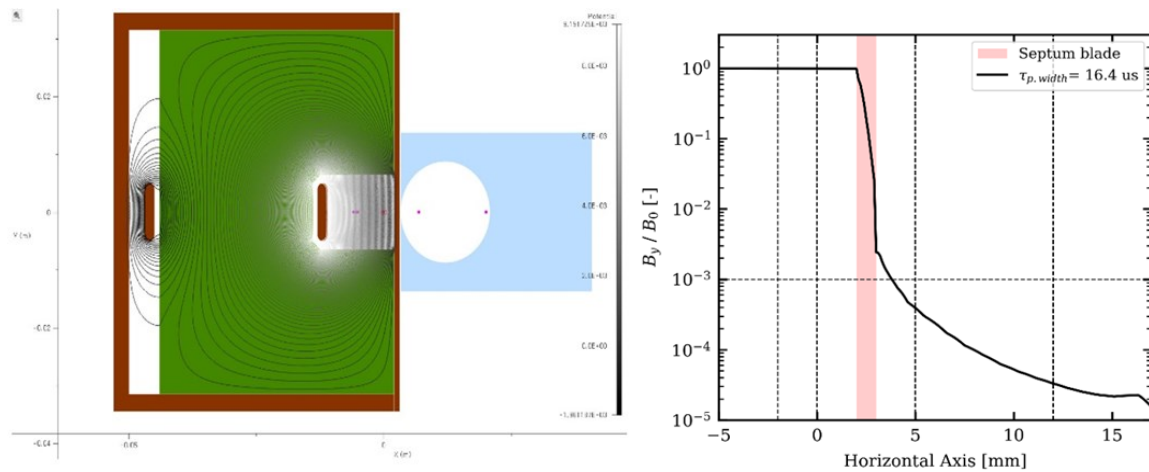
<Figure 2.1.6.67> 3D CAD model of BTSTNS prototype.

<Table 2.1.6.22> Technical parameters of BTSTNS

Parameters	Values	Unit
Particle	e-	-
Kinetic energy	4	GeV
-Magnetic rigidity	13.34	Tm
Magnetic length	0.5	m
Bending angle	1.432	deg
-Central field	0.6672	T
-Field integral	0.3336	Tm
Pulse type	Half-sine	-
Pulse width	16.4	μ s
Repetition rate	2	Hz
Peak current	6.919	kA
Full gap	13	mm
Full width	16	mm
Septum thickness	1	mm
Inductance	1.516	nH
Resistance	4.71	m Ω
Ohmic heat/pulse	2.034	J

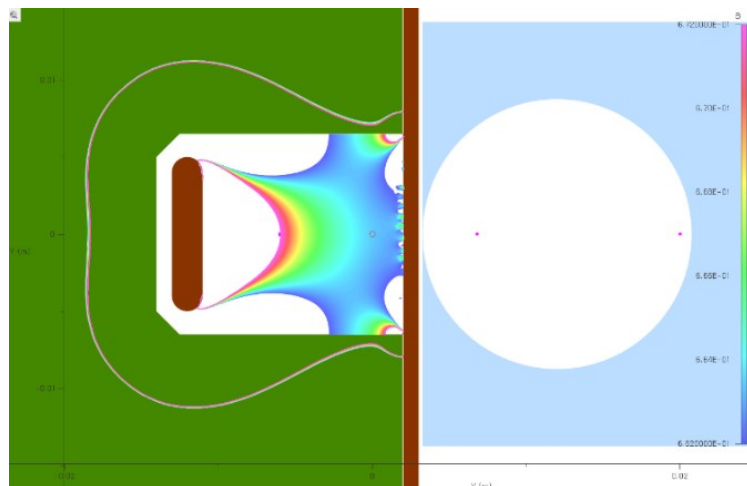
Resistive heating of the conductor is 2 J per pulse. Considering the maximum repetition rate, the total heat dissipation remains at about 4 W, making additional cooling unnecessary.

The central magnetic field is approximately 0.667 T, and the horizontal leakage field distribution outside is shown in <Figure 2.1.6.68>. With a blade thickness of 1 mm, the field decay factor for a half-sine pulse width of 16.4 μs is around 0.003. Further attenuation occurs within the aluminum vacuum chamber, ultimately reducing the leakage field at the bumped orbit to below 0.0006 T.



<Figure 2.1.6.68> Field distribution & leakage field analysis of BTSTNS.

The figure below shows the uniform field distribution within $\pm 0.1\%$. It can be observed that a consistent magnetic field is formed over most of the beam path.

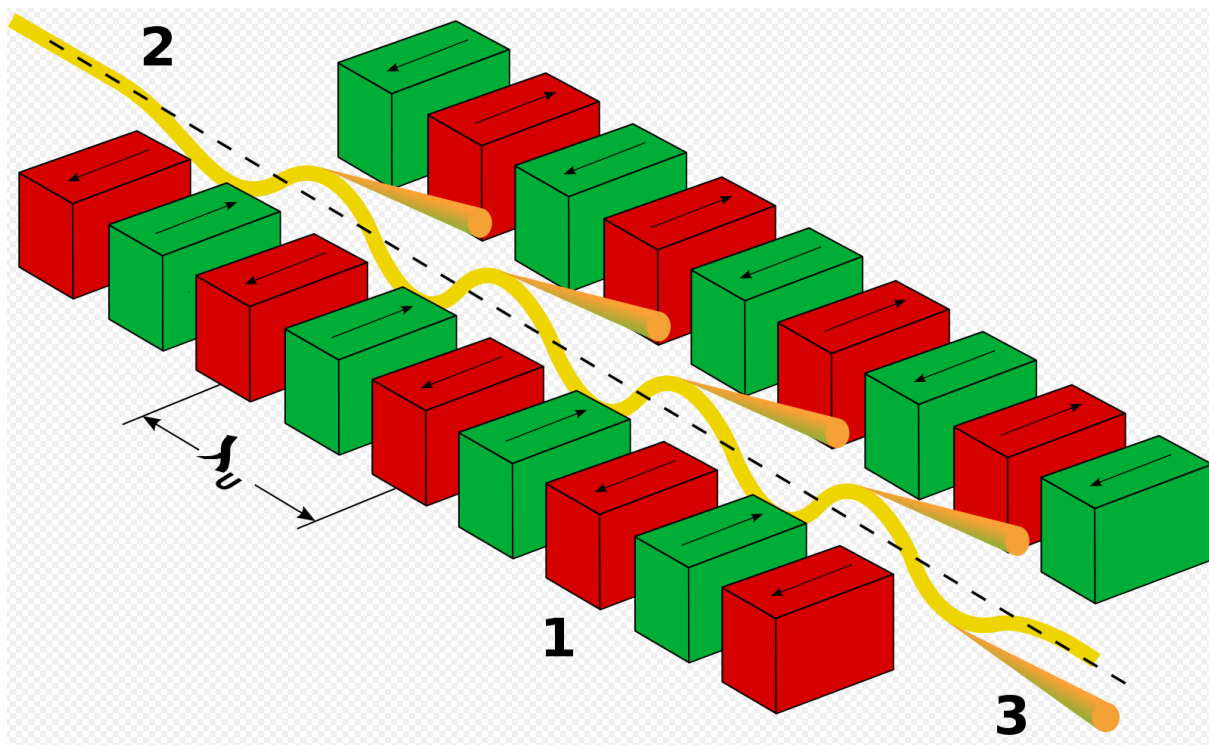


<Figure 2.1.6.69> Field uniformity of BTSTNS.

2.1.7 Insertion Devices and Light Source

A. In Vacuum Undulator

Out of the ten beamlines to be built in Phase 1 of 4GSR, 1 beamline will use one of the center bends as the synchrotron source, 2 beamlines will use elliptically polarizing undulators (EPUs) to generate the circularly polarized light, and the remaining seven beamlines will use in-vacuum undulators, which are undulators placed in a vacuum. Undulators do not determine the performance of the storage ring lattice but purely generate light, as shown in the schematic drawing of <Figure 2.1.7.1>. In <Figure 2.1.7.1>, permanent magnets (SmCo₅) and Fe poles arrangements are shown, which results alternating magnetic field distribution along the beam. The alternating north and south poles generate alternating magnetic fields, which cause the electrons to move in a sinusoidal pattern. Through this motion, the electrons emit synchrotron radiation, and particularly in the case of undulators, the brightness of the emitted light increases by the square of the number of sine motion periods. Due to these characteristics, undulators have been used as the primary light source since the advent of the third generation of synchrotron light sources.



<Figure 2.1.7.1> Schematic drawing of an undulator.

In particular, for magnetic structures such as in-vacuum undulators, SPring-8 in Japan developed a technology for placing a magnetic structure inside a vacuum chamber to achieve a short magnetic period and high effective magnetic flux density. It has been widely applied

in synchrotron radiation sources worldwide. We also plan to apply the In-Vacuum Undulator (IVU) technology to the seven beamlines in phase 1. Although similar devices have already been developed and applied to PLS-II, they need to be upgraded to fit the 4GSR. The main upgrade points are as follows:

- The 4GSR straight section will be longer than the PLS-II straight section (C beamline), so the design magnetic length of an IVU is about 3.0 m.
- Since the minimum gap will be 5.0 mm to reflect the low emittance and beam stay clear of 4GSR, a new structural design is required to withstand the increased magnetic force, and longer magnetic length.

The previous IVUs used in PLS-II underwent final magnetic field measurements before assembling the vacuum chamber. In that case, it relied solely on the mechanical assembly's precision, and no magnetic field measurement was conducted after the final vacuum chamber assembly. To resolve this uncertainty, preparing the required tooling at the design stage may be necessary to allow field measurements even after assembling the vacuum chamber.

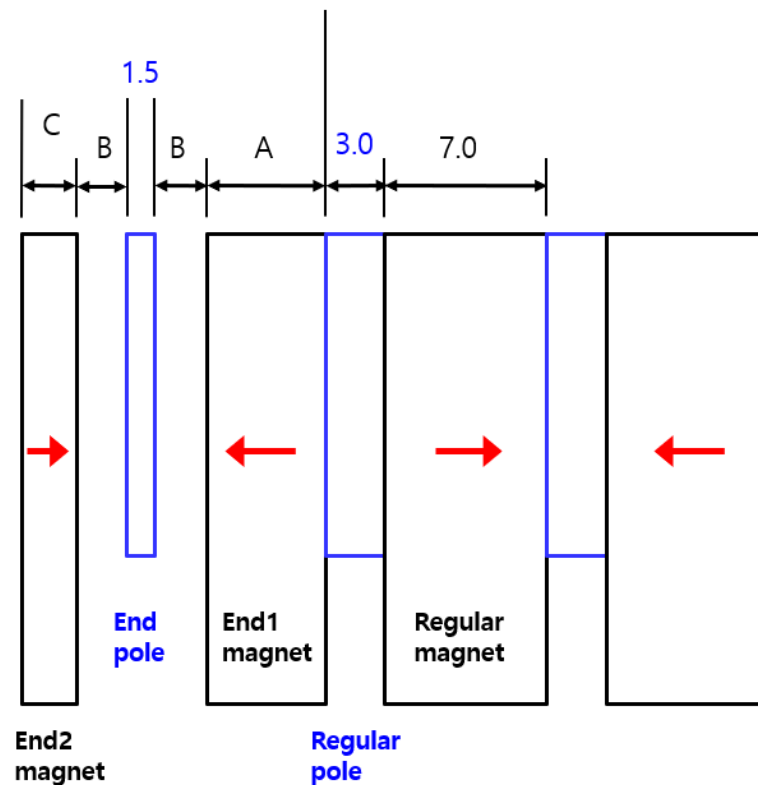
Besides the 20 mm period IVU, it is necessary to prepare for the possibility of using 22 mm and 24 mm undulators.

An IVU magnet material should be resistant to the electron beam and gamma-ray radiation because magnetic structures are positioned close to the electron beam and used for an extended period. Considering these factors, a rare earth permanent magnet of the $\text{Sm}_2\text{Co}_{17}$ series will be used. This magnet has a residual magnetic flux density of $B_r = 1.13 \text{ T}$, about 10% lower than the Nd series, but has higher radiation resistance. This $\text{Sm}_2\text{Co}_{17}$ permanent magnet is corrosion-resistant and has a high Curie temperature of 660°C , where the magnetic property is lost. Therefore, its stability is so excellent that no additional cooling is required even when baking the vacuum chamber. However, its drawbacks include lower B_r by 10% and higher cost than the Nd series rare earth magnets, and its brittleness requires careful handling.

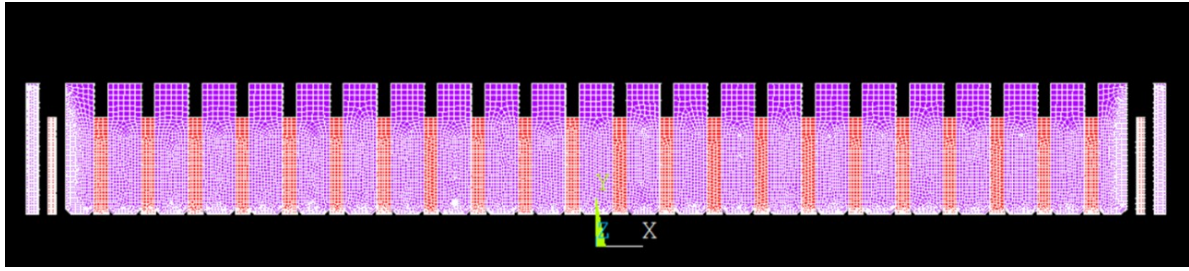
All permanent magnets should be coated to be applicable in an Ultra High Vacuum (UHV) environment. Permendur with a high saturation magnetic flux density of 2.3 T or ordinary low carbon steel with a saturation magnetic flux density of 2.05 T to 2.10 T can be used for the pole material. In the case of shorter periods, where the peak field is lower, using

Vanadium Permendur provides a 2 to 3% gain in the peak field, but it is expensive and difficult to procure. Low-carbon steel is deemed sufficient for our purposes and will be used as the pole material. A finite element method (FEM) simulation was used to perform calculations on the undulator to determine the optimal geometry of the poles and permanent magnets.

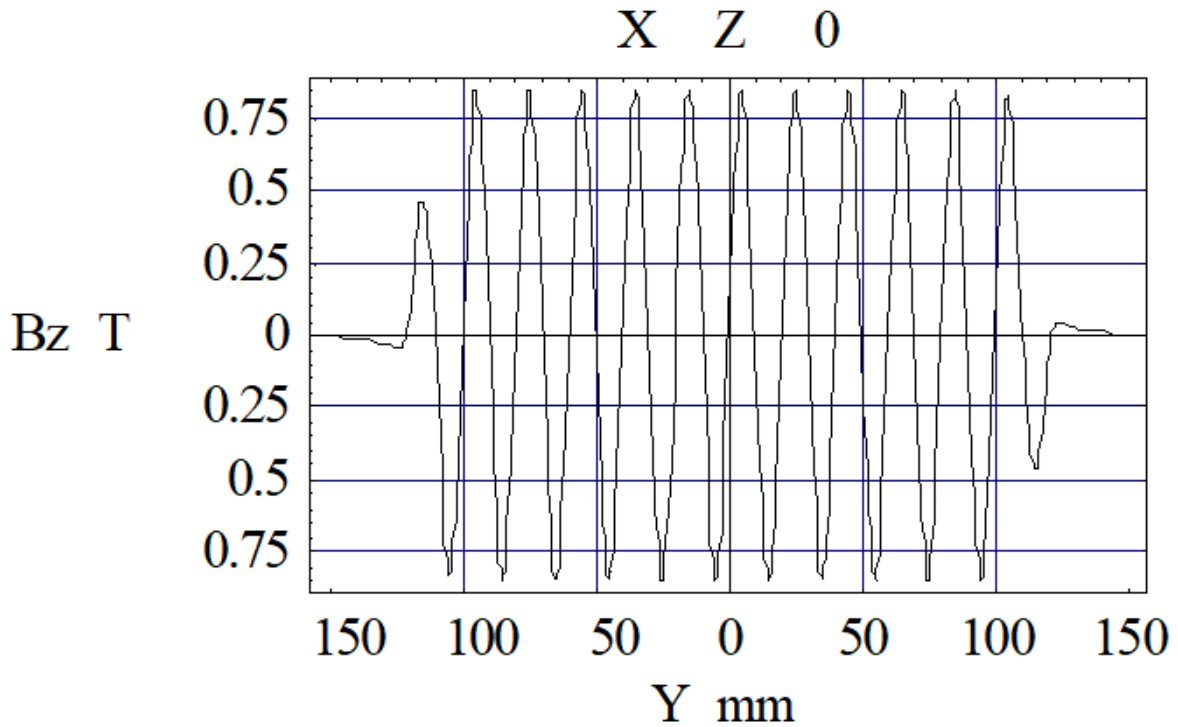
Due to limitations in computer resources, the entire geometry was not analyzed. However, the analysis was conducted, including the number of periods until the magnetic flux density reached a sufficiently periodic shape. The magnet geometry in the end part was adjusted to the thickness of the end pole and end magnet and the distance between them so that the field reached a periodic shape with minimal transient. <Figure 2.1.7.2> shows the geometry of the end magnet, and <Figure 2.1.7.3> shows the 3D FEM model. The purple represents the permanent magnet, and the red represents the ferromagnetic pole. <Figure 2.1.7.4> shows the z-direction distribution of the magnetic flux density calculated through FEM. The calculation result is for a 6.0 mm pole gap.



<Figure 2.1.7.2> Optimization of an IVU end magnet and pole geometry.



<Figure 2.1.7.3> IVU 3D FEM model.



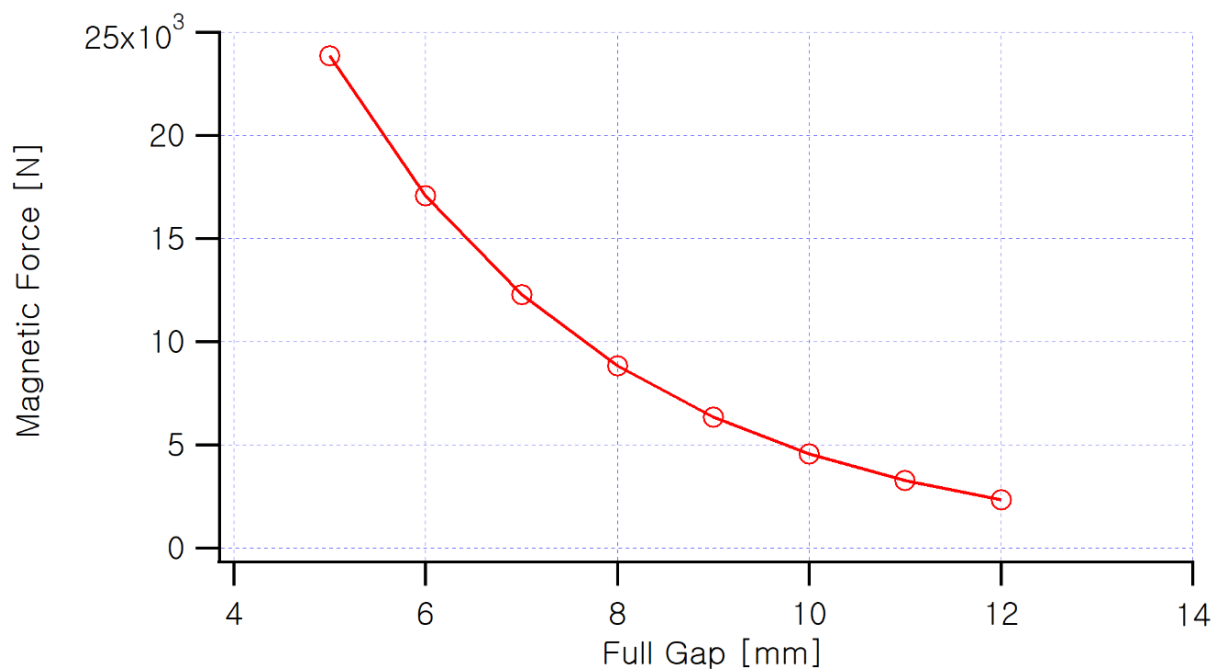
<Figure 2.1.7.4> Flux density profile of IVU20 at gap = 6.0 mm.

In addition to this, it is also possible to use undulators with 22 mm and 24 mm periods in the beamline. The total magnetic length is estimated to be about 3.0 m, and the overall length, including RF bellows and vacuum components, is estimated to be about 3.5 to 3.6 m. <Table 2.1.7.1> summarizes the parameters of $\text{Sm}_2\text{Co}_{17}$ and low carbon steel undulators with periods of 20 mm, 22 mm, and 24 mm, a length of 3.0 m, and a minimum pole gap of 5.0 mm.

As the undulator pole gap changes, the inner girder supporting the magnetic structure inside the vacuum chamber is subjected to forces such as magnetic force, gravity, and atmospheric pressure due to vacuum. This deformation of the inner girder can lead to deformation of the magnetic structure and degrade the performance of the undulator, so it should be limited to within a few microns. To achieve this, the strength and dimensions of

the inner girder made of aluminum should be optimized, the design of the supporting rod connecting the inner girder and outer girder should be optimized, and a compensation spring should be designed and installed to compensate for the magnetic force at a small pole gap. <Figure 2.1.7.5> shows the calculation results of the magnetic force according to the pole gap. At the minimum pole gap, a force of about 5 tons is applied, and at a 5.0 mm gap, the magnetic force acting on one side of the magnetic structure is about 23 kN or about 2.3 tons.

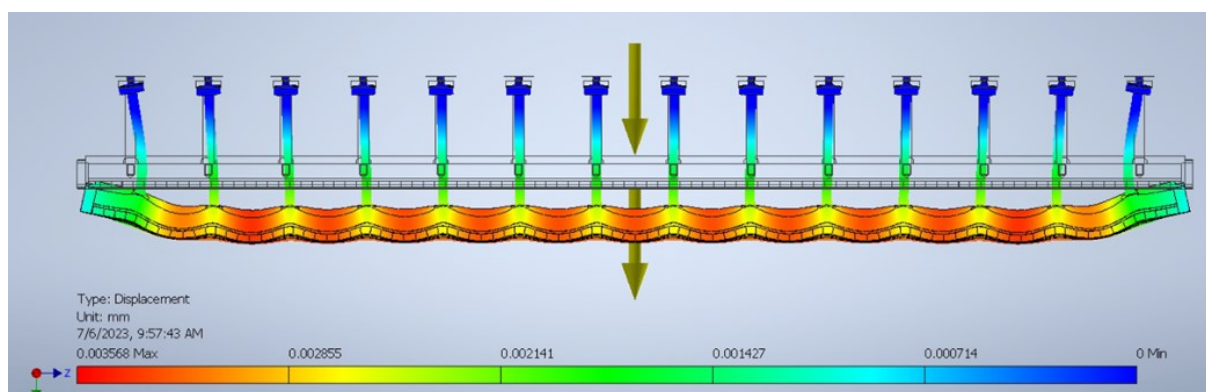
<Figure 2.1.7.6> shows the calculation results of the deformation of the magnetic structure under the magnetic force and various load conditions. When the distance between suspension rods is set to 215 mm (with a total of 28 suspension rods), a maximum displacement of about $3.46 \mu\text{m}$ can be obtained. <Figure 2.1.7.7> shows the deformation calculation results of the entire structure, including the outer girder.



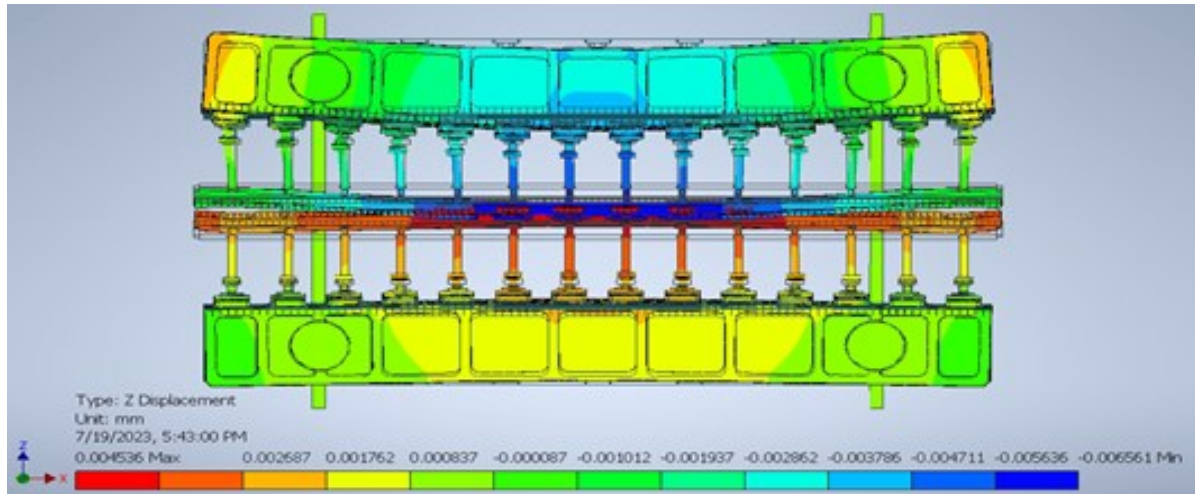
<Figure 2.1.7.5> Magnetic force calculation result depending on pole gap.

<Table 2.1.7.1> Main parameters of the 4GSR in-vacuum undulators

Parameters	Values			Remark
Period length [mm]	20	22	24	Three period depending on the beam line
Period number of full fields	149	135	124	-
Total magnetic length [m]	≤ 3.0	≤ 3.0	≤ 3.0	-
Magnet material	Sm ₂ Co ₁₇	Sm ₂ Co ₁₇	Sm ₂ Co ₁₇	For better resistance to the radiation
Undulator type	Hybrid	Hybrid	Hybrid	-
Working gap range [mm]	5.00 to 16	5.00 to 16	5.00 to 16	Max gap is flexible.
Max Effective field [T]	1.021	1.127	1.225	-
Max K	1.907	2.316	2.747	-
Precision of gap change [μ m]	< 1.0	< 1.0	< 1.0	-
Total Power [kW]	12.71	15.49	18.30	@4 GeV, 400 mA
Peak PD [kW/mrad ²]	170.0	170.6	170	@4 GeV 400 mA
e-beam energy loss [keV]	31.8	38.7	45.8	-
e1 [keV]	2.70	1.88	1.33	fundamental energy
Vacuum pressure with beam [Torr]	$< 3.0 \times 10^{-9}$	$< 3.0 \times 10^{-9}$	$< 3.0 \times 10^{-9}$	-
Impedance [m Ω]	≤ 80	≤ 80	≤ 80	-



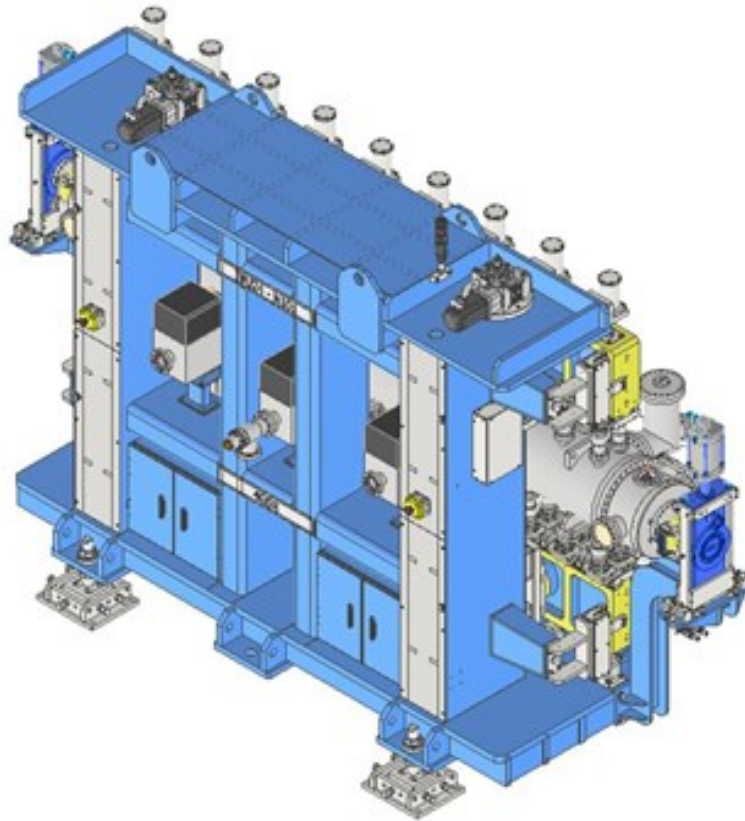
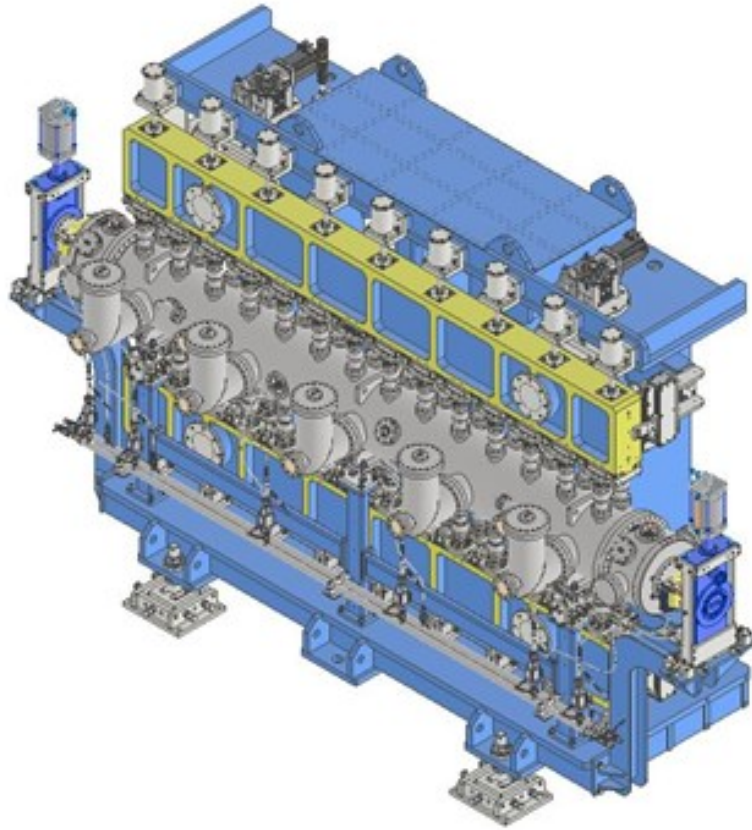
<Figure 2.1.7.6> Deformation calculation result of a magnetic structure.



<Figure 2.1.7.7> Deformation of an IVU inner girder and outer girder based on 3.0 m length.

Additionally, when baking the vacuum chamber, an IVU should protect the magnets from heat, so cooling channels need to be installed to maintain the temperature below the operating temperature of permanent magnets. Also, to avoid interference caused by the thermal expansion difference between the chamber and the magnetic structure, the bellows should have enough internal diameter to accommodate this difference. Moreover, to prevent deformation due to the force exerted when the magnetic structure thermally expands, an LM guide should be installed to allow sliding in the longitudinal direction. A 50 μm thick Ni foil and 50 μm thick Cu foil should be covered to the magnetic structure surface to ensure electrical continuity. Ni, being a magnetic material, secures contact with the magnetic structure, while Cu, with its low resistivity, minimizes heating due to the image current seen by the electron beam and reduces impedance. Flexible RF fingers are installed at both ends of the undulator to maintain electrical continuity between the foil and the storage ring chamber even when the gap changes.

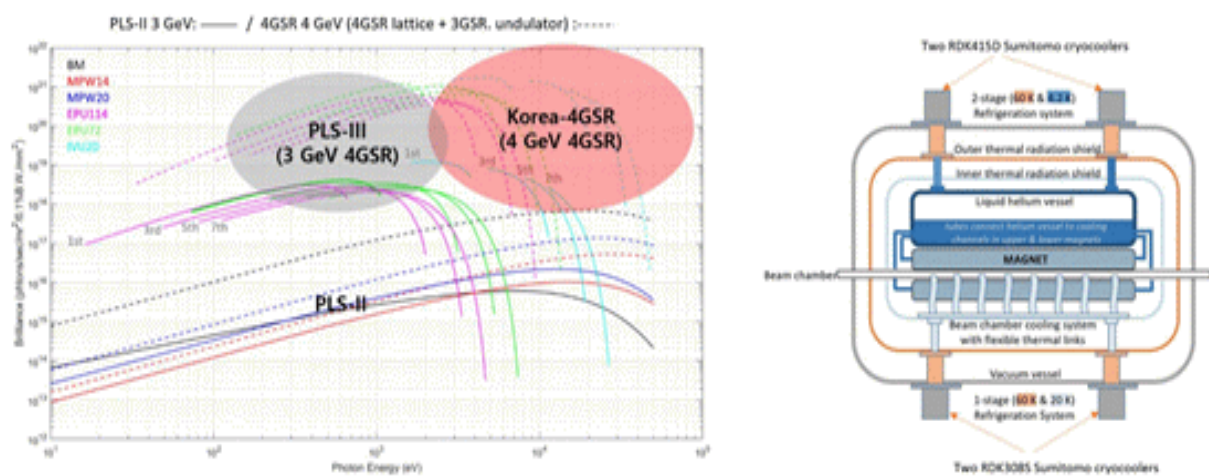
Based on these mechanical, structural, magnetic, and engineering calculations, an IVU that meets the specifications of 3.0 m in length, a minimum pole gap of 5 mm, and a period of 20 to 24 mm has been designed, and the final 3D drawings are shown in <Figure 2.1.7.8>. The 2D drawings for manufacturing the key components are attached in the appendix.



<Figure 2.1.7.8> IVU isometric view after the final 3D design.

B. High-performance Components for Insertion Devices: High Temperature Superconducting Wavelength Shifter

Most insertion devices scheduled for 4GSR are bright in the X-ray regime below 10 keV. While most organic material analyses are possible with these light sources, analyzing smaller structures at the atomic and molecular level or the electronic structure spectroscopy of high atomic number metals requires shorter wavelength (higher energy) light sources. For this reason, several institutions operate Wiggler magnets with a maximum flux density of 5 T, which can generate hard X-rays above 100 keV at operating energies of 3 to 4 GeV, enabling the experiments above.



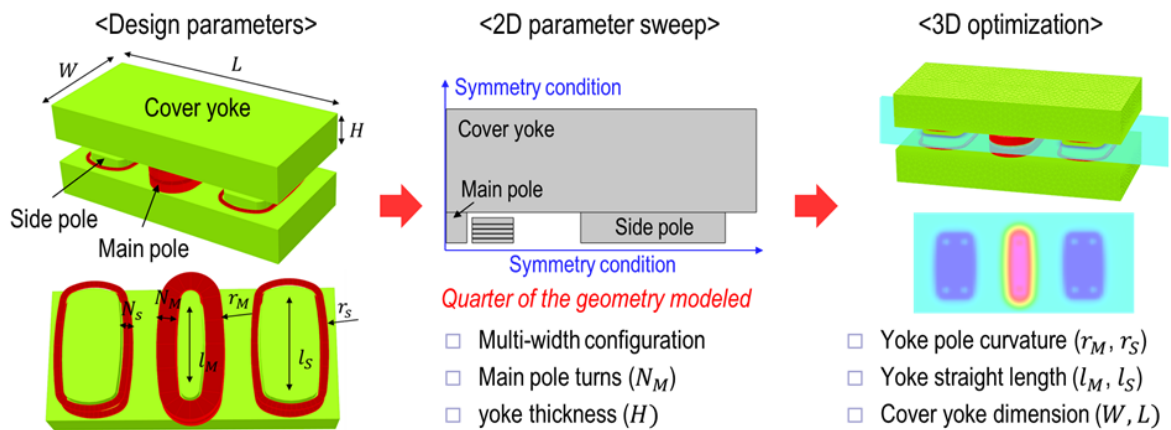
<Figure 2.1.7.9> Distribution of photon energy and brightness that can be extracted from domestic synchrotron radiation facilities (left) and the cooling system structure of a typical low-temperature superconducting insertion device (right).

Several 7 T class low-temperature superconducting wavelength shifters and 4 T class multi-pole wigglers installed in foreign synchrotron radiation facilities all adopt a cooling system using 4 K liquid helium, as shown in <Figure 2.1.7.9>, to make the coils in a superconducting state. This cooling system presents various issues, including long and costly cool-down and warm-up, damage to the helium cooling system during quenching accidents, and high construction costs. These problems directly lead to a reduction in annual operating hours.

The second detailed study on the localization of high-performance insertion device components proposes an alternative to the above issues by using NI-HTS (non-insulated high-temperature superconducting) coil sets to significantly improve the operating temperature from 4 K to above 20 K and develop insertion devices adopting conduction cooling instead of liquid helium baths.

(1) Magnet Design

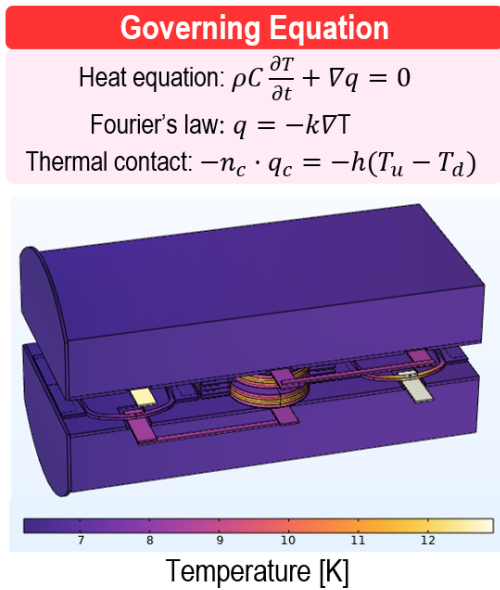
In this study, we developed the world's first insertion device using high-temperature superconductivity and conduction cooling. Despite achieving a strong magnetic flux density of over 5 T, this combination has a volume only 1/8 that of conventional magnets due to high current density in the coils and a simple cooling system. To reduce wake impedance heating, the pole-to-pole gap was limited to 12 mm, and for the safe operation of the current leads and coils, the operating current was restricted to below 200 A. The finite element design of the designed magnet body is shown in <Figure 2.1.7.10>.



<Figure 2.1.7.10> 2D and 3D finite element design of the 5 T class wavelength shifter.

(2) Cooling

For efficient operation, a thermal analysis was conducted to operate with one PT815 freezer, confirming the safety of the storage ring operation. The total heat generation was less than 10 watts in the second stage and less than 65 watts in the first stage, verifying an available cooling capacity of 18 and 75 watts, respectively. These figures include various potential heat sources during operation (contact heat, radiative heat transfer, coil's resistive heating, and wake impedance heating caused by the beam).

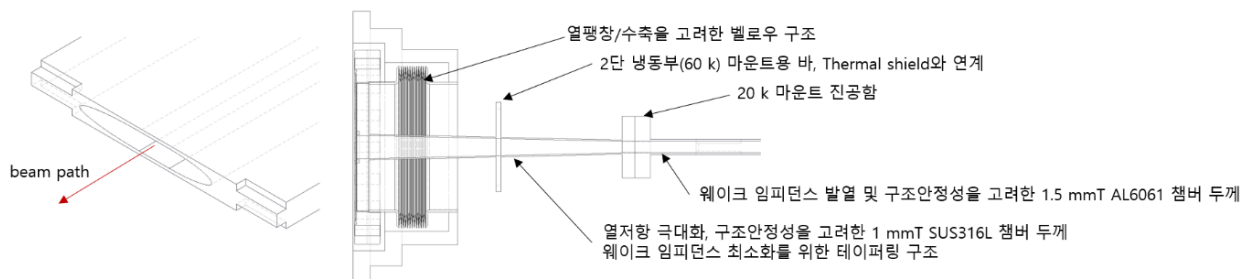


Heat source [W]		2 nd stage	1 st stage
Conduction	Magnet support	<1	<1
	Beamduct support	<0.1	<1
	Beamduct conduction	1.8	9.4
Radiation	Radiation	0.1	16.1
Resistance	Resistive joint	0.16	0
	NI leakage current	<1	0
	Current lead	0.3	33.6
Beam	Image current + Wake impedance	3.3	
	Synchrotron radiation	<1	<1
Total [W]		<10	<65.5
Cooling margin [W]		18	75

<Figure 2.1.7.11> Table of heat equation, heat distribution diagram, and heat analysis results.

(3) Cryogenic Vacuum Chamber

If the vacuum chamber heating due to the beam exceeds the design margin, it cannot be used as a storage ring light source. Also, if the thermal resistance from room temperature to the cryogenic section is low, there is a high risk of quenching due to heat intrusion from the atmosphere. Therefore, we devised a 1 mm thick vacuum chamber structure that is thin enough to have high thermal resistance and allows only minimal structural deformations. Also, using dissimilar bonding, the inner vacuum chamber is made of aluminum, which generates less heat, and the outer vacuum chamber is made of stainless steel (SUS 316L), which has a high thermal resistance.



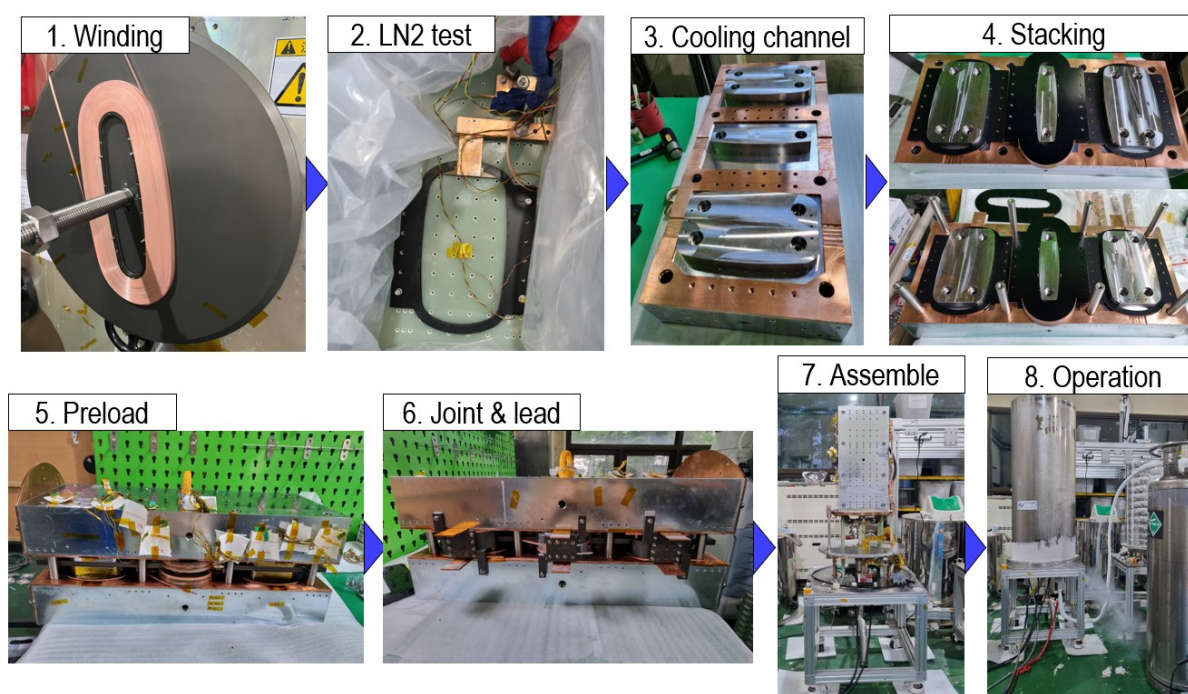
<Figure 2.1.7.12> Vacuum chamber structure.

<Table 2.1.7.2> Analysis of wake impedance heating

Conductivity [S/m]	Loss factor [V/pC]	Heating per bunch [W]	Total heating [W]
Low temperature (SUS + Al)	0.007027	0.01243	3.73

(4) Assembly

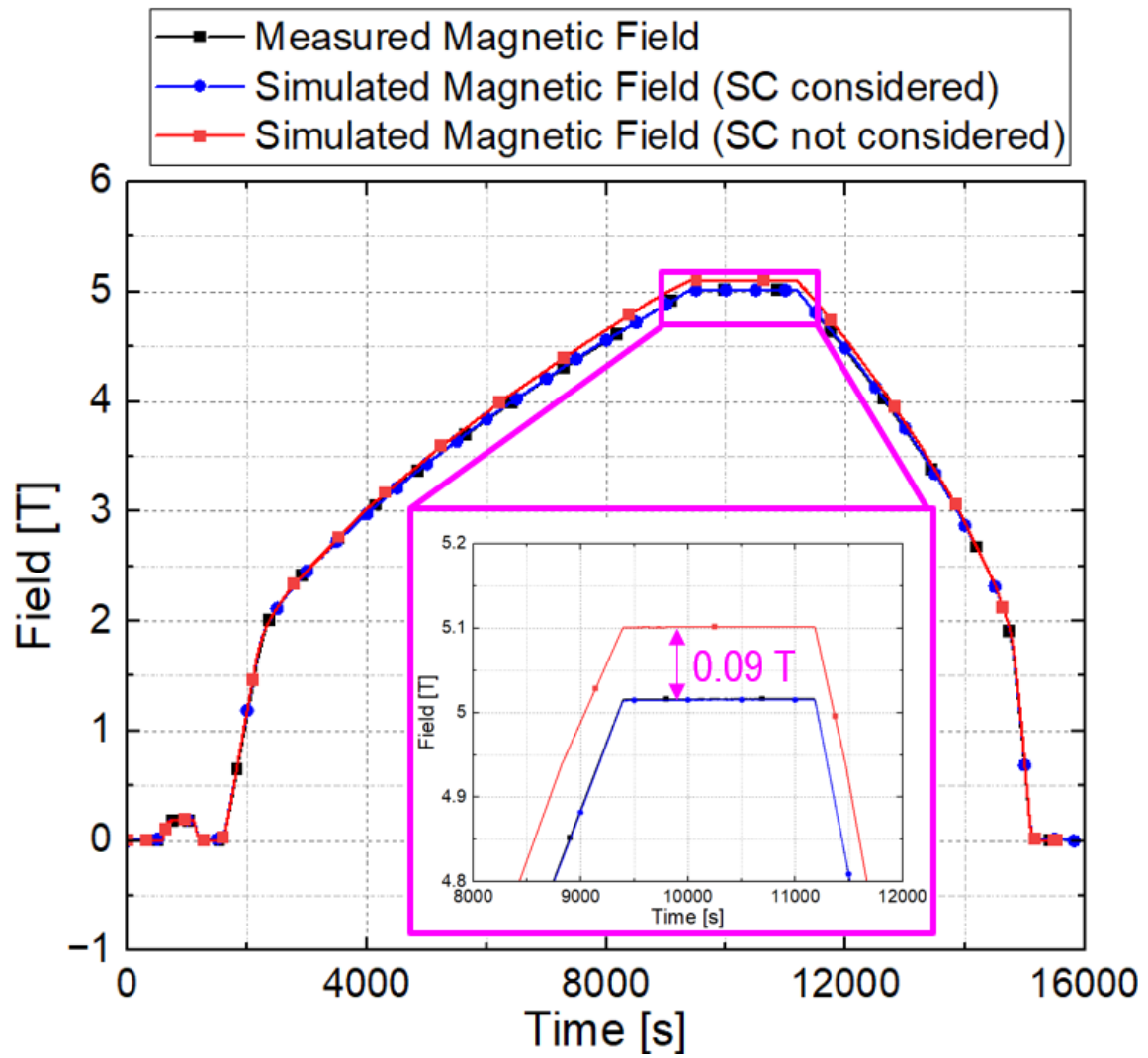
The assembly proceeded in the following order: ① winding of the coil sets, ② nitrogen cooling conduction test of individual coil sets, ③ cooling channel wiring in the yoke, ④ coil sets stacking, ⑤ preload tightening, ⑥ combining the joints and current leads, ⑦ assembly, and ⑧ operation test. After assembly, a separate cooling test was also conducted.



<Figure 2.1.7.13> Wavelength shifter: assembly and experiment process.

(5) Experiment

Before the end of the research project, cooling test and conduction test were successfully completed. The target of 5 T central magnetic field was successfully measured, and the results are shown in <Figure 2.1.7.14>.



<Figure 2.1.7.14> Cooling and conduction test results of HTS Wavelength shifter (High-performance insertion device: No-insulation High Temperature Superconducting Insertion Device). 5 T was successfully realized.

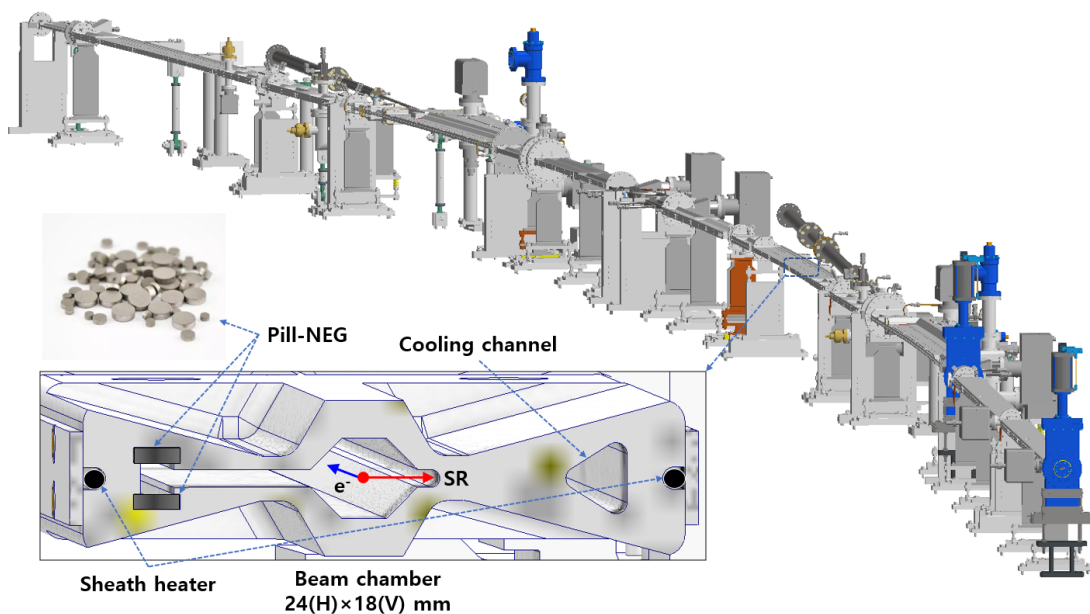
2.1.8 Vacuum System

A. Overview

The vacuum system must maintain a stable and appropriately sized ultra-high vacuum (UHV) environment to ensure electrons, generated from the electron gun, are accelerated through a 26 m linac, then gain energy in a 770 m booster ring, and are subsequently reliably stored in an 800 m storage ring.

To achieve stable beam operation, the vacuum system must maintain an ultra-high vacuum (UHV) condition, typically below 10^{-9} mbar, to minimize beam-gas interactions that can cause beam loss and degrade beam quality. Furthermore, careful design considerations are required to mitigate beam impedance, which can impact beam stability and performance. The vacuum chamber geometry, surface properties, and material selection play a crucial role in reducing wakefield effects and managing resistive wall impedance.

The storage ring has a small emittance of 62 pm·rad, requiring an arrangement of numerous strong magnets. This imposes spatial constraints in the vacuum system design, leading to low gas conductance in the vacuum tube. To address this issue, similar facilities such as MAX IV, SIRIUS, ESRF EBS, APS-U, and HEPS have extensively adopted NEG-coated vacuum chambers. Taking a different approach, the Korea-4GSR vacuum system is designed to resolve this challenge using an aluminum vacuum chamber with inserted Pill-NEG. (<Figure 2.1.8.1>)

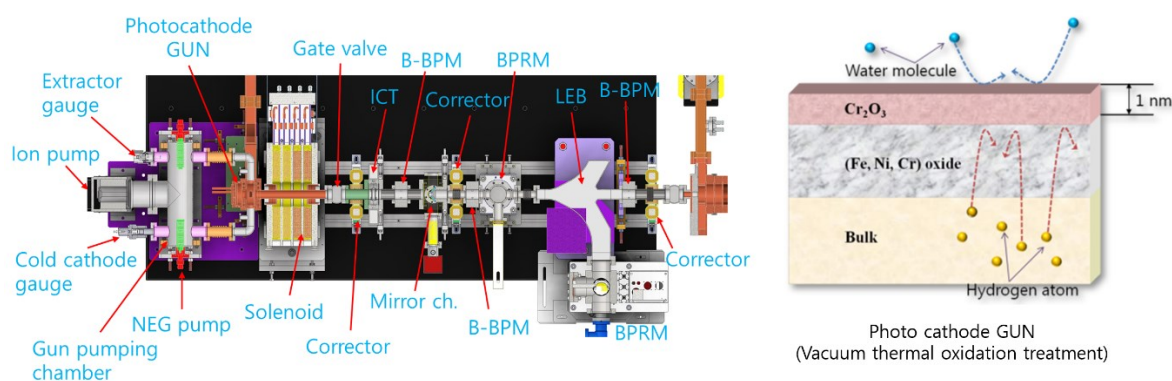


<Figure 2.1.8.1> Storage ring vacuum system of the Korea-4GSR.

B. Linac Vacuum System

The linear accelerator (Linac) vacuum system consists of an electron gun, accelerating columns, waveguides, and diagnostic devices. The electron gun's vacuum level should be maintained below 10^{-10} mbar for sustained operation. To prevent RF breakdown and electron scattering, the accelerating column and waveguide—which transmit high-power, high-frequency waves—are designed to operate at a vacuum level of 10^{-8} mbar or lower.

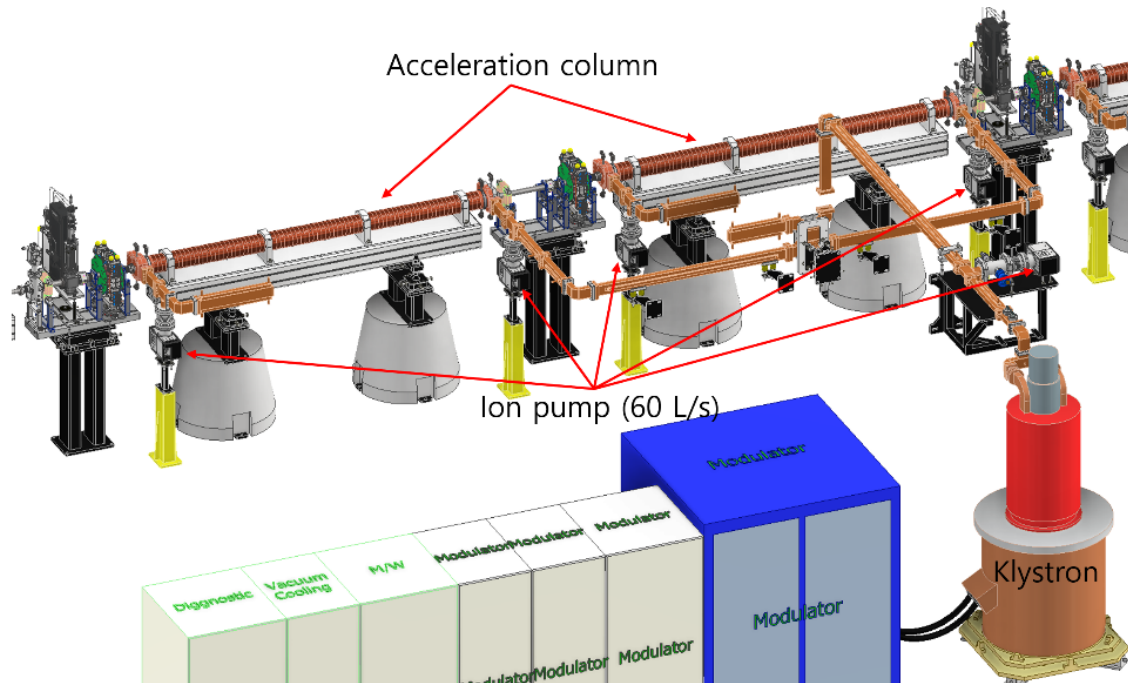
The surface of the electron gun is susceptible to contamination by particles such as carbon compounds, leading to dark current generation, which directly impacts the electron gun's lifetime. To maximize the photocathode's lifespan, the vacuum level inside the gun chamber is recommended to be maintained below 10^{-10} mbar. To achieve this, the electron gun vacuum system uses a 60 L/s sputter ion pump combined with a 400 L/s non-evaporable getter (NEG) as shown in <Figure 2.1.8.2>. In addition, to effectively suppress hydrogen outgassing from the bulk, the electron gun vacuum chamber undergoes vacuum thermal oxidation (VTO) treatment, forming a high-density chromium oxide layer on the stainless steel surface. For accurate measurement of the ultra-high vacuum (≤ 10 mbar) inside the electron gun chamber, an extractor gauge is necessary to minimize the effects of X-ray-induced currents and electron-stimulated desorption (ESD). A cold cathode ultra-high vacuum gauge with a fast interlock response time is also used to ensure the prompt activation of the vacuum valve in the event of a vacuum burst, thereby protecting critical components such as the electron gun and RF components.



<Figure 2.1.8.2> GUN and G2L section.

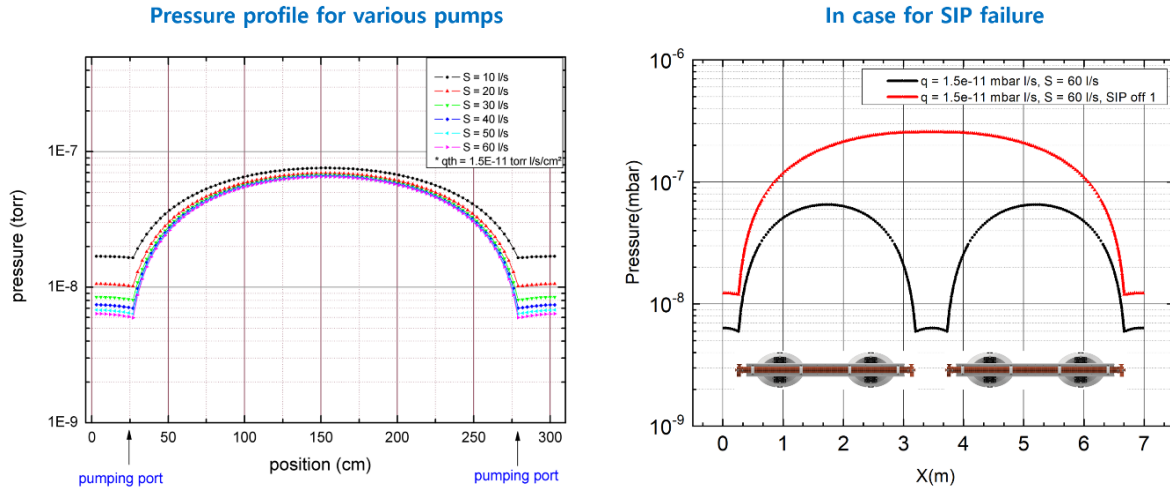
The linac consists of four 2980 mm long accelerating columns, along with various electron beam diagnostic devices and magnets positioned between the columns. The waveguide, which transmits high-frequency waves from the klystron to the two accelerating

columns, is approximately 20 meters in length. To prevent electrical breakdown in these components, the vacuum level should be kept below 10^{-7} mbar, while a pressure of 10^{-5} mbar or lower is required to minimize electron scattering. Typically, the vacuum system maintains a base pressure in the medium range of 10^{-9} mbar after RF conditioning, and a working pressure of around 10^{-8} mbar during operation. The waveguide is made of oxygen-free copper with a thermal outgassing rate (q_{th}) of less than 3×10^{-11} mbar·L/(s·cm²), and its internal dimensions (34×72 mm) conform to the WR284 standard, providing sufficient conductance to achieve ultra-high vacuum (UHV). In contrast, although the accelerating columns are also made of oxygen-free copper with a similarly low gas release rate, their internal diameter of just 22 mm and length of 3 meters result in poor vacuum conductance. <Figure 2.1.8.3> illustrates the accelerating column structure with vacuum components.



<Figure 2.1.8.3> Accelerating column structure with vacuum components.

<Figure 2.1.8.4> shows vacuum profiles for various pumping speeds and the locations of ion pumps. Sputter ion pumps with a pumping speed of 60 L/s, located at both ends of the accelerating column, are sufficient to maintain the vacuum level at a low 10^{-8} mbar. Even in the event of a failure of one of the sputter ion pumps, the average pressure of the system remains below 10^{-7} mbar.



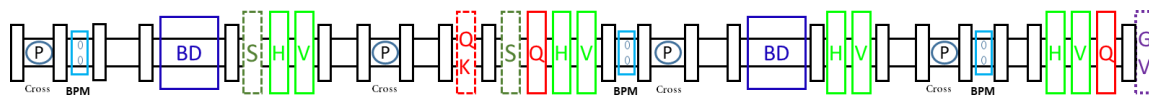
<Figure 2.1.8.4> Vacuum profiles for various pumping speeds and the locations of ion pumps.

C. Booster Vacuum System

(1) Overview and requirements of the booster vacuum system

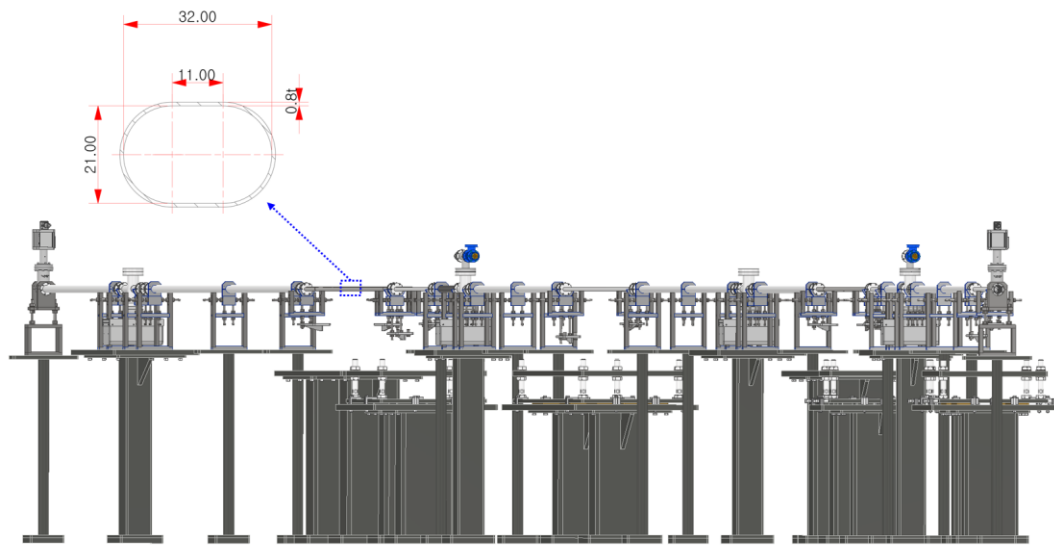
The booster vacuum system provides an optimal vacuum environment tailored to the appropriate dimensions, enabling the acceleration of 0.2 GeV electrons received from the linear accelerator to 4 GeV before transferring them to the storage ring. The booster accelerates electron bunches with a maximum current of 0.0012 amperes within a 250-millisecond ramp-up time of the electromagnets.

The booster consists of 30 cells. Four of these cells, located near the high-beta cells of the storage ring, include one dipole magnet with a bending angle of 5.02° , one dipole magnet with a bending angle of 6.07° , four quadrupole magnets, and three sextupole magnets. The remaining 26 cells, arranged in a repeating structure, consist of two dipole magnets with a bending angle of 6.07° , two quadrupole magnets, and two sextupole magnets. Additionally, a total of 10 skew quadrupole magnets are placed in specific cells: #3, #5, #8, #11, #13, #18, #20, #23, and #26. The typical layout of a single cell is shown in <Figure 2.1.8.5>.



<Figure 2.1.8.5> Layout of a single cell of the booster vacuum system
(B: dipole magnet chamber, Q, QK: quadrupole magnet chamber, S: sextupole magnet chamber, C: corrector chamber, D: straight section chamber).

The booster vacuum system is divided into 30 vacuum sectors, with one gate valve installed per cell to simplify maintenance. A super door is installed at the injection section of the storage ring, and the remaining three super doors are positioned at 90-degree intervals around the section to facilitate the transport of large equipment. When equipment is moved through these super doors, the chamber must be removed. To prevent the entire cell from being vented to air during this process, two additional gate valves are installed near each super door. As shown in Figure 3.1.8.6, the modeling of one booster cell vacuum chamber is presented.



<Figure 3.1.8.6> Cross-sectional dimensions of the magnet chambers and the one-cell model of the booster vacuum system.

The inner cross-section of the booster vacuum chamber is designed in a racetrack shape, as illustrated in Figure 3.1.8.6, taking into account the beam stay clear and the vertical gap of the magnets. The chamber is fabricated from stainless steel with a wall thickness of 0.8 mm. For the straight sections without magnets, the chamber is designed with a diameter of 38.7 mm and a thickness of 2 mm.

The booster accelerates electrons by varying the magnetic field strength of the electromagnets, during which induced currents are generated on the surface of the vacuum chamber. Among the various effects of induced currents, from a vacuum perspective, they can lead to increased outgassing due to the temperature rise of the chamber, which should be considered. During the short acceleration cycle, electron beam loss due to scattering with gas molecules is negligible, so a vacuum level of approximately 10^{-8} mbar is sufficient. The main source of outgassing in the booster is thermal desorption, while outgassing caused by synchrotron radiation contributes only a small percentage.

(2) Eddy current heating effect

To minimize the effects of eddy currents, the material for the dipole magnet vacuum chamber must have high electrical resistivity. 316L stainless steel is suitable as it has relatively high electrical resistivity, excellent mechanical strength, low magnetic permeability, ease of fabrication, and superior vacuum properties.

When a magnetic field pulse is generated in the magnet chamber, eddy currents are induced in opposition to the changing magnetic field. These currents can cause heating of the chamber and affect the stability of the electron beam. In particular, when the vacuum chamber has a racetrack shape cross-section, the eddy currents can be approximated as shown in (Equation 2.1.8.1).

$$I = \frac{\dot{B}dR^2 \sin \phi}{\rho} \quad (\text{Eq. 2.1.8.1})$$

In (Equation 2.1.8.1), d is the thickness of the chamber wall, and R is the radius of the chamber cross-section, with units in meters m. ρ is the electrical resistivity of 316L stainless steel, which is $7.4 \times 10^{-7} \Omega\text{-m}$. The vacuum chamber cross-section is racetrack shape, and ϕ is 90° . When the electron beam energy changes from 0.2 GeV to 4 GeV, the magnetic field changes at a frequency of 2 Hz, and the maximum value of \dot{B} reaches 5.8 T/s. The energy dissipated per unit time in the vacuum chamber due to eddy currents is given by (Equation 2.1.8.2).

$$P = \frac{4\dot{B}^2 dLR^3}{\rho} \left(\frac{\phi}{2} + \frac{\sin 2\phi}{4} \right) \quad (\text{Eq. 2.1.8.2})$$

For the booster dipole magnet chamber, the cross-sectional radius is 12 mm, and the length L is 1.8 m. In this case, the eddy current generated in the vacuum chamber, as calculated using (Equation 2.1.8.1), is approximately 0.79 A. The average power per dipole magnet chamber is about 0.25 W, with a power density of 10^{-3} W/cm^2 . Therefore, the resulting temperature rise and the associated thermal outgassing are expected to be negligible. Similarly, for the multipole magnet chambers, the average power density is also below 10^{-3} W/cm^2 , so the temperature rise and thermal outgassing are considered insignificant.

<Table 2.1.8.1> Eddy current and energy dissipation per unit time in the dipole magnet chamber

	\dot{B} (T/s)	ρ ($\Omega\cdot\text{m}$)	d (m)	ϕ (rad)	R (m)	L (m)	I (A)	P (W)
Dipole magnet	5.8	7.4×10^{-7}	0.0007	1.57	0.012	1.45	0.79	0.25

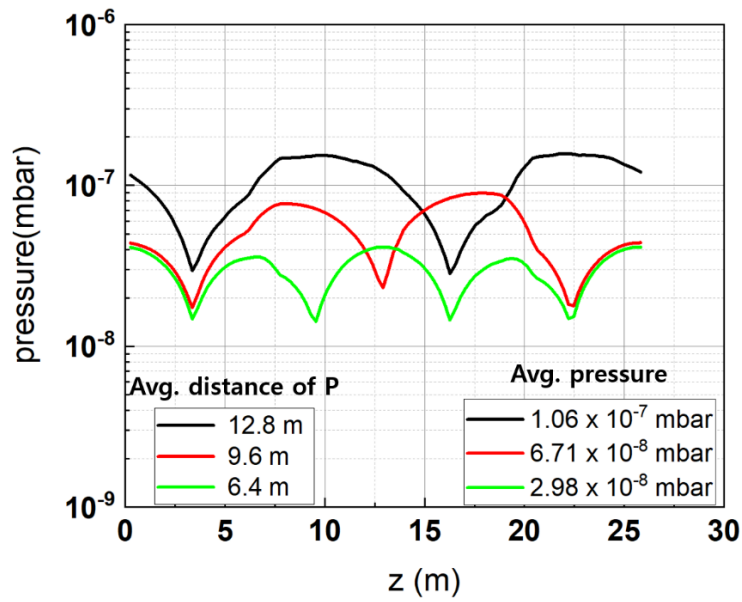
(3) Photon stimulated desorption (PSD) and vacuum requirements

The booster vacuum chamber is made of 316L stainless steel. The thermally induced outgassing rate on a clean stainless steel surface decreases to below 1×10^{-10} mbar·L/(s·cm²) within a few hours after the start of vacuum pumping. The main gas components are water (H₂O), hydrogen (H₂), and carbon monoxide (CO). This corresponds to an outgassing of $< 1.16\times 10^{-7}$ mbar·L/(s·m) per unit length.

The second source of outgassing is photon-stimulated desorption (PSD). When the electron beam passes through the dipole magnets, it emits strong X-rays. These photons interact with the chamber walls, generating photoelectrons, which trigger a chain reaction that releases gas molecules from the surface. The total photon flux Γ for the booster is given in (Equation 2.1.8.3).

$$\Gamma = 8.08 \times 10^{17} I E \quad (\text{Eq. 2.1.8.3})$$

In (Equation 2.1.8.3), I is the electron beam current with units in mA, and E denotes the electron beam energy with units in GeV. According to this equation, the total number of photons generated during acceleration from 0.2 GeV to 4 GeV over 250 milliseconds at a beam current of 1.2 mA is estimated to be approximately 2.0×10^{18} . The number of gas molecules released is proportional to the PSD rate of the surface and varies depending on the surface condition, even for the same material. In the booster, photons are primarily concentrated in a narrow region along the central plane inside the vacuum chamber. During commissioning, the PSD rate can reach below 1×10^{-4} within a short period. Based on this rate, the outgassing rate for the magnet chamber is expected to be approximately 5×10^{-9} mbar·L/(s·m) per unit length, which is about 4% of the thermally induced outgassing rate and thus negligible.



<Figure 2.1.8.7> Vacuum pressure distribution and average pressure according to pump distance.

Therefore, in analyzing the vacuum level of the booster, it is sufficient to consider only thermally induced gas desorption. Using a typical gas desorption rate of 1×10^{-10} mbar·L/(s·cm²) per unit area, the vacuum distribution for one booster cell based on the spacing of vacuum pumps is shown in <Figure 2.1.8.7>. According to the calculation results, installing four sputter ion pumps with a pumping speed of 60 L/s at intervals of no more than 6.5 m per cell can achieve an average vacuum level of better than 3×10^{-8} mbar.

Additionally, performing bake-out during installation in the tunnel is expected to further improve the vacuum level. During acceleration, electron beam losses occur due to elastic scattering between electrons and atomic nucleus and bremsstrahlung scattering. Assuming a vacuum level of 1×10^{-7} mbar, the electron beam loss over 250 msec is expected to be below 1×10^{-4} , which is negligible.

<Table 2.1.8.2> Molflow+ simulation parameters and average pressure calculation results

Molflow+ simulation parameters				Results
outgassing rate (H ₂)	pumping speed (L/s)	average distance to pump (m)	number of pumps per cell	average pressure (mbar)
1×10^{-10} mbar L/s/cm ²	60	12.8	2	1.06×10^{-7}
		9.6	3	6.71×10^{-8}
		6.4	4	2.98×10^{-8}

(4) Vacuum chamber design, thermo-structural analysis, and fabrication techniques

The booster vacuum chamber is made of 316L stainless steel. The dipole magnet chamber has a racetrack-shaped cross-section with a thickness of 0.8 mm and a curved shape, featuring bending angles of 6.07° and 5.02° . Its length is approximately 1.8 m. The multipole magnet vacuum chamber is straight, also with a racetrack-shaped cross-section and a thickness of 0.8 mm, and has a maximum length of approximately 1.3 m. The straight section chamber, which is not associated with magnets, uses a standard 2.75-inch pipe. Structural analysis using ANSYS was performed to evaluate the stress and deformation of the dipole magnet vacuum chamber under atmospheric pressure.

The dipole and multipole magnet vacuum chambers are manufactured from racetrack-shaped pipes formed by drawing process, and both ends are welded to Conflat (CF) flanges..

<Table 2.1.8.3> Structural analysis and eddy current calculation results of the dipole magnet chamber according to material and thickness

	Wall (mm)	Deformation (μm)	Max.stress	I_{eddy} (A)
SS 316L	0.3	-266.64	4.96	0.339
	0.7	-119.27	2.45	0.790
	1.0	-86.45	1.77	1.129
	1.2	-73.65	1.50	1.354
Inconel 625	0.3	-321.03	4.95	0.199
	0.7	-143.59	2.41	0.464
	1.0	-104.08	1.76	0.663
	1.2	-86.64	1.50	0.795

○ Vacuum monitoring and control

Four sputter ion pumps, each with a pumping speed of 60 L/s, are installed per cell. Thus, the vacuum pressure of the booster can be monitored primarily by measuring the pump current using ion pump controllers. In addition, two cold cathode vacuum gauges are installed per cell to monitor the vacuum during initial pump-down operations. These gauges are also connected to an interlock system, enabling automatic closure of vacuum valves and emergency shutdown of critical components, such as the RF system and injection devices, in case of vacuum failures.

D. Storage Ring Vacuum System

(1) Overview and design strategy of the storage ring vacuum system

The storage ring operates at an electron beam energy of 4 GeV and can store multiple electron beam bunches, supporting a total current of up to 400 mA. The synchrotron radiation emitted by the dipole magnets releases energy at a rate of 400 kW. To minimize electron beam loss, the vacuum system of the storage ring must provide low impedance while maintaining an ultra-high vacuum to ensure a long beam lifetime. The vacuum system consists of vacuum chambers, pumps, gauges, valves, and control devices designed to sustain these conditions.

Several key challenges must be addressed in constructing the storage ring vacuum system:

Compared to conventional storage rings, a greater number of magnets are densely arranged, limiting the available space for vacuum components, which must be carefully managed.

The vacuum chamber has a narrow cross-section to fit within the tight spacing of the magnet poles, reducing gas conductance, which must be compensated for in the design.

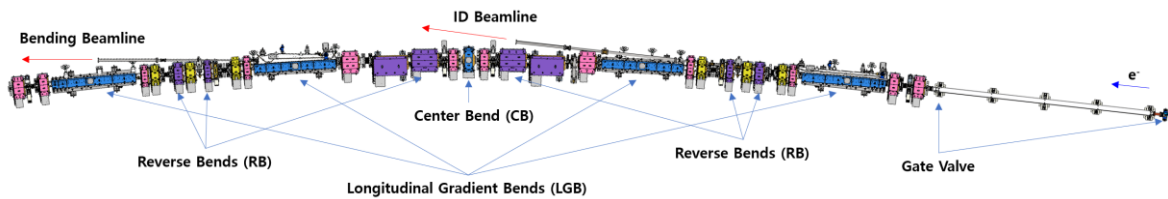
The introduction of a reverse bending magnet (RB) necessitates a detailed analysis of the radiation path. The system must be designed to efficiently absorb the heat load generated by the RB while preventing damage to other accelerator components.

The system must also handle the high-density thermal loads induced by synchrotron radiation from the strong center bending (CB) magnets, which operate at 1.96 T.

The storage ring consists of 28 cells, each comprising a curved section of approximately 22 m and a straight section of about 6.5 m. The curved sections contain a dipole magnet, quadrupole and sextupole magnets, a correction magnet, and a beam position monitor (BPM). Additionally, a beam extraction tube is installed in the curved sections to direct synchrotron radiation toward the beamline. (<Figure 2.1.8.8>)

Among the straight sections, one of the specially designated high-beta sections is allocated for the installation of the storage ring injection system, while another accommodates four RF cavities. Additionally, two of the regular straight sections are planned to contain the remaining RF cavities. In the remaining 24 straight sections, insertion devices (IDs) can be installed to provide synchrotron radiation for beamline experiments. RF-shielded gate valves are installed at both ends of each curved section, isolating them

from the straight sections. When considering the segments between the gate valves as independent vacuum sections, the storage ring consists of a total of 56 vacuum sections.



<Figure 2.1.8.8> Configuration of a single cell in the storage ring.

To address these challenging issues, the design strategy of the storage ring vacuum system has been devised as follows:

Distributed pumping system using “**Pill-type NEG**s”

In-situ bake-out: Bake-out and NEG activation conducted inside the tunnel

Optimized beam cleaning: Maximizing chamber wall exposure to synchrotron radiation for rapid beam conditioning

Two-step installation process:

- Pre-assembling magnets and vacuum chambers on a girder outside the tunnel
- Connecting chambers between girders using bellows inside the tunnel

Low-impedance design:

- 24×18 octagon-shaped e-beam channel with 4 mm high winglets for synchrotron radiation handling
- Transition angles kept below 1:10
- Gate valves with comb-type RF-shielding
- No components protruding into the beam channel (cross-section changes only in the winglet)

(2) Lifetime

The average pressure in the storage ring should be designed to be maintained below 1×10^{-8} mbar. At this vacuum degree, the residual gas component is mostly hydrogen partially mixed with carbon monoxide. The effect of residual gas on the electron beam lifetime is realized via three mechanisms:

electron-electron elastic collision scattering (σ_e), electron-atomic elastic collision scattering (σ_N), and electron-atomic inelastic collision scattering (Bremsstrahlung, σ_B). The collision cross-sectional areas σ_e and σ_N gradually decrease as the energy of the electron beam increases, whereas σ_B does not depend on the electron beam energy at the GeV level. The cross-sectional areas of the three types of collisions are commonly proportional to the atomic number Z of the residual gas. The lifetime τ_{B-G} due to beam gas scattering is calculated as

$$\tau_{B-G} = \frac{1}{nc(\sigma_e + \sigma_N + \sigma_B)} \quad (\text{Eq. 2.1.8.4})$$

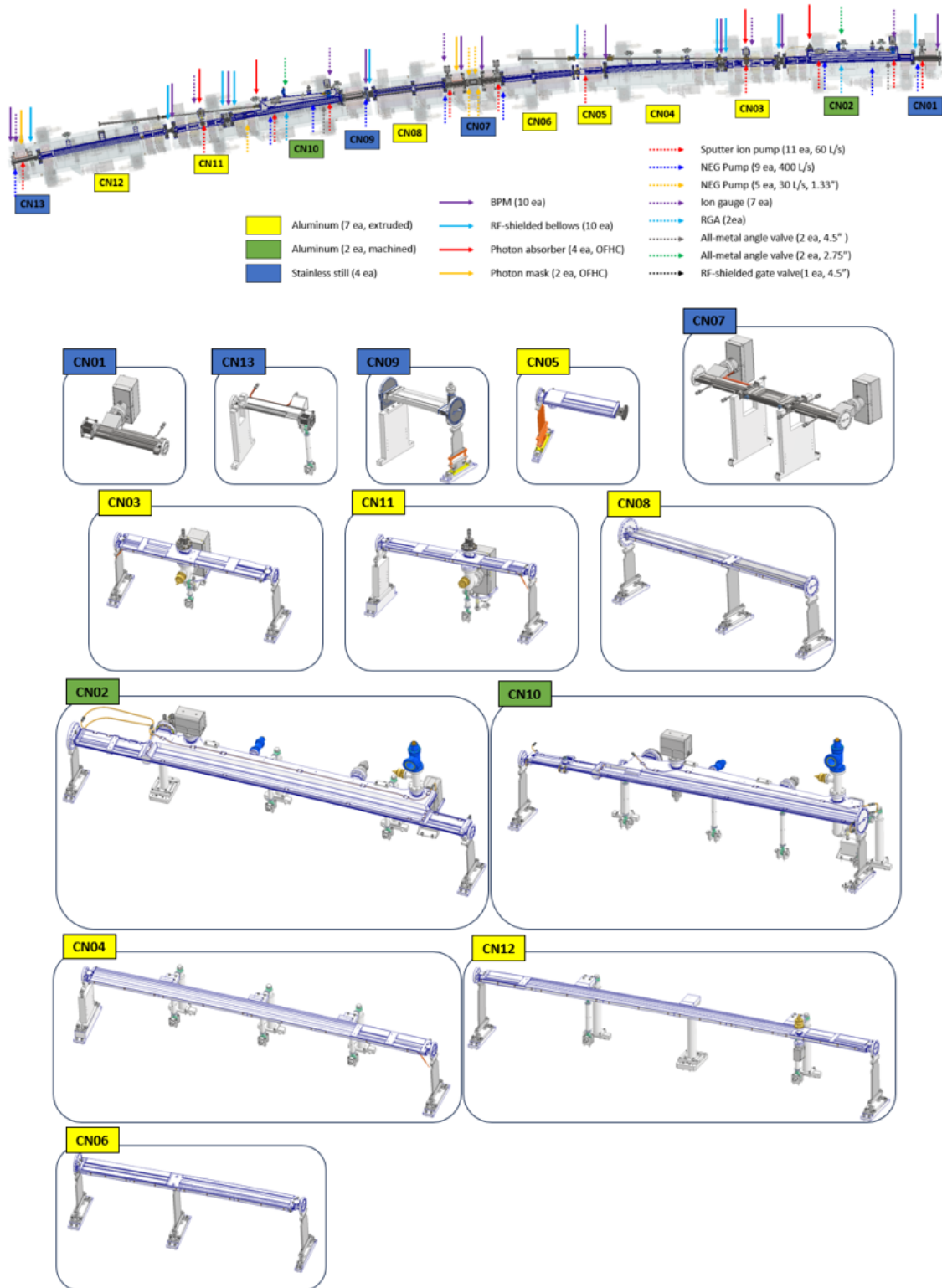
where c refers to the electron velocity at 3×10^{10} cm/sec, and n refers to the gas density, which can be calculated as $2.4 \times 10^{16} \times p$ [cm⁻³] for pressure p [mbar]. The beam-gas scattering lifetime for a mixture gas made up of 86% hydrogen and 10% carbon monoxide of 1×10^{-9} mbar is as shown in <Table 2.1.8.4>. At a vacuum degree of 1×10^{-8} mbar, the beam-gas scattering beam lifetime τ_{B-G} is approximately 10 hours, which is sufficiently longer than the Touschek beam lifetime [7] of several hours due to electron-electron scattering in a bunch. Nevertheless, it is desirable to maintain a vacuum degree of 10^{-9} mbar or more because ionized gas particles may be confined due to the short bunch interval between electron beams and cause ion instability.

<Table 2.1.8.4> Beam-gas scattering cross-sectional area and beam-gas scattering lifetime for mixed gases made up of 86% hydrogen, 2% methane, 1% water, 10% carbon monoxide, and 1% carbon dioxide at 10^{-9} mbar

1. Total beam-gas lifetimes (nTorr h)		H2	CH4	H2O	CO	CO2
1. W/O IVUN	313.16	1150.68	112.98	128.10	53.02	32.81
		86.0%	2.0%	1.0%	10.0%	1.0%
		1,338.0026	5,648.947	12,809.891	530.2312	3,281.065905
2. With IVUN	99.20	414.05	37.12	41.22	16.09	9.93
		86.0%	2.0%	1.0%	10.0%	1.0%
		481.45569	1,855.931	4,121.8575	160.89928	992.6854164
		99.19756				
2. Bremsstrahlung lifetime (nTorr h)						
1 and 2. With or W/O IVUN	340.47	1232.18	122.27	138.99	57.97	35.89
		86.0%	2.0%	1.0%	10.0%	1.0%
		1,432.7719	6,113.469	13,899.1	579.70379	3,588.634155
		99.19756				
3. Coulomb lifetimes (nTorr h)		H2	CH4	H2O	CO	CO2
1. W/O IVUN	3905.10	17396.62	1486.89	1634.64	621.31	382.83
		86.0%	2.0%	1.0%	10.0%	1.0%
		20,228.627	74,344.53	1,63463.65	6,213.0782	3,8282.70694
2. With IVUN	139.98	623.60	53.30	58.60	22.27	13.72
		86.0%	2.0%	1.0%	10.0%	1.0%
		725.11766	2,664.962	5,859.5366	222.71471	1,372.286262

(3) Vacuum chambers and components

The vacuum chambers for the curved sections primarily consist of extruded aluminum chambers with integrated Pill-NEGs, and stainless steel chambers for fast correctors and Beam Position Monitors (BPMs). Additionally, two machined aluminum chambers are used for photon beam extraction, as depicted in <Figure 2.1.8.9>. The numerous Pill-NEGs serve as the primary pumping mechanism, while eleven sputter ion pumps (60 L/s) and ten NEG cartridges (400 L/s) provide supplementary pumping. Vacuum quality is monitored by five ion gauges and two Residual Gas Analyzers (RGAs). To accommodate thermal expansion and facilitate installation, ten RF-shielded bellows are incorporated.



<Figure 2.1.8.9> Configuration of the vacuum components in a storage ring curved section.

(4) Vacuum profile calculation

The pressure of the storage ring during beam operation is determined by the Photon Stimulated Desorption (PSD). As the electron beam passes through the dipole magnet and its path bends, the electron beam emits a large number of photons, which hit the wall of the downstream vacuum chamber to generate photo-induced electrons. The secondary electrons generated at this time hit the chamber wall again, and induce degassing. The PSD rate η refers to the number of gas molecules emitted per photon, weakly dependent on the energy of the photon and the angle of incidence and strongly dependent on the surface state of the chamber wall. Although the initial PSD rate is as high as a few percent, the PSD rate rapidly decreases as the exposure of photons increases with the continuation of the operation. The photon exposure is mainly represented as the product of the beam current [A] and the exposure time [h], and the relationship between the PSD rate and dP/dI is shown in <Figure 2.1.8.10>. In this log-log graph, the PSD rate slope is usually found to be approximately 0.6 \sim 0.7. The amount of light Γ during beam operation in the storage ring is represented as

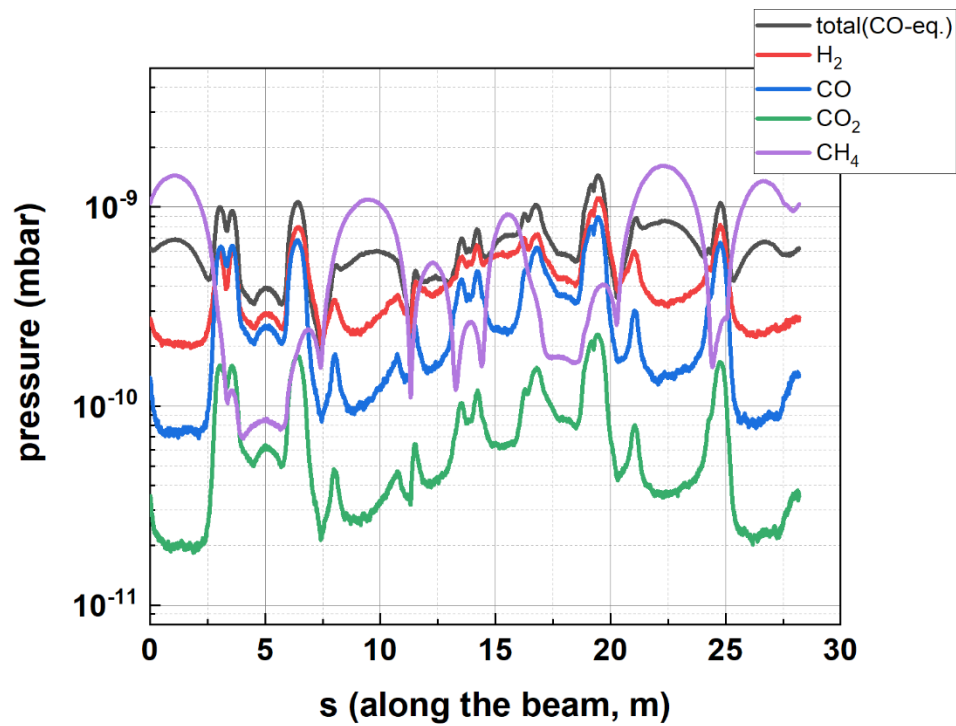
$$\Gamma = 8.08 \times 10^{17} \times I(\text{mA}) \times E(\text{GeV}). \quad (\text{Eq. 2.1.8.5})$$

At 4 GeV and 400 mA, the total photon flux (Γ) in the storage ring is 1.3×10^{21} photons/s, with a flux density of 1.6×10^{18} photons/s/m per unit length. If the photon-stimulated desorption (PSD) yield (η) is 1×10^{-6} , this results in the release of 1.6×10^{12} molecules/s/m, equivalent to 6×10^{-8} mbar·L/s/m of gas. To achieve an ultra-high vacuum of approximately 10^{-10} mbar, a pumping speed of at least 100 L/s/m is required.

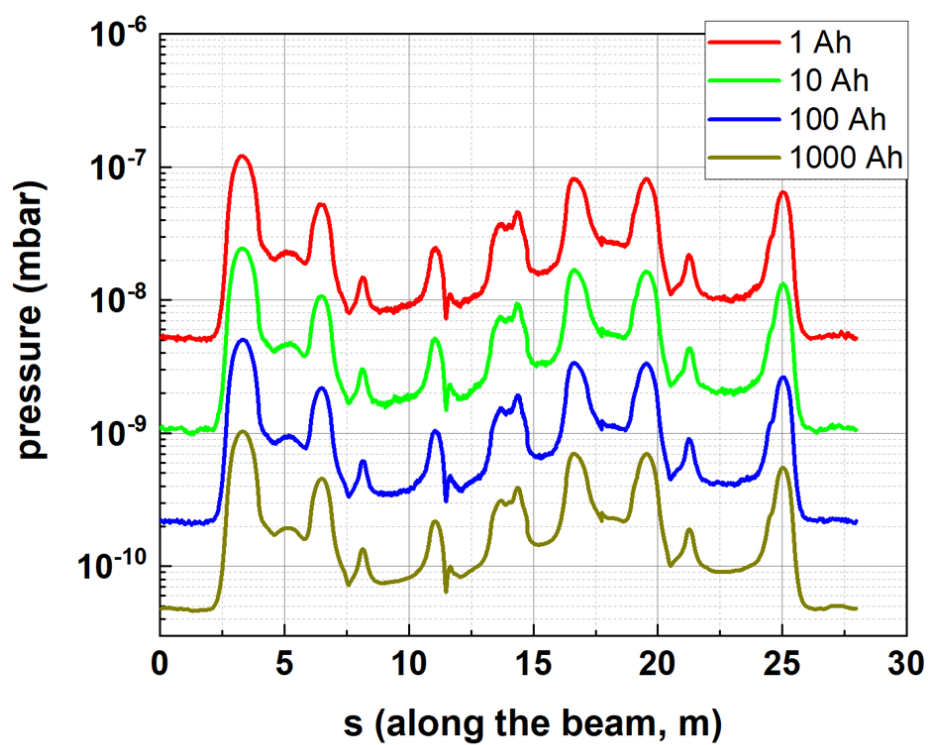
The NEG strip, composed of a Zr-V-Fe alloy, provides a pumping speed of over 1000 L/s/m. While a distributed vacuum pumping system meets the capacity requirements, its installation is constrained by the limited space within the vacuum chamber. The Pill-NEG, as shown in <Figure 2.1.8.1>, has been successfully deployed and operated in the PLS-II storage ring for several years, demonstrating its effectiveness as a distributed vacuum pumping solution. Although the Pill-NEG has a lower pumping speed compared to conventional NEG strips, its ability to fit within confined spaces makes it a viable alternative for storage ring applications, provided that its pumping efficiency can be enhanced. With an activation temperature of 320°C for 24 hours, the Pill-NEG achieves a pumping speed of 50 L/s/m per unit length. When arranged in two rows, a total pumping capacity of 100 L/s/m can be obtained.

The PSD was calculated using the software programs SynRad and MolFlow [13, 14], and

in conjunction with this, the vacuum degree distribution during storage ring operation was simulated as shown in <Figure 2.1.8.11>.



<Figure 2.1.8.10> Partial pressure profile at fully cleaned stage.



<Figure 2.1.8.11> CO equivalent total pressure profile during beam operation.

(5) Photon absorber and beam handling in storage ring

Managing the powerful photon beam generated by bending magnets or insertion devices in synchrotron accelerators is critical to maintaining the performance of the accelerator. Photon beams of Korea-4GSR have high intensity and a wide spectrum characteristic, and if these photon beams are not effectively blocked, thermal loads are continuously imposed on the devices constituting the storage ring. Analysis of the photon beam and structural design that absorbs and cools are essential to keep the storage ring in an ultra-high vacuum and to extend the lifetime of the accelerator device and vacuum components.

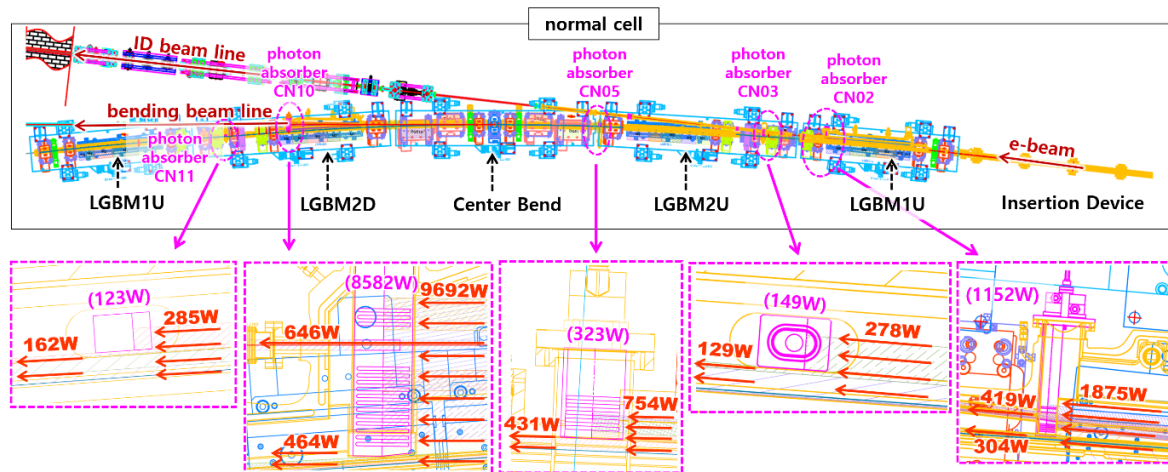
The table below shows the distribution of photon flux power, which is the photon beam energy by the bending magnets of the storage ring excluding the insertion device, and the energy absorbed by the vacuum chambers and the photon absorbers to effectively block this photon beam.

<Table 2.1.8.5> Photon beam distribution of normal 1 cell by bending magnets

Photon Flux Power Distribution	
1 cell photon power absorbed by the chambers [kW]	3.12
1 cell photon power absorbed by the absorbers [kW]	11.47
1 cell photon power to the beamlines [kW]	1.07
total power of 1 cell [kW]	15.66

<Table 2.1.8.6> Photon flux power absorbed by the photon absorbers and vacuum chambers

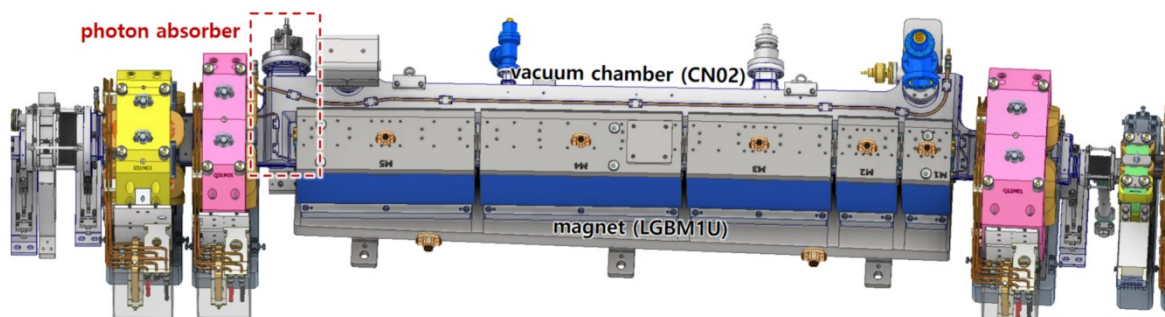
Photon Absorption Device			
Photon Absorber [W]		Vacuum Chamber [W]	
CN02 absorber	1,152.0	CN02	24.8
CN03 absorber	148.9	CN04	312.2
CN05 absorber	323.2	CN06	1375.6
CN07 mask	652.6	CN08	93.0
CN10 absorber	8,583.1	CN09	1.2
CN11 absorber	87.3	CN10	213.2
CN13 mask	442.5	CN12	559.3
ID chamber mask	83.6	ID Chamber	542.8
total power [W]	11,473.2	total power [W]	3,122.1



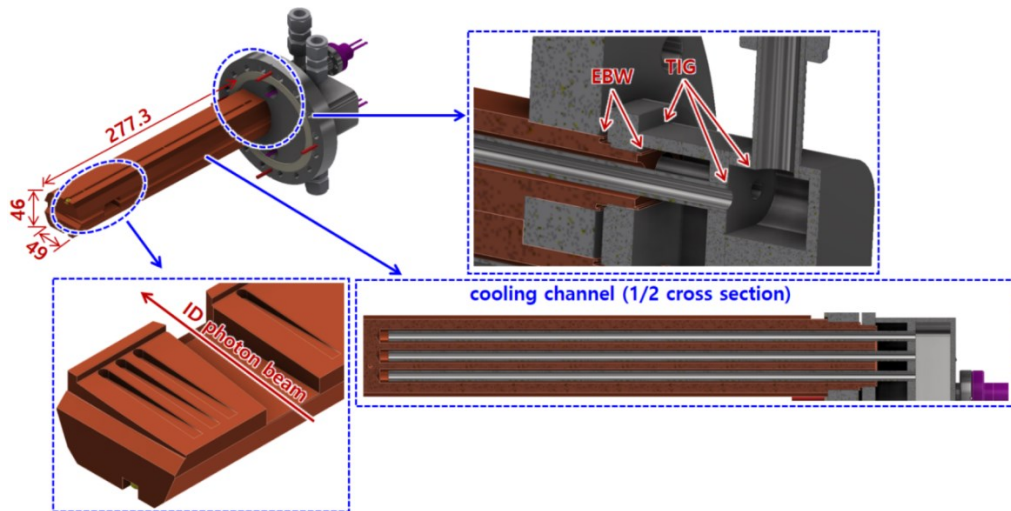
<Figure 2.1.8.12> Flux power distribution absorbed by photon absorbers.

○ Photon absorber CN02

The photon absorber installed in the vacuum chamber CN02 provides the insertion device photon beam to the beamline and absorbs the remaining photon beams to protect the vacuum chamber. The opening angle of the photon beam of the insertion device provided as the beamline is designed to be ± 1.5 mrad (horizontal) \times ± 1.0 mrad (vertical). In addition, it is designed to stably absorb the photon beam generated from EPU98, which has the largest size, spreading angle, and intensity of the photon beam among the insertion devices, and to avoid interference with the vacuum chamber and surrounding magnets. The interlock condition of the electron beam trajectory for device protection is ± 0.1 mrad ± 400 μ m, and the photon absorber is designed to be safe from the leaking photon beam even if the electron beam trajectory at both ends of the insertion device deviates to the allowable maximum.



<Figure 2.1.8.13> The location of the CN02 photon absorber.

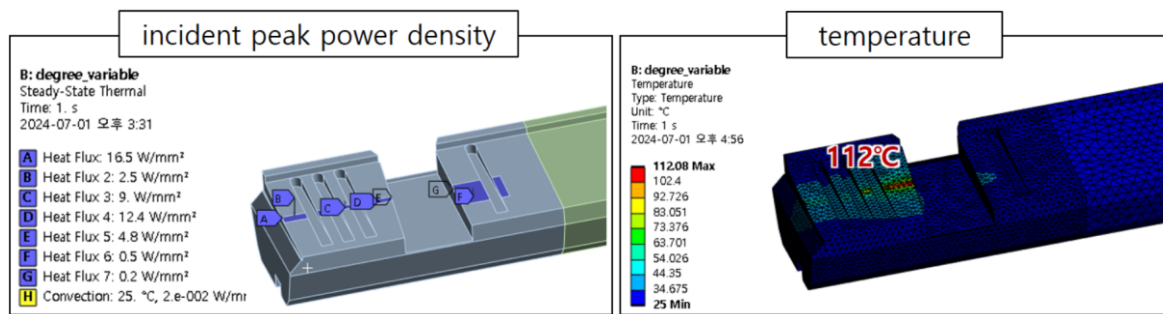


<Figure 2.1.8.14> Dimension and internal shape of the photon absorber CN02.

The photon flux absorbed by the CN02 photon absorber is a photon beam by the bending magnet LGBM1U and the LGBM1D magnet in the previous cell, and the photon flux power is 1,152W. The photon absorber is designed as a cooling channel to disperse heat and be sufficiently cooled by the LCW. The peak power density was examined by adjusting the incident angle to satisfy the mis-alignment condition $\pm (1\text{mrad} + 0.4\text{mm})$. The analysis results below are based on the case where the incident angle is 7 degrees, and the maximum temperature is 112°C.

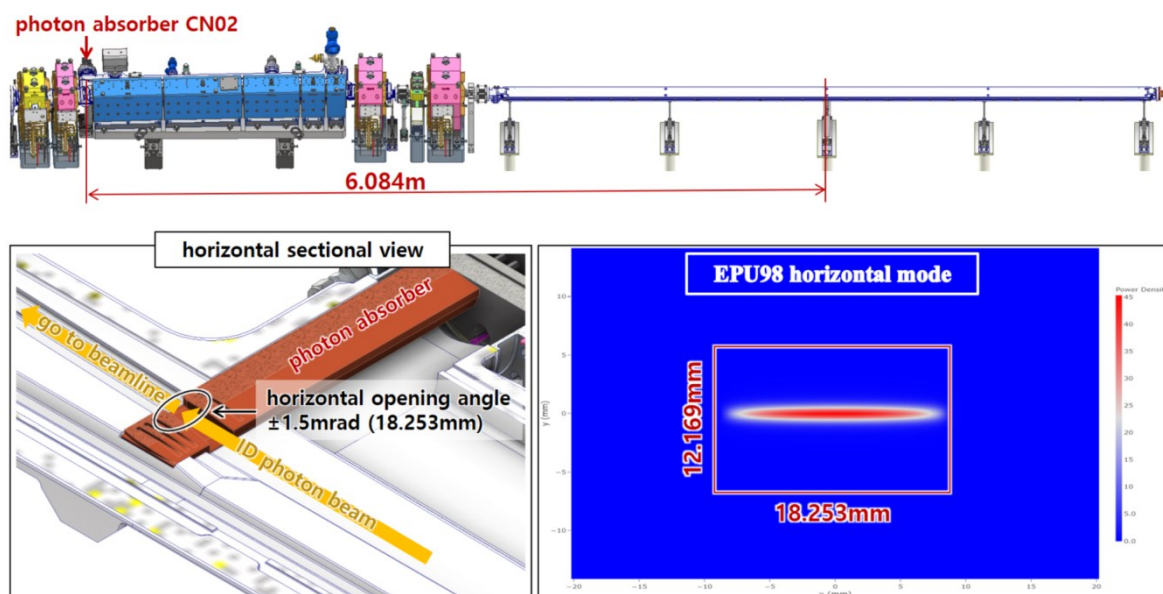
<Table 2.1.8.7> Photon flux power absorbed by the photon absorber CN02

Source magnet	B [T]	Incident angle [°]	Power [W]	Incident peak power density [W/mm ²]
M5 (LGBM1D)	0.734	7	154.3	0.5
M1 (LGBM1U)	0.734	7	373.1	12.4
M2 (LGBM1U)	0.430	7	309.0	9.0
M3 (LGBM1U)	0.287	7	311.0	2.5
M4 (LGBM1U)	0.197	7	4.7	16.5
total power			1152.0	

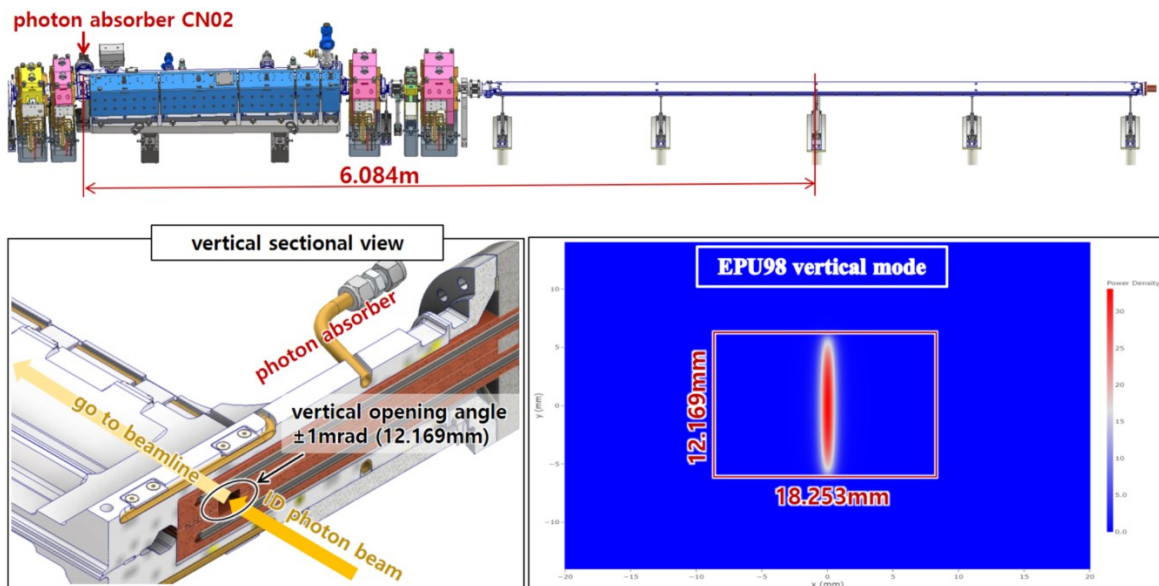


<Figure 2.1.8.15> Peak power density and temperature absorbed by the photon absorber CN02.

The photon flux absorbed by Photon absorber CN02 must absorb not only the photon beam by the bent magnet but also the photon beam generated by the insertion device except for the desired passage angle in the beamline. In the case of the insertion device photon beam, flux power analysis and temperature analysis were performed for vertical mode and horizontal mode based on EPU98.

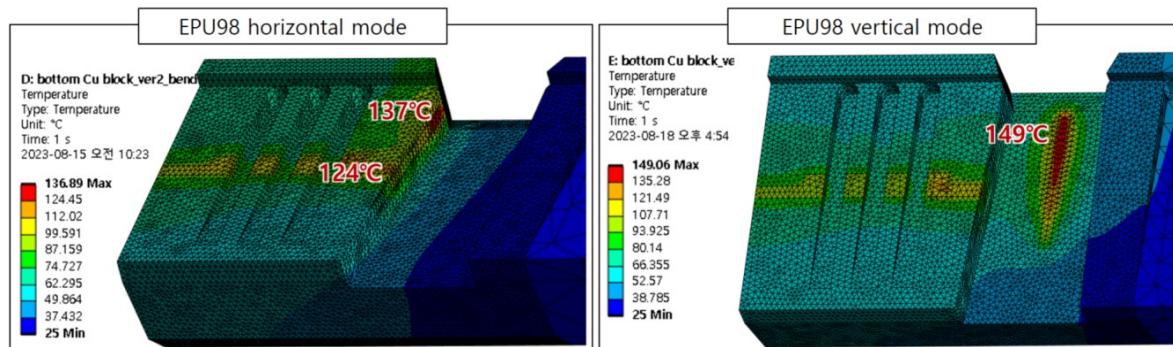


<Figure 2.1.8.16> The location of the photon absorber CN02 and opening angle for horizontal mode.



<Figure 2.1.8.17> The location of the photon absorber CN02 and opening angle for vertical mode.

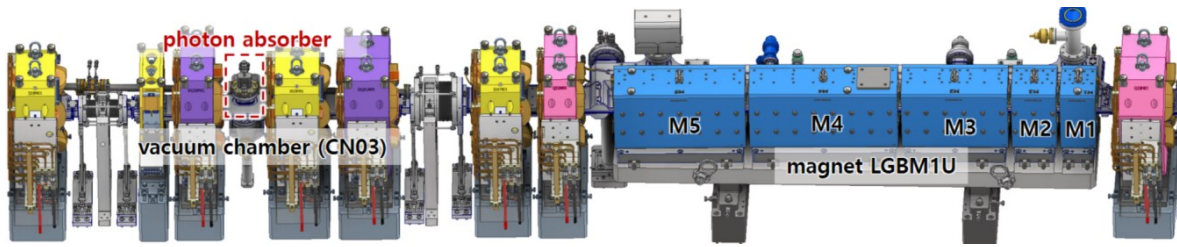
The following figure shows the results of temperature analysis for the photon flux by bending magnets and EPU98.



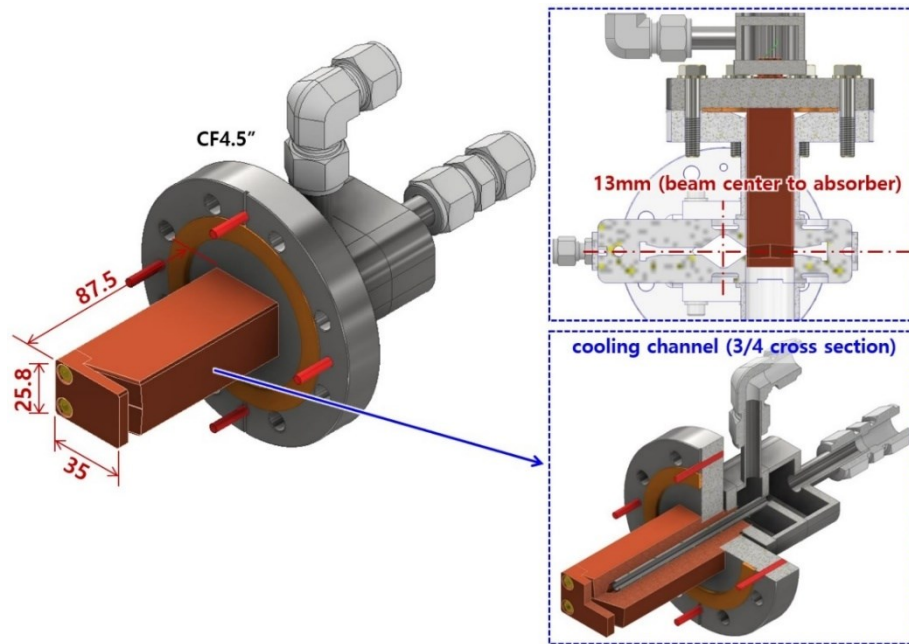
<Figure 2.1.8.18> Temperature analysis for horizontal mode and vertical mode of EPU98.

○ Photon absorber CN03

The photon absorber installed in the vacuum chamber CN03 absorbs a part of the photon beam by the bending magnet LGBM1U to protect the vacuum chamber CN03 and the RF shielded bellows. The CN03 photon absorber is a vertical type and absorbs a photon beam generated by the M4 magnet of the bending magnet LGBM1U. The photon flux power absorbed by the CN03 photon absorber is 149W.



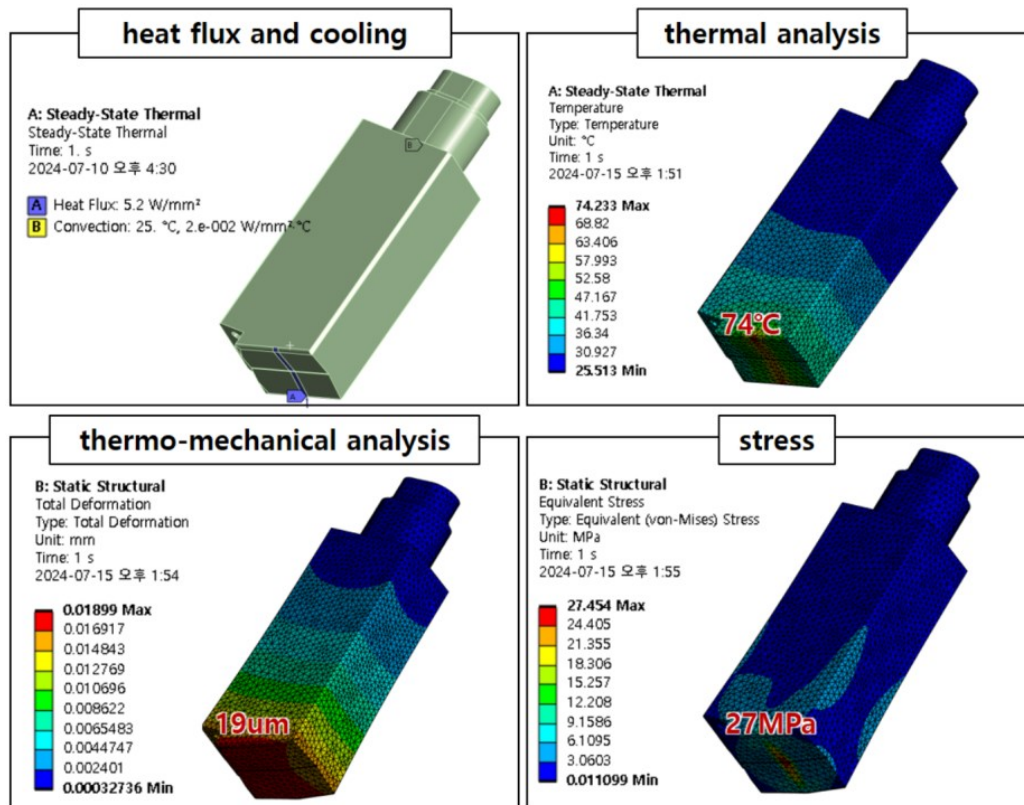
<Figure 2.1.8.19> The location of the photon absorber CN03.



<Figure 2.1.8.20> Dimension and internal shape of the photon absorber CN03.

<Table 2.1.8.8> Photon flux power absorbed by the photon absorber CN03

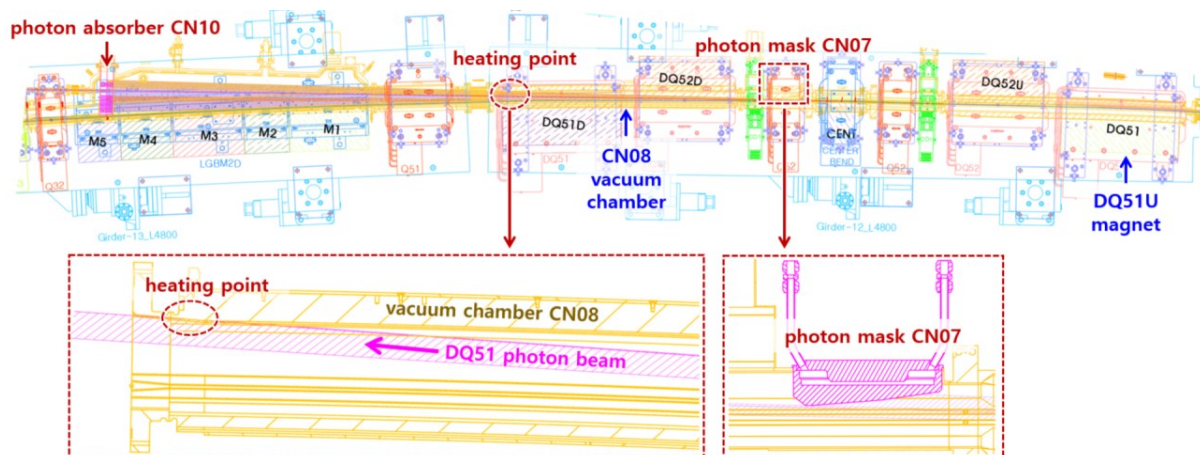
Source magnet	B [T]	Incident angle [°]	Power [W]	Incident peak power density [W/mm ²]
M4 (LGBM1U)	0.197	16	149	5.2
total power			149	



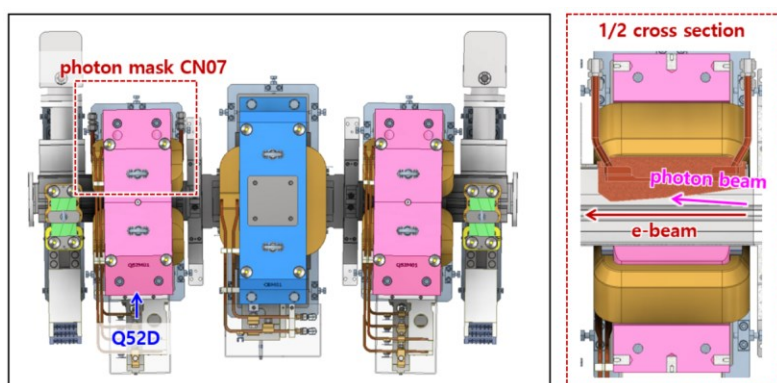
<Figure 2.1.8.21> Thermal and structural analysis results of the photon absorber CN03.

○ Photon mask CN07/CN08

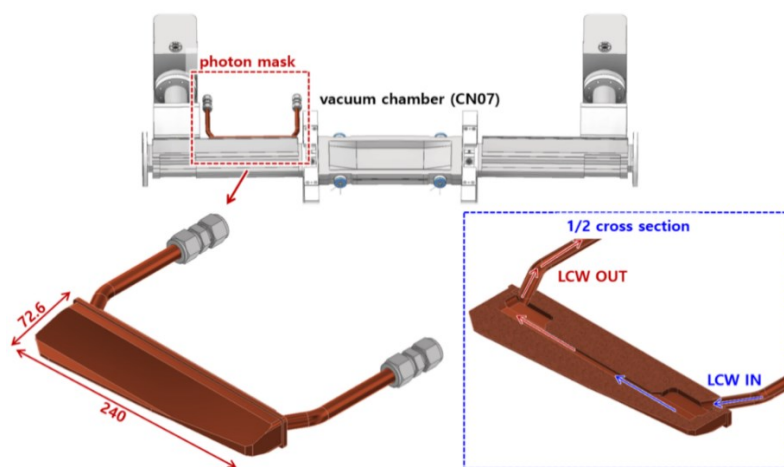
The photon mask CN07 is installed in the vacuum chamber CN07 in which the center bend magnet is installed and partially absorbs the photon beam by DQ51U. The photon beam that the photon mask could not absorb is absorbed by CN08 vacuum chamber in the downstream and the photon absorber by CN10. The design of the photon mask is difficult because five electromagnets are installed in the vacuum and the photon mask is installed inside the magnet cores of the electromagnet Q52D.



<Figure 2.1.8.22> The location of the photon mask CN07 and distribution of photon beam.



<Figure 2.1.8.23> The location of the photon mask CN07.

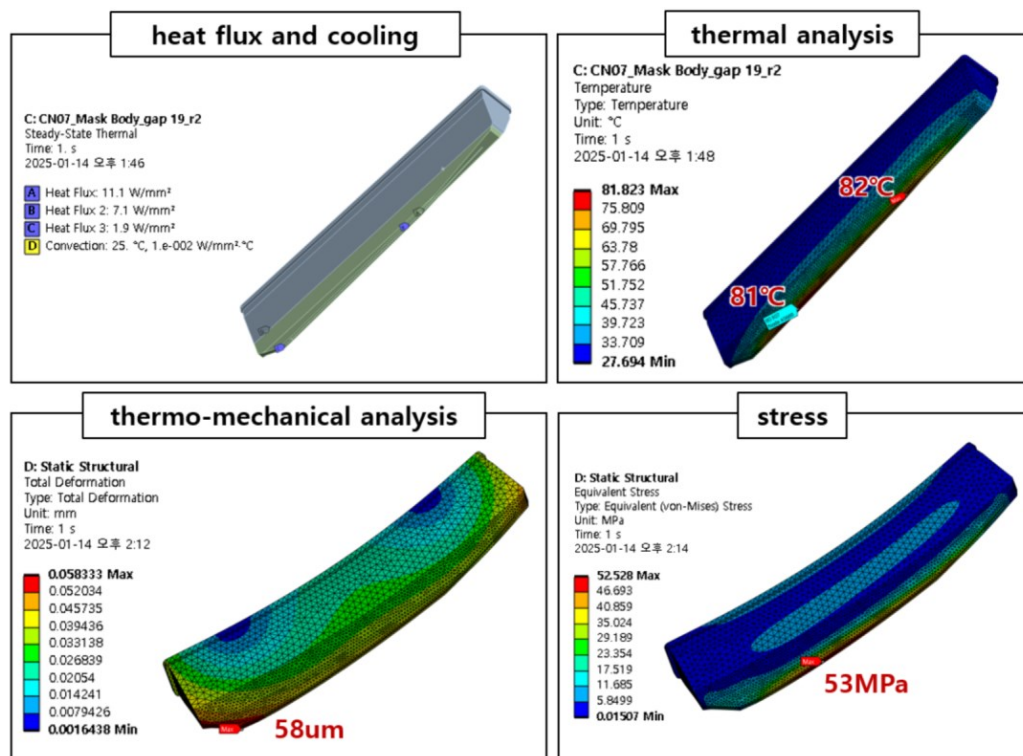


<Figure 2.1.8.24> Dimension and internal shape of the photon mask CN07.

The amount of photon flux power absorbed by the vacuum chamber CN08 in downstream varies depending on the amount of photon flux power absorbed by the photon mask CN07. Therefore, during the design of the photon mask CN07, the thermal analysis is performed while adjusting the incident angle and the amount of absorbed flux power. Additionally, the temperature of the vacuum chamber CN08 is also simulated in connection with this analysis.

<Table 2.1.8.9> Photon flux power absorbed by the photon mask CN07

Source magnet	B [T]	Incident angle [°]	Power [W]	Incident peak power density [W/mm²]
DQ51U	0.565	10.2	307	11.1
		6.1	337.6	7.1
		1.6	8.1	1.9
total power			652.7	

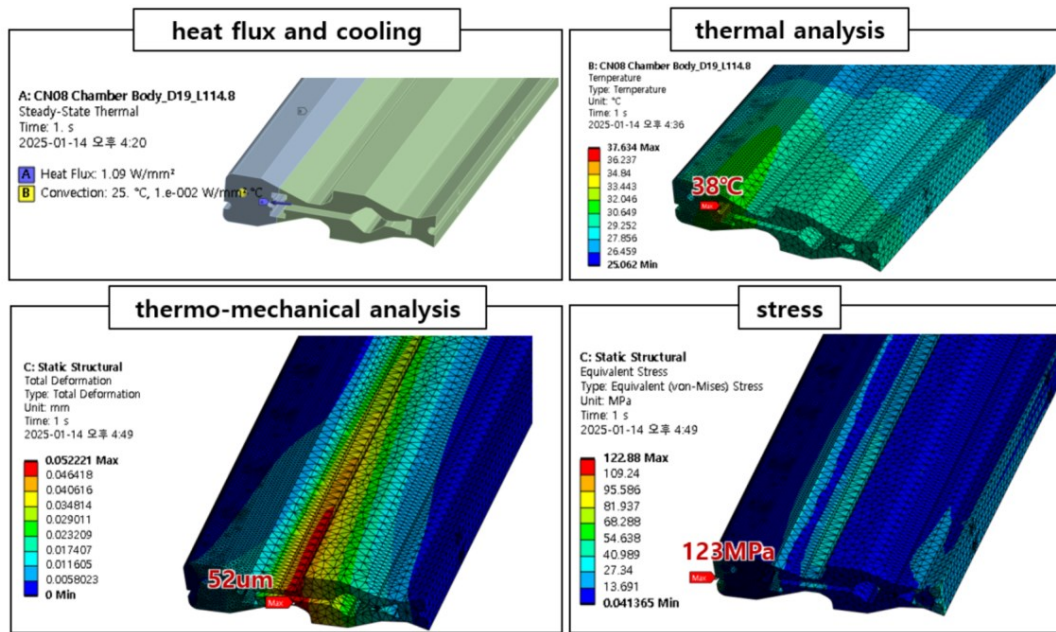


<Figure 2.1.8.25> Thermal and structural analysis results of the photon mask CN07.

The photon beam that photon mask CN07 does not absorb is partially absorbed by the vacuum chamber CN08 in the downstream, and it is confirmed that the vacuum chamber CN08 stably absorbs the photon flux power in terms of temperature and structure. Vacuum chamber CN08 is fabricated using aluminum A5083-H321, and the yield strength of A5083 is generally known as 215 MPa to 295 MPa. In this analysis, the yield strength is set to 200 MPa at room temperature and 0.5% strain.

<Table 2.1.8.10> Photon flux power absorbed by the vacuum chamber CN08

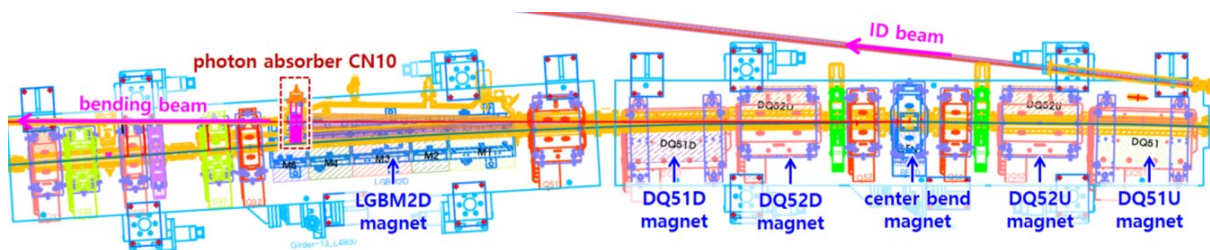
Source magnet	B [T]	Incident angle [°]	Power [W]	Incident peak power density [W/mm²]
DQ51U	0.565	3.0	93	1.09
total power			93	



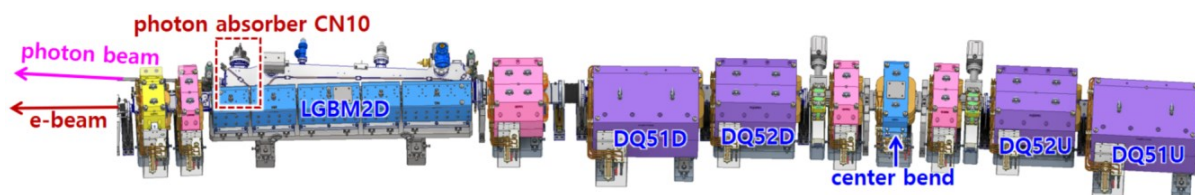
<Figure 2.1.8.26> Thermal and structural analysis results of the vacuum chamber CN08.

○ Photon absorber CN10

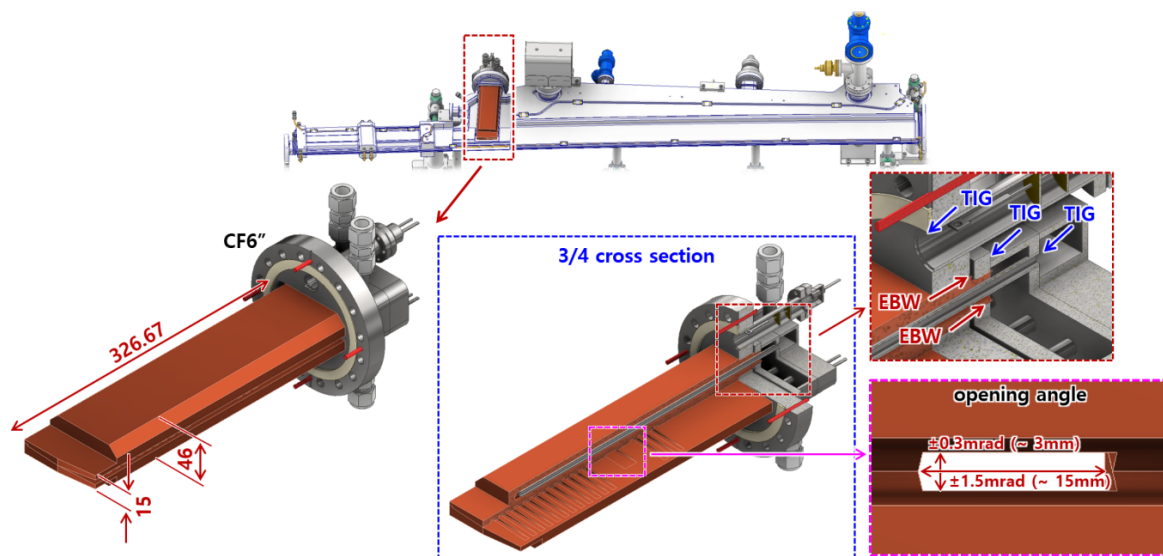
The photon absorber installed in the vacuum chamber CN10 provides the center bend magnet photon beam to the beamline and absorbs the rest of the photon beam to protect the vacuum chamber. The opening angle of the center bend magnet photon beam provided to the beamline is designed to be ± 1.5 mrad (horizontal) \times ± 0.3 mrad (vertical). To protect the downstream vacuum chamber, the photon absorber CN10 must absorb the photon beams by DQ51U, DQ52U, DQ52D, DQ51D, and LGBM2D electromagnets. Therefore, the photon absorber CN10 is designed to sufficiently absorb unnecessary photon beams while avoiding interference with nearby devices as much as possible.



<Figure 2.1.8.27> Distribution of photon beam absorbed by photon absorber CN10.



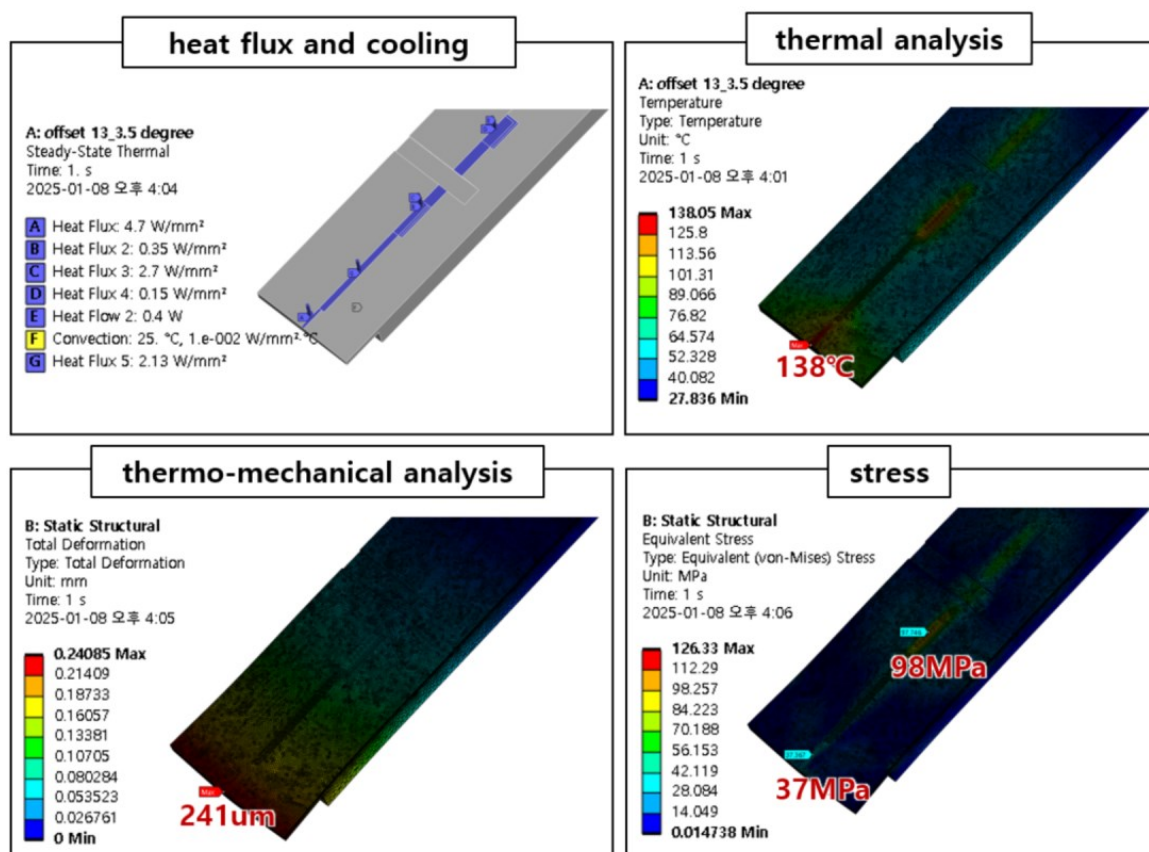
<Figure 2.1.8.28> The location of the photon absorber CN10 and distribution of bending magnets.



<Figure 2.1.8.29> Dimension and internal shape of the photon absorber CN10.

<Table 2.1.8.11> Photon flux power absorbed by the photon absorber CN10

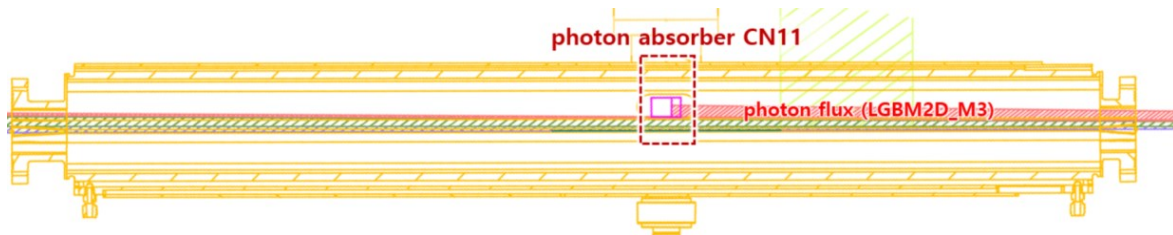
Source magnet	B [T]	Incident angle [°]	Power [W]	Incident peak power density [W/mm ²]
DQ51U	0.565	3.5	428.7	4.0
DQ52U	0.166	3.5	139.8	0.2
Center Bend	1.994	3.5	2,671.6	2.6
Center Bend	1.994	3.5	2,671.6	2.6
DQ52D	0.166	3.5	139.8	0.4
QD51D	0.565	3.5	2,120.2	1.9
M1 (LGBM2D)	0.312	3.5	410.1	4.4
total power			8,581.8	



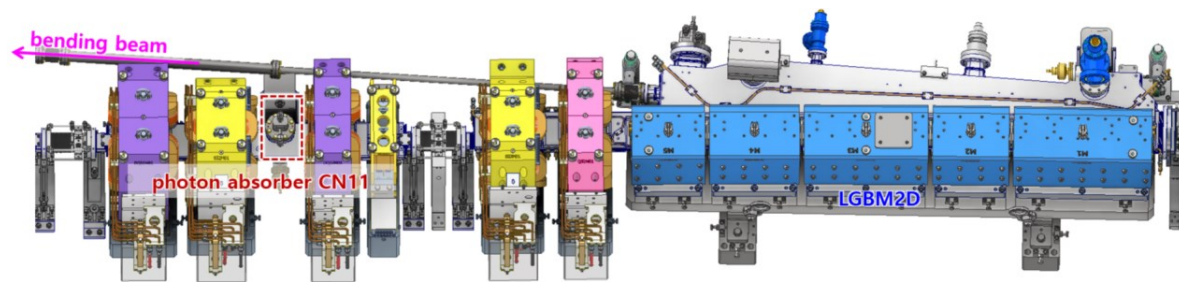
<Figure 2.1.8.30> Thermal and structural analysis results of the photon absorber CN10.

○ Photon absorber CN11

Photon absorber CN11 is installed in a vertical direction on the vacuum chamber CN11. It absorbs a part of the photon beam by the third magnet M3 of LGBM2D, allowing the extra photon beam to pass stably without being absorbed by the vacuum chamber CN11. The shape of the photon absorber CN11 has the same shape as the photon absorber CN03.



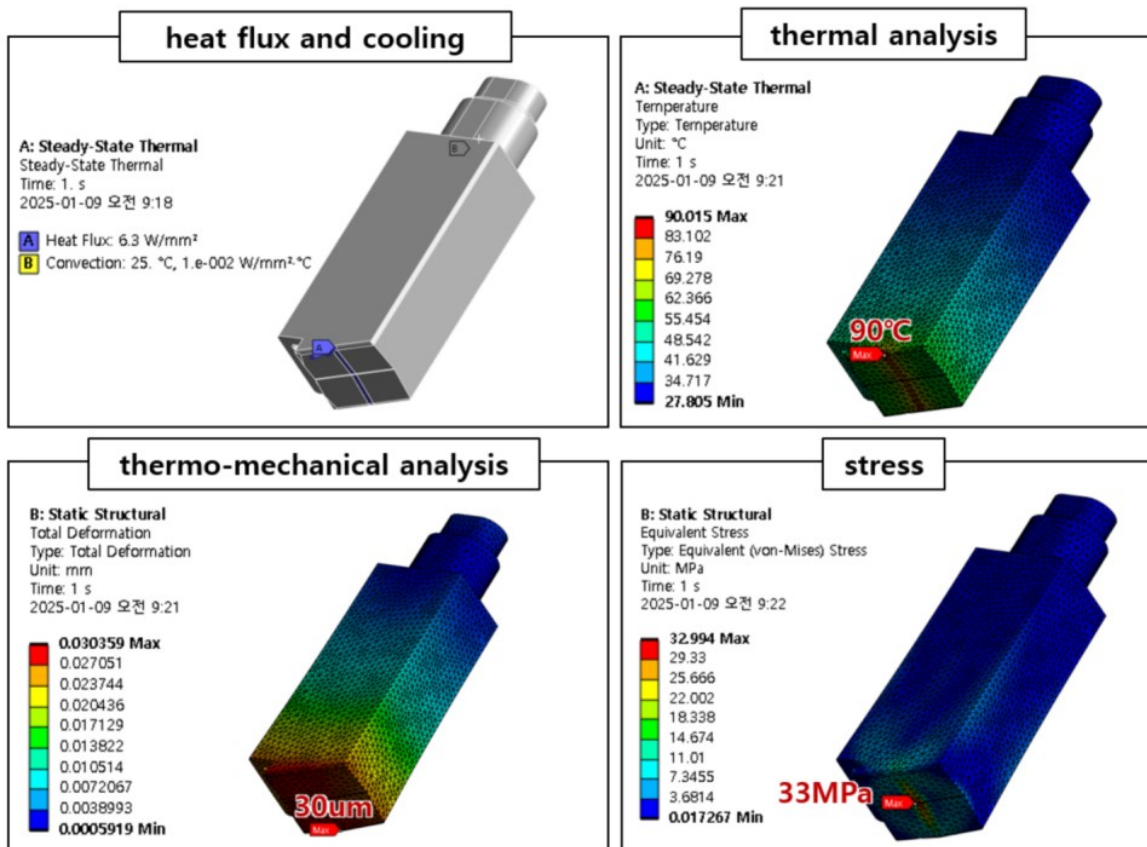
<Figure 2.1.8.31> Distribution of photon beam absorbed by photon absorber CN11.



<Figure 2.1.8.32> The location of the photon absorber CN11.

<Table 2.1.8.12> Photon flux power absorbed by the photon absorber CN11

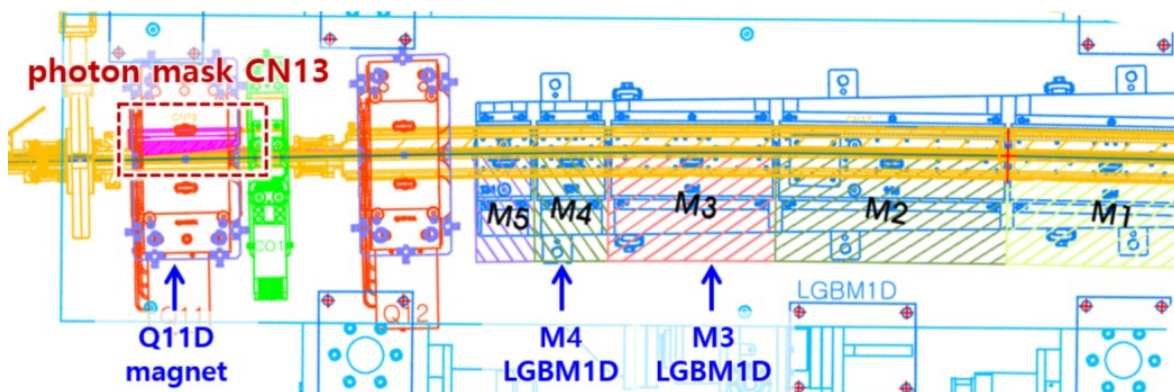
Source magnet	B [T]	Incident angle [°]	Power [W]	Incident peak power density [W/mm ²]
M3 (LGBM2D)	0.203	16	123	6.3
total power			123	



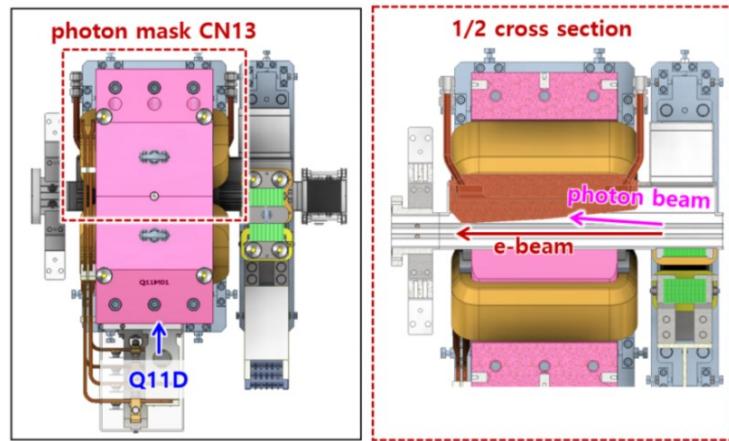
<Figure 2.1.8.33> Thermal and structural analysis results of the photon absorber CN11.

○ Photon mask CN13

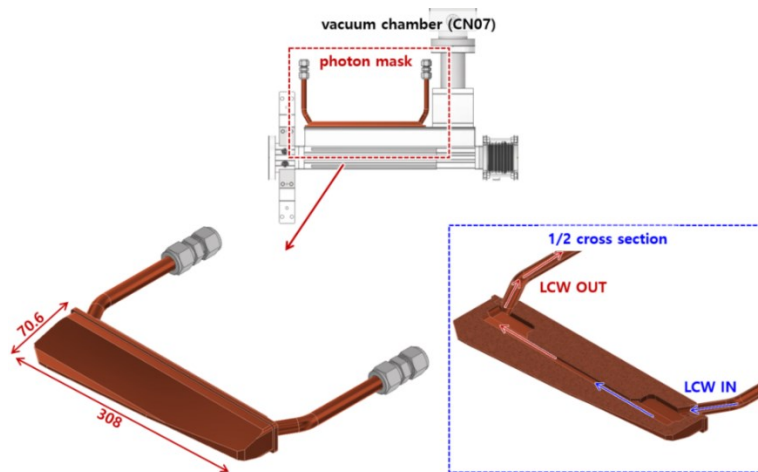
Photon mask CN13 is installed in the vacuum chamber CN13, and partially absorbs the photon beam by the third magnet M3 and the fourth magnet M4 of LGBM1D, allowing the extra photon beam to pass stably through the vacuum chamber CN13 and the RF shielded bellows in downstream.



<Figure 2.1.8.34> Distribution of photon beam absorbed by photon mask CN13.



<Figure 2.1.8.35> The location of the photon mask CN13 and nearby devices.

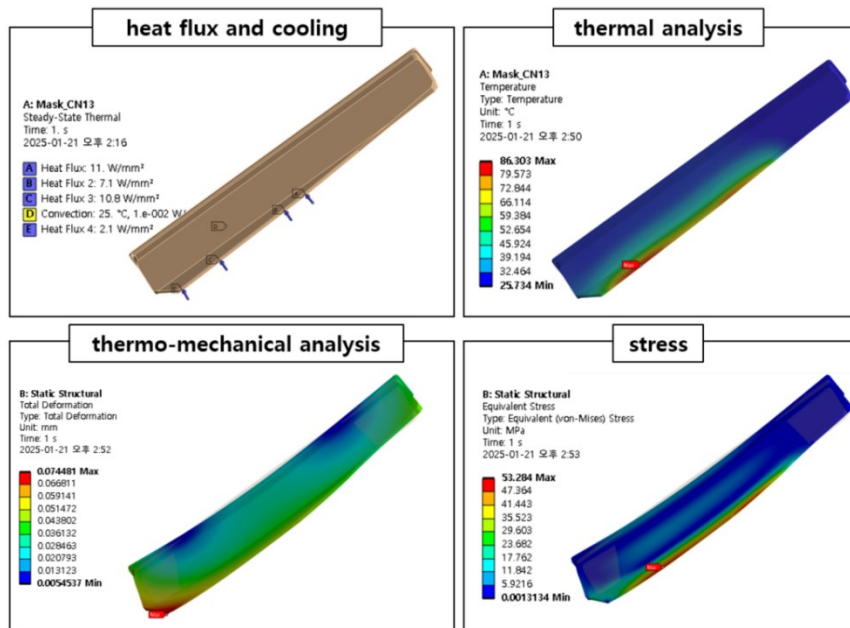


<Figure 2.1.8.36> Dimension and internal shape of the photon mask CN13.

The design of the photon mask CN13 is completed by temperature analysis according to various shapes because photon mask CN13 is greatly affected by the flux power density and temperature increase depending on the incident angle and cooling water path design. The photon beam is not absorbed by the mask is absorbed by another photon mask and the vacuum chamber in the straight section.

<Table 2.1.8.13>1 Photon flux power absorbed by the photon mask CN13

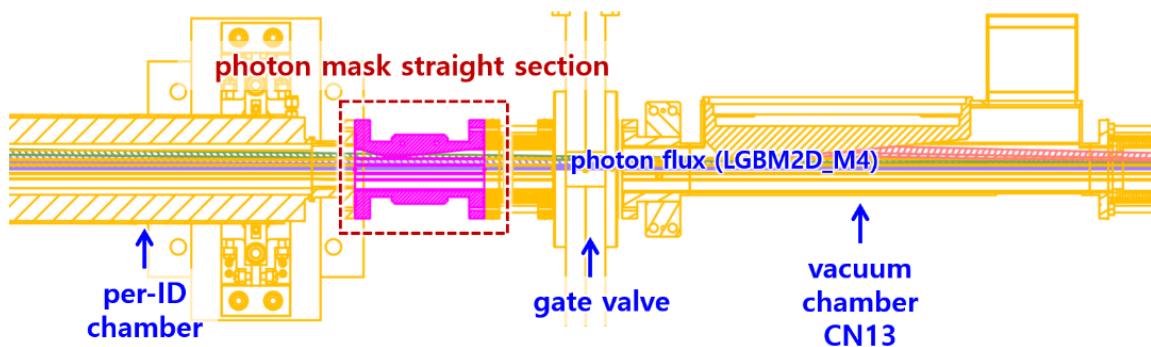
Source magnet	B [T]	Incident angle [°]	Power [W]	Incident peak power density [W/mm ²]
M3 (LGBM1D)	0.287	7.1	174	11.0
M3 (LGBM1D)	0.287	3.9	110.3	7.1
M4 (LGBM1D)	0.430	3.7	158.2	10.8
total power			442.5	



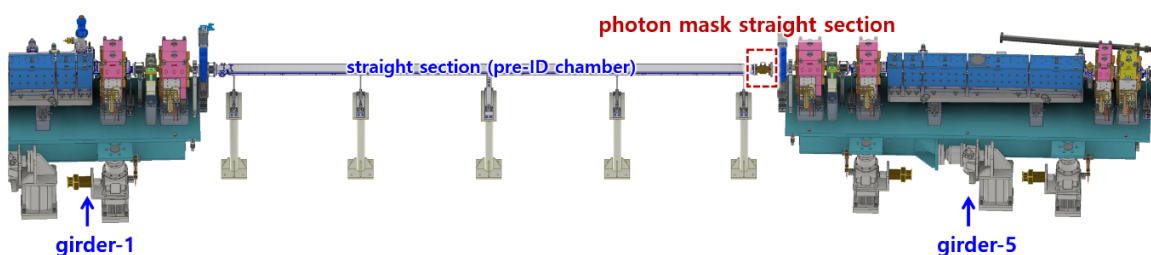
<Figure 2.1.8.37> Thermal and structural analysis results of the photon absorber CN13.

○ Straight section photon mask

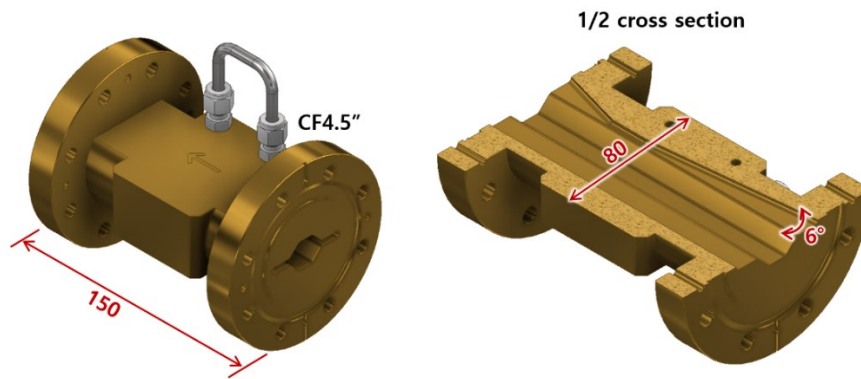
Between the ARC sections, there is a straight section for the installation of an insertion device, and at the beginning of the straight section, mask-type photon absorber is installed to protect the vacuum chamber in the straight section from the photon beam generated by the LGBM2D magnet.



<Figure 2.1.8.38> Distribution of photon beam absorbed by straight section mask.



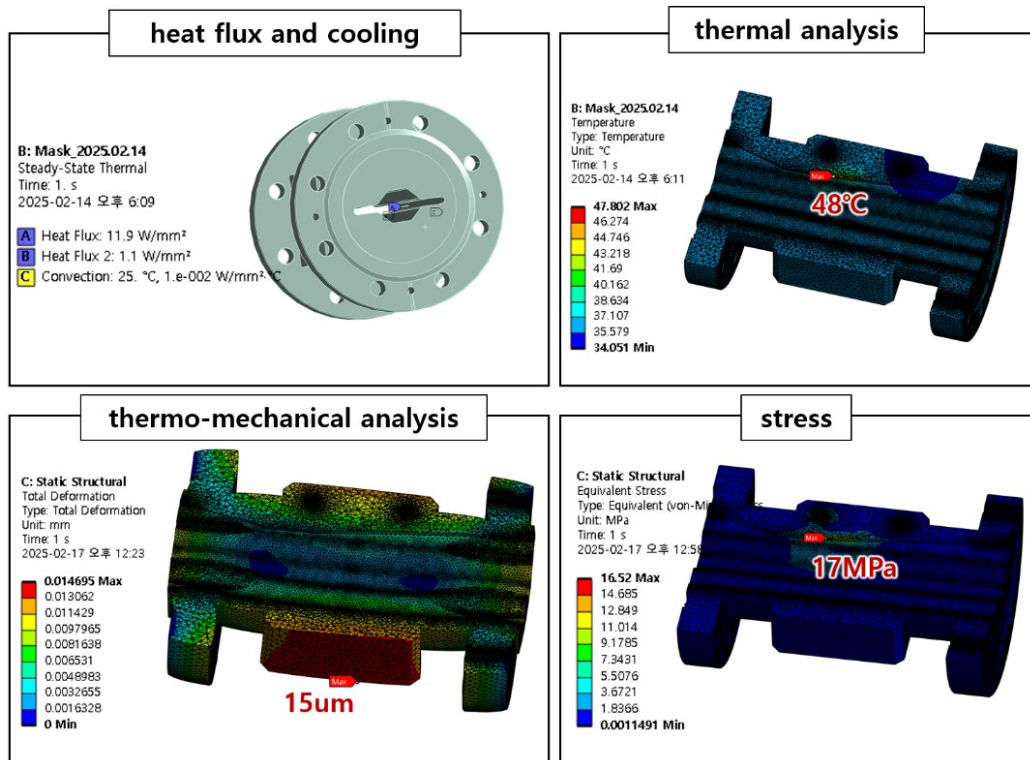
<Figure 2.1.8.39> The location of the photon mask and nearby devices.



<Figure 2.1.8.40> Dimension and internal shape of the straight section photon mask.

<Table 2.1.8.14> Photon flux power absorbed by the straight section photon mask

Source magnet	B [T]	Incident angle [°]	Power [W]	Incident peak power density [W/mm ²]
M4 (LGBM2D)	0.430	6.6	83.6	11.9
total power			83.6	

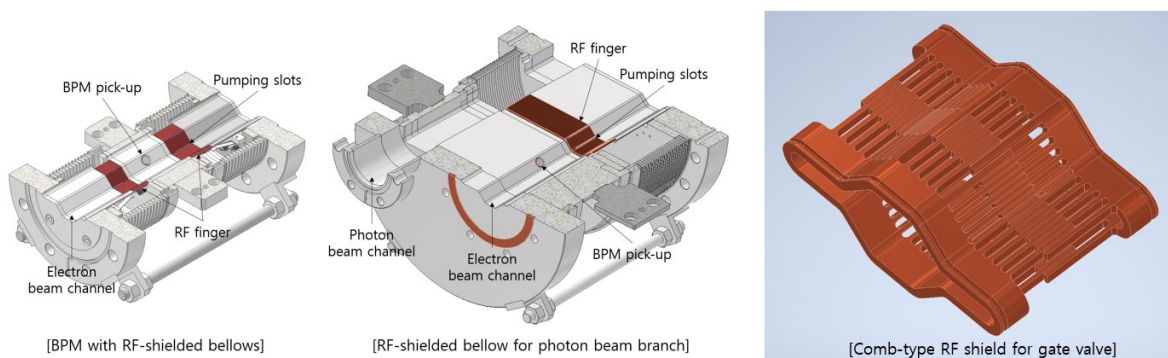


<Figure 2.1.8.41> Thermal and structural analysis results of the straight section photon mask.

(6) RF shielding and flange joint

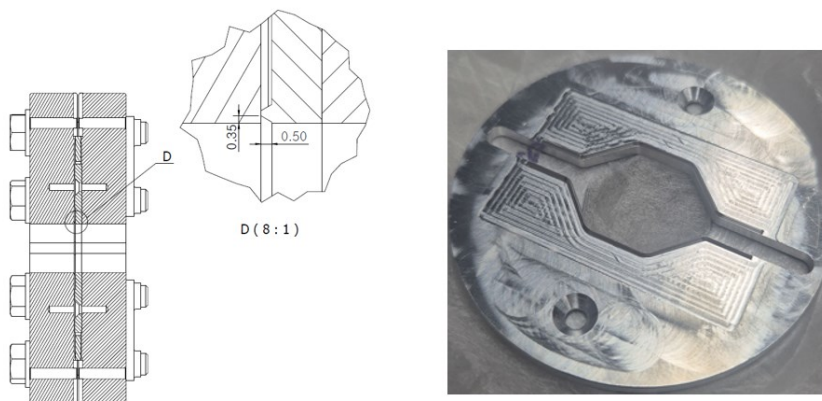
The RF shielding and flange joint in the storage ring vacuum system are designed to ensure both electrical continuity and vacuum integrity under dynamic mechanical conditions. Inside the bellows, a sliding-type RF finger (<Figure 2.1.8.42>) is adopted to accommodate mechanical deformation while maintaining continuous RF contact. Thin pumping slots are provided to compensate for the bellows' flexibility and to facilitate vacuum pumping.

In the gate valve, a comb-type RF shielding structure (<Figure 2.1.8.42>) is employed to minimize the impedance typically induced by conventional flexible, bending-type RF fingers. This configuration provides improved RF performance while preserving mechanical tolerance during valve operation.



<Figure 2.1.8.42> RF-shielded bellow and gate valve

The vacuum chamber flanges are fabricated from bi-metal materials, ensuring compatibility between dissimilar metals used in the vacuum system. Vacuum tightness is maintained with a copper gasket on a ConFlat-type knife edge, and RF continuity across the flange interface is secured using an aluminum RF bridge, as shown in <Figure 2.1.8.43>.



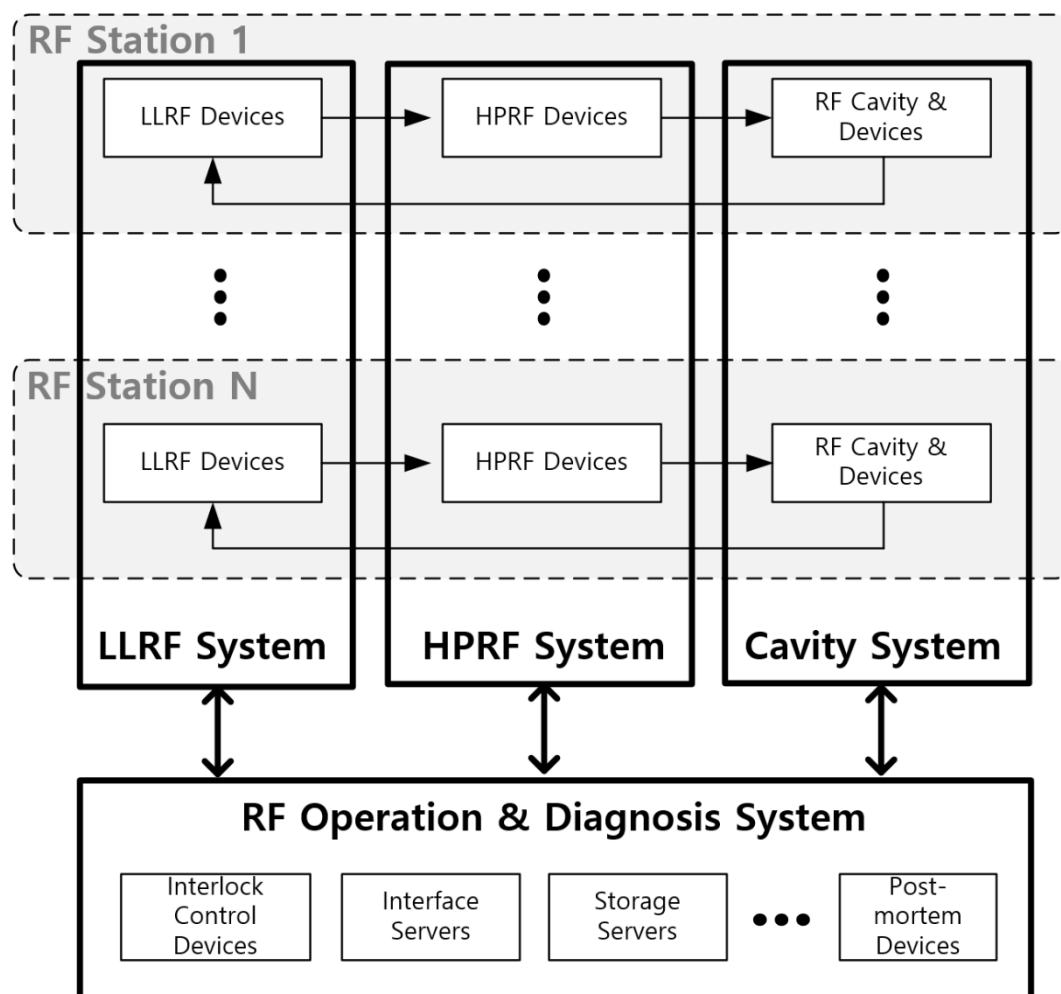
<Figure 2.1.8.43> RF contact for flange joint

References

- [1] J.C. Herrera, "Eddy Current Effect in the AGS Vacuum Chamber," AGSCD Technical Note No. 49, April 22, 1966.
- [2] Chao and M. Tigner, "Handbook of Accelerator Physics and Engineering," World Scientific, 1st edition, 1998, p. 397.
- [3] Chao and M. Tigner, "Handbook of Accelerator Physics and Engineering," World Scientific, 1st edition, 1998, p. 183.
- [4] D. Kramer, "CERN Accelerator School," CERN 99-05, p. 307, 1999.
- [5] K. A. Mohammad et al., "IOP Conf.: Mater. Sci. Eng.," vol. 36, 012012, 2012.
- [6] J. F. Grubb, "Allegheny Ludlum Corp., The Minerals, Metals and Material Society," p. 629, 1997.
- [7] Bernardini et al., "Phys. Rev. Lett.," vol. 10, p. 407, 1963.
- [8] Y. Suetsugu and K. Kanazawa, "IEEE Proc. 1993 Particle Accel. Conf.," p. 3860, 1994.
- [9] S. Heikkinen, "Doctoral Thesis, School of Sci. Technol., Aalto Univ., Finland," Nov. 2014.
- [10] "GlidCop is a dispersion-strengthened copper alloy by SCM Metal Products, North Carolina, USA."
- [11] Y. Suetsugu et al., "J. Vac. Sci. Technol. A," vol. 27, p. 1303, 2009.
- [12] "ANSYS is an engineering simulation and 3-D design software that calculates the thermal and mechanical conditions, sold by ANSYS Corp."
- [13] "SynRad+ is part of MolFlow+ code from CERN, which traces photons to calculate flux and power distribution on a surface caused by synchrotron radiation."
- [14] "MolFlow+ is a Monte-Carlo simulation code for ultrahigh vacuum systems with complex geometries and surface conditions, available at www.molflow.web.cern.ch."
- [15] Y. Suetsugu et al., "Rev. Sci. Instrument.," vol. 78, 043302, 2007.

2.1.9 RF System

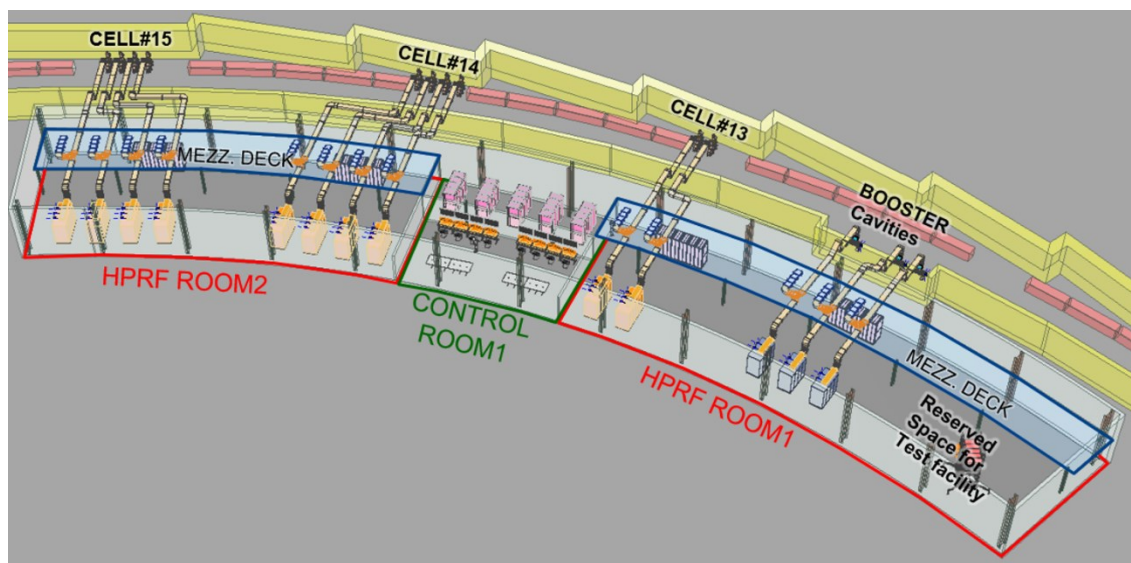
The RF system occupies the largest proportion in terms of cost for construction and operation among the components of modern storage ring as synchrotron radiation source, and directly affects the characteristics, capacity, availability, and reliability of synchrotron radiation. These attributes are the basic requirements of modern synchrotron light sources. Therefore, the design of the RF system involves finding a balance between optimizing these factors and adhering to budgetary constraints.



<Figure 2.1.9.1> Configuration of RF system.

The RF system is divided into subsystems, including RF cavity, high power RF system that generates and supplies RF output, and low level RF system that manages the interaction between the beam and RF system. As shown in <Figure 2.1.9.1>, each RF station is comprised of components from these subsystems.

In the storage ring of the 4GSR, a total of 10 cavities will be placed in the straight sections 13, 14, and 15 of the storage rings, as shown in <Figure 2.1.9.2>. Four cavities will be installed in the high beta section of straight section 15, while another four will be placed in straight section 14. The remaining two cavities will be placed in the straight section 13. The remaining space will be used for installing a short insertion device or additional cavity. To consolidate the RF devices, including the booster cavities, within a single RF building, three booster cavities will be placed adjacent to the storage ring cavities. The RF building will be also strategically located near the utility and electrical rooms to minimize the length of cooling piping and electrical cables.



<Figure 2.1.9.2> Layout of RF building.

Inside the RF building, two high-power device rooms are placed with a control room between them for easy interconnection between spaces. The LLRF cabinets will be located as close as possible to the corresponding straight sections to minimize the length of the cavity pick-up lines. A false floor (double-floor structure) is applied beneath the control room and LLRF cabinets, allowing all signal lines to run underground. A mezzanine is placed in the RF building for installing circulators and dummy loads. The space beneath the mezzanine will serve to store spare parts or install LLRF cabinets. and the space below the mezzanine level can be utilized for storing spare parts or installing LLRF cabinets. On the top of the mezzanine, monorail crane will be installed for maintenance of circulators and dummy loads.

A. Storage Ring RF System

(1) Overview of the Storage Ring RF System

① Role and Functions of the Storage Ring RF System

The RF system of the storage ring is a complex device that integrates control, vacuum, and cooling systems in addition to RF-related subsystems. The storage ring RF system has two primary functions. First, the RF system compensates for the energy loss of the charged particle beam by synchrotron radiation. The charged particle beam consisting of 1,332 bunches, loses approximately 1.5 MeV of energy with each revolution due to the effects of bending magnets and nine insertion devices. The RF cavity compensates the lost energy as the beam passes through cavity, thereby maintaining both the beam energy and orbit, which ensures the continuous synchrotron radiation emission. The second function of the RF system is to influence the longitudinal motion of the beam. This motion determines the primary operating parameters of the charged particle beam and contributes to maintaining the beam stability. The force applied to the electron beam in the storage ring is expressed by the following equation (Equation 2.1.9.1).

$$\vec{F} = -q\vec{E} - q(\vec{v} \times \vec{B}) \quad (\text{Eq. 2.1.9.1})$$

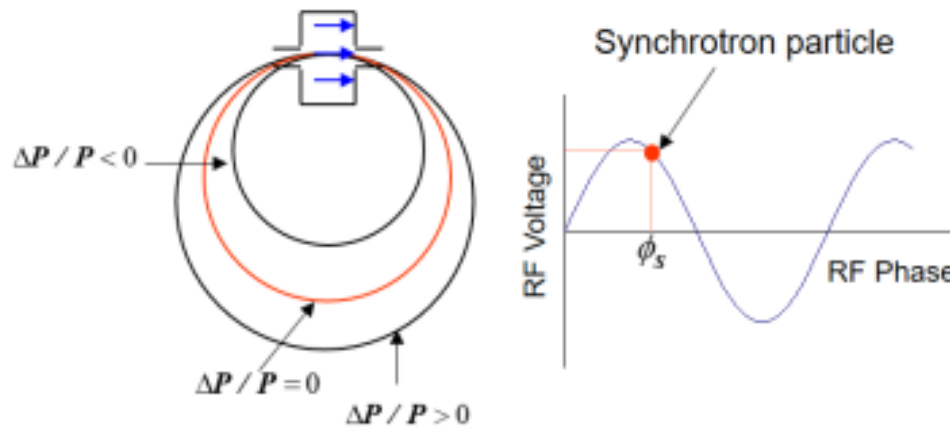
q : electric charge, \vec{E} : accelerating electric field, \vec{B} : magnetic field

Energy is the dot product of force and velocity.

$$\begin{aligned} |\vec{F} \cdot \vec{v}| &= |-q\vec{E} \cdot \vec{v} - q\vec{v} \cdot (\vec{v} \times \vec{B})| \\ &= |-q\vec{E} \cdot \vec{v} - q(\vec{v} \times \vec{v}) \cdot \vec{B}| \\ &= qE v \end{aligned} \quad (\text{Eq. 2.1.9.2})$$

(Equation 2.1.9.2) demonstrates that the force of magnet applies to the electron beam, influencing its orbital motion, and the energy can only be supplied through the RF cavity. This energy directly impacts several factors, including bunch size, Touschek beam lifetime, beam emittance, dynamic bucket height, and synchronous stability. <Figure 2.1.9.3> shows that a bunch with a large momentum ($\Delta\rho > 0$, ρ : momentum) travels a longer path compared to the ideal bunch ($\Delta\rho \equiv 0$), while a bunch with lower momentum ($\Delta\rho < 0$) travels a shorter path. The bunches that travel along the shorter path arrive at the RF cavity sooner and consequently receive more energy, whereas those on the longer path arrive later

and receive less energy. This dynamic leads to a passive correction of the bunches back to the design orbit. <Table 2.1.9.1> summarizes the RF parameters essential for the operation of the storage beam.



<Figure 2.1.9.3> Conceptual diagrams of Synchronous stability.

<Table 2.1.9.1> RF parameters required for storage ring beam operation (9 IDs)

Parameter	Values
Energy [GeV]	4.0
Current [mA]	400
Emittance [pm-rad]	61
Circumference [m]	799.297
Revolution frequency [MHz]	0.375070
Harmonic number	1332
Electron energy loss/turn [keV]	1,509.245
Beam loss power by synchrotron radiation [kW]	603.84
RF frequency [MHz]	499.593469
Accelerating Voltage [MV]	3.52

② Requirements and Design Considerations for RF System

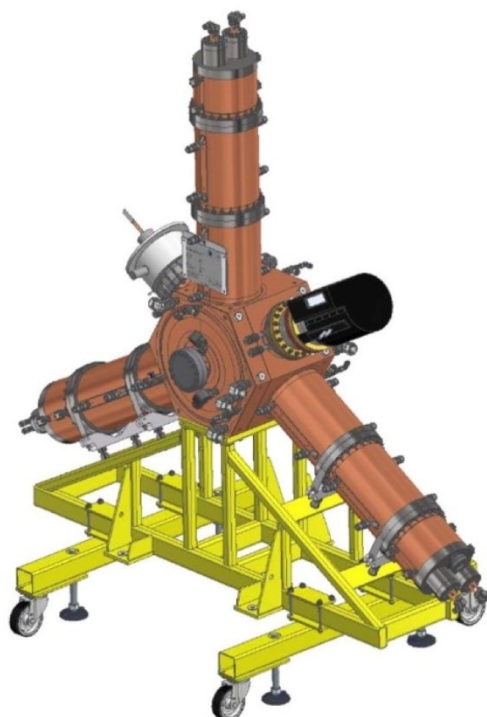
In the design procedure of the storage ring, the RF system is a critical device that allows the lattice design to be realized for the purpose of utilizing the radiation source. Once the lattice design parameters and the qualitative and quantitative characteristics of the radiation source are determined, the main parameters for the RF system are selected to compensate for the corresponding energy loss, ensuring that the particle beam maintains continuous and stable motion. Moreover, it is essential to develop a robust system that can maintain RF characteristic parameters to ensure the stability of the beam orbit by the lattice design. The size of the RF system is determined based on the energy loss due to synchrotron radiation and accelerating electric field derived from the lattice design. The specifications of the RF system components are then defined to sustain beam stability.

The RF cavity is designed to minimize the electromagnetic fields generated by its high order modes (HOM), regulate noise and distortion of the high-power RF devices, and define the feedback control parameters in low power RF devices to manage the interaction between the RF system components and the beam. In the operation of the storage ring, the RF system serves as a complex and fundamental device that directly influences the operation of the entire facility, statistically accounting for approximately 40% to 50% of the total annual beam dump attributed to various components. Therefore, it is crucial to design a device that is robust and stable while sufficiently implementing the functionalities that meet the main specifications.

(2) Storage Ring RF Cavity

In the storage ring, the bunch of electrons loses energy due to the electromagnetic field of the magnets, the insertion device (ID), and so on. The RF cavity is used to supply the lost energy. The super conducting RF cavities and the normal conducting RF cavities are employed in roughly the same ratio at 4th generation synchrotron radiation source worldwide.

Currently, in the construction the 4th generation synchrotron radiation accelerator in Korea, the normal conducting RF cavity is employed to reduce the downtime needed to recover normal beam conditions, thereby maximizing user beam time. Since the effect of beam instability caused by high order mode (HOM) on the cavity is significant, there are plans to install cavities with HOM absorber system.



<Figure 2.1.9.4> EU-HOM damped Cavity.

The EU-HOM damped cavity shown in <Figure 2.1.9.4>, designed by BESSY in Germany, is one of the few normal conducting cavities with a HOM absorber that is currently in operation worldwide 3rd and 4th generation synchrotron radiation accelerators. <Table 2.1.9.1.2-1> shows the main parameters of the EU-HOM damped cavity.

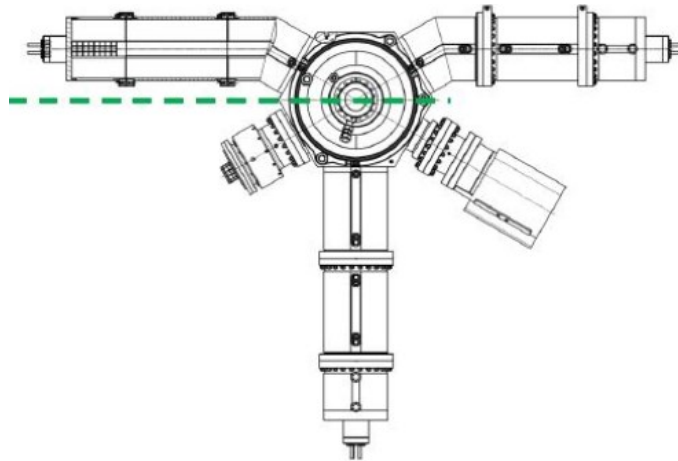
<Table 2.1.9.2> EU-HOM damped Cavity Parameters

parameter	value
Flange to flange length [m]	0.5
Max. power coupler [kW]	120
unloaded quality factor	>29,000
shunt impedance [MΩ]	3.40
coupling factor	1 to 5

Each cavity needs a space of less than 0.5 meters for installation, and a loop type coupler has been selected so that its coupling factor can be adjusted from 1 to 5. Additionally, the coupler can supply up to 120 kW RF power to the cavity.

Currently, this type cavity has been employed in ESRF-EBS, ALBA, BESSY-II,

Diamond, and other accelerators. Additionally, in ALS-U and PETRA-IV, they are fabricating or testing the cavity for installation. Particularly, ESRF-EBS fabricated the cavity after redesigning it due to a frequency difference, and ALS-U modified the shape of the HOM absorber, as shown in the <Figure 2.1.9.5>, because of space limitations during installation. Both facilities made slight design changes before installation.



<Figure 2.1.9.5> ALS-U HOM damped Cavity [1].

Reference

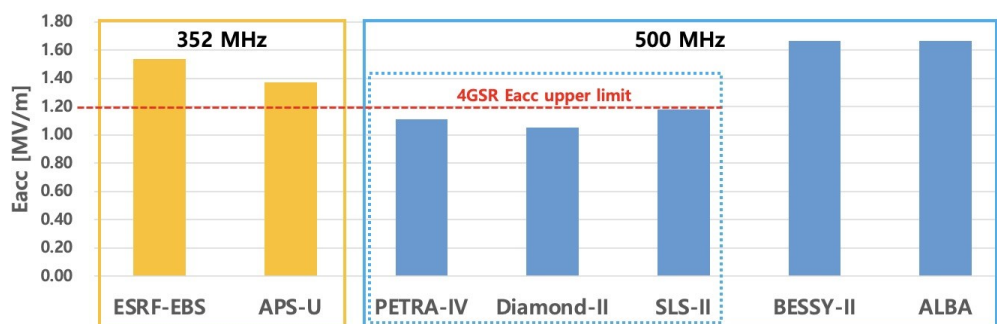
[1] K. Baptiste, "ALS-U Plans for the RF Systems," presentation.

<Table 2.1.9.3> EU-HOM damped Cavity operating conditions

Light Source	Frequency [MHz]	#of Cavity	Gap Voltage [kV]	Beam Current [mA]	Eacc	Maker	Remark
ESRF-EBS	352	13	500	200	-	RI	
			462				
APS-U	352	12	530	200	-	RI	
PETRA-IV	500	24	333	200	1.11	-	
Diamond-II	500	8	338	300	1.13	RI	
BESSY-II	500	4	750 (Max.)	300	2.50 (Max.)	RI	Operating
			500	200	1.67		
ALBA	500	6	700 (Max.)	400	2.33 (Max.)	RI	Operating
			500	200	1.67		

<Table 2.1.9.3> shows the frequency, number of cavities, accelerating voltage, and other parameters for each accelerator using or planning to use the EU-HOM damped cavity.

ESRF-EBS, with a frequency of 352 MHz, has an RF accelerating voltage of 500 kV or more. However, PETRA-IV and Diamond-II, which use 500 MHz cavities and are either recently planned or under construction, have their accelerating voltages set to 350 kV or less. If this value is converted into the accelerated electric field (E_{acc}), it is about 1.1 MV/m. At this point, the acceleration length inside the cavity is 30 cm. BESSY-II and ALBA, which were manufactured relatively early, were designed for a maximum voltage of 700 kV or more but are currently operating at a lower voltage of 500 kV or less to ensure stable operation. (Refer to *PETRA-IV system design concept*.) At 500 kV operation, the accelerated electric field is 1.67 MV/m. It was reported that ALBA experienced 15 arcing trips in 2017. Based on this, PETRA-IV determined that the accelerating voltage should be set to approximately 333 kV, corresponding to an accelerated electric field of 1.0 MV/m, for stable operation of the EU-HOM damped cavity. Diamond-II selected a similar accelerating voltage. (Refer to *PETRA-IV Proposal of an RF System for PETRA-IV_M. Eber_DESY_Tech_NOTE_2019_Germany*.) Therefore, since the same cavity is planned for the multi-purpose radiation accelerator, it was decided to set the maximum acceleration voltage to 360 kV and operate below this value. At this time, the accelerated electric field corresponding to the maximum voltage is 1.20 MV/m. <Figure 2.1.9.6> shows the accelerated electric field of operating or planned synchrotron radiation accelerators. In the graph, the blue dotted box highlights synchrotron radiation accelerators that are currently under construction or planned. In the case of SLS-2, although it does not use the EU-HOM damped cavity, other normal conducting RF cavities operate at a similar level of accelerated electric field. The red dotted line represents the accelerated electric field corresponding to the upper limit of the acceleration voltage in a multipurpose synchrotron radiation accelerator.



<Figure 2.1.9.6> Accelerating RF electric field of EU-HOM damped Cavity.

<Table 2.1.9.4> show the main RF parameters of the multipurpose synchrotron radiation accelerator.

<Table 2.1.9.4> Main Parameters of Korea Multi-purpose synchrotron radiation
accelerator

Parameter	Value	
Frequency [MHz]	499.593	f ₀
Beam energy [GeV]	4.0	E ₀
Beam Current [mA]	400	I _b
Accelerating Voltage [MV]	3.52	V _{cav}
Harmonic number	1332	
revolution frequency [MHz]	0.375070	f _{rev}
momentum compaction factor	7.775×10^{-5}	α
synchrotron tune	3.411×10^{-3}	Ω_s
Longitudinal damping time [ms]	16.792	τ_s
transverse damping time x/y [ms]	10.545/19.432	$\tau_{x,y}$
Total energy loss per turn [MeV]	1.509	E _{loss}

For every revolution of electrons in the storage ring, 1.098 MeV is lost due to the magnets, 0.352 MeV is lost due to the nine Insertion Devices (IDs), and 0.060 MeV is lost due to the vacuum chamber, among other factors. Therefore, the total energy lost in one turn is 1.509 MeV. To compensate for this lost energy and ensure stable beam operation, a 3.52 MV RF voltage has been determined, which is generated using the EU-HOM damped cavities.

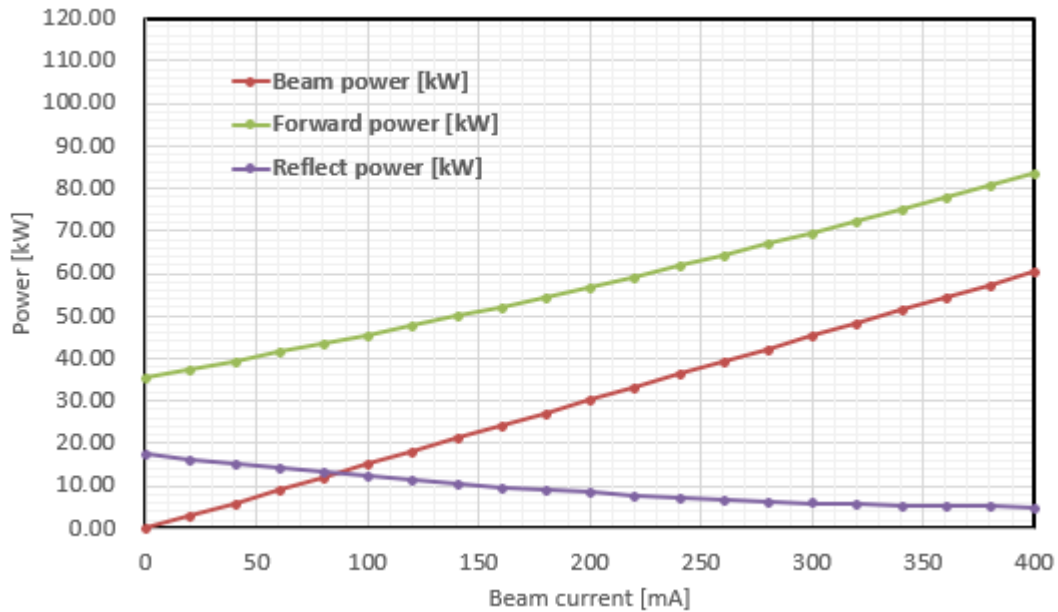
<Table 2.1.9.5> RF power and Key parameters according to number of cavities (9 IDs)

# of cavity	8	9	10	11	12
R over Q [Ω]	113.68	113.68	113.68	113.68	113.68
Unloaded Q	29909	29909	29909	29909	29909
Shunt impedance [M Ω]	3.40	3.40	3.40	3.40	3.40
gap voltage [kV]	440.00	391.11	352.00	320.00	293.33
Eacc [V/m]	1.466	1.304	1.173	1.067	0.978
Fixed coupling factor	4.5	4.5	4.5	4.5	4.5
Dissipated power [kW]	28.47	22.50	18.22	15.06	12.65
Loss power @ HOM absorber	5.00	5.00	5.00	5.00	5.00
beam power @ 400 mA [kW]	75.46	67.08	60.37	54.88	50.31
forward power [kW]	110.07	94.91	83.63	74.96	68.12

<Table 2.1.9.5> shows the RF power and operating variables base on the number of cavities. In this table, shunt impedance used the following equation, and the RF power lost by the HOM absorber was conservatively applied by 5 kW. And considering the 400 mA operation, the coupling factor was fixed at 4.5 for all cavity configuration the Table.

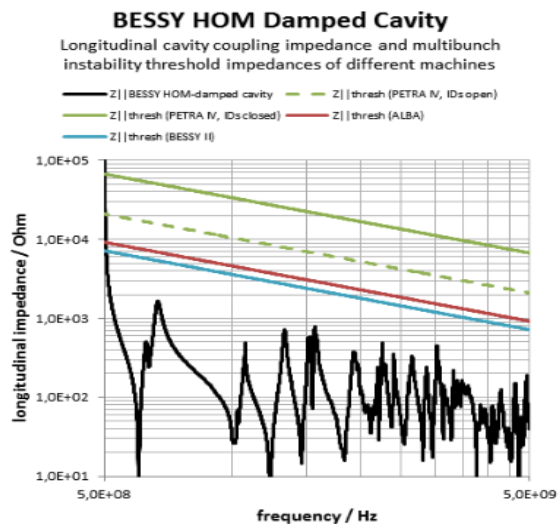
$$R_{sh} = \frac{V^2}{2P_c} \text{ (shunt impedance)}$$

Increasing the number of cavities has the advantage of making operation easier by lowering the RF voltage applied to each cavity. However, as the number of cavities increases, it takes up more installation space and reduces the number of available beamlines. Therefore, to satisfy both the maximum RF voltage of 360 kV (Eacc 1.2 MV/m) and the coupler's allowable power limit of 120 kW, the minimum number of cavities required is 10. <Table 2.1.9.5> shows the values set for the capacity operation from 8 assuming a cavity failure during operation to 12 corresponding to 1 MV/m, which is a stable acceleration electric field selected by PETRA-IV. (*PETRA-IV RF Proposal*) The coupling factor used in this calculation is also shown. If one of the 10 operating cavities fails, the RF power supplied to the coupler increases to around 120 kW. While it is still possible to operate by keeping the power below the coupler's allowable limit, if two cavities fail, the operation will exceed the coupler's allowable power.

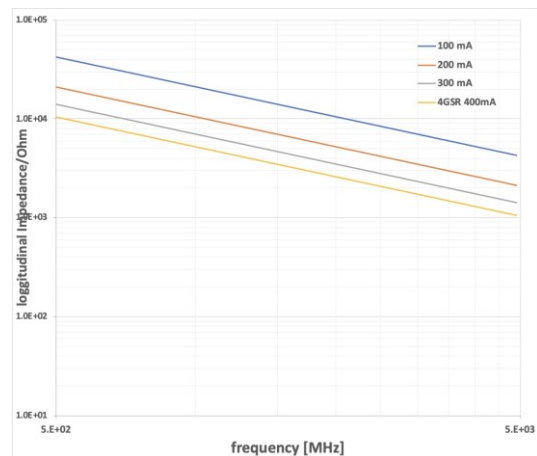


<Figure 2.1.9.7> RF power Required for Beam Current with 10 Cavities.

<Figure 2.1.9.7> shows the forward and reflected power according to the beam current as a graph when 10 cavities are installed. If 10 cavities operations are planned, about 84 kW RF power at the coupler is required for 400 mA operation, and a larger RF power amplifier is required including transmission loss and operation margin to satisfy this value.

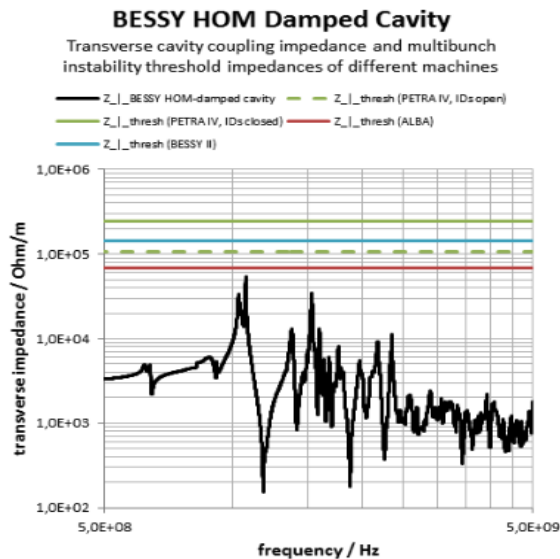


<Figure 2.1.9.8> Longitudinal wake Impedance and Threshold Impedance of Coupled Bunch Instability (CBI).

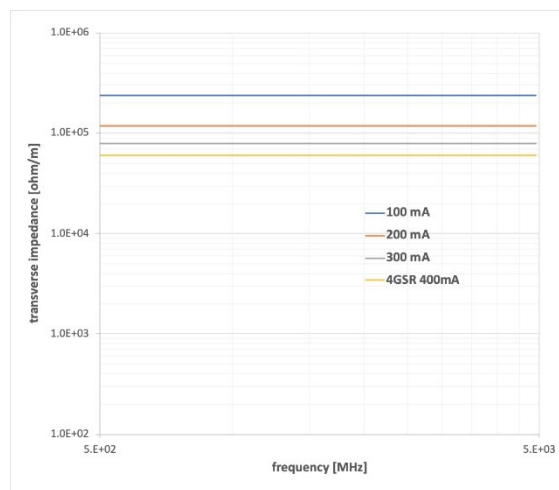


<Figure 2.1.9.9> CBI Threshold Impedance for Beam Current with 10 Cavities.

<Figure 2.1.9.8> shows the longitudinal wake impedance in the beam's direction of travel for the EU-HOM damped cavity, as well as the Coupled Bunch Instability (CBI) threshold impedance of other laboratories as a function of frequency. The threshold impedances for PETRA-IV, ALBA, and BESSY are represented by green, red, and blue lines, respectively. The black line represents the wake impedance of the EU-HOM damped cavity according to frequency. It can be seen that the wake impedance of the EU-HOM damped cavity does not exceed the CBI threshold impedance across the entire frequency range. When 10 cavities are used as parameters for the current multi-purpose synchrotron radiation accelerator, the CBI threshold impedance as a function of frequency is calculated as shown in <Figure 2.1.9.9>. At 400 mA, the calculated value follows the same trend as the CBI threshold impedance of ALBA. Therefore, it can be concluded that the use of the EU-HOM damped cavity is less affected by CBI due to HOM.



<Figure 2.1.9.10> Vertical wake Impedance and Threshold Impedance of Coupled Bunch Instability (CBI).

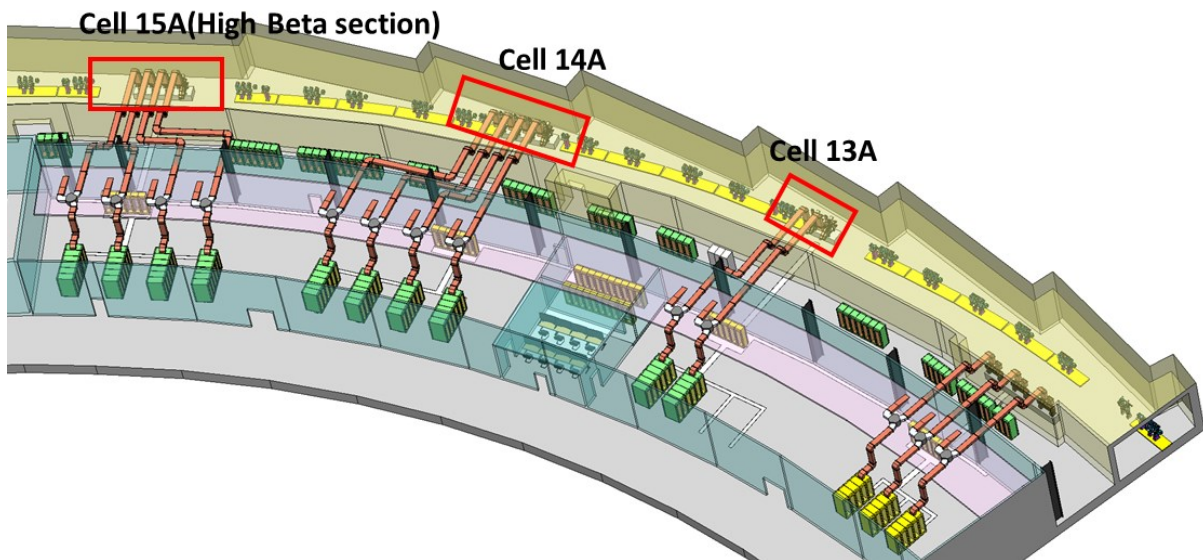


<Figure 2.1.9.11> CBI Threshold Impedance for Beam Current with 10 Cavities.

Similarly, <Figure 2.1.9.10> shows the vertical wake impedance of the EU-HOM damped cavity and the CBI threshold impedance of other laboratories. As with the beam direction, the CBI thresholds for PETRA-IV, ALBA, and BESSY are represented by green, red, and blue lines, respectively. The vertical wake impedance of the EU-HOM damped cavity is shown as a black line, and it can be seen that the threshold does not exceed 5 GHz. When 10 cavities are used as parameters for the current multi-purpose synchrotron radiation accelerator, the vertical CBI threshold impedance is calculated as shown in <Figure

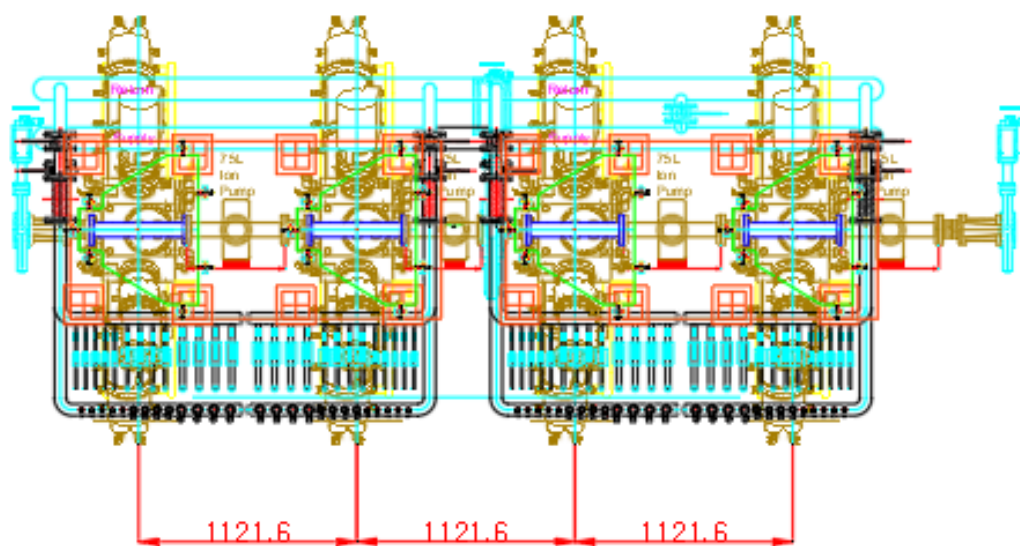
2.1.9.11>. The calculated value for vertical beam CBI also follows a similar trend to the CBI threshold impedance of ALBA at 400 mA. The threshold value is reached at around 1 GHz, but it is lower than the threshold in other frequency ranges. Therefore, it can be concluded that the use of the EU-HOM damped cavity is also less affected by vertical CBI due to HOM.

The EU-HOM damped cavities will be arranged as follows: two in the storage ring straight section 13A, four in section 14A, and four in the High Beta section 15A, as shown in <Figure 2.1.9.12>. Each cavity will be part of an individual RF station to minimize interference with other cavities and will be installed in dedicated RF building to facilitate maintenance. Specifically, only two cavities will be installed in section 13A, providing space for relatively short insertion devices (IDs). If additional RF voltage is needed in the future, this space can also be used for installing additional RF cavities.



<Figure 2.1.9.12> Cavity layout in the storage ring.

An ion pump was installed in front of each cavity to maintain the vacuum level below 1×10^{-9} mbar, and a photon mask was placed between the cavities to reduce radiation damage.

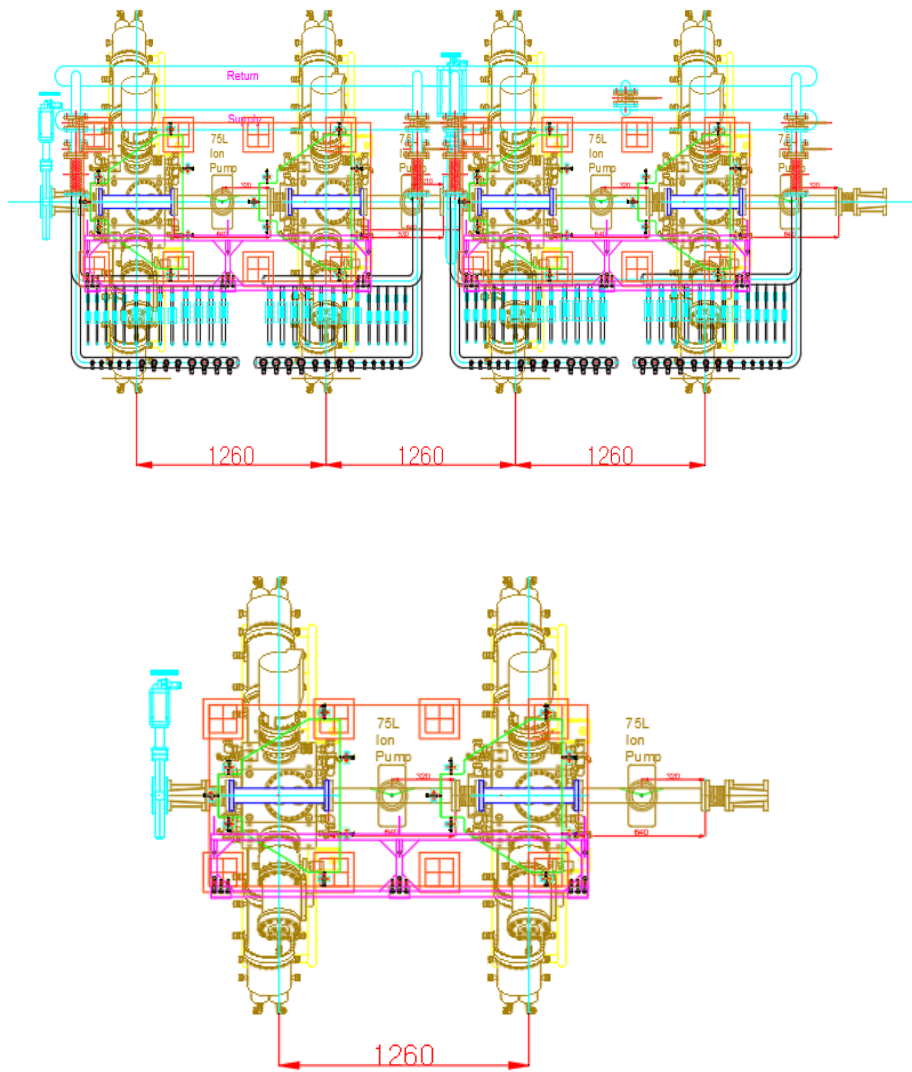


<Figure 2.1.9.13> 15A high beta section – Cavity layout.

<Table 2.1.9.6> Phase difference according to cavity position in 15A section

Cavity	Distance between cavity centers	Relative time deviation (Δt) from the first cavity	Relative phase deviation ($\Delta\phi$) with respect to the first cavity
15A-c1			
15A-c2	1121.6 mm	3.74 ns	313.43°
15A-c3	1121.6 mm	7.48 ns	266.85°
15A-c4	1121.6 mm	11.22 ns	220.28°

As shown in <Figure 2.1.9.13>, the distance between cavities in the High Beta section 15A is 1121.6 mm. The time interval from the center of the first cavity to the center of the next cavity is 3.74 ns, which corresponds to a phase shift of 313.43°.



<Figure 2.1.9.14> 14A, 13A Straight section – Cavity layout.

<Table 2.1.9.7> Phase difference according to cavity position in 13, 14A section

Cavity	Distance between cavity centers	Relative time deviation (Δt) from the first cavity	Relative phase deviation ($\Delta\phi$) with respect to the first cavity
14A-c1			
14A-c2	1260 mm	4.33 ns	58.44°
14A-c3	1260 mm	8.65 ns	116.88°
14A-c4	1260 mm	12.97 ns	173.32°
13A-c1			
13A-c2	1260	4.33 ns	58.44°

Similarly, as shown in <Figure 2.1.9.14>, the spacing between cavities in the straight sections 14A and 13A is 1295.6 mm. This corresponds to a time interval of 4.33 ns from the center of the first cavity to the center of the next cavity, and a phase shift of 58.44°.

(3) Storage Ring High-Power RF System

The capacity of the high-power RF system according to the number of RF cavities required to satisfy the beam physics is shown in <Table 2.1.9.8>. Considering the operational margin and the maximum allowable power of the RF cavities, at least 10 high-power RF systems are required. In this case, the output of each RF amplifier must be at least 118 kW. To ensure uninterrupted beam operation in case of a failure in one RF cavity, the rated output of each RF amplifier needs to be approximately 150 kW.


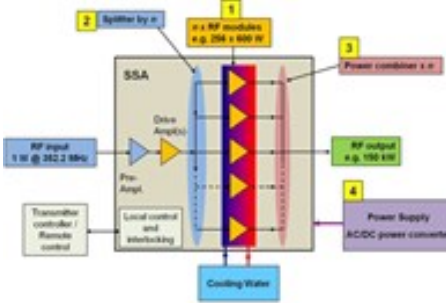
<Table 2.1.9.8> High power RF power as per the number of storage ring RF cavities

	Number of cavities	8	10	12
Cavity	Required power to coupler [kW/unit] (case of single cavity failure)	110.07 (131.30)	83.63 (94.91)	68.12 (74.96)
Transmission	Reflect power [kW/unit]	1.14	0.04	0.16
	Transmission line loss (Pt/unit)	10	10	10
SSPA	Output power of HPRF [kW/unit] (Case of single cavity failure)	151.99 (178.87)	118.51 (132.80)	98.89 (107.54)
	Rated power of SSPA [kW/unit]	190	150	130

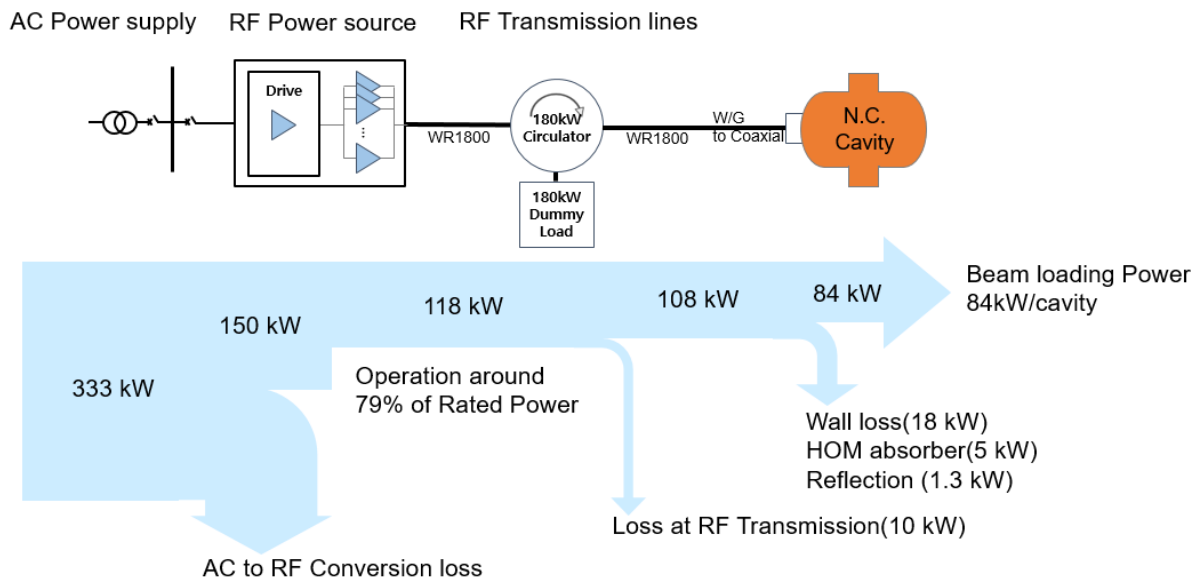
For the selection of a high-power RF amplifier for the storage ring, two types of amplifiers, 150 kW, 500 MHz 'Klystron' and 'Solid State Power Amplifier (SSPA)', were evaluated and compared. The klystron has demonstrated excellent performance in this frequency and power range over the past several decades. However, the recently developed SSPA has shown superior performance. Its efficiency and reliability have improved, and its signal-to-noise ratio (SNR) is better. Additionally, as shown in <Table 2.1.9.9>, unlike the klystron, the SSPA does not require high voltage or X-ray shielding equipment. In the event of a failure, only components such as RF modules need to be replaced for the SSPA, whereas the klystron requires the replacement of the entire unit, making maintenance easier with the SSPA. The required installation space for the SSPA has also been reduced continuously, making it possible to install in less space compared to the klystron. Moreover, the cost of

the SSPA continues to decrease, while the price of the Klystron increases annually. Considering all these considerations, the SSPA is determined to be technically and economically suitable as the high-power RF amplifier for the storage ring.

<Table 2.1.9.9> Comparison between Klystron and Solid state RF Amplifier

Characteristics	Klystron	SSPA
		
HV Power supply	HV Protection required X-ray shielding required Phase noise by PWM Voltage ripple (abt. -50dBc)	No need HV provisions No X-ray shielding Lesser phase noise (abt. -68dBc)
Operational Efficiency	abt. 40%	abt. 50%
Modularity /Redundancy	Lower redundancy Klystron should be replaced where it's failed	Very High redundancy except Driver module fails Operable with several module fails
Durability and Obsolescence	Longer durability Could be Obsolescence in future	Each module has shorter lifetime but maintenance is easy

To ensure beam operation even if a failure occurs in the RF stations, the RF system is configured into 10 independent stations. This design ensures that a single failure in one RF device does not affect the adjacent devices. During accelerator operation, full reflection can occur from the RF cavities. Therefore, high-power circulators and dummy loads are applied. The transmission line employs EIA standard WR1800 waveguide, known for its low loss and high stability. The configuration of the high-power RF system is shown in <Figure 2.1.9.15>. Additionally, each stage's energy flow is indicated, providing information on the required power and cooling capacity.



<Figure 2.1.9.15> High-power RF system's configuration and energy flow.

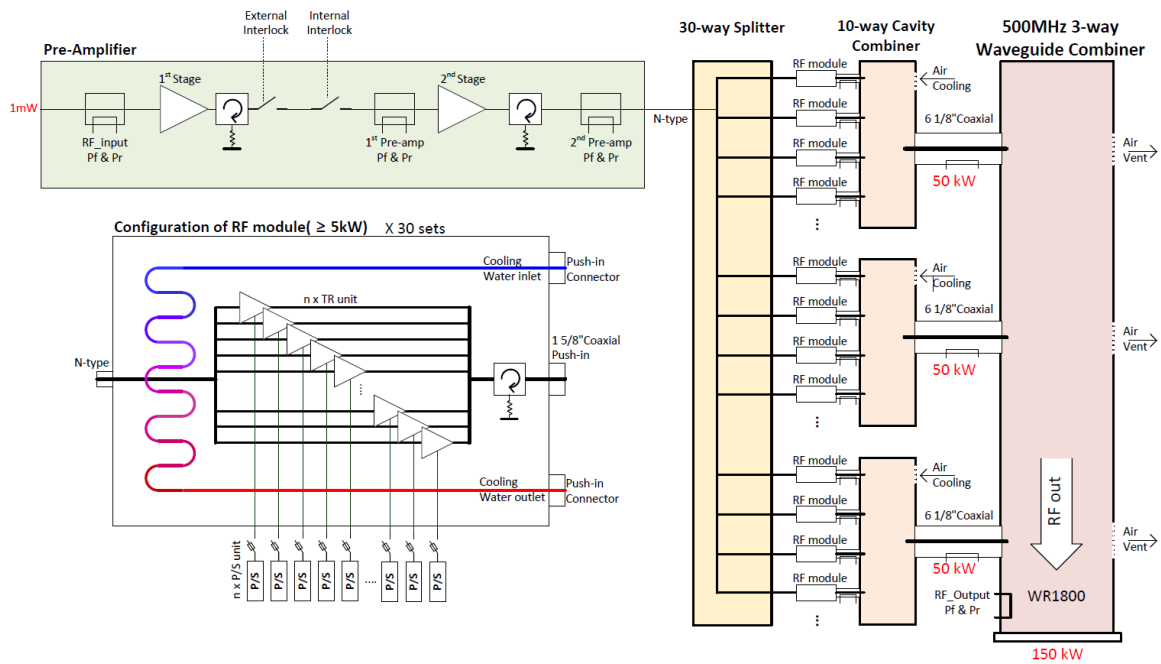
① Solid State Power Amplifier (SSPA)

The individual components, configuration, and requirements of the SSPA are shown in the conceptual diagram in <Figure 2.1.9.16>. The required RF power and monitoring points at each amplification stage from the input stage are indicated, clearly specifying the specifications of each component. Connectors and specifications for the input/output stages and connection points are also marked to finalize the interface with other systems.

Considering the operational requirements of the accelerator, which must continuously provide beam service throughout its operating period, independent bias power supplies are configured for each amplification transistor. This allows the system to continue operating even in the event of a component failure, ensuring beam operational stability and enabling the replacement of faulty components during maintenance after operations are completed.

In addition, to protect the SSPA from RF reflection that may occur during accelerator operation, circulators and dummy loads are applied to each RF module. By adopting this method, the output VSWR of the SSPA can be maintained at approximately 1.5.

For easy replacement of RF modules, plug-in type cooling lines and RF connectors are used. Furthermore, independent bias power supplies are applied to each transistor to minimize the impact of internal failures. To accommodate installation space and output scalability, a waveguide combiner is used for the final-stage RF combiner. The main specifications of the SSPA are summarized in <Table 2.1.9.10>.



<Figure 2.1.9.16> Conceptual diagram of 150kW Solid state RF amplifier.

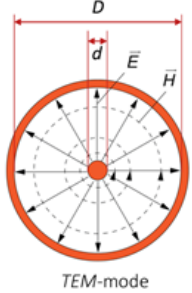
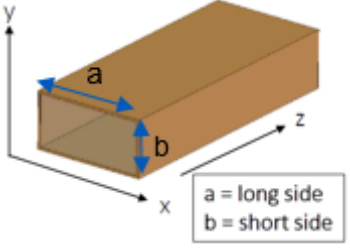
<Table 2.1.9.10> Specification of 500 MHz cw 150 kW SSPA

Equipment	Parameter	Value
Solid State RF Amplifier	RF rating	500MHz cw, BW ≥ ±1MHz
	In / Out Power	0 dbm_max / >150 kW
	Gain Flatness	0.5 dB within BW 0.5 dB from 50 to 110 kW
	Output Power Stability	0.5% Vp-p
	Phase Variation & Stability	3° / dB, 0.5° @ rated power
	Efficiency	>50% @ P1dB
	Input/output Z	50 Ω
	Harmonics / Spurious	<-36 dBc / <-70 dBc
	RF Ports	In: N-type / Out: WR1800
	Operability	Up to 5% of RF module failure

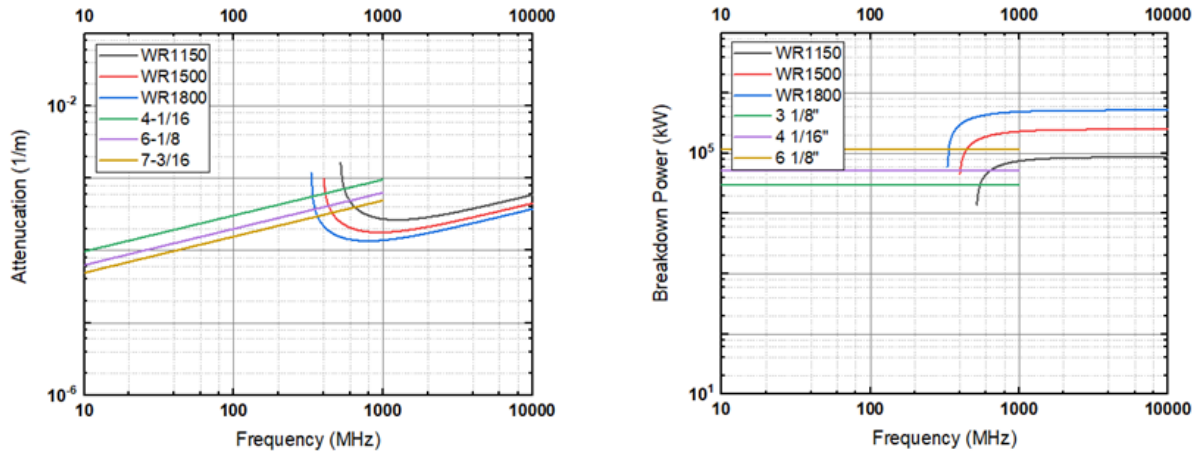
② High-Power RF transmission

To select a high-power RF transmission line, two options were considered: the coaxial line and the rectangular waveguide. The coaxial line operates in TEM mode, which has no cut-off frequency, whereas the rectangular waveguide operates in TE₁₀ mode, resulting in a cut-off frequency that depends on the length of its long side. For transmitting RF at 500 MHz, suitable waveguides include WR1500, WR1800, and WR2100.

<Table 2.1.9.11> Comparison between Coaxial line vs Rectangular waveguide

	Coaxial lines	Rectangular Waveguide
Structure		
Attenuation [1/m]	$\alpha = \underbrace{\frac{1}{2 \cdot Z} \cdot \frac{1}{\pi} \cdot \left(\frac{1}{d} + \frac{1}{D} \right) \cdot \sqrt{\frac{\mu\omega}{2\sigma}}}_{\alpha_{resistive}} + \underbrace{\pi f \frac{\sqrt{\epsilon_r}}{c_0} \cdot \tan\delta}_{\alpha_{dielectric} = 1.048 \cdot 10^{-8} \cdot f \cdot \tan\delta}$ $\alpha_{resistive} = \frac{1}{2 \zeta_0 \log \frac{D}{d}} \left(\frac{R_d}{d} + \frac{R_D}{D} \right), \zeta_0 = 377 \text{ ohm}$ <p style="text-align: center;"><small>Wave impedance in free space R_d & R_D : Surface resistance</small></p>	$\alpha_{wg} = \frac{2R_s \left[1 + \left(\frac{f_{cut}}{f} \right)^2 \right]}{a \zeta_0 \left[1 - \left(\frac{f_{cut}}{f} \right)^2 \right]^{0.5}}$ <p style="text-align: center;"><small>, $\zeta_0 = 377 \text{ ohm}$ Wave impedance in free space</small> <small>, $R_s = 0.075$ for Al Surface resistance</small></p>
Handling Power [kW]	$P_{peak} = \frac{E_d^2 d^2}{\zeta_0} \pi \log \frac{D}{d}$ <p style="text-align: center;"><small>, $\zeta_0 = 377 \text{ ohm}$ Wave impedance in free space</small> <small>, $E_0 = 3 \text{ MV/m}$ Break down voltage of Dry air</small></p>	$P_{wg} = \frac{E_d^2 a^2}{\zeta_0} ab \sqrt{1 - \left(\frac{f_{cut}}{f} \right)^2}$ <p style="text-align: center;"><small>, $\zeta_0 = 377 \text{ ohm}$ Wave impedance in free space</small> <small>, $E_0 = 3 \text{ MV/m}$, $b = a$ Break down voltage of Dry air</small></p>

As shown in <Table 2.1.9.11>, attenuation is related to the surface resistance and the distance over which the RF signal is transmitted. Once the structural distance required to satisfy a characteristic impedance of 50 Ω is determined, the attenuation is ultimately governed by the surface resistance. Typically, in a coaxial line, copper is used for the inner conductor to improve transmission efficiency, while aluminum is used for the outer conductor. In contrast, rectangular waveguides are generally made entirely of aluminum to reduce weight. The attenuation and power handling characteristics of both coaxial lines and rectangular waveguides at a characteristic impedance of 50 Ω, as a function of frequency, are shown in <Figure 2.1.9.17>.



<Figure 2.1.9.17> Attenuation and power handling of Coaxial line & Rectangular waveguide.

As summarized in <Table 2.1.9.12>, considering the 500 MHz frequency and approximately 150 kW of power handling, the WR1800 rectangular waveguide demonstrates the best characteristics as a high-power RF transmission line.

<Table 2.1.9.12> Comparison of Coaxial line vs Rectangular waveguide

Parameters	Coaxial line		Rectangular Waveguide	
	6 1/8"	9 3/16"	WR1500	WR1800
Frequency	-	-	492 to 749 MHz	410 to 625 MHz
Average Power handling	abt. 80 kW	abt.170 kW	422 to 475 kW	658 to 928 kW
Attenuation [dB/m] @ 500 MHz	0.0067 dB/m (1.17 dB/40m)	0.0035 dB/m (0.60 dB/40m)	0.0027 dB/m (0.47 dB/40m)	0.0021 dB/m (0.35 dB/40m)
Transmission Loss [kW]	35.3 kW	19.3 kW	15.4 kW	11.8 kW
Installation cross-section	0.0725 m ²	0.170 m ²	0.0724 m ²	0.1045 m ²

Although a circulator was applied to each RF module of the SSPA, a 180 kW-class 3-port circulator and dummy load were additionally implemented to account for potential full reflection during accelerator operation. The S-parameters of the circulator and dummy load, required to achieve the output VSWR of 1.5 as specified by the SSPA, are summarized in <Table 2.1.9.1.13>. In this scenario, the worst-case condition assumes that all phases of the

standing wave are superimposed at port 1 (the output port of the SSPA). For this case, the circulator must have an isolation of at least 22 dB, and the dummy load must have a return loss of at least 28 dB. However, considering a sufficient margin of safety, the specification requirements were set with a circulator isolation of 26 dB and a dummy load return loss of 30 dB.

<Table 2.1.9.13> VSWR by Circulator's isolation and Dummy load's return loss

Case	Circulator		Dummy	Return Loss @ Port1	VSWR
	Insertion Loss	Isolation	Return Loss		
1	0.1 dB	28 dB	28 dB	18.59 dB	1.27
2		26 dB		17.19 dB	1.32
3		24 dB		15.71 dB	1.39
4		22 dB		14.14 dB	1.49
5		20 dB		12.49 dB	1.62

To compensate for changes in the circulator's characteristics due to temperature variations, a Temperature Compensation Unit was applied. Additionally, an Arc Sentry was implemented for arc protection. The key specifications of the 3-port circulator and dummy load are summarized in <Table 2.1.9.14>.

<Table 2.1.9.14> Specification of 3 port Circulator and Dummy load

Equipment	Parameter	Value
3 Ports Circulator	RF ratings	500 MHz cw, BW $\geq \pm 1$ MHz, ≥ 180 kW
	Acceptable Reflect Power	100% at any phase
	Insertion loss @ fc	≤ 0.1 dB
	Isolation @ fc	≥ 26 dB
	RF Ports	3ports, WR1800
	Controller	Temp. Compensation. and ARC protection
Dummy Load	RF Rating	500 MHz cw, BW $\geq \pm 1$ MHz, ≥ 180 kW
	Connection	WR1800
	Return Loss @ fc	≤ -30 dB
	RF absorber	Ferrite with water cooled
	ARC protection	4 of View port Required

(4) Storage Ring Low Level RF System

The low-level RF(LLRF) system is a device that controls the interaction of a charged particle beam with an RF system and is essential for stable beam operation. While the particle beam passes through the storage ring, it is influenced by various disturbances such as mechanical vibrations from vacuum devices and cooling devices, beam loading, power supply ripples, and noise from RF systems. The LLRF system mitigates the effects of these disturbances to within the performance requirements by feedback control. The LLRF system not only performs fundamental feedback control functions such as amplitude/phase control and resonance frequency control but also provides additional functions, including monitoring the status of the RF system, and processing interlock signals for equipment protection.

① RF Control Stability Requirements

The longitudinal stability of the beam is primarily controlled by the LLRF system, and any residual beam instability is further damped by the longitudinal feedback system. Phase fluctuations or jitter in the accelerating RF voltage can cause longitudinal oscillations in the bunch beam. Therefore, precise control of the phase and amplitude of the accelerating electric field within the RF cavity is critical, particularly in high current/high energy storage rings with low beam emittance. In general, the magnitude of the beam jitter should be kept within 10% of the bunch length, and the synchronous phase stability in the RF cavity is defined by the following equation.

$$\Delta\phi_b = (10\%) \frac{2\pi f_0 L_b}{c} = 0.244^\circ \quad (\text{Eq. 2.1.9.3})$$

Here, f_0 is the resonant frequency of the RF cavity ($= 499.593469$ MHz), L_b is the bunch length ($= 0.004079$ m), and c is the speed of light in vacuum. Since the RF power supplied to the particle beam from the RF cavity is equal to the beam loss power (P_b), and P_b and beam current (I_b) must be constant to keep the beam stability constant, the RF amplitude stability requirement can be derived from the phase stability requirement by differentiating the following equation.

$$P_b = I_b V_c \cos \phi \quad (\text{Eq. 2.1.9.4})$$

From the above equations, the required RF stability in the storage ring RF system must be controlled within 0.271% for amplitude and 0.244° for phase. Therefore, the target stability for amplitude and phase was set to 0.1% and 0.1° , respectively.

<Table 2.1.9.15> RF stability requirements of LLRF system

Parameter	Tolerance	Target
Amplitude stability	0.271%	0.1% (rms)
Phase stability	0.244°	0.1° (rms)
Parameter	Tuning range	Resolution
Resonance frequency	±1 MHz	10 Hz

② Functional Requirements

The storage ring LLRF system performs various functions to compensate for the beam energy loss caused by synchrotron radiation and to stabilize the acceleration voltage to achieve the required momentum acceptance. In order to keep the accelerating electric field inside the RF cavity within the RF tolerance from disturbances, the amplitude and phase of the RF signal applied to the high-power RF system are feedback controlled. It also compensates for resonance frequency changes inside the cavity caused by temperature variations using a tuner. In addition, the LLRF system includes interlock functions to protect the RF system components and data acquisition, storage, and diagnostic functions for monitoring the RF signals from each point in the system. The detailed functions required for a storage ring LLRF system are as follows

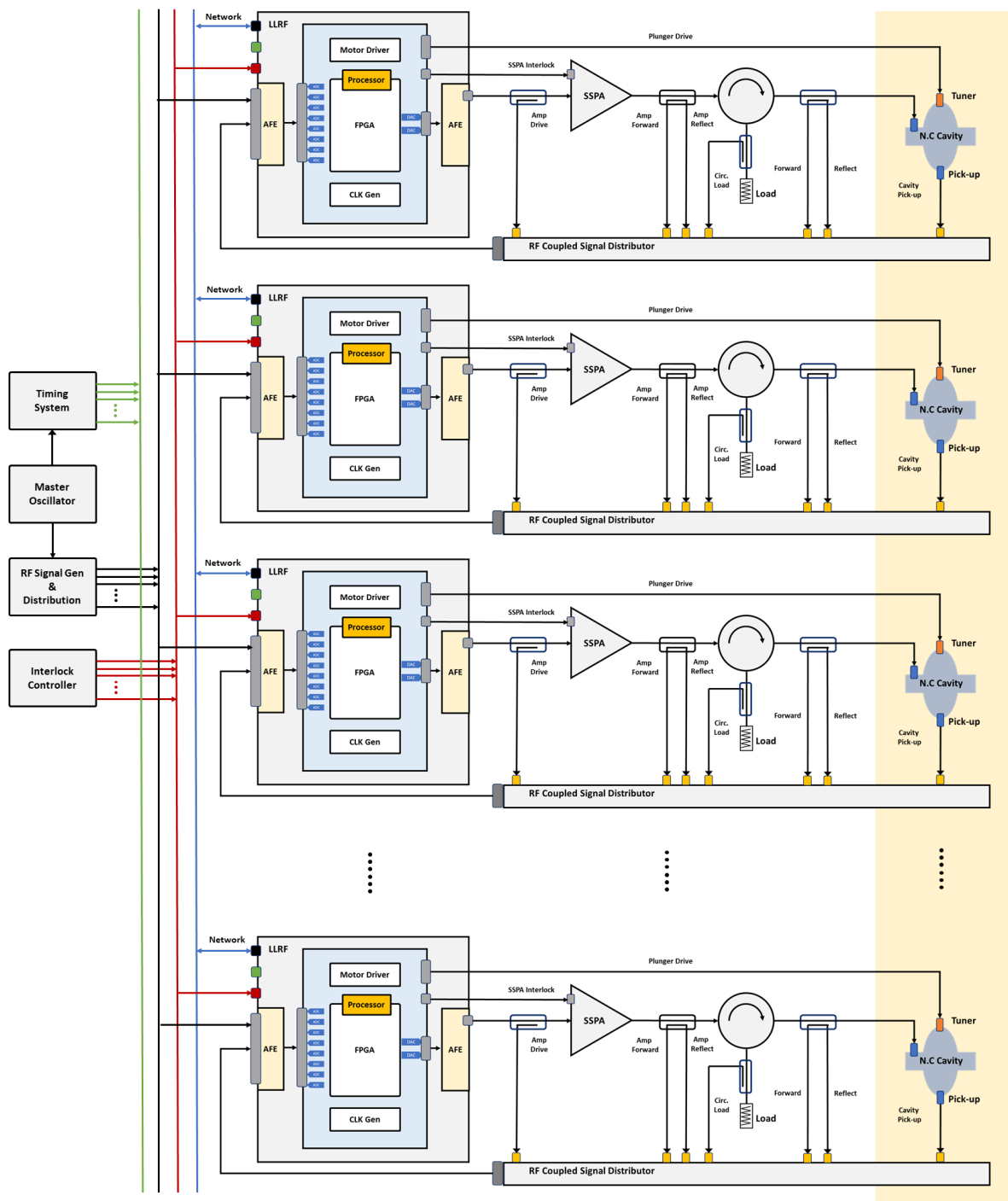
○ RF signal feedback control and interlock signal processing

- Amplitude/phase feedback control of SSPA drive signal for accelerating electric field stabilization inside cavity (Open loop / close loop operation)
- Automatic compensation of the resonance frequency due to mechanical change of the cavity
- Shut-down of SSPA drive signals in response to external interlock (MIS/PSI) and cavity faults (vacuum, temperature, etc.)

○ Data acquisition/Storage/Diagnostics

- Acquisition and storage of data related to cavity field, cavity input forward/reflected signals, drive signals, and internal diagnostic signals (loop error, filter coefficients, PI gain, etc.), post-mortem function
- Monitoring of the mechanical behavior of the tuner (tuner position, limit switch, direction, etc.)
- Housekeeping functions for hardware (power supply voltage, board temperature, etc.)

③ Configuration of the LLRF System and Integration with Other Systems

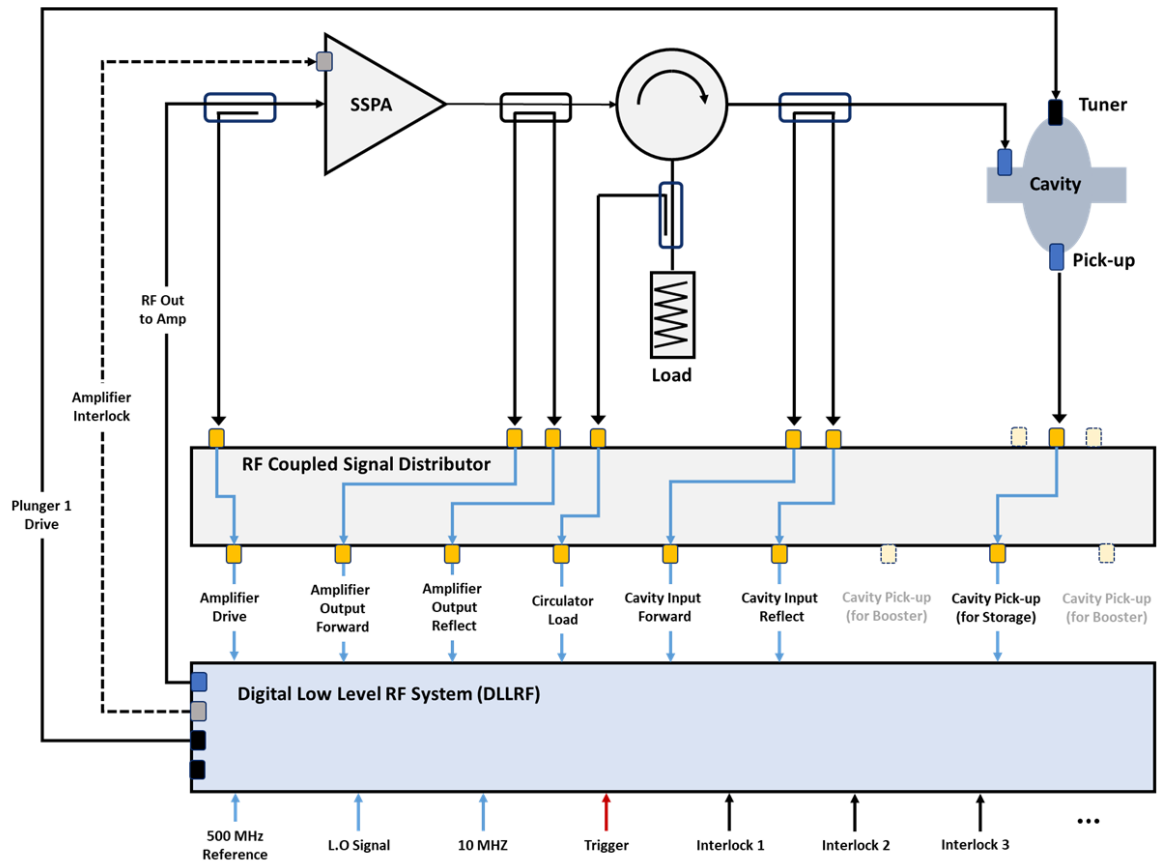


<Figure 2.1.9.1.18> Configuration of the storage ring RF system and connection of the LLRF system with other systems.

As shown in <Figure 2.1.9.18>, each RF cavity in the storage ring RF system is planned to be operated by independent SSPP (Solid State Power Amplifier) and LLRF system, which is advantageous for device control and maintenance. The LLRF system consists of an analog

Front-end (AFE) for frequency conversion of input/output RF signals and a digital board for digital signal processing. It receives RF reference signals and local oscillator (LO) signals required for feedback control from an external master oscillator and RF generation/distribution devices. When implementing precision control using a digital signal processing system, the performance requirements for signal processing become more stringent as the frequency of the input analog signal increases, and the error caused by sampling jitter increases.

Therefore, A feedback control method was applied by converting the RF signal to intermediate frequency (IF). In selecting the IF frequency, various factors need to be considered, such as sensitivity to clock jitter, latency requirements during digital signal processing, LO signal stability, filtering requirements of IF signal, and ease of supply of components during system implementation. Based on these considerations, the IF signal frequency was set to 50 MHz. The LLRF system receives the signals detected from each point of the high-power RF system such as RF cavity, SSPA, and circulator through the coupled RF signal distribution device. It also performs exception handling according to the operating situation with the interlock system for equipment and personnel protection. As shown in <Figure 2.1.9.19>, or RF feedback control, it processes input signals such as cavity field pick-up, cavity input forward/reflect signals, and operates in synchronization with the reference signal provided by the RF reference signal. Additionally, to diagnose the operational status of the RF system and handle anomalies, it receives SSPA input/output signals, circulator reflect signals, and load reflect signals for RF shutdown. The LLRF system control drive tuner motor control signal and shares the RF ready signal, fast RF shut off signal, and high-power RF permit signal for interoperability with the SSPA.

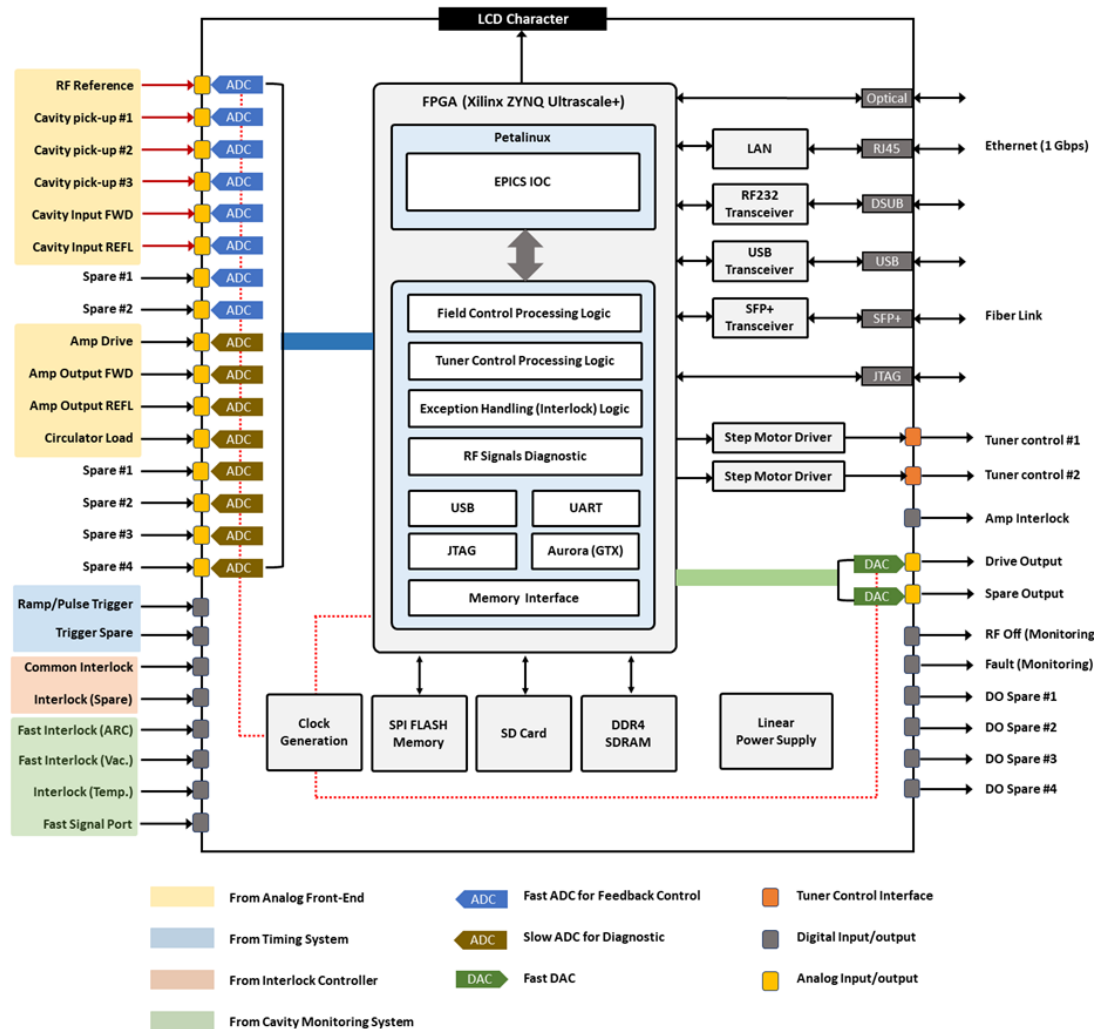


<Figure 2.1.9.19> RF signal layout for RF cavity control.

④ LLRF System Hardware Interface and Main Specifications

Considering the desired RF stability requirements, functional requirements, and interoperability with other systems, the hardware interface of the LLRF system was configured as shown in <Figure 2.1.9.20>. Using Xilinx Zynq chip with SoC (System on Chip) technology, it is possible to install Petalinux OS on the processor embedded in the FPGA without installation of additional SBC (single board computer) or MCU (Micro Controller Unit). The installed OS implements an EPICS IOC to enable the control logic and interface for feedback control, and fast ADCs and DACs with a sampling rate of over 100 MHz are applied for controlling and diagnosing RF signals. Inside the digital board, a PLL (Phase Lock Loop) chip for clock signal generation is applied to drive the ADC/DAC and FPGA, and it is configured to embed flash memory for booting itself, SD card for OS porting, and DDR memory for data storage. For communication with external systems, LAN for ethernet, serial communication (RS-232 or RS-485), USB, and SFP+ (Small Form-factor Pluggable) interfaces are applied, and a motor driver is embedded to control the tuner motor. In case of the power supply for digital board, a linear type power supply or SMPS with equivalent performance (ripple characteristic of 1mV or less) will be applied, and a character

LCD will be installed to monitor the status of the LLRF system. The hardware configuration and main specifications of the digital board are summarized in <Table 2.1.9.16> and <Table 2.1.9.17>.



<Figure 2.1.9.20> Hardware configuration and interfaces on the digital board.

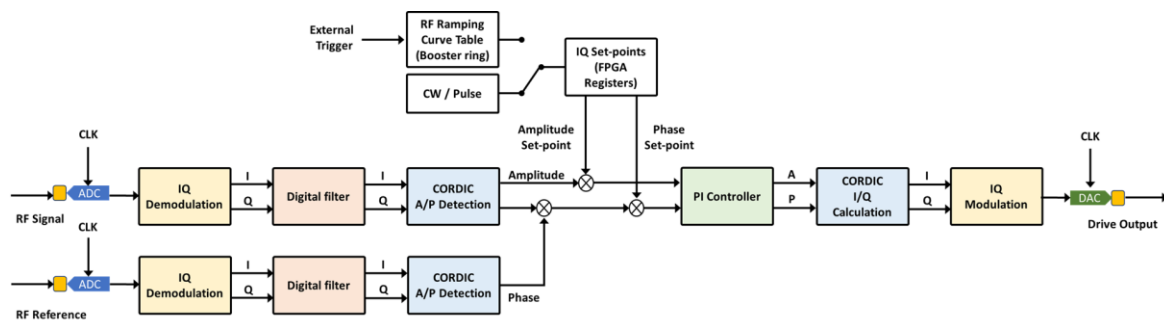
<Table 2.1.9.16> Configuration of the LLRF system hardware

Item	Implementation Detail
Chassis	19-inch rack, Character LCD
	Linear power supply or Ultra low ripple & noise power supply
	Analog Front-end (for Up/Down conversion) / Digital board
	Step motor driver (2 ea)
	PLL chip
	Flash memory, SD card, DDR4
Interface	Ethernet port
	JTAG port
	USB port
	Serial port (RS-232 / RS-485)
	SFP+ port

<Table 2.1.9.17> Main specification of LLRF system

Classification	Parameter	Value
General specification	Operating frequency	500 MHz \pm 1 MHz
	FPGA chip	Xilinx Zynq ultrascale+
	External trigger	2 inputs, rising/falling edge
RF Inputs	Number of channels	8 (fast) / 8 (slow)
	Channel-to-channel isolation	>65 dB
	Full scale input level	10 dBm
	Spurious-free dynamic range	>65 dB
	IF frequency	50 MHz
	LO frequency	450 MHz
	Fast ADC clock	40 MHz (250 MSPS max.)
	Amplitude dynamic range	\geq 25 dB
	Amplitude resolution	<0.01%
	Amplitude stability	<0.1% (upper 10 dB range)
	Phase resolution	<0.01°
	Phase stability	<0.1° (upper 10 dB range)
RF outputs	Output channel No.	2
	Full scale drive	10 dBm Max.
Feedback processing	Direct loop delay	<1000 ns
	Control scheme	CW / Pulse / Ramping
Interlocks	Number of digital inputs	>20
	Number of digital outputs	>20

⑤ RF Digital Signal Processing and Feedback Control



<Figure 2.1.9.21> Digital signal processing for cavity field control.

○ RF digital signal processing

In the LLRF system, RF feedback control is performed by digital signal processing algorithms such as digital filter, CORDIC (COordinate Rotation DIgital Computer), and PI (Proportional Integral) controller as shown in <Figure 2.1.9.21>. It allows the selection of both pulse mode and continuous wave (CW) mode. Additionally, it provides open loop mode for conditioning process and closed loop mode for cavity field control.

○ RF signal sampling and IQ demodulation

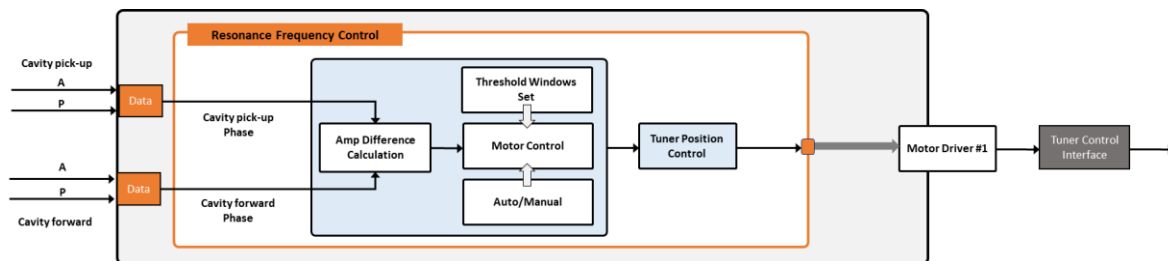
The signal detection of the accelerating electric field inside the RF cavity is based on the IQ demodulation method of the RF signal. The most intuitive method for IQ demodulation is IQ sampling, which is simple to implement and has good latency characteristics. However, a drawback of IQ sampling is that odd-order harmonic components generated during the sampling process overlap with the fundamental frequency, making it difficult to distinguish them. An alternative is the non-IQ sampling method, which is easier to distinguish the harmonic components generated during the sampling process from the fundamental frequency, but requires additional processing delay. Therefore, both sampling methods should be tested during the prototype development stage, and the optimal method should be determined through further refinement. For the IQ sampling method, a sampling frequency of 40 MHz is being considered, and for the non-IQ sampling method, sampling frequencies of 68.75 MHz and 137.5 MHz are being considered. We plan to conduct performance tests on various options to select the optimal sampling conditions within the applicable sampling frequency range of the ADC.

○ Cavity field control

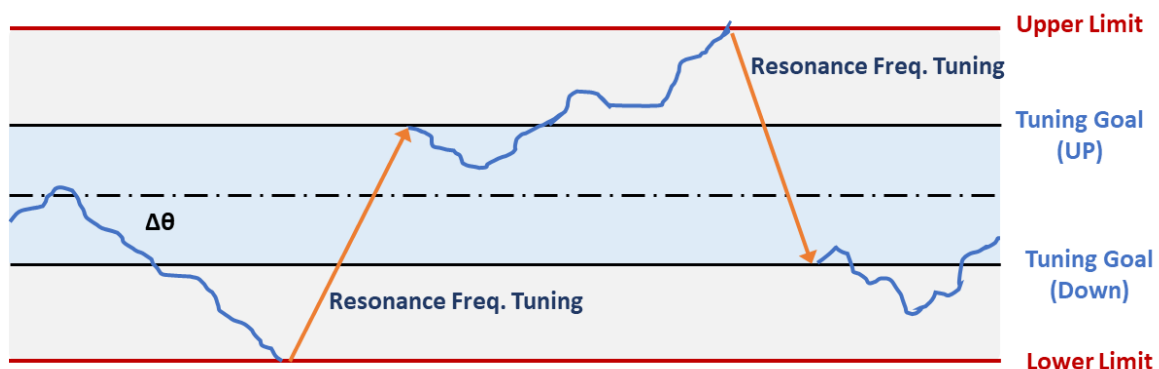
Cavity field control is primarily performed in Generator Driven Resonator (GDR) control mode. When the signal picked up from the RF cavity and the reference signal are input to the digital board, the IQ signal calculated through the IQ demodulation process and the digital filtering process is compared with the set value to calculate the error. The calculated error is compensated by PI control, and the corrected IQ signal is modulated and generated to RF output signal through the DAC, if the RF reflected wave does not exceed the set reference value.

○ Tuning loop control

For the control of the resonant frequency of the RF cavity, as shown in <Figure 2.1.9.22> and <Figure 2.1.9.23>, the phase difference between the pick-up signal and the forward signal is calculated to determine the detune angle. If the calculated detune angle exceeds the preset threshold, the motor is driven to adjust the detune angle so that it follows the target value within the predefined limits, thus enabling feedback control.

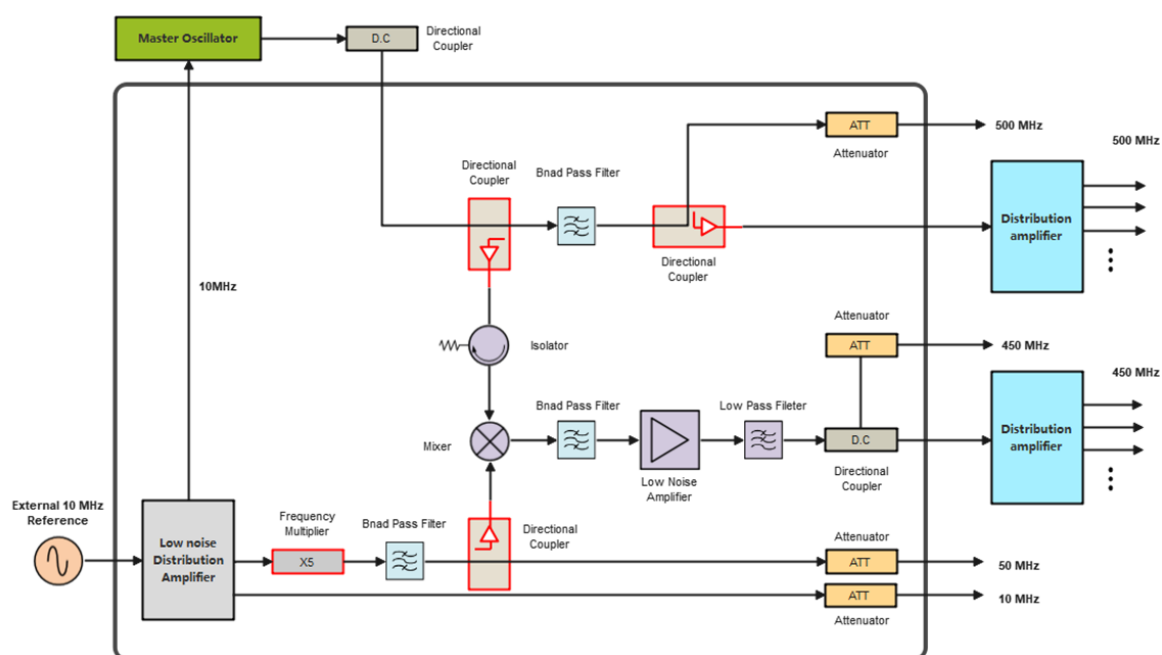


<Figure 2.1.9.22> Digital signal processing for resonance frequency.



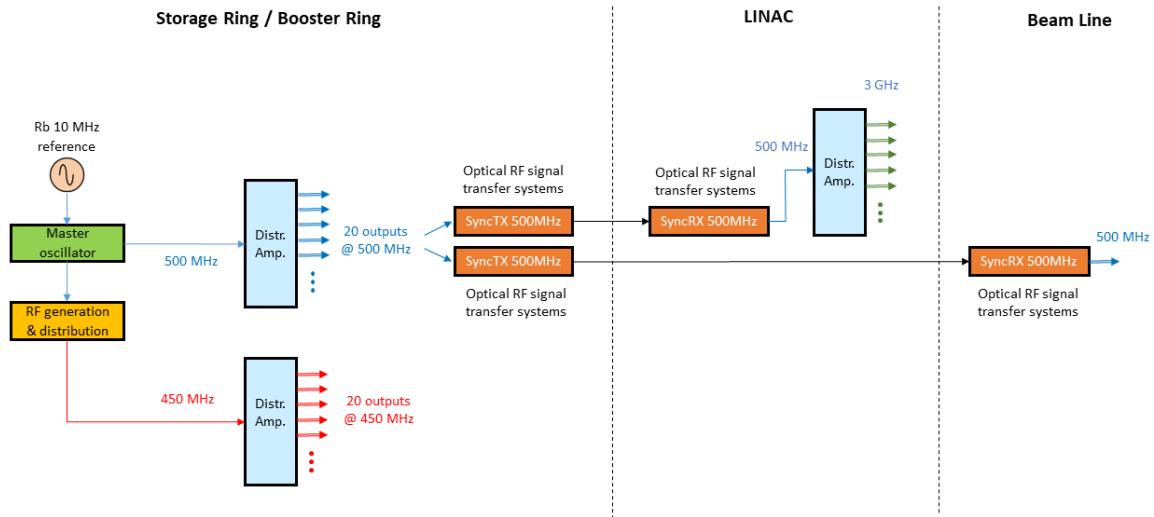
<Figure 2.1.9.23> Principles of Resonant Frequency Control.

⑥ Master Oscillator and RF Reference Signal Distribution



<Figure 2.1.9.24> Configuration of the RF generation and distribution systems.

The master oscillator is a source for generating RF reference signals that are distributed to LINACs, booster RF systems, storage RF systems, timing systems, beam diagnostic systems, laser system-based experiments, and beam lines. The master oscillator output must have extremely low phase noise characteristics to ensure stable synchronization between systems requiring RF reference signals and must be tunable in response to frequency variations caused by daily or annual changes in machine circumference. In addition, as the frequency of the output RF signal changes, the phase shift must be continuous. In order to generate RF reference signals with stable phase noise characteristics, a commercially available RF signal generator (RMS jitter: within a few tens of fs), which is used in various accelerator facilities and has been verified, will be used as a master oscillator. For the external 10 MHz reference signal input to the master oscillator, a Rubidium oscillator with good frequency stability characteristics is used for precise signal generation. Based on the RF reference signal output from the master oscillator, the 500 MHz signal and 450 MHz LO signal required for the LLRF system are generated and distributed by the RF generation and distribution system as shown in <Figure 2.1.9.24>.



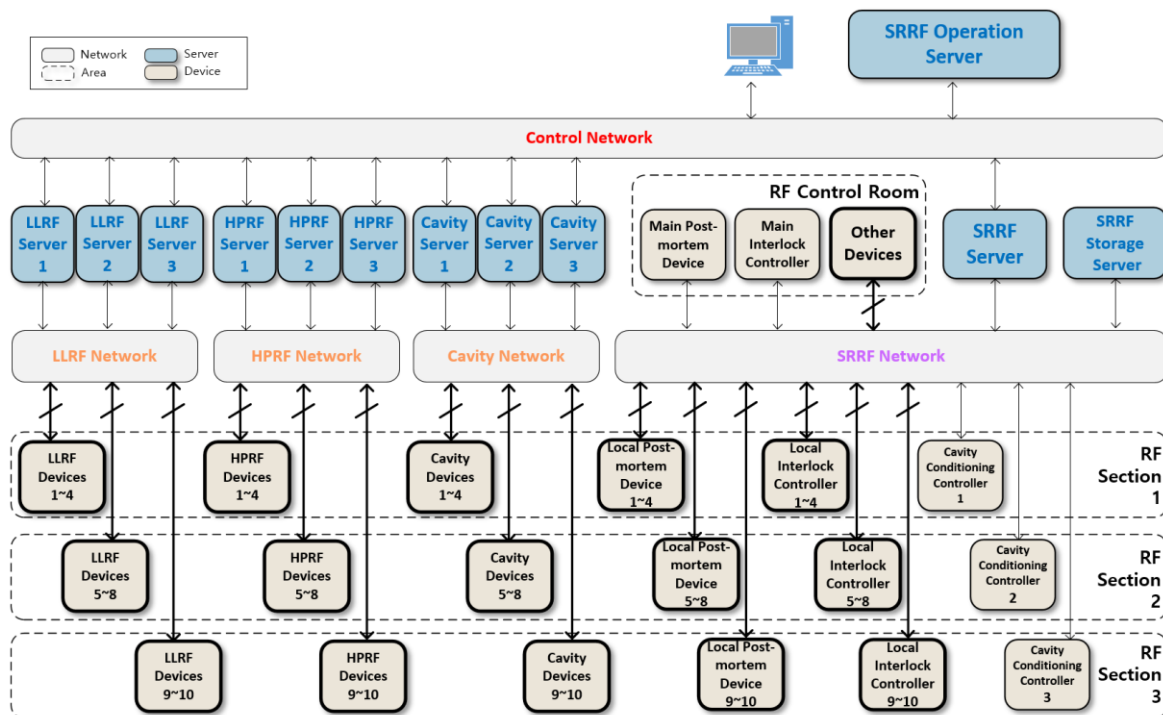
<Figure 2.1.9.25> RF reference signal distribution.

In the case of the storage ring RF station, booster ring RF station, and timing system, the master oscillator will be located near these systems. However, the LINAC station will be located several hundred meters away, which could result in RF signal loss, interference due to external temperature changes, and EMI (Electromagnetic Interference) during RF reference signal transmission. To deliver the RF reference signal to the LINAC station while maintaining jitter characteristics within hundreds of femtoseconds under such disturbances, a commercial optical RF signal transmission device will be used. The overall configuration of the RF reference signal distribution is shown in <Figure 2.1.9.25>.

(5) Storage Ring RF Operation and Diagnostic System

① Networks for RF System in the Storage Ring

The storage ring RF system is composed of subsystems (LLRF, HPRF, Cavity) and each subsystem has a dedicated local network to ensure stability and security as shown in <Figure 2.1.9.26>

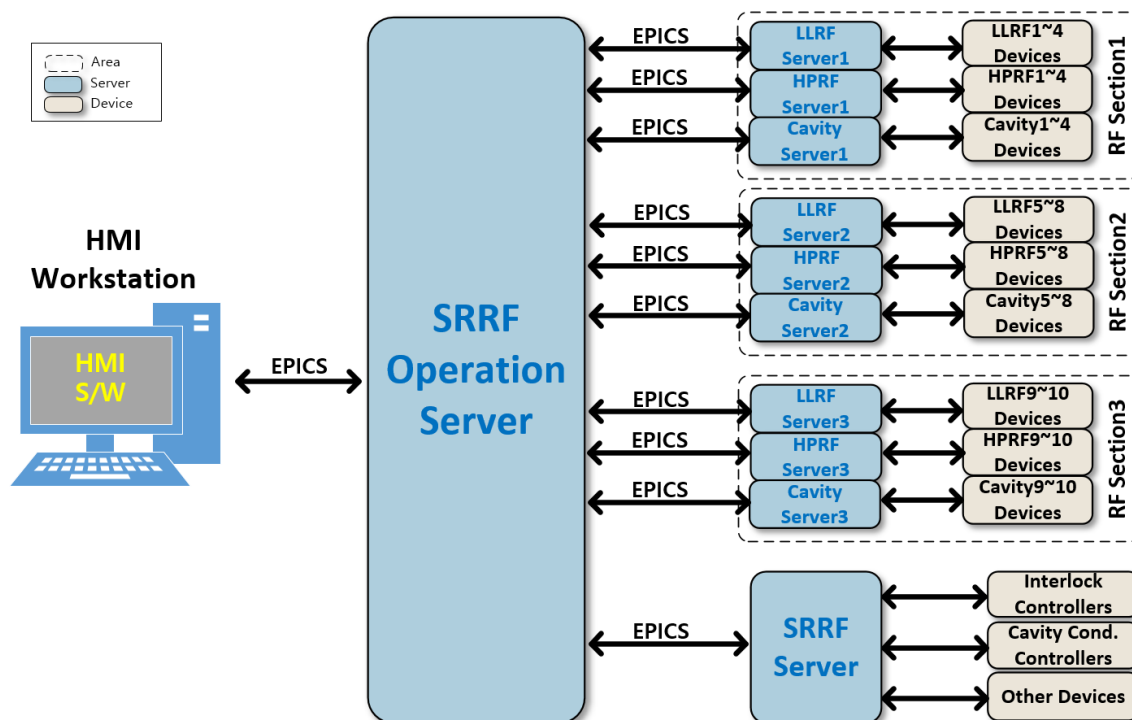


<Figure 2.1.9.26> Concept of networks for the SRRF.

A server to support EPICS (Experimental Physics and Industrial Control System) IOC (Input / Output Controller) service is needed in each RF subsystem to support the protocol and connect between a local network and the control network.

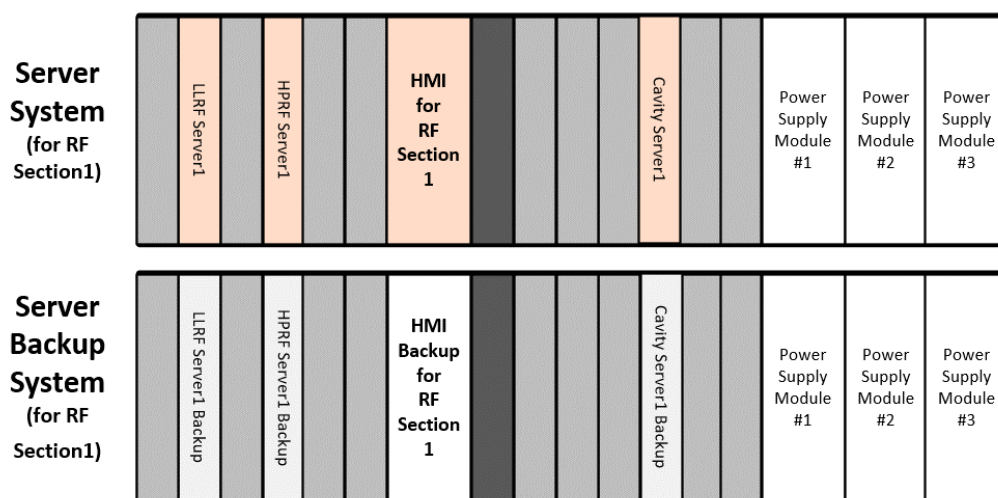
② Storage Ring RF Server System

Each EPICS IOC will support their own RF subsystem. The storage ring RF system should be operated without human interference by mode selection through the automatic control server. If necessary, an operator can control RF subsystems using the HMI software, as shown in <Figure 2.1.9.27>.



<Figure 2.1.9.27> Control diagram of the SRRF.

The cPCI (compact-Peripheral Component Interconnect) is a famous platform for industrial devices. The SRRF System uses cPCI computer modules for each EPICS IOC. 4 computer modules (for LLRF server1, HPRF server1, HMI for RF section-1 and cavity server-1) are included in a server chassis and a backup chassis is always ready for fast recovery as shown in <Figure 2.1.9.28>.



<Figure 2.1.9.28> Composition of the server system for the RF section1.

The following is a specification for the Server System.

<Specification of cPCI chassis>

3U cPCI backplane with 12 peripheral slots

2 + 1 Hot-swappable 500W + 250W cPCI power supply (support three 250W PSUs)

Temperature, voltage, and fan monitoring LEDs

Hot-swappable cooling fans & filters

<Specification of cPCI computer module>

cPCI 3U 1 slot (4HP) computer module

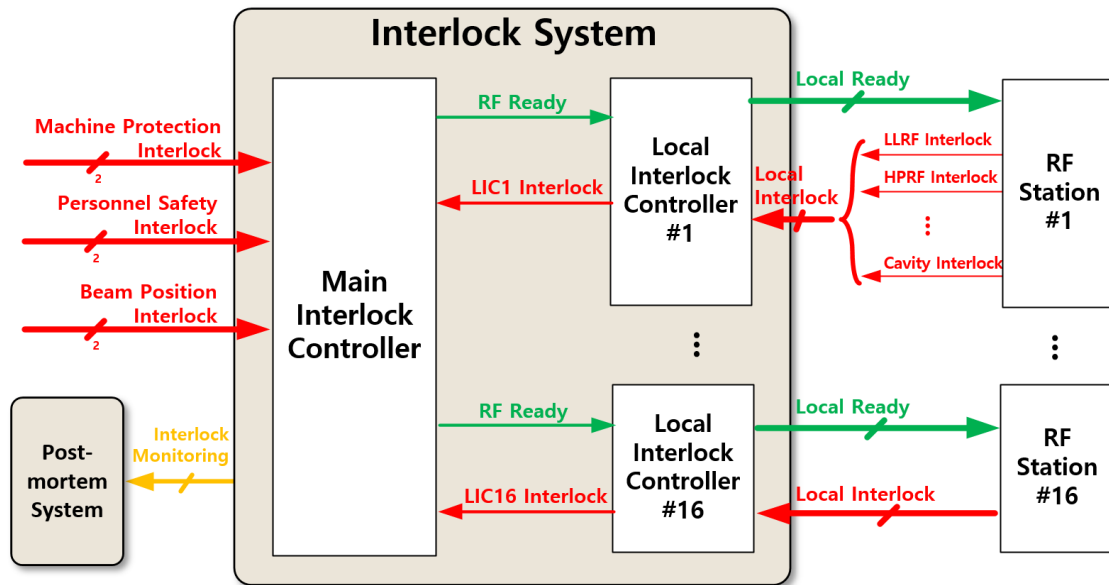
≥Quad-core Intel Atom x7-E3950 1.6GHz processor

≥4GB DDR3 memory · ≥512GB SSD M.2 SATA

≥2 gigabit ethernet, 1 USB, 1 display port

③ RF Interlock System in Storage Ring

The interlock system is designed to protect systems during unexpected operating conditions and interacts with various devices of RF station using interlock signals and ready signals. The system is composed of 16 LICs (Local Interlock Controllers) and a MIC (Main Interlock Controller) as shown in <Figure 2.1.9.29> It will cover the 16 RF stations for the storage-ring. The MIC will stop providing RF power to cavities, when the external interlock signals such as Machine Protection Interlock, Personnel Safety Interlock, or Beam Position Interlock are triggered. The LIC collects the status signals from each RF components and generates “ready” or “non-ready” signals, which are then passed to the master interlock system.



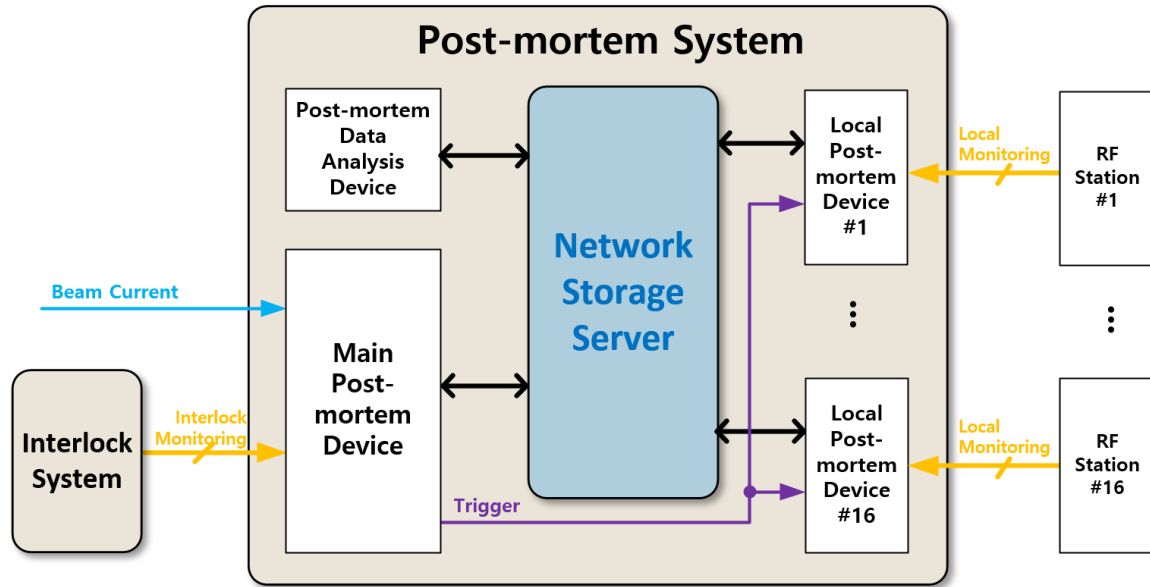
<Figure 2.1.9.29> Block diagram of the RF interlock system for storage ring.

A RF-dump can be triggered by external interlocks, local interlocks or a force stop command from the operator. The RF-dump time (the interval from the generation of the interlock signal to the actual RF shutdown) is a critical parameter for ensuring the safety of both personnel and machines. The desired RF-dump time for the storage ring RF system is defined as 100 us to include a safety margin.

④ Post-Mortem System for Storage Ring RF System

Monitoring signals from RF stations and the interlock system are recorded by the post-mortem during abnormal beam event. The usual recorded data is stored automatically on the network storage server along with the event. Additionally, the primary parameters for diagnostics should be logged in the quick recordable media of the post-mortem within a specified time window such as ± 1 second.

To merge and analysis the logged data, the system includes a post-mortem data analysis device as shown in <Figure 2.1.9.30>. To accurately identify the changes in parameters at the time of the fault and determine the cause of the fault, the post-mortem should have more than 1 MS/s sampling rate and more than 1M points record length each input channel.



<Figure 2.1.9.30> Block diagram of the post-mortem system for storage ring RF system.

(6) 3rd Harmonic RF Cavity

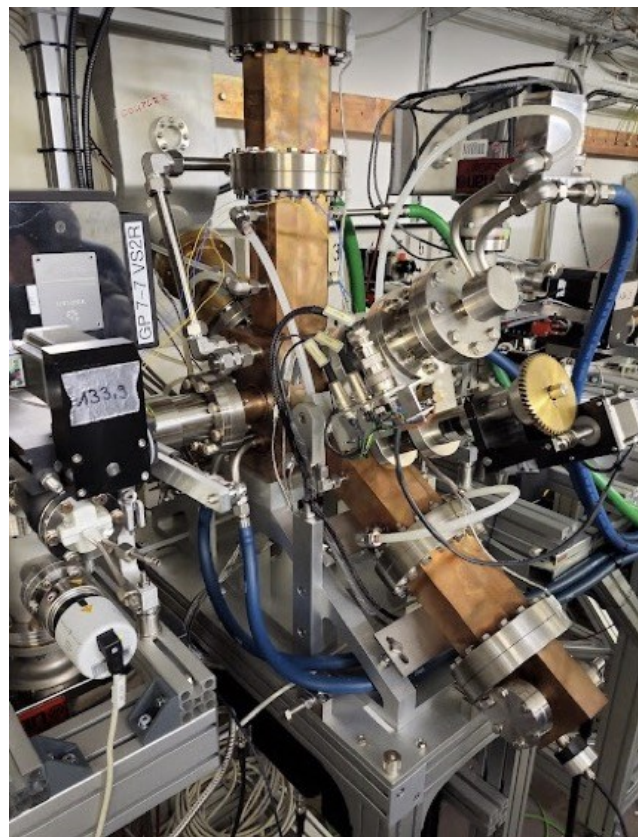
A high order mode (HOM) harmonic cavity is required to mitigate the reduction in beam lifetime caused by Touschek scattering and intra-beam scattering, both of which result from the low beam emittance of high-current.

In 4th generation synchrotron radiation accelerators, reducing emittance is crucial for increasing beam brightness. However, lowering the emittance increases the electron density within the bunch for high-current, leading to reduced beam lifetime and increased emittance due to Touschek scattering and intra-beam scattering. To address this, if voltage with a different intensity and phase from the main cavity is added to the primary RF voltage, it reduces the electron density inside the bunch. This causes the voltage phase at the bunch center to shift, elongating the bunch and decreasing charge density. As a result, high order mode (HOM) harmonic cavities, which serve this purpose, have been installed in both 3rd and 4th generation synchrotron radiation accelerators.

There are four types of 3rd harmonic cavities used in synchrotron radiation accelerators. The first is the normal conducting passive type cavity, which generates a field using the beam-induced field within the normal conducting cavity. The second is the normal conducting active type cavity, which creates a field by supplying RF power from an external source to the coupler. The third is the superconducting passive type cavity, which utilizes

the beam-induced field within a superconducting cavity. Finally, the fourth is the superconducting active type cavity, which generates a field by providing RF power to a superconducting cavity through an external source, and this approach is adopted at HEPS.

In the multi-purpose synchrotron radiation accelerator, the main cavities in the storage ring have been changed from superconducting cavities to normal conducting cavities. Since the main cavities have been defined as normal conducting, it is considered more cost-effective to also adopt the 3rd harmonic cavity as a normal conducting type, and thus this option is being considered first. In this regard, a normal-conducting 3rd harmonic cavity is being primarily examined, and among the possible designs, the ALBA type has been considered first because it shares a similar configuration with the main cavity and can be applied without major modifications. The ALBA-type cavity was designed by modifying EU-HOM damped cavity (main cavity), in which the frequency range was scaled up from the 500 MHz band to the 1.5 GHz band, and it has been manufactured by a domestic company in Korea. This cavity is currently being tested after installation in the BESSY-II storage ring. <Figure 2.1.9.31> shows a photo of the actual installation at BESSY-II. The main characteristics of ALBA 3rd harmonic cavity is shown in <Table 2.1.9.18>.



<Figure 2.1.9.31> normal conducting 3rd harmonic cavity.

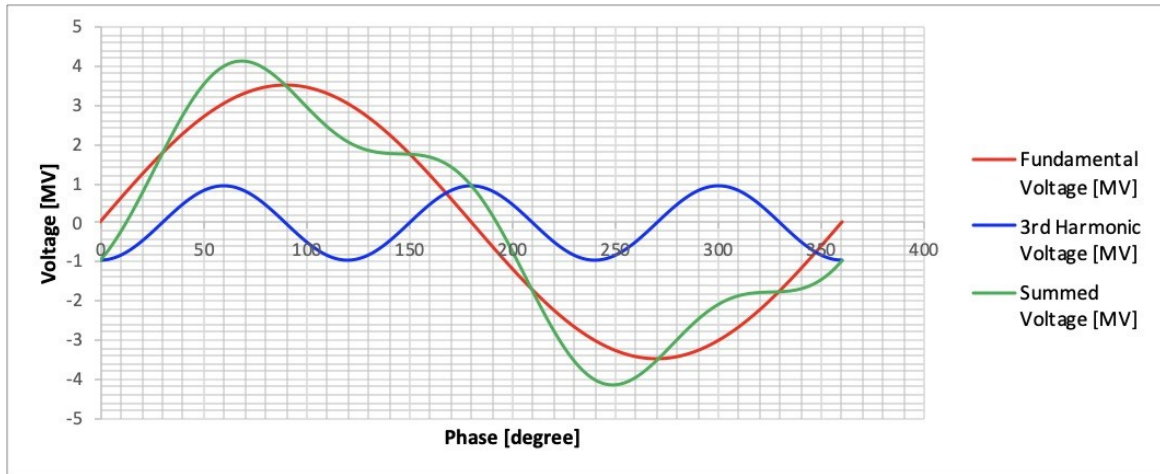
<Table 2.1.9.18> Normal Conducting 3rd Harmonic Cavity Key Parameters

parameter	value
Frequency [GHz]	1.5
Max. power coupler [kW]	20
unloaded quality factor	>14,000
shunt impedance [MΩ]	1.2
coupling factor	1.0 to 3.0
Tuning range [MHz]	6.0
Max. Accelerating Voltage [MV]	0.185

The acceleration voltage of the high order harmonic cavity mentioned in the 'PETRA-IV CDR' is given by the following equation.

$$V_{\text{HHC}} = V_{\text{RF}} \sqrt{\frac{1}{n^2} - \frac{1}{n^2-1} \left(\frac{U_0}{e_0 V_{\text{RF}}} \right)^2} \quad (\text{Equation 2.1.9.5})$$

The acceleration voltage V_{RF} required for the storage ring, the energy loss per turn U_0 , and the harmonic mode n are given by the following equation. For the storage ring, V_{RF} is 3.5 MV, U_0 is 1.877 MeV, and n is 3, yielding a V_{HHC} of 0.96 MV. Therefore, considering a 15% margin, an acceleration voltage of 1.1. MV is needed for the 3rd harmonic cavity. Based on the acceleration voltage of 0.185 MV for ALBA's 3rd harmonic cavity <Table 2.1.9.1.6-1>), which is currently being tested, a total of 6 or more 3rd harmonic cavities are required for stable operation in the multi-purpose synchrotron radiation accelerator. <Figure 2.1.9.32> shows the ideal acceleration voltage, applying the storage ring's main frequency of 500 MHz and the 3rd harmonic cavity frequency of 1.5 GHz, with a phase difference of 270° for V_{RF} and 0.96 MV for V_{HHC} .



<Figure 2.1.9.32> Superposition of Main RF Cavity and 3rd Harmonic Cavity Fields.

B. Booster Ring RF System

(1) Overview of the Booster Ring RF System

Unlike the previous PLS-II, which was fully accelerated by a linear accelerator and sent to the storage ring, the 4GSR uses a booster injection method, in which the electrons are first accelerated to 200 MeV in the linear accelerator before entering the booster and accelerated to 4 GeV in the booster. In the booster, the RF system is responsible for supplementing the energy lost by the incident electrons per booster rotation and providing sufficient energy during the energy ramping process. At a booster output energy of 4 GeV, the energy loss is 1671 keV, and the acceleration voltage to compensate for this loss and provide sufficient acceleration is 3 MV.

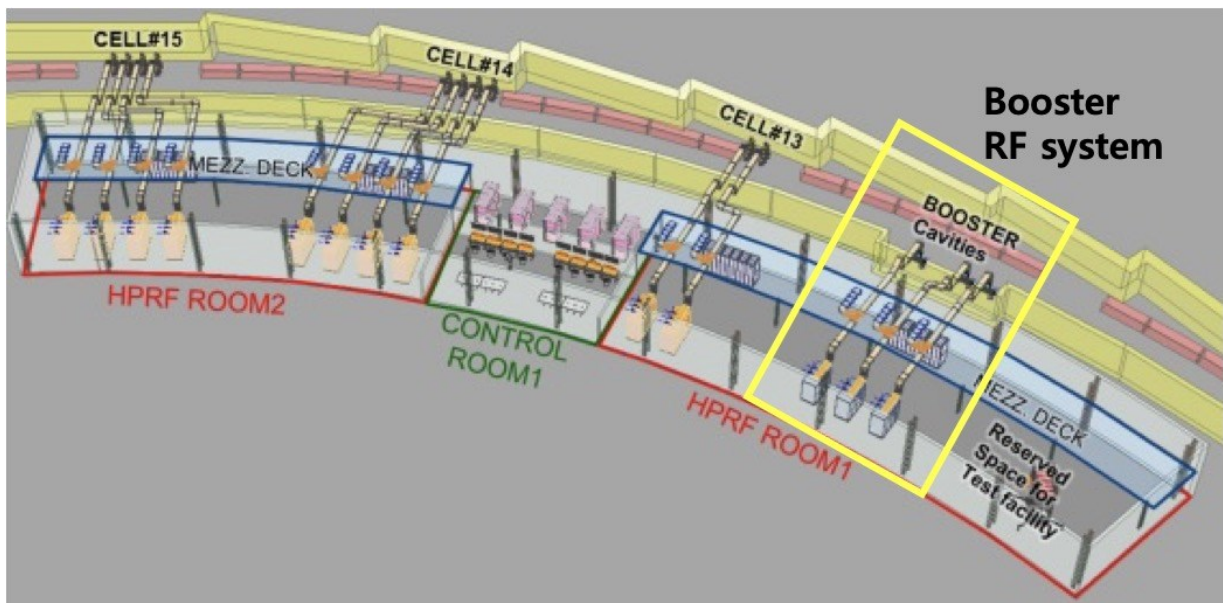
The main RF-related parameters of the 4GSR booster are shown in <Table 2.1.9.19>.

<Table 2.1.9.19> Primary specifications of booster ring

Parameter	Value	
Frequency [MHz]	499.594	f_0
Beam energy [GeV]	0.2 to 4.0	E_0
Beam Current single/multi [mA]	1/3 mA	I_b
Accelerating Voltage @ 0.2 GeV [MV]	0.3	V_{inj}
Accelerating Voltage @ 4.0 GeV [MV]	3.0	V_{ext}
Circumference [m]	773	-
Harmonic number	1,288	-

Revolution frequency [kHz]	387.9	f_{rev}
repetition rate [Hz]	2	-
Synchrotron Frequency [kHz]	4.24	-
Energy loss per turn @ 4.0 GeV [MeV]	1.671	E_{loss}

The booster ring is concentric with the storage ring and shares a tunnel with the storage ring. The booster ring RF cavity, which is placed deeper than the storage ring, is located next to the straight section 13A where the storage ring main cavity is installed. The other RF devices are located in the RF Building, as is the storage ring RF system. In <Figure 2.1.9.33>, the yellow boxed area shows the booster RF system.



<Figure 2.1.9.33> Booster RF System Placement - Place the storage ring main cavity close to the RF system. Yellow boxed area.

(2) Booster Ring RF Cavity

The booster RF cavity serves to accelerate electrons from 200 MeV to 4 GeV and provides the necessary acceleration voltage to compensate for the energy loss as electrons circulate in the booster. To select a type of RF Cavity that meets the specifications of the multi-purpose synchrotron radiation accelerator booster, a study was conducted on the cavities used by global synchrotron radiation accelerator boosters. <Table 2.1.9.20> presents the frequency, energy, circumference, energy loss per turn, and cavity type for global synchrotron radiation boosters that are either operational or currently under construction.

<Table 2.1.9.20> Specifications for Booster RF Cavities in Synchrotron Radiation Accelerators Worldwide

Light source	f_0 [MHz]	Energy [GeV]	Circumference	Repetition rate [Hz]	Energy loss [keV]	Cavity type (#of cavity)	Total Gap Voltage (one Cavity)
ESRF-EBS	352	0.2→6.0	298	4	4,500	5 cell LEP (4)	9.00 (2.25)
APS-U	352	0.45→6.0	368	2	-	5 cell LEP (4)	8.30 (2.07)
PETRA-IV	500	0.45→6.0	316.8	2, 5	4,040	5 cell (9)	12.00 (1.33)
Diamond-II	500	0.1→3.5	163.8	5	947	PETRA 5 cell (2)	2.00 (1.00)
SLS-2	500	0.1→2.4	270	3	-	ELETTRA single cell (1)	0.50 (0.50)
HEPS	500	0.5→6.0	454	1	4,000	PETRA 5 cell (6)	8.00 (1.33)
NSLS-II	500	0.2→3.0	158.4	1	686	PETRA 7 cell (1)	1.20 (1.20)
SIRIUS	500	0.15→3.0	496.8	2	721	PETRA 5 cell (1)	1.05 (1.05)
SSRF	500	0.15→3.5	180	2	1,159	PETRA 5 cell (2)	1.74 (0.87)
TPS	500	0.15→3.0	496.8	3	586	PETRA 5 cell (1)	1.2
BESSY-II	500	0.05→1.9	96	10	-	PETRA 5 cell (1)	-
ALBA	500	0.1→3.0	249.6	3	627	PETRA 5 cell (1)	1.00

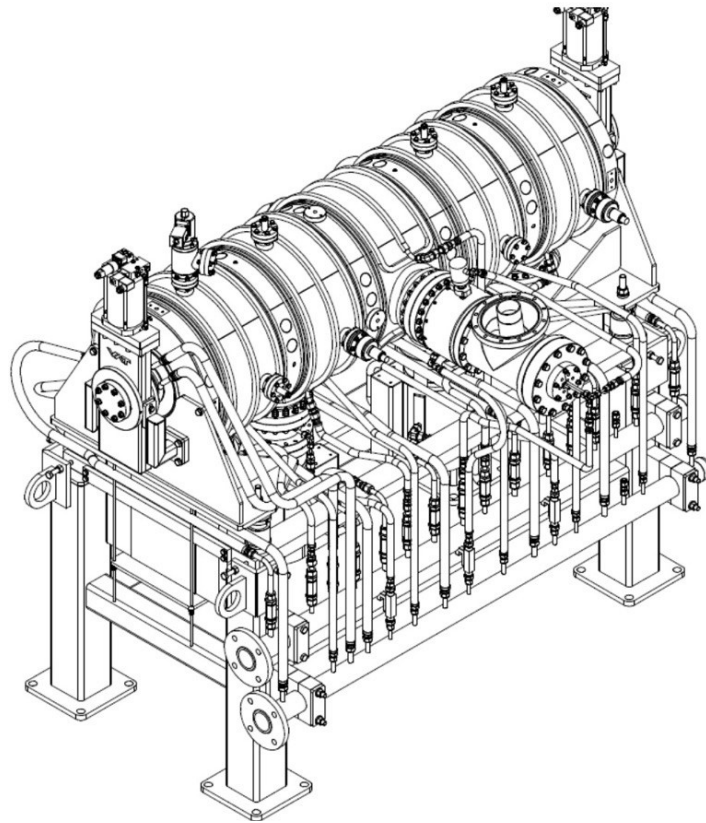
ESRF-EBS and APS-U, which operate at a frequency of 352 MHz, use a 5-cell LEP type cavity, while most synchrotron radiation accelerators operating in the 500 MHz band use a 5-cell PETRA-type cavity. SLS-2 is the accelerator that chose a single-cell cavity for the booster to match the storage ring cavity type, while all other accelerators use multi-cell cavities. Generally, multi-cell cavities are preferred over single-cell cavities for their greater efficiency in reducing installation space and costs, which is why they are widely used in booster applications.



<Figure 2.1.9.34> LEP 5 cell Cavity installed in ESRF-EBS (left), PETRA 5 cell Cavity installed in BESSY-II (right).

The PETRA-type 5-cell cavity, as shown in <Figure 2.1.9.35>, which has already been

validated for performance in other synchrotron radiation accelerators, was selected for its cost efficiency. This choice reduces space requirements and the number of cavities and RF devices needed.



<Figure 2.1.9.35> PETRA type 5 cell Cavity.

<Table 2.1.9.21> Main Parameters of PETRA type 5 cell Cavity

Parameter	Value
Flange to flange length [m]	1.65
Max. power coupler [kW]	120
unloaded quality factor	>29,000
shunt impedance [MΩ]	15
coupling factor	1.0 to 3.0
Tuning range [MHz]	1.0
Accelerating Voltage @ 60 kW [MV]	1.3

<Table 2.1.9.21> shows the main parameters of the PETRA-type cavity. The circumference of the multi-purpose synchrotron radiation booster is 772.893 meters, which is similar to that of the storage ring, as both are installed in the same tunnel. In the booster's single-bunch mode, the beam current is 1 mA, and the output energy is 4 GeV. To achieve this, a 3.0 MV acceleration voltage is necessary to compensate for the energy loss. With three 5-cell cavities installed, approximately 35 kW of RF power from a coupler is needed to produce 1 MV of acceleration voltage per cavity. Due to the low beam current in the booster, most of the RF power is dissipated as heat in the cavity, with only a small portion transferred to the beam for energy compensation and acceleration. As the RF power delivered to the beam is minimal, the calculated coupling factor (β) is close to 1. However, to account for potential errors in RF power settings, the coupling factor for the booster RF cavities is planned to be operated at 1.20. <Table 2.1.9.22> summarizes the acceleration voltage, coupling factor (β), and required RF power for operating three PETRA-type 5-cell cavities in the multi-purpose synchrotron radiation booster. The loss power (P_c) at this time was calculated using the following equation, with R_{sh} set to 15 MΩ.

$$P_c = \frac{V_c^2}{2R_{sh}} \text{ [W]}, \quad R_{sh} = (R/Q) \cdot Q_0 \text{ [M}\Omega\text{]}$$

<Table 2.1.9.22> 5 cell Cavity operating Parameters in Korea Multi purpose Synchrotron Radiation Accelerator

Parameter	Value
Total Accelerating Voltage @ 4 GeV	3.0 MV
Number of Cavity	3
Accelerating Voltage unit Cavity	1.0 MV
Coupling factor, β	1.20
RF power @ coupler unit cavity	34.41 kW
Dissipated power unit Cavity (P_c)	33.33 kW
Beam loading power unit Cavity	1.7 kW

If one of the three RF cavities fails during operation, the required RF power was calculated based on the assumption that only two RF cavities are operational. In this case, the RF cavity will be operated at a gap voltage of 1.3 MV. With two cavities in operation, the power (P_c) required at the coupler is 56.33 kW, and approximately 64 kW of RF power is needed when accounting for transmission losses. <Table 2.1.9.23> summarizes the required power based on the number of RF cavities. Here, the transmission loss was estimated to be 10% of the total power, and the power (P_b) transmitted to the beam is 1.7 kW at 4 GeV.

<Table 2.1.9.23> Required RF power according to Number of Cavities

	P_c	P_b	$P_{loss} (\leq 10\%)$	P_t
2 cavities	56.33 kW	1.7 kW	5.8 kW	63.83 kW
3 cavities	33.33 kW	1.7 kW	3.5 kW	38.53 kW

In order to share the main parts of the storage ring, the Cavity of the boot ring is different in form from the main Cavity, but the Input Coupler and tuner drive parts are made the same and interchangeable, reducing the supply and maintenance time and supply cost in the event of a failure.

(3) Booster Ring High-Power RF System

① High-Power RF Amplifier

In the field of accelerators, the power amplifiers used can generally be categorized into klystron power amplifiers, which utilize klystrons, and solid-state power amplifiers (SSPA), which use RF transistors. In the booster ring of the multi-purpose synchrotron accelerator, where high output power of up to around 80 kW is required, it is more advantageous to choose a solid-state power amplifier (SSPA) rather than a klystron amplifier, which requires high-voltage power supplies and vacuum conditions. SSPAs operate at low voltages below 50 VDC and offer superior reliability and operational efficiency.

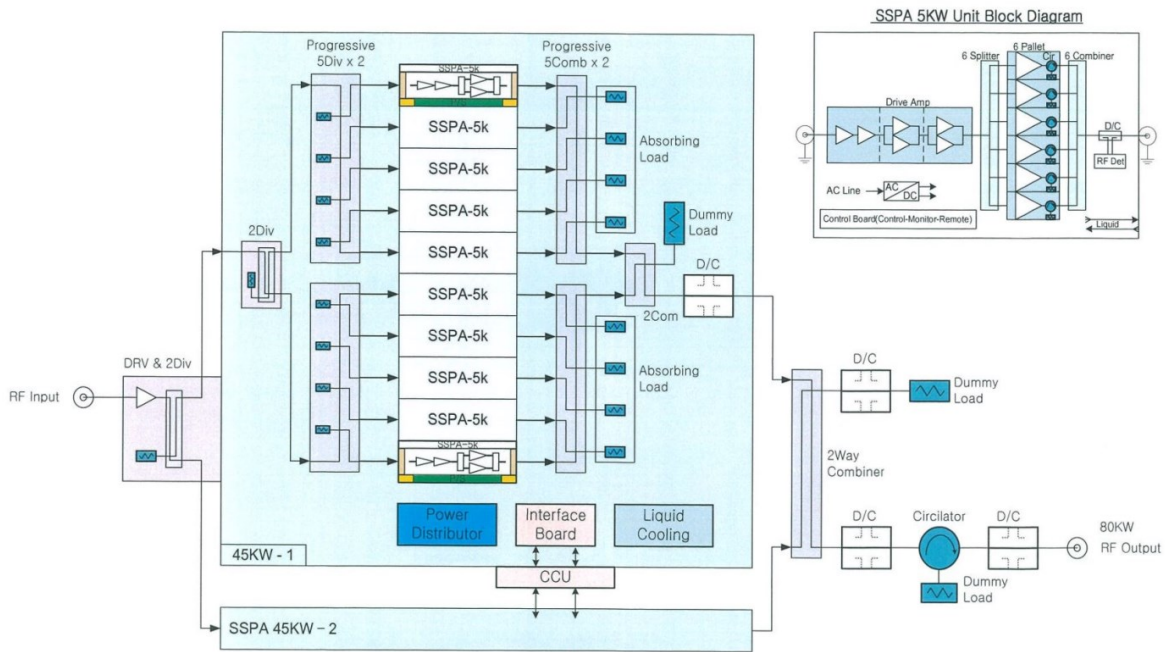
Moreover, modern semiconductor-based power amplifiers (SSPA) exhibit better noise performance than the currently used klystron-based amplifiers. In long-term operation, SSPAs are more efficient than klystron amplifier systems, resulting in reduced operational power costs.

Therefore, considering factors such as stability, reliability, cost, operation, and maintenance, an 80 kW-class high-power SSPA was selected for the multi-purpose synchrotron accelerator booster.

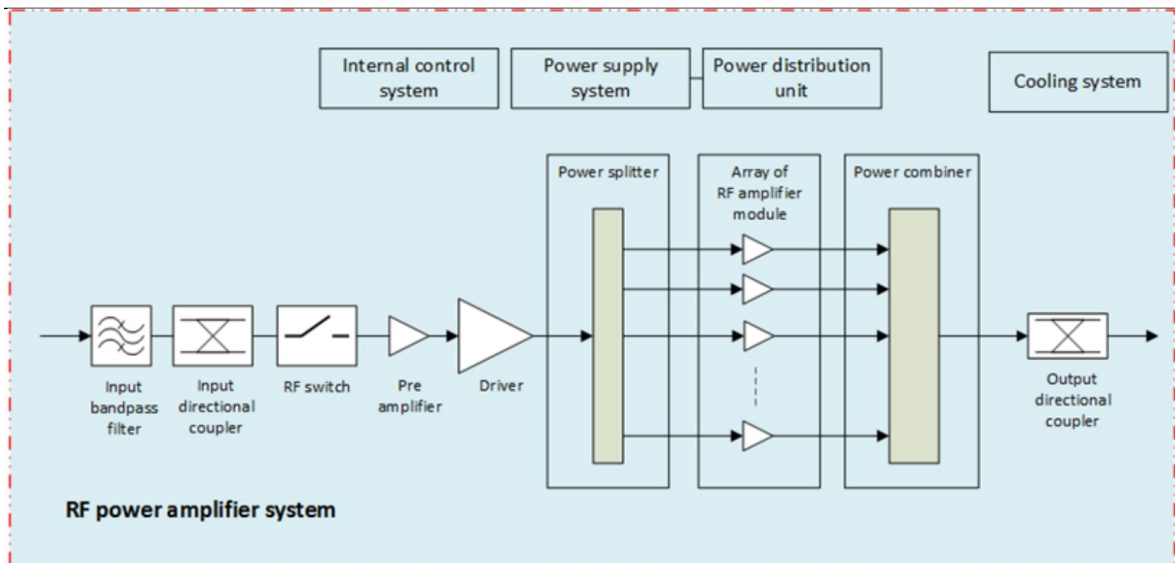
② Solid State Power Amplifier (SSPA)

The configuration of the booster ring SSPA is detailed in <Figure 2.1.9.36> and <Figure 2.1.9.37>. Essentially, the booster ring SSPA can apply the same specifications as the storage ring SSPA. However, unlike the storage ring, which operates in continuous wave mode, the booster ring SSPA must perform repeated ramping operations from zero to operational output.

In a high-speed pulse amplifier, the transistor bias current must increase rapidly in accordance with the required pulse. To ensure this, the inductance value of the bias power supply needs to be sufficiently low. When the output of each transistor is approximately 750 W, with a bias voltage of 50 V and a DC-to-RF efficiency of about 50%, the required bias current is approximately 30 A (calculated as $I = 750 \text{ W} \times 2 / 50 \text{ V}$). Therefore, the inductance value of the DC bias power supply must be adjusted to allow the current to increase from 0 to 30 A within the ramping time of 200 ms.



<Figure 2.1.9.36> 80 kW SSPA block diagram (1).



<Figure 2.1.9.37> 80 kW SSPA block diagram (2).

The specifications for the 80 kW SSPA used for booster cavity are detailed in <Table 2.1.9.24>.

<Table 2.1.9.24> Specification of SSPA for Booster RF Cavity

SSPA requirements	
Nominal output power (@P1dB)	80 kW (CW)
Frequency	500 MHz \pm 2 MHz (flatness <0.5 dB)
Input Power	0 dBm (1 mW) for nominal output
Load VSWR	better than 1.22:1(>20 dB) w / Load or Circulator
Output flange	WR1800
Operation mode	CW Ramp (1 to 80 kW/0.2 s) Pulse (100 us/10 Hz)
Amplification class	AB
Efficiency at nominal power	>50% (AC to RF)
Cooling water temperature	25 \pm 1°C (supplied by PAL)
Water cooling temperatures for Pallet amplifiers	<35 \pm 1°C
Power stability	less than 0.5dB (@1 hour @25 \pm 1°C)
Phase stability	less than 3° (@1 hour @25 \pm 1°C)
Harmonic & Spurious	<-30 dBc & <-60 dBc
Phase Noise (short-term stability)	<-90 dBc @1 kHz
Protection	over-reflected input output current temperature
Monitoring	input power output power current for each module cooling temperature water pressure & flow
Control	Local & Remote w/ EPICS
HMI control panel	>17" monitor
Rack size	less than 2.0m(W) \times 1.8m(D) \times 2.2m(H)
including items: remote control PC, FAT, SAT	
including spares - SSA modules: 10% of 80 kW	

Additionally, the SSPA is cooled using Low Conductivity Water (LCW). Even if up to 5% of the RF amplification modules experience a failure, sufficient reliability and redundancy must be ensured so that normal operation can continue without triggering the interlock to shut off the RF switch. Faulty modules are typically replaced during the next scheduled maintenance.

③ High-Power RF Transmission Line

To reliably transmit the amplified 80 kW output from the SSPA to the cavity, a WR1800 waveguide was selected. While a 6-1/8" EIA coaxial line could also be used, the decision was made considering installation, maintenance, and compatibility with the storage ring HPRF system.

The circulator is positioned between the SSPA and the RF cavity to bypass excessive reflection to a dummy load, preventing damage to the amplifier. It also ensures impedance matching, allowing for smooth RF transmission and operation.

During normal operation, the dummy load is connected to the circulator to absorb reflections from the cavity. During maintenance, the connection to the cavity is shorted so that full reflection is absorbed by the dummy load through the circulator, making it easier to measure the SSPA's output. Two types of dummy loads are available: a coaxial water load and a WR1800 ferrite load. The ferrite type was selected for the booster ring dummy load due to its superior return loss characteristics and the fact that the RF signal and cooling water do not come into direct contact, ensuring more stable operation.

The specifications for RF system transmission components determined for the multi-purpose synchrotron accelerator are listed in <Table 2.1.9.25>.

<Table 2.1.9.25> Specification of RF transmission lines

Transmission	Circulator	Dummy Load	Directional Coupler	Flexible waveguide
WR1800	WR1800 type	Ferrite type return loss: < -30 dB	60 dB	WR1800 Horizontal 1 ea Vertical 1 ea

<Table 2.1.9.26> RF control target specifications for Booster ring LLRF systems

Parameter	Value
Nominal RF frequency (MHz)	499.593975 MHz
Repetition rate (ramping) (Hz)	2
RF resonance frequency range (MHz)	499 to 501 MHz
Amplitude stability (%) (@ cw operation)	<1 (rms)
Amplitude stability (%) (@ ramping)	< ± 2 (rms)
Phase stability (°) (@ cw operation)	< ± 1 (rms)
Phase stability (°) (@ ramping)	< ± 2 (rms)
Phase control range (°)	-180° to +180°
Field flatness (%)	< ± 2

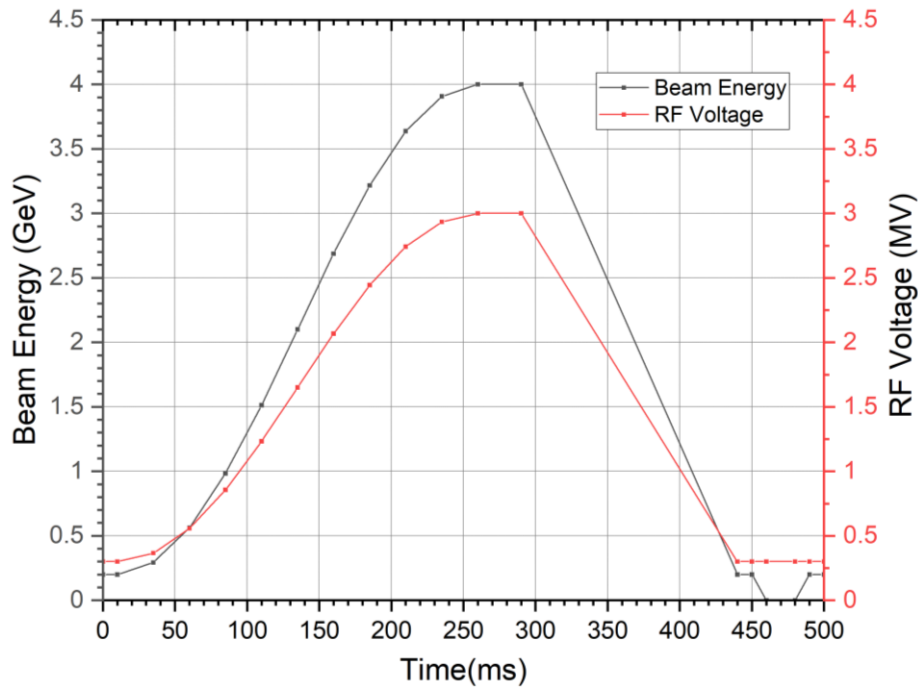
② Design and Fabrication of a Booster LLRF System

The LLRF system for boosting ring requires RF voltage ramping control and field flatness control functions in addition to the functions required for the LLRF system for storage ring, but can share many parts in terms of hardware and software. Therefore, considering the ease of system development and compatibility with the storage ring LLRF system, the booster ring LLRF system has been designed to expand its functions based on the hardware configuration and specifications of the storage ring LLRF system. The LLRF system for 4GSR has been designed based on technologies (hardware, algorithms, etc.) that have been verified and successfully applied to various accelerator facilities through prior development cases. Additionally, it will be designed and manufactured in parallel with prior research on high-speed sampling in the GHz band, high-speed data acquisition, and development of integrated digital boards based on SoC technology, which have become easier to implement due to advances in FPGAs, ADC/DAC, PLL chips, etc.

③ RF Ramping and Amplitude/Phase Control

The booster ring RF cavity accelerates the electrons from 200 MeV to 4 GeV at a repetition rate of 2 Hz, compensating for the energy lost as the electrons circulate in the booster ring. Consequently, the accelerating voltage does not remain constant but has a ramping profile as shown in <Figure 2.1.9.39>. The RF voltage ramps up and down from 0.3 MV to 3.0 MV in corresponding to the change in beam energy, and this process is triggered by the signal from an external timing system as a reference signal. The defined RF set-point table for RF ramping is applied to the FPGA control logic of the LLRF system. For the ramp profile step, the final specifications suitable for 4GSR booster ring operation will

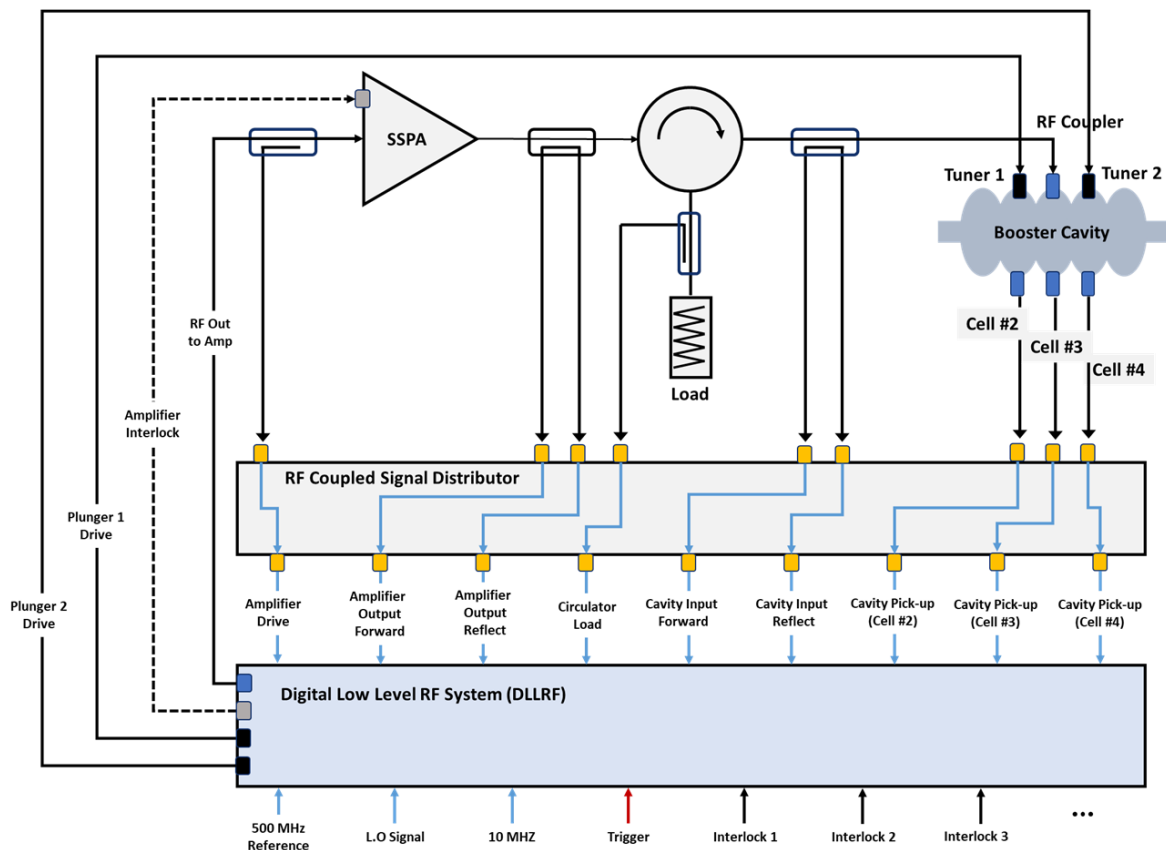
be selected by referring to international case studies. (SSRF: 50 set-point (repetition rate: 1 Hz) / NSLS-II: 512 set-point (repetition rate: 1 Hz) / TPS: 1024 set-point (repetition rate: 3 Hz)) The amplitude and phase control are performed through the same signal processing as the storage ring LLRF system. When the signal picked up from the RF cavity is input to the digital board through IQ sampling (or non-IQ sampling) and digital filtering, the calculated errors are corrected by PI control.



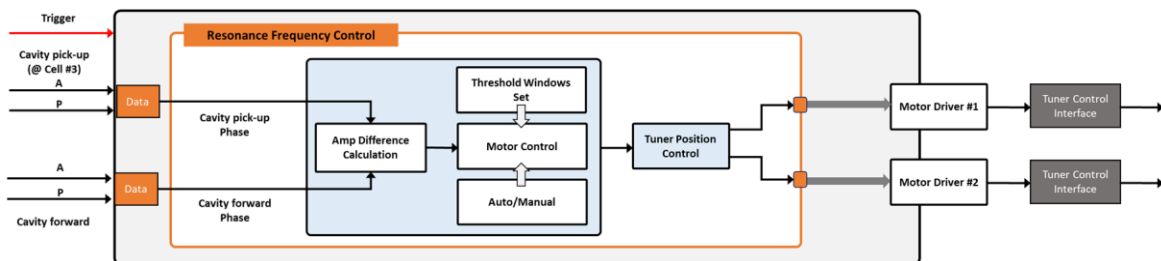
<Figure 2.1.9.39> Ramping curves of beam energy and RF acceleration voltage.

④ Tuning Control and Field Flatness Control for Booster Ring RF System

Unlike the single cell cavity for storage ring, the PETRA type cavity for booster ring is a 5-cell cavity. Therefore, it requires additional field flatness control function to maintain a uniform distribution of the accelerating field inside each cavity cell. As shown in <Figure 2.1.9.40>, the PETRA type cavity is equipped with two plungers. In addition to the pick-up port for resonance frequency and amplitude/phase control (located in cell 3), there are additional pick-up ports for field flatness monitoring installed in cells 2 and 4 of the cavity. The tuning loop control and field flatness loop control are managed by tuners that adjust the positions of the two plungers. As shown in <Figure 2.1.9.41>, the phase difference between the pick-up signal from cell 3 and the forward signal is calculated. If the resulting detune angle exceeds the defined tuning threshold, both tuners are adjusted in the same direction to maintain the resonance frequency within the target value.

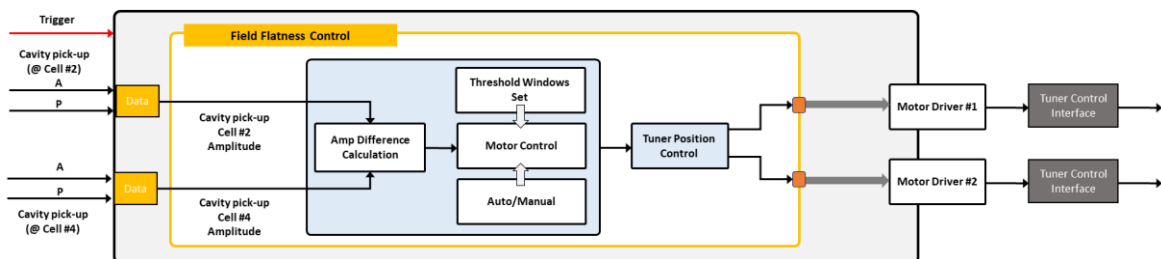


<Figure 2.1.9.40> Signal layout for booster ring RF cavity control.

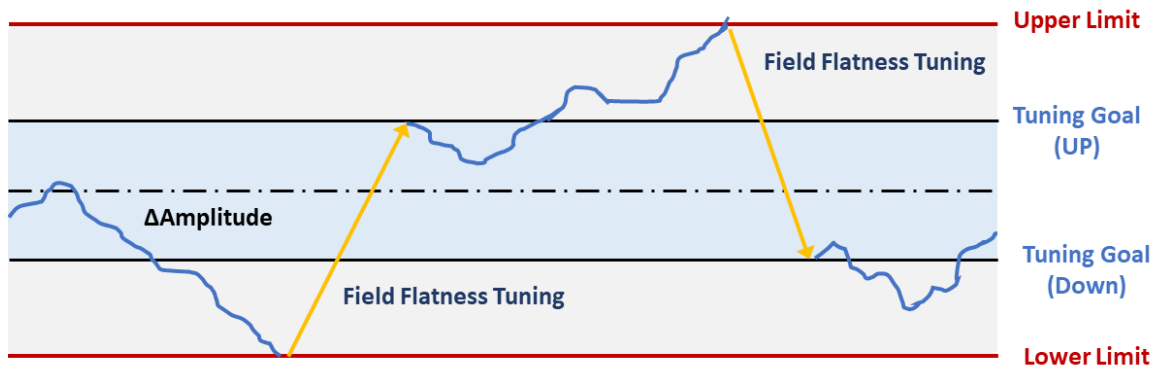


<Figure 2.1.9.41> Digital signal processing for resonance frequency control.

As shown in <Figure 2.1.9.42> The difference in field strength within the cells calculated from the pick-up signals of cell 2 and 4, is monitored. If the difference exceeds the field flatness threshold, the two tuners are operated in opposite directions to maintain the field intensity within the target value.

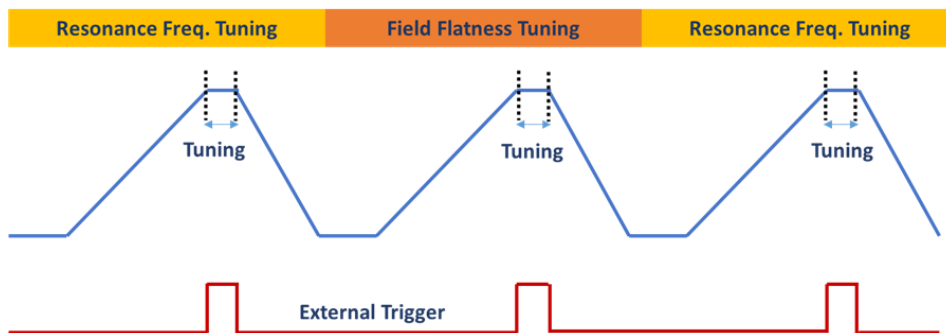


<Figure 2.1.9.42> Digital signal processing for field flatness control



<Figure 2.1.9.43> field flatness control

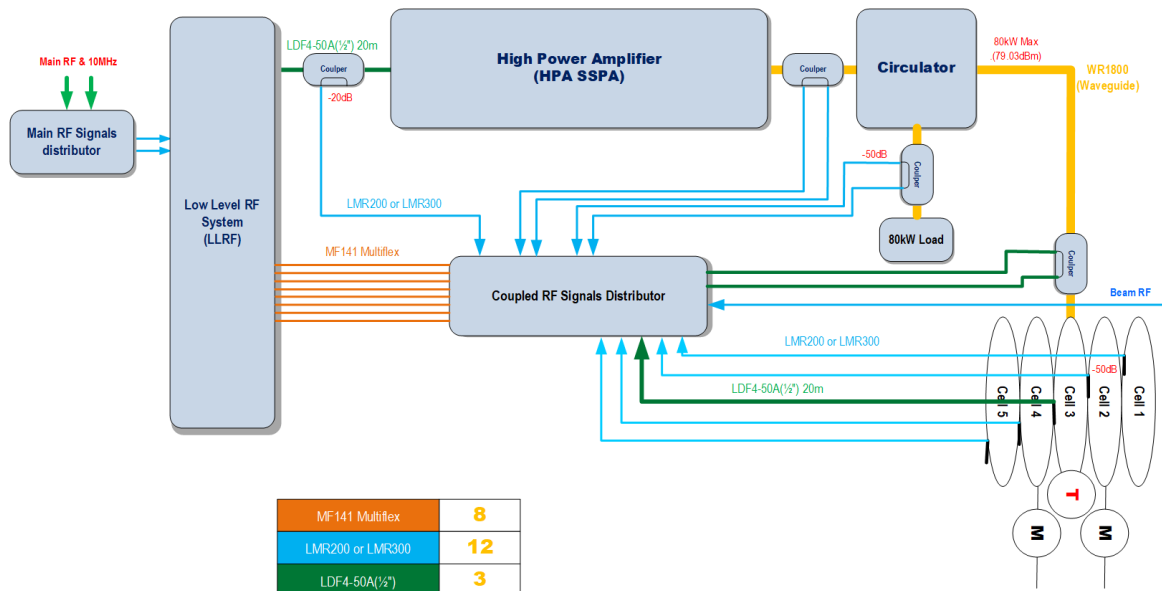
The tuning loop and field flatness loop control are only activated when the RF acceleration voltage is in top-up mode, and the tuning loop control and field flatness control loop are sequentially operated in alternation and synchronized with an external trigger as shown in <Figure 2.1.9.44>.



<Figure 2.1.9.44> Tuning loop / field flatness control sequence for booster LLRF systems

⑤ Distribution and Transmission of RF Signals

The RF signal input and output configuration of the booster ring RF device is as shown in <Figure 2.1.9.44>. The maximum power of the RF signal applied to the RF cavity is expected to be 80 kW (79.03 dBm), and the RF signal output from the waveguide coupler (60 dB) is up to 0.08 W (19.03 dBm).



<Figure 2.1.9.45> RF signal transmission for booster ring

The RF signal transmission at each RF terminal will be designed to reduce RF phase changes due to the environment, and the RF signal level will be adjusted. For the RF signal transmitted through the waveguide coupler, we plan to use a coaxial cable with a relatively large diameter, low loss, and small phase change. (In case of LDF4-50A cable, it has the insertion loss within 1 dB (based on 20 meters) and the change within 0.1 degrees at room temperature.)

2.1.10 Magnet Power Supply (MPS)

A. Overview

All the magnets of the storage ring are powered by individual magnet power supplies (MPS), while the magnets of the booster ring are connected in series, excluding low-capacity MPS. The advantages and disadvantages of individual power supply and series connection powering are as follows:

○ Individual Power Supply

- High freedom in controlling the B-field of each magnet.
- Lower stored energy in each magnet connected to the MPS allows emergency shutdown via Crowbar Switch, enhancing safety.
- High insulation is not required due to the relatively lower output voltage.
- An increased number of output cables, but they can be installed over the shortest distance without crossing other equipment, reducing EMI/EMC issues.
- Favorable for air-cooling, leading to the effect of distributed heat sources.
- Lower output voltage compared to series connection facilitates modular configuration of MPS, which has many advantages.
- Each MPS is required to be highly accurate to provide the same current to the same type of magnets.
- Timing synchronization is required for identical operation.
- The B-field of each magnet can change due to hysteresis, which requires control.
- Easy to maintain spare parts.

○ Series connection

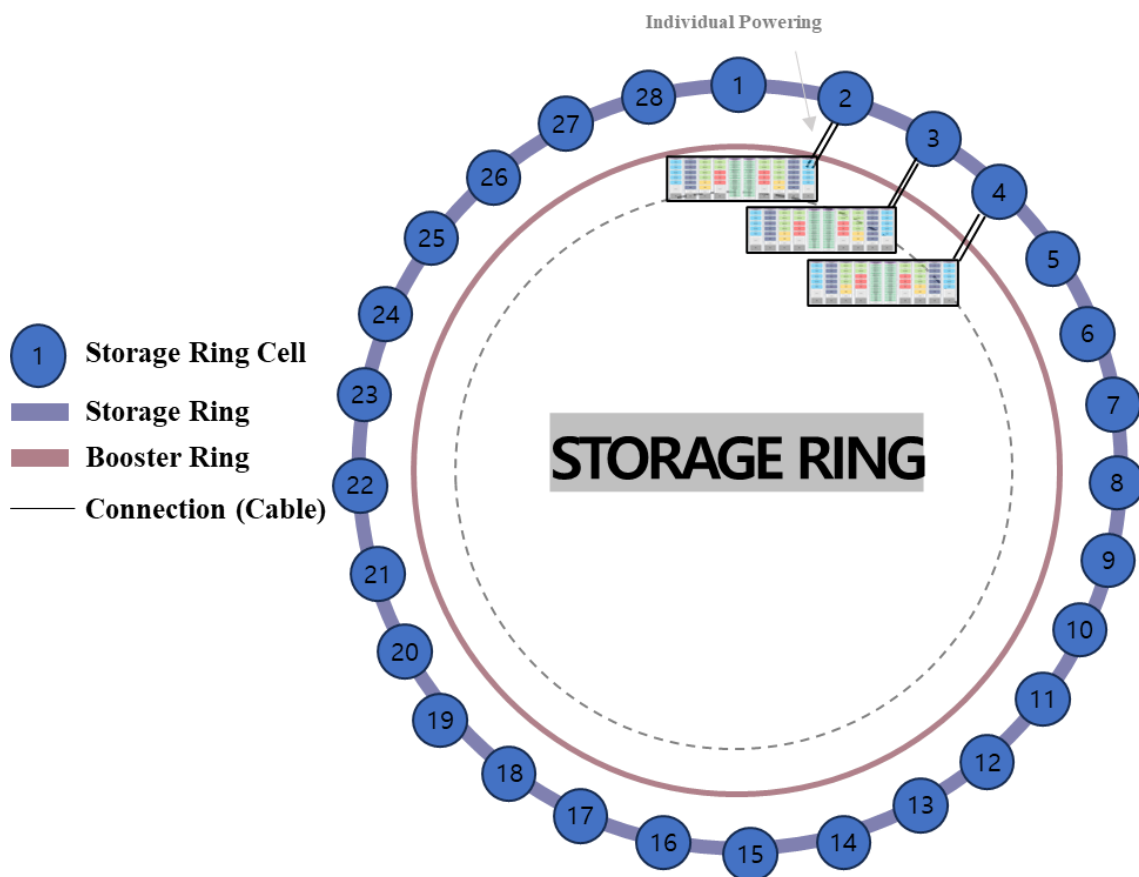
- As the same current is supplied to all the magnets connected in series, it is advantageous to generate the same B-field in those magnets.
- Although the output cable length increases, the number of output cables to be maintained

and managed decreases.

- Water cooling is advantageous and lowers cost because the number of power supplies is small.
- The number of MPS that need maintenance and diagnosis is small.
- MTTR (Mean Time To Repair) is relatively long.

B. Storage Ring MPS

The MPS for the storage ring is distributed over 28 locations, just like the 28 periodic sectors of the magnets, providing power to each individual magnet. The schematic diagram of this configuration is shown in <Figure 2.1.10.1> below.



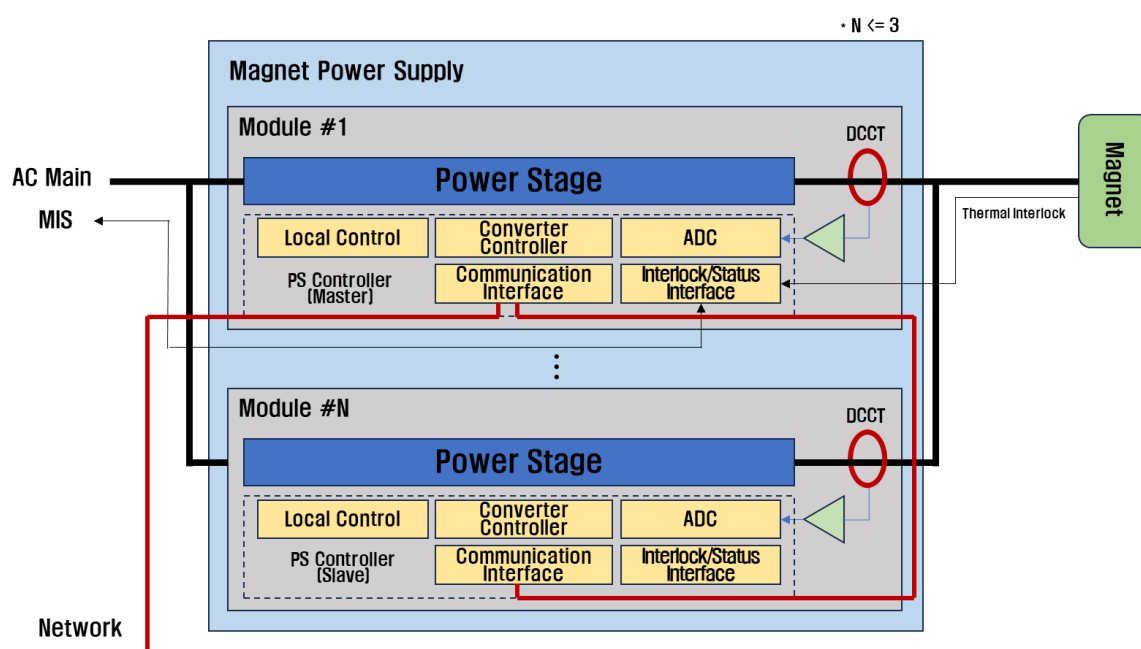
<Figure 2.1.10.1> Configuration of storage ring MPS connection

<Table 2.1.10.1> Storage ring modular magnets: specifications and cable

Magnet Type	Magnet Name	Magnet Qty		Magnet Resistor (Ohm)	Magnet Inductance (H)	Current (A)	Trim	Cable (AWG/KCMIL)
		Qty/Sec	Total					
Center Bend	Central BM	1	28	0.0313	0.023	228.5	-	300
Quad-Bend & Reverse Bend	DQ31U	1	28	0.068	0.037	119.1	T	4/0
	DQ32U	1	28	0.0488	0.0223	119.8	T	4/0
	DQ51U	1	28	0.128	0.167	225.0	T	300
	DQ52U	1	28	0.169	0.098	102.4	T	4/0
	DQ52D	1	28	0.169	0.098	102.4	T	4/0
	DQ51D	1	28	0.128	0.167	225.0	T	300
	DQ32D	1	28	0.0488	0.0223	119.8	T	4/0
	DQ31D	1	28	0.068	0.037	119.1	T	4/0
Quadrupole	QHU1	1	2	0.068	0.037	34.9	-	4/0
	QHU2	1	2	0.068	0.037	59.9	-	4/0
	QHU3	1	2	0.068	0.037	95.2	-	4/0
	QHU4	1	2	0.068	0.037	38.5	-	4/0
	Q11U	1	26	0.0754	0.04	105.8	-	4/0
	Q12U	1	26	0.068	0.037	89.3	-	4/0
	Q31U	1	28	0.0537	0.026	120.4	-	4/0
	Q32U	1	28	0.0537	0.026	120.4	-	4/0
	Q51U	1	28	0.1031	0.062	114.8	H/V	4/0
	Q52U	1	28	0.068	0.037	122.9	H/V	4/0
	Q52D	1	28	0.068	0.037	122.9	-	4/0
	Q51D	1	28	0.1031	0.062	114.8	-	4/0
	Q32D	1	28	0.0537	0.026	120.4	-	4/0
	Q31D	1	28	0.0537	0.026	120.4	-	4/0
	Q12D	1	26	0.068	0.037	89.3	-	4/0
	Q11D	1	26	0.0754	0.04	105.8	-	4/0
	QHD4	1	2	0.068	0.037	38.5	-	4/0
	QHD3	1	2	0.068	0.037	95.2	-	4/0
	QHD2	1	2	0.068	0.037	59.9	-	4/0
	QHD1	1	2	0.068	0.037	34.9	-	4/0
Sextupole	S31U	1	28	0.0331	0.00587	117.6	H/V/SQ	4/0
	S32U	1	28	0.0331	0.00587	117.6	H/V/SQ	4/0
	S33U	1	28	0.0359	0.00587	117.6	H/V/SQ	4/0
	S33D	1	28	0.0359	0.00587	117.6	H/V/SQ	4/0
	S32D	1	28	0.0331	0.00587	117.6	H/V/SQ	4/0
	S31D	1	28	0.0331	0.00587	117.6	H/V/SQ	4/0

<Table 2.1.10.2> Storage ring bipolar magnets: specifications and cable

Magnet Type	Magnet Name	Magnet Qty		Magnet Resistor (Ohm)	Magnet Inductance (H)	Current (A)	Cable (AWG or KCMIL)
		Qty/Sec	Total				
Octupole Magnet	Q31U	1	28	3.35	0.51	3.6	6
	Q31D	1	28	3.35	0.51	3.6	6
Quad-Bend& ReverseBend	Trim	8	224	-	-	-	6
Quadrupole	H-Corr(Q51)	2	56	1.712	0.062	3.432	6
	V-Corr(Q51)	2	56	1.712	0.062	3.432	6
Sextupole+ Slowcorrector	H-Corr	6	168	0.83	0.02634	8	6
	V-Corr	6	168	0.83	0.03506	7.1	6
	Skew Q	6	168	0.21	0.00686	7.1	6
Fast-Slow Corrento	H-Corrector	4	112	0.082	0.018	13.76	6
	V-cCorrector	4	112	0.215	0.022	17.3	6
	Skew Q	4	112	-	-	-	6
ID	Undulator H	9	18	-	-	-	6
	Undulator V	9	18	-	-	-	6
Active Shim	Active Shim	24	24	-	-	-	6



<Figure 2.1.10.2> Modular composition of storage ring large capacity MPS

<Table 2.1.10.1> and <Table 2.1.10.2> show the required specifications and cables for large-capacity (Modular) and small-capacity (Bipolar) MPS, respectively. The large-capacity storage ring MPS is designed with a modular structure that supplies the necessary current to the magnet through up to two parallel connections of MPS. As shown in <Figure 2.1.10.2>, it is composed of a high level of modular structure, where each module can operate independently, separated from the input power. The specifications for the modular MPS and the small-capacity MPS are shown in <Table 2.1.10.3>, and the interface specifications are shown in <Table 2.1.10.4>.

<Table 2.1.10.3> Storage ring MPS: detailed specifications

Specifications	Modular MPS	Bipolar MPS
Output Current	140 A	±20 A
Output Voltage	40 V	±20 V
Maximum Average Power	5.6 kW	400 W
Maximum Peak Power	5.6 kW	400 W
Topology	Unipolar	Bipolar (4-Quadrant)
Control Mode	Constant Current (CC) & Constant Voltage (CV)	
Output Setting Resolution -CC/CV	>19-bit	
Output Read back Resolution	24-bits	
Response time	>1 kHz	>10 kHz
Current Accuracy	<100 ppmP-P	<100 ppmP-P
Temperature Coefficient	<30 ppm	<40 ppm
Long Term Stability (8 hr)	<20 ppm	<30 ppm
Short Term Stability (30 min)	<10 ppm	<20 ppm
Reproducibility	<30 ppm	<40 ppm
Repeatability	<30 ppm	<40 ppm
Line Regulation	<±40 ppmP-P	<±50 ppmP-P
Load Regulation	<±40 ppmP-P	<±50 ppmP-P
Output Current Ripple	<30 ppmP-P	<40 ppmP-P
Cooling	Water/Air	Air (front-to-rear)
Maximum Efficiency	>90%	
Power Factor	>0.98 @full load	
PARALLELING Option	O (≤2 modules)	X

Input Ratings	Three-phase: 380 VAC/60 Hz (±10%)	Single-phase: 220 VAC/60 Hz (±10%)
DC Link Voltage	TBD *	
Operating Ambient Temperature	0 to 40 °C	
Size	<19"×3U	<19"×1U
Communication Interface	EthernetTCP-IP, SFP/SFP+	
Drivers	EPICS	
Local Control	Colordisplay with multi-function rotary switch	
Internal fault status	OutputOver-Current and Over-Voltage Over-Temperature / DC-LinkUnder-Voltage / Earth Leakage Current / Regulation Fault	
Hardware Protection	Input Fuses / Output Free-Wheeling Diodes (Crowbar)	
External ports	User-configurable "dry" contacts External input interface: 4 EA - Web Browser: Disable, High, Low selectable External output interface - 2set magnetic relay and 2set solid state relay - Normal Close 1, Normal open 1: 1set Trigger Input	
Extra Features	Waveform execution / Remote Firmware Update / Web server	

<Table 2.1.10.4> Storage ring MPS: interface specifications

	Item	Sub-item	Description	Additional Information	Note
1	Controller	Digital Control	DSP	TMS320F28377D	equivalent or higher
			FPGA	Xilinx Zynq UltraScale+ MPSoC	equivalent or higher
2	Mode		Local/ Remote		
3	Remote Interface	Ethernet	EPICS embedded	Xilinx Zynq UltraScale+ MPSoC or higher	PV is separately specified
		Web Browser			Oscilloscope function MPS Parameter Set enabled PV modifiable

4	Display	Output current	Digits	Integer	2-line 16 characters LCD is used
		Output voltage	Digits		
		System state	LED	Run, Interlock communication, Heartbeat	Device Status displayed (Displays status of key diagnostic points in MPS) Heartbeat is On/Off every second by DSP
		Mode	Local/Remote		Displayed on LCD

Power is supplied through the configuration of a modular structure MPS composed of two modules of the Longitudinal Gradient Bending Magnet, one module of the Center Bend Magnet, one module of the Quad-Bend and Reverse Bend Magnet (the DQ51 Magnet comprises two modules), one module of the Quadrupole magnet, and one module of the Sextupole magnet. In other words, 46 modules are applied per sector. <Table 2.1.10.5> and <Table 2.1.10.6> show the total required modules, the number of required MPS, and the output margin for the storage ring magnets.

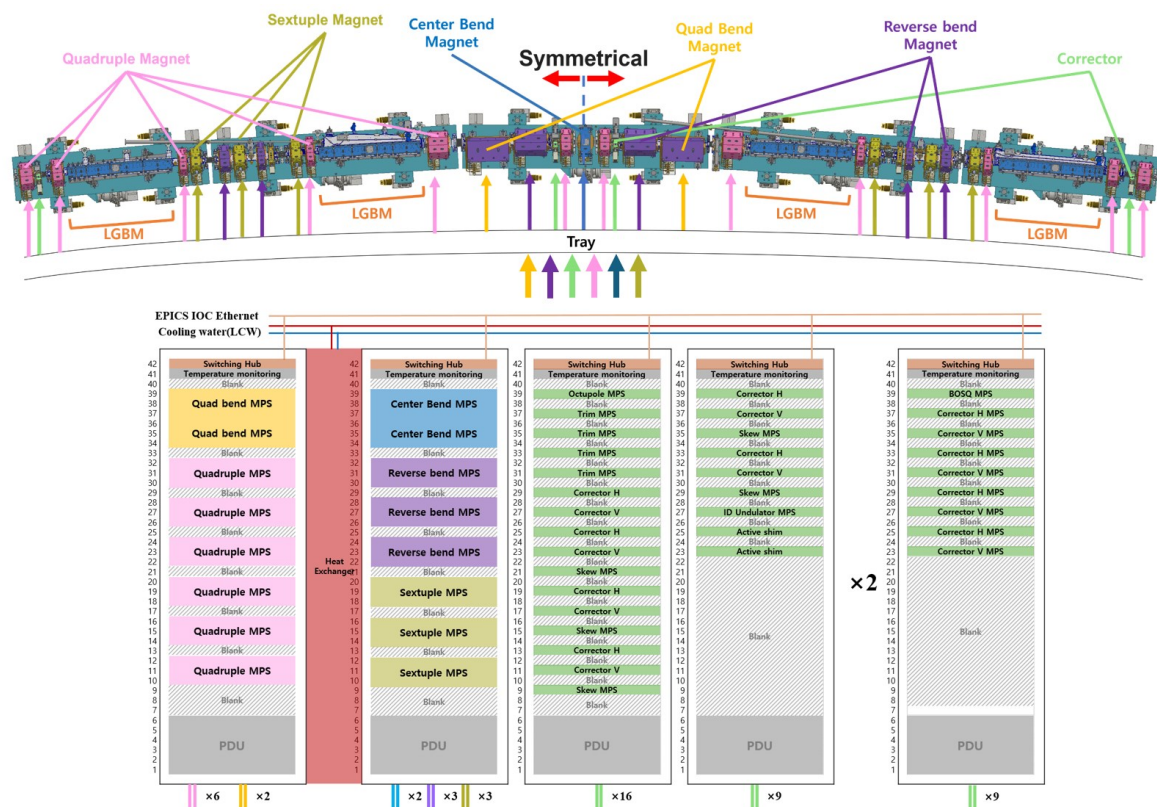
<Table 2.1.10.5> Storage ring modular (large-capacity) MPS:
required numbers and output margin

Load Magnet	Magnet Qty		Module Qty	Total Module Qty	Magnet Current (A)	Magnet Voltage (V)	MPS Rated Current (A)	MPS Rated Voltage (V)	Current Margin (%)	Voltage Margin (%)
	Qty/Sec	Total								
Central BM	1	28	2	56	228.5	7.15	280	40	18.4	82.1
DQ31U	1	28	1	28	119.1	8.1	140	40	14.9	79.8
DQ32U	1	28	1	28	119.8	5.26	140	40	14.4	86.9
DQ51U	1	28	2	56	225	28.7	280	40	19.6	28.3
DQ52U	1	28	1	28	102.4	17.31	140	40	26.9	56.7
DQ52D	1	28	1	28	102.4	17.31	140	40	26.9	56.7
DQ51D	1	28	2	56	225	28.7	280	40	19.6	28.3
DQ32D	1	28	1	28	119.8	5.26	140	40	14.4	86.9
DQ31D	1	28	1	28	119.1	8.1	140	40	14.9	79.8
QHU1	1	2	1	2	34.90	2.50	140	40	75.1	93.7
QHU2	1	2	1	2	59.89	4.30	140	40	57.2	89.3
QHU3	1	2	1	2	95.25	6.84	140	40	32.0	82.9
QHU4	1	2	1	2	38.55	2.77	140	40	72.5	93.1
Q11U	1	26	1	26	105.80	8.79	140	40	24.4	78.0
Q12U	1	26	1	26	89.33	6.41	140	40	36.2	84.0
Q31U	1	28	1	28	120.40	7.13	140	40	14.0	82.2

Q32U	1	28	1	28	120.40	7.13	140	40	14.0	82.2
Q51U	1	28	1	28	114.80	13.04	140	40	18.0	67.4
Q52U	1	28	1	28	122.90	8.82	140	40	12.2	78.0
Q52D	1	28	1	28	122.90	8.82	140	40	12.2	78.0
Q51D	1	28	1	28	114.80	13.04	140	40	18.0	67.4
Q32D	1	28	1	28	120.40	7.13	140	40	14.0	82.2
Q31D	1	28	1	28	120.40	7.13	140	40	14.0	82.2
Q12D	1	26	1	26	89.33	6.41	140	40	36.2	84.0
Q11D	1	26	1	26	105.80	8.79	140	40	24.4	78.0
QHD4	1	2	1	2	38.55	2.77	140	40	72.5	93.1
QHD3	1	2	1	2	95.25	6.84	140	40	32.0	82.9
QHD2	1	2	1	2	59.89	4.30	140	40	57.2	89.3
QHD1	1	2	1	2	34.90	2.50	140	40	75.1	93.7
S31U	1	28	1	28	117.616632	3.89	140	40	16.0	90.3
S32U	1	28	1	28	117.616632	4.22	140	40	16.0	89.5
S33U	1	28	1	28	117.616632	3.89	140	40	16.0	90.3
S33D	1	28	1	28	117.616632	3.89	140	40	16.0	90.3
S32D	1	28	1	28	117.616632	4.22	140	40	16.0	89.5
S31D	1	28	1	28	117.616632	3.89	140	40	16.0	90.3
				1,072						

<Table 2.1.10.6> Storage ring bipolar (small-capacity) MPS:
required numbers and output margin

Magnet Type	Magnet Qty		MPS Qty	Magnet Current (A)	Magnet Voltage (V)	MPS Rated Current (A)	MPS Rated Volage (V)	Current Margin (%)	Voltage Margin (%)
	Qty/Sec	Total							
O31U	1	28	28	3.6	12.07	20	20	82.0	39.7
O31D	1	28	28	3.6	12.07	20	20	82.0	39.7
Quad-Bend& ReverseBend	8	224	224	-	-	20	20	-	-
H-Corr(Q51)	2	56	56	3.432	5.875	20	20	82.8	70.6
V-Corr(Q51)	2	56	56	3.432	5.875	20	20	82.8	70.6
H-Corr	6	168	168	8	6.7	20	20	60.0	66.5
V-Corr	6	168	168	7.1	5.9	20	20	64.5	70.5
Skew Q	6	168	168	7.1	1.5	20	20	64.5	92.5
H-Corrector	4	112	112	13.76	1.13	20	20	31.2	94.4
V-cCorrector	4	112	112	17.3	3.72	20	20	13.5	81.4
Skew Q	4	112	112	-	-	20	20	-	-
Undulator H	9	18	18	-	-	20	20	-	-
Undulator V	9	18	18	-	-	20	20	-	-
Active Shim	24	24	24	-	-	20	20	-	-

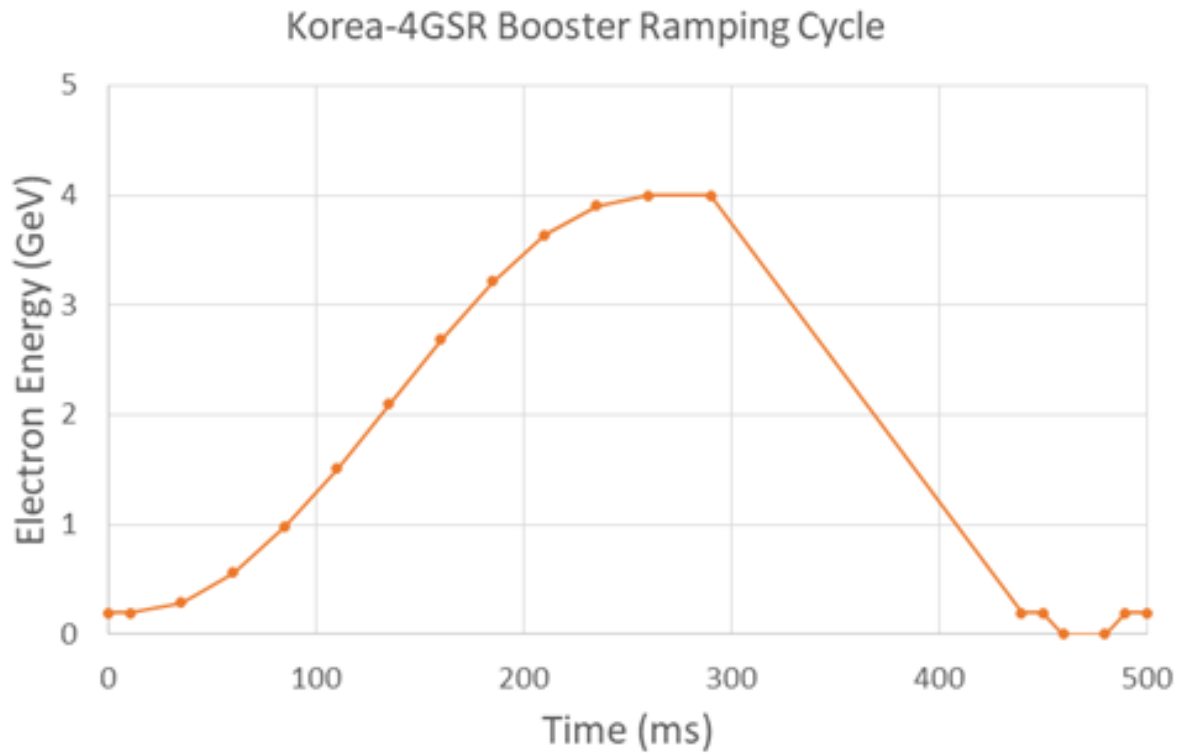


<Figure 2.1.10.3> Storage ring MPS rack configuration

<Figure 2.1.10.3> shows the configuration of the storage ring MPS rack. It is installed according to the 42U EIA standard rack specifications for each sector (panel width of 19 inches, approximately 482.6 mm, and panel height in multiples of 1.75 inches, approximately 44.45 mm). Each sector consists of 10 racks, and based on a total of 28 sectors, 280 racks are distributed.

C. Booster Ring MPS

As shown in <Figure 2.1.10.4>, the booster ring operates at 2 Hz ramping. It is configured in series to facilitate commissioning, supplying the same current to the series-connected magnets to create a uniform B-field for each magnet.



<Figure 2.1.10.4> Booster ring MPS: Ramping Profile

<Table 2.1.10.7> Booster ring large-capacity MPS: specifications and cable

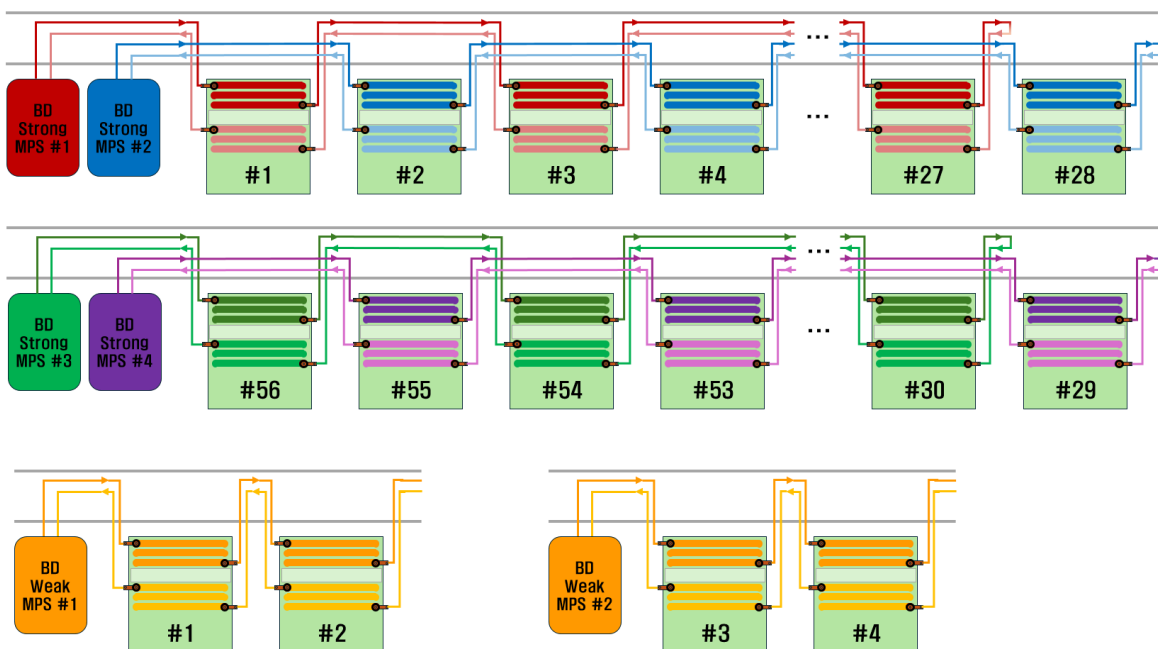
Magnet Type	Magnet Name	Magnet Qty	Resistor (Ohm)	Inductance (H)	Current (A)	Trim	Configuration	Cable (AWG/KCMIL)
		Total						
Dipole Bending	BD Strong	56	0.02283	0.0177	465.7	-	28 Series/ 2 Parallel * 2	600
	BD Weak	4	0.02283	0.0177	385.1	-	2-Series, 2-Series	600
Quadrupole	Quad54	54	0.0371	0.0117	147	SQ	27-Series, 27-Series	4/0
	Quad4	12	0.0371	0.0117	147	SQ	4-Series, 4-Series, 4-Series	4/0
Sextupole	S Strong	30	0.0137	-	21.4	-	30-Series	4/0
	S Weak	30	0.006	0.0001517	64.1	-	30-Series	4/0

<Table 2.1.10.8> Booster ring small-capacity MPS: specifications and cable

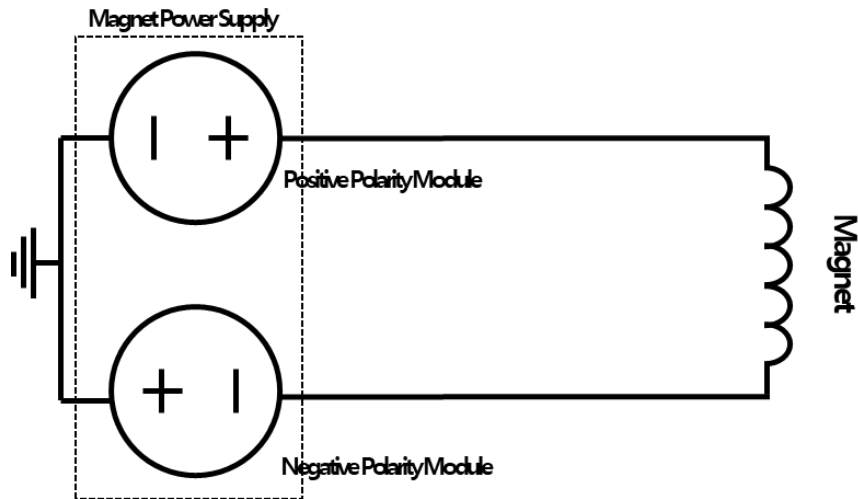
Magnet Type	Magnet Name	Magnet Qty	Resistor (Ohm)	Inductance (H)	Current (A)	Voltage (V)	Power (W)	Cable (AWG/KCMIL)
Quadrupole	Skew Q	10	1.2977	0.0468	3.51	4.55	16	10
Fast-Slow Corrector	Corrector H	120	-	-	-	-	-	-
	Corrector V	120	-	-	-	-	-	-

<Table 2.1.10.7> and <Table 2.1.10.8> show the required specifications and cables for DC operation of large and small capacity booster MPS, respectively. For example, all 56 dipole bending magnets should be connected in series. After connecting them all in series, if it operates at 2 Hz ramping, a 1 MW (peak) class MPS with an output voltage of more than 3 kV is required. However, there are disadvantages: It is difficult to configure to compensate for EMI and parasitic inductance in the output cable during ramping operation, and high-insulation special cables and magnet insulation of over 3 kV are required.

To reduce the burden on MPS and overcome these disadvantages, the connection of the dipole magnets is configured, as shown in <Figure 2.1.10.5>.



<Figure 2.1.10.5> Connection configuration of the booster ring dipole magnets.



<Figure 2.1.10.6> Configuration of internal modules in the booster ring MPS.

The booster ring dipole magnet consists of four individual windings, with two windings each for the upper and lower windings. By connecting one winding from each dipole magnet in series, four MPS will be operated simultaneously (parallel operation) to supply power to the booster ring dipole magnets. Also, when connecting in series, the upper and lower windings are connected in a cross-configuration (Winding 1 (upper) → Winding 3 (lower) → Winding 2 (upper) → Winding 4 (lower)) to form an identical B-field even if MPS's have output differences, facilitating easy commissioning. The cables for connecting different magnets are configured so that the current directions are opposite to each other, thus reducing parasitic inductance and EMI.

Furthermore, as shown in <Figure 2.1.10.6>, the internal configuration of MPS is connecting in series two internal modules, with one module giving positive voltage and the other module giving negative voltage, with grounding connected in the middle of the modules. It allows the output cables and magnets to have dielectric strength equivalent to half of the MPS output voltage from the grounding. It also has the configurational advantage of lowering the rated voltage of the MPS capacitor bank, which receives energy feedback from the magnet during the ramping operation.

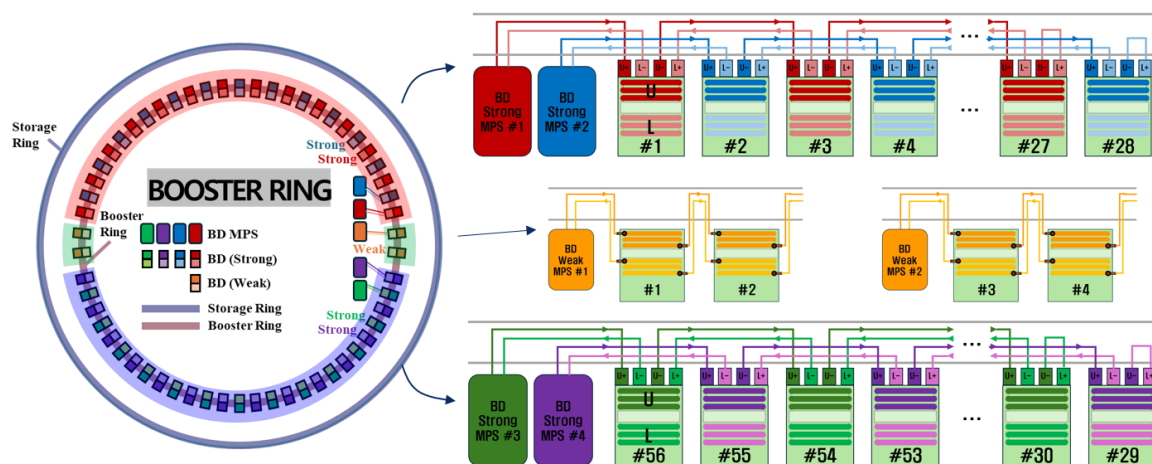
The specifications of the booster ring high-capacity MPS during 2 Hz ramping operation, after the above configuration and series connection, are shown in <Table 2.1.10.9>.

<Table 2.1.10.9> Booster ring large-capacity MPS: specifications

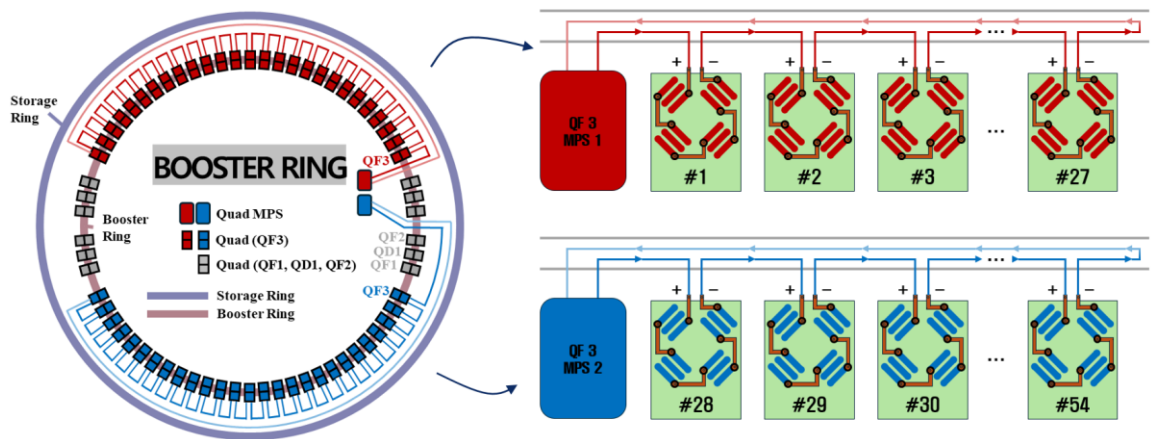
Magnet Type	Magnet Name	Magnet Qty	Total Resistor (Ohm)	Total Inductance (H)	Peak Current (A)	Peak Voltage (V)	Peak Power (W)	Apparent Power (VA)	Configuration
		Total							
Dipole Bending	BD Strong	56	0.3196	0.2478	465.7	1,048.1	488,108	270,000	28 Series/ 2 Parallel * 2
	BD Weak	4	0.0457	0.0354	385.1	165.6	63,781	35,000	2-Series, 2-Series
Quadrupole	Quad54	54	2.2410	0.6329	147	520.7	76,553	42,000	27-Series, 27-Series
	Quad4	12	0.1660	0.0469	147	137.0	20,147	11,000	4-Series, 4-Series, 4-Series
Sextupole	S Strong	30	0.0038	0.1500	113.9	102.5	11,676	6,500	30-Series
	S Weak	30	0.0038	0.1500	38.2	34.4	1,313	730	30-Series

The booster ring low-capacity MPS has a configuration where one magnet is powered by one power supply, just like the storage ring MPS.

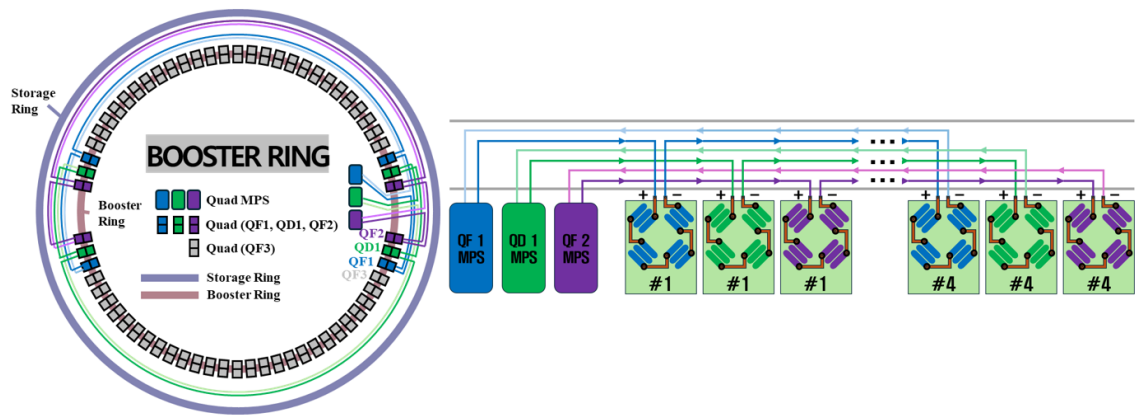
<Figure 2.1.10.7> shows the connection configuration of the booster ring MPS. The large-capacity MPS are placed in one location within the storage ring shed to facilitate maintenance, management, and integration of spare parts, while the low-capacity MPS are distributed within the storage ring shed.



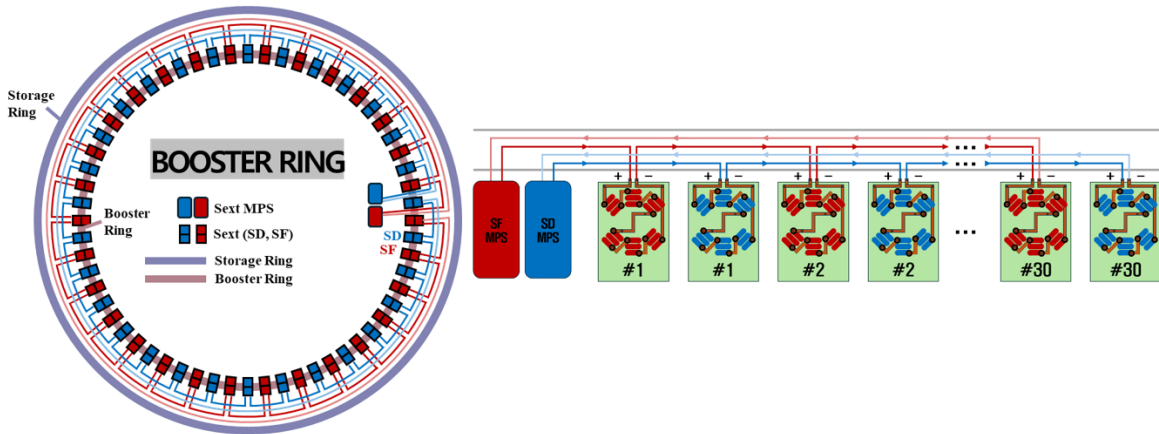
(a)



(b)



(c)



(d)

<Figure 2.1.10.7> Connection configuration of booster ring MPS:

(a) Bending Dipole (b) Quadrupole, (c) QF/QD, (d) Sextupole.

<Table 2.1.10.10> provides detailed specifications of the booster ring dipole/quadrupole MPS, applying the same MPS to the two magnets to facilitate spare parts management and maintenance. <Table 2.1.10.11> shows detailed specifications of the booster ring sextupole MPS, which is configured by changing one module of the storage ring MPS to do four quadrant operation. For other booster ring low-capacity MPS, the configuration of the storage ring low-capacity MPS will be applied.

<Table 2.1.10.12> shows the required numbers and the output margin of the booster ring large-capacity MPS.

<Table 2.1.10.10> Booster ring dipole/quadrupole MPS: detailed specifications

Specifications	Booster Ring MPS
Output Current	±600 A
Output Voltage	±1,000 V (Each Module 500 V×2)
Average Power	200 kW
Peak Power	600 kW
Topology	Bipolar (4-Quadrant)
Control Mode	Constant Current (CC) & Constant Voltage (CV)
Output Setting Resolution -CC/CV	>19 bits
Output Read back Resolution	24 bits
Small Signal Bandwidth (-3dB)	>1 kHz
Current Accuracy	<100 ppmP-P
Temperature Coefficient	<30 ppm
Long Term Stability (8 hr)	<20 ppm
Short Term Stability (30 min)	<10 ppm
Reproducibility	<30 ppm
Repeatability	<30 ppm
Line Regulation	<±40 ppmP-P
Load Regulation	<±40 ppmP-P
Output Current Ripple	<30 ppmP-P
Cooling	Water/Air
Maximum Efficiency	>90%
Power Factor	>0.9 @full load
Series Option	O (up to 2 modules)
Input Ratings	Three-phase: 380 VAC/60 Hz (±10%)
DC Link Voltage Ripple	TBD *
OperatingAmbientTemperature	0 to 40 °C
Communication Interface	EthernetTCP-IP, SFP/SFP+
Local Control	Colordisplay with multi-function rotary switch
Internal fault status	OutputOver-Current and Over-Voltage Over-Temperature / DC-LinkUnder-Voltage Earth Leakage Current / Regulation Fault
Hardware Protection	Input Fuses / Output Free-Wheeling Diodes (Crowbar)
External ports	User-configurable "dry" contacts / External input interface: 4 EA - Web Browser: Disable, High, Low selectable External output interface - 2set magnetic relay and 2set solid state relay - Normal Close 1, Normal open 1: 1set / Trigger Input
Extra Features	Waveform execution / Remote Firmware Update / Web server

<Table 2.1.10.11> Booster ring sextupole MPS: detailed specifications

Specifications	Booster Ring MPS
Output Current	±200 A
Output Voltage	±200 V
Average Power	50 kW
Peak Power	400 kW
Topology	Bipolar (4-Quadrant)
Control Mode	Constant Current (CC) & Constant Voltage (CV)
Output Setting Resolution -CC/CV	>19 bits
Output Read back Resolution	24 bits
Small Signal Bandwidth (-3dB)	>1kHz
Current Accuracy	<100 ppmP-P
Temperature Coefficient	<30 ppm
Long-Term Stability (8hr)	<20 ppm
Short-Term Stability (30 min)	<10 ppm
Reproducibility	<30 ppm
Repeatability	<30 ppm
Line Regulation	<±40 ppmP-P
Load Regulation	<±40 ppmP-P
Output Current Ripple	<30 ppmP-P
Cooling	Water/Air
Maximum Efficiency	>90%
Power Factor	>0.9 @full load
Input Ratings	Three-phase / 380 VAC/60 Hz (±10%)
DC Link Voltage Ripple	TBD *
OperatingAmbientTemperature	0 to 40 °C
Communication Interface	EthernetTCP-IP, SFP/SFP+
Drivers	EPICS
Local Control	Colordisplay with multi-function rotary switch
Internal fault status	OutputOver-Current and Over-Voltage Over-Temperature / DC-LinkUnder-Voltage Earth Leakage Current / Regulation Fault
Hardware Protection	Input Fuses / Output Free-Wheeling Diodes (Crowbar)
External ports	User-configurable "dry" contacts / External input interface: 4 EA - Web Browser: Disable, High, Low selectable External output interface - 2set magnetic relay and 2set solid state relay - Normal Close 1, Normal open 1: 1set Trigger Input
Extra Features	Waveform execution / Remote Firmware Update / Web server

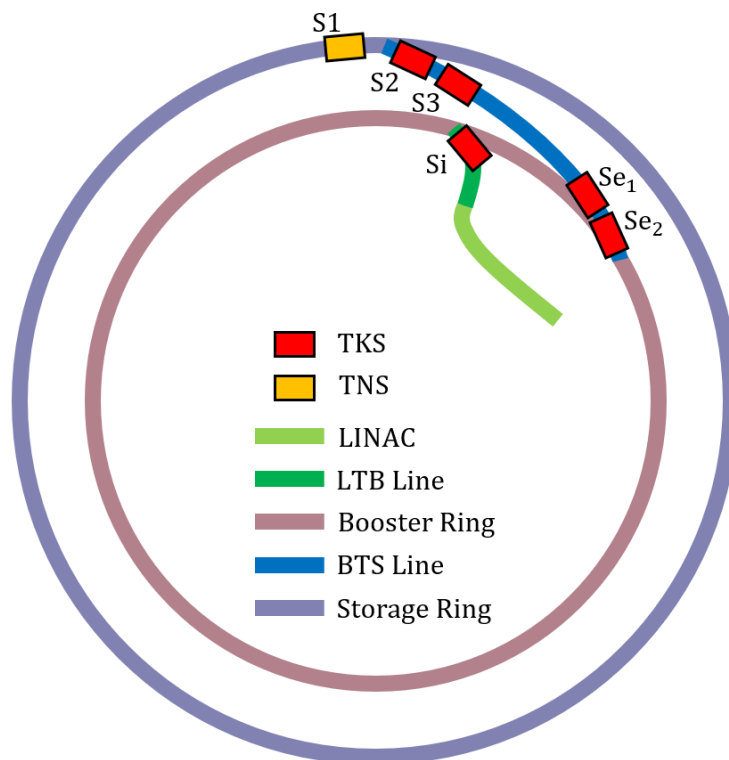
<Table 2.1.10.12> Booster ring large-capacity MPS: required numbers and output margin

Magnet Name	Magnet Qty	MPS Qty	Magnet Peak Current (A)	Magnet Peak Voltage (V)	MPS Rated Current (A)	MPS Rated Voltage (V)	Current Margin (%)	Voltage Margin (%)
	Total							
BD Strong	56	4	465.7	785.55	+600	±1,200	22.4	12.7
BD Weak	4	2	385.1	92.80	+600	±300	35.8	44.8
Quad54	54	2	147	779.00	+200	±600	26.5	13.2
Quad4	12	3	147	57.70	+200	±200	26.5	31.5
S Strong	30	1	113.9	102.77	+200	±200	68.0	48.8
S Weak	30	1	38.2	34.47	+200	±200	68.0	82.8
Skew Quadrupole	10	10	3.51	4.55	±20	±20	-	-
Corrector H	120	120	-	-	±20	±20	-	-
Corrector V	120	120	-	-	±20	±20	-	-

2.1.11 Pulsed Septum Magnet Power Supply

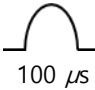
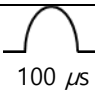
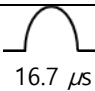
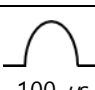
A. Overview

During the injection and extraction process, the septum electromagnet plays a crucial role in switching the beam path. In the 4GSR accelerator, electrons are accelerated up to 200 MeV in the linear accelerator (LINAC) before being transferred to the booster ring (Booster Ring, BR) via the LINAC to Booster (LTB) transfer line. In this LTB section, a septum magnet is used to precisely guide the beam into the booster ring. Subsequently, in the booster ring, the electrons are further accelerated to 4 GeV and then extracted through the Booster to Storage (BTS) line, finally being injected into the storage ring (SR). The septum magnets used in this process include the LINAC to Booster Thick Septum Magnet (LITKS), Booster to Storage Ring Thick Septum Magnet (BTSTKS), and Booster to Storage Ring Thin Septum Magnet (BTSTNS), with their respective roles and positions shown in <Figure 2.1.11.1>.



<Figure 2.1.11.1> Configuration of pulsed septum magnet in 4GSR.

<Table 2.1.11.1> Characteristics of pulsed septum magnet & power supply.

Magnet type	Number	Current waveform	Energy storage	I_{magnet}	Switching type
Booster injection thick septum Si	1	 100 μs	C: 290 μF V_c : 850 V	5,600 A	Solid-state switch
Booster extraction thick septum Se_1, Se_2	2	 100 μs	C: 200 μF V_c : 1,350 V	6,700 A	Solid-state switch
Storage ring injection thin septum $S1$	1	 16.7 μs	C: 10 μF V_c : 4,000 V	7,000 A	Solid-state switch
Storage ring injection thick septum $S2, S3$	2	 100 μs	C: 200 μF V_c : 1,350 V	6,700 A	Solid-state switch

Each septum magnet is designed as a pulsed electromagnet and is powered by a pulsed power supply (PS). Depending on the system requirements, the size of the magnet, bending angle, and peak magnetic field are designed differently. Accordingly, the specifications of the power supply also vary for each magnet.

<Table 2.1.11.2> Specification of pulsed septum magnet.

Septum Magnet	LITKS	BTSTKS	BTSTNS
Type	Pulsed	pulsed	pulsed
Number of Used	1	4	1
Bending angle [deg]	20.0	3.0	1.432
S mag length [mm]	500	1,250	500
Peak B_0 [T]	0.47	0.56	0.67
Peak Current [kA]	5.6	6.7	7.0
Inductance [μH]	1.23	2.67	0.76
Half-sine Pulse Width [μs]	100.00	100.00	16.7

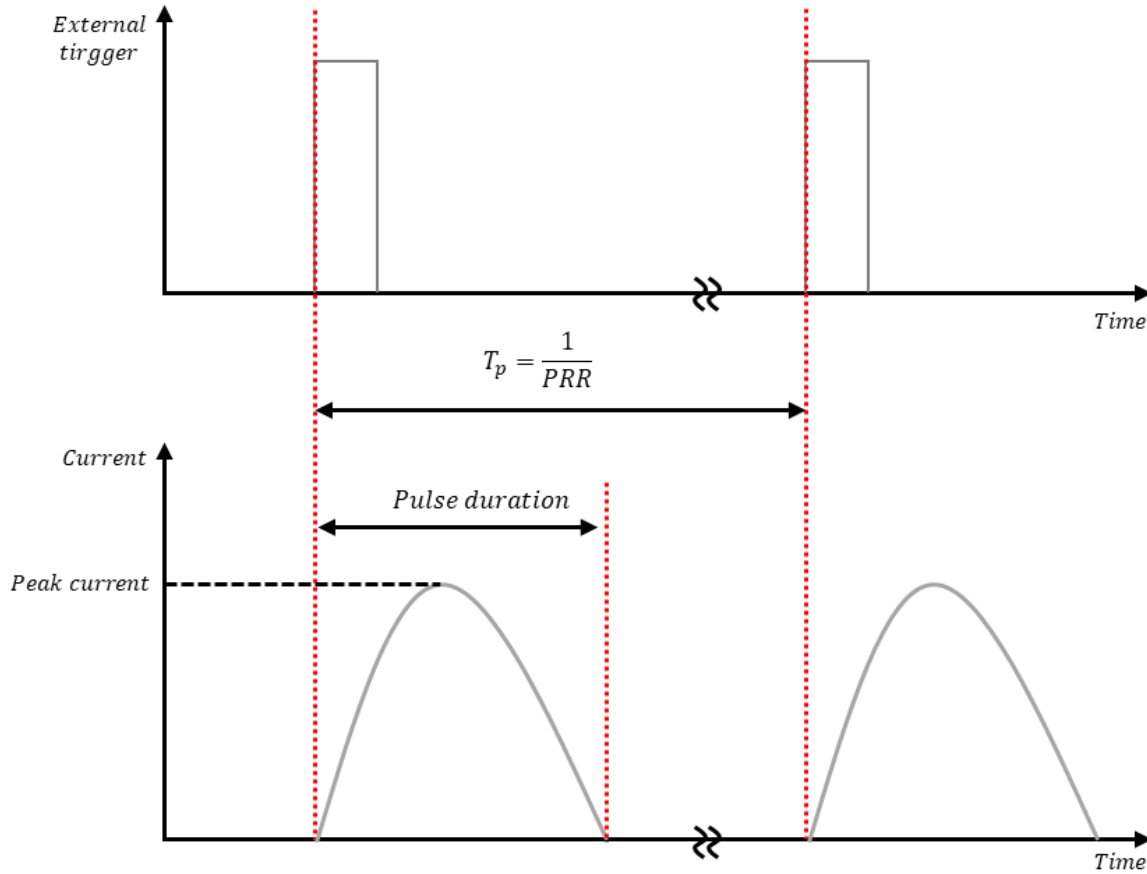
B. Specifications of the Pulsed Septum Magnet Power Supply

The power supply is designed to match the specifications of the septum magnet and consists of three types: LITKS_PS, BTSTKS_PS, and BTSTNS_PS. All of these power supplies utilize a half-sine current waveform and operate at a pulse repetition rate (PRR) of 2 Hz. The half-sine current waveform <Figure 2.1.11.2> generates a unipolar pulse, facilitating the injection and extraction of the electron beam into and from the booster ring and storage ring. The key electrical specifications of each power supply are summarized in <Table 2.1.11.3>.

<Table 2.1.11.3> Specification of pulsed septum magnet power supply.

Magnet & PS		LITKS_PS	BTSTKS_PS	BTSTNS_PS
Septum Magnet	Number of used	1	4	1
	Current waveform	Half sine	Half sine	Half sine
	Peak current	5.6 kA	6.7 kA	7.0 kA
	Magnet inductance	1.23 μH	2.67 μH	0.76 μH
	Pulse duration	100 μs	100 μs	16.7 μs
	Pulse repetition rate	2 Hz	2 Hz	2 Hz
	Charging voltage	0.85 kV	1.35 kV	4.0 kV
Pulsed Septum Magnet Power Supply	Max. peak voltage	1.5 kV	2.0 kV	5.9 kV
	Max. peak current	10 kA	10 kA	10 kA
	Capacitance	290 μF	200 μF	10 μF
	Total inductance ¹⁾	3.23 μH (1.23+2)	4.67 μH (2.67+2)	2.76 μH (0.76+2)
	Stability	<100 ppm _{RMS}	<100 ppm _{RMS}	<100 ppm _{RMS}
	Average power	>660 W	>780 W	>320 W
	CCPS peak power	>990 J/s	>1,130 J/s	>400 J/s

The total inductance refers to the combined inductance of the entire system, including the magnet, cables, and system inductance.



<Figure 2.1.11.2> Output waveform of pulsed septum magnet power supply.

Each pulsed power supply has different pulse duration, charging voltage, and peak current characteristics. The pulse duration for LITKS_PS and BTSTKS_PS is 100 μs , while for BTSTNS_PS, it is 16.7 μs . The peak current is designed according to the magnet's requirements, with values of 5.6 kA, 6.7 kA, and 7.0 kA, respectively, to generate the necessary magnetic field for electron beam injection.

The pulsed power supply is designed with charging voltage and capacitance values based on system requirements. The charging voltages for LITKS_PS, BTSTKS_PS, and BTSTNS_PS are 0.85 kV, 1.35 kV, and 4.0 kV, respectively, with corresponding capacitance values of 290 μF , 200 μF , and 10 μF . These differences are closely related to the required peak current, pulse duration, and total inductance (including the magnet, cables, and semiconductor switches) of each system.

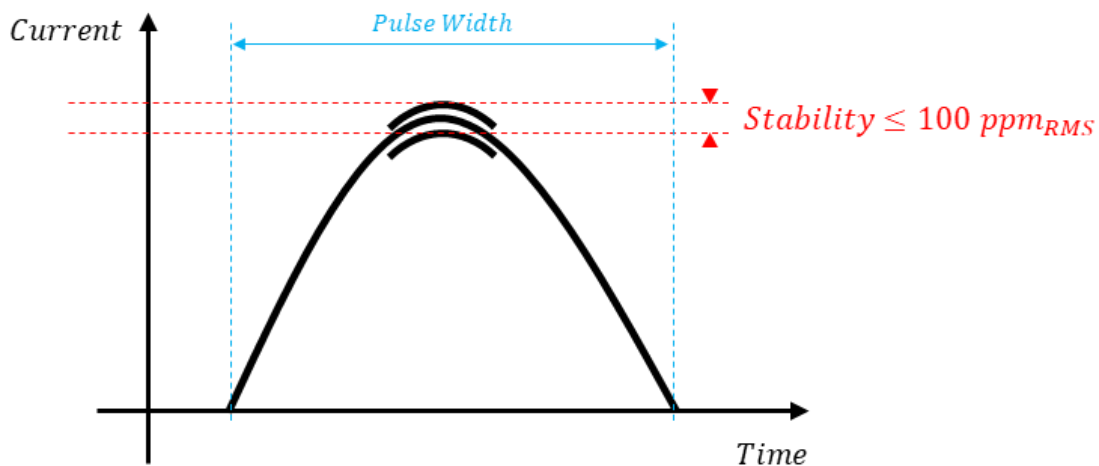
In terms of power, simulations indicate that the average power consumption is at least 660 W for LITKS_PS, 780 W for BTSTKS_PS, and 320 W for BTSTNS_PS. Additionally, the peak power of the capacitor charging power supply (CCPS) is optimized to meet the power

supply requirements, with LITKS_PS at 990 J/s, BTSTKS_PS at 1.13 kJ/s, and BTSTNS_PS at 400 J/s.

Precision and stability are critical factors in the operation of pulsed power supplies, as shown in <Figure 2.1.11.3>. To ensure precise current control, the current stability is maintained at 100 ppm RMS. This high level of precision ensures that the same pulse current can be supplied consistently over long-term operation, significantly improving system reliability.

The stability of the output current is closely related to the performance of the CCPS. Achieving precise stability requires increasing the switching frequency of the CCPS. To accomplish this, a series-resonant converter utilizing a soft-switching technique is employed in the design. Additionally, low timing jitter is associated with the performance of the main switch. Typically, the timing jitter of a thyatron used in high-voltage pulsed power applications is around 2 ns. However, solid-state switches offer a timing jitter performance of just a few hundred picoseconds. Furthermore, solid-state switches have a virtually infinite lifespan, making them advantageous in terms of maintenance.

The half-sine current waveform is generated by each power supply unit and is designed based on the key specifications summarized in <Table 2.1.11.3>. These specifications enable the pulsed power supply to maintain high precision and stability, ensuring that the septum magnet operates at optimal performance.

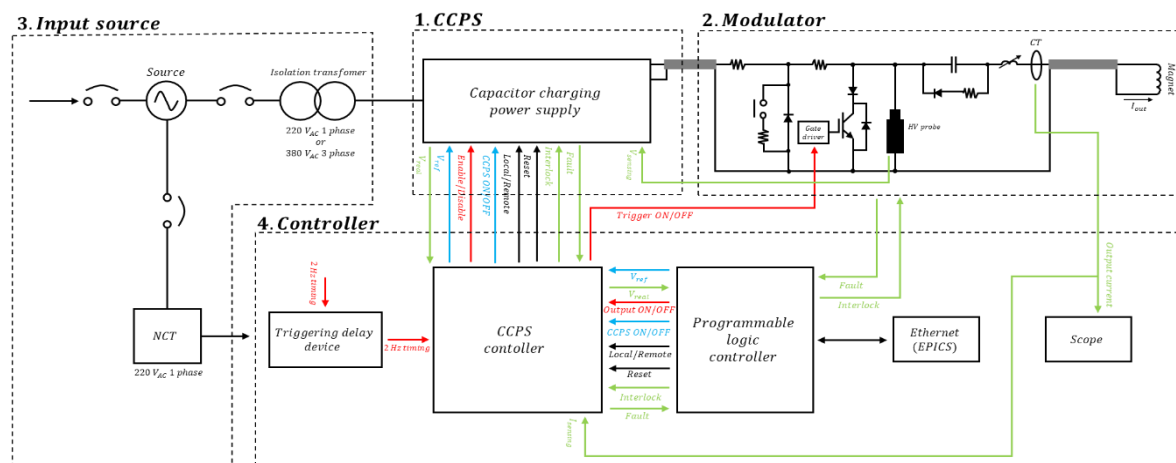


<Figure 2.1.11.3> Stability and timing jitter of pulsed septum magnet power supply.

C. Design of the Pulsed Septum Magnet Power Supply

The pulsed septum magnet power supply can be categorized into four main components based on its functional role, as shown in <Figure 2.1.11.4> :

1. CCPS (Capacitor Charging Power Supply): Charges the capacitor to the target voltage.
2. Modulator: Resonates the charged capacitor with the electromagnet to generate a half-sine current output.
3. Input Source: Provides input power to the CCPS and controller, with isolation achieved through a transformer.
4. Controller: Monitors the real-time status of the modulator and CCPS, delivering trigger signals and commands to each unit. It also communicates with the upper-level control system via EPICS.



<Figure 2.1.11.4> Entire diagram of pulsed septum magnet power supply.

The pulsed septum magnet power supply fundamentally generates a sine wave through the resonance of an inductor and a capacitor. By adjusting the capacitance and inductance values, it is possible to control the pulse width, characteristic impedance, and peak current. The operational sequence is illustrated in <Figure 2.1.11.5>.

(a) Capacitor Charging

The CCPS charges the capacitor to the target voltage with a constant current. During this process, a small amount of current flows into the magnet, but since its magnitude is very small and in DC form, it can be ignored. Voltage sensing is performed using an HV probe, which reads the voltage and sends a signal to the CCPS to turn it off.

(b) Discharge of Capacitor Energy into the Magnet

When the CCPS turns off, an ON signal is sent to the gate driver. This activates the main switch, allowing the stored energy in the capacitor to discharge into the magnet. At this stage, the capacitor and magnet resonate, generating a sine-wave-shaped current.

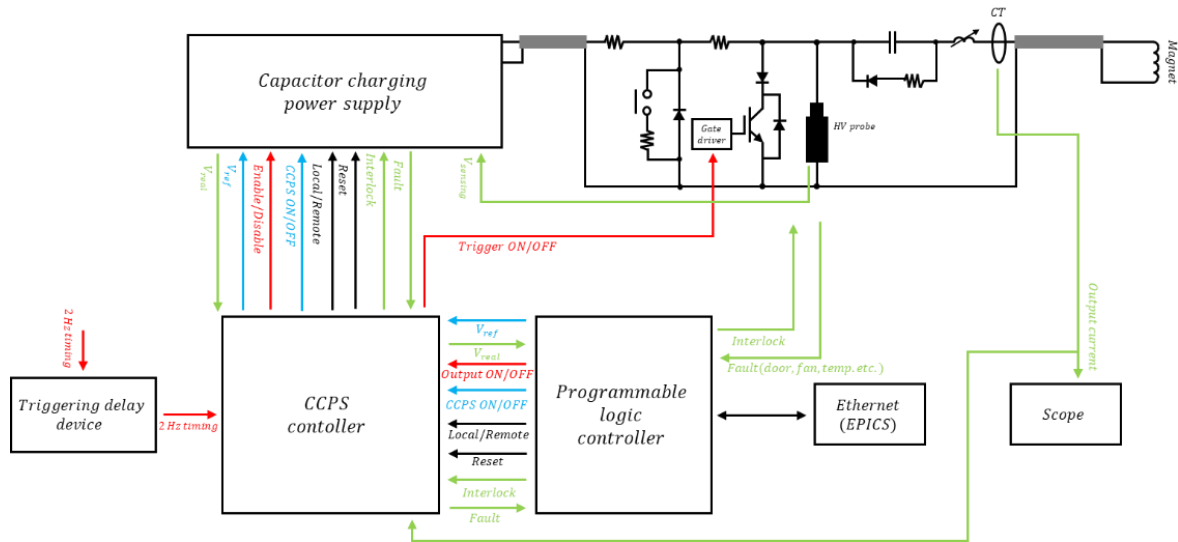
(c) Capacitor Discharge and Energy Dissipation

After the current flowing through the magnet reaches its peak and starts decreasing, the capacitor voltage becomes negative. At this point, the diode connected in parallel with the capacitor conducts, dissipating energy through a resistor. As a result, the output current gradually decreases.

(d) Capacitor Energy Dissipation

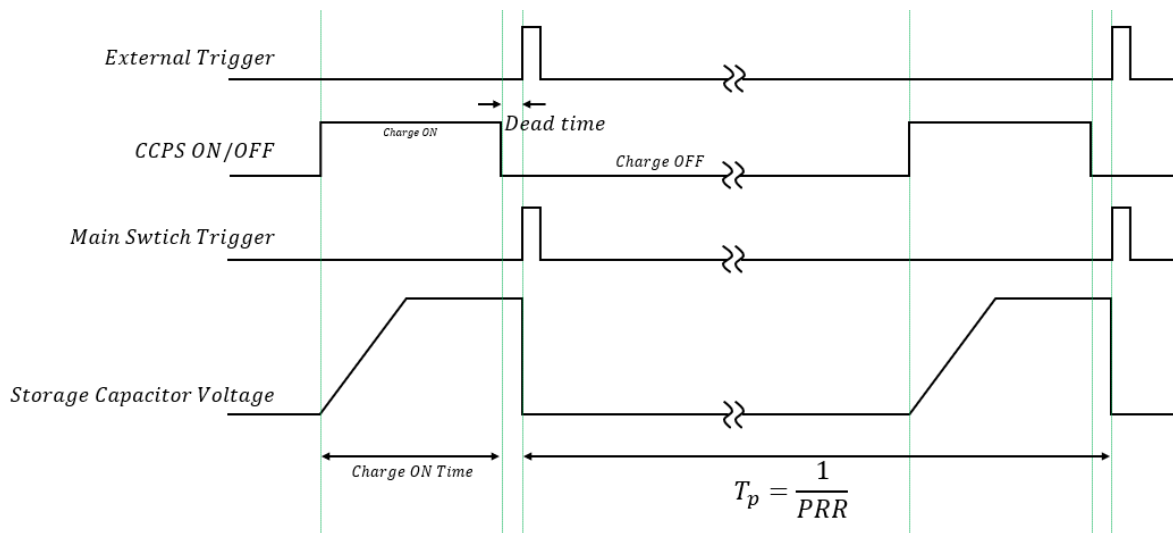
When the current flowing through the magnet reaches zero, it would typically reverse due to resonance. However, the blocking diode connected in series with the main switch prevents this reversal. Instead, to dissipate the reverse voltage across the capacitor, a small amount of current flows through the magnet. Since this current is very brief and small in magnitude, it can be considered negligible.

Next, the control sequence of the pulsed septum magnet power supply is explained. The entire control process is managed through the PLC and the CCPS controller, as shown in <Figure 2.1.11.6>. The power supply receives signals from the upper-level system via EPICS, which are then transmitted by the PLC to the CCPS controller. Additionally, the PLC monitors the status of the power supply and reports it to the upper-level system through EPICS. This allows for real-time monitoring of component failures and safety issues, ensuring reliable operation.



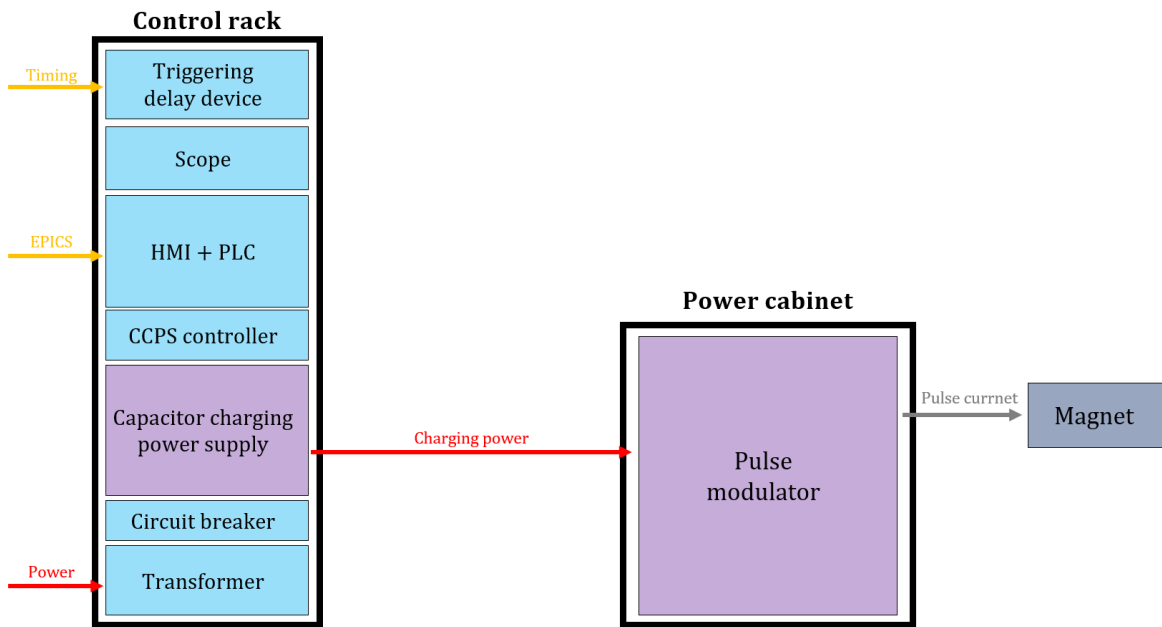
<Figure 2.1.11.6> Control sequence of pulsed septum magnet power supply.

<Figure 2.1.11.7> illustrates the operation sequence of the controller over time. The pulsed septum magnet power supply operates at a fundamental frequency of 2 Hz. When an external 2 Hz trigger signal is received, the CCPS begins charging the capacitor after a predetermined delay. To maintain stability, the pulsed septum magnet power supply performs voltage regulation once the target voltage is reached. After the CCPS turns off and a dead time elapses, the second external trigger signal activates the gate driver, causing the capacitor to discharge.

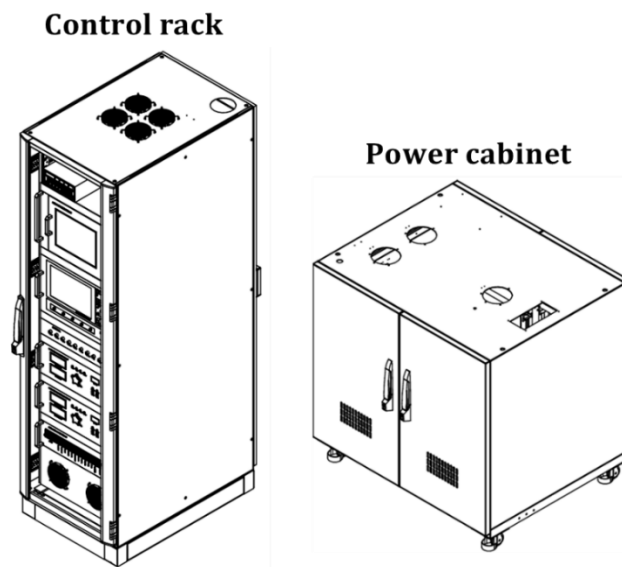


<Figure 2.1.11.7> Control timing flow chart.

To improve the efficiency of management and maintenance, the pulsed septum magnet power supply is divided into a Control Rack and a Power Cabinet, as shown in <Figure 2.1.11.8>. The Control Rack consists of a triggering delay device, PLC, and CCPS controller, while the Power Cabinet houses the CCPS and modulator.



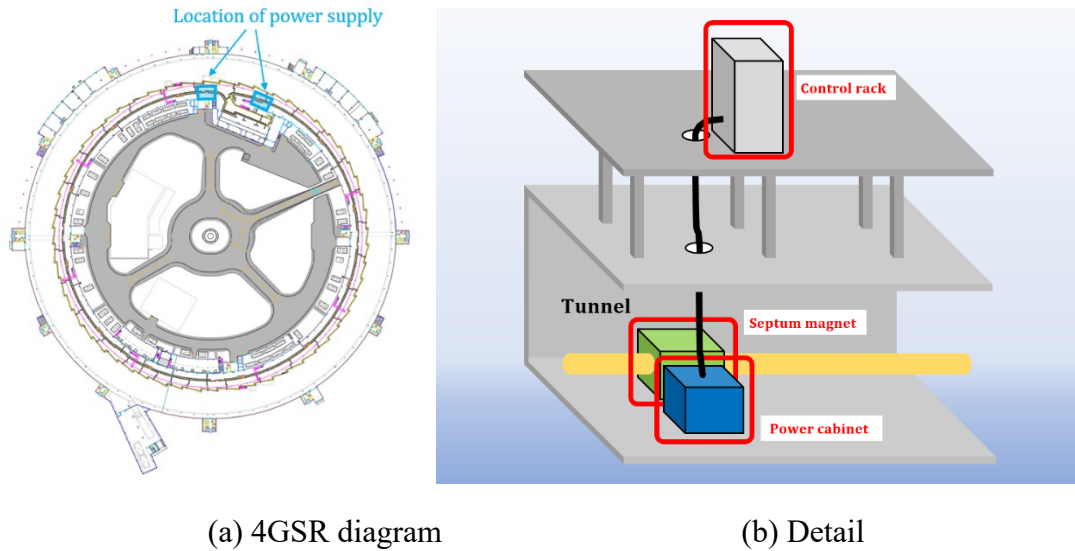
(a) Diagram



(b) 3D model

<Figure 2.1.11.8> Configuration of pulsed septum magnet power supply.

The power supply is designed, as shown in <Figure 2.1.11.8>, to minimize the cable length between the supply and the magnet, thereby reducing inductance. Additionally, to isolate the surrounding environment from electromagnetic noise generated by the high-voltage power supply, a dedicated space has been allocated above the septum magnet.

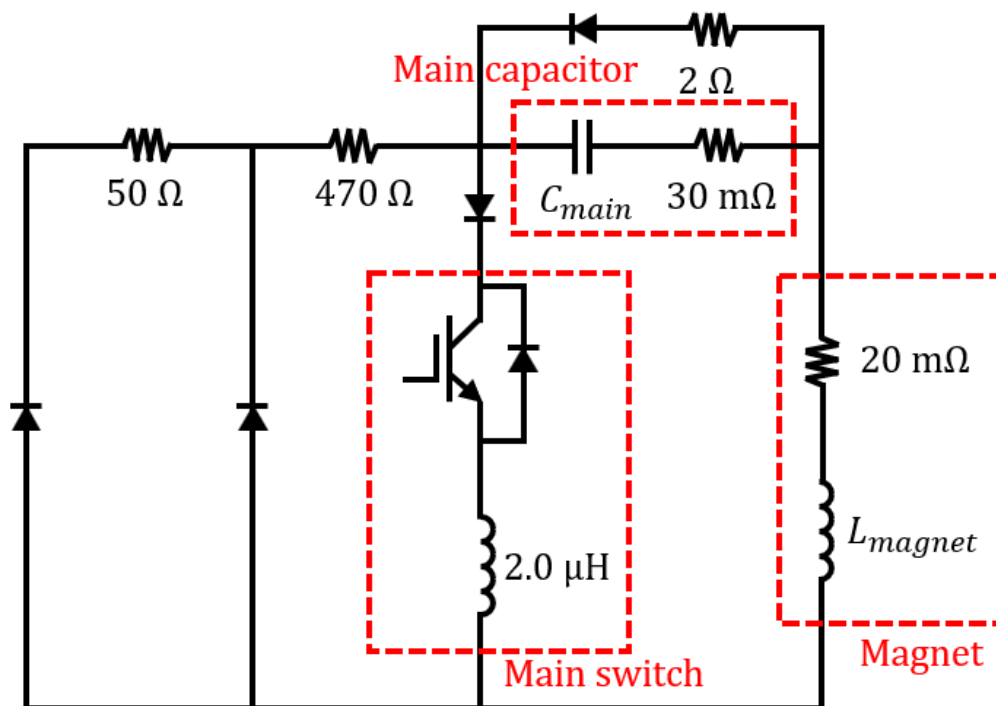


<Figure 2.1.11.9> Location of pulsed septum magnet power supply.

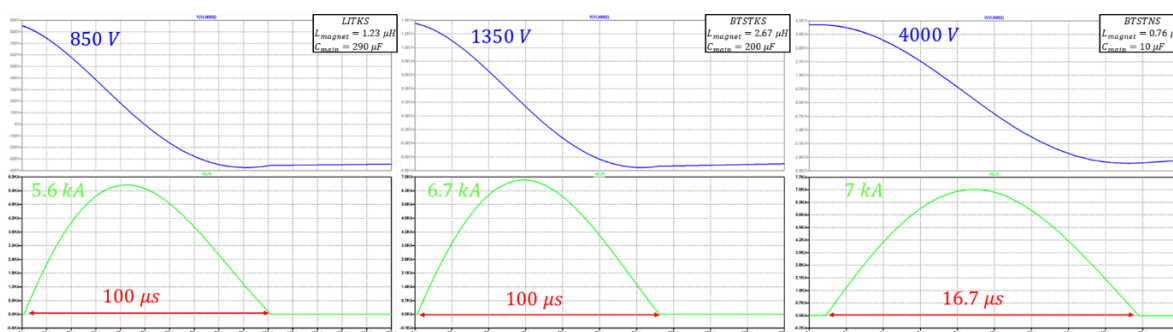
D. Simulation for Parameter Verification

The parameters in <Table 2.1.11.3> were verified through LTspice simulations, and the simulation circuit diagram is shown in <Figure 2.1.11.10>. The simulation models the main capacitor and magnet as equivalent components while incorporating parasitic elements such as system resistance and inductance.

Finally, the designed parameters for LITKS_PS, BTSTKS_PS, and BTSTNS_PS were validated using the LTspice simulation circuit, with the results presented in <Figure 2.1.11.10>.



<Figure 2.1.11.10> Simulation circuit with the value for each part.



<Figure 2.1.11.11> Result waveform of LTspice simulation
(blue line: charging voltage, green line: output current).

2.1.12 Beam Diagnostics and Control

A. Beam Diagnostic Device

The 4th generation storage ring beam, characterized by a multi-band structure, features a small cross-sectional beam emittance and beam size. In this report, the designed emittance is approximately 60 [pm.rad], which is about 1/100 of the 3rd generation storage ring PLS-II's design emittance of 5800 [pm.rad]. Compared to the existing 3rd generation storage ring, the significantly reduced cross-sectional area of the vacuum chamber and the inclusion of multiple superconducting accelerating cavities increase the likelihood of heating due to wake impedance and can heighten multi-bunch beam instabilities. Furthermore, the incorporation of a photocathode electron gun and the multi-bunch injection method may require bunch-by-bunch time-resolved energy beam diagnostics in the injector section.

Therefore, to address several challenging beam-diagnostics issues, instruments such as BPMs and FOFB need to be developed further and established in line with the specifications of the 4th generation storage ring. Other diagnostic devices either adopt methods already used in the 3rd generation storage ring (PLS-II) or are implemented at an improved level based on existing devices.

<Table 2.1.12.1> Types and Quantities of Diagnostic Devices

	Devices	Parameter	Quantities per section				
			LINAC	LTB	BR	BTS	SR
1	BPM	Beam Position	10	8	120	8	288
2	BPRM (YAG/OTR)	2D Profile, Emittance	7	6		3	
3	X-ray Diagnostic Hutch	Beam Size, Emittance, Energy Spread					1
4	Visible light Diagnostic Hutch	Beam Size, Emittance, Bunch Length & Purity			1		3
5	Slow BLM	Beam Loss (slow)	1	1	4	1	14
6	Fast BLM	Beam Loss (fast)			5		30
7	ICT	Pulse Beam Current	2	1		2	
8	DCCT	DC Beam Current			1		2
9	PBPM	Photon Beam Position					20
10	Tune Monitor	Tune			1		1
11	TFS/LFS	Multi-bunch Feedback					3
Total Number of Diagnostic Devices by Section			20	16	132	14	362

(1) Overview

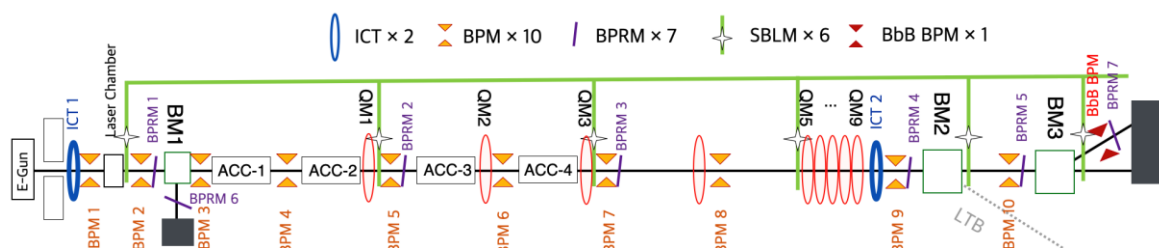
Table <3.1.12.1> outlines the types and quantities of representative diagnostic devices that will be installed in the industrial-support multipurpose synchrotron accelerator, categorized into five different sections.

In <Table 2.1.12.1>, each section corresponds to (1) LINAC, (2) LTB (Linac To Booster), (3) BR (Booster Ring), (4) BTS (Booster ring To Storage ring), and (5) SR (Storage Ring)*, and a Stripline (STRL) Type BPM may be used instead of a Button (BTN) Type BPM in the linear accelerator.

(2) Overview of Diagnostics in LINAC

<Table 2.1.12.2> Beam Parameters of LINAC and its measurements

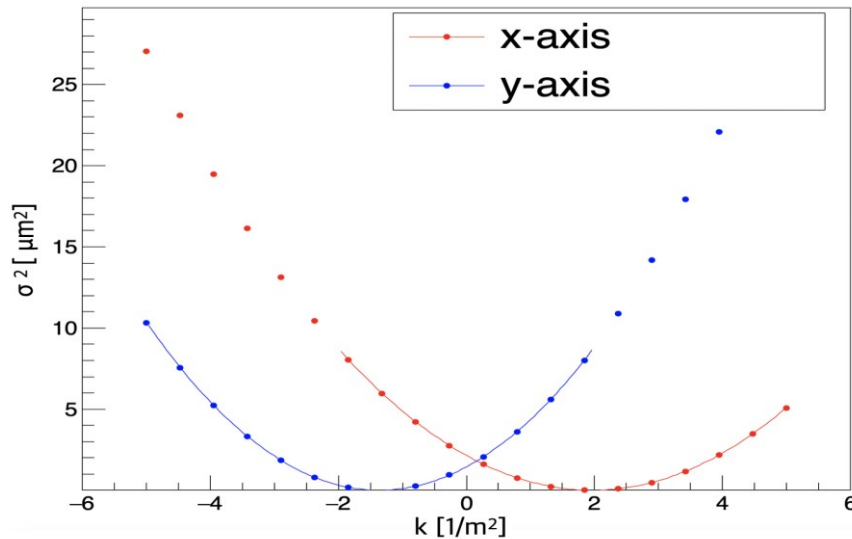
Beam Parameter	Instrument and Measurement
Position	BPM×10, BPRM×7
Profile	BPRM×7
Pulse Charge	ICT×2, BPM×10 (relative)
Energy	Bending Magnet & BPRM×2 (4 MeV, 200 MeV)
Multi-bunch Energy	Vertical kicker, Bending Magnet BPRM×1
Emittance & Twiss	Quadrupole Magnet Scan & BPRM
Beam Loss	Slow BLM×6 Channels



<Figure 2.1.12.1> Configuration of diagnostic devices in LINAC.

The configuration of diagnostic devices in the LINAC are shown in <Figure 2.1.12.1> and the beam parameters and measurement and diagnostic methods are summarized in <Table 2.1.12.2>. Seven beam properties are measured using five diagnostic devices in the LINAC, as detailed below:

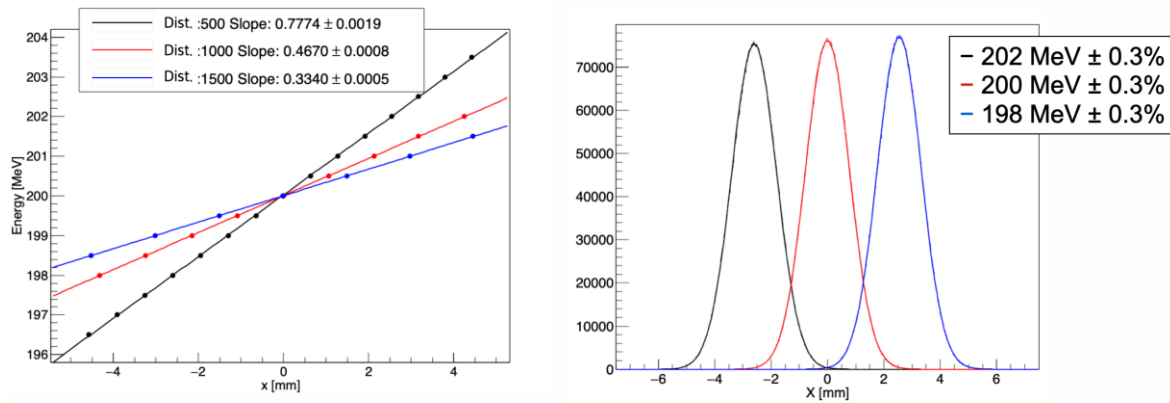
- Beam Position and Profile measurement: Beam positions are measured with 10 BPMs, and both beam position and profiles are measured with 7 BPRMs.
- Emittance & Twiss Parameter Measurement: The emittance and Twiss parameters are measured using Q-Scan with BPRM 4 and QM3.



<Figure 2.1.12.2> Q-Scan Simulation result using QM3 and BPRM4.

<Figure 2.1.12.2> shows the results of the Q-Scan simulation after the acceleration section. The input emittance and Twiss parameters for this simulation are derived from linear accelerator simulation results. Although the maximum k value for the QMs in the linear accelerator is 15, since the focus is at around ± 2 , the k value for Q-scan range was set from -5 to 5. The X-axis of <Figure 2.1.12.2> represents the k value of the QMs and the Y-axis represents the square of the beam size. Emittance and Twiss parameters were estimated by analyzing the relationship between beam size and k value. With BPRM pixel size of $20 \mu\text{m}$, the emittance error can be measured within 0.1%, and the α , β parameters within a 5% error.

- **Energy & Energy Spectra Measurement:** The energy spectra are measured using BPRM 6/7 and BM1/3 for E-gun Section/beam Analysis Section. BM1 is 90 degrees bending dipole magnet of the same specifications as used in PAL-XFEL, while BM3 is 20 degrees bending angle dipole magnet which is the same specifications as BM2 used for LTB transport.



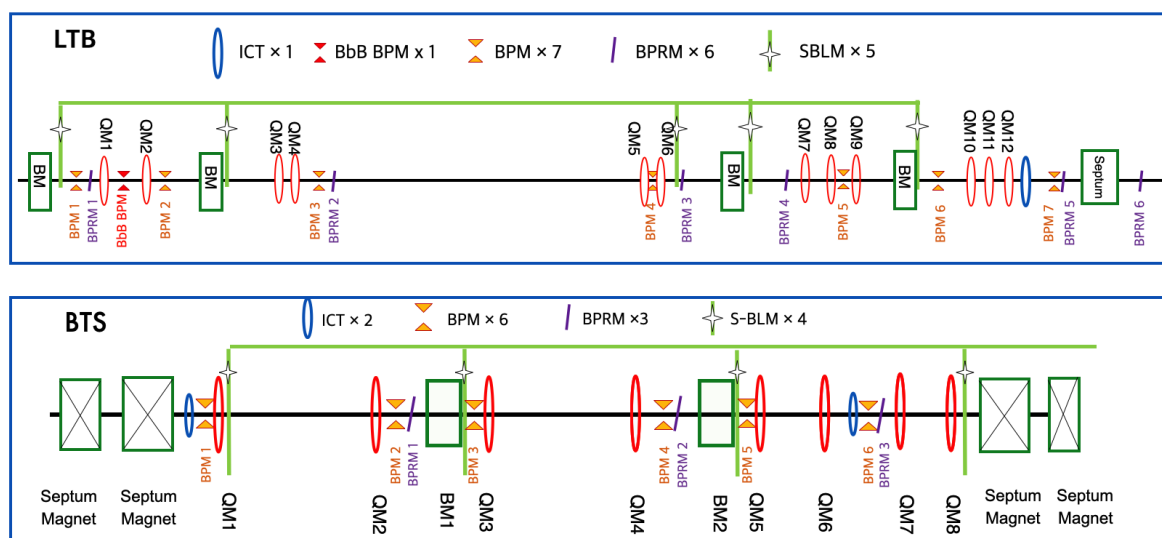
<Figure 2.1.12.3> Simulation result of energy measurement at beam analysis section.

<Figure 2.1.12.3> presents the simulation results of energy measurement in the 200 MeV diagnostic line. The energy distribution and resolution simulation study were achieved using ELEGANT. Considering the measurement of ± 2 MeV, Distance between BPRM 7 and BM 3 was set to 500 mm <Figure 2.1.12.3 left>. <Figure 2.1.12.3> right shows the simulation results for beam energies of 202, 200, and 198 MeV, with an energy distribution of 0.3%. The accuracy and resolution of energy and its distribution are less than 0.1%.

- In multi-bunch mode, 64 bunches are emitted at 2 ns intervals over a span of 128 ns. Since the energy of each bunch depends on the RF power and emission timing, measuring the energy of individual bunches enables feedback control for the RF and emission timing of the linear accelerator.

To achieve this, a Bunch-by-Bunch BPM (BbB BPM) is installed 400 mm downstream of BM3 at the end of the BAS line. The dispersion at the installation location is 0.26 m. Considering the position resolution of the BbB BPM, which is $20 \mu\text{m}$, the system can measure the energy of each bunch with a resolution of 15 keV.

(3) Overview of Diagnostics in LTB & BTS (Beam Transportation)

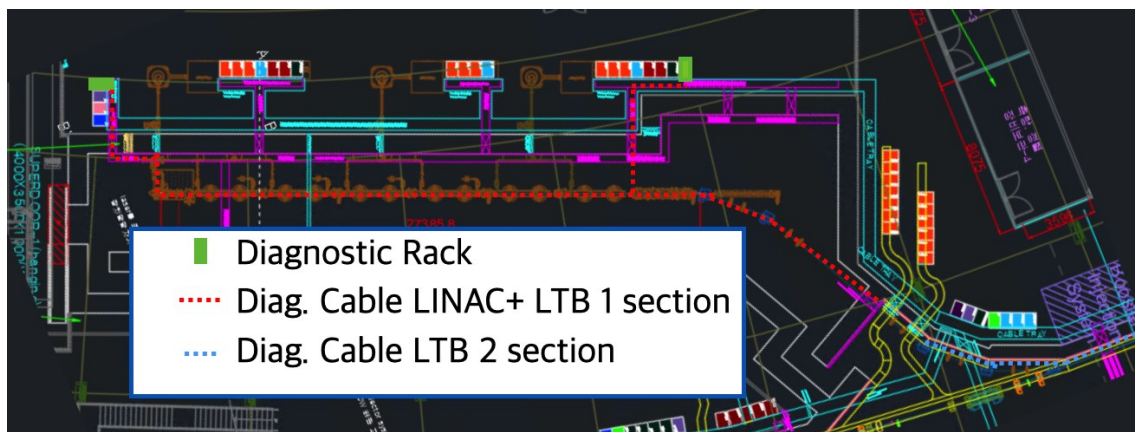


<Figure 2.1.12.4> Configuration of diagnostics devices in LTB & BTS.

<Figure 2.1.12.4> illustrates the configuration of diagnostic devices in the LTB and BTS beam transport lines. The LINAC to Booster Ring (LTB) and Booster Ring to Storage Ring (BTS) transport lines utilize four types of diagnostic devices to measure beam charge, beam position and shape, and beam loss. The arrangement and location of these diagnostic devices are shown in <Figure 2.1.12.5>, and the measurement methods for each beam parameter are described below:

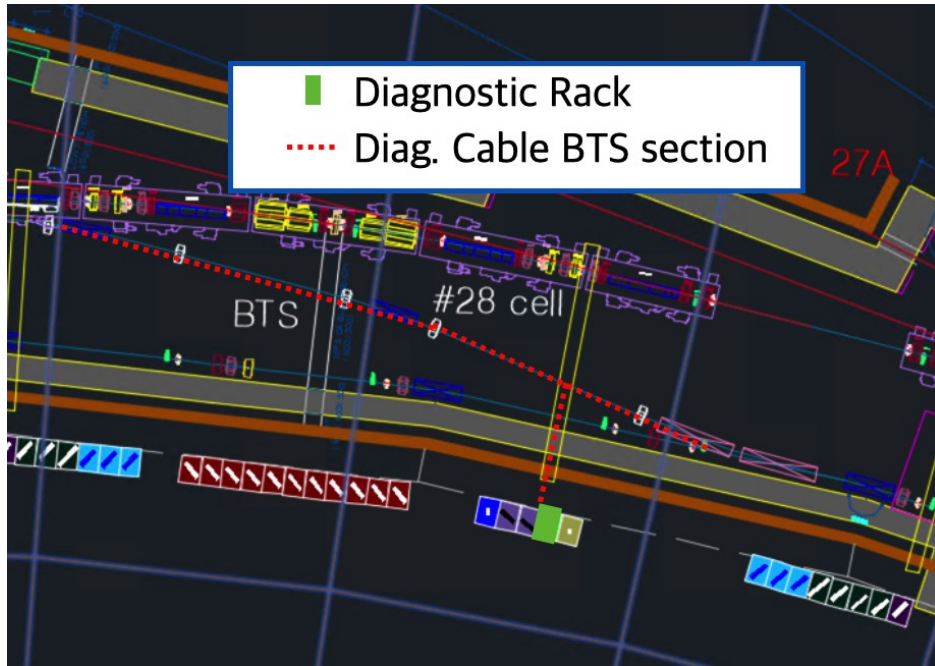
- **Beam Charge Measurement:** ICTs are installed at the end of the LTB and at both ends of the BTS. The beam transmission rate in the LTB is measured by comparing the charge at the end of the LTB with the charge at the end of the LINAC. In the BTS, the charge is measured during injection from the BR and extraction into the Storage Ring, with the transmission rate determined by comparing these two measurements.
- **Beam Position Measurement:** Eight BPMs are installed in the LTB to measure beam position, one of which (marked in red triangle in <Figure 2.1.12.4>) is a BPM for bunch-by-bunch energy measurement (BbB BPM). The BbB BPM measures the energy of each bunch during normal operation. It is positioned where the dispersion is 0.45 m, enabling bunch-by-bunch energy measurement with a resolution of 9 keV, given the 20 μ m position resolution of the BbB BPM. Although it takes a few seconds to analyze data using a broadband oscilloscope, making it not real-time, the data is still valuable for feedback as the RF environment does not change rapidly.

- **Beam Profile Measurement:** Six BPRMs are installed in the LTB. The first BPRM is used for energy distribution measurement, the third for emittance measurement, and the others for beam profile and center position measurement. The first BPRM is installed at a point where the dispersion is 0.33 m, providing an energy and energy distribution resolution of 3 keV, considering the 5 μm position and size resolution of the BPRM. The last BPRM is placed just after the LTB septum magnet, at the point where the LTB and Booster Ring converge, to measure the beam shape just before injection into the Booster Ring.
- **Beam Loss Measurement:** Beam loss monitors are installed at five locations in the LTB and four in the BTS, using multi-channel modules for each transport line.
- **Cable Configurations of LINAC and Beam Transport line**



<Figure 2.1.12.5> Cable Configurations in LINAC and LTB.

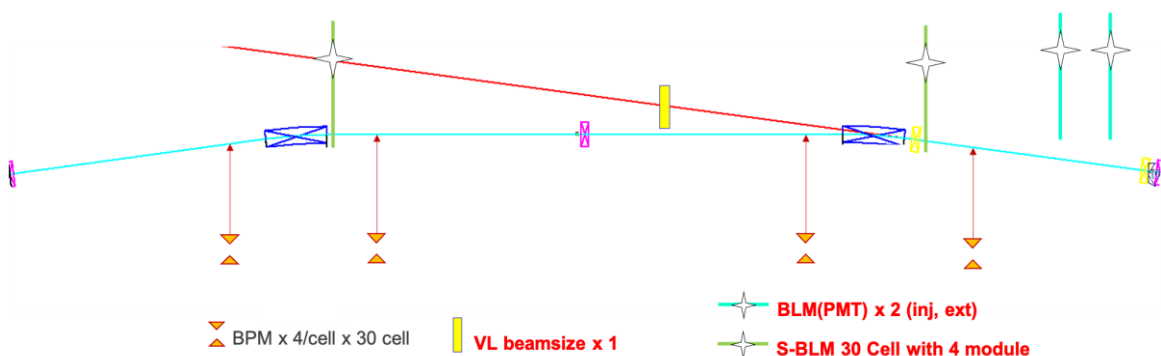
<Figure 2.1.12.5> shows the cable connections between the LINAC and LTB diagnostic devices. A shielding wall separates the LTB from the storage ring tunnel, preventing the cable tray from passing over it. As a result, the upstream diagnostic devices in the LINAC and LTB are controlled and signal-analyzed from the LINAC diagnostic device rack, while the downstream half of the LTB devices are controlled and signal-analyzed from the LTB rack. The maximum cable length for LINAC + LTB1, considering the tray height, is 45 meters. Detailed information about cable connections for each device type is provided in the section summarizing the diagnostic devices.



<Figure 2.1.12.6> Cable configuration in BTS.

<Figure 2.1.12.6> shows the cable connections in the BTS. The BTS uses the beam diagnostic rack of #28-1 in the control shed, with a maximum cable length of 30 meters from the beam diagnostic rack to the diagnostic devices. Detailed information about the cable connections for each device type is provided in the section summarizing the diagnostic devices.

(4) Overview of Diagnostics in Booster Ring



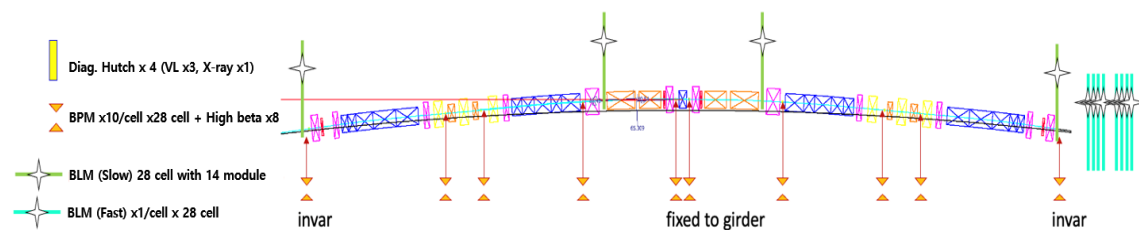
<Figure 2.1.12.7> Configuration and Location of Diagnostic Devices in the Booster Ring.

The booster ring employs four button BPMs (Beam Position Monitors) per cell, requiring a total of 120 BPMs across 30 cells. These BPMs are installed both upstream and downstream of every dipole magnet.

Because the booster ring is located in the same tunnel as the main storage ring, it shares the dose-type beam loss monitors with the main ring. Consequently, five fast dose-type beam loss monitors-including two units at the injection and extraction sections-are installed for the booster. In addition, four multi-channel slow beam loss monitors are used to measure total beam loss around the booster ring. Outside the injection/extraction regions, fiber-based multi-channel beam loss monitors are utilized to separately measure beam loss in the booster ring without interference from the storage ring.

Diagnostics for beam size, chromaticity, and emittance are conducted at a single visible light diagnostic hatch installed in the booster ring. One DCCT (Direct Current Current Transformer) is installed and operated for beam current measurements. The booster ring also has a dedicated tune monitor for tune measurement.

(5) Overview of Diagnostics in Storage Ring



<Figure 2.1.12.8> Configuration and Location of Diagnostic Devices in the Storage Ring.

A total of ten BPM (Beam Position Monitor) installation points are planned per cell. Specifically, two are located upstream and downstream of each insertion device (ID), four between corrector magnets, two inside the longitudinal gradient dipole magnet, and two around the super-bend magnets. With 28 cells in the storage ring design and eight additional BPMs in the high-beta straight sections, the total number of BPMs required for operation is 288.

Beam size, energy spread, and emittance measurements are performed simultaneously in two separate locations using a slit and an interferometer. Absolute beam size is measured using photons generated near the RF cavity straight section, where the dispersion is nearly zero, while relative size changes are monitored using photons from the longitudinal gradient dipole magnet region. Consequently, at least four beam diagnostic hatches are needed. These hatches extract visible light for streak camera measurements and fill pattern monitoring.

Among the four hutches, one is dedicated to X-ray-based beam diagnostics.

For beam loss monitoring, 30 dose-type beam loss monitors are installed around the storage ring—one in each arc section and two in each high-beta straight section. Additionally, 14 multi-channel slow beam loss monitors are deployed to measure overall beam loss in the ring. Beam current is continuously monitored by two DCCTs (Direct Current Current Transformers) placed along the beam path.

Finally, two bunch-by-bunch feedback systems are installed in the storage ring: the TFS (Transverse Feedback System) and the LFS (Longitudinal Feedback System), each operating to maintain stable beam conditions.

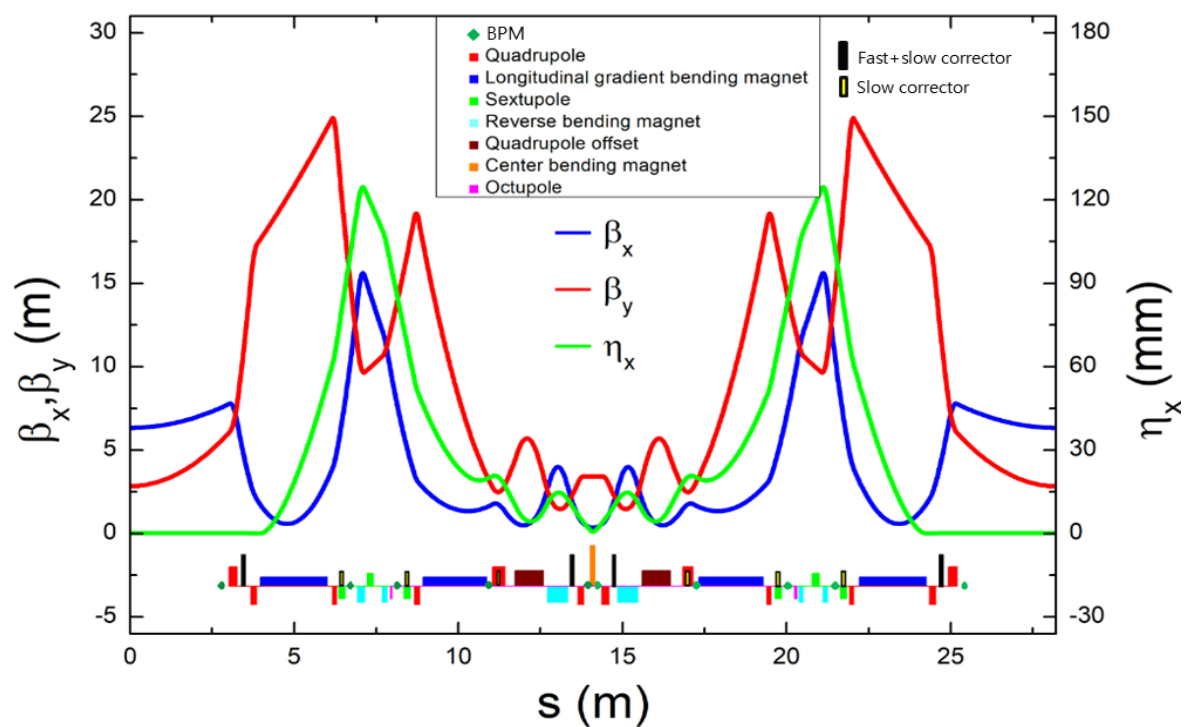
B. Summary of Beam Diagnostic Devices by Type

(1) Beam Position Monitor (BPM)

A total of 288 Beam Position Monitors (BPMs) are installed in the 4GSR storage ring. Excluding the high-beta straight section, each of the remaining 28 cells is equipped with 10 BPMs.

<Figure 2.1.12.9> shows the locations of the BPMs and correctors for a single cell of the 4GSR storage ring, while <Table 2.1.12.3> presents the beta functions at each BPM location.

Both the 4GSR storage ring and the booster employ button-type pickup designs to implement their beam position monitors. Compared to conventional third-generation storage rings, both the beam size and the vacuum chamber dimensions in the storage ring are smaller. This necessitated an optimized design aimed at minimizing the wake impedance budget in the BPM. In addition, to reduce the thermal load on the BPM pickups, the pickup antennas were designed using two insulators with different dielectric constants.



<Figure 2.1.12.9> Layout of the BPM and Corrector in One Cell of the 4GSR Storage Ring.

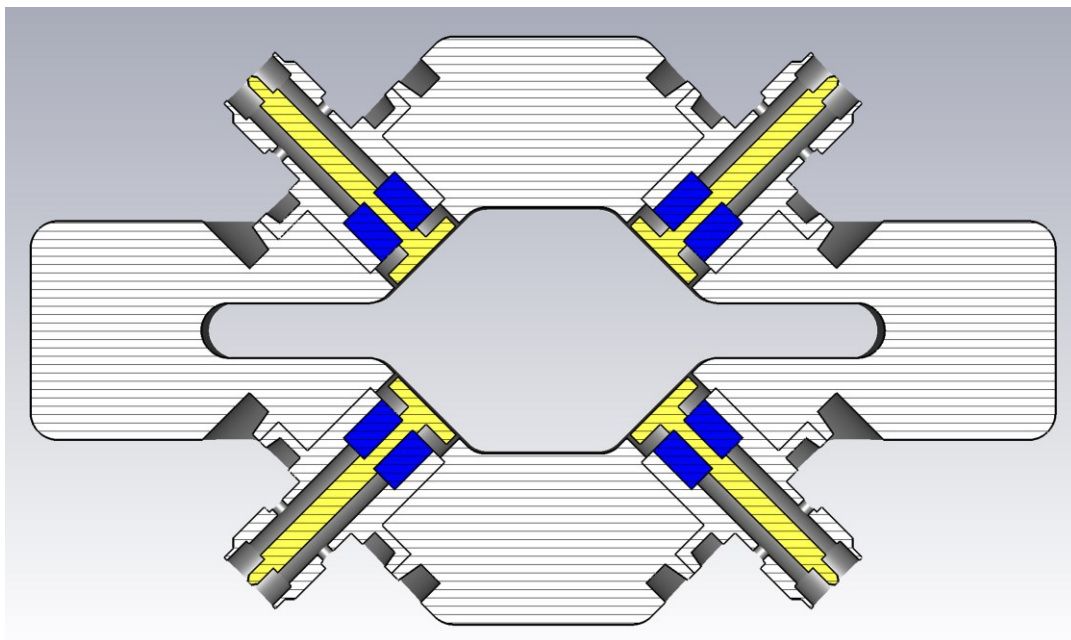
<Table 2.1.12.3> Beta Functions at the BPM Positions

Element Name	Type	Location [m]	β_x [m]	η_x [mm]	β_y [m]
MONI1U02	Fast BPM	2.940000	7.698924	0.204329	5.883431
MONI2U02	Fast BPM	6.853048	12.614888	111.809349	12.440296
MONI3U02	Slow BPM	8.072548	8.324628	89.041717	13.331988
MONI4U02	Fast BPM	10.952965	1.661979	20.162768	3.103496
MONI5U02	Fast BPM	13.913640	0.455929	2.634210	3.420795
MONI5D02	Fast BPM	14.291640	0.455927	2.634210	3.420796
MONI4D02	Fast BPM	17.252315	1.661978	20.162768	3.103499
MONI3D02	Slow BPM	20.132732	8.324620	89.041717	13.331992
MONI2D02	Fast BPM	21.352232	12.614888	111.809349	12.440296
MONI1D02	Fast BPM	25.265280	7.698888	0.204329	5.883427

○ SiO₂ BPM Design

The first BPM design employed a SiO₂ glass insulator with a dielectric constant of 4 to develop the BPM pick-up, and a prototype was manufactured by Kyocera in Japan. An optimized design was implemented using an insulator with a low dielectric constant to minimize the wake impedance budget. The fabrication method of the SiO₂ glass insulator utilizes a high-temperature sealing process that leverages differences in the coefficient of thermal expansion. This approach enables more precise production and ensures uniform manufacturing tolerances during mass production compared to antennas that use alumina ceramic insulators.

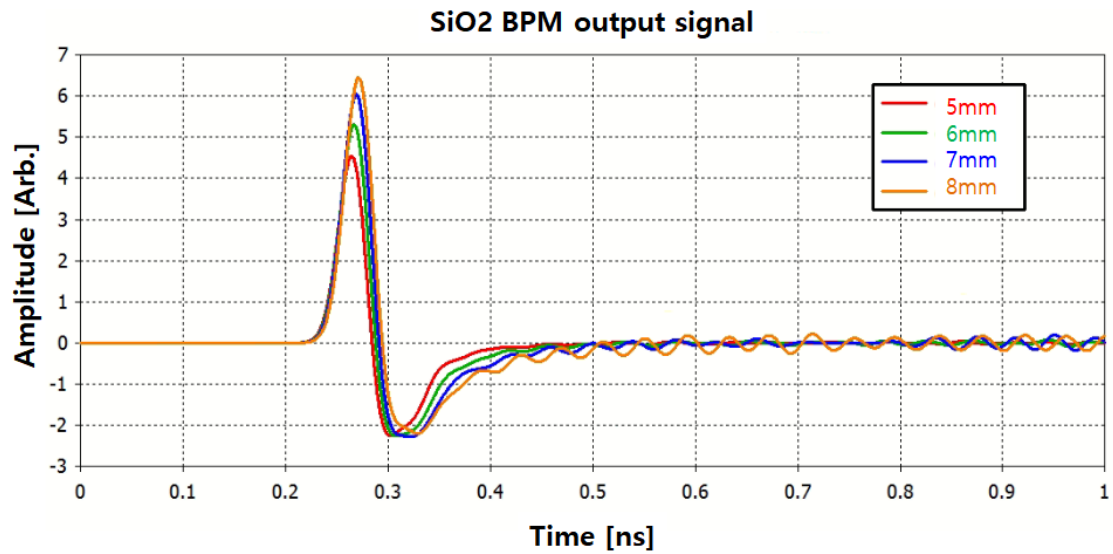
<Figure 2.1.12.10> shows the cross-sectional view of the SiO₂ BPM. The SiO₂ glass pick-up antenna was designed using SiO₂ glass (with a dielectric constant of 4) as the insulator. Instead of employing a brazing method, the antenna was fabricated using a high-temperature sealing process, which allowed the use of molybdenum—due to its similar coefficient of thermal expansion to that of the insulator—in the design. Additionally, the housing of the antenna was constructed using KOVAR, considering its thermal expansion properties.



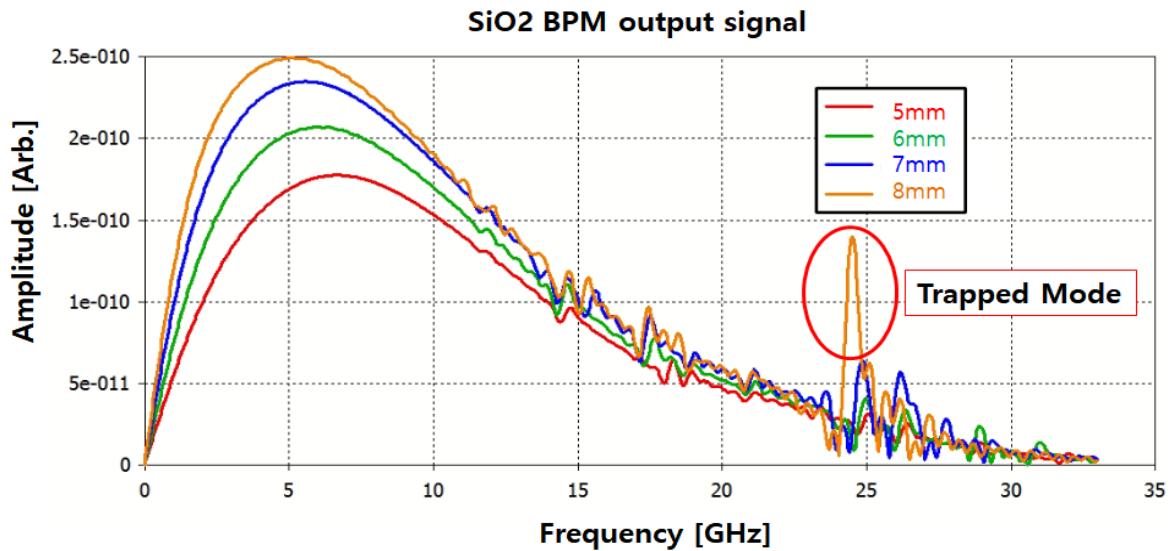
<Figure 2.1.12.10> 4GSR SiO₂ BPM Cross-Section.

In designing a button BPM, the most critical parameter is the size of the button. A smaller button reduces the wake impedance; however, it also decreases the output signal strength. Therefore, it is essential to optimize these two factors to determine the optimal button size. Through this optimization process, the button size for the 4GSR Button BPM was

determined to be 6 mm. <Figures 3.1.12.11> and <Figure 2.1.12.12> show the results of the button size optimization simulations.



<Figure 2.1.12.11> 4GSR SiO₂ BPM Output Signal Waveforms According to Button Size.



<Figure 2.1.12.12> FFT of the 4GSR SiO₂ BPM Output Signal According to Button Size.

For the 8 mm button, a trapped mode was observed in the 25 GHz band. For the sake of fabrication ease for both the 4GSR vacuum chamber and the BPM antenna, a 6 mm button was ultimately chosen.

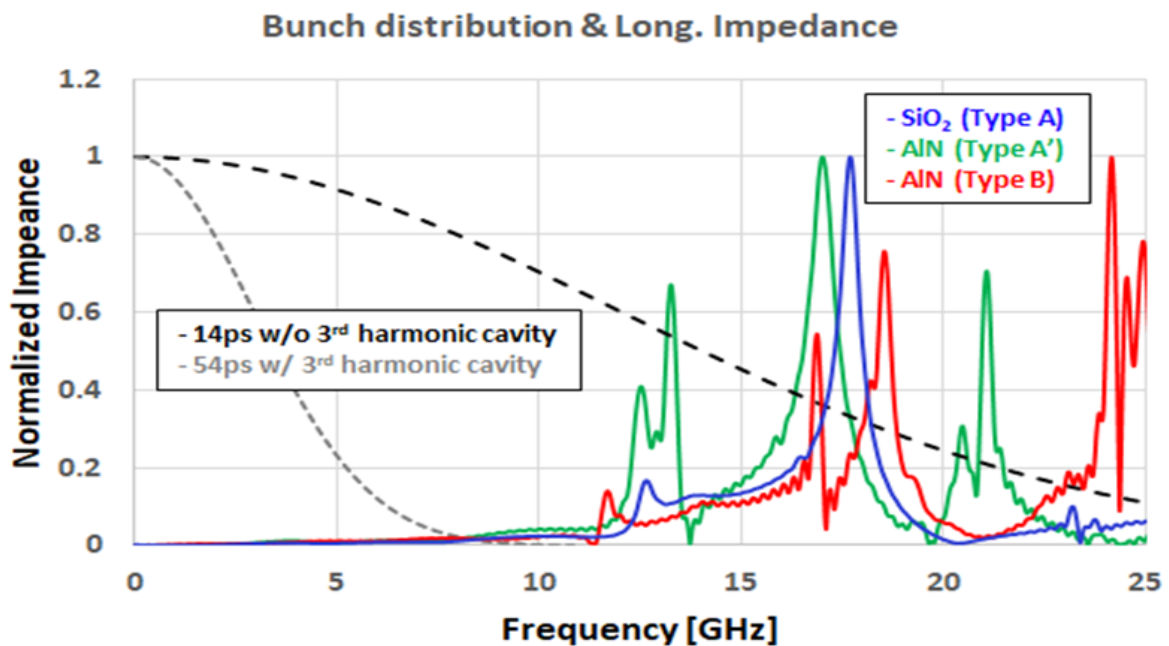
In addition to button size, optimization simulations were performed on various parameters, including the button height, shape, dielectric constant of the insulator, the thickness and height of the insulator, the button gap size, and impedance matching related to the antenna pin thickness. As a result, the SiO₂ BPM was designed as shown in <Figure 2.1.12.10>.

Among these variables, the dielectric constant of the insulator was the most critical consideration in the BPM antenna design. A lower dielectric constant shifts the wake impedance to a higher frequency band. Since the overall heat loss generated in the BPM is proportional to the product of the wake impedance (in the frequency domain) and the beam bunch distribution, shifting the wake impedance to a higher frequency band reduces the integral of this product, thereby decreasing the total heat loss in the BPM. (Equation 2.1.12.1) and (Equation 2.1.12.2) illustrate the formulas used to calculate the heat loss generated in the BPM.

$$k_{loss} = \int ds W_L(s) \lambda(s) \quad (\text{Eq. 2.1.12.1})$$

$$P_{loss}[\text{W}] = MQ [\text{nC}]^2 f_0 [\text{k Hz}] 10^{-3} k_{loss} \quad (\text{Eq. 2.1.12.2})$$

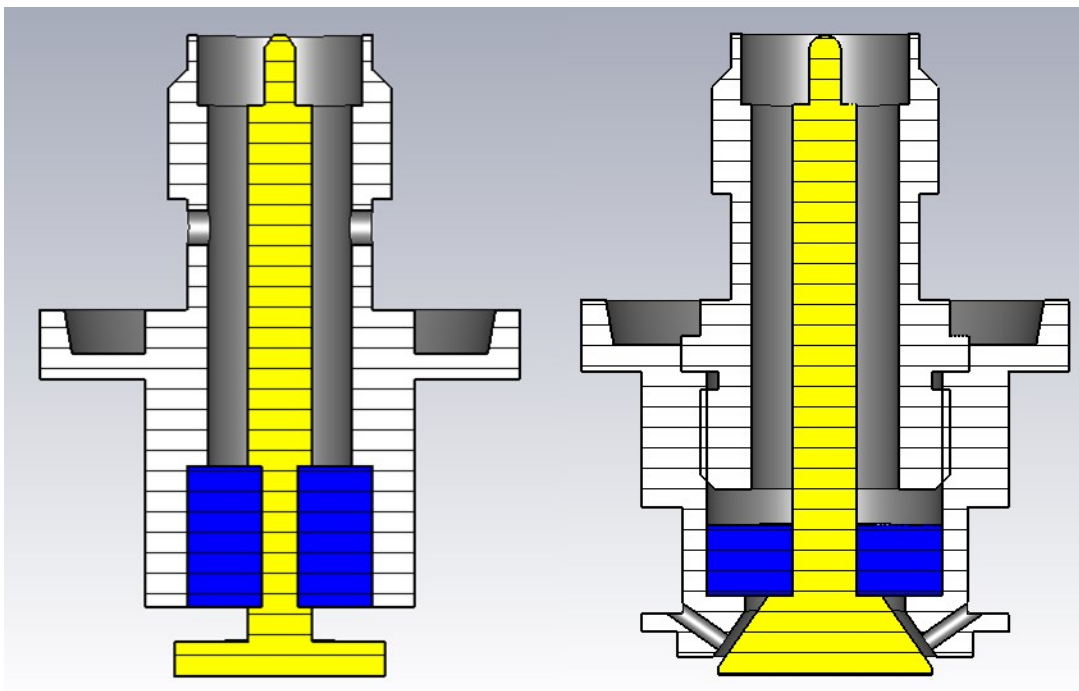
Here, k_{loss} is the heat loss variable, M is the number of beam bunches, Q is the bunch charge, and f_0 is the revolution frequency of the storage ring.



<Figure 2.1.12.13> Longitudinal Wake Impedance According to the Insulator Dielectric Permittivity and BPM Antenna Design.

In the same BPM design, using an insulator with a higher dielectric constant result in the wake impedance being generated at a lower frequency band compared to using an insulator with a lower dielectric constant. However, even when using a high dielectric constant insulator, optimizing the shape of the BPM antenna can shift the wake impedance frequency band to a higher range. Based on this consideration, the 4GSR BPM adopted a second antenna design by referencing the optimized BPM antenna designs of SOLEIL and SIRIUS, which utilized alumina ceramics.

<Figure 2.1.12.13> shows that, compared to the SiO₂ BPM design, when the dielectric constant is changed to that corresponding to alumina-based insulators and the button antenna is optimized into a bell shape, the wake impedance appears at a higher frequency band. Ultimately, the Type A flat shape design was completed using an SiO₂ glass insulator, while the Type B bell shape design was completed using an alumina-based insulator. <Figure 2.1.12.14> shows the BPM antenna using the Type A design with an SiO₂ insulator and the BPM antenna using the Type B design with an alumina insulator.



<Figure 2.1.12.14> Optimized Design of the Type-A SiO₂ BPM Antenna (Left) and Type-B Alumina BPM Antenna (Right).

○ Al_2O_3 Alumina Ceramic Pick-up BPM Design

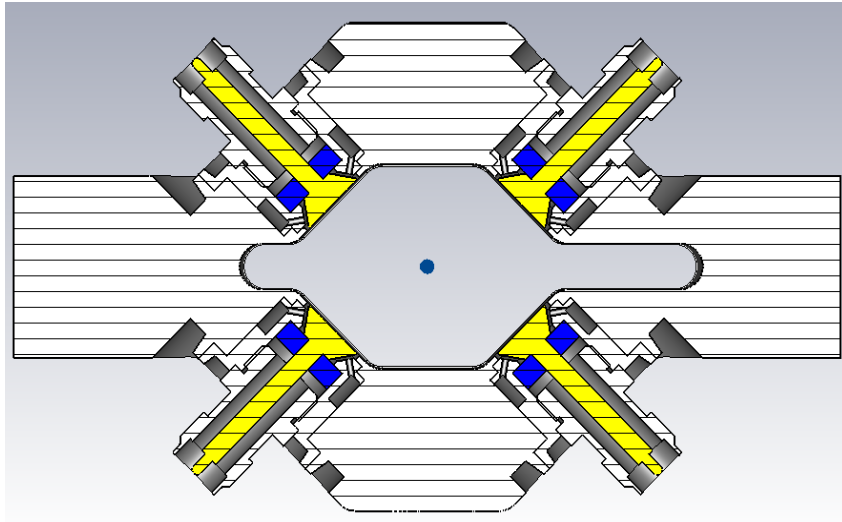
The second BPM design was developed using a traditional Al_2O_3 alumina ceramic insulator with a dielectric constant of 9 to 9.9 for the BPM pick-up. A prototype was manufactured at the Pohang Accelerator Laboratory, and through technology transfer of the manufacturing process, plans are underway to domestically produce the mass-produced units.

An optimized Bell-shape design was implemented to minimize the wake impedance budget resulting from the high dielectric constant of the alumina ceramic disk. Since the button head must be fabricated in a bell shape, its manufacturability is lower compared to conventional pick-up antennas. However, this design can reduce the wake impedance budget to a level similar to or even lower than that of the SiO_2 insulator design. Moreover, its high thermal conductivity allows for rapid dissipation of heat from the antenna when a thermal load occurs.

To achieve these performance characteristics, the ceramic is processed to a thin 2 mm thickness, and the complex structure of the antenna manufacturing process necessitates very precise tolerance management during mass production. The post-assembly antenna stiffness, which is difficult to verify through simulation, will be validated by performing various stiffness tests on the prototype.

Among the candidate materials for alumina-based insulators, the selected materials were AlN (Aluminum Nitride) with a dielectric constant of 9, and the traditional ceramic material Al_2O_3 (Alumina). Although AlN offers a lower dielectric constant and higher thermal conductivity compared to Al_2O_3 , it was ultimately decided to use Al_2O_3 after comprehensive evaluation, due to difficulties in finding manufacturers with extensive domestic and international experience and because its production cost is higher than that of SiO_2 .

<Figure 2.1.12.15> shows a cross-sectional view of the optimized Al_2O_3 Bell-shape BPM design.



<Figure 2.1.12.15> Cross-Section of the Optimized Tyep-B Alumina BPM.

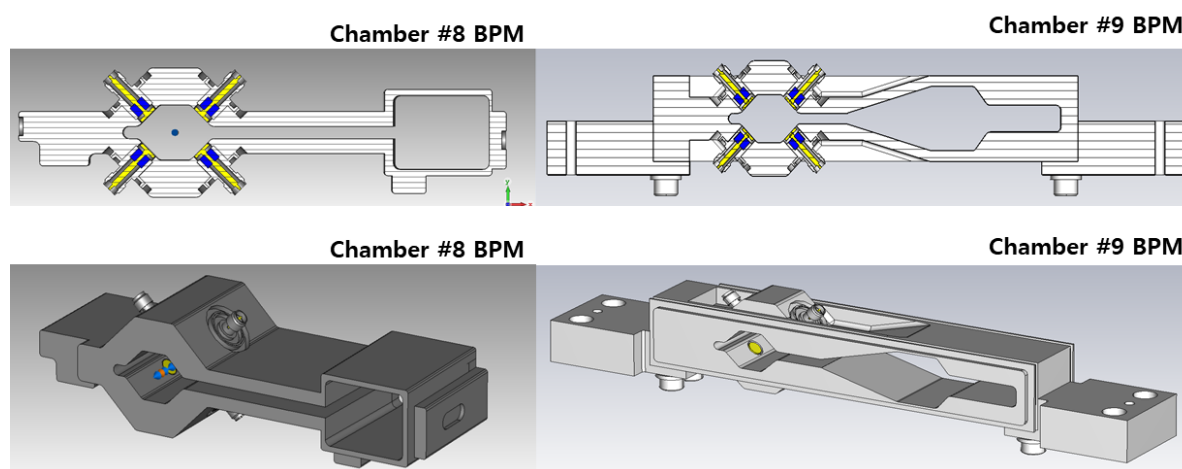
The Al_2O_3 BPM antenna is assembled using two housings. The upper housing, which connects to the SMA connector, is machined from SUS 316L, while the lower housing-used for ceramic brazing-is machined from KOVAR. In <Figure 2.1.12.15>, the blue area represents the Al_2O_3 alumina ceramic, and the antenna pin is fabricated from titanium. <Table 2.1.12.4> displays the parameters of the storage ring BPM determined through the optimization design.

<Table 2.1.12.4> Storage Ring BPM Parameter Table

	SiO ₂ BPM (Type A)	Al ₂ O ₃ BPM (Type B)
Button size	6 mm	6 mm
Button thickness	1 mm	2.2 mm
Button shape	Flat	Bell
Gap size	0.35 mm	0.35 mm
Insulator	SiO ₂ ($\epsilon_r = 4$)	Al ₂ O ₃ ($\epsilon_r = 9.9$)
Insulator diameter	5.3 mm	6.6 mm
Insulator height	4 mm	2 mm
Inner pin diameter	1.8 mm (1mm for Insulator)	1.8 mm
Impedance	50 Ω	50 Ω
Housing material	Kovar	Kovar/SUS316L
Pin material	Molybdenum	Titanium
Pin type	RP SMA male	RP SMA male
Insulator assemble method	HT sealing	Brazing

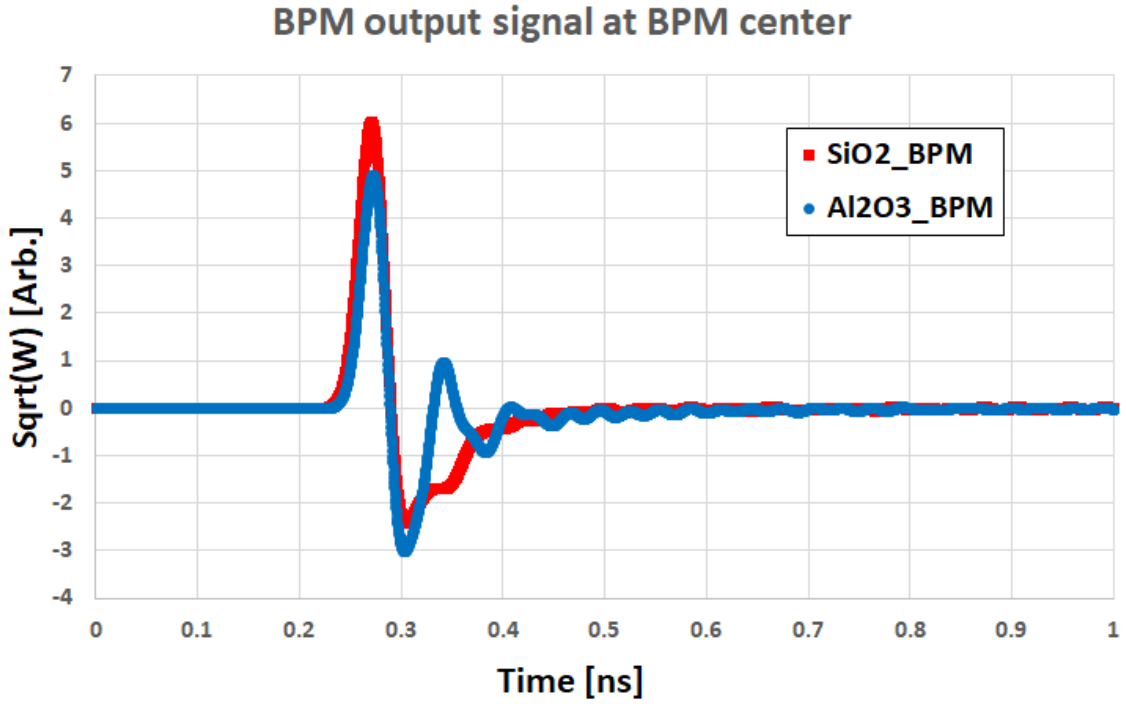
○ BPM Calibration Factor

The BPM calibration factor is largely dependent on the button size and the shape of the vacuum chamber. In the case of 4GSR, the most representative BPM vacuum chamber cross-section is that of the bellows flange BPM, as shown in <Figures 3.1.12.10> and <Figure 2.1.12.15>. Although there are five different types of BPM vacuum chambers depending on their location, the cross-sectional area of the beam pipe where the antenna is installed is identical, so its impact on the BPM calibration factor is minimal. <Figure 2.1.12.16> illustrates examples of the cross-sections for BPM vacuum chambers No. 8 and No. 9.

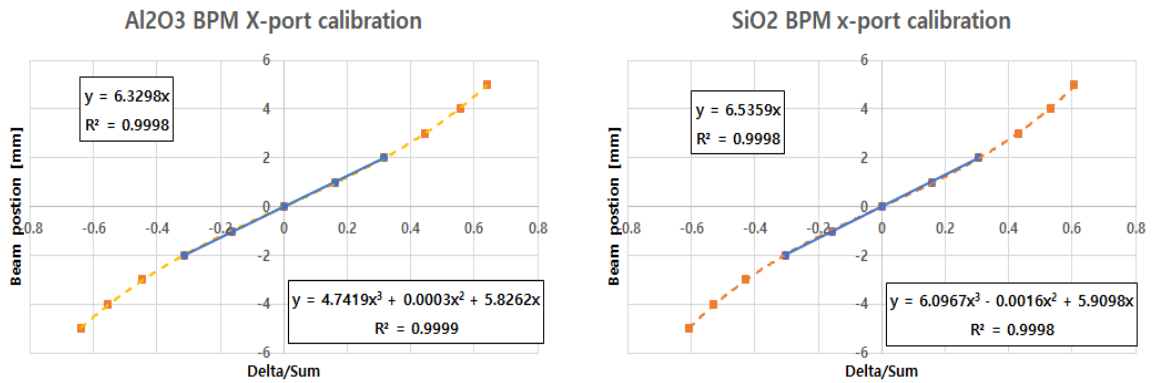


<Figure 2.1.12.16> Cross-Sections of the 8th and 9th 4GSR BPM Vacuum Chambers.

The calibration factor for the 4GSR BPM was calculated using the most basic design-the bellows flange vacuum chamber. Although the vacuum chamber shape is the same, slight variations in the BPM calibration factor occur due to differences in the output signal amplitude and waveform of each BPM antenna. <Figure 2.1.12.17> shows the output signal waveforms for the SiO_2 BPM and the Al_2O_3 BPM when the bunch length is 3.66 mm. The SiO_2 BPM exhibits a cleaner waveform and higher signal amplitude. However, for TDP (Time Domain signal Processing), where the beam position is calculated by integrating the absolute value of the signal, the variation in the integrated value does not show significant differences.



<Figure 2.1.12.17> 4GSR BPM output signals.



<Figure 2.1.12.18> Horizontal calibration factor of 4GSR SiO₂ BPM & Al₂O₃ BPM.

<Figure 2.1.12.18> shows the simulation results for the calibration factor of the 4GSR BPM. The beam position is calculated based on the following formula by integrating the absolute values of the BPM's 4-port output signals.

$$x_{pos} = k_{cal} \times \frac{(A-B+C-D)}{(A+B+C+D)} + offset = k_{cal} \times x_{DoS} + offset \quad (\text{Eq. 2.1.12.3})$$

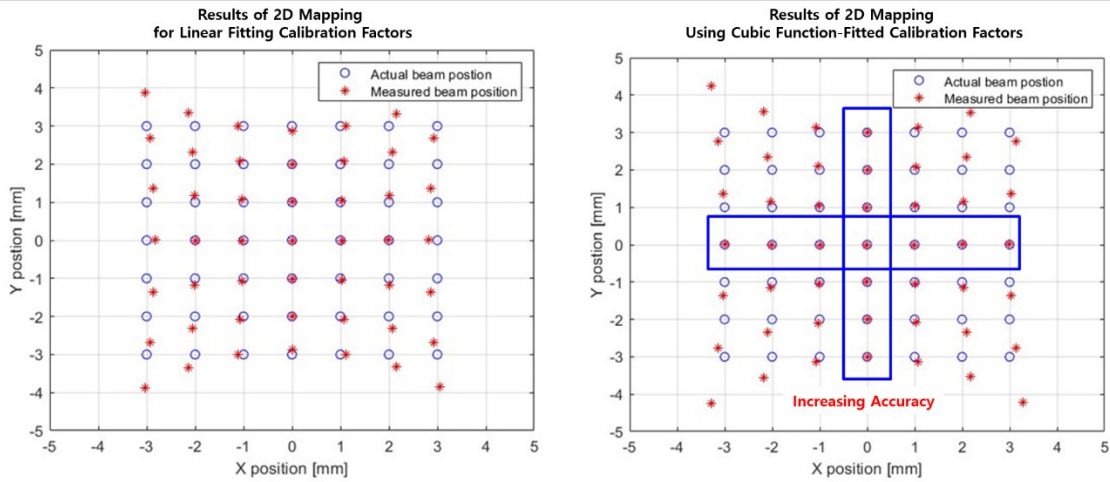
The horizontal linear calibration factor for both BPMs is similar, measuring 6.54 mm for

the SiO₂ BPM and 6.33 mm for the Al₂O₃ BPM. In the vertical direction, the calibration factor is 11.61 mm for the SiO₂ BPM and 11.2 mm for the Al₂O₃ BPM. Since the vacuum chamber of the 4GSR BPM is wider in the horizontal direction than in the vertical, the beam position can be measured more precisely horizontally than vertically. <Table 2.1.12.5> shows the simulation results for the calibration factors of the two BPMs.

<Table 2.1.12.5> SR BPM calibration simulation results

	SiO ₂ BPM (Type A)	Al ₂ O ₃ BPM (Type B)
Linear fit x-port	6.54 mm	6.33 mm
Linear fit y-port	11.61 mm	11.2 mm
Poly fit x-port	C1 = 6.0967, C2 = -0.0016, C3 = 5.9098, offset = 0	C1 = 4.7419, C2 = 0.0003, C3 = 5.8262, offset = 0
Poly fit y-port	C1 = 19.326, C2 = -0.0019, C3 = 10.998, offset = 0	C1 = 19.326, C2 = -0.0019, C3 = 10.998, offset = 0

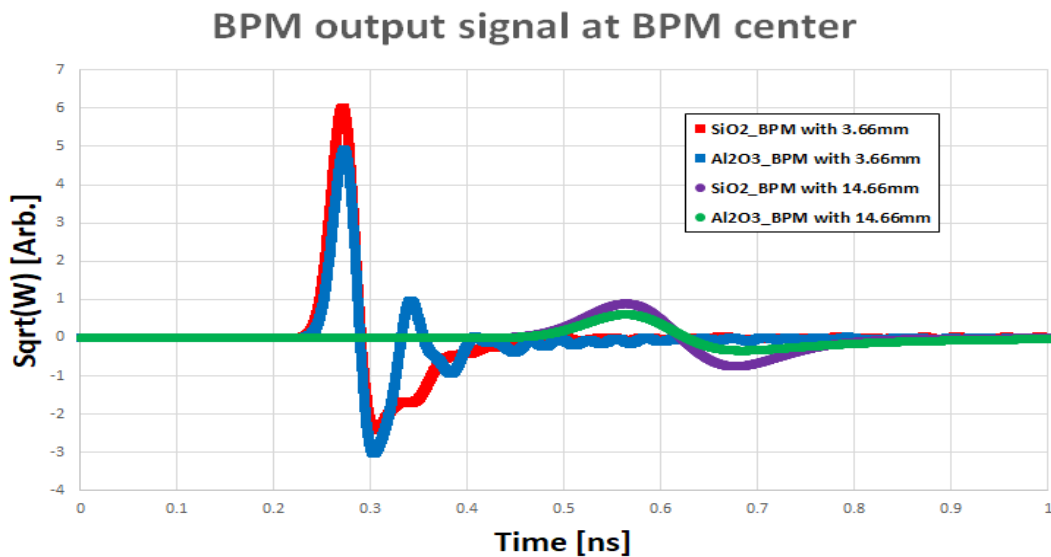
At the beginning of commissioning, it is difficult to align the beam position precisely at the center. Therefore, a method is employed where a look-up table is created based on 2D mapping data to align the beam position to the center. In preparation for initial commissioning, 2D mapping look-up tables are generated using both the linear calibration factor and the poly fit calibration factor. <Figure 2.1.12.19> shows the 2D mapping results of the 4GSR BPM using both linear fit and poly fit methods. When using the linear fit calibration factor, beam position accuracy is maintained within ± 2 mm on-axis. If the poly fit is used, high accuracy can be achieved within ± 3 mm. However, the accuracy off-axis decreases; therefore, during the early stages of commissioning, it is preferable to perform Beam Based Alignment (BBA) using the linear fit calibration factor and the look-up table.



<Figure 2.1.12.19> 2D mapping simulation results of 4GSR BPM.

○ Thermal Analysis of 4GSR BPM

When the 3rd harmonic cavity is absent, the 4GSR storage ring exhibits a bunch length of 3.66 mm, whereas with the 3rd harmonic cavity the bunch length is 14.66 mm. Since initial commissioning might be carried out without the 3rd harmonic cavity, it is essential that the 4GSR BPM operates reliably even with a 3.66 mm bunch length. <Figure 2.1.12.20> shows the changes in the BPM's output signal amplitude and waveform depending on whether the 3rd harmonic cavity is present.

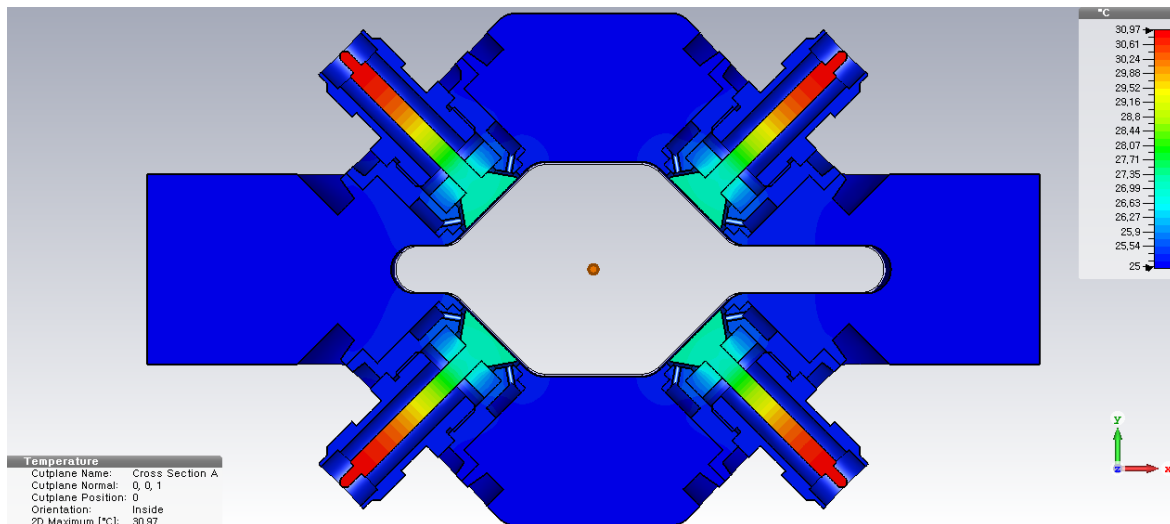


<Figure 2.1.12.20> 4GSR BPM output signals with/without 3rd harmonic cavity.

As the bunch length decreases, the influence of the wake field generated within the BPM chamber becomes stronger, necessitating a fast and precise feedback system to suppress it. <Table 2.1.12.6> summarizes the power dissipation and the maximum temperature rise in the storage ring BPM for cases with and without the operation of the 3rd harmonic cavity. An ambient temperature of 25 °C was assumed. When the electron beam passes through the center of the BPM, significant heat is not generated; however, prolonged beam operation at currents above 250 mA without the 3rd harmonic cavity and feedback system may result in heat loss that deforms the button insulator and the antenna pin. For example, if the BPM is operated at a beam current of 250 mA without the 3rd harmonic cavity and the entire 250 mA beam impinges on the button, the temperature of the antenna pin could rise by more than 240 °C. Therefore, if operating the 3rd harmonic cavity becomes challenging, the beam current must be limited to 250 mA or less. <Figure 2.1.12.21> illustrates the heat loss distribution for the Al₂O₃ BPM when operating at 250 mA without the 3rd harmonic cavity.

<Table 2.1.12.6> SR BPM Power dissipation and Max temp. at centered beam

	SiO ₂ BPM (Type A)		Al ₂ O ₃ BPM (Type B)	
	Total P_loss [W]	Max Temp. [°C]	Total P_loss [W]	Max Temp. [°C]
250mA without 3 rd harm. cavity	3.28	44.2	2.093	31.0
400mA without 3 rd harm. cavity	8.4	74.1	5.35	40.3
250mA with 3 rd harm. cavity	0.081	25.5	0.052	25.15
400mA with 3rd harm. cavity	0.21	26.7	0.13	25.38



<Figure 2.1.12.21> Thermal simulation results of 4GSR Al₂O₃ BPM without 3rd harmonic cavity for 250mA beam operation condition.

○ Mechanical tolerance and TDR measurement of Proto-type Pick-ups

The prototypes of the 4GSR BPM pickup antennas were fabricated in two types. As mentioned earlier, one model uses a SiO₂ glass insulator while the other uses an Al₂O₃ insulator. The SiO₂ pickup was manufactured at Kyocera in Japan, whereas the Al₂O₃ pickup was initially processed by a domestic company and then brazed at the Pohang Accelerator Laboratory. <Figure 2.1.12.22> shows the two prototype pickup samples. The SiO₂ pickup was constructed using three components-a molybdenum antenna pins, a SiO₂ glass insulator, and a KOVAR housing-while the Al₂O₃ pickup was assembled from four components-a titanium antenna pin, an Al₂O₃ ceramic insulator, and two housings made of KOVAR and SUS316L.



<Figure 2.1.12.22> Prototype sample photo showing two types of pickups for the 4GSR BPM: SiO₂ pickups on the left and Al₂O₃ pickups on the right.

Fifty samples of each type were produced, and after fabrication, the manufacturing tolerances were measured. The results confirmed that the SiO₂ pickups were manufactured with high precision. <Table 2.1.12.7> shows the measured tolerance results for five samples, and the measurements for all 50 samples were found to be similar to those in the table.

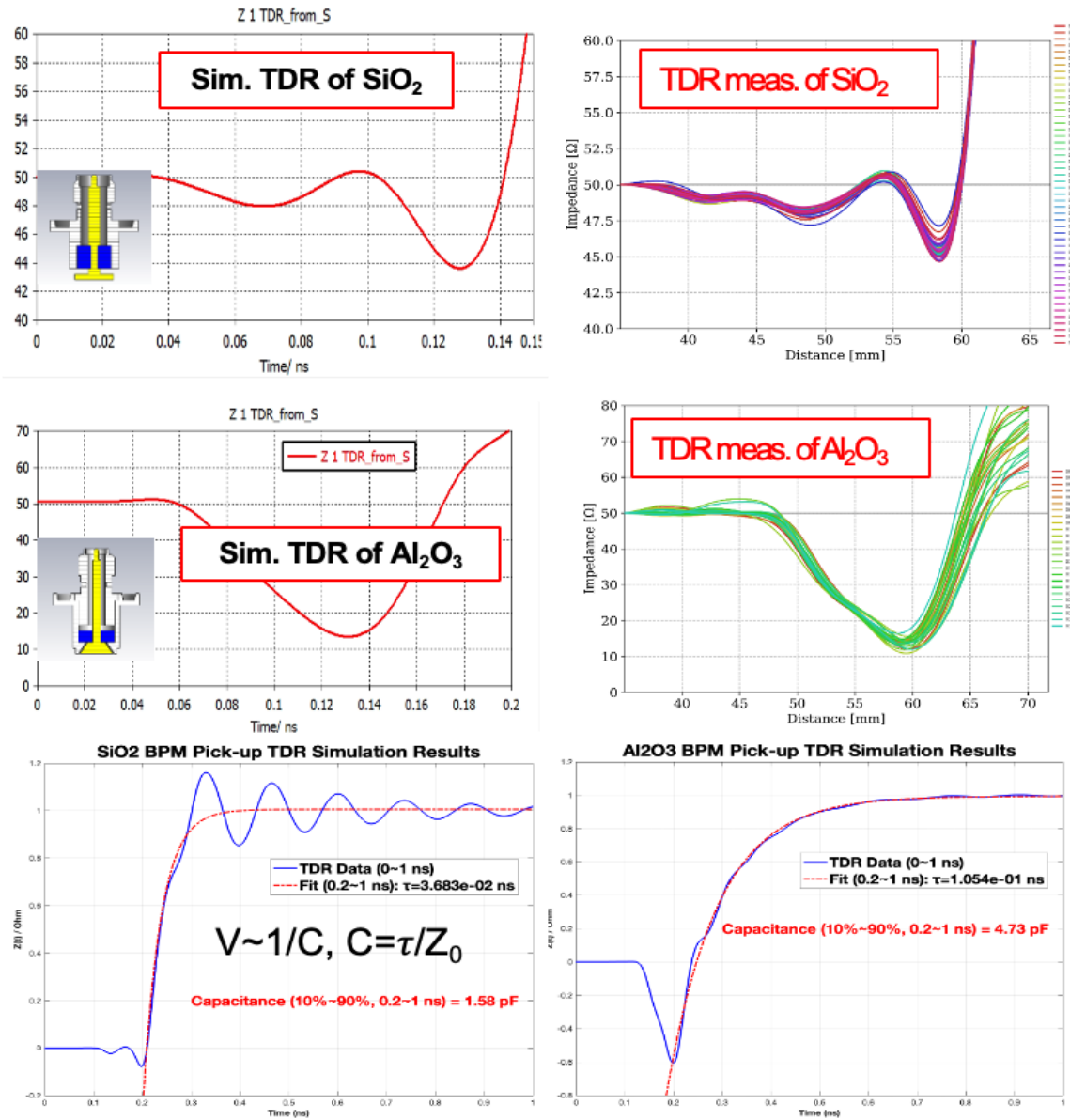
<Table 2.1.12.7> Tolerance measurements of two proto-type pick-ups for 4GSR BPM

SiO ₂ sample	Pin Head Diameter				Pick-up Outer Diameter				Pick-up welding rip diameter			
	Measureemnts			Average	Measureemnts			Average	Measureemnts			Average
#3	6	6	6	6.00	7.67	7.67	7.67	7.67	13.67	13.67	13.66	13.67
#14	6.01	6	6.01	6.01	7.68	7.68	7.69	7.68	13.67	13.69	13.68	13.68
#28	5.99	6.01	6.01	6.00	7.67	7.67	7.67	7.67	13.68	13.67	13.68	13.68
#39	6	6.01	6	6.00	7.68	7.67	7.68	7.68	13.67	13.68	13.68	13.68
#41	6	6	6.01	6.00	7.68	7.66	7.67	7.67	13.68	13.69	13.67	13.68
Average (mm)				6.00				7.67				13.68
STD (mm)				0.002				0.01				0.005
STD (%)				0.04				0.07				0.04
Al ₂ O ₃ sample	Pin Head Diameter				Pick-up Outer Diameter				Pick-up welding rip diameter			
	Measureemnts			Average	Measureemnts			Average	Measureemnts			Average
#2	5.96	5.96	5.96	5.96	10.3	10.29	10.3	10.30	13.69	13.7	13.69	13.69
#7	5.99	5.99	5.99	5.99	10.31	10.3	10.31	10.31	13.74	13.73	13.74	13.74
#13	5.96	5.97	5.96	5.96	10.33	10.33	10.32	10.33	13.68	13.75	13.73	13.72
#19	6	5.98	5.98	5.99	10.28	10.3	10.27	10.28	13.66	13.68	13.7	13.68
#23	5.95	5.95	5.96	5.95	10.29	10.28	10.27	10.28	13.69	13.69	13.69	13.69
Average (mm)				5.97				10.30				13.70
STD (mm)				0.01				0.02				0.02
STD (%)				0.25				0.16				0.15

Based on the measured tolerances, the primary samples were classified by size, and TDR (Time-Domain Reflectometry) measurements were performed sequentially according to that classification. Through the TDR measurements, the actual impedance and capacitance of the pickups were determined, which served as the basis for evaluating the final performance of the pickup antennas. TDR is a technique in which a high-speed pulse is injected into the pickup and the reflected waveform is measured over time, allowing for an assessment of the electrical characteristics and the detection of any structural defects in the pickup. In this experiment, identical pulses were applied under the same conditions to BPM pickups

incorporating two types of insulators (SiO_2 and Al_2O_3), and the reflected waveforms were observed using a high-bandwidth TDR measurement system. By dividing the time difference (τ) over a specific interval by the reference impedance (Z_0), the capacitance (C) of the pickup antenna was calculated. In addition, by analyzing both the magnitude of the reflected voltage and the changes in the waveform, the differences in the pickup structure and material characteristics were quantitatively evaluated.

As shown in <Figure 2.1.12.23>, the experimental results indicated that the SiO_2 pickup exhibited a lower capacitance compared to the Al_2O_3 pickup (approximately 1.58 pF vs. approximately 4.73 pF) and demonstrated a more favorable signal response in relatively higher frequency ranges. This is interpreted as the smaller capacitance producing a larger reflected voltage and inducing rapid waveform changes over a short time interval. On the other hand, while the Al_2O_3 pickup offered superior heat resistance and mechanical stability, maintaining concentricity during the brazing process was challenging, and variations in ceramic thickness could potentially result in increased capacitance. Although each material has its own advantages and disadvantages, for the 4GSR BPM the SiO_2 pickup, which shows greater signal variation with beam position, can achieve superior beam position resolution. Moreover, even if a more precise and demanding brazing process is introduced during mass production, it would be difficult to obtain uniform performance from the Al_2O_3 pickup, and the manpower required for performance verification would be significant. Consequently, the final design adopted the pickup utilizing a SiO_2 insulator.

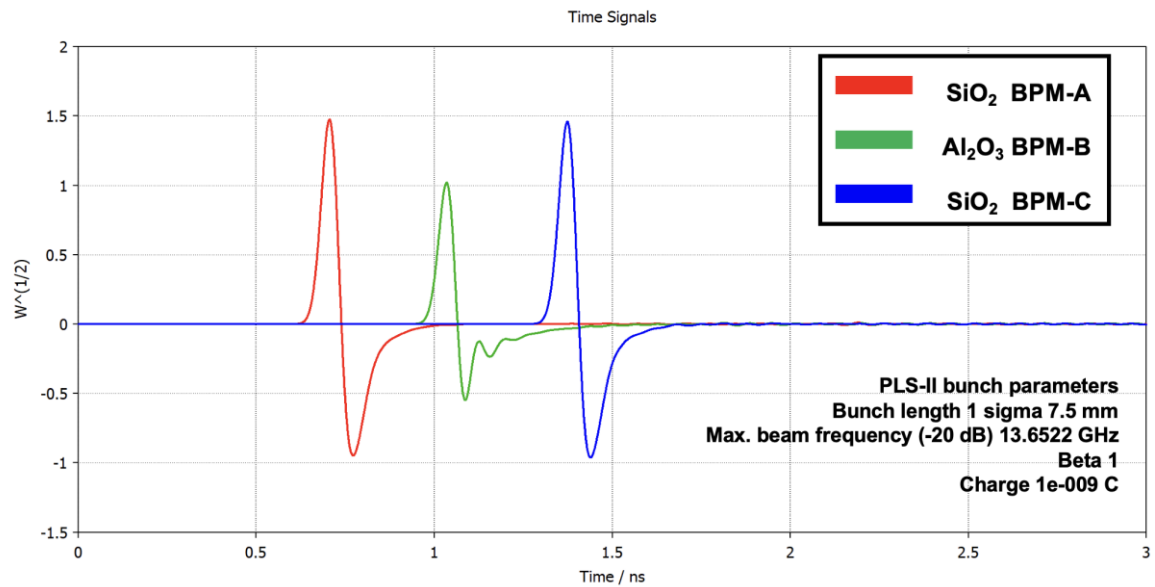


<Figure 2.1.12.23> TDR measurements results by using two types of pickups for the 4GSR BPM: SiO₂ pickups on the left and Al₂O₃ pickups on the right.

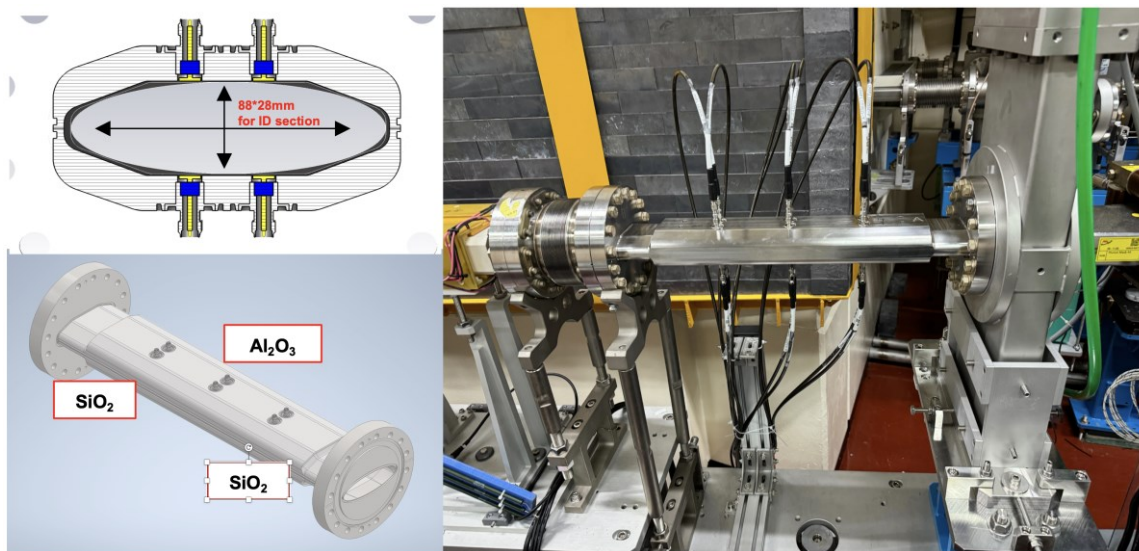
○ Test BPM beam test with 4GSR BPM pick-ups at PLS-II

After fabricating the 4GSR BPM pickup antenna prototypes, beam tests were conducted to indirectly evaluate their suitability for operation in the actual 4GSR accelerator. These tests aimed to determine whether the 4GSR BPM exhibited performance largely consistent with simulation results based on the PLS-II storage ring beam parameters. <Figure 2.1.12.24> shows the simulation results obtained by installing the 4GSR BPM prototype pickup antennas in a dummy chamber. Both the beam parameters and chamber geometry were based on those of PLS-II, and a total of 12 prototype pickups were installed to

implement three BPMs in the dummy chamber. SiO₂ BPMs were installed on both sides of the chamber, with an Al₂O₃ BPM positioned in the center (see <Figure 2.1.12.25>). When comparing the simulation results with the TDR measurement outcomes, it was observed that the SiO₂ BPM exhibited a stronger output signal intensity.

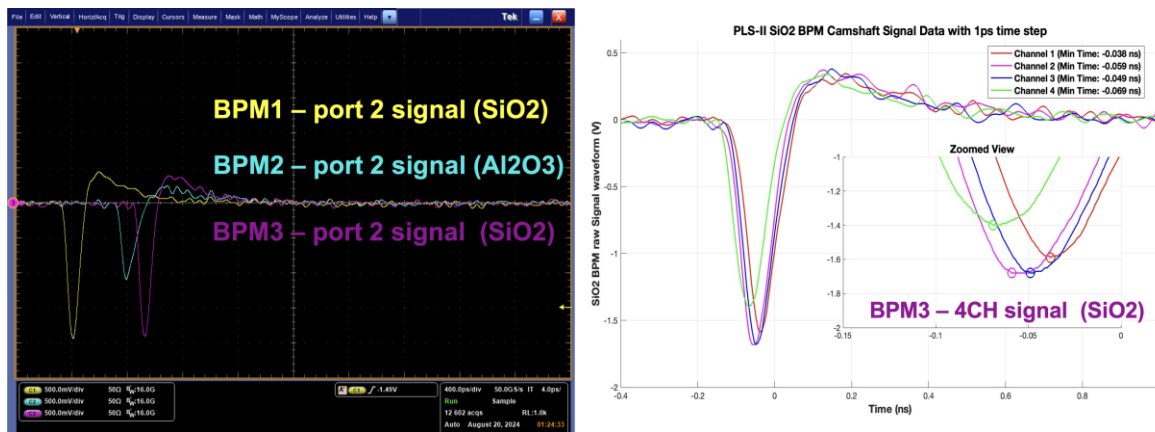


<Figure 2.1.12.24> 3D simulation of Test BPM for the beam test at PLS-II storage ring.



<Figure 2.1.12.25> Installation of Test BPM for the beam test at PLS-II storage ring.

<Figure 2.1.12.25> shows a test dummy chamber BPM installed in the ID section of cell 7 in the PLS-II storage ring. The connection from the BPM to the BPM electronics in the control shed outside the storage ring was made using a single coaxial SMA cable. This configuration ensured that the phase differences among the four cables per BPM were maintained within an error margin of only 20 ps. Prior to performing the beam position resolution test, the original waveform of the BPM signal was measured using a high-performance oscilloscope with a 16 GHz analog bandwidth and a 50 GS/s sampling rate. The measured BPM output signal exhibited the same results as the 3D simulation. Therefore, it has been confirmed that the results of the 3D simulation using the 4GSR BPM chamber will closely match the actual BPM signals to be measured in the future 4GSR storage ring.

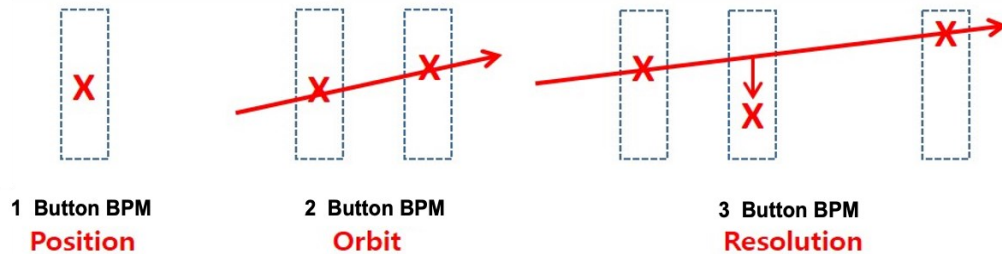


<Figure 2.1.12.26> Raw BPM signals from three different BPMs (left) and camshaft beam signals from BPM3 with the SiO₂ pick-up(right). For the beam test, four pick-ups of each BPM are connected using single SMA coaxial cables, achieving a phase difference of less than 30 ps.

<Figure 2.1.12.26> shows the raw signals of three BPMs measured using a high-performance oscilloscope. The left image displays the three signal waveforms from the same output port (port 2) of each BPM, while the right image presents the four output signals from BPM3 (SiO₂ BPM). The signals shown in the figure are an enlarged view of the storage ring camshaft signal waveform, demonstrating a phase difference of approximately 30 ps based on the maximum peak value. Although the phase difference between the cables measured using TDR equipment was 20 ps, the phase difference measured based on the camshaft bunch was approximately 30 ps, which is within the target of 1 cm for the 4GSR BPM RF cable installation.

After confirming the characteristics of the raw signals, the beam position resolution was measured using the three BPMs. The beam test was conducted in the storage ring top-up

mode. The beam position resolution using the three BPMs was determined by applying the SVD method to calculate the expected beam position from two BPMs, and then measuring the RMS of the residual values between the calculated and the actually measured beam positions. <Figure 2.1.12.27> illustrates the principle and formula for measuring the BPM beam position resolution using the SVD method.



Predicted position(ADC counts) for BPM1-Y was calculated as follow equation,

- Predicted position of BPM1-Y = $a_1 \cdot \text{BPM2-Y} + a_2 \cdot \text{BPM3-Y} + a_3 \cdot \text{BPM1-X} + a_4 \cdot \text{BPM2-X} + a_5 \cdot \text{BPM3-X} + a_6 \cdot \text{BPM1-Sum} + a_7 \cdot \text{BPM2-Sum} + a_8 \cdot \text{BPM3-Sum} + a_9$
- Residual of BPM1-Y = Measured BPM1-Y – Predicted BPM1-Y
- The beam position resolution proportional to $1/(\text{beam charge})$.

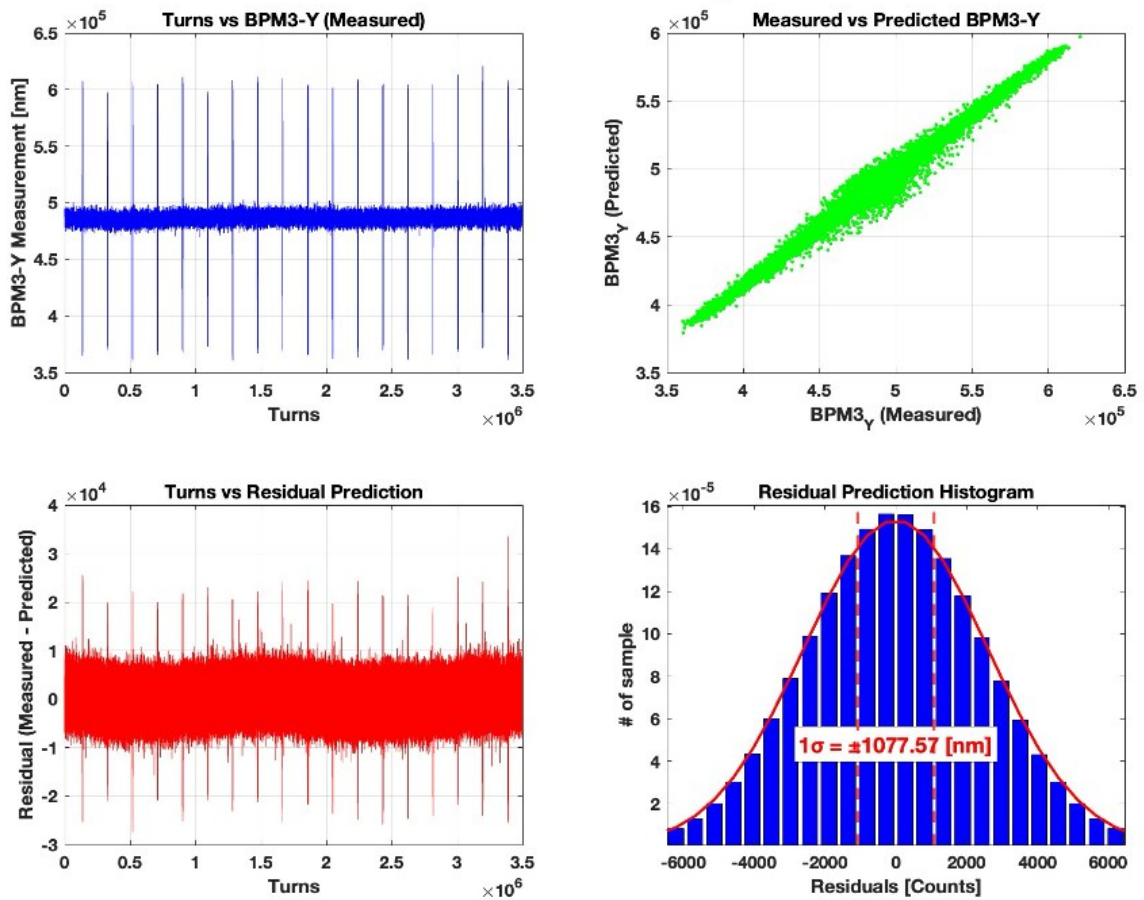
$$\text{Norm. Resolution} = \text{Geometrical factor} \times \frac{\text{RMS of residual}}{\text{Calibration factor}} \times \frac{\text{Measured beam charge}}{\text{Nominal beam charge}}$$

<Figure 2.1.12.27> Position resolution calculation by using three BPMs with SVD method.

The beam position resolution test was conducted using Turn by Turn (TbT) BPM data collected over 3.5 million turns. The DAQ system for acquiring the TbT data was the Libera Brilliance+, synchronized with the PLS-II storage ring's machine clock and a 10 Hz trigger signal. In addition, it was confirmed that the three BPMs were operating normally as they were synchronized through the BPM electronics.

During the data collection phase, 1,000 TbT data points were acquired 3,500 times, resulting in a total of 3.5 million turns of data collected over a period of one hour. This allowed for the measurement of stable beam orbits and beam position resolution in both the X and Y directions under overall beam operation conditions, including top-up injection. <Figure 2.1.12.28> shows the Y-direction beam position resolution measurement result of BPM3. The expected beam position at BPM3 was calculated using BPM1 and BPM2, and the beam position resolution of the BPM was determined based on the residual between the calculated and the actually measured beam positions.

BPM3-Y Position Analysis



<Figure 2.1.12.28> The measured beam position resolution of BPM3-Y.

Using the same method, the beam position resolution for the remaining BPMs was also measured, and the results are summarized in <Table 2.1.12.8>. In the case of the SiO₂ BPM, a beam position resolution of approximately 1 to 1.5 μm was obtained in the top-up mode at 300 mA, while the Al₂O₃ BPM exhibited a beam position resolution of approximately 2.1 to 2.7 μm . Extrapolating these results to the 4GSR 400mA top-up operating mode, it is anticipated that the SiO₂ BPM could achieve a beam position resolution of around 0.8 to 1.1 μm .

<Table 2.1.12.8> The measured and expected beam position resolution of 4GSR BPM

TbT resol.	BPM-A (SiO ₂)	BPM-B (Al ₂ O ₃)	BPM-C (SiO ₂)
X-port (300mA Meas.)	1.52 um	2.70 um	1.50 um
X-port (400mA Exp.)	1.14 um	2.03 um	1.13 um
Y-port (300mA Meas.)	1.30 um	2.16 um	1.08 um
Y-port (400mA Exp.)	0.975 um	1.62 um	0.81 um

(2) BPM Electronics

The 4GSR storage ring is equipped with a total of 288 beam position monitors (BPMs), as mentioned earlier. Since one BPM electronics unit can connect to 4 BPMs, the storage ring requires a total of 72 BPM electronics units. To elaborate further, each cell of the 4GSR storage ring consists of 10 BPMs. Among these, 8 BPMs are used for Fast Orbit Feedback (FOFB) and the remaining 2 are used for Slow Orbit Feedback (SOFB). Based on these feedback characteristics, the configuration of the electronics and BPMs was determined as follows:

One unit of 4GSR BPM electronics processes the data from 4 BPMs.

For the 8 BPMs connected to the FOFB controller, they are grouped into two sets of 4 (left and right, based on the CB), each set being connected to one electronics board (see <Figure 2.1.12.29>).

The remaining 2 slow BPMs are connected to one BPM electronics unit. As shown in <Figure 2.1.12.29>, one BPM electronics unit is installed per 2 cells, thereby connecting 4 slow BPMs in total.

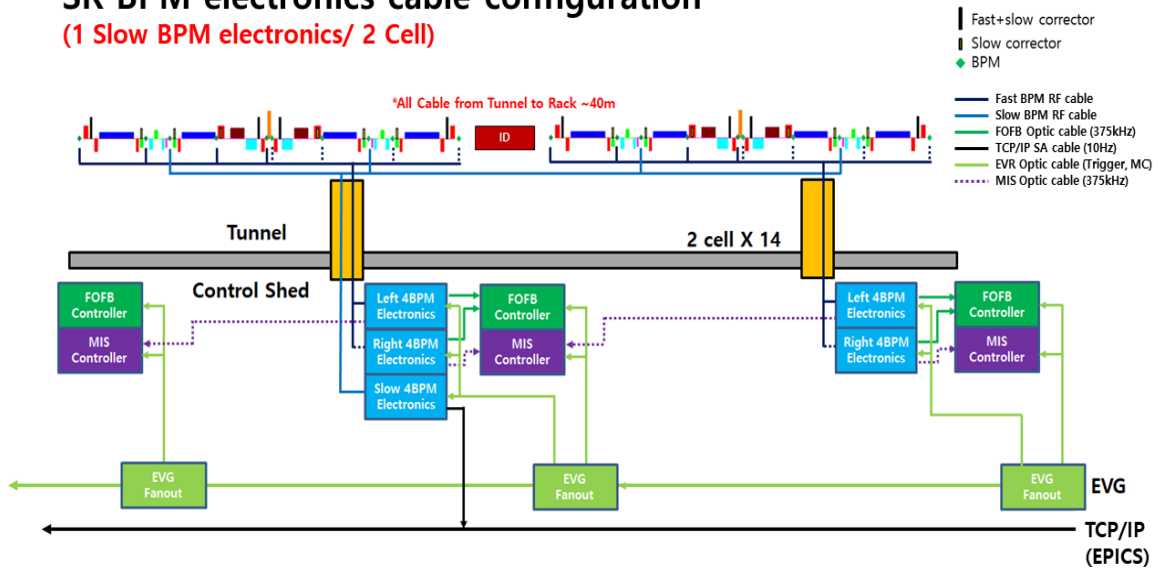
Thus, a total of 5 BPM electronics units are configured to process the data from 20 BPMs across 2 cells. In addition, for the non-symmetric cells in the high beta straight sections, a total of 4 BPMs are installed, which are connected to one BPM electronics unit to measure the beam position. In summary, 70 BPM electronics units are installed for the 28 symmetric cells, and 2 BPM electronics units are installed for the two high beta straight sections.

<Table 2.1.12.9> Number and Positions of the 4GSR BPM and Electronics per Cell

Location	Number of BPM in 1 Cell	Number of BPM electronics in 1 Cell	BPM Type
Arc Cell	8	2	Fast BPM
Arc Cell	2	0.5	Slow BPM
High beta Straight	4	1	Fast BPM
Total	288	72	-

SR BPM electronics cable configuration

(1 Slow BPM electronics/ 2 Cell)



<Figure 2.1.12.29> SR BPM electronics cable configuration per two symmetry cells.

○ BPM Cable Configuration

The BPM has 4 output ports, meaning that 4 cables form one complete set. Three types of cables are used to connect the BPM in the tunnel to the BPM electronics in the control shed:

BPM Cable: This cable is directly attached to the BPM. Since the BPM pickup antenna is mechanically delicate, using a heavy and stiff cable may apply excessive force, potentially causing damage or cracks in the pickup antenna, which could lead to vacuum leaks. Therefore, a flexible cable with minimal transmission loss and a length of approximately 1 m is directly connected to the pickup. The other end is then connected to the diagnostics cable via an adapter.

Diagnostics Cable: This cable is used for long-distance transmission between the tunnel

and the control shed. It must have low transmission loss, with an expected length of about 40 m for Fast BPM and 50 m for Slow BPM.

Extension Cable: This cable connects directly to the BPM electronics. The diagnostics cable is attached to the extension panel adapter of the BPM rack, and on the opposite end, the extension cable links the adapter to the BPM electronics. The expected length of the extension cable is within 1 to 2 m.

○ **Specifications**

(i) Pickup Cable and Extension Cable Specifications

- Connector: SMA (M) - SMA (M)
- Cable: Refer to [4GSR BPM Cable Specifications]
- Length: 1 to 2 m
- Loss Variation: ± 0.1 dB at 500 MHz for all cables
- Length Variation: Less than 1 mm for all cables, or phase matching within 0.7° at 500 MHz

(ii) Diagnostics Cable Specifications

- Connector: SMA type (M) - SMA type (M)
- Length: 40 to 50 m (to be verified on site)
- Loss Variation: For a set of 4 cables, less than 0.4 dB at 500 MHz
- Length Tolerance: For a set of 4 cables, less than 1 cm

(iii) Pickup Panel Specifications

- Configuration: Equipped with 1×4 adapters
- Adapter Type: SMA (F) - SMA (F)
- Panel Fastening Screws Material: SUS (must be non-magnetic)

(iv) Extension Panel Specifications

- Configuration: 19" 3U or 4U, equipped with 4×16 adapters
- Adapter Type: SMA (F) - SMA (F)

(v) 4GSR BPM Cable Specifications

The Pickup Cable, Diagnostics Cable, and Extension Cable all use the same grade of specifications and must comply with the requirements outlined in <Table 2.1.12.10>, which details the specifications for the 4GSR BPM cables.

<Table 2.1.12.10> Specification of 4GSR BPM cable

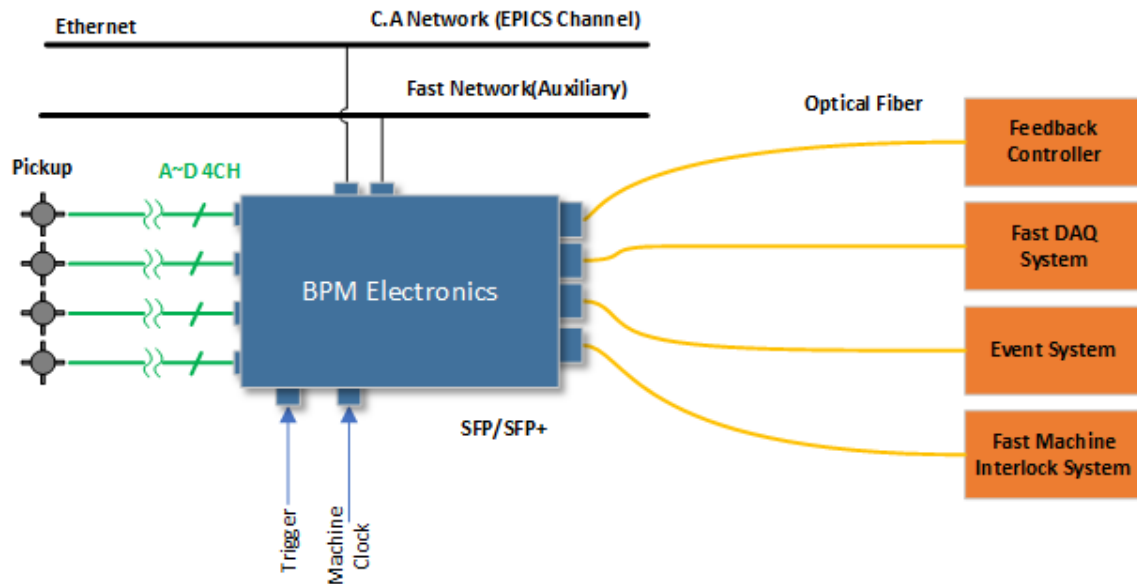
Specification	4GSR BPM cable
Operating Frequency	0 Hz to 26.5 GHz
Maximum VSWR	1.25:1
Impedance (Nominal)	50 Ω
Amplitude Stability in Insertion Loss	< ± 0.05 dB
Phase Stability vs Temperature	2°
Attenuation at 500 MHz Frequency	< -0.3 dB/m
Velocity of Propagation	83%
Shield Effectiveness (Through 18 GHz)	< 100 dB
Temperature Ranges (°C)	-55° to +150°
Minimum Bend Radius	28 mm
Crush Resistance (kg-f/cm)	41.2

○ BPM Electronics Hardware Configuration

The 4GSR BPM electronics is designed to acquire and process Turn by Turn (TbT) data. Although the electronics are classified as Fast BPM electronics and Slow BPM electronics based on whether they connect to the feedback controller or directly transmit data to EPICS, the same performance-equivalent electronics are used in both cases. Therefore, in the future, the Slow BPM electronics can also be used to acquire TbT data if needed.

<Figure 2.1.12.30> illustrates the hardware configuration of the 4GSR BPM electronics. It features a 16-channel RF signal input port that allows connection to 4 BPMs, thereby enabling the calculation of TbT data from these 4 BPMs. Additionally, 4 SFP/SFP+ ports are utilized to transmit the TbT data at a rate of 375 kHz via optical fiber to the FOFB controller, Fast DAQ server, and Fast Machine Interlock System. The remaining SFP port is connected to the internal EVR of the electronics, which decodes event signals from the EVG (Event Generator) to generate the trigger signal and Machine Clock (MC).

The following section presents the design target specifications for the 4GSR BPM electronics.



<Figure 2.1.12.30> Connection Configuration of the Main I/O Ports of the 4GSR BPM Electronics.

○ 4GSR BPM Electronics Hardware Configuration

1. Key Design Specifications for 4GSR BPM Electronics

Assumes a pickup calibration factor of 10 mm.

2. Resolution: The BPM electronics must satisfy the following resolution specifications under each operating condition:

TBT (up to 375 kHz, 1024 multi-bunch, 400 mA): $\leq 1 \text{ } \mu\text{m rms}$

TBT (up to 375 kHz, commissioning, single-bunch, 0.1 to 1 mA): $\leq 100 \text{ } \mu\text{m rms}$

FA (1 kHz): $\leq 100 \text{ nm rms}$

SA (up to 10 Hz): $\leq 20 \text{ nm rms}$

3. Long Term Stability: (Based on an environment of $\pm 0.5 \text{ } ^\circ\text{C}$)

Day Drift: $\leq \pm 0.2 \text{ } \mu\text{m}$

To meet these specifications, the electronics must incorporate a calibration function. When using TDP (Time Domain Processing) logic, a calibration function utilizing a crossbar switch and calibration tone is being considered. In contrast, when using FDP (Frequency Domain Processing), calibration will be performed via a pilot tone method.

4. Mechanical Specifications

I/O Ports:

- SFP/SFP+ Ports: 4 (for Event, FOFB Data, Machine Interlock, and Fast DAQ)
- RF Input Channels: 4 channels (A, B, C, D) per 4 BPMs
- RF Input Connector: SMA
- Trigger Channel: 1 LEMO port
- MC Clock: 1 LEMO port
- A/B Contact: 1 unit (for either A or B contact)
- TCP/IP Ports: 2 (for Control Network and Fast Network)
- Power: 1 port (220 V)
- Size: 19-inch sub-rack, 4 U or less (depth TBD)

5. Electrical Specifications

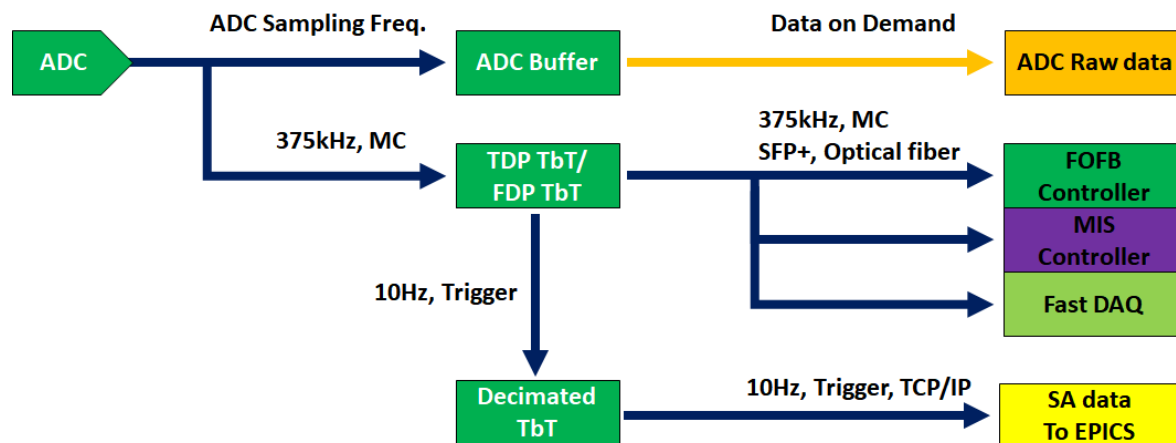
- RF Input VSWR: ≤ 1.2 (at 500 MHz, BW 20 MHz)
- RF Input Frequency: 500 MHz
- Max Input Power: ≤ 12 dBm
- RF Gain: ≥ 20 dB
- Gain Control / Step: ≥ 30 dB / 0.5 dB
- Dynamic Range: ≥ 50 dB

6. Software Specifications

- Control Toolkit: EPICS 7
- Embedded EVR Functionality: Included
- Network Booting: Supported
- Remote FPGA File Update: Supported

<Figure 2.1.12.31> illustrates the data flow of the 4GSR BPM system. Raw data, acquired in synchronization with the ADC sampling frequency, is stored in an ADC buffer and

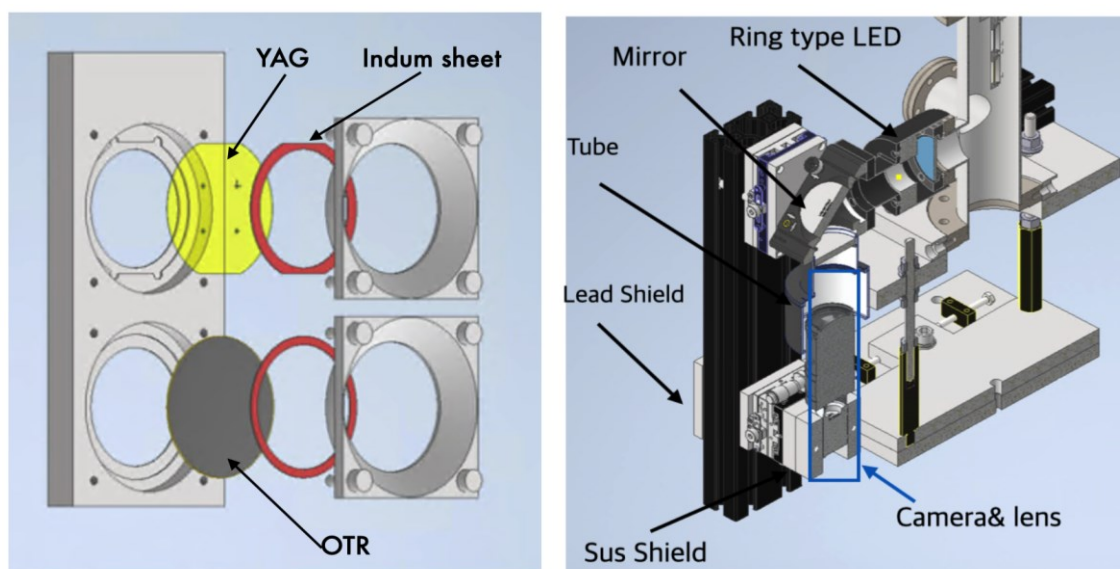
provided upon user request. This raw data is synchronized to either 375 kHz or the machine clock (MC) and is transmitted turn-by-turn (TbT) as beam position information to three application endpoints via the SFP+ ports. Finally, the TbT data is synchronized with a 10 Hz trigger and delivered as SA (Slow Acquisition) data to EPICS via the TCP/IP port. The TbT data is used for FOFB, while the SA data is used for global closed orbit calculations.



<Figure 2.1.12.31> 4GSR BPM Electronics Data Flow.

(3) Beam Profile Monitor

1) BPRM Hardware Configuration



<Figure 2.1.12.32> 3D Drawing of the BPRM Screen frame and the BPRM Chamber.

The Beam Profile Monitor (BPRM) is a device that measures the beam profile using a YAG fluorescent screen and an OTR screen.

<Figure 2.1.12.32> shows the 3D design of the BPRM. The frame has a 25 mm diameter fluorescent screen and an OTR screen installed vertically with a 35 mm space. Indium sheets are used to fix the screens to the frame and prevent damage from electrical shocks. The fluorescent screen features cross markers at 8 mm intervals for camera coordinate calibration. This frame is installed at a 45-degree angle to the beam direction and is inserted using a three-position actuator. The actuator operates pneumatically and has a positional accuracy of 0.1 mm during repeated operations. However, the positional accuracy along the Y-axis does not affect the profile measurement. Optical devices and cameras are installed at a 90-degree angle to the beam direction to measure the beam profile using the fluorescence/OTR light emitted from the screen selected by the actuator. To minimize radiation damage of camera, Camera is set diagonal position of the beam's vertical/horizontal plane using additional mirror. The camera and mirror are mounted on a stage that allows precise angle and position adjustments, which is crucial when measuring with OTR. An aluminum tube is used from the optical view port of the chamber to the camera to block external light. Additionally, an LED is installed in front of the view port to verify and adjust the position of the screen frame using the LED even after installation on the beam-line.

2) Optical devices

<Table 2.1.12.11> Specification table of camera and lens

Camera		Lens	
Shutter	Global	Focal length	75 mm
Pixels	1440×1080	Optical Mag	×0.15 to ×0.35
Pixel Size	3.45 μm	WD	<500 mm (300mm)
Sensor size	5 mm×3.7 mm	FoV @ 300 mm	25 mm×20 mm
FPS	>10 fps	DOF @ 300 mm	7.6 mm
Mount	C type	Lens size	Up to 50 mm
ADC	12 bits	Resolution	3.45 μm

In the 4GSR LINAC and transport line, the beam size is expected to be between 100 to 500 μm in most cases. For 5 μm target resolution, required screen area of a pixel is 20 μm × 20 μm . Consequently, we selected a camera and lens targeting at a working distance (WD) of 300 mm, as specified in <Table 2.1.12.11>.

Using the chosen camera and lens, images can be captured with pixel sizes of 15 μm in the Y-axis and 20 μm in the X-axis. The depth of field (DOF) of the lens is 7.6 mm which is enough depth of that the coordinate calibration using 8 mm spaced cross markers.

The fluorescent screen, specifically YAG, has a saturation limit. The measured saturation level of YAG is 13 fC/ μm^2 [1][2]. For 100 μm beam size, this corresponds to a saturation charge of 0.9 nC. To mitigate this issue, pulses with higher charge are measured using the OTR screen, which does not suffer from saturation at these levels.

<Table 2.1.12.12> The number of photoelectrons detected by the CMOS sensor when a 3 nC pulse is incident on the YAG screen

Beam Size	YAG
100 μm	6.609E+05
200 μm	1.656E+05
500 μm	2.652E+04
1000 μm	6.631E+03

The camera CMOS sensor can measure up to 10,000 photoelectrons per pixel. To prevent saturation, the light output from the fluorescent screen and OTR screen was investigated. The number of photoelectrons detected by the YAG screen can be expressed by the following formula:

$$N_{PE} = E_{dep} \times Y \times \pi r_L^2 / (4\pi r_d^2) \times M_{px} \times QE \times N_e, \quad (\text{Eq 3.1.12.4})$$

Where $\pi r_L^2 / (4\pi r_d^2)$ is solid angle to the lens, M_{px} is amplitude ratio of Center pixel, Y is light yield of YAG in [Photon/MeV], QE is Quantum efficiency of CMOS Sensor. E_{dep} is energy deposition in the YAG which is estimated using Geant4. The result of energy deposition by 5MeV to 4GeV energy range of single electron is 250 keV in the screen.

The saturation levels for different beam sizes with 3 nC of electrons incident on the screen are presented in <Table 2.1.12.12>. For a beam size of 100 μm , a 1/100 ND filter is required to prevent saturation. Therefore, after investigating the beam sizes at various BPRM positions, appropriate ND filters are selected.

OTR light is emitted at specific angles at the boundary surface. The formula of OTR light yield and emission angle are given:

$$N_{ph} = \frac{\alpha}{\pi} (2\ln\gamma - 1) \ln \frac{\nu_2}{\nu_1} \quad (\text{Eq 3.1.12.5}),$$

$$W(\omega, \theta) = \frac{e^2 \beta^2}{\pi^2 c} \frac{\sin^2 \theta}{(1 - \beta^2 \cos^2 \theta)^2} \quad (\text{Eq 3.1.12.6})$$

Here, β and γ are represent the relativistic speed and Lorentz factor, respectively, θ is the emission angle, and ν denotes the wavelength. The number of photoelectrons detected by the camera sensor can then be determined from these relationships.

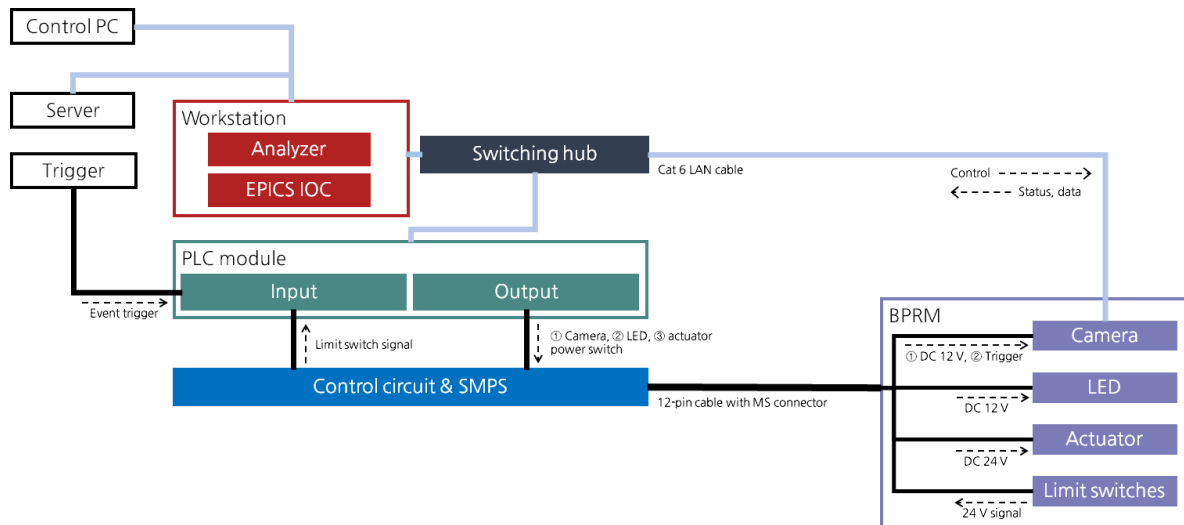
$$N_{PE} = N_{ph}(\gamma) \times A(\gamma) \times QE \times N_e \times M_{px} \quad (\text{Eq. 2.1.12.7})$$

<Table 2.1.12.13> The expected number of photoelectrons generated by OTR light for different beam energies.

Energy [MeV]	A	Nph/Ne
5 [MeV]	0.03%	3.441E+00
100 [MeV]	27.9%	2.087E+04
200 [MeV]	55.9%	4.814E+04
4,000 [MeV]	97.5%	1.316E+05

$N_{ph}(\gamma)$ represents the total number of emitted photons, and $A(\gamma)$ is the ratio of photons that reach the camera lens to the total emitted photons. For a screen-lens working distance of 300 mm and an emission wavelength of 500-600 nm, <Table 2.1.12.13> shows the maximum number of photoelectrons detected by the sensor and the lens arrival ratio for a beam size of 200 μm . Even when using OTR, an ND filter is necessary to measure the 4 GeV energy in the BTS. The light yield of OTR is approximately one-tenth that of YAG, so the fluorescent screen is used for low charge measurements, and the OTR screen is used for high charge measurements.

3) BPRM control device configuration



<Figure 2.1.12.33> BPRM System configuration.

The configuration of the BPRM system is illustrated in <Figure 2.1.12.33>, and its key features are described below:

- **Installation:** Seven BPRMs are installed in the LINAC, six in the LTB, and three in the BTS. All BPRMs are controlled from the LINAC control shed.

- **Camera Connections:** Coaxial cables with BNC connectors are used for the trigger signals, while LAN cables of Cat 6 or higher are used for image signal transmission and

camera control. To avoid interference with other diagnostic and control networks, the camera data, which can be large, is directly connected to a dedicated analysis workstation, forming an independent network.

- **BPRM Controller:** The controller manages the camera power supply and actuator control. A 12-core cable is used to connect the camera power and actuator. The camera captures and transmits images within a $100\ \mu\text{s}$ time window after receiving a trigger signal, or a wider time window if required. The data is then read and analyzed by the PC.

- **Environmental Stability:** The BPRM operates with DC voltage, and the camera signals are transmitted digitally. As a result, cable length does not affect control or data acquisition, and the system is not sensitive to temperature variations, eliminating the need for temperature- and humidity-controlled racks.

- **Analysis PC:** The analysis PC, equipped with EPICS IOC, controls the camera and exchanges analysis results via Ethernet.

(2) Beam Charge/Current Measurement

In the LINAC and beam transport lines, the total charge of pulses is measured using an ICT, while the beam current in the Booster Ring (BR) and Storage Ring (SR) is measured using a DCCT.

1) Measurement of Beam Charge in the LINAC and Beam Transport Lines

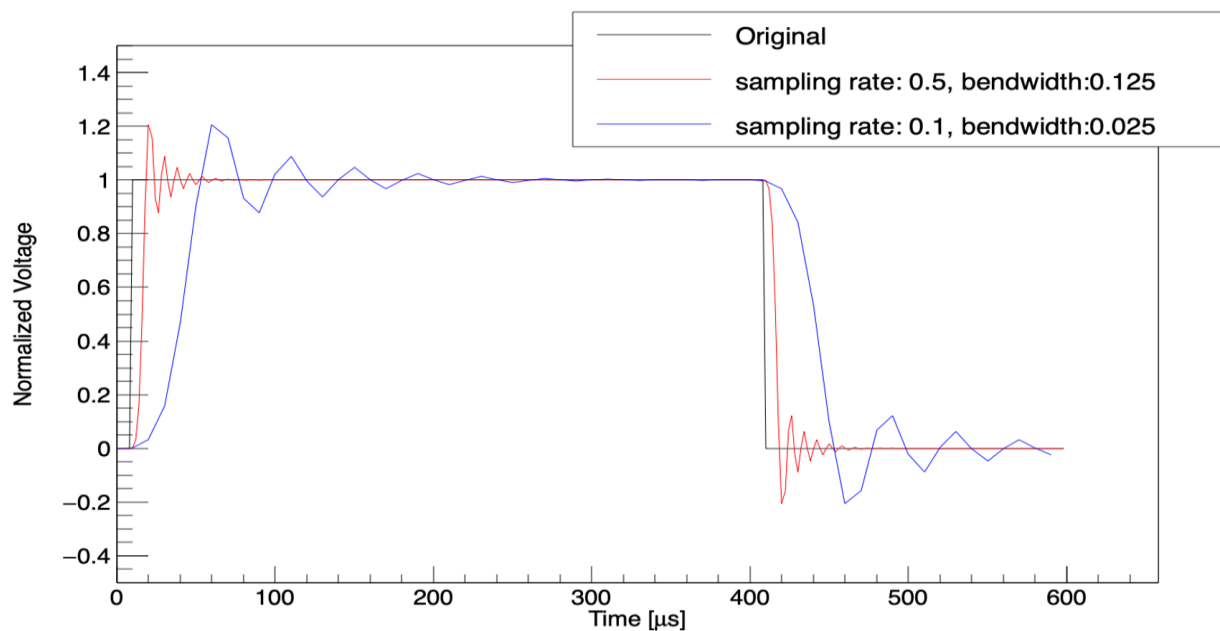
The 4GSR LINAC operates in both Multi Bunch (MB) mode and Single Bunch (SB) mode. Using an Integrated Current Transformer (ICT), the total charge of beam pulse in both modes. We use the commercial in-flange ICT from Bergoz and installed it at various points along the LINAC and transport lines to measure the total charge upon beam injection and extraction.

○ Integrate Current Transformer

<Table 2.1.12.14> Specifications of ICT and It's Digitizer

	Parameter	Value
Bergoz ICT	Range	0 to 40 nC
	Trigger Rate	0 to 60 Hz
	Resolution	0.2 pC (4 nC Range)
	Flange	2.75 Inch
	length	40 mm
	output	± 7 V
	Droop	20%/μs
Digitizer	Sampling Rate	>500kSPS
	Bandwidth	>125kHz
	Trigger Rate	>10 Hz
	Input	> ± 7 V

We select ICT-5.0-LD in-flange with its specifications detailed in <Table 2.1.12.14>. This model can measure up to 40 nC with a resolution of 2 pC. To minimize droop when measuring multi-bunches, we selected Low Droop (LD) option, resulting in a droop error of 0.1%.



<Figure 2.1.12.34> Simulation Study of ICT output readout with 125kHz and 25kHz bandwidth digitizer.

The Bergoz ICT readout module outputs ± 7 DCV for $400 \mu\text{s}$. According to the manual, the signal must be averaged over at least $200 \mu\text{s}$ for accurate measurement. The rise time of the ICT readout module's output signal is $7 \mu\text{s}$, with a maximum integration period of $50 \mu\text{s}$. Therefore, the output voltage will be measured in the $150 \mu\text{s}$ to $350 \mu\text{s}$ range following the trigger signal. The simulation results for determining the required specifications of the digitizer ADC are shown in <Figure 2.1.12.34>. The black line represents the actual signal considering the rise/fall time, and the colored lines represent waveforms from two types of ADC specifications. Using a 16-bit ADC with a sampling rate of 500 kSPS and a bandwidth of 125 kHz, the signal stabilizes after $100 \mu\text{s}$, and averaging 1,000 bins of voltage measurements results in negligible digitizer error.

A total of 5 ICTs are installed: 2 in the LINAC, 1 in the LTB, and 2 in the BTS. To control these and process the data, a total of 3 control units are installed, one in each region. Each control unit can manage up to 4 ICTs.

2) DC Current Transformer

The DCCT is a device used to measure the beam current installed in each ring to measure the circulating beam current. Commercial In-Flange NPCTs from Bergoz with custom designed beam pipe cross-section.

<Table 2.1.12.15> Requirements of DCCT & Digitizer

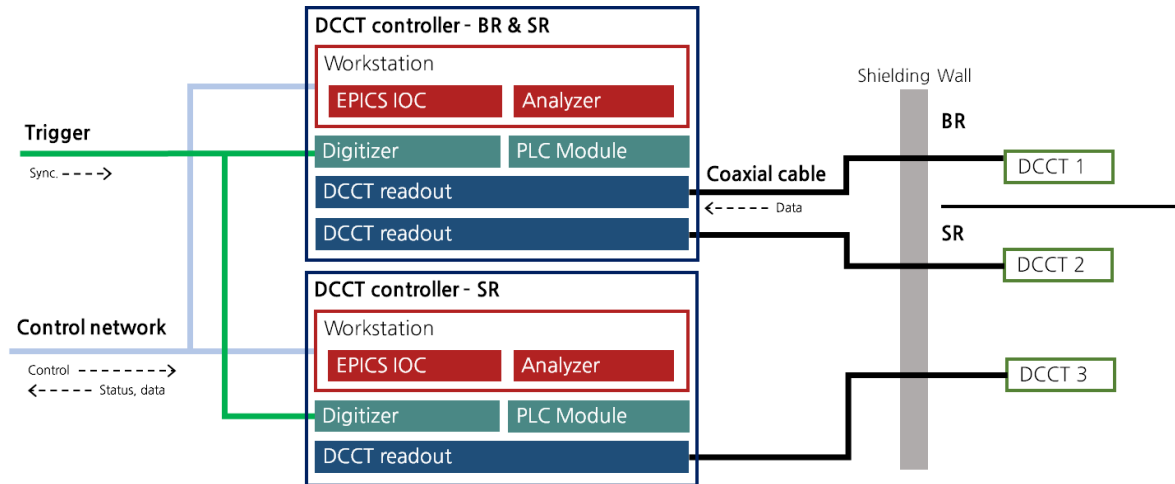
	Parameter	Value
DCCT Bergoz NPCT	Range	$\leq 40 \text{ A}$
	Resolution	$0.5 \mu\text{A}$
	Baking	$< 100 \text{ }^\circ\text{C}$
	Output	$\pm 10 \text{ V}$
Digitizer	Sampling Rate	$> 100\text{kSPS}$
	Bandwidth	DC
	Trigger Rate	10 Hz
	Input Range	$> \pm 10 \text{ V}$

The Bergoz NPCT outputs a high impedance ± 10 DCV signal, so the performance of the digitizer is not significantly affected. Therefore, the same specification digitizer as used for the ICT signal analysis module is employed. DCCT specification and digitizer requirements are shown in <Table 2.1.12.15>.

The DCCT is damaged at temperatures exceeding 100°C . According to Bergoz's report,

the device recorded 58°C after operating for over an hour without a cooling system at 500 mA, indicating no issues. This was confirmed to be suitable for the 4GSR conditions as well. However, to avoid damage from high temperatures during vacuum baking, the DCCT is installed away from the vacuum baking section.

3) Configuration of ICT/DCCT



<Figure 2.1.12.35> DCCT connection configuration of the entire storage ring.

The configuration of ICT and DCCT connections is illustrated in <Figure 2.1.12.35>. The detailed configurations are outlined below.

- ICT: One ICT is installed in the LINAC, one in the LTB, and two in the BTS. The cable connecting the ICT to the Readout Module through the tunnel uses a 50 m coaxial cable provided by the manufacturer.
- DCCT: One DCCT is installed in the BR and two in the SR. Similarly, the cable connecting the DCCT to the Readout Module through the tunnel uses a dedicated cable provided by the manufacturer.
- Configuration: The ICT and DCCT connection setup consists of a workstation, a control module, and a CT.
- Workstation: This performs control and analysis tasks, with an EPICS IOC installed to enable remote control and data acquisition via Ethernet.
- Control Module and Readout Module: These are connected using a DB9 cable, utilizing 8-bit TTL signals to control the measurement range and calibration intensity. And the same digitizer/control module is used for both ICT and DCCT.

- **Environmental Stability:** The sensors and readout modules of the ICT and DCCT are minimally affected by temperature-induced signal changes.

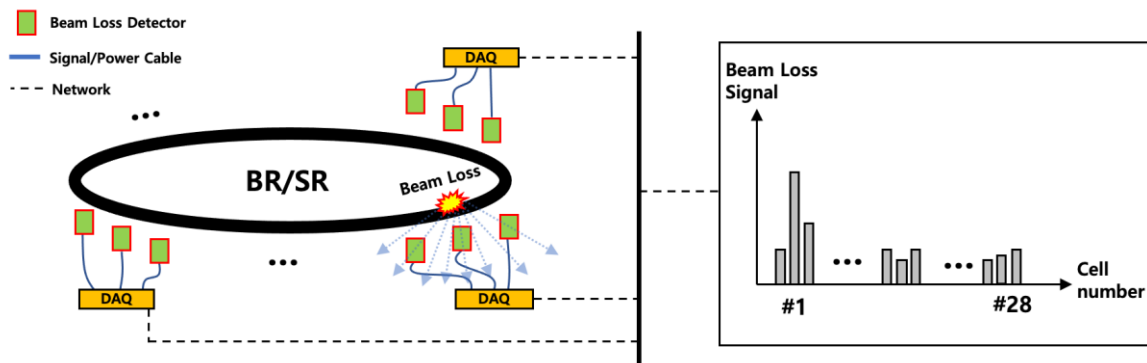
(4) Beam Loss Monitor

<Table 2.1.12.16> Comparison between fast and slow beam loss monitor

	Fast Beam Loss Monitor	Slow Beam Loss Monitor
Devices	Scintillator + photomultiplier	Scintillator + CMOS Camera
position	Storage Ring, Booster Ring	LINAC, LTB, BTS, BR, SR
Sampling	≥ 375 kSPS	100 to 500 SPS
Channels	4	24
Target	Turn by Turn Beam loss, Priority: timing	Main for LINAC, LTB, BTS Sub for SR, BR Priority: Position

In the 4GSR ring, primarily fast beam loss monitors will be used, supplemented by slow beam loss monitors. The low repetition rate of the LINAC and beam transport lines will rely on slow loss monitors to measure beam loss. The functions and requirements for beam loss monitors in the 4GSR ring are summarized in <Table 2.1.12.16>.

1) Fast Beam Loss Monitor



<Figure 2.1.12.36> Configuration and principle of beam loss measurement by F-BLM.

<Table 2.1.12.17> Specifications of F-BLM

Scintillator		PMT		Digitizer	
Rising Time	<1ns	Rising time	<1ns	bandwidth	50MHz
Light Yield	10,000/MeV	Gain	>10 ³	Sapling Rate	125MSPS
Pulse Width	<10 ns	response wavelength	visible	Trigger Rate	5MHz
Peak Wavelength	visible			V resolution	12 bits

The Fast beam loss monitor (F-BLM) is a detector with rapid response and data acquisition speed, capable of accurately timing beam loss at the turn-by-turn (TbT) level in the Booster Ring and Storage Ring. <Figure 2.1.12.36> shows the configuration and principle of the F-BLM, and <Table 2.1.12.17> lists the specifications commercial product. The F-BLM detector consists of a scintillator and PMT, with a data acquisition device having a sampling rate of 125 MSPS and a maximum trigger rate of 5 MHz, which is sufficient to measure the turn-by-turn revolution rate of 375 kHz.

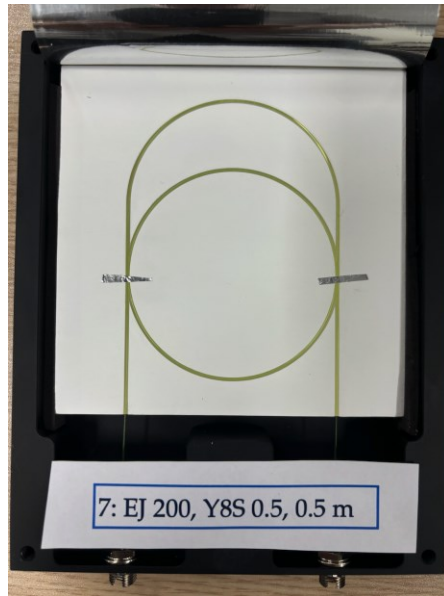
2) Slow Beam Loss Monitor

The slow beam loss monitor (S-BLM) in the 4GSR is primarily used in the LINAC and beam transport lines and serves to locate beam loss in the ring.

The 4GSR S-BLM is developed with reference to monitors from other institute, using optical fibers and a camera. <Figure 2.1.12.37> illustrates the configuration and operation principle of the current prototype S-BLM. The S-BLM comprises a scintillator, beam transport optical fibers, and a CMOS camera, with the performance of the components used in the prototype summarized in <Table 2.1.12.18>.

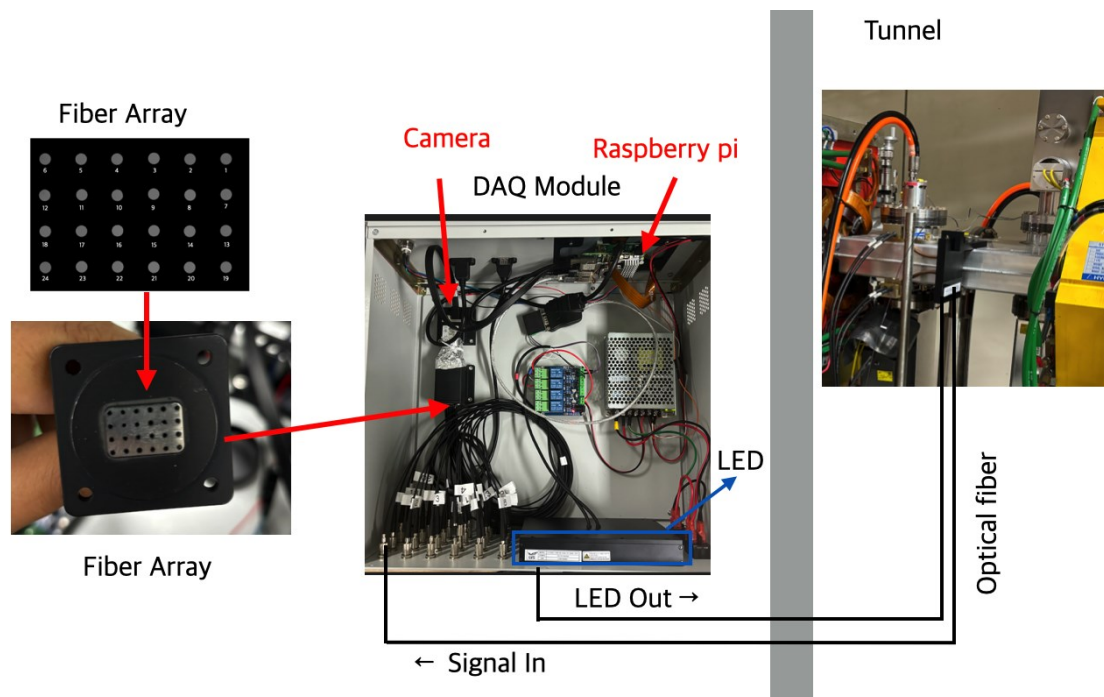
<Table 2.1.12.18> Specifications of Camera and Scintillation plate for S-BLM Prototype

Camera		Scintillation Plate	
Interface	USB 3.0	size [mm]	100×100×10
Sensor	CMOS, 1/2.9"	bandwidth [nm]	400 to 500
Resolution	720×540	Peak wavelength [nm]	425
FrameRate	525 fps	rise time [ns]	0.9
Bit Depth	12 bits	decay time [ns]	2.1
Conformity	GenICam, SBVision	Yield [# /keV]	≤10,000



<Figure 2.1.12.37> S-BLM Detector consists of scintillator with blue light coating, wavelength shift fiber and two FC connector ports.

<Figure 2.1.12.37> shows a detector composed of a scintillator and a wavelength-shifting optical fiber, which absorbs blue light and emits green light. The entire assembly is enclosed in an aluminum box with two input/output ports. One port connects to the DAQ camera, and the other to a calibration LED.



<Figure 2.1.12.38> BLM DAQ System.

<Figure 2.1.12.38> shows the structure of the data acquisition and analysis module of the prototype S-BLM. The prototype DAQ module includes 24 optical input ports, 24 optical output ports, a camera for signal measurement, an LED for calibration, and a single-board computer for camera control and signal analysis. The optical fiber bundle from the 25 input ports is arranged in a 4x6 grid in front of the camera lens, allowing for the measurement of light emission from the optical ports to determine the loss location, as shown in the example on the left top of <Figure 2.1.12.39>. Calibration LEDs are installed at the output optical ports, enabling loss measurement and calibration by measuring the light intensity exiting from the output port. The camera operates at a maximum frequency of 500 Hz, which is sufficiently fast for the LINAC and beam transport lines. While it is slower for the ring, it is significantly more cost-effective than high-speed beam loss monitors, allowing for extensive installation to locate losses.

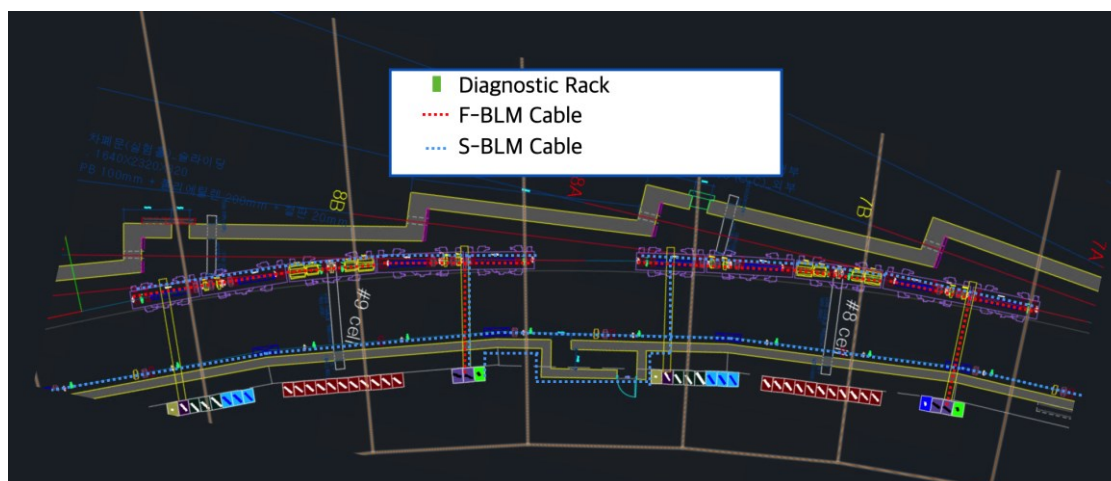


<Figure 2.1.12.39> (Left) The result of Testing at PLS II, (Right) setting up S-BLM on the PLS II beam pipe.

<Figure 2.1.12.39> presents the test results at PAL-PLS II, demonstrating the measurement of losses during electron beam injection into the accelerator. Black is reference beam loss detector positioned at injection section, and red is installed at behind of second BM of Cell #3. The results show that slow BLM detect beam loss by beam injection and low energy particles.

In the LINAC, LTB, and BTS, a single DAQ module will be used for each, with 4-6 detectors installed in each section. In the BR, 60 detectors will be installed behind the bending magnets. And eight detectors per superperiod will be installed in SR.

3) Beam Loss monitor Line Configuration



<Figure 2.1.12.40> BLM optical fiber cable connection.

<Figure 2.1.12.40> illustrates the BLM cable connection configuration, with the features described below:

In the SR, each cell will have one 4-channel DAQ module for F-BLM and one 25-channel DAQ module for S-BLM for every two cells. Thus, each SR cell will have four F-BLM detectors and ten S-BLM detectors.

For F-BLM in the SR, a 40 m cable provided by the supplier will be used, considering the tray height. For S-BLM, a 60 m optical cable will be used as there are no cable trays above the straight sections of the storage ring, requiring connections outside the tunnel.

In the Booster Ring, F-BLMs will be installed at critical injection and extraction sections, with 60 S-BLM detectors installed at each bending magnet using four modules and 120 m optical cables. The prototype S-BLM has successfully tested with a 120-meter cable, and the F-BLM specifications support up to 100 meters, ensuring reliable beam loss measurements.

C. Orbit Feedback System

(1) Slow & Fast Orbit Feedback system

In a storage ring, several factors can contribute to beam orbit distortions. The specific sources of these distortions may vary based on the design and operating environment of the storage ring. However, the main vibration sources that typically cause beam orbit distortions include magnetic vibrations, mechanical vibrations, temperature fluctuations, and various external influences.

Magnetic vibrations occur when electromagnets-such as standard magnets and pulsed magnets-generate vibrations as current passes through them. These magnetic-induced disturbances can directly affect the beam's trajectory. In addition, mechanical vibrations arise from the storage ring's structural components, including magnets, girders, and other support equipment. These components are susceptible to external influences such as environmental vibrations, changes in the insertion device (ID) gap, and vibrations originating from the low-conductivity water (LCW) system. Such mechanical disturbances represent one of the primary causes of beam orbit distortions.

Temperature fluctuations within the storage ring can induce gradual thermal expansion or contraction of various components, thereby affecting the beam orbit over time. Moreover, external factors-such as nearby road traffic, vibrations from surrounding building structures, and even natural disasters-can impose irregular vibrational forces on the storage ring, further exacerbating orbit distortions.

To mitigate these effects and achieve the desired beam orbit stability, vibration reduction systems and correction techniques must be incorporated into both the design and operation of the storage ring. In the 4GSR storage ring, this challenge is addressed by employing two distinct feedback systems that operate in parallel to suppress vibration effects across various frequency ranges.

The orbit correction system in the 4GSR storage ring is designed on a cell-by-cell basis, with each cell equipped with 10 beam position monitors (BPMs) and 10 correctors. A subset of these devices-specifically, 8 fast BPMs and 4 fast correctors per cell-is dedicated to capturing turn-by-turn (TbT) beam position data. This data is used to generate new orbit correction setpoints at a high rate of 15.6 kHz. The fast correctors then utilize these setpoint values to perform rapid orbit corrections.

Simultaneously, the remaining slow BPMs and slow correctors work in tandem with the fast system, operating at a slower rate of 2 Hz, to determine the closed orbit for the entire storage ring. This dual feedback approach ensures that the overall beam orbit is maintained within the required stability parameters.

The 4GSR feedback system initiates with the slow orbit feedback (SOFB) process. The entire storage ring, comprising 288 fast BPMs, 288 slow BPMs, and an equivalent number of fast and slow correctors, is used to calculate and correct the closed orbit at 2 Hz. The corrected closed orbit obtained through this process serves as the new reference orbit (Ref. Orbit).

Subsequently, the fast orbit feedback (FOFB) system takes over. This system utilizes fast BPMs and fast correctors to measure deviations from the reference orbit on a per-cell basis and corrects these deviations at a rate of 10 kHz. Although there is no centralized master feedback controller for the entire storage ring, the FOFB controllers in each cell exchange information with adjacent cells on every turn. This distributed control mechanism allows each cell to compute the required kick angle for rapid beam orbit correction based on the cumulative orbit variation information across the storage ring.

<Table 2.1.12.19> of the original design report details the target parameters achieved by the 4GSR feedback system, underscoring the performance goals and the rigorous control strategy implemented to maintain beam orbit stability.

<Table 2.1.12.19> Specification goal of 4GSR Beam stability

Type	Data	Spec.	Conditions
Position Resolution [RMS]	Turn by Turn (375 kHz)	1 um rms	400 mA, 1,024 bunch
	SA (10 Hz)	20 nm rms	
	Turn by Turn (375 kHz)	100 um rms	0.1 to 1 mA (Commissioning)
	SA (10 Hz)	1 um rms	
Beam Current Dependence	-	Up to 1 um	0.1 to 400 mA
Absolute accuracy	-	<500 um	Before BBA
		<5 um	After BBA
Long-term Stability	-	±0.2 um	Daydrift
		1 um rms	Weekdrift

○ Diagnostic Hutch

The diagnostic beamlines for the multi-purpose synchrotron accelerator are primarily installed in Cell-15, immediately following the long straight section. All facilities are located above the tunnel and are designated as VDH-S15, VDH-S15B, and VDH-B16. "VDH" stands for Visible Light Diagnostic Hutch; "S" indicates the storage ring, "B" indicates the booster ring, and the number corresponds to the section number. If there is no final letter in the name, the light source is a Longitudinal Gradient Bending Magnet (LGBM). When the name ends with "B," the center bend is used as the light source.

<Table 2.1.12.20> Diagnostic Hutch Summary

Hutch Name	Measured parameters	Location
VDH-S15	Beam size, Emittance	SR, Cell 15, LGBM1
VDH-S15B	Bunch length, Bunch phase, Fill pattern	SR, Cell 15, CB
VDH-B16	Beam size, Mechanical vibration	BR, Cell 16, CB
XDH-S15B	2-Dim profile, Emittance, Energy spread	SR, Cell 15, CB

The primary function of the diagnostic beamline is to measure the transverse beam size and the longitudinal position & size (i.e., signal timing and temporal width) using

synchrotron radiation. For transverse beam size measurements, one approach involves measuring at locations where the electron beam's beta function and dispersion function are identical, allowing cross-checks of the same physical quantity. Additionally, by measuring the transverse beam size at different locations, one can separate chromatic effects to determine both vertical and horizontal emittances. The measurement method employs a visible-light interferometer operating near a wavelength of 450 nm.

In recently constructed similar facilities (DLSRs), issues have been reported where the long distance to the source reduces the beam size resolution below the target, or where the limited space within the photon beam transport vacuum chamber causes stray reflections inside the opening angle. Under these conditions, using a visible-light interferometer becomes difficult, leading some facilities to switch to an X-ray source. To prepare for such scenarios, the XDH-S15B beamline (an X-ray beam diagnostic hutch at the storage ring's Section 15 center bend) has been established as a contingency diagnostic beamline.



<Figure 2.1.12.41> Detailed Locations of Diagnostic Beamlines:
 Three VDH & XDH(Reserved).

The longitudinal beam information is monitored using a streak camera and an avalanching photodiode to track bunch length, longitudinal beam instability, bunch filling pattern, and bunch purity. In addition, a fast photodiode paired with a wide-band digitizer provides online data on the bunch length and phase.

○ VDH-S15 Beamline Design

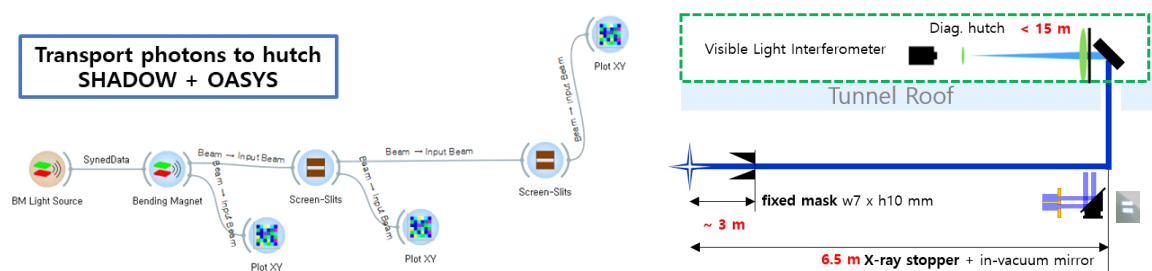
VDH-S15 is positioned along the extension of the cell's straight section because it utilizes the 0.7 T region of the initial gradient section in the downstream LGBM of the long straight section. An in-vacuum mirror is installed in the tunnel's vacuum chamber as close as possible to the light source, allowing the beam to be extracted vertically through a 6-inch quartz window. This in-vacuum mirror is engineered with structures to minimize heat intrusion from X-rays, to facilitate cooling, and to adjust its vertical position based on the detected X-

ray position. The light source information for VDH-S15 is provided in <Table 2.1.12.21>.

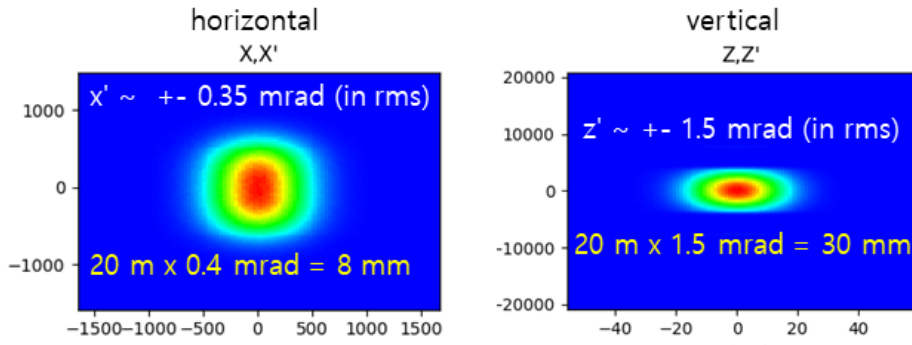
<Table 2.1.12.21> VDH-S15 Light Source Specifications

Parameters	Horizontal	Vertical
Beta function (β) [m]	1.54	17.72
Dispersion (η) [m]	2.62e-4	0
E. Spread (δ) [%]	0.13	
Emittance (ϵ_{rms}) [μm]	59.0	5.90
B Field Strength [T]	0.734	
Beam Size (σ) [μm]	9.53	10.2

Using the determined lattice, the beam profile at S15 was analyzed using the SHADOW and OASYS programs. The process involved defining the LGBM light source and the photon mask, transporting the beam, omitting the in-vacuum mirror, and carrying the beam to the optical table, while tracking the relationships between the photon energy, position, and angle during the calculation. Based on the divergence information of the desired visible point light source, when the source size is converted on the optical device at the diagnostic table, it comes out to be approximately 8 mm (rms) horizontally and 30 mm (rms) vertically, confirming that there is no issue in utilizing interferometers, etc.



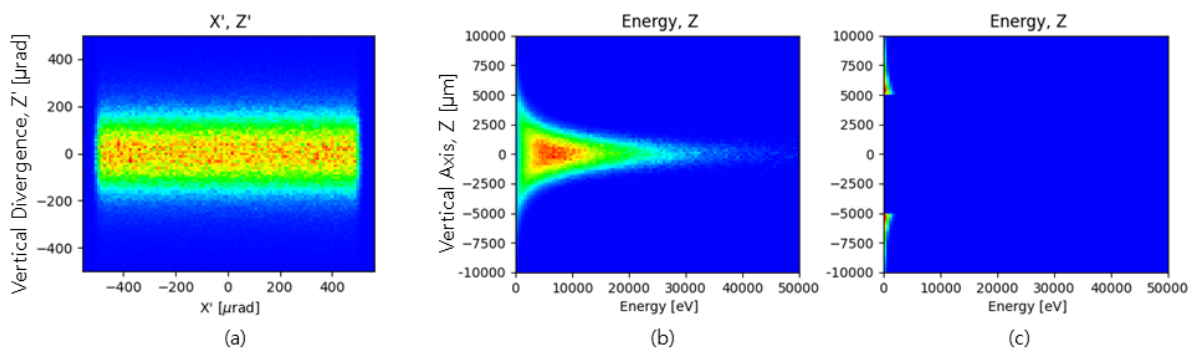
<Figure 2.1.12.42> Simulation Model (Left) and Schematic Diagram of the VDH-S15 (Right).



<Figure 2.1.12.43> Phase Distribution of the 2 to 4 keV Visible Point Source.

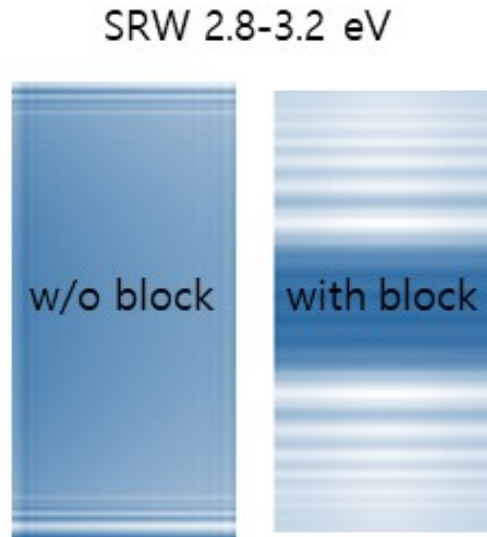
For visible light reflection, the in-vacuum mirror requires a shielding function to prevent heat load and mechanical deformation caused by X-rays. To achieve this, the energy and angular distributions of the photons from the light source must be reviewed so that an appropriate X-ray blocker or X-ray transparent component can be placed at the correct location. The horizontal and vertical angular distributions of the dominant heat source-X-ray photons with energies above 50 keV-are as shown below: horizontally, the distribution is broad, while vertically it follows a Gaussian distribution.

The X-ray region that is irrelevant for visible beam diagnostics has an angular distribution of $\pm 115 \mu\text{rad}$ (rms), which corresponds to a distribution of about $\pm 0.8 \text{ mm}$ on the transverse plane at a point 7 to 8 m away, where the in-vacuum mirror is expected to be installed. When this distribution is converted into the size at 7 m after the X-ray blocker, it is approximately 0.8 mm. For more than 96% shielding efficiency, using 3-sigma (i.e., multiplying by 6 to cover the full size), the required width is 4.8 mm.



<Figure 2.1.12.44>

- (a) Horizontal and vertical angular distributions of the heat-source X-rays above 50 keV,
- (b) Energy-vertical spatial distribution of the heat-source X-rays before shielding,
- (c) Energy-vertical spatial distribution of the heat-source X-rays after shielding.



<Figure 2.1.12.45> Visible Light Distribution on the Final Optical Table.

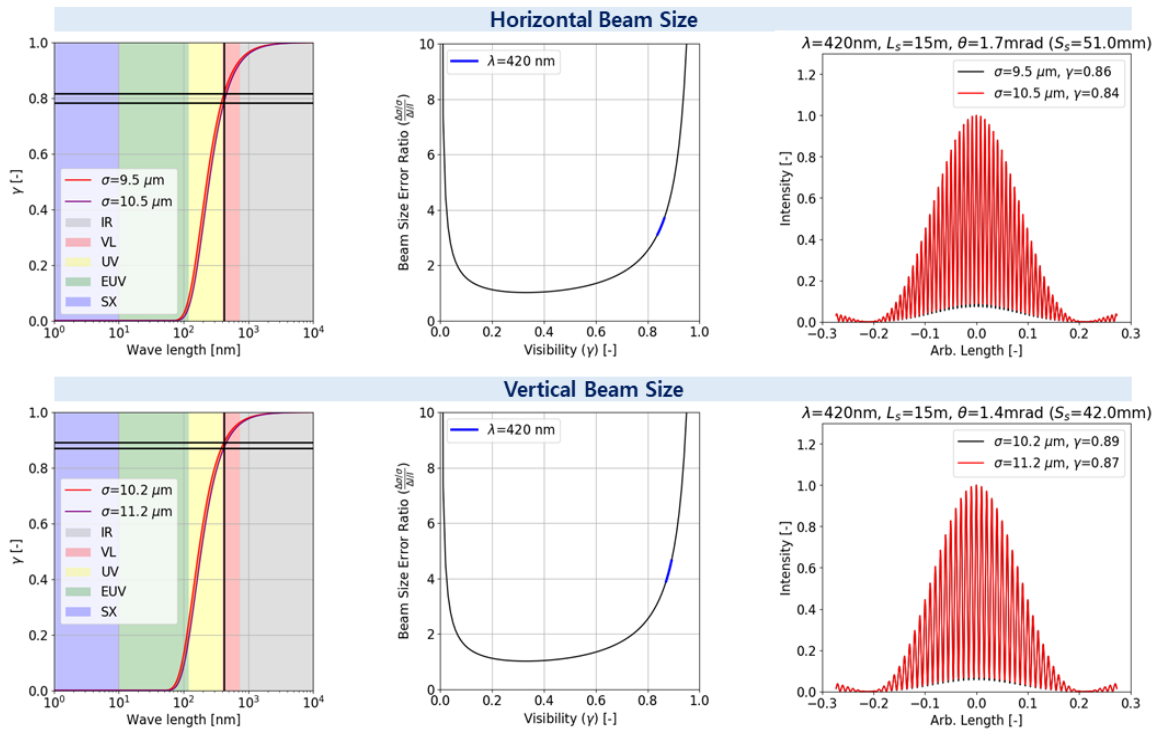
○ VDH-S15B Beamline Design

As with the calculations for VDH-S15, the light source characteristics are as described below, and X-ray shielding was implemented using the same method. However, since the designed lattice results in a beam size of approximately $4\text{-}5\text{ }\mu\text{m}$ at the Center Bend-and considering a systematic error estimate of $1\text{ }\mu\text{m}$ -the beam size measurement becomes insignificant.

<Table 2.1.12.22> VDH-S15B Light Source Specifications

Parameters	Horizontal	Vertical
Beta function (β) [m]	0.366	3.435
Dispersion (η) [m]	$6.54\text{e-}4$	0
E. Spread (δ) [%]	0.13	
Emittance (ϵ_{rms}) [pm]	59.0	5.90
B Field Strength [T]	1.994 (0.186 m)	
Beam Size (σ) [μm]	4.7	4.5

However, it is the bending light source with the highest photon flux due to its high magnetic field strength of around 2 T. Therefore, real-time measurements of bunch length, bunch filling pattern, and bunch purity are performed using a streak camera and photodiode, which benefit from the high photon flux.



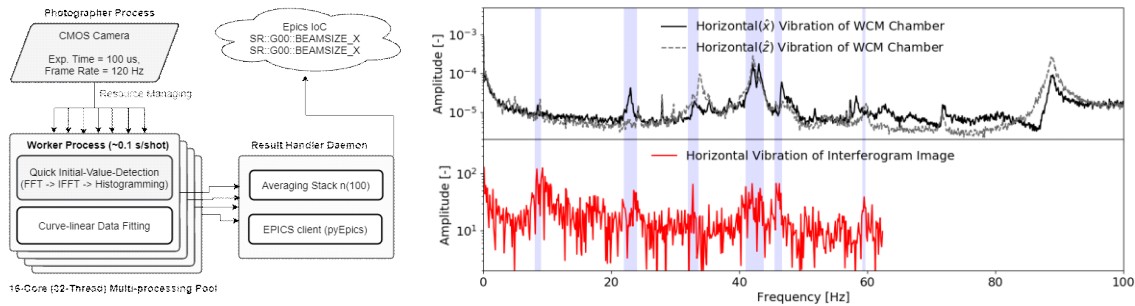
<Figure 2.1.12.46> Designed Interferometer's Vertical (Top) and Horizontal (Bottom) Interference Pattern (γ), Intensity Sensitivity $\frac{\Delta\sigma/\sigma_0}{\Delta I/I_0}$, and Image Simulation Results.

○ Interferometer: Beam Size & Emittance Measurement

The visible light interferometer is installed at VDH-S15 in the storage ring and at VDH-B1 in the booster. The design parameters assume a 420 nm wavelength, a 1.2 m focal length, a 15 m distance from the light source, and a slit width of approximately 4 to 5 cm. Under these conditions, the interference fringe (γ) is formed at about 0.8 horizontally and about 0.9 vertically. The intensity sensitivity is around level 4 for all cases. This means that, if the image brightness is resolvable to roughly 400 levels, the beam size resolution would be approximately $0.1 \mu\text{m}$, which indicates a sufficiently effective design. However, when considering factors such as the white noise from CMOS sensors and optical wavefront errors from lenses or mirrors, a conservative estimate suggests that the resolution may degrade by over ten times (resulting in a systematic error of about $1 \mu\text{m}$ or more). Therefore, careful attention must be paid to noise reduction and signal processing.

○ Mechanical Vibration Measurement

When sufficient photon flux is available, beam vibrations below 100 Hz can be measured solely by the interferometer. By employing short exposure times and multi-core data processing, it is possible to capture interferogram images at rates exceeding 200 frames per second—a capability already demonstrated in the PLS-II diagnostic beamline. This system is scheduled for installation at VDH-S15 and VDH-B1, with the processing logic and measurement data illustrated in the figure below. Additionally, if a line scan camera (operating at 2000 to 4000 frames per second) is used, kHz-level beam vibrations can be measured given adequate photon flux. Due to its low cost, this setup is planned for implementation.



<Figure 2.1.12.47> Parallel Processing Logic for Interferometer Vibration Measurement (Left), and Comparison of Actual Table Vibration with Interferometer Beam Vibration Measurements (Right).

○ Emittance & Momentum Spread

The beam size is given by the following relationship. After LOCO is conducted during the maintenance period and commissioning, the beta function (β) and chromatic dispersion (D) become fixed constants.

$$\langle x \rangle = \sqrt{\beta_0 \varepsilon + D_0 \Delta p/p} \quad (\text{Eq. 2.1.12.8})$$

By measuring the beam size at two different locations using the visible light interferometer and solving the two equations simultaneously, both the emittance and momentum spread can be determined. Although this method is feasible when using XDH-S15B, there is a possibility of reduced precision because the beam size is close to the resolution limit of the measurement devices.

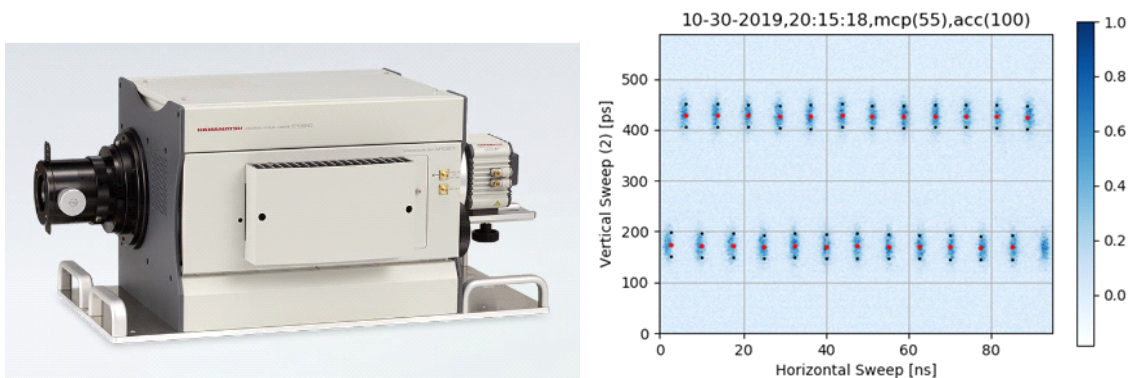
XDH-S15B is an X-ray pinhole camera diagnostic beamline. It is a system in which the

image formed on a scintillation plate-after passing through a monochromator, central X-ray block, and zone plate-is observed via a mirror. In the conventional pinhole method, the hole is thick and narrow for X-ray shielding, which leads to unavoidable diffraction patterns.

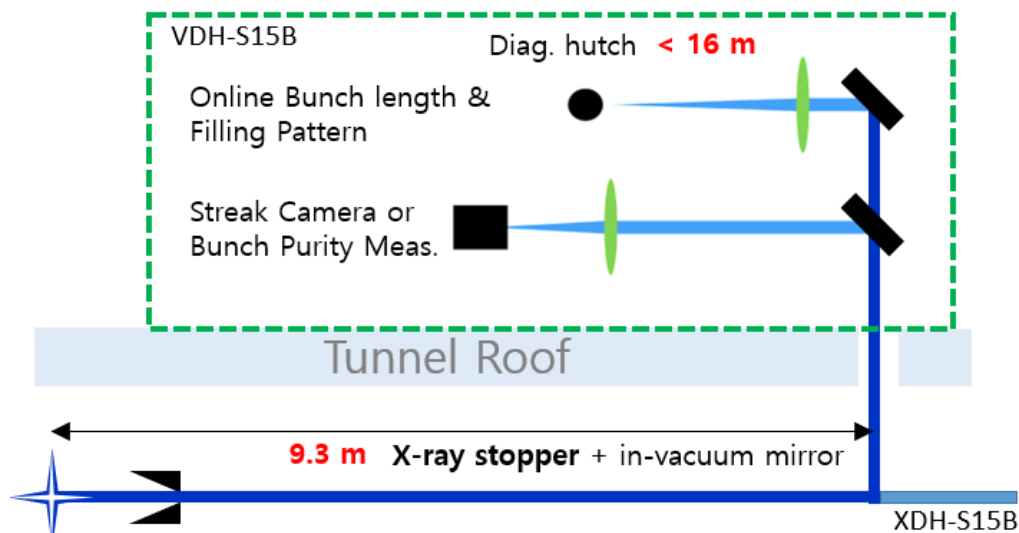
○ Emittance & Momentum Spread

The VDH-S15B visible light diagnostic beamline is configured above the tunnel, as shown in the figure. Using a vacuum mirror with an aperture, the visible light is extracted up to the tunnel, while the central X-rays are transported to the downstream XDH-S15B. The VDH-S15B visible light diagnostic beamline employs a streak camera to observe various multi-bunch instabilities. In most cases, it monitors longitudinal instabilities, though transverse information can also be observed when needed.

To accurately observe the temporal characteristics of the electron or photon beam, a Hamamatsu streak camera is used for diagnostics. With an expected unit bunch length in the storage ring of approximately 20 ps, the system is configured with either a single or dual synchroscan to achieve a resolution of about 2 ps. This device is installed and utilized in the visible light diagnostic beamline.

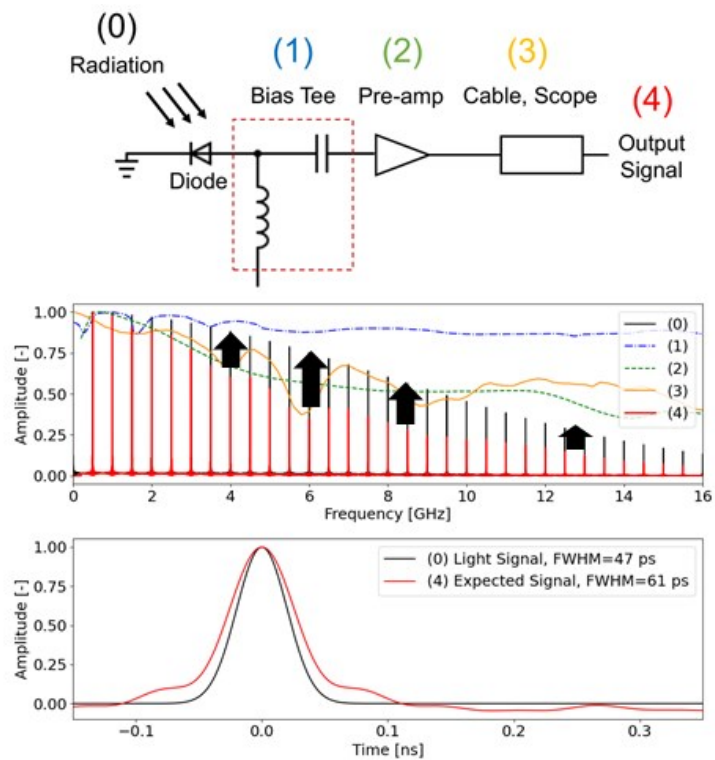


<Figure 2.1.12.48> Streak Camera (Left), and the Analyzed Image of the PLS-II Bunch Captured by the Streak Camera (Right).



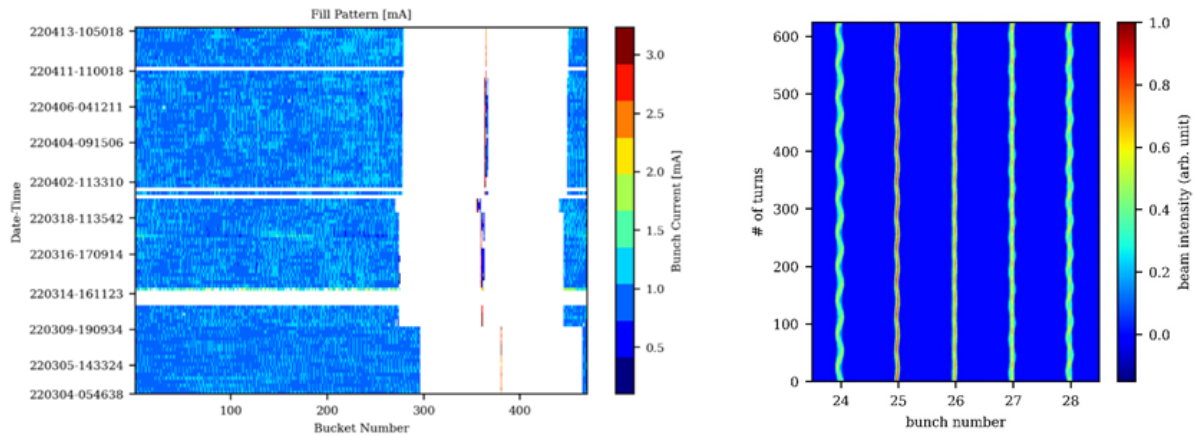
<Figure 2.1.12.49> VDH-S15B Diagnostic Beamline Configuration.

The bunch length monitor, based on an MSM photodiode (metal-silicon-metal Schottky diode), diagnoses and provides real-time bunch length and per-bunch phase information. It analyzes the time-resolved signal from the photodiode, which is excited by synchrotron radiation, using a high-performance broadband digitizer with 100 GS/s sampling rate and 15 GHz analog bandwidth.



<Figure 2.1.12.50> Photodiode Connection (Left), and Operating Principle (Right).

This system is implemented in PLS-II, and in addition to the bunch length, it can also measure in real time the filling pattern information as well as the coupled mode instability.



<Figure 2.1.12.51> Online Filling Pattern Measurement Using the Photodiode System (Left), and Beam Instability Monitoring (Right).

D. TFS, LFS: Multi-bunch Feedback System

In order to obtain an extremely bright photon beam in a fourth-generation synchrotron radiation accelerator, it is essential to store the highest possible beam current in the storage ring. To achieve a higher beam current, it is important to either increase the bunch charge or stably store a larger number of electron bunches within the ring. Generally, the beam bunches in the storage ring undergo transverse (betatron) and longitudinal (synchrotron) oscillations, which naturally damp over time. However, as numerous bunches circulate in the ring, interactions with devices such as RF cavities, vacuum chambers, and BPMs generate wakefields that, in turn, act back on the beam. This feedback can lead to a nonlinear effect known as coupled bunch mode instability (CBMI). When the wakefields amplify the oscillations in both the transverse and longitudinal directions beyond the level of natural damping, the bunches become unstable. Moreover, since the intensity of the electromagnetic fields produced by the bunches is proportional to the bunch charge, these instabilities generally increase with the beam current. As a result, as the beam current increases, the instabilities become more pronounced and may induce beam loss, thereby limiting the maximum storable current in the ring. Therefore, to suppress beam instabilities and increase the maximum stored beam current, a multi-bunch feedback system capable of damping instabilities in both the transverse and longitudinal planes is required.

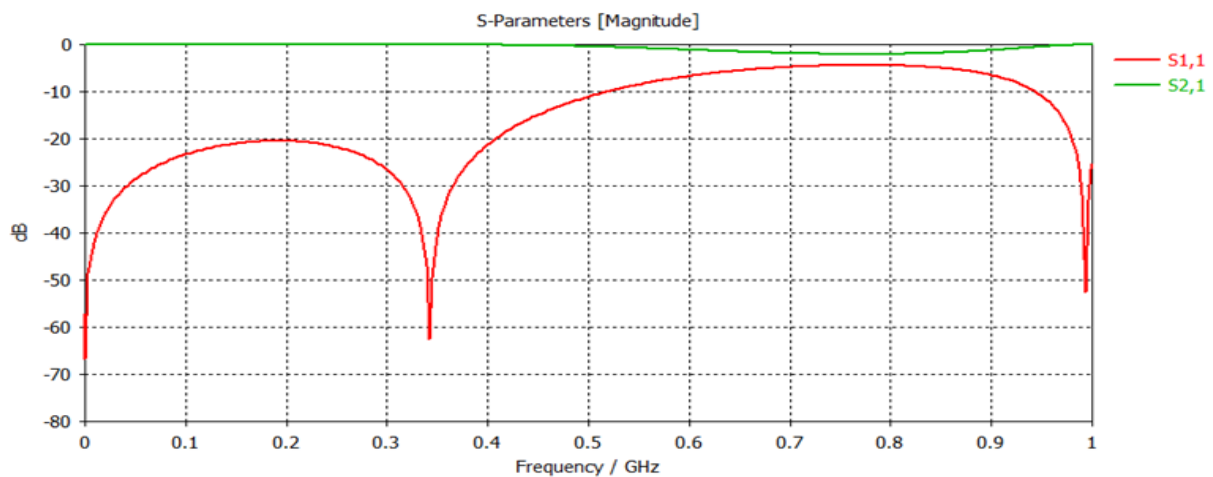
(1) Hardware

The operating frequency range of the TFS is approximately from $f_{RF} / 0.5$ h to $f_{RF} / 2$. The kicker used for transverse multi-bunch feedback is a stripline device that operates in the TEM mode. For independent operation in both the horizontal and vertical directions, identical TFS kickers are installed with a 90° rotation relative to each other. The high-frequency power output from the wide-band RF amplifier is applied to the downstream ends of the striplines via a 180° splitter, while the upstream end is terminated with a $50\ \Omega$ dummy load.

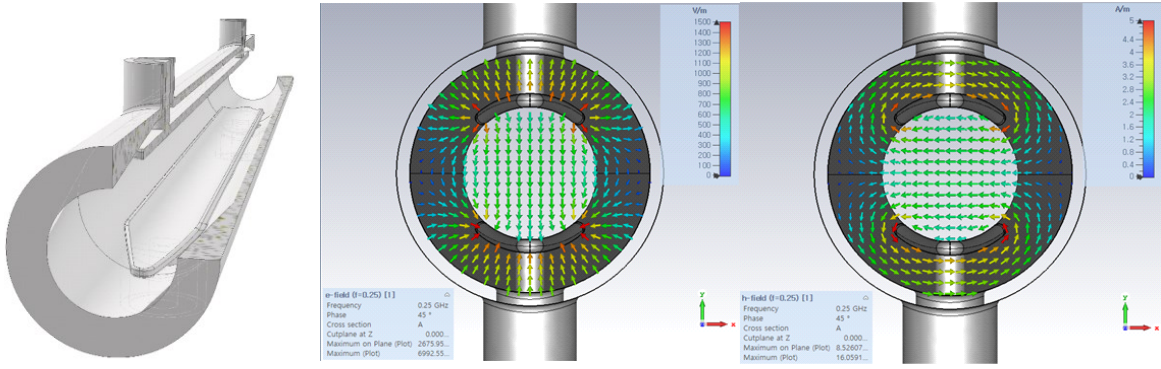
Key points in the load design include:

1. Ensuring that the reflected power within the designated frequency range is below 2%.
2. Implementing appropriate impedance matching-where the even mode and odd mode deviate slightly from $50\ \Omega$ -to minimize power supply damage due to wake impedance.
3. Achieving a minimum kick angle of $1.5\ \mu\text{rad}$ for a power level of 500 Watts.

Below is the result of the physical design.



<Figure 2.1.12.52> Voltage Reference, and the Reflection and Transmission Coefficients of the TFS Odd Mode (180° Phase Difference).

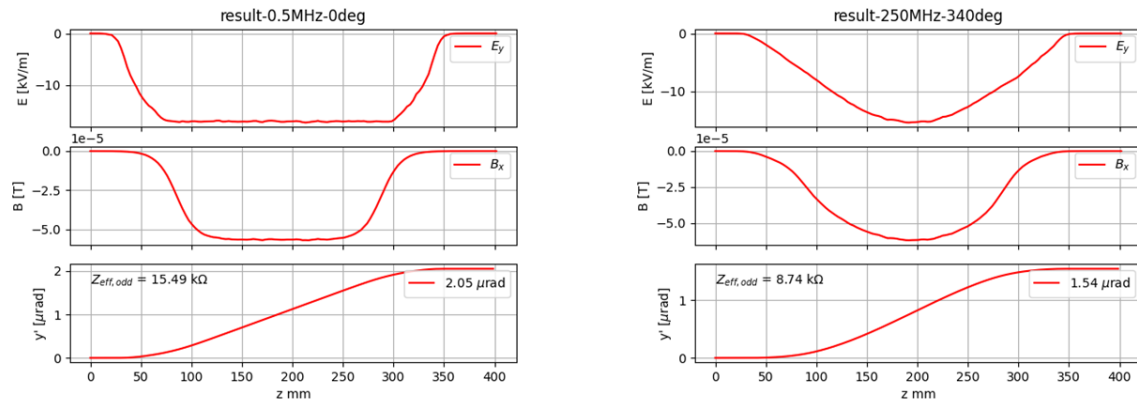


<Figure 2.1.12.53> TFS Cavity Geometry and the Correct E and H Field Patterns (From Left to Right in Sequence).

Instead of relying on analytical methods with large error margins (i.e., estimating the impedance using representative geometric values and modeling the kicking angle based on that), a full 3D time-varying traveling wave simulation was employed. This simulation utilized both the electric and magnetic field distributions to perform actual electron beam tracking. As a result, a kicking angle that incorporates the transit time factor for the given RF power was obtained, and a realistic effective shunt impedance was calculated. The effective shunt impedance used in the numerical beam tracking is summarized in the following equation (Equation 2.1.12.9).

$$R_{\perp} T^2 = \frac{\left(\frac{1}{q} \int [E_y(t) + cB_x(t)] c dt\right)^2}{P_0} \quad (\text{Eq. 2.1.12.9})$$

Since an actual 500 W wideband amplifier will be used, P_0 is assumed to be 484 W. For the TFS stripline kicker operating at 0.5 MHz and 250 MHz, actual electron tracking was performed to design the system. Power is applied in the downstream direction so that both the electric (E) and magnetic (H) fields deliver force in the same direction to the electrons. In order to perform calculations that account for the transit time, forward beam tracking was directly carried out in the traveling wave, and the results are shown in <Figure 2.1.12.54>.

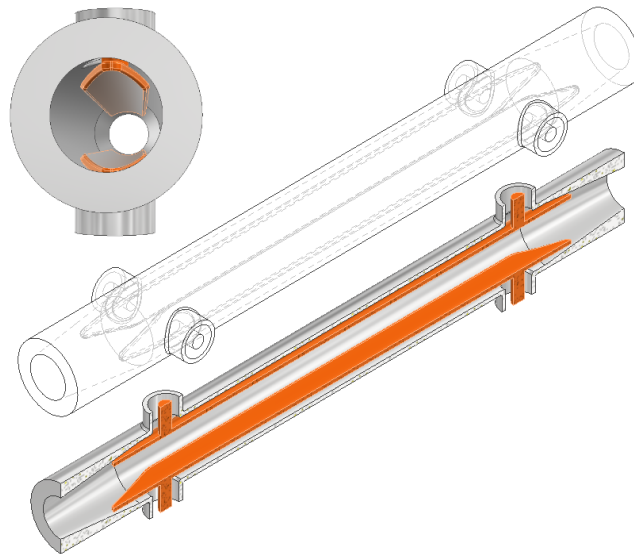


<Figure 2.1.12.54> Electron Beam Tracking Simulation Results
(Left: 0.5 MHz Operation, Right: 250 MHz Operation).

Consequently, the TFS cavity was designed to deliver a $2 \mu\text{rad}$ kick per cavity at 484 W for lower-frequency instabilities, and a $1.5 \mu\text{rad}$ kick per cavity for the highest-frequency instabilities in multi-bunch beam instability scenarios.

<Table 2.1.12.23> TFS cavity parameter

Parameters	Values
Electrode Length (L) [mm]	300
Impedance Z_{odd} [Ω]	49.75
Impedance Z_{even} [Ω]	To Be updated
Kick angle [μrad]	1.5 to 2.0
Eff. Shunt Impedance [k Ω]	8.74 to 15.49
Input Power / Cavity [W]	<500

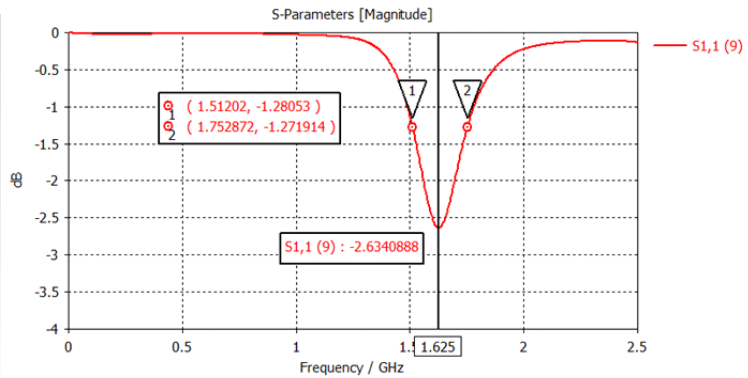
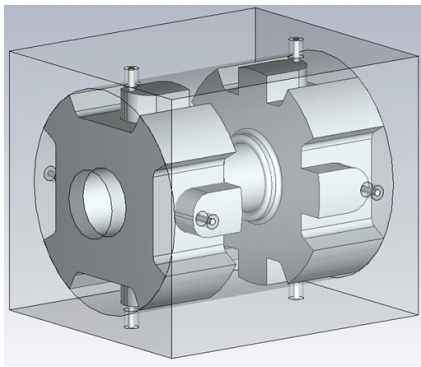


<Figure 2.1.12.55> Designed TFS Kicker.

○ LFS Kicker

The LFS cavity, like the TFS, must be capable of correcting all possible multi-bunch instabilities; therefore, it needs to support frequency operation from $n f_{RF}$ to $(n + 1/2) f_{RF}$. In a multipurpose synchrotron radiation accelerator, an RF cavity of around 500 MHz is typically used. By choosing an integer $n = 3$, the center frequency f_c is set to 1.625 GHz with a half-bandwidth f_{BW} of 125 MHz (i.e., $f_c \pm f_{BW}$). The reason for selecting three times the RF frequency is twofold:

1. to implement a cavity geometry of an appropriate size for installation
2. to achieve a quality factor and shunt impedance that are suitable for operation.



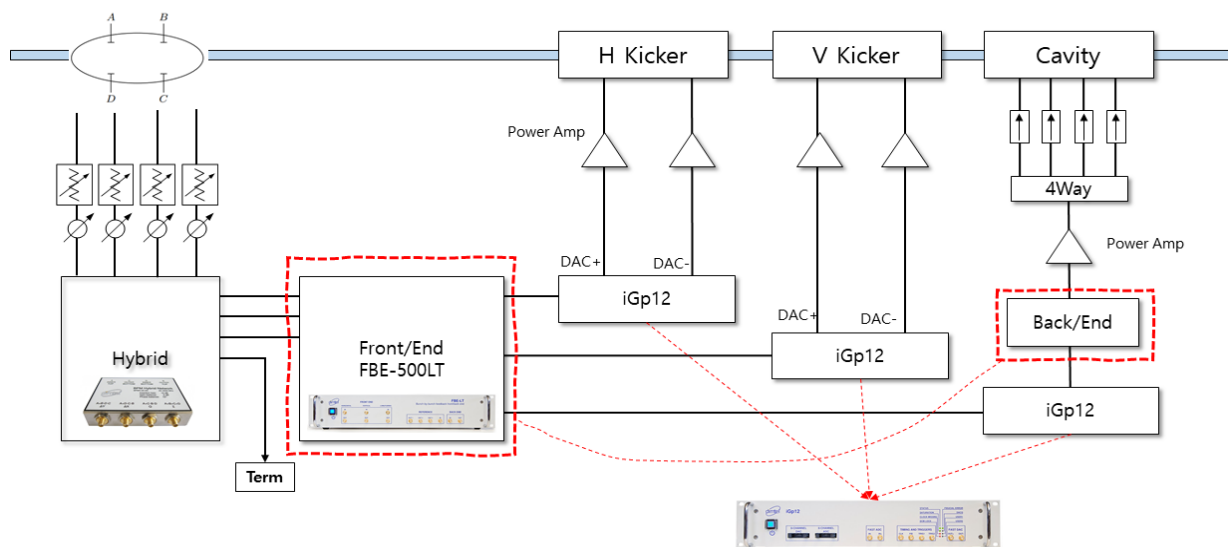
<Figure 2.1.12.56> LFS Kicker Cavity.

In terms of coupling structure, the LFS kicker cavity geometry follows the DAΦNE style, while its near-absence of a nose cone resembles the BESSY-II design, resulting in an intermediate form. The design goal for the loaded quality factor loaded Q is approximately 6.5 ($= f_c / f_{BW} = 2n + 0.5$) at the center frequency of 1.625 GHz. Although the cavity has eight ports, only two are used, with the remaining ports terminated at 50 Ω using commercial dummy loads.

(2) Multi-bunch feedback system configuration

As mentioned earlier, the multi-bunch feedback system operates in two principal directions. The transverse feedback system measures the position of each bunch and uses a Stripline kicker to minimize the position differences among the bunches in the multi-bunch train, thereby reducing the betatron damping time. Meanwhile, the longitudinal feedback system measures the phase differences among the bunches in the train and uses a longitudinal cavity kicker to keep the spacing between bunches uniform. <Figure 2.1.12.57> illustrates the overall configuration of the multi-bunch feedback system.

Beam Position Monitors (BPMs) are installed in the storage ring to measure the beam position and phase for multi-bunch feedback. The feedback kickers are placed in a section where the beam phase advances by 90 degrees from the BPM location. The signals from the BPM pass through a hybrid, which provides SUM and Δ (Delta) signals to the Front-end electronics. In the Front-end stage, amplitude control, phase control, filtering, and optional down-conversion of the BPM signals are performed. Finally, in the feedback processor, the feedback angle for the transverse kicker and the RF phase for the longitudinal cavity kicker are calculated to execute multi-bunch feedback in each direction. The processor for the multi-bunch feedback system will be built using a commercial product from Dimtel, the iGp12.



<Figure 2.1.12.57> The configuration of TFS/LFS Feedback system for 4GSR.

References

- [1] Novokshonov et al., "Scintillator Non-Proportionality Studies at PITZ," IBIC 2022, Kraków, Poland.
- [2] R. Yang et al., "Development of a YAG/OTR Monitor for Beam Halo Diagnostics," IBIC 2018, Shanghai, China.
- [3] D. Martin et al., "Evaluation of Bergoz Instrumentation NPCT," Bergoz Internal Report.
- [4] L. Torino and K. Scheidt, Proceedings of the 7th Int. Beam Instrumentation Conf., IBIC 2018, China.
- [5] Ozkan Loch, C. Ischebeck, and R. Stampfli, Proceedings of the 10th International Beam Instrumentation Conference, Rep. of Korea.

2.1.13 Beam Instability and Feedback

A. Overview

The performance of the storage ring is quantified by brightness, which is proportional to the beam current. Therefore, during storage ring operation, the beam current is increased to the highest possible value. However, the maximum operating current is limited by beam instability. Beam instability is determined by two factors: the storage ring impedance and the operating current, with the instability threshold being inversely proportional to these factors. Hence, to achieve the target maximum current of 400 mA, it is necessary to minimize the storage ring's impedance and prepare a bunch-by-bunch feedback system. This section will discuss the impedance status of the Korea-4GSR for successful 400 mA operation, beam instability in the storage ring, and the feedback systems required to control it

B. Impedance

The impedance generated in the storage ring can be broadly categorized into two types: Resistive Wall (RW) impedance and Geometric impedance. In the case of the 4GSR, the influence of Resistive Wall impedance has increased due to the reduced aperture. Therefore, as shown in <Table 2.1.13.1>, a significant portion of the vacuum chambers is made of high-conductivity aluminum. A few chambers, due to engineering requirements, are made of relatively lower-conductivity stainless steel. The fingers of the bellows and the coated parts of the In-vacuum undulator (IVU) are made of copper, while the kicker chamber for injection is made of alumina coated with a 3 μm thick layer of titanium.

<Table 2.1.13.1> Material length and conductivity

Material	Length (m)	Conductivity (s/m)
Aluminum	648.21	2.46E7
Stainless steel	82.52	1.35E6
Copper	66.05	5.8E7
Titanium coated alumina	2.52	3.33E5, 1E-12
Total	799.30	

The vacuum chamber in the arc section of the Korea-4GSR features a pentagon-shaped beam channel with a width of 24 mm and a height of 18 mm. At both ends of the channel, there are antechambers for vacuum pumping and X-ray shielding. The straight sections contain 26 Insertion Device (ID) sections and 2 High-beta sections. During the initial construction phase, 8 of the 26 ID sections are planned to house in-vacuum undulators (IVUs), and 1 section will house an elliptically polarizing undulator (EPU). However, here we assume that there will ultimately be a total of 19 IVUs and 5 EPUs, considering the future effects of the RW impedance from the additional IVUs and EPUs.

The IVUs for the Korea-4GSR are being designed with a length of 3 meters, with a minimum vertical gap of 5 mm and 15 mm. <Table 2.1.13.2> lists the parameters used to calculate the RW impedance of the Korea-4GSR. The pentagon-shaped vacuum, center bend, and EPU chambers were approximated as ellipses for calculation purposes, while the IVU and injector kicker chambers were approximated as parallel plates. The RW impedance was calculated using ImpedanceWake2D [1]. The IVU was calculated under two scenarios: with an open vertical gap of 15 mm and a closed gap of 5 mm.

<Table 2.1.13.2> Cross-section of vacuum chambers

Chamber type	Shape	Values
Vacuum chamber	Ellipse	Major axis 10 mm, minor axis 9 mm
Center bend chamber	Ellipse	Major axis 10 mm, minor axis 4.87 mm
In-vacuum undulator chamber	Parallel plates	Width 15 mm
Elliptical polarized undulator chamber	Ellipse	Major axis 10 mm, minor axis 7.5 mm
Injection kicker chamber	Parallel plates	Width 5 mm

The geometric impedance was calculated for the vacuum components using GdfidL [2]. In the geometric impedance calculations performed with GdfidL, a bunch length of 1 mm was used, and wake lengths of 1 meter or 10 meters were given in the simulation. Additionally, for the transverse impedance calculations, the beam offset was set to three times the mesh size, and the impedance and wakefield results were normalized for the given offset.

The Korea-4GSR has a total of 288 BPMs (Beam Position Monitors), and currently, two types of feedthroughs are being considered: Glass-Ceramic and Alumina. In this TDR phase,

the impedance budget reflects the glass feedthrough BPM, which has higher impedance compared to the optimized alumina feedthrough BPM.

The flanges of the vacuum chambers primarily use CF flanges, but to mitigate impedance effects, the area near the vacuum where the beam passes is surrounded by an RF contact spring made of copper-beryllium alloy. If only the CF flange is used, the beam would experience an impedance effect similar to a pillbox cavity with a length of approximately 0.1 mm. This could lead to long-range wakefield effects and heating issues at the flanges. Therefore, the Korea-4GSR minimizes the wakefield effects generated by the beam by surrounding the area near the vacuum at the flange joints with RF contact springs. In the GdfidL simulations, the flange was modeled as a thin strip with a width of 1 mm and a thickness of 0.1 mm placed in the center of the beam pipe.

In the Korea-4GSR, the vacuum chamber has ante-chambers on both sides. These ante-chambers contain ports for vacuum pumping, NEG getters, photon masks, and absorbers. By locating these components in the ante-chambers rather than the main beam channel, the impedance generated by the beam is minimized.

The Korea-4GSR has adopted the EU-type Higher Order Mode (HOM)-damped RF cavity, which is a normal conducting cavity, as its main RF cavity. HOMs can induce multi-bunch instability, which has led many 3GSR facilities to adopt superconducting RF cavities. However, the EU-type HOM-damped cavity effectively mitigates HOMs using dampers, as demonstrated by facilities such as Diamond and ESRF [3]. Therefore, in this section, we considered only the single-bunch effect caused by the HOM in the main RF cavity, rather than the multi-bunch effect.

Longitudinal feedback systems (LFS) and transverse feedback systems (TFS) have been prepared to suppress coupled-bunch mode instabilities that may occur in the Korea-4GSR. These systems each provide a kick to the beam in the storage ring, opposite to the impedance in the longitudinal and transverse directions, to suppress instability. However, the LFS and TFS kickers themselves also generate significant impedance, which must be included in the impedance calculation of the storage ring.

The bunch length of the Korea-4GSR is 4 mm RMS without a higher harmonic cavity (HHC) and 14 mm with an HHC. Considering the possibility that increasing the bunch length using HHC might be difficult in the early stages of commissioning, the loss factors, kick factors and longitudinal effective impedance were investigated for bunch length of 4

mm. The definitions used for calculating the loss factor, kick factor and effective impedance are given below in (Equation 2.1.13.1), (Equation 2.1.13.2) and (Equation 2.1.13.3).

$$\kappa_z = - \int_{-\infty}^{\infty} \lambda(s) W_z(s) ds, \quad (\text{Eq.2.1.13.1})$$

$$\kappa_{x,y} = - \int_{-\infty}^{\infty} \lambda(s) W_{x,y}(s) ds, \quad (\text{Eq.2.1.13.2})$$

$$\left| \frac{Z_{\parallel}}{n} \right|_{eff} = \frac{\int_{-\infty}^{\infty} d\omega Z_{\parallel}(\omega) \frac{\omega_0}{\omega} h_m(\omega)}{\int_{-\infty}^{\infty} d\omega h_m(\omega)} \quad (\text{Eq.2.1.13.3})$$

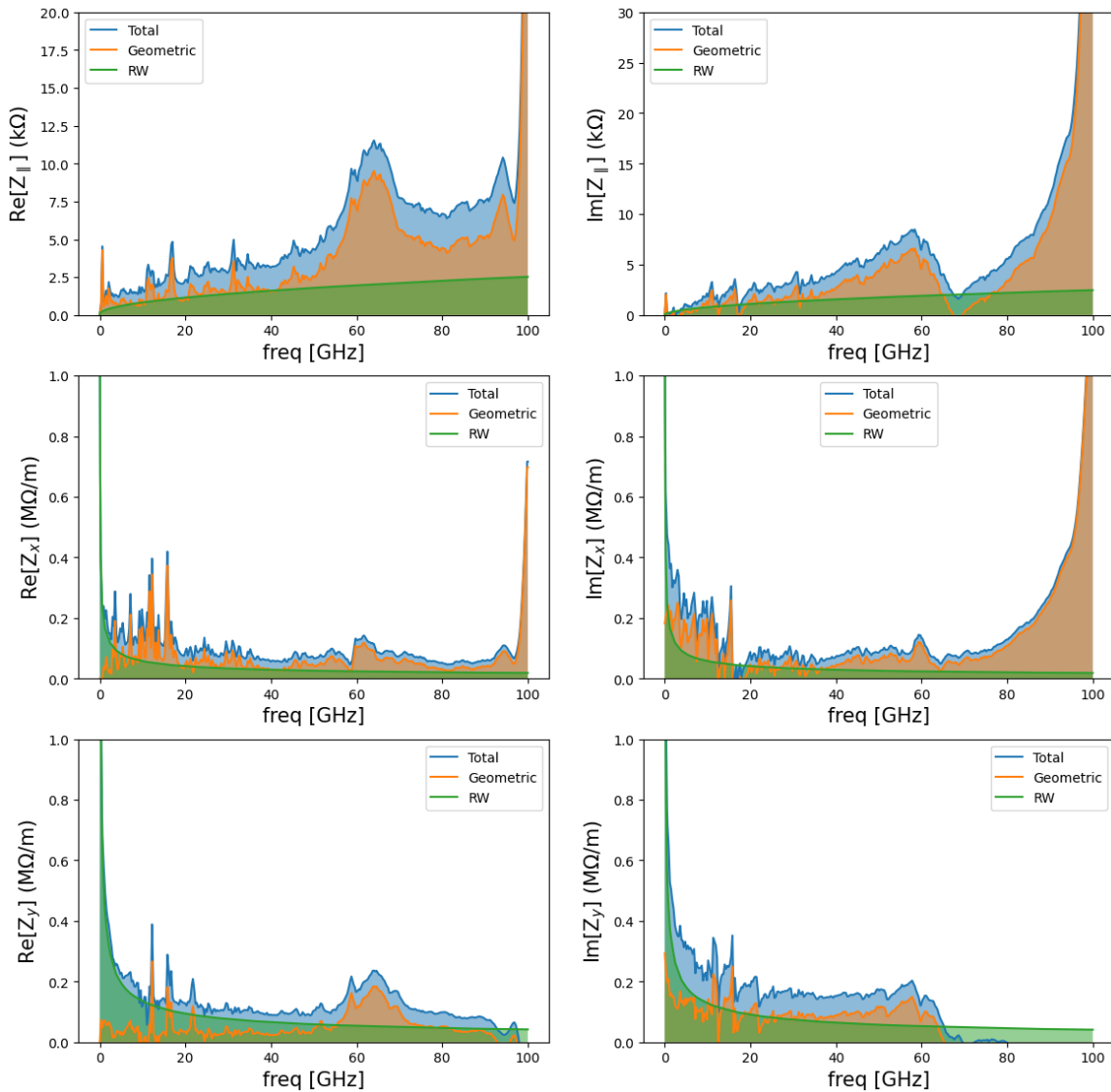
In the equations mentioned above, $\lambda(s)$ represents the longitudinal density of the beam, while $W_z(s)$ and $W_{x,y}(s)$ are the longitudinal and transverse wakefields, respectively. $Z_{\parallel}(\omega)$ is longitudinal impedance which is Fourier transform of $W_z(s)$, ω_0 is revolution frequency and h_m is bunch spectral density.

<Table 2.1.13.3> Korea-4GSR components loss, kick factors and effective impedance with bunch length of 3.6 mm

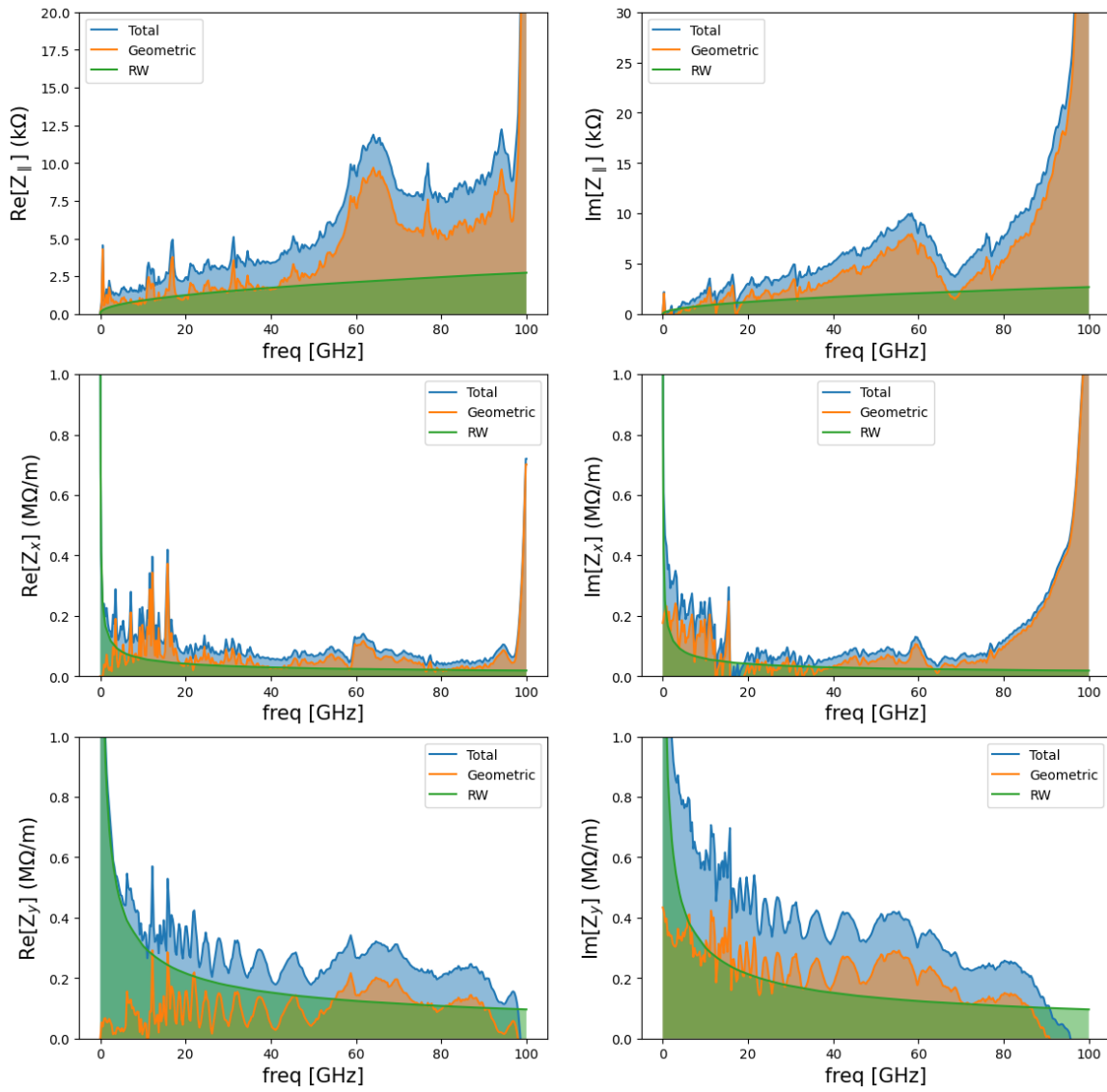
Name	number	$ Z_{\parallel}/n _{eff}$ [mΩ]	κ_z [V/pC]	$\langle\beta_x\rangle\kappa_x$ [V/pC]	$\langle\beta_y\rangle\kappa_y$ [V/pC]
RW (IVU open/close)	1	108.39/109.72	15.93/16.38	8,401.81/8,349.82	38,666.48/48,084.69
500 MHz cavity	12	5.14	1.22	73.44	30.59
BPM	176	0.16	0.03	19.34	19.87
BPM bellows	112	0.22	0.03	135.23	-6.08
RF Components	1	20.54	2.00	1,546.41	462.85
LGBM chamber	56	0.22	0.03	44.71	-104.78
LFS	1	5.37	1.67	711.62	419.58
Comtype gate valve	80	0.86	0.01	26.04	7.95
Bellows	168	0.04	0.00	1.97	16.17
TFS x	1	0.65	0.21	-105.35	58.27
TFS y	1	0.65	0.21	7.47	151.57
Transitions	1	25.23	0.20	-83.44	869.63
DCCT	2	0.14	0.06	33.68	39.20
Pump	84	0.02	0.00	6.53	-2.73
Flange joint	700	0.02	0.00	2.28	6.05
IVU gap (open/close)	19	0.04/0.69	0.00	-5.19/44.71	10.90/-104.78
Total		380.95/394.63	47.59/48.05	36,942/37,838	45,584/52,804.60

<Table 2.1.13.3> presents the loss factors, kick factors, and effective impedance of individual components within the storage ring. Although the current Korea-4GSR design includes seven in-vacuum undulators (IVUs) with two elliptically polarized undulators (EPUs), we assumed 19 IVUs and five EPUs in this section. For the resistive wall (RW)

impedance, a distinction was made based on whether the gaps of all 19 in-vacuum undulators (IVUs) are set to a minimum of 5 mm (closed) or a maximum of 16 mm (open). Among the four longitudinal gradient bending magnet (LGBM) chambers in the arc section, two include photon extraction holes and photon absorbers, whose impedance contributions are accounted for. The LF, HF, and VF kickers represent longitudinal feedback (LF), horizontal feedback (HF), and vertical feedback (VF) kickers, respectively. The RF components include an RF trapper from the straight section to the RF cavity and an RF translation chamber with vacuum pumping holes and a photon absorber. <Figures 2.1.13.1> and <Figure 2.1.13.2> illustrate the real and imaginary parts of the impedance with the IVU gaps in the closed and open positions. The horizontal impedance remains constant regardless of whether the IVUs are open or closed because the RW impedance model for the IVU, based on a parallel plate approach, does not affect the horizontal impedance.



<Figure 2.1.13.1> Longitudinal, horizontal and vertical impedance with 19 in-vacuum undulator open.



<Figure 2.1.13.2> Longitudinal, horizontal and vertical impedance with 19 in-vacuum undulator close.

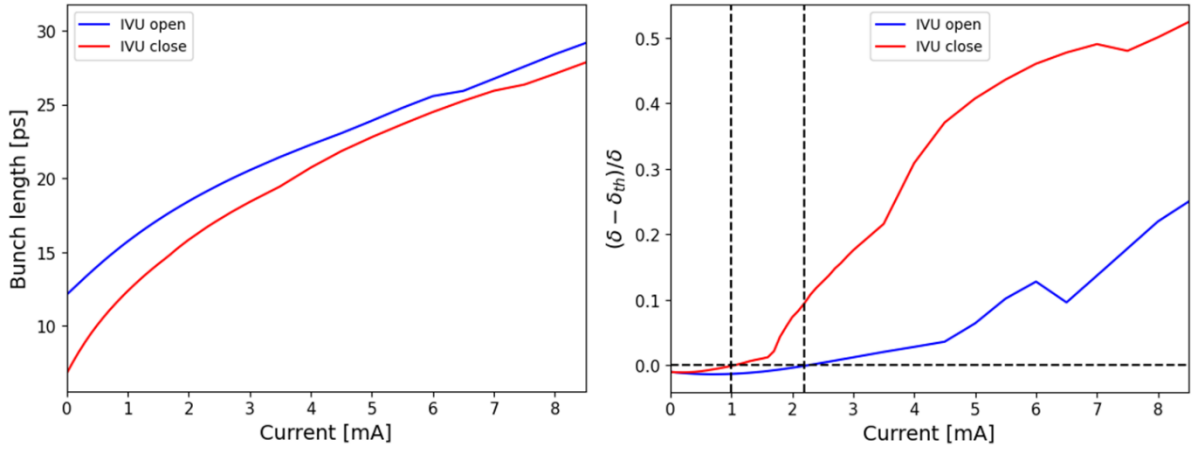
C. Beam Instability (Collective Effect)

Impedance can lead to various instabilities, which are categorized into two types: single-bunch instability and coupled-bunch mode instability. Single-bunch instability occurs when a single bunch becomes unstable due to the impedance it generates. Notable examples include microwave instability, which increases both bunch length and energy spread, and transverse-mode coupling instability (TMCI), which affects the emittance and orbit of the electron beam. In this section, instability tracking simulations were conducted using PyAT [4], employing impedance data from the previous section. Additionally, two lattices (19 IVU gaps are opened closed) and the absence of harmonic cavities were considered.

First, let's predict the effects of microwave instability in Korea-4GSR through analytical and numerical calculations. (Equation 2.1.13.4) define the Keil-Schnell-Boussard criterion, which are used to evaluate microwave instability.

$$\left| \frac{Z_{\parallel}}{n} \right|_{eff} < (2\pi)^{\frac{3}{2}} \frac{E_0 |\eta_p| \sigma_z \sigma_{\delta}^2}{e^2 N_0 c}, \quad (\text{Eq.2.1.13.4})$$

The above formulas involve the beam energy E_0 , slip phase factor η_p , bunch length σ_z , beam energy spread σ_{δ} , electron charge e , number of electrons per bunch N_0 , speed of light c , and the bunch spectrum h_m . According to the Keil-Schnell-Boussard criteria, the required effective impedance for 400 mA operation is 90 and 45 m Ω for IVU gaps open and close, respectively. However, the effective impedance of the Korea-4GSR exceeds 400 m Ω . Given the conservative nature of the Keil-Schnell-Boussard criteria, it is likely that a higher current can be injected in actual operation than the threshold indicates. Therefore, it is essential to determine a realistic threshold for microwave instability through tracking simulations.



<Figure 2.1.13.3> The microwave instability simulations using the bare lattice (blue) and the 24-ID lattice (red) show threshold currents of 2.2 mA and 1.0 mA, respectively. The threshold current is defined as the point at which the energy spread increases by 1 % compared with the zero-current value.

The MWI simulations did not include intrabeam scattering (IBS), transverse impedances, and two cases were analyzed: all 19 IVU gaps open and all closed. When the 19 IVU gaps are closed, additional longitudinal damping occurs, and the main RF voltage, natural bunch length, and energy spread differ from those of the IVU open. < Figure 3.1.12.3> presents the results of incorporating the calculated longitudinal impedance of Korea-4GSR into tracking simulations, showing the mean bunch length and energy spread as functions of single-bunch current. The numerical tracking results indicate that the MWI threshold currents for the open and closed IVU configurations are 2.2 mA and 1.0 mA, respectively, 32 times higher than the analytical estimates. The threshold current is defined as the point where the energy spread increases by more than 1% relative to the zero-current value.

Another important single-bunch instability is transverse mode coupling instability (TMCI), which affect transverse stability and emittance. The analytical TMCI threshold at a given chromaticity can be calculated as shown in [6],

$$I_{th} = \frac{4\sqrt{\pi}\alpha_c E \sigma_\delta}{e} \frac{1}{\beta \text{Im}(Z_\perp)_{eff}} \quad (\text{Eq.2.1.13.5})$$

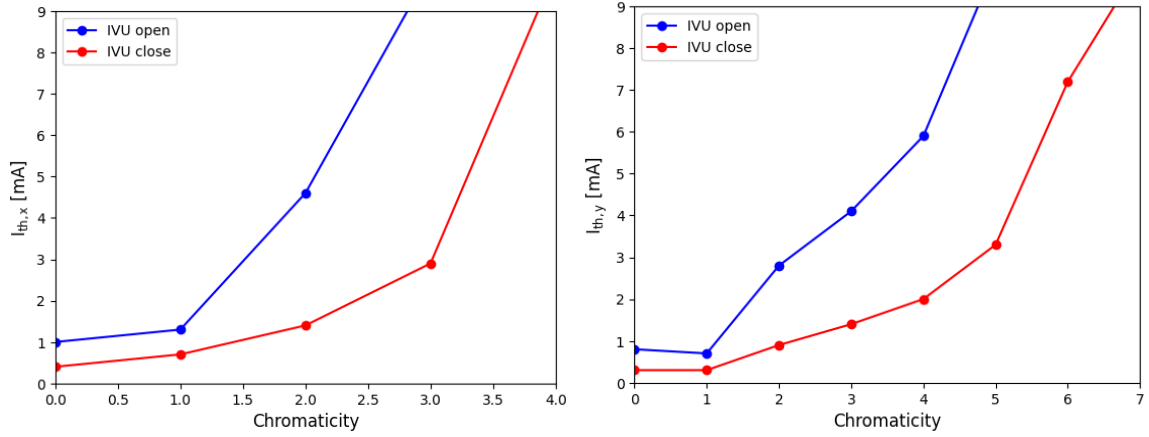
where α_c is momentum compaction factor, E is beam energy, σ_δ is natural energy spread and β is the average beta function. In this study, we utilized beta-weighted transverse impedance to determine the effective impedance instead. <Table 2.1.12.4> compares the analytical threshold current with the numerical tracking results at zero chromaticity. The simulation performed with 360,000 particles, taking into account both transverse longitudinal impedances. The threshold current was identified as the point at which the transverse beam size began to exhibit significant variation. A large discrepancy was observed between the analytical and numerical threshold currents because the analytical estimation considered only the transverse impedances, whereas the tracking simulations included both transverse and longitudinal contributions.

<Table 2.1.13.4> Analytical and numerical TMCI threshold current at zero chromaticity

	Analytical threshold current	Threshold current from tracking
Horizontal (IVU open/ close)	1.7/ 1.7 mA	1.0/ 0.4 mA
Vertical (IVU open/ close)	1.1/ 0.7 mA	0.8/ 0.3 mA

Korea-4GSR is planned to operate in a 400 mA brightness mode with 1,024 bunches, corresponding to a single-bunch current of 0.4 mA. As shown in <Table 2.1.13.4>, the closed 19-IVU configuration can stably operate up to a single-bunch current of 0.3 mA. Several methods can be employed to increase the TMCI threshold current, one of which is to raise the chromaticity. <Figure 2.1.13.4> illustrates the simulation results for the TMCI threshold currents at various chromaticity values. As expected, higher chromaticity leads to a higher TMCI threshold. With a chromaticity of 2, both horizontal and vertical planes exhibit threshold currents exceeding 1 mA, which is sufficient for the brightness mode. When the chromaticity exceeds 7, the TMCI threshold current surpasses 10 mA.

Each bunch in the total 1,024 bunches contains beam charge of 1 nC. Consequently, coupled-bunch mode instabilities (CBMIs) can arise from resistive-wall (RW) impedance, ion collisions, and higher-order modes (HOMs) of the RF cavities. Due to the reduced chamber aperture, the RW impedance has increased significantly, becoming a major source of transverse CBMI. (Eq. 2.1.13.6) assumes rigid-body bunch motion and represents the betatron frequency shift induced by the impedance as the bunches undergo betatron oscillations.



<Figure 2.1.13.4> TMCI threshold currents for the horizontal (left) and vertical (right) planes with different chromaticity values. The blue and red lines represent the IVU-open and IVU-closed configurations, respectively.

Coupled bunch mode instability induced by resistive wall at zero chromaticities can be described as

$$\Omega_{\mu} - \omega_{\beta} = -i \frac{4\pi n_b N_b r_0 \omega_0 c}{Z_0 8\pi \gamma_0 v_{\perp}} \sum_{p=-\infty}^{\infty} Z_{\perp} \{ \omega_{\beta} + (\mu - n_b p) \omega_0 \}, \quad (\text{Eq. 2.1.13.6})$$

$$Z_{\perp}(\omega) = \frac{1}{\beta_{\perp}} \sum_{i, \text{element}} \beta_{\perp, i} Z_{\perp, i}(\omega), \quad (\text{Eq. 2.1.13.7})$$

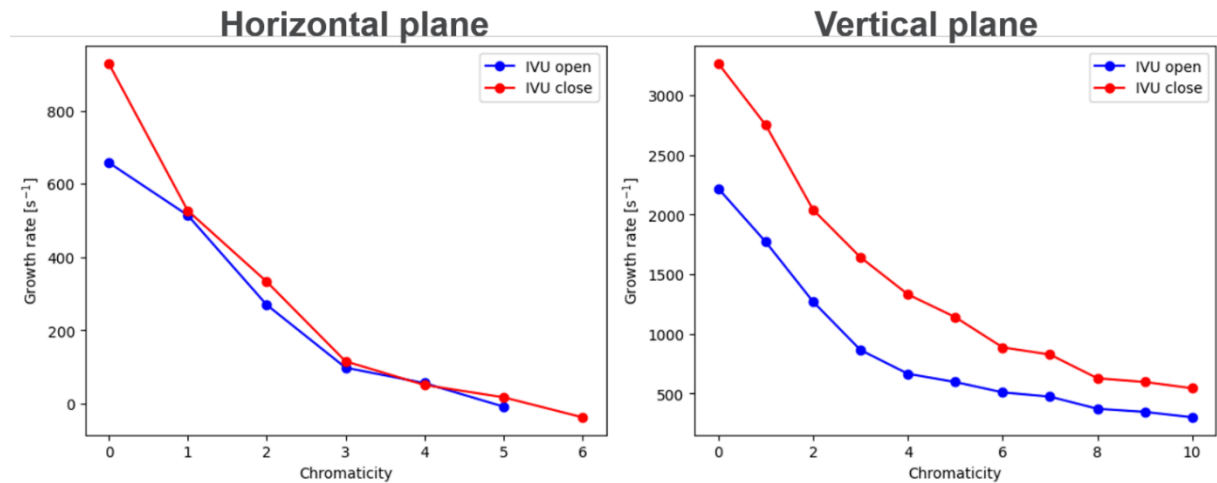
Ω_{μ} is mode frequency, ω_{β} denotes the betatron frequency, n_b denotes the number of bunches in the storage ring, N_b denotes the number of electrons per bunch, r_0 denotes the classical electron radius, ω_0 denotes the revolution frequency, Z_0 denotes the vacuum impedance, γ_0 denotes the Lorentz factor of the beam, v_{\perp} denotes the transverse tune, and μ denotes the mode number. The real part of (Eq. 2.1.13.6) represents the frequency shift due to impedance, while the imaginary part indicates the growth rate.

<Table 2.1.13.5> Growth rate comparison at chromaticity of 0 when IVU gaps are closed.

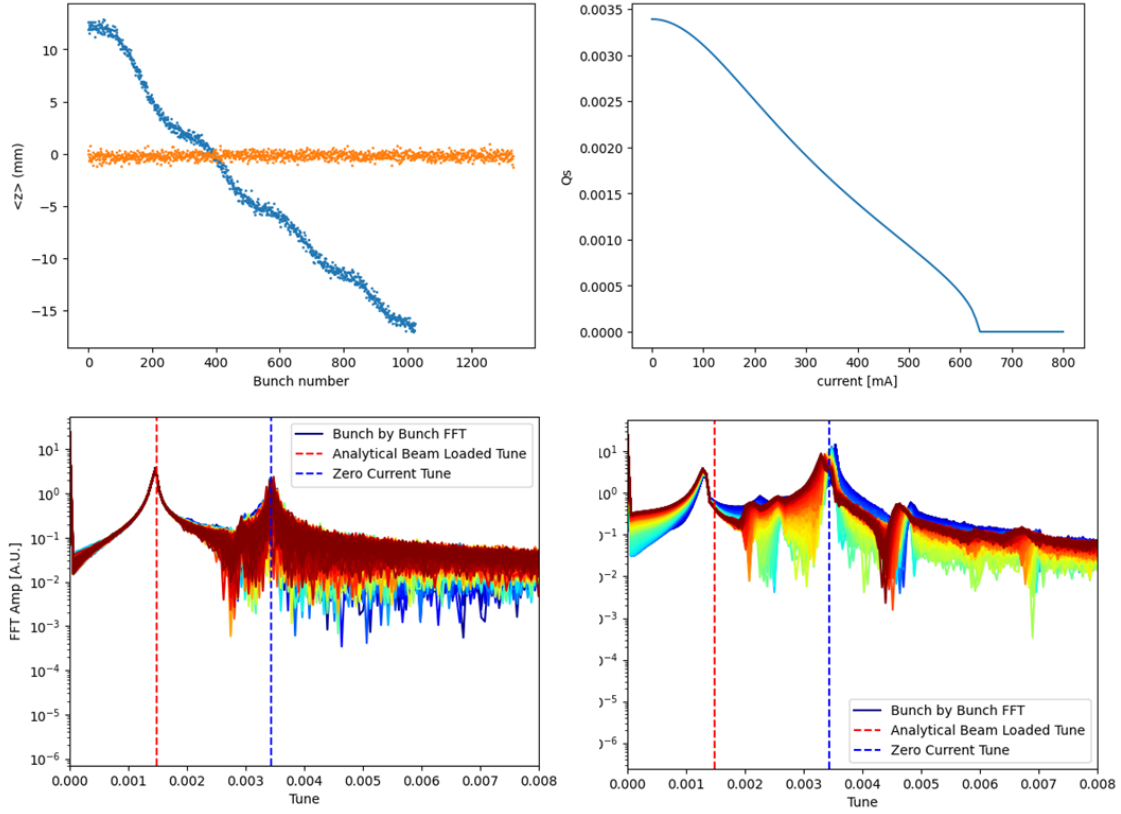
	Analytical [s ⁻¹]	Simulation [s ⁻¹]
Horizontal (IVU open/close)	53.54 / 53.54	657.56 / 928.21
Vertical (IVU open/close)	2563.29 / 4402.78	2216.47 / 3264.92

Analytical and numerical tracking calculations of the resistive-wall (RW)–induced CBMI growth rates were performed at a beam current of 400 mA. <Table 2.1.13.5> summarizes the analytical and numerical growth rates for a chromaticity of zero. The numerical tracking simulations also employed beta-weighted impedances. From the numerical results, turn-by-turn beam position data were analyzed using singular value decomposition (SVD) to extract the growth rates from the temporal evolution and to identify the dominant spatial modes [7]. Because the RW model of the IVU is based on a parallel-plate geometry, no horizontal growth-rate variation appears in the analytical model, whereas the simulations yield growth rates of 657.56 s^{-1} and 928.21 s^{-1} for the horizontal plane. In the vertical plane, the analytical and simulated results show similar growth rates.

Similar to the TMCI case, higher chromaticity can effectively mitigate the RW-induced CBMI. <Figure 2.1.13.5> shows the growth rate as a function of chromaticity. In the horizontal plane, a chromaticity above 6 is sufficient to suppress the RW-induced CBMI. However, in the vertical plane, suppression does not occur until the chromaticity reaches approximately 10, where the corresponding growth rates for the IVU-open and IVU-closed configurations are 229.31 s^{-1} and 542.54 s^{-1} , respectively. Since the vertical radiation damping rates for the IVU-open and IVU-closed cases are 51.5 s^{-1} and 138.7 s^{-1} , respectively, a bunch-by-bunch feedback system may be required to maintain vertical stability.



<Figure 2.1.13.5> Simulation results of horizontal (left), vertical (right) growth rate with 19 IVUs open and close.



<Figure 2.1.13.6> Beam-loading simulation for main RF cavity. Left top: Longitudinal mean positions of bunches, with blue dots representing the case when the number of bunches is 1,024 and orange dots for 1,332. Right top: Analytical synchrotron tune shift (Eq. 2.1.12.8) resulting from beam-loading. Left bottom: Bunch-by-bunch synchrotron tune results for a bunch number of 1,332. Right bottom: Bunch-by-bunch synchrotron tune results for a bunch number of 1,024.

We investigated beam-loading simulations for transient effects. The Korea-4GSR has a harmonic number of 1,332, but only 1,024 buckets will be filled with bunches. Due to the ion clearing gap, transient effects from beam-loading may arise. In this simulation, two cases were studied: one with the number of bunches (Nb) set to 1,024, and the other with Nb set to 1,332. When Nb = 1,332, no transient effect is present, allowing for the analytical calculation of the synchrotron tune shift as shown in [8].

$$\omega_s = \sqrt{\omega_{s0}^2 + K\omega_{rf} \sin 2\psi} \quad (\text{Eq.2.1.13.7})$$

where ω_{s0} unperturbed synchrotron frequency, K loaded quality factor, ω_{rf} rf frequency, ψ detuning angle. The analytical tune shift and tracking results are presented in <Figure 2.1.13.6>. The simulated total beam current is 400 mA for both cases. Due to the transient effect, the longitudinal mean positions change linearly, while the Nb = 1,332 case

maintains consistent positions. Additionally, the transient effect results in a greater shift than the expected synchrotron tune shift. However, despite the presence of the transient effect, the Nb = 1,024 case experiences no particle loss.

As mentioned in the impedance management section, Korea-4GSR effectively suppresses the higher-order modes (HOMs) in the normal-conducting RF (NCRF) cavities using dedicated HOM dampers. <Figure 2.1.13.7> shows the NCRF impedance spectra of Korea-4GSR and the threshold shunt impedance for HOM-induced CBMI, given by (Eq. 2.1.13.8):

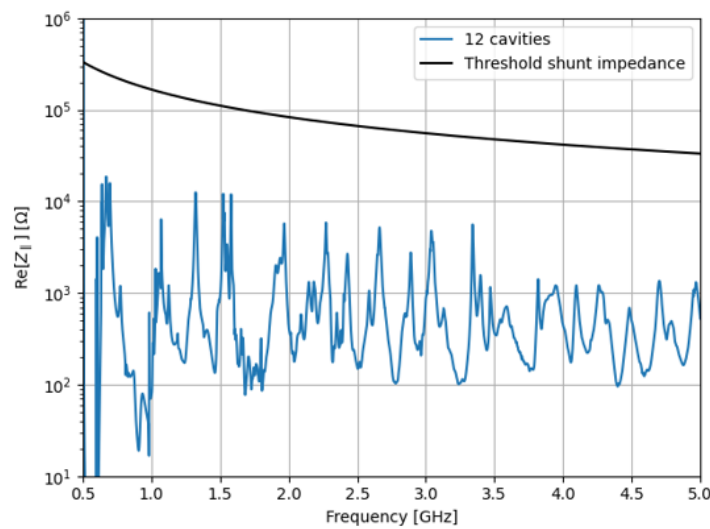
$$R_s = \frac{2EQ_s \alpha}{\tau_s f} \quad (\text{Eq.2.1.13.8})$$

where E is the beam energy, Q_s is synchrotron tune, τ_s is longitudinal damping time, α is momentum compaction factor, and f is frequency. Analytical estimations indicate that the HOMs of the NCRF cavities cannot induce CBMI in the Korea-4GSR.

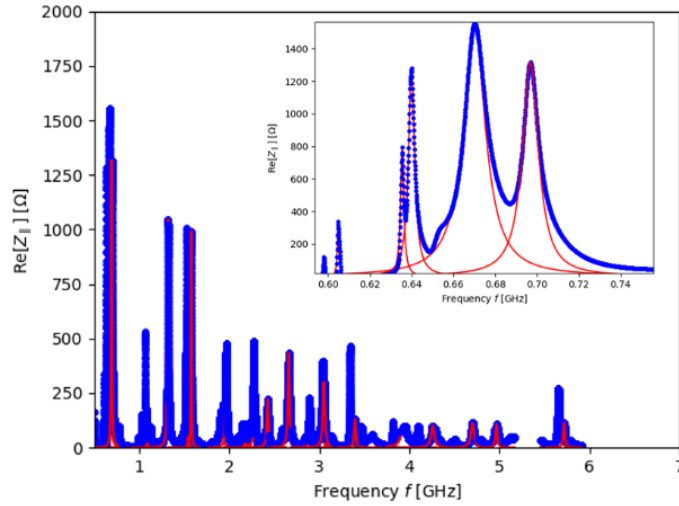
In addition, numerical tracking simulations were performed using the NCRF cavity's HOM components. The HOM frequencies, shunt impedances, and quality factors were obtained by fitting the approximated cavity impedance model expressed as (Eq. 2.1.13.9):

$$\text{Re}Z(f) \approx \frac{R_s}{1+(2Q\frac{f-f_r}{f_r})^2}, \quad (\text{Eq.2.1.13.9})$$

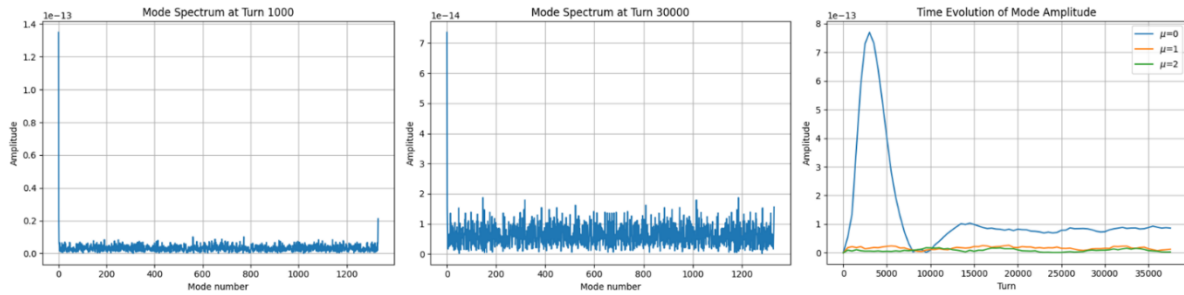
where R_s is shunt impedance, Q is quality factor, and f_r is resonant frequency. The fitting results are presented in <Figure 2.1.13.8>



<Figure 2.1.13.7> NCRF cavity impedances and CBMI threshold shunt impedance line.



<Figure 2.1.13.8> NCRF cavity impedances and HOM fitting.



<Figure 2.1.13.9> Modal analysis to estimate the NCRF HOM induced CBMI.

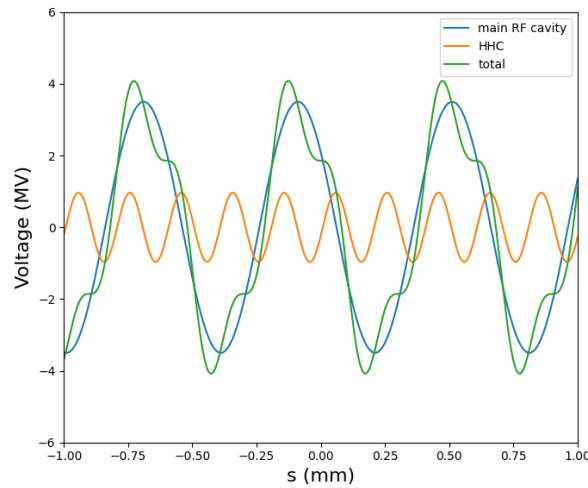
The simulation was performed with 1,332 bunches, each containing 1,000 particles. Only the NCRF cavity HOMs were considered in the CBMI analysis. The results are illustrated in <Figure 2.1.13.9>. As expected from the analytical estimation, no dominant coupled-bunch modes were observed in the simulation results.

D. Harmonic Cavity (Bunch-Lengthening Cavity)

In 4GSR, the lattice is designed to reduce dispersion, which in turn decreases the emittance. As a result, the momentum compaction factor is small, leading to a shortened bunch length. The reduced emittance and shorter bunch length increase the likelihood of electron collisions within the bunch. This shortens the Touschek lifetime, causes an emittance growth due to the Intrabeam Scattering (IBS) effect, and makes beam instabilities more likely to occur. In 4GSR, the bunch length is 4 mm, but as mentioned in the beam

physics section, the bunch length should ideally be extended to around 15 mm to achieve better performance.

There are two options for the Higher Harmonic Cavity (HHC): a normal conducting option and a superconducting option. These can be further categorized into active HHCs, which use external RF power, and passive HHCs, which utilize beam loading. For 4GSR, the primary consideration is an active system normal conducting cavity, similar to the main RF system. Traditional normal conducting cavities can induce severe beam instability due to the Higher Order Modes (HOM) generated as the beam passes through. However, Korea-4GSR is considering an HOM-damped cavity, which suppresses HOMs, similar to the main RF cavity. This TDR assumes the use of an NC HOM-damped cavity for the HHC.



<Figure 2.1.13.10> The main RF voltage, HHC voltage, and total RF voltage based on the bare lattice.

To increase the bunch length, one can either increase the momentum compaction or install a Harmonic Cavity (HHC). However, since increasing the momentum compaction also leads to an increase in emittance, the 4GSR utilizes an HHC to extend the bunch length. The HHC uses a frequency that is an integer multiple of the main cavity frequency to adjust the slope of the total voltage, thereby increasing the bunch length. The total RF voltage and phases are given as follows,

$$V(t) = V_{RF} \sin(\omega_{RF}t + \phi_s) + kV_{RF} \sin(n\omega_{RF}t + n\phi_h), \quad (\text{Eq.2.1.13.10})$$

$$k = \sqrt{\frac{1}{n^2} - \frac{1}{n^2-1} \left(\frac{U_0}{eV_{RF}} \right)^2}, \quad (\text{Eq.2.1.13.11})$$

$$\tan(n\phi_n) = -\frac{\frac{nU_0}{eV_{RF}}}{\sqrt{(n^2-1)^2 - \left(n^2\frac{U_0}{eV_{RF}}\right)^2}}, \quad (\text{Eq.2.1.13.12})$$

Here, n is the harmonic number of the HHC, V_{rf} and ϕ_s represent the voltage and phase of the main RF cavity, ϕ_h is the phase of the HHC, U_0 is the energy loss per turn, and e is the electron charge. As shown in <Figure 2.1.13.10>, these conditions flatten the voltage around the synchronous particle, thereby increasing the beam length. In the 4GSR, a main RF frequency of 500 MHz is used, and the HHC employs the 3rd harmonic (1,500 MHz) to achieve a bunch length of 15 mm. Based on this, the voltage and phase of the main RF cavity and HHC are given in <Table 2.1.13.6>

<Table 2.1.13.6> The required main RF cavity voltage, HHC voltage, and phase for the cases of bare lattice and SR with IDs included

	Without IDs	With 9 IDs
Main RF voltage (MV)	3.03	3.5
Main RF phase (degree)	155.95	152.24
HHC voltage (MV)	0.93	1.05
HHC phase (degree)	351.54	350.05

When applying the parameters from the 'without IDs' case in <Table 2.1.13.6> to the simulation, it was calculated that the bunch length, initially 3.8 mm, was maintained at around 14.5 mm, and both the fractional energy and energy spread remained within acceptable limits. However, in the simulation, the effects of the wakefield generated as the beam passes through the cavity were not considered. Typical wakefield effects include Robinson instability and phase transient beam loading, and there are also effects from HOMs (higher-order modes) that are not fully eliminated by the damper. Robinson instability can be addressed by tuning the cavity, and HOM effects can be mitigated through longitudinal feedback cavities. However, beam loading has a significant impact on bunch lengthening due to factors such as bunch charge and filling pattern, so ongoing research is being conducted on this topic.

References

- [1] "IRIS IW2D," *GitLab CERN*, <https://gitlab.cern.ch/IRIS/IW2D>.
- [2] "GDFIDL," <http://www.gdfidl.de/>.
- [3] M. Abbott et al., "Diamond-II Technical Design Report."
- [4] "ATCollab," *AT Documentation*, <https://atcollab.github.io/at/index.html>.
- [5] R. Nagaoka and K. L. F. Bane, "Collective effects in a diffraction-limited storage ring," *Journal of Synchrotron Radiation*, vol. 21, pp. 937–960, 2014.
- [6] N. Mounet, "The LHC Transverse Coupled-Bunch Instability," No. 5305, EPFL, 2012.
- [7] L. Carver et al., "Beam loading simulations in PYAT for the ESRF," *Proceedings of the 14th International Particle Accelerator Conference*, Venice, Italy, 2023.

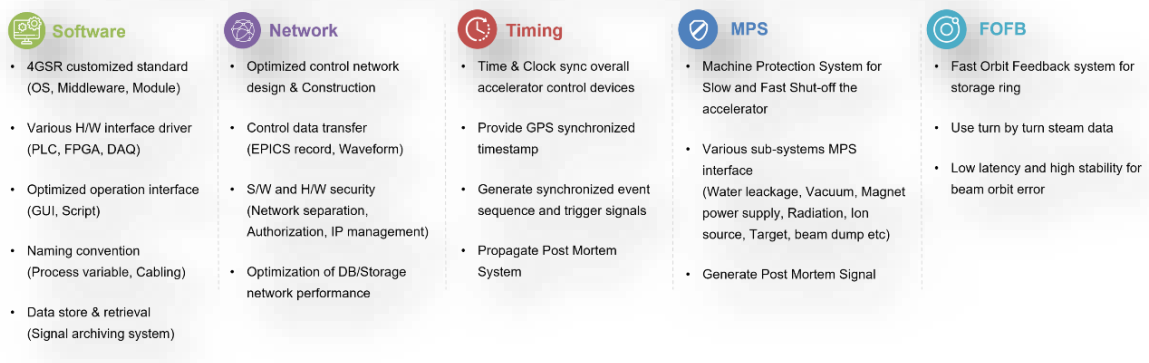
E. Integrated Control System

(1) Overview

The multipurpose synchrotron radiation accelerating system requires a dedicated control system that integrates various heterogeneous systems into a single, cohesive system due to the nature of the system. To achieve this integration, different devices are integrated and operated within the EPICS (Experimental Physics and Industrial Control System) middleware framework. The integrated control system is established in the integrated control room, supporting the control of all of the various elements of an accelerator by monitoring all signals from the distributed local devices. Before building heterogeneous systems into an integrated system, categorizing and standardizing the diverse systems that may be derived indiscreetly according to their performance and purpose is crucial for preventing potential significant cost losses in the future. Standardizing the control system should proceed more rapidly than constructing the multipurpose synchrotron radiation facility. Also, since the accelerator is a facility that will operate for several decades, it is important to consider the expandability and flexibility of the system for long-term operation, and these considerations should be fully reflected in the initial construction of the control infrastructure. The goal is to develop and apply an integrated control system that ensures the stability, reliability, expandability, and availability of the 4GSR by carrying out a series of tasks from the design of the accelerator's integrated control system to its completion.

Goals

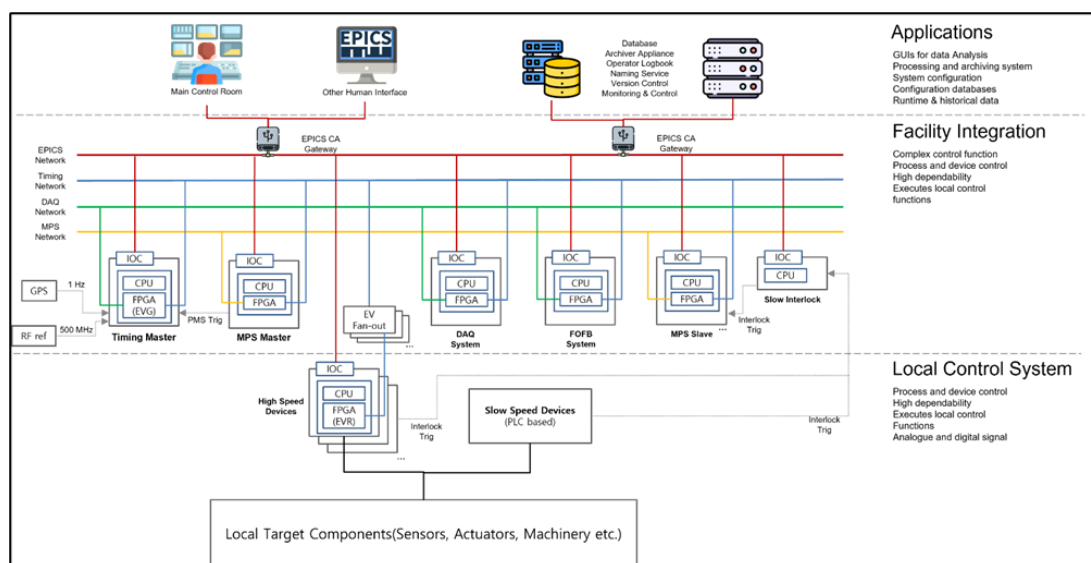
- To read, change and record all raw signals from all equipment of the accelerator and all logic signals
- To provide an effective standards : graphical user interface(GUI), operating system(OS), database, network, standard hardware, version control
- To oversee all equipment, alert operators, end-users, or both to fault conditions, and could provide tools in order to analyze any fault quickly



<Figure 2.1.13.7> The goals and core technologies of the central control system.

(2) Control System Configuration

The control system of a multipurpose synchrotron radiation accelerator uses EPICS as the software framework to integrate the environment of distributed heterogeneous devices. EPICS serves as a distributed control system middleware with an Ethernet communication layer. Each local device in the 4GSR should be configured using an EPICS IOC (Input Output Controller). This setup can be seen as the boundary that distinguishes between the local control system and the integrated control system. When designing the 4GSR's integrated control system structure, one needs to consult the diagram below.



<Figure 2.1.13.8> Architecture of the integrated control system.

The 4GSR is structured around four types of networks: the EPICS network, the Timing network, the DAQ (Data AcQuisition) network, and the MPS (Machine Protection System) network. The EPICS network, also known as the control network, connects each local control system with the integrated control system in the 4GSR. The Timing network is an optical communication network designed to transmit high-speed event signals defined in the Timing system to devices that require precisely synchronized signals. The DAQ network is an optical communication network used to transmit large volumes of data, such as NArray and waveform data, separate from typical control signals. It is used to enhance the stability of the network through the separation. The MPS network is an optical communication network designed to transmit quickly signals from diagnostic devices like BPM (Beam Position Monitor) and BCM (Beam Current Monitor) as well as trip signals from RF (Radio Frequency) devices that supply power to the electron beam. These signals could pose critical threats to the accelerator.

○ **Standardization of software**

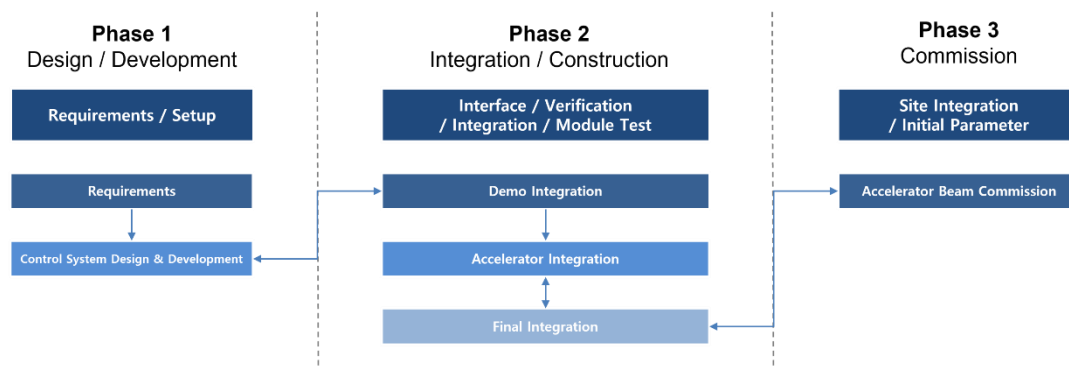
The EPICS middleware is an operating system-independent open-source program. However, standardization guidelines for operating EPICS have been established to prevent various unregulated operating environments. In cases where necessary dependencies on operating systems and system management arise, system maintenance and operational costs will be minimized through separately prepared exceptional items. The standard software management guidelines for running 4GSR are as follows:

- ① EPICS Middleware: EPICS7 7.0.7 or later
- ② Base Operating System: Debian and Redhat-based Linux 64bit
 - Debian 11, Ubuntu 22.04 or later
 - Rocky 7 or later
 - Xilinx - SoC (PetaLinux)
- ③ Display (GUI: Graphic User Interface) Manager: Phoebus
- ④ Centralized Storage System:
 - EPICS Archiver Appliance on Network Attached Storage (NAS)
 - Storage Area Network (SAN) for array data
- ⑤ Industrial Protocol: ModbusTCP
- ⑥ EPICS CA (Channel Access) Gateway: Redundant on L4 switch
- ⑦ Database: MariaDB
- ⑧ Version Control: GitLab

(3) Control System Development Cycle

The development cycle of the control system for the 4GSR project is coordinated according to the project's schedule and is broadly divided into three stages. The first stage involves analyzing the requirements and developing the design for the control system to operate the 4GSR comprising devices. In this process, prototypes or commercial product tests are conducted, leading to the second stage of construction and integration. Once the second stage is completed, the final third stage involves conducting the actual operation. Verification procedures should be established at each stage, and the control system

integration should be completed based on the verified results.



<Figure 2.1.13.9> Control system development cycle.

○ Verification between Phase 1 and 2

Verification of the EPICS middleware system integration

Validation of the interface of the commercial uTCA-based timing system

Verification of the Timing System

Verification of the Fast Orbit Feedback System (FOFB)

Verification of the fast Data Acquisition (DAQ) System

Verification of Machine Protection System (MPS): Machine Interlock System (MIS) and Fast Orbit Interlock (FOI)

○ Verification between Phase 2 and 3

I/O verification for each module (verification according to all Local Systems)

Integration and linkage test of each system

Parameter settings for the 4GSR commissioning

Operation modes according to the commissioning scenario

Linkage test of beam physics applications with the commissioning

(4) Configuration of Integrated Control System Infrastructure

The integrated control system will establish the computing infrastructure to be included in the central operation room and server room, along with the 4GSR operation environment that must operate on top of this infrastructure.

○ **Software development for operation**

The 4GSR utilizes EPICS middleware to create a systematic system from various heterogeneous devices. Multiple programs for accelerator operation (UI (User Interface) and high-level applications) should also be intimately integrated with EPICS, and it is necessary to develop various EPICS-based operational modules for the stable operation of the 4GSR. Such EPICS-based operational modules include a CA gateway for OPI and control networks, WebOPI supporting web-based EPICS signal monitoring, Channel Finder supporting Elastic Search, Logbook for recording accelerator operating circumstances or anomalies, and Alarms for EPICS signal Alarm Events.

○ **Infrastructure configuration**

① Configuration of the central operation room

- Display wall
- Operation environment
- Operator interface server configuration
- Public network configuration
- Control network configuration
- Personal Safety Interlock monitoring system
- Monitoring system for control shed and tunnel
- Emergency manual buttons
- Public address system
- Server room configuration
- Operational server configuration
- Configuration of accelerator operation-related servers (EPICS IOC server, OPI (Operator Interface) server, Archive server)
- Storage system configuration
- Data backup and storage system configuration
- Control network's backbone switch configuration (EPICS Control, Timing, MPS, DAQ networks)

- Temperature and humidity control
- Power redundancy and UPS (Uninterruptible Power Supply)

② Network configuration

- Configuration of MDS in the server room and each FDF (Fiber Distributed Frame)
- Dedicated line for 48-core closed network
- EPICS control network with 4 cores (10 G redundancy)
- Timing network with 4 cores (redundancy)
- FOFB network with 4 cores (redundancy)
- MPS network with 4 cores (redundancy)
- DAQ network with 4 cores (redundancy)

○ **Standard installation script**

A standard installation script will be developed to standardize the development environment for internal and external personnel involved in developing the 4GSR accelerator to prevent issues related to discrepancies between developing and operating the control system software. This environment is designed to enable the consistent development and operation of systems controlling a number of devices.

The `install_scripts` is an automated installation script for the EPICS development environment, supporting the installation of EPICS Base, EPICS synApps, and EPICS Extensions in Debian, Ubuntu, and Rocky environments. When installing the development environment through the `install_scripts`, the script automatically configures packages dependent on the installation items. However, administration authority is required to install and configure dependency items.

The open-source EPICS middleware should be configured in a standard environment in an account of the host where EPICS is installed. A `setEpicsEnv.sh` file containing the environment variables used by EPICS will be created.


```
Auto Installation script
Enter the number of you want to install
1 : EPICS V7 version 7.0.7
2 : EPICS synApps
3 : EPICS extension
0 : Exit script
Enter the number : 0
```

<Figure 2.1.13.10> The install_scripts execution screen.

In the script, EPICS Base consists of the OS (Operation Interface) interface libraries, CA client and server libraries, and device and driver support, forming the core of EPICS. The EPICS module is the synApps module, a collection of libraries containing essential libraries such as Asyn, StreamDevice, and Autosave. EPICS Extensions compose EDM (Editor/Display Manager) and MEDM (Modif Editor and Display Manager) in the src folder to manage the display. EPICS IOC and EPICS lib folders, which are not included in the script installation items, contain self-developed IOC and library codes.

After installing all items, it is possible to verify the installation of the Base, module, and extensions on the execution screen, as shown in the figure below.

```
example@example:/usr/local/epics/EPICS7$ tree -L 2
├── base
├── epics_ioc
│   ├── control_ioc
│   └── local_ioc
├── epics_lib
├── extensions
├── modules
│   └── synApps
└── setEpicsEnv.sh

9 directories, 1 file
```

<Figure 2.1.13.11> Completed EPICS Base installation signal on the screen.

In addition to the EPICS Base development libraries, the libraries to be used in the 4GSR are composed of the module directories, which consist of the development code directory that forms the interfaces related to the integrated control system and another development code directory for local device control systems. For configuration management, codes related to development should be operated by establishing an open-source-based configuration management tool.

(5) Integrated local control system

The 4GSR integrated control system requires significant effort to understand the platforms of the control systems configured in each local device and to provide the EPICS interface for integrating the control systems of local devices. Various forms of heterogeneous systems are considered between the local devices, and many EPICS interface modules should be considered to integrate these systems with EPICS. Since the various devices comprising the accelerator have individual control systems, integrating the various forms of heterogeneous systems introduces complexity. The indiscriminate integration of heterogeneous systems can lead to complications in maintaining and configuring for operation in the future.

For system integration after minimizing unnecessary heterogeneous systems, it is essential to understand the requirements of each device and then proceed with standardizing the systems based on performance and purpose. For maintainability and efficiency, heterogeneous systems should be minimized, and standardization should align with the performance and objective of each device.

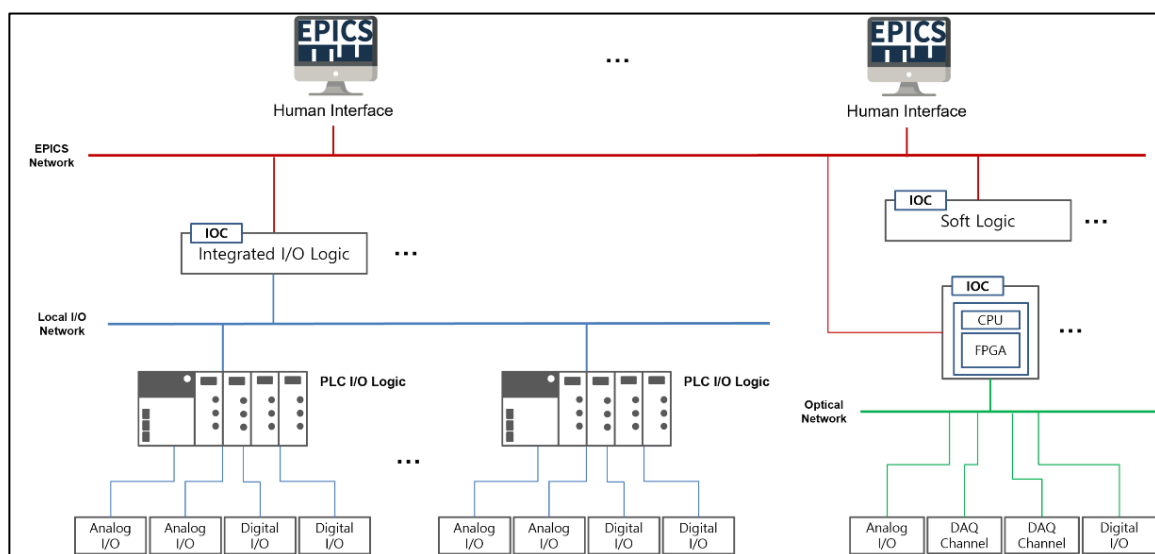
To standardize the development of the central control system, UI guidelines, naming convention, and IOC development guidelines have been prepared and distributed for the local control systems. These guidelines provide technical instructions for the control systems, allowing developers to maintain a consistent coding style and maximize development efficiency. The UI guidelines cover design principles, layout, colors and themes, icons, graphic elements, and accessibility to provide consistent user experiences. The design should emphasize consistency, user-oriented principle, and responsiveness, recommending layout configuration, color, theme settings, and intuitive icons and graphics utilizing Phoebus. Also, the design should consider accessibility so all users can easily utilize the system.

The naming convention defines the naming rules for EPICS PV (Process Variable). The

purpose is to clarify the meaning of signals through a consistent naming scheme. The IOC development guidelines provide necessary instructions for managing dependencies between system components and for writing modular code. They include an overview of the IOC, its components, setup and configuration methods, and testing and debugging procedures to support developers in working efficiently. It enhances system flexibility and maximizes code reusability.

These guidelines are essential for maintaining consistency between central and local control systems while maximizing efficiency throughout development.

○ Configuration of the local control system



<Figure 2.1.13.12> Architecture of the local control system.

The control system configuration of a local device is broadly divided into two areas: PLC (Programmable Logic Controller)-based Slow Processing area and FPGA (Field Programmable Gate Arrays) based Fast Processing area. As illustrated in the figure above, the PLC I/O data in the slow processing area is integrated using EPICS IOC and ethernet-based industrial TCP/IP (Transmission Control Protocol/Internet Protocol) protocols. The fast processing area is integrated within the middleware of FPGA logic and an embedded CPU (Central Processing Unit) on a semiconductor-based System on-chip (SoC).

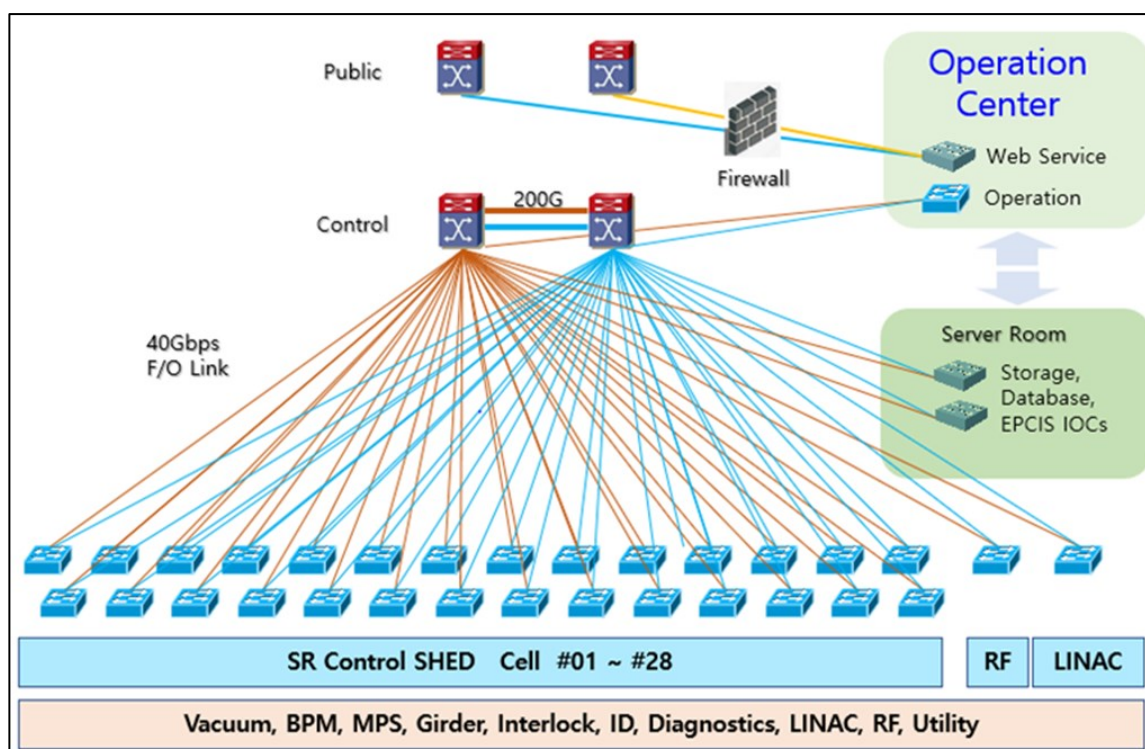
<Table 2.1.13.8> Standardized modules for local control software development

Device Controller	Detail		EPICS Module	Related System
PLC	- Industrial Communication Protocol (ModbusTCP)		ModbusTCP	Vacuum Slow Interlock
Programmable SoC	Xilinx Zynq	- Vivado (FPGA code) - Peta Linux (Xilinx Linux Kernel) - Linux Device Driver	asyn Stream user-driver	Timing FOI FOFB LLRF
Serial Controller	- MOXA serial server - Ethernet to RS232 / 485 - SCPI standard serial command - Embedded EPICS IOC Controller		asyn Steram	Magnet Power Supply Vacuum

F. Design of Control Infrastructure

(1) Network Design

The network infrastructure should be configured so that the operational information of all devices required for accelerator operation can be monitored and controlled in real-time from the central operation room. All required data of devices, such as storage ring control shed, linear accelerator, RF, air conditioning and utility, and beamline ID (Insertion Device), are collected in the server room. The server room is where data from EPICS IOC control devices for controlling various devices and data processing are stored, and traffic is concentrated there. The collected data is sent at high capacity and high speed on the network to the operators or beam physics and diagnostic agents either visually or in the form of extracted data. In addition, when designing the control network, the installation of optical cables should be considered from the beginning of the building construction, and the design should secure an optical path that can transmit a large amount of data at high speed in advance. For network expandability, a centralized topology was selected for ease of adding/removing equipment.



<Figure 2.1.13.13> Control Network Topology.

When providing data to general users and experts in charge of each device in a remote experiment environment, using an EPICS gateway is advantageous for saving traffic and enhancing security, and it is possible to manage and transmit PV data effectively. All data-transfer processes should be designed for ease of control, and it is important to optimize the performance and speed of the network and reflect this in the design. This approach ensures the efficiency and reliability required for remote experimentation.

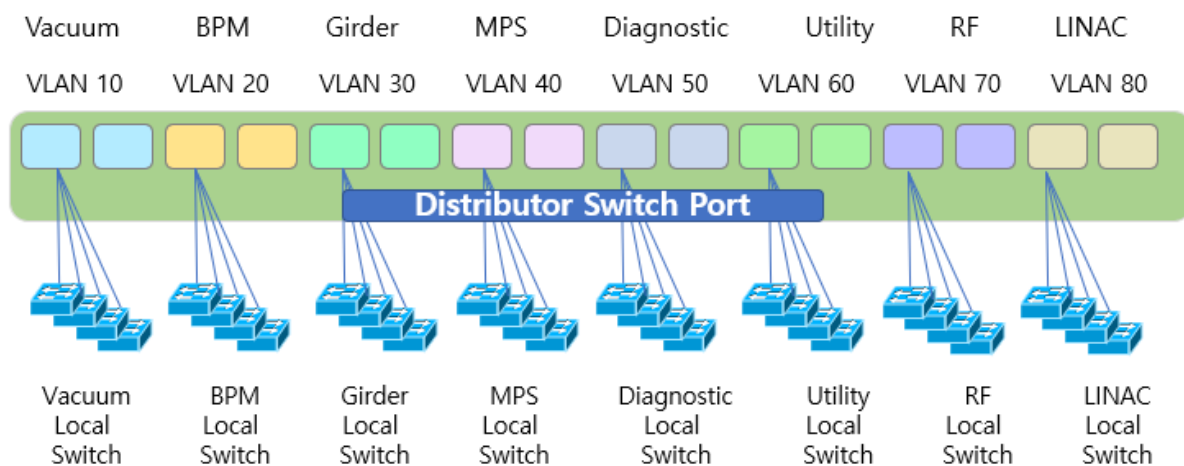
○ Classification of VLANs by device group

The system will be organized using a VLAN (Virtual Local Area Network) for each device. By setting up a VLAN per device, it is possible to minimize the broadcast traffic sent to all nodes per event and to increase performance and efficiency. VLANs logically unify physically distributed networks to achieve centralization.

The VLAN ID assigned to each device enables differentiating subsystems, which requires using a network switch that supports VLANs. Devices differentiated by VLAN ID can form independent networks even if they use the same switch. It maximizes the efficiency of network management.

In a VLAN-implemented system, devices with the same VLAN ID can communicate

freely with each other, while communication between devices belonging to different VLANs is done through the main backbone router. This allows network traffic to be effectively separated and managed. Moreover, configuring independent VLANs for each device can enhance security between subsystems. It improves the network efficiency and safety. Properly utilizing VLANs can improve the overall quality and reliability of the network in many ways, including performance, efficiency, security, and management.



<Figure 2.1.13.14> VLAN ID Allocation for Devices.

○ Device IP addressing

For efficient network operation, it is necessary to systematically assign IP addresses to each device. For this purpose, principles and appropriate policies for IP address management should be established and operated. All end devices connected to the control network should not be assigned IP addresses arbitrarily but should be assigned according to a consistent procedure established by the network administrator. Utilizing management tools for efficient IP address management is also required.

IPv4 can be used by selecting the 10.0.0.0 band, a private IP band, or the bands from 172.16.0.0 to 172.31.255.255. In a large-scale control system, class A private IPs (10.0.0.0) are used to assign IP addresses intuitively and effectively. Each device operator is given a private IP band network and assigned IP addresses in the order of the devices.

The following IP assignments are based on the IP Class A addressing system and are subject to change in the future in consultation with public and control network managers.

10.10.0.0: public Network

10.100.0.0 to 10.199.0.0: Accelerating devices' IP assignment range

10.101.0.0: Vacuum

10.102.0.0: BPM

10.103.0.0: Girder

10.104.0.0: Magnet Power Supply

10.105.0.0: Diagnostic

10.106.0.0: RF

10.107.0.0: Linear accelerator

10.108.0.0: Utility

10.109.0.0: Common

10.110.0.0: etc.

From 10.200.0.0 to 10.251.0.0: Beamline control devices' IP assignment range

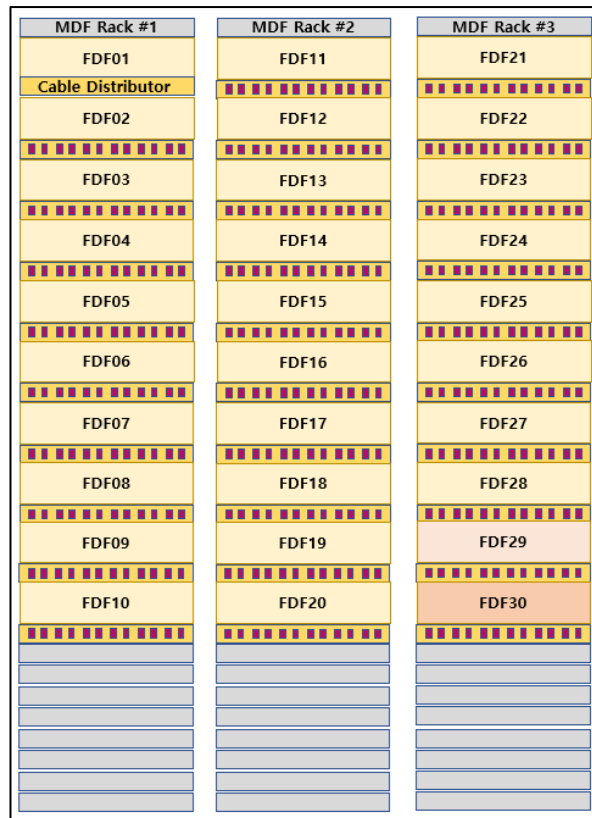
○ Network's optical cable configuration

For the placement of the MDF (Main Distribution Frame) optical cable and MDF rack for the control system network infrastructure, it is suggested to adjust the FDF rack position to avoid mutual interference with the on-site control system rack and to place the network rack in the center of each cell to maximize the connection efficiency.

The figure below shows the MDF Rack layout in the control system server room. The MDF rack is the central hub of the control system's network branch, connecting and centralizing the various networks.

The installed on-site FDF racks consist of FDF racks distributed in 30 locations, such as the storage ring control shed, RF system, and linear accelerator, and concentrated to the MDF in the server room through an optical cable. The optical cable end will be processed in the construction infrastructure while the racks are connected to the switch through optical media in the control system. Considering the straightness of the optical cable, it is necessary to reserve space for cable movement and leave the bottom of the rack empty as a passage for the optical cable.

The purpose of the 48-core optical cable in each cell is to be configured as a dual system and used for transmission and reception. The other purpose is to transmit the system's control signal. The optical cable can be utilized not only for data networks but also for independent networks, MIS, BPM high-capacity data, FOFB, and timing networks.



<Figure 2.1.13.15> MDF rack layout.

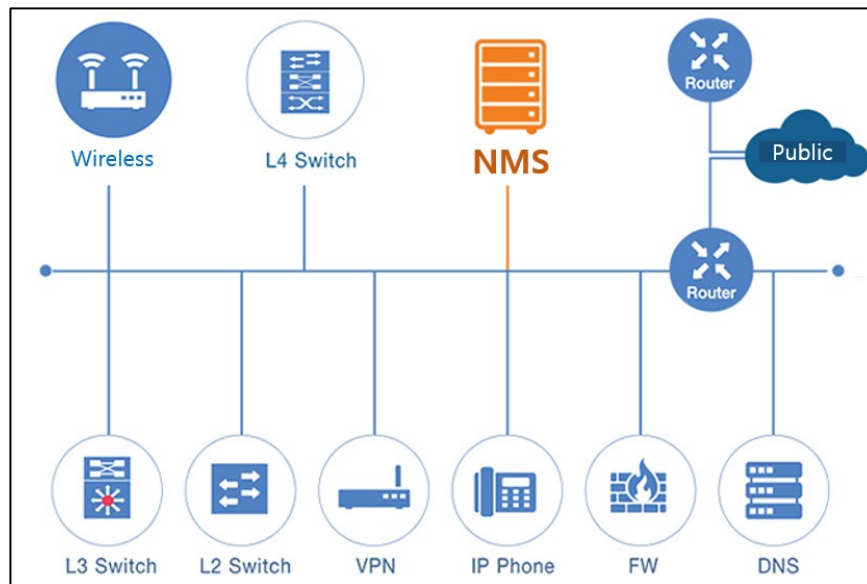
- Maintaining the network stability

The Network Management System (NMS) is key in network operation. The importance of NMS is especially evident in large-scale network environments. Since large networks have a wide variety of equipment and complex structures, directly managing them is quite difficult. In these environments, NMS enables efficient management and operation of the networks and plays a vital role in quickly diagnosing and resolving potential problems.

The NMS monitors information, such as the network equipment status, traffic, and malfunctions, in real-time and optimizes network performance based on the information. It is also essential for maintaining network stability by enhancing network security and enabling immediate response to failures. Therefore, adopting an NMS is essential for efficient network management and reliable operation in large-scale network environments.

The NMS should provide various functions, such as security management, bandwidth management, and performance analysis, to support network operations efficiently. First, it monitors the operating status of network equipment in real-time and collects the status quantitatively to provide predictive analysis. Second, it detects failures and generates alarms to notify administrators so that they can respond quickly. Third, it tracks changes in network

configuration information and provides reports to maintain configuration consistency. Therefore, the NMS plays an essential role in supporting control network operations and improving the reliability and efficiency.



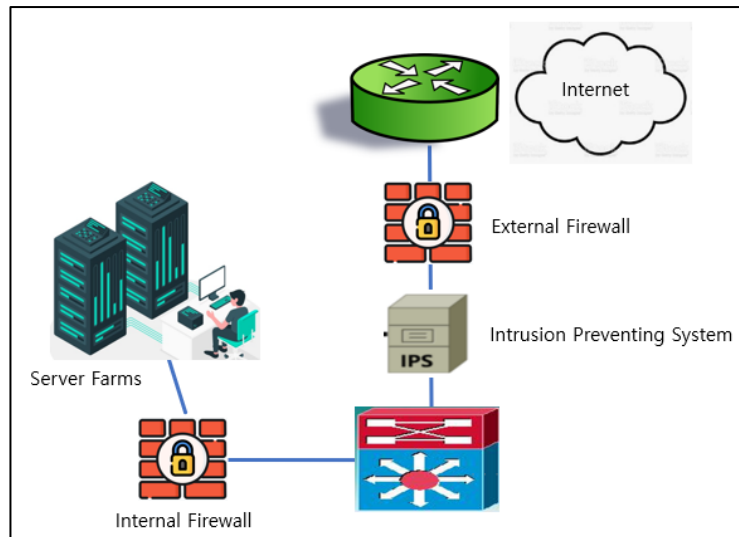
<Figure 2.1.13.16> NMS management environment.

○ Network security

The accelerator control system is a national security facility, and a policy should be set to disallow external connections in principle. It should be isolated from the outside Internet in an emergency to prevent hacker attacks or malicious access and enable independent accelerator operation. The ultimate purpose of network security is to protect various devices and keep the network safe from potential threats.

Enhanced security aims to minimize exposure to risks, such as external intrusion, data leakage, and malware infection, and to protect the institution's sensitive information and data.

Therefore, the accelerator control network should strengthen its security and establish appropriate security policies and defense mechanisms. It is necessary to manage authorized and unauthorized traffic, such as IP and protocol management on firewall equipment and automatic blocking of harmful traffic using IPS (Intrusion Prevention System) equipment. Adopting these security technologies and procedures is essential to keep the network secure.

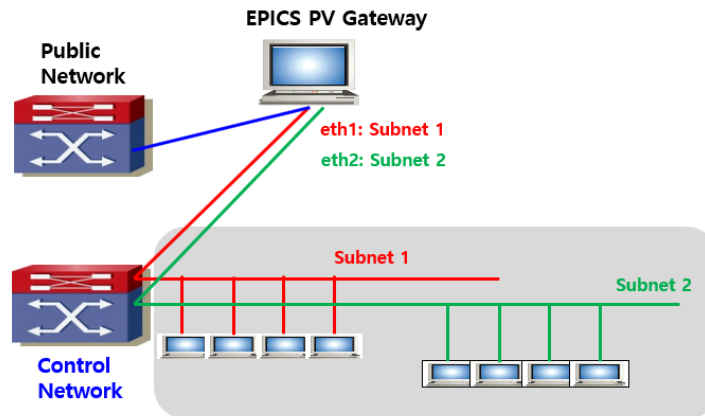


<Figure 2.1.13.17> Network security.

The 4GSR accelerator control network will be operated as a closed network. Remote experimentation, development, debugging, and updates in a closed network environment require more restrictions and security than in a general network. Closed networks are protected from external attacks but have limited interactions with external resources. To minimize manual work and increase efficiency in a closed network environment, using isolated network zones or establishing a management system in the central control system is considered. In a closed network environment, connection to the outside world is restricted due to the security policy. Therefore, automating OS patching and kernel package updates is important. In the case of kernel packages, the central management system provides the automatic update function, which is validated in an isolated test environment and then implemented. Once validation is complete, the update function is automatically distributed to the operating environment. In such a closed network environment, it is possible to keep the system up-to-date and manage it efficiently by building the central management system and automating OS patches and software updates.

○ EPICS PV Gateway

PV Gateway is an EPICS CA server that provides a means for multiple clients to access PVs and at the same time, a CA client that has only one connection to the IOC server that generates the PVs. In other words, the PV Gateway acts as an intermediary responsible for communications between other systems or devices and the EPICS system. The gateway role can protect the IOC server while restricting access to the PVs of IOC devices. It runs on computers with multiple network cards, and the client and server can be on different subnets.



<Figure 2.1.13.18> PV Gateway.

The EPICS PV Gateway facilitates communication with other systems and efficiently manages the flow of data, increasing the flexibility and expandability of the EPICS system. The EPICS system can be utilized in various ways through the PV Gateway, including integration with various control systems, data analysis, and remote monitoring.

The PV Access, a new protocol adopted by EPICS, is a high-performance network communication protocol for signal monitoring and scientific data interconnecting services. PV Access utilizes IP multicasting instead of the conventional UDP (User Datagram Protocol) broadcasting method of a CA. Multicasting using PV Gateway is a very useful way to use network resources and deliver data to specific groups more efficiently than the previous broadcasting method. It plays an important role in managing and delivering traffic effectively, especially in complex networks.

PV Access utilizes load balancers to distribute traffic concentrated across network segments by appropriately routing client requests to each group. This reduces network load and improves overall system performance. Using multicasting optimizes the frequency and size of PV data transmissions, minimizing bandwidth usage. In other words, multicasting can manage bandwidth more efficiently than broadcasting. Multicasting can also provide reliable service by prioritizing important PV data, such as real-time control data. It ensures key data transmission in the network environment and improves the overall QoS (Quality of Service) level. Therefore, it can effectively manage traffic in a complex network environment through various methods, such as network load balancing and bandwidth saving.

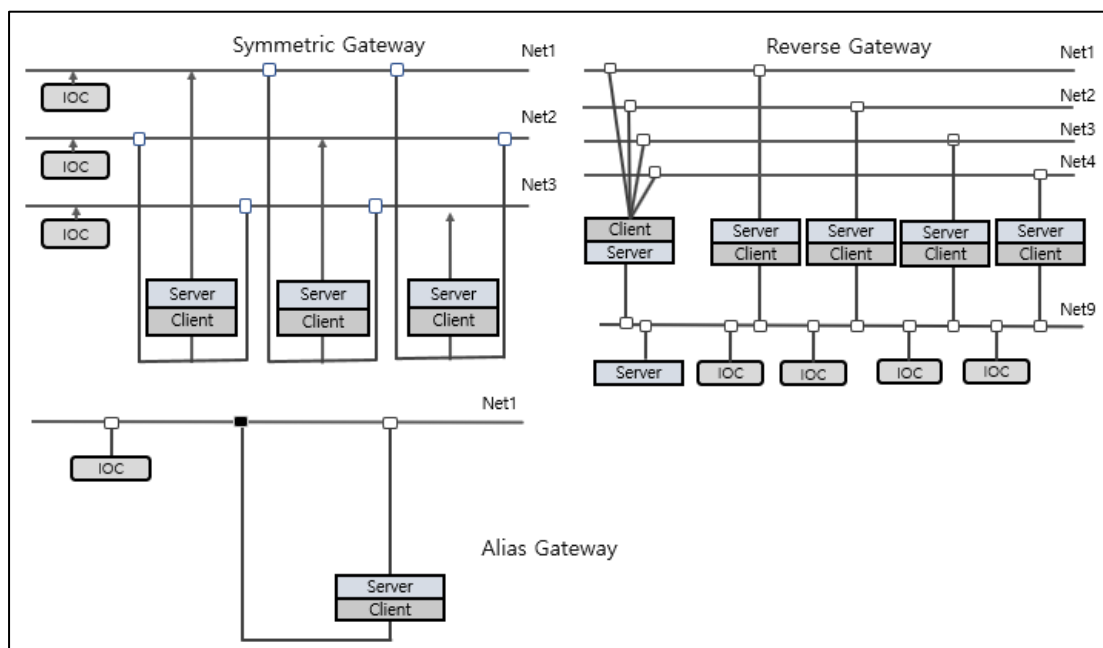
The EPICS Gateway version 2 works with any standard EPICS Base 3.14.6 or later and has improved performance and functions over previous versions. This means that it can

handle tens of thousands of PVs while processing hundreds of thousands of events per second. The access security setting in the configuration file defines PV name patterns that allow or deny access in the 'gateway.pvlist' file. The 'gateway.access' file defines access security rules.

There are three purposes for using the EPICS Gateway: First, to allow multiple clients to access a PV, the IOC server provides a mechanism to allow only one connection. Second, it provides access to the PV from one subnet to another. Thirdly, it strengthens security by restricting access to the IOC PV.

There are three types of EPICS PV gateways: symmetric, reversed, and alias. Symmetric gateways are used to find one PV on two or more different subnets, while reversed gateways are used to access the internal PVs of other gateways. To prevent loops, reversed gateways should accept only one other gateway and their internal process variables and deny all other gateways' internal PVs. Alias gateways are used only for aliasing PVs on a subnet.

In summary, the PV gateway aims to minimize the impact of connecting to PV on IOC performance and to provide multiple users with convenient access to IOC PV.



<Figure 2.1.13.19> Architecture of EPICS PV Gateways.

(2) Hardware Platform

The open hardware platform for high performance has evolved continuously in the order of PC-104, COM EXPRESS, VME (Versa Module Europa), cPCI, ATCA (Advanced Telecommunications Computing Architecture), and MicroTCA (Micro Telecommunications Computing Architecture). With each generation, stability and performance have increased proportionally. The ongoing development of the 4GSR control system is focused on TCA family platforms, which belong to the high-performance area.

The most recent MicroTCA was officially introduced by PICMG (PCI Industrial Computer Manufacturers Group) in 2010. While MicroTCA cannot accommodate more I/O configurations than the previously used ATCA due to space issues, it is a highly energy-efficient, compact, and economical new modular computer system. MicroTCA incorporates many advantages of ATCA AMC (Advanced Mezzanine Card) and has been designed with reusability in mind to allow previously developed AMC boards to be used within the MicroTCA system.

In high-energy physics, where particle accelerator control systems are studied, MicroTCA.4 has been rapidly adopted and is now used in many areas of science. MicroTCA.4 refers to a more robust version suitable for challenging physical environments and has significantly expanded hardware standards through its own version management of the hardware platform. The key benefits of the TCA family hardware platform that the 4GSR control group aims to use are as follows:

<Table 2.1.13.9> MicroTCA key benefits and feature

MicroTCA Key Benefits and Features
Better signal quality than VME and CPCI
Better flexibility and scalability than VME and CPCI, addressing low-cost, mid-range, and high-performance applications
Support for Rear Transition Module
Best mixture of state-of-the-art interfaces like PCIe, SRIO, Gbe, XAUI
Re-use of modules like IP (Industrial Pack), PMC, and others
Carriers for XMC, FMC, and other new module standards
Competitive with industrial PC technology and small form factors
Definition of different levels of ruggedization from "no" to "full"
Redundancy built into the standard, no longer proprietary
Built-in error detection, isolation, and protection

(3) Design of Central Operation Room

The central operation room of the 4GSR serves as a comprehensive monitoring and control room, equipped with the IT and network infrastructure necessary for the operation and beam diagnostics of the accelerator. In the central operation room, all signals related to the 4GSR accelerator can be monitored, and the devices that comprise the accelerator should be controllable.

○ Configuration of the central operation room environment

The central operation room is designed as a place where shift operators operate and monitor the accelerator around the clock, focusing on ergonomic conditions. The environment in the central operation room should minimize environmental factors that impair the operators' judgment and provide a setting that satisfies operational efficiency, convenience, and comfort.

① Display wall

To use the display wall more efficiently, a hardware-based video matrix switch or software-based screen transition solutions will be employed to create a diverse and flexible system.

② Operation interface

The configuration of Operator Interface PCs and the network should proceed in the central operation room so that the operators can monitor and control the accelerator's operational status.

③ Server room

The server room for the 4GSR integrated control system is where the backbone switch of the control network operates, and the storage system that holds data generated through the operation of the accelerator and the control devices for the accelerator are stored. The control server room is a restricted access area accessible only to authorized personnel. For the estimation of the 4GSR control system scale, the EPICS system size of the currently operating PLS-II was examined, and a relative scale for the 4GSR was derived.

<Table 2.1.13.10> Summary of the PLS-II EPICS system

Object	Count
Server EPICS	10
IOCs	about 350
Database	1
Process Variables (PV)	about 40,000
PV Archived	4,969
GUI Pannels	18

The PLS-II storage ring has 12 cells. For the scale estimation of the 4GSR system with 28 cells, the increase in the number of signals due to the advancement of digital controllers is considered, leading to a scale estimation of 2.5 times that of PLS-II. The integrated control system of 4GSR is estimated to have approximately 875 IOCs and 100,000 PVs. However, since 4GSR is a complex accelerator, its complexity will directly affect the number of I/Os, and the impact of technological advancements should also be considered. Introducing new technologies may require additional monitoring systems for more precise control.

For reference, similar fourth-generation synchrotron accelerators handle more IOCs and PVs; NSLS-II has more than 1,000,000, Sirius has more than 500,000, and ESRF-EBS has more than 1,500,000 EPICS PVs. It is also necessary to build a server system that matches the scale, considering future upgrades and expansions.

The estimation for the servers required for the minimum system setup in the 4GSR control system is shown in <Table 2.1.1.27> below.

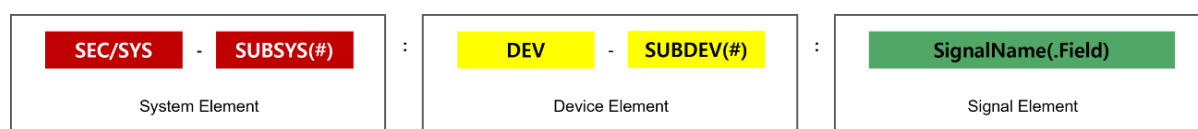
<Table 2.1.13.11> Servers required in the 4GSR

Server	Description	Quantity	Note
Storage System	Centralized EPICS data storage	1	- 100TB useable for 5 years - Flash Disk
	-EPICS control & data monitoring -Expected signal: 50k or more -Expected data rate: 20 TB/y -9 months online - 5 years archive - Older data on tape		
	Centralized experimental data storage for DAQ	1	- 120 TB useable for 1 month (15.6 kHz)
	-Beam diagnostics and experiment data -BPM data rate (15.6kHz) -BPM data rate (375kHz) -9 months online - 1 month archive - Older data on tape – <i>undecided</i>		- 2 PB useable for 1 month (375 kHz) - Flash Disk
Backup Storage System	Backup storage based on data backup policy	1	- SATA Disk
CA Gateway	Configuration of OPI and control network's channel access connection	6	- Workstation level - Failover
Archiver Appliance	EPICS PV signal archiving to the storage system	2	- 2 TB useable RAM disk for short-term storage
WebOPI	EPICS signal monitoring and web-based summary of experimental data without setting the EPICS environment	2	- Server level
EPICS Extension	Management of channel finder and other extensions that users can use to easily search EPICS PVs using Elasticsearch	8	- Server level
Logbook	Log creation to record accelerator operation status or notable matters.	3	- Server level
Alarm	Alarm Event sever for EPICS signals	3	- Workstation level
EPICS IOCs	Soft IOC server for the 4GSR operation	12	- Server level
Database	Archiver metadata and operation data	2	- Server level
Boot	The TFTP (Trivial File Transfer Protocol) server for booting the accelerator's embedded devices	3	- Server level
Control Development	Program development and test server	3	- Server level
Device Monitoring	Accelerator devices monitoring server	3	- Server level

(4) Naming Convention

The naming convention of the 4GSR control system is a set of rules for naming signals and devices to control the entire accelerator and monitor signals. The 4GSR control system can be organized and integrated by adopting a naming convention across all subsystems. With an efficient naming system, it is possible to recognize quickly such information as what the signal is, where it is located, and which device it is associated with. All signals should be given unique names to prevent confusion and conflicts. In particular, the uniqueness of control system signals on the EPICS middleware is a strict requirement.

The following naming convention for the 4GSR may be modified through discussions between groups. In the EPICS-based control system, signals are represented as Process Variables (PVs), and the names determined by the naming convention will be used across all areas, including the UI, software, and database for the 4GSR.



<Figure 2.1.13.20> Naming convention of 4GSR EPICS PV.

The above diagram shows three elements (System, Device, and Signal) for assigning unique names to signals, with each element separated by a colon (:). The System and Device may also have sub-Systems and sub-Devices. The naming rules for each element are as follows:

SEC/SYS: Naming for zones or Systems

SUBSYS: Naming for sub-Systems

DEV: Naming for Devices

SUBDEV: Naming for sub-Devices

: Naming for sub-Device numbering

Signal Name: Naming for signals

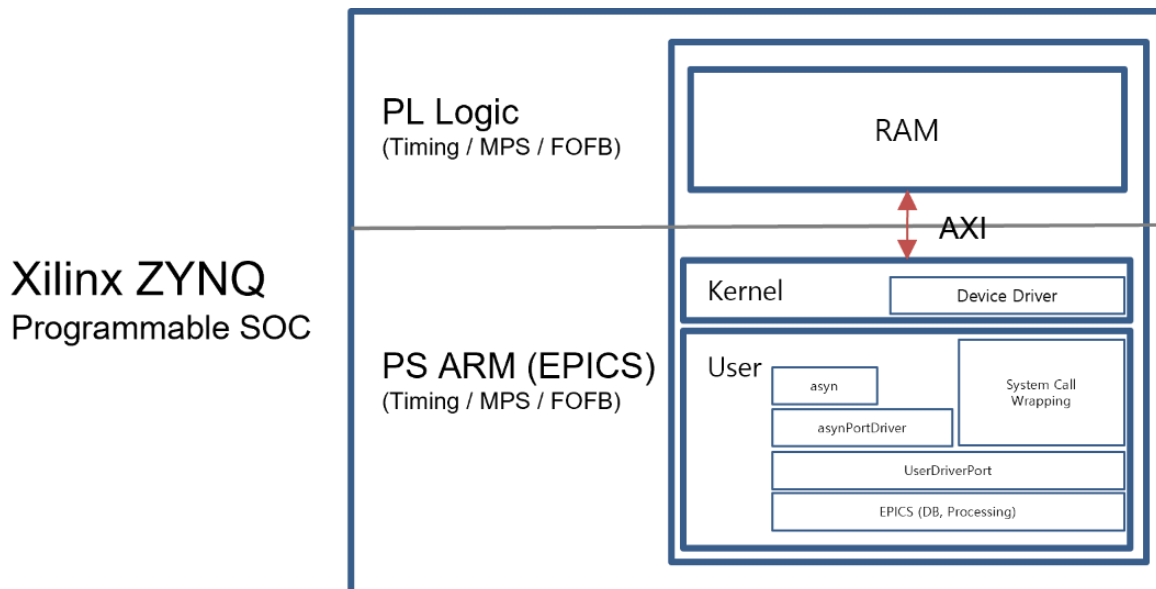
Field: Naming for PV field name

(Based on the naming rules defined in EPICS Record, the user cannot define it.)

Another important aspect of the defined naming convention is that it maximizes software reusability for systems that repeat for each accelerator lattice cell. Unique names are assigned based on their unique System and Device names to signal names that repeat by section, Cell1, Cell2, and the software that composes the corresponding I/O signals is structured through macro definitions.

G. Core control system

The core control system of the integrated control system utilizes FPGA to minimize overhead and network latency in real-time control systems. Xilinx's ZYNQ SoC, an integrated chip of an FPGA with ARM cores, is used after mounting an operating system on the FPGA chip. Employing Peta Linux to load the Linux kernel here can create the basic Linux device driver code from the synthesized bitstream developed using FPGA HDL.



<Figure 2.1.13.21> Development using ZYNQ SoC.

Developing a SoC (System on Chip) for high-speed control is divided into the PL (Programmable Logic) and PS (Processing System) regions. The PS region, which mounts an ARM CPU, requires the Linux operating system to be ported, and the EPICS middleware is applied after cross-compile. In the PL region, The FPGA critical logic should be executed.

The PS region builds the Linux kernel in the ARM core most commonly used in embedded systems. The EPICS middleware should be built using the GNU toolchain on the Linux OS. After building the EPICS middleware, the EPICS asynchronous libraries should be standardized, and the interface should be established through the FPGA firmware and the

system calls. After the development of an interface module with FPGA entering Linux kernel space in the Linux user space, the EPICS interface module should be developed using the system calls of the user space and the EPICS asynchronous libraries.

The update of the FPGA-based high-speed control system is carried out using TFTP (Trivial File Transfer Protocol), providing a fast and efficient method for transmitting firmware and configuration files. A TFTP server is set up on the network within the integrated control system, and the latest firmware and configuration files are uploaded to the server. After that, the network settings of the FPGA controller are configured. On lower-level FPGAs, a TFTP client is implemented via a processor or embedded software. The FPGA controller need to be connected to the TFTP server to request and receive the necessary files. The integrity of the received files is verified through checksums, and the verified files are loaded onto the FPGA and applied. When necessary, the FPGA is rebooted to activate the new firmware.

This update method using TFTP is straightforward and enables reliable and efficient updates in FPGA-based high-speed control systems through its fast transmission speed and standardized support.

(1) Event Timing System

The event timing system refers to a system that coordinates and synchronizes events in a precise order over time. This system provides precise timing to local devices installed in the 4GSR. The system consists of one Event Master (EVM), multiple Event Fanouts (EVF), and multiple Event Receivers (EVR), as shown in the figure below. Each local device receives event, trigger, and time stamp information from the EVR. The event timing signals provided to the local devices are TTL or optical signals. If the local device receives an event as an optical signal, the local device receives both the event information and the time stamp. However, the EVR must be embedded in the local device. A protocol developed by Micro Research Finland (MRF) is used to facilitate the configuration of local devices with built-in EVR. This protocol allows the use of EVR FPGA IP function and the functions within commercial equipment (e.g., I-Tech Libera Brilliance + BPM).

The event system will be configured based on the mTCA.4 form factor. The figure below shows an example of an EVR configured using the mTCA.4 infrastructure. This configuration requires CPU, MCH, Chassis, and Power designed according to the mTCA.4 form factor. Also, optical and coaxial cables should be installed for the overall system

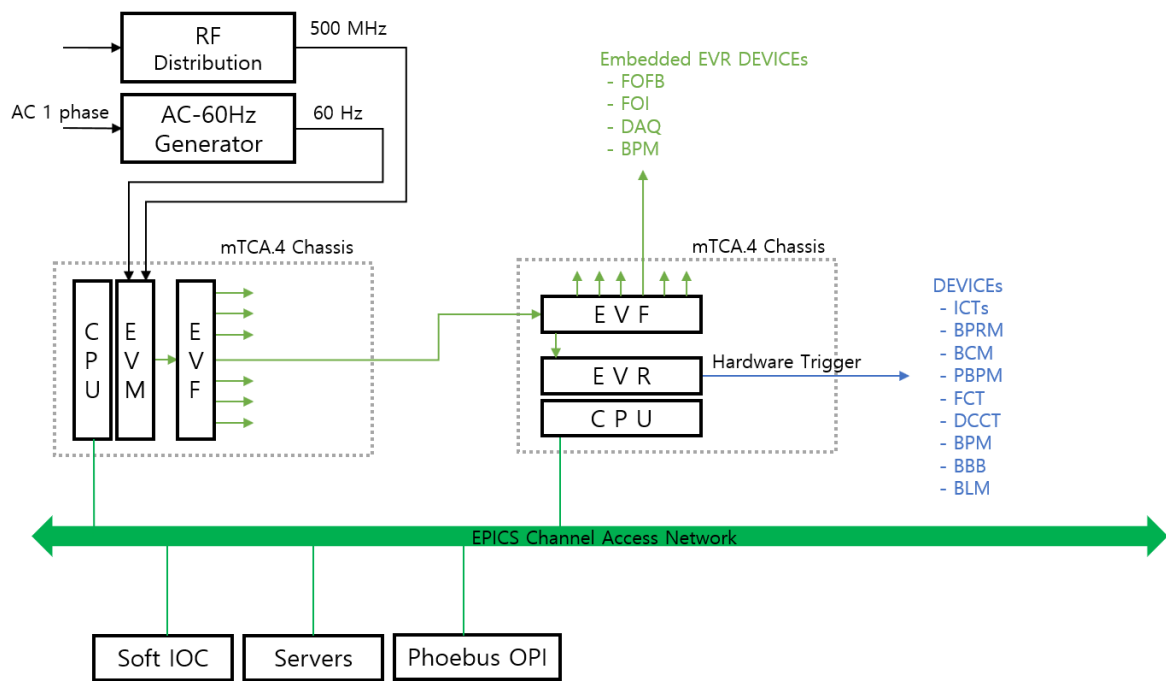
configuration.



<Figure 2.1.13.22> An example event timing system configured using mTCA.4 infrastructure.

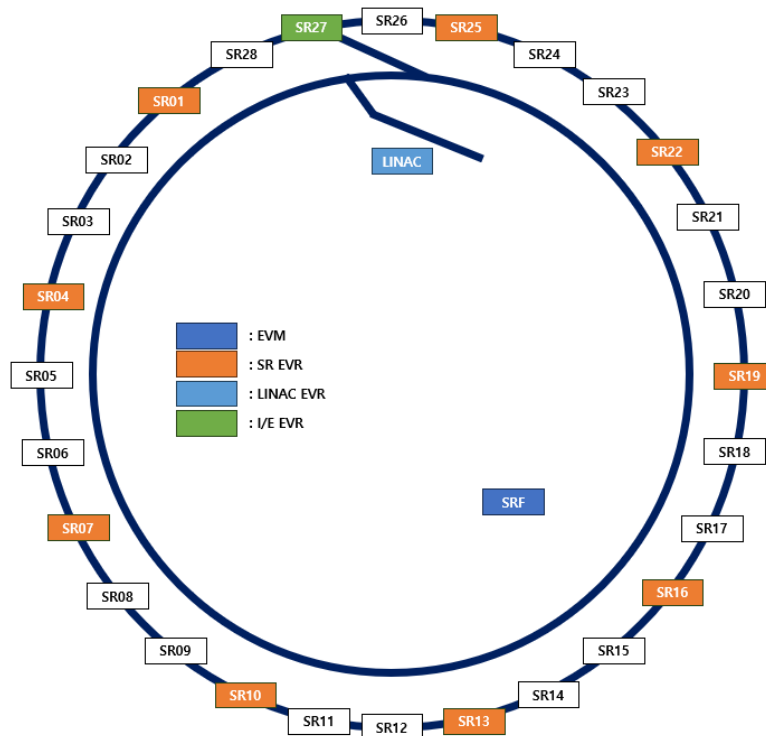
○ Placement of EVM, EVF, and EVR

The event timing system operates with clock synchronization. Clock synchronization is crucial in securing the reliability and accuracy of the entire system by synchronizing events across multiple EVRs and accurately coordinating data communication and control actions. The Master Oscillator provides these clock synchronization signals. Therefore, the EVM should be located close to the Master Oscillator. The EVM also operates by synchronizing the RF clock provided by the Master Oscillator and the AC phase 1 signal. The AC 60 Hz is generated based on the zero-cross point, which is the most phase-stable region of the AC phase 1 signal, and this signal is provided to the EVM. The events synchronized with AC phase 1 are transmitted to multiple EVRs through the EVF. Therefore, multiple EVMFs (Event Master's Fanout) are installed in the mTCA where the EVM is located, and the output signals of the EVMFs are connected to multiple EVRFs (Event Receiver's Fanout) installed in the storage ring. The figure below shows a detailed block diagram showing the EVM configuration and how local devices with built-in EVRs and EVRs composed of mTCA.4 are connected to EVRFs. Devices with built-in EVRs receive events and implement their own trigger functions, while devices without built-in EVRs are provided with hardware trigger signals from mTCA.4.



<Figure 2.1.13.23> Detailed block diagram of the event timing system.

One or more EVR and EVF modules should be installed per mTCA.4 chassis to reduce over-installation of mTCA.4 chassis and unnecessary elements or costs. Also, they should be appropriately placed to prevent the possible transmission loss and reflections caused by the increased length of the trigger output signal cable. Accordingly, the cable should provide low loss and excellent signal quality. The linear accelerator (LINAC) has a total length of 50M. One set of LINAC EVR is installed in the LINAC center to provide signals from the e-gun to the LINAC kicker. Storage ring (SR) has 28 cells with a length of 28 meters per cell. EVRs are installed in every 3 cells in their center to provide signals to the left and right cells. Therefore, there are a total of 9 sets of mTCA.4 chassis in the storage ring. The remaining cell of the SR is where LTB and BTS meet, and 1 set of I/E EVR (Injection/Extraction EVR) is installed in the cell. The figure below shows the overall layout of the event timing system.



<Figure 2.1.13.24> The overall layout of the event timing system.

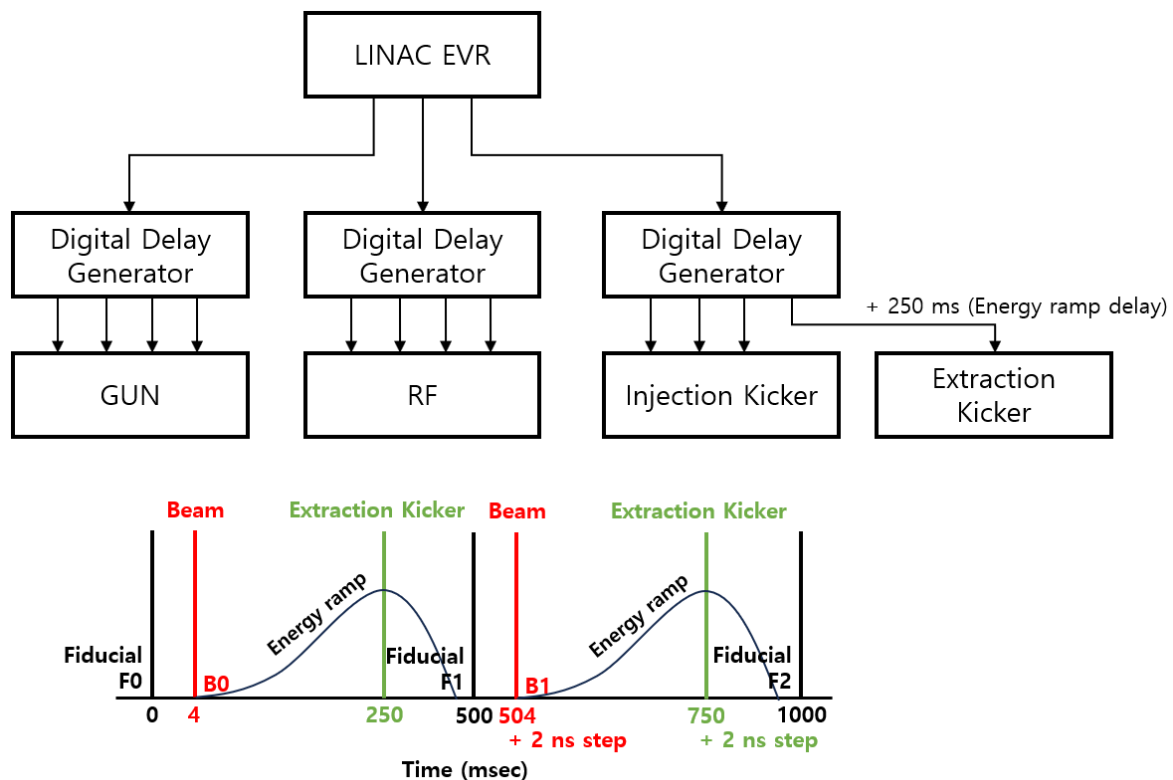
○ Event Types and Timing

LINAC & KICKER: A 2 Hz trigger signal is provided to all devices in the LINAC section to match the electron-beam drive repetition rate. The Klystron should be operated in the section with the highest AC voltage for efficient operation. Therefore, the beam generation should be delayed approximately 4 ms from the AC 60 Hz zero cross. The generated beam passes through the booster ring and enters the buckets of the storage ring. Tuning the delay to the RF frequency to ensure that the electron bunches fall into the desired buckets is a critical step in accelerator operation and one of the key roles of the event timing system. The delay resolution of 2 ns is required to match the spacing between the buckets in the storage ring, which is achieved by using the DG645, a precision digital delay generator. The four output signals of the DG645 are used to provide triggers for the injection and extraction kickers. The event timing system, LINAC EVR, provides timing signals to the DG645 and provides software tools to design bucket injection patterns.

Booster & Storage Ring: The 200 MeV electron beam generated by the LINAC is ramped in the booster ring to a beam energy of 4 GeV. The ramp-up time is expected to be about

250 ms. Once the ramp-up is complete, the extraction timing is generated to inject the beam into the storage ring buckets. The revolution clock, the time it takes to make one revolution within the storage ring, requires precise timing to maintain the high energy and stability of the storage ring. The event timing system provides revolution clock timing for each harmonic number of the booster and storage ring (booster: 387.88 kHz, storage ring: 375.07 kHz). It also provides 10 Hz timing for data acquisition and experimental control.

The figure below illustrates the block diagram and timeline for injecting electrons into buckets in 2 ns steps. The LINAC EVR provides timing signals to each of the precision delay generators, the precision delay generators adjust the LINAC delays to match the injection pattern into buckets, and the output signal for the Extraction Kicker adds a delay equal to the energy ramping time. This format allows beams generated in 2 Hz cycles to be injected into different buckets. The GUN and RF should have different event codes so that they can be operated separately from the beam. The energy ramping delay is adjusted in the precision delay generator associated with the Extraction Kicker.



<Figure 2.1.13.25> LINAC EVR block diagram and Injection / Extraction timeline.

The 4GSR timing system has been decided to adopt the Micro Research Finland (MRF) product. Many accelerator facilities worldwide use MRF products, and the decision was

made to adopt the mTCA platform, which has better specifications and performance than the old VME platform. The mTCA can support software development and system integration and precisely tune the output signal delay of the EVR firmware. To enable precise delay control, the UNIV-TTL-DLY module can be utilized to optimize the clock and timing management of the system. Also, delay drift occurs when transmitting signals over optical cables due to the length deviations of optical cables or temperature changes. To compensate for this, fine-tuning is required, which is a method to adjust the delay time for events to travel back and forth from the EVM to the local device. To use the delay compensation feature that measures and compensates for delay drift, the fanout connecting the EVM and local devices also needs a delay compensation feature. So, developing a fanout module is considered.

The existing mTCA-based fanout module is inefficient for 4GSR because it only has seven SFP transceiver ports, while the new timing system has a built-in EVR, which requires many ports. Therefore, the fanout module is unfavorable to the timing system in terms of structure and cost. That is why developing an mTCA-based or standalone fanout module is considered.

(2) Fast Orbit Feedback System

The FOFB (Fast Orbit Feedback) system is designed to effectively attenuate noise and vibrations that impact the electron beam orbit in the storage ring, ensuring a stable beam orbit in a synchrotron radiation source. The 4GSR storage ring comprises 28 cells, each equipped with 10 Beam Position Monitors (BPMs) and 10 correctors. The FOFB system uses 8 BPMs and 4 correctors (vertical and horizontal combined) in each cell, excluding 2 slow BPMs and 6 slow correctors.

○ Key Components and Functionality

- **BPMs and Correctors:** The BPMs continuously monitor the beam position while the correctors adjust the beam's trajectory to maintain a stable orbit. Using high-speed data from the BPMs, the correctors make real-time adjustments to correct any deviations caused by noise or vibrations.
- **FPGA-Based Low-Latency System:** The core of the FOFB system is a low-latency, firmware-based setup built on FPGA technology. This setup allows for high-performance parallel processing, essential for real-time noise and vibration suppression in the storage ring. The FPGA's ability to rapidly process data and

execute corrective actions is crucial for maintaining beam stability.

○ **Network Design for FOFB**

- **Dedicated Network:** For the stability and reliability of the FOFB system, a dedicated network is designed to facilitate the transmission and reception of data with minimal errors. This network is optimized for low latency and high throughput, which are critical for the real-time operation of the FOFB system.
- **Redundancy and Reliability:** The communication links within the FOFB network are configured with redundancy and reliability in mind. Redundant links help prevent data loss and ensure continuous operation even when one part of the network fails. This design ensures that the system can process and respond to data in real-time, which is essential for effectively suppressing disturbances in the electron beam.

The integration of FPGA technology with a robust, dedicated network enables the FOFB system to maintain a stable beam orbit by quickly responding to and correcting any disturbances, thus ensuring the reliable operation of the synchrotron radiation facility.

○ **Hardware**

The FOFB system is a critical system that requires high-speed computational performance and stability. This system is implemented using FPGA technology with an MPSoC (Multi-Processor System on Chip) architecture. MPSoC is divided into two main components: the PS (Processing System) and the PL (Programmable Logic).

- **PS (Processing System)**

The PS section is designed to run a Linux operating system and an EPICS IOC. This part manages the system at a high level and is in charge of communications. It interacts with the reliable operating system and EPICS IOC to process user commands through them.

- **PL (Programmable Logic)**

The PL section handles the core functions of the controller and is where firmware is executed for data computation and processing. It functions in real time. It is critical for the system's real-time response and data handling capability.

○ **Communication and interfaces**

Communication between the PS and PL is facilitated by the AMBA (Advanced

Microcontroller Bus Architecture) bus, with different ports designed for specific purposes:

- GP (General Purpose) Port: Used for general-purpose data transmission, allowing for a wide range of data to be sent and received.
- HP (High Performance) Port: Provides a high bandwidth, low latency interface for high-performance data transmission.
- ACP (Accelerator Coherency Port): Manages data coherency between firmware and memory, ensuring consistent data handling.

Within the PL, the primary communication protocols used are AXI (Advanced eXtensible Interface) and AXIS (AXI Stream):

- AXI Protocol: Suitable for large-scale data transmission, operating in burst mode based on memory addresses. This is ideal for transmitting large volumes of data, such as the response matrix, between components like BRAM (Block Random Access Memory) and DDR RAM.
- AXIS Protocol: Designed for streaming data processing, utilizing channels such as Tready, Tdata, and Tvalid for data streaming. This protocol is ideal for real-time computation and can be used for internal communication within FPGA logic, minimizing the latency of the FOFB controller.

○ **High-Speed Communication**

The system employs SFP+ ports capable of handling bandwidths up to 16 Gb/s to ensure high-speed or low-latency communication. Data communication with the BPM electronics supports serial communication through optical media, while communication with the fast MPSs (Magnet Power Supply) supports gigabit-speed connections. An RJ45 port enables independent EPICS IOC communications via the Linux operating system within the PS section.

This carefully designed structure and use of specific communication protocols make sure that the FOFB controller is both stable and high-performing, capable of reliable data processing and real-time operation. The system architecture supports the effective mitigation of disturbances in the electron beam orbit, contributing to the overall stability and reliability of the synchrotron radiation facility.

○ **FOFB System Network**

The control network for the FOFB system is composed of three main networks in order

The FOFB dedicated network is employed for the controllers to send and receive beam position and status information. This data communication must support high-speed communication using fast and reliable fiber optic communication. Its sub-networks enable connections to BPM electronics and fast Magnet Power Supply. The event timing network is used to synchronize the FOFB controllers. It receives timing and trigger information to enable precise synchronization among all FOFB controllers.

The diagram illustrates the EPICS CA Network architecture. At the top, three horizontal lines represent the **FOFB Network** (purple), **Timing Network** (yellow), and **EPICS CA Network** (blue). Below these, three **FOFB Controller** units are shown, labeled **#N-1**, **#N**, and **#N+1**. Each controller is connected to the three networks via multiple lines. Below controller **#N-1** is a dashed box containing **BPM Electronics**. Below controller **#N** is a dashed box containing four **Fast MPS (H)** modules and four **Fast MPS (V)** modules. Below controller **#N+1** is a dashed box containing four **Fast MPS (V)** modules. Arrows indicate data flow: blue arrows for EPICS CA Network, yellow arrows for Timing Network, and purple arrows for FOFB Network. A specific connection labeled **Aurora 8b10b** is shown between the BPM Electronics and the Fast MPS modules. A **UDP/IP** connection is also shown between controllers **#N** and **#N+1**.

① FOFB Network

2 - 469

support reliable and high-speed optical communication, satisfying the data transmission requirements of the FOFB system. LC-type connectors provide small size and high performance, maintaining the reliability and performance of the fiber optic network.

The FOFB network sends the measured beam position values received from other FOFB controllers placed over the storage ring. This process allows all controllers to share the beam position measurement values of the 28 cells.

② Event Timing Network

The FOFB controllers are distributed across the 28 cells of the storage ring. Since a master-slave structure is not adopted, global synchronization within the entire system is essential. To achieve this, they receive various information necessary for synchronization from the Event Timing System. This information includes the revolution clock, trigger, and timestamp.

Achieving global synchronization requires a dedicated event timing network that provides reliable communication to each controller. Each FOFB controller can maintain synchronization using accurate timing information obtained through this network.

To accomplish this goal, it is necessary to implement an embedded EVR (Event Receiver) function. This function allows the controllers to synchronize at the correct time.

③ EPICS Network

The EPICS network runs EPICS IOC for the control within the FOFB controllers. Unlike the dedicated FOFB network, users transmit and receive data through the EPICS network to issue commands or monitor measured data.

④ BPM Electronics Network

The BPM electronics use the same multimode optical fiber cables as in the FOFB network, to transmit measured beam positions to the FOFB controllers via serial communication. The FOFB controllers are assigned two SFP+ ports and receive measured beam positions from four BPMs through a port.

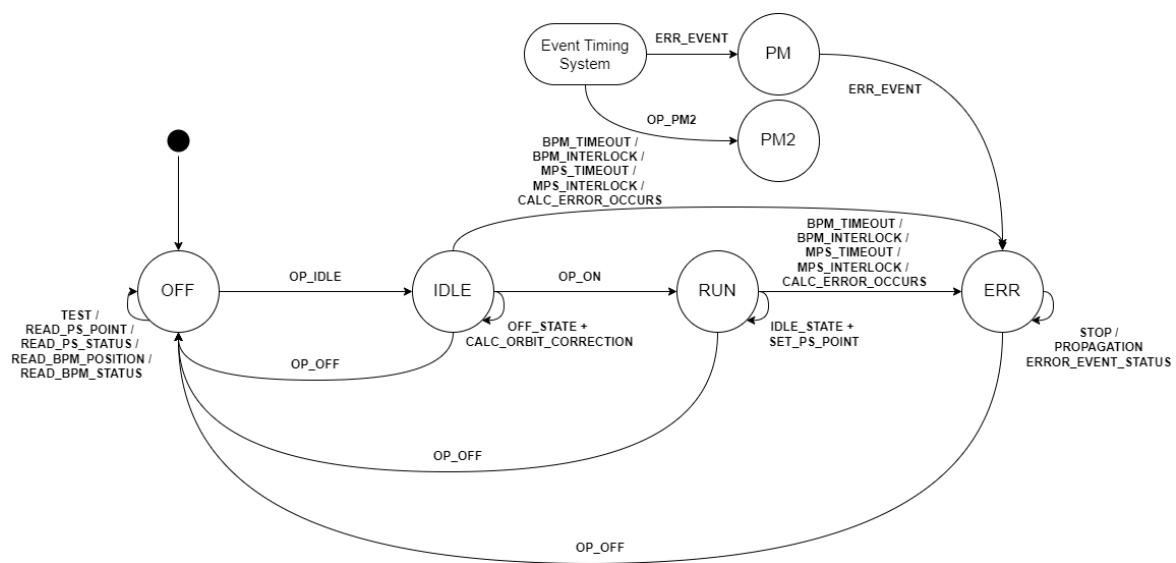
⑤ Fast Magnet Power Supply Network

The fast Magnet Power Supply was designed based on the UDP/IP protocol, which uses Ethernet protocols. Since the UDP/IP protocol supports high performance and reliable communication, it is suitable for power devices. Also, 8b/10b or 64b/66b protocols can be

used for low latency. Four fast Magnet Power Supplies for horizontal orbit correction and four fast Magnet Power Supplies for vertical orbit correction are placed in each cell of the storage ring. These power supplies can be connected in a daisy chain to enhance data transmission and efficiency. Therefore, stable communications between the FOFB controllers and fast Magnet Power Supplies should be ensured.

(3) FOFB Controller's States and Transition Diagram

The FOFB controller has six states and state transitions, as outlined below, to ensure accurate system operations and prevent unintended exceptions. The FOFB controllers strictly manage the state transitions to maintain system stability.



<Figure 2.1.13.27> FOFB controller's state transition diagram.

① OFF Mode

The OFF mode is designed to operate in a test mode for various purposes. In addition, it will continuously receive the status and read points from the fast Magnet Power Supplies to verify their proper operations. Similarly, the BPM electronics will be kept in a standby state, allowing the FOFB controllers to continuously receive the BPM status and current beam position information and comprehend information about surrounding devices before the FOFB system is activated.

② IDLE Mode

The IDLE mode builds on the operations of the OFF mode by utilizing beam position information to check for orbit correction. This mode serves to verify whether the entire FOFB system is ready to operate by checking the global synchronization status between the

BPM electronics and the FOFB controllers and ensuring that the orbit correction values are calculated correctly to confirm the fast Magnet Power Supplies set point. If any calculation errors or interlocks from other devices occur, the system transitions to the ERR mode.

③ RUN Mode

The RUN mode sends the calculated set points to the fast Magnet Power Supplies in addition to the functions and operations of the OFF and IDLE modes. This marks the transition to a state where the FOFB system operates normally. As feedback operates correctly, any operational errors or status information from other devices are monitored at this stage.

④ ERR Mode

The ERR mode is activated when an error is received from the calculation results or other devices, causing the feedback to stop. At this point, all FOFB controllers receive information about the controllers that have entered ERR mode via the FOFB network and transition to the ERR mode. The error information is provided as control data through the EPICS network so that users can identify the cause of the issue.

⑤ PM (Postmortem) Mode

The PM mode transitions to the ERR mode when the controller receives a PM event code from the event timing system. PM responds to an interlock signal from events outside the FOFB system, such as beam dumps. In this case, while the FOFB controllers are performing feedback, they store data related to the PM event to help identify the cause. When a PM event is received, information such as beam position or correction details can be checked through the EPICS network.

⑥ PM2 (Postmortem 2) Mode

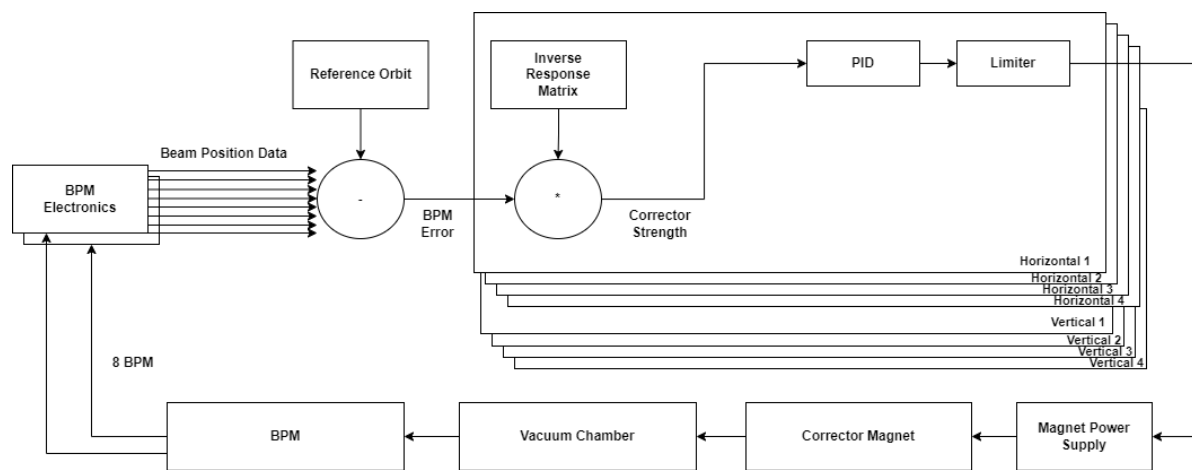
The PM2 mode generates events from the event timing system when users want to check the data in the PM buffer. This mode is used for checking the data accumulated in the buffer without transitioning to the ERR mode, while feedback operations can continue uninterrupted.

(4) FOFB Calculation

The FOFB calculation should meet real-time processing requirements and use parallel processing to minimize latency. Also, to handle potential additional delays, such as internal

jitter or uncertain situations in the firmware, it is essential to secure approximately 10 to 15% of leeway from the target time.

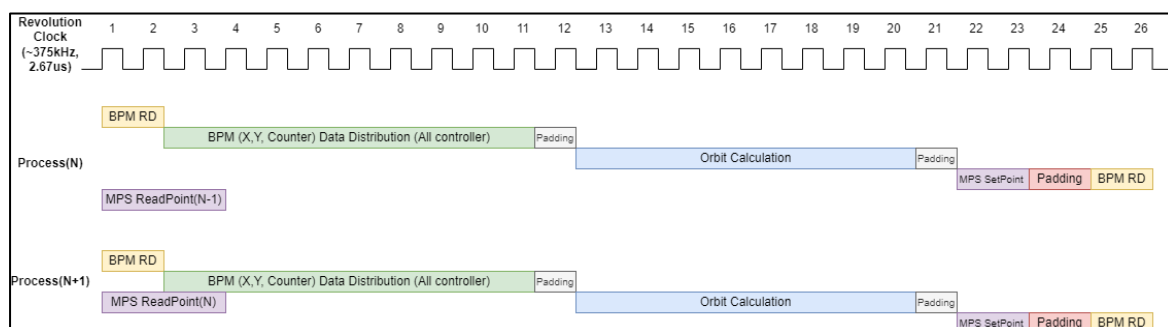
In the first step of the calculation, the beam position data obtained from the BPM electronics is processed to determine the beam's position, and the BPM error is obtained. In the second step, corrector strengths are calculated using the BPM errors and the IRM (Inverse Response Matrix). In the final step, the corrector strengths are processed, passing through a digital filter and a PID (Proportional-Integral-Derivative) control algorithm. After obtaining the outcome data, the minimum and maximum current values are checked by a limiter to derive the final setpoint values, which are then transmitted to the fast Magnet Power Supplies to control the beam position.



<Figure 2.1.13.28> FOFB flow chart.

○ FOFB timeline

The FOFB operates at 375 kHz, the storage ring revolution clock, with the goal of executing all FOFB tasks within 22 clock cycles. Satisfying the repetition rate of 15.6 kHz (approximately 64 microseconds) requires completing all FOFB tasks within 22 clock cycles (approximately 56 microseconds).



<Figure 2.1.13.29> FOFB timeline.

The operation of the FOFB system is represented by <Figure 2.1.1.23>, and the data processing procedure for each task is as follows:

○ **BPM Data Reading (BPM RD)**

The BPM data reading begins at the first rising edge of the clock signal (Clock N), where the system collects BPM data, including X and Y coordinates and Counter values.

○ **BPM Data Distribution (BPM (X, Y, Counter) Data Distribution)**

After collecting the BPM data, data distribution starts. All controllers receive the latest BPM data to synchronize the system.

○ **Padding**

Following data distribution, the system undergoes a padding period for several clock cycles. This padding reflects delays between data processing steps, ensuring the system can smoothly transition to the next step. The padding duration is measured in clock cycles and can be adjusted by system requirements.

○ **Orbit Calculation**

After the padding ends, the orbit calculation begins. This phase involves calculating the appropriate Magnet Power Supply setting values for feedback purposes in real-time based on the collected BPM data.

○ **Padding**

After the orbit calculation, there is another padding period of a few clock cycles. This padding prepares for the delay between the orbit calculation and the next phase.

○ **Magnet Power Supply Setpoint**

Following the padding time, the Magnet Power Supply setpoint is adjusted at the rising edge of the next clock signal. This adjustment synchronizes the Magnet Power Supply setpoint based on the calculated values.

○ **Padding**

After the Magnet Power Supply Setpoint adjustment, there is another padding period for a few clock cycles. This padding prepares for the delay between the setpoint adjustment and the next step.

○ BPM Data Reading (BPM RD)

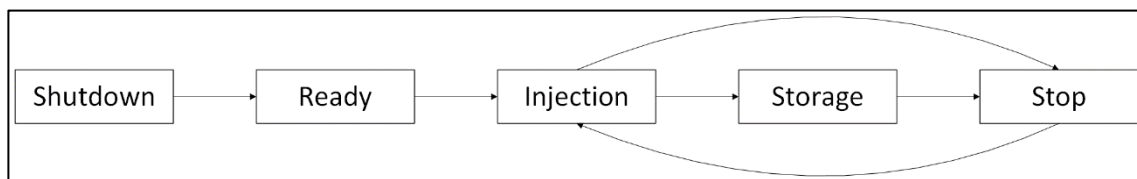
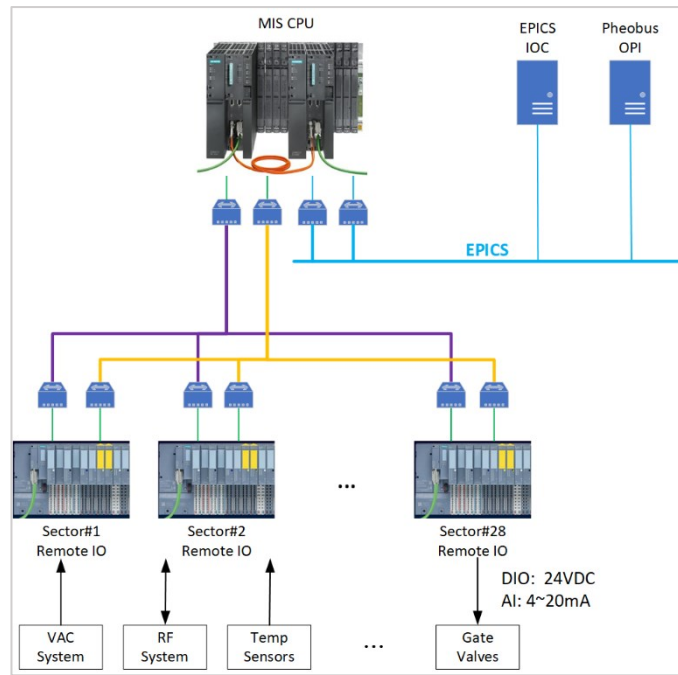
Finally, at the rising edge of the next clock signal (Clock N+1), the system reads the BPM data again. After that, it is identical to the first BPM RD. This step is repeated periodically to ensure continuous data collection by the system.

(5) Machine Protection system

Machine Interlock System

Machine Interlock System

MIS (Machine Interlock System) is a system that prevents operations that may cause harm to related devices when a malfunction or a harmful situation occurs in each device configured throughout the accelerator during accelerator operation. It is an essential element of accelerator operation. MIS is classified by area, level, and device according to each accelerator operation policy and aims to protect each device. In the MPS (Machine Protection System), MIS mainly covers signals with relatively slow response speeds and low importance among various classifications of signals. For signals generated by an interlock situation, which are recognized by the central device from local devices and transmitted to the final destination, differences in speed exist depending on the route. However, MIS is designed with minimized signal routes so that the difference in speed by signal will be minimal. The controller of MIS is a PLC (Programmable Logic Controller), which is widely used in various fields of industry and experimental physics. Since various PLC guidelines are provided for securing system reliability and responding to failures, configuring a more robust system is more accessible with PLC than with other types of controllers. MIS is basically configured to ensure high availability by considering device failure situations (PLC product failure, power outage, etc.). In addition, a high-reliability design is essential, considering the safety and reliability of the data. The connection between the Central and Local PLC uses industrial Ethernet protocols such as Profinet to intimately exchange data. It also features the ability to provide services for users by linking with EPICS IOC.



The figure above illustrates the sequence of MIS in the early stage. This sequence, once the accelerator operation scenario is finalized, will be thoroughly supplemented to align with the operation scenario.

- **Shutdown:** MIS-off state. This state indicates that MIS undergoes regular maintenance or the whole accelerator undergoes long-term maintenance.
- **Ready:** Standby state before MIS execution. In this state, MIS checks whether the MIS controller and each accelerator device are in normal contact.
- **Injection:** This is the state where the electron beam is injected into the storage ring. If a Machine Fault occurs during the injection, Injection mode immediately changes to Beam Dump mode.

- **Storage:** This is the state where the electron beam is stored in the storage ring. Storage mode immediately changes to Beam Dump mode if a Machine Fault occurs during beam storage.
- **Stop:** This is the state where the accelerator is stopped after the electron beam dump. MIS maintains the latch state until the faulted device manager and the operation room confirm. After the device check is completed, Stop mode moves to Injection mode, and the electron beam starts to be injected again.

The above figure briefly shows the relationships between Central MIS, Local MIS, EPICS, and peripheral devices. The MIS PLC of 4GSR is divided into a total of 28 cells, correspondingly to the 28 cells of the 4GSR storage ring, to manage the entire area of the accelerator. A rack is located in each cell to collect signals from peripheral devices and also generate and transmit interlock status. All signals collected/generated through the MIS PLC will be connected to the EPICS network to be displayed in the central operation room, allowing the system users to monitor and command the MIS. MIS is represented in three layers, and each layer is represented as follows.

○ **The Device & System Layer:**

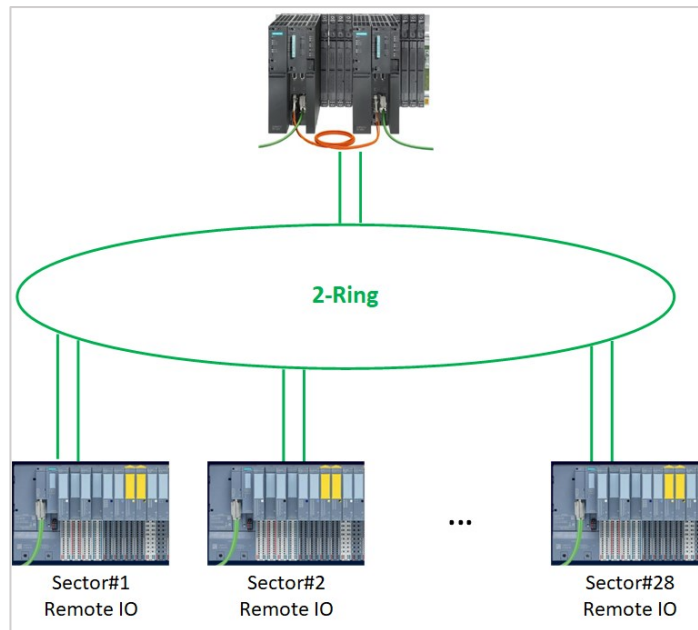
This layer has a protection function for devices related to accelerator operation. It protects itself and transmits the status to other related systems when it detects a problem by watching itself. It also receives interlock signals from related systems for control.

○ **The MIS Local Layer:**

This layer collects status signals provided by devices related to accelerator operation by purpose (area, function) and transmits them to the Central MIS. It also receives the result signals analyzed by the Central MIS and sends them to the Device & Equipment Layer.

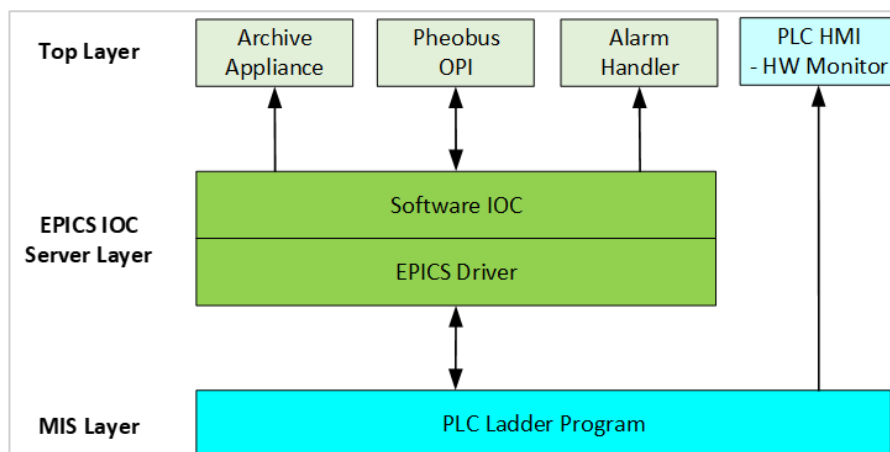
○ **The MIS Central Layer:**

This layer monitors and analyzes collected data by purpose (area, function) to monitor and protect devices.



<Figure 2.1.13.32> MIS ring topology.

The above figure shows the communication topology between PLCs used in MIS. To ensure the high availability and reliability of each MIS, Central MIS is configured by applying redundant CPUs, network redundancy, and power redundancy. Particularly, the communication connections between PLCs are configured in a ring topology so that if a communication failure or hardware failure occurs in any Local PLC, data can be promptly routed through another Local PLC, allowing the Central PLC to make accurate judgments of data. The Central PLC is configured to assess problems immediately and take appropriate actions. All signals from both the Local and Central PLC are connected to the higher-level EPICS Network, enabling communication with the MIS EPICS IOC at remote locations and ultimately providing services to the end-user.



<Figure 2.1.13.33> SW architecture.

The above figure expresses the SW architecture of MIS, showing the relationship between the software used in each layer.

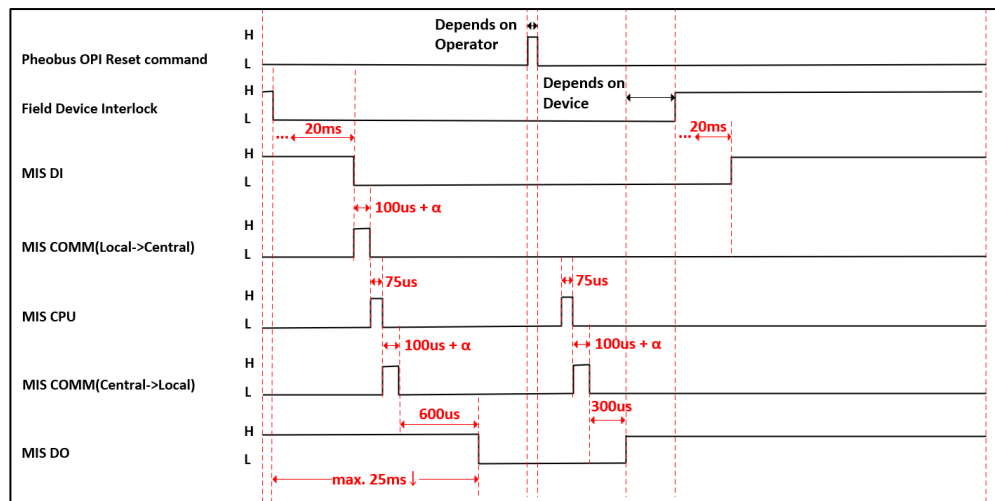
○ Top Layer:

This layer aims to serve users or operators. It is divided into Archive Appliance for data storage, OPI allowing users to monitor and control MIS signals, Alarm Handler expressing the MIS alarm status, and PLC HMI monitoring the MIS PLC status by areas.

○ EPICS IOC Server Layer:

This layer connects the EPICS to the PLC and relays it to the top layer. It enables linking PLC and EPICS through the EPICS Driver and EPICS IOC.

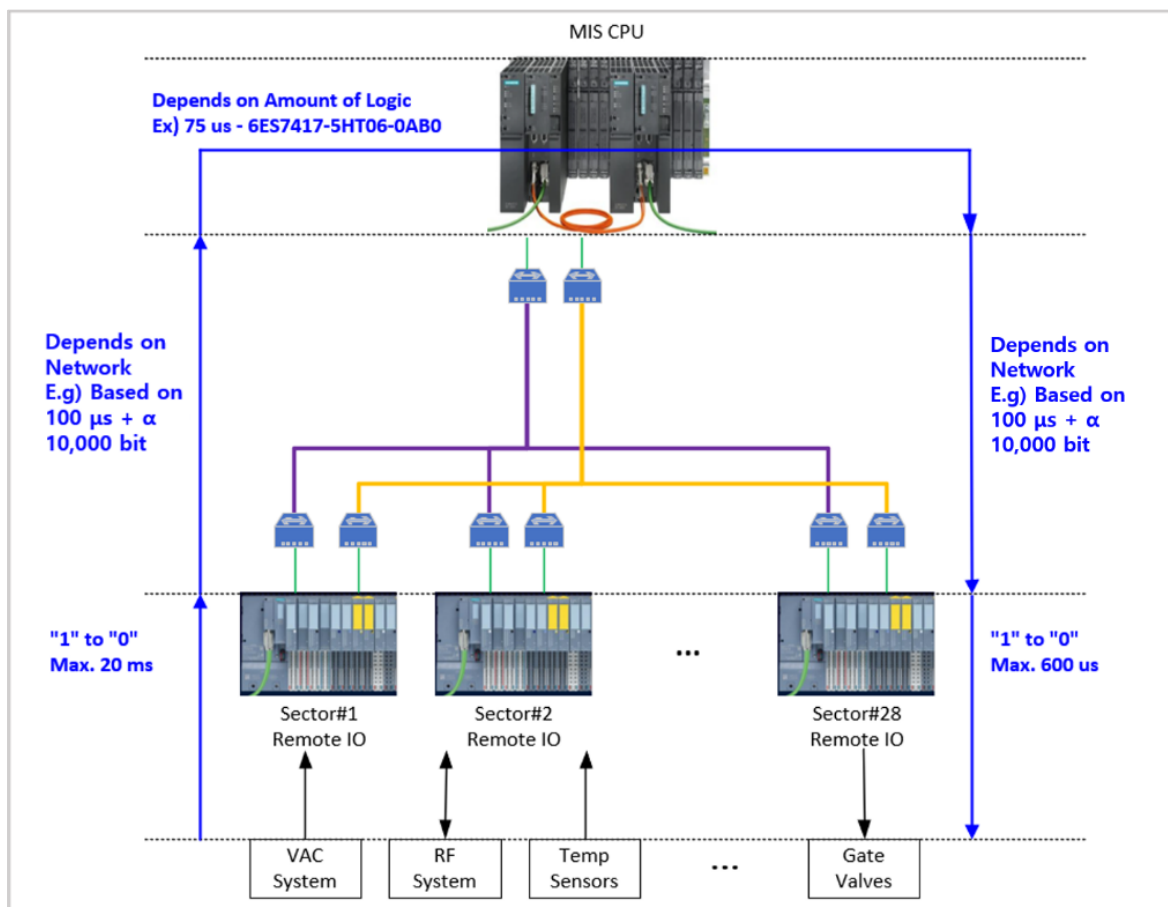
○ MIS Layer:



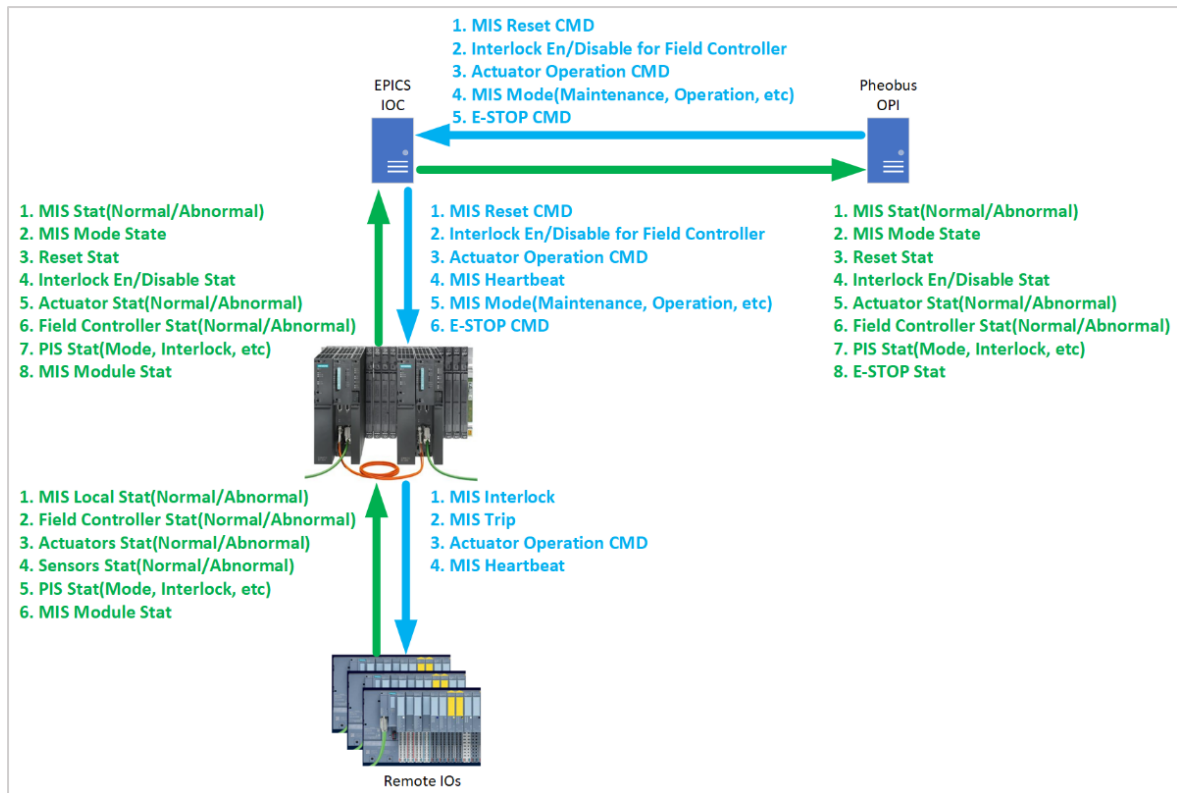
<Figure 2.1.13.34> MIS fault reset commands and fault processing timing.

This layer represents the software layer that contains all PLC Logic of Central/Local MIS. The above figure shows MIS's fault reset commands and fault processing timing. The interlock signals generated from Local PLC and Central PLC should remain in Latch status until the user presses the Reset button to process them. The communication health between MIS EPICS IOC and the Central and Local PLCs should always be checked through data such as Heartbeat. In addition, when linking with systems other than PLC, communication and system health should always be checked through H/W or S/W Heartbeat.

Each Local PLC receives interlock signals generated from local devices through DI or AI cards and outputs the signal values processed after being calculated via the logic of the Central PLC or Local PLC to send them to each local system to respond to the interlock situation without disruption. The MIS network should be configured redundantly in consideration of the possible communication failures to guarantee no communication disconnection between the Central PLC and the Local PLC. The MIS PLC and electrical equipment should be installed inside the 19'rack so that it cannot be accessed by anyone other than for maintenance purposes.



<Figure 2.1.13.35> Local/Central MIS timing.



<Figure 2.1.13.36> Signal flow diagram.

The figure above shows the signal flow diagram that illustrates the kinds and steps of signals exchanged by the MIS layers. Through this block diagram, it is possible to know indirectly how the signal of each step converts, passing through the devices for each hardware and software.

<Table 2.1.12.28> below summarizes the conditions and actions for MIS interlock during accelerator operation. It shows that conditions for MIS Interlock change according to the status of PSI and MIS peripheral devices. This table needs to be updated continuously and will be flexibly changed according to the operational policy for 4GSR.

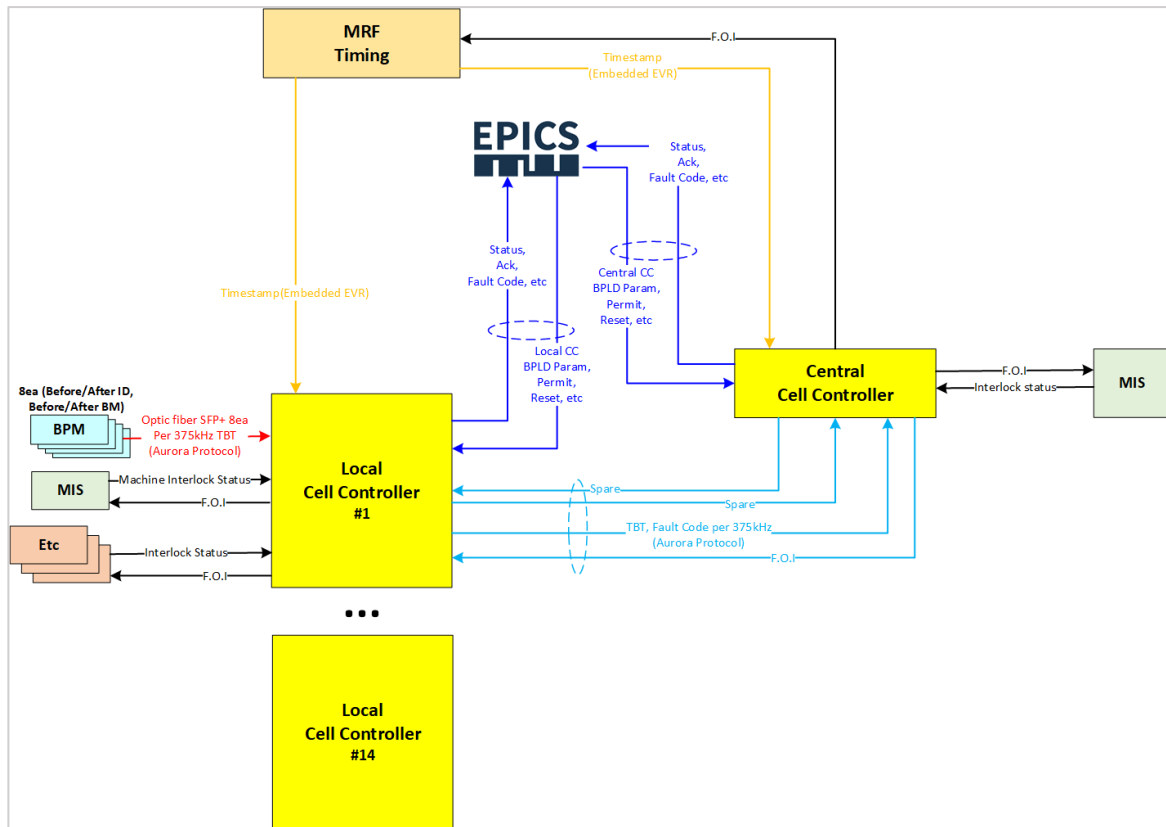
<Table 2.1.13.12> Interlocking conditions and actions

Condition	Action	Acting System	Note
PSI in No Access mode; MIS in Operation Mode - Beam Dump Request from Beam Lines - SR vacuum chamber temperature (Photon Stop) Interlock - ID Interlock Request - FOI Interlock Request	Beam dump	MIS	-
PSI in No Access mode; MIS in Operation mode - SR BPM orbit Interlock	Beam dump, Interlock signal transmission	FOI	-
PSI in Restricted Access or No Access mode; MIS in Operation or Maintenance mode; No stored beam - SR vacuum Interlock	Gate valve closing	MIS	-
PSI in Restricted Access or No Access mode; MIS in Operation or Maintenance mode; No stored beam - SR vacuum Interlock	Beam dump, Gate valve closing	MIS	-

The MIS should be configured and developed to respond flexibly to situations such as the operation and maintenance of the accelerator by connecting with a personal safety system via hard-wired interface or communication.

○ Fast Orbit Interlock

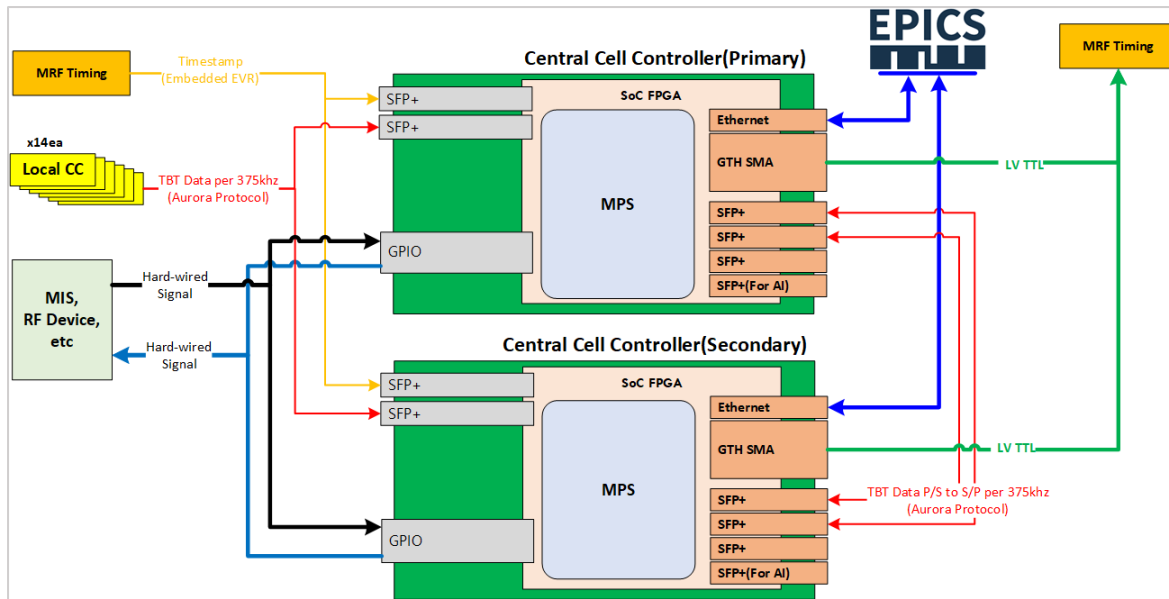
The purpose of FOI (Fast Orbit Interlock) is to prevent situations where the radiation from circulating electron beam can hit and damage the BMs (bending magnet) or IDs during operation when the beam deviates from normal orbit in the storage ring and to protect the devices. Therefore, the FOI system collects the beam position data at the BPMs before/after BMs and before/after IDs. These data represent the beam trajectory state synchronized with the timing system. The FOI collects and analyzes these data to judge the beam deviation state and quickly outputs the beam dump signal, sending the interlock signal to the peripheral devices. These data and the state of the devices should be informed at the central operation room to notify them of the beam deviation from the orbit during operation. In addition, when the Orbit Interlock occurs due to beam deviation during operation, TBT (Turn By Turn) data is collected for 1,000ms (375,000th) before and after the signal is generated. The collected data should be used to analyze the cause of beam deviation.



<Figure 2.1.13.37> FOI (Fast Orbit Interlock) system architecture.

The figure above illustrates the FOI architecture. The FOI is divided into the Master Cell Controller and Local Cell Controller, which will be composed of the same chips and same circuits. However, the software and peripheral interfaces will be different depending on the role.

Local CC will be synchronized with the timing system at 375 kHz, and the beam location information from BPMs will be collected during this cycle via high-speed serial communication using the Aurora Protocol. The beam position data collected from the BPMs are turn-by-turn (TBT) data for the beam trajectory. Each local CC is designed to have Aurora-Protocol-based high-speed serial communication ports that can communicate with BPM and Central CC. Each Local CC calculates the beam trajectory using the data from 4 BPMs located before and after the BMs or IDs to determine the FOI occurrence and triggers signals to nearby MISs, RF devices, and other peripheral devices. Central CC should frequently check the beam motion integrity via mutual communication and signals and enable the component's own response to failures.



<Figure 2.1.13.38> Central CC (Cell Controller) architecture.

The figure above shows the Central CC (Cell Controller) architecture. The Central CC should be dually configured with the same type of controllers, such as primary and secondary controllers, to prevent interruption during operation. Each Central CC board always operates to receive the same data from Local CCs. However, the EPICS IOC runs only one soft IOC at a time. It means that only either the primary or secondary controller runs the soft IOC. Basically, the primary controller has high priority, but if it has problems such as hardware malfunction, the secondary controller judges the state of the primary controller and may get the priority to run soft IOC. The redundancy of the Central CC is for the continuous functioning of the FOI without stopping. The output of the redundant controllers will be decided after judging the state of the two controllers by logic via the external gate logic board. Also, the Central CC will be developed to enable internal programs to be downloaded remotely by users so that the mutual operational health can be frequently checked through mutual communications and signals to enable the components' own response to failures.

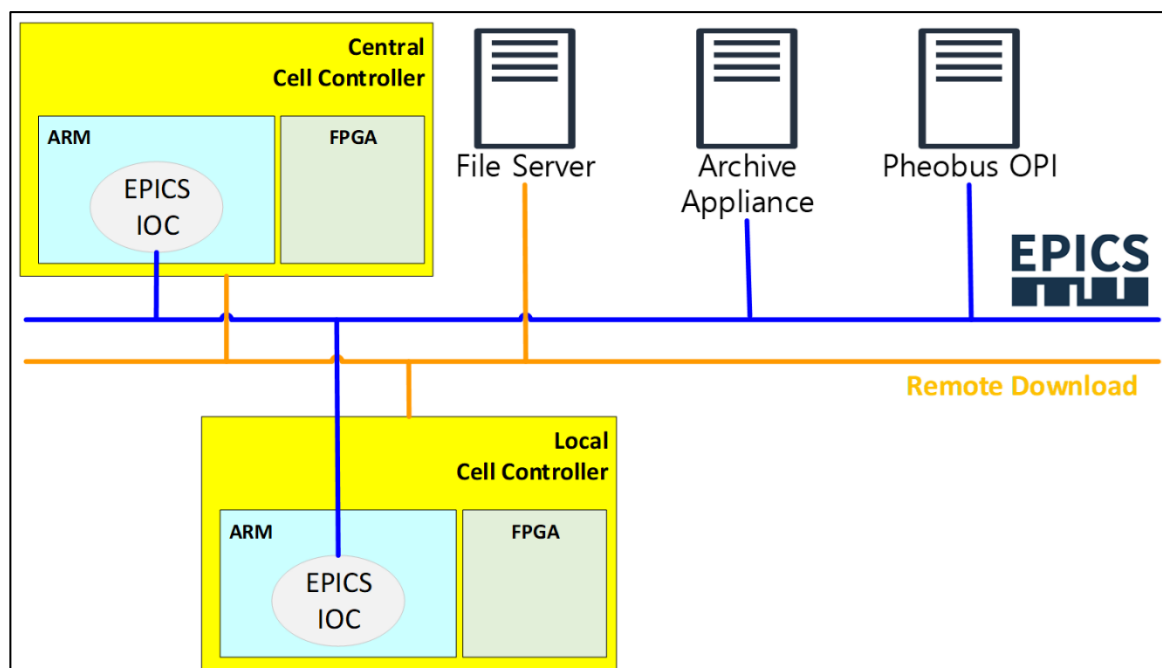
○ FOI Signal List

<Table 2.1.13.13> FOI Input/Output Signal List

Classification	FOI In/Out	Description	Note
Time Stamp	In	Timing System Time Stamp	
ID Status	In	ID Gap status and other	
DCCT value	In	Beam Current or Normal/Abnormal Status	
BPM data	In	X, Y, and Sum	
Timing Event	In	Operation Event	
MIS Interlock	In	MIS Interlock Output	
Fast Orbit Interlock to MIS	Out	FOI Interlock Output	
Fast Orbit Interlock to Timing System	Out	FOI Interlock Output	
Fast Orbit Interlock to RF Device	Out	FOI Interlock Output	
Fast Orbit Interlock to Peripheral Device	Out	FOI Interlock Output	

The Table above shows FOI's Input/Output signal list. The FOI orbit interlock data can be divided into input data that can judge the beam trajectory, parameter data that can determine whether orbit interlock is executed, and data that generates orbit interlock after calculation. The FOI devices related to the I/O of each data are various and will be developed considering each signal level.

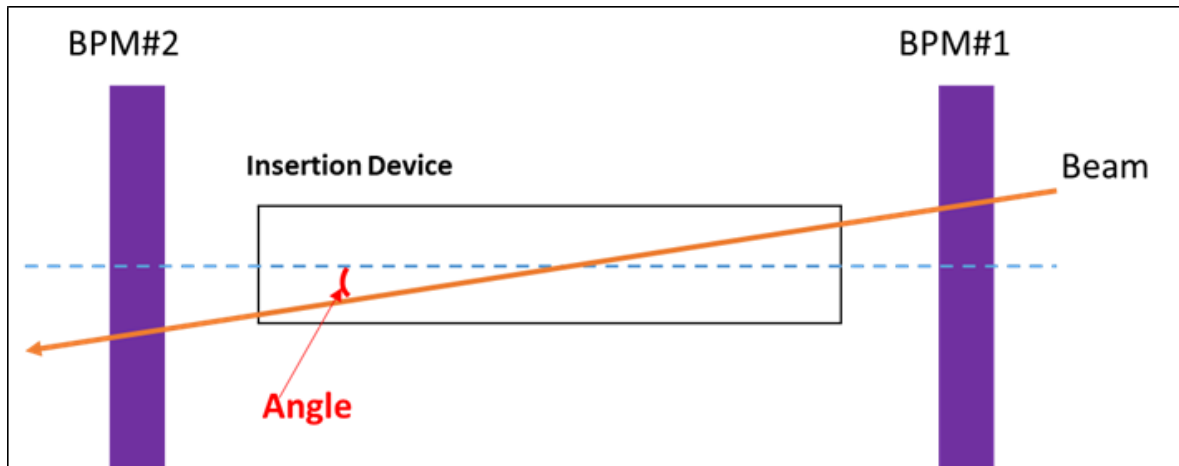
○ Software and Network Composition



<Figure 2.1.13.39> Configuration of FOI hardware and software.

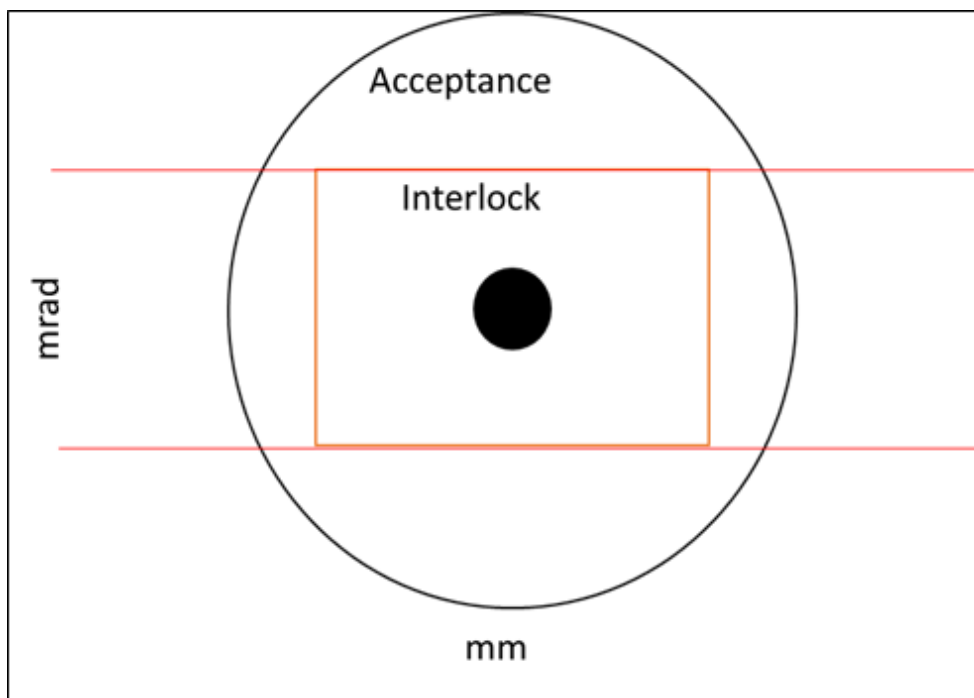
The figure above shows the configuration of the FOI hardware and software. The Local and Central CC consist of ARM and FPGA parts. The ARM operating system should be the Peta Linux for software development, and the EPICS IOC will be developed and operated based on the EPIC7 version. In the case of internal logic development, VIVADO will be used. The FOI functions will be implemented through connections to the EPICS network, remote download network, and data-saving network.

○ Orbit Interlock Acceptance



<Figure 2.1.13.40> An example of beam angle detection.

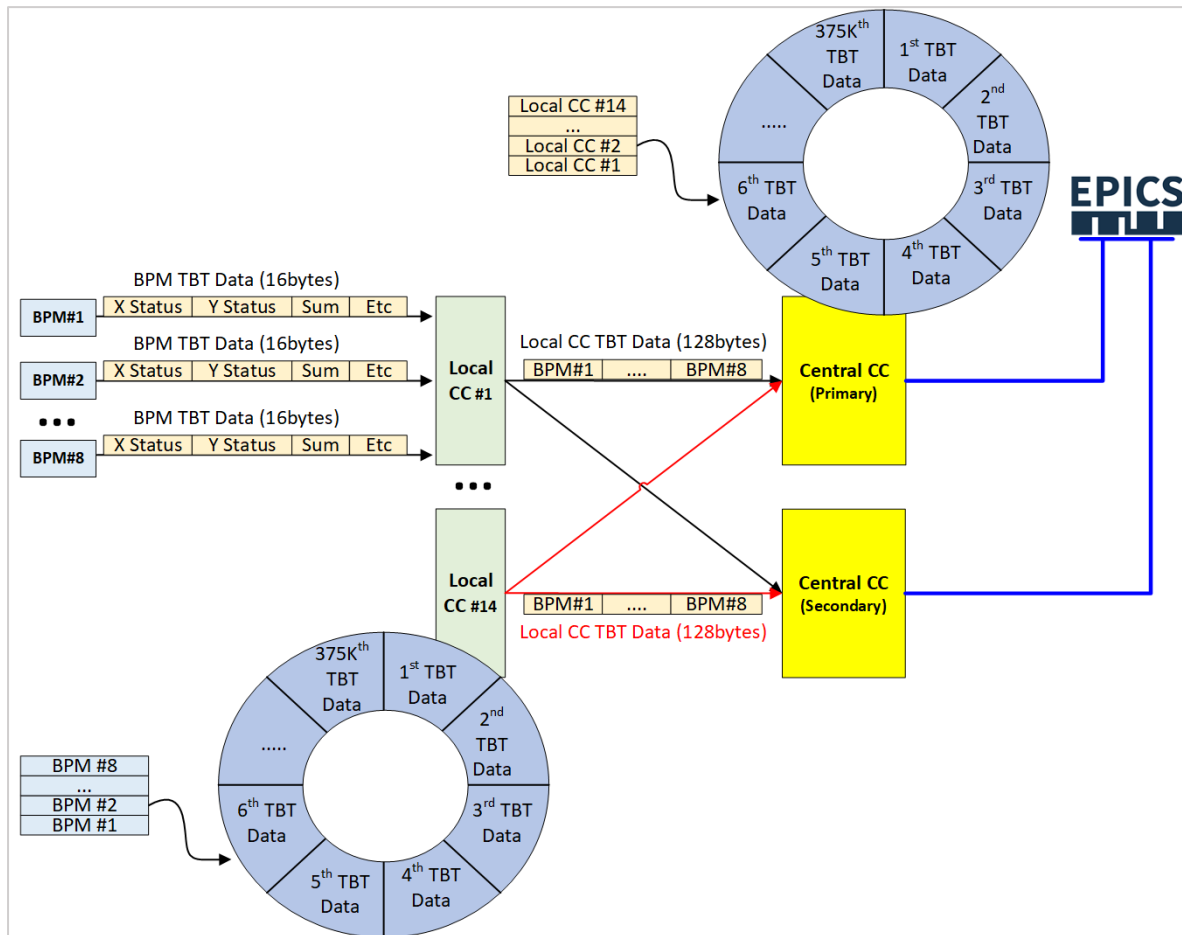
The figure above shows an example of beam angle detection. Two BPMs will be located before/after each BM and ID, and the beam position data will be collected when the beam passes BPM#1 and BPM#2. Based on this data, it is determined whether or not the beam is out of normal trajectory.



<Figure 2.1.13.41> An example of the acceptance for orbit interlock.

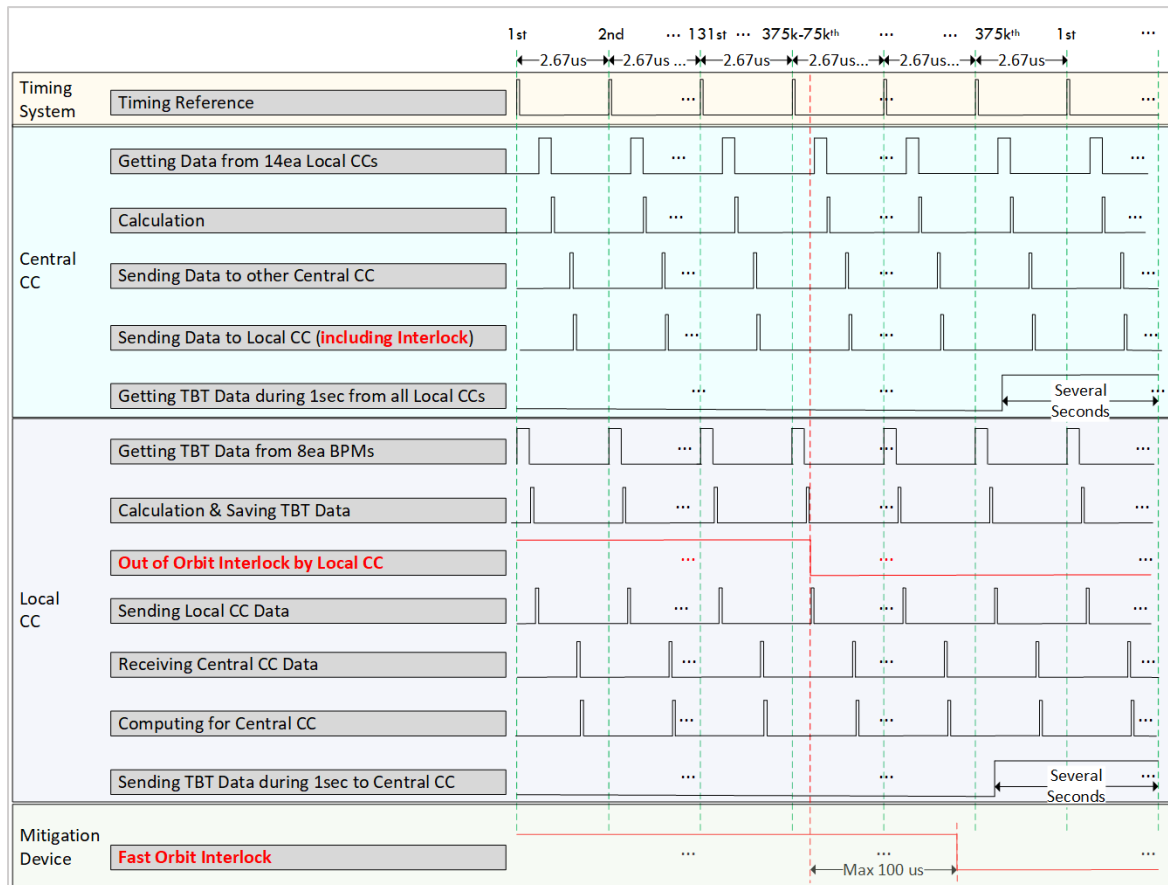
The figure above shows an example of the acceptance of orbit interlock during storage ring operation. The detailed acceptance criteria for orbit interlock should be defined based on the beam position information and angle when the beam passes an ID or BM. Since sufficient data will accumulate after operating the accelerator for some time, the detailed criteria will be defined later.

○ Data Processing



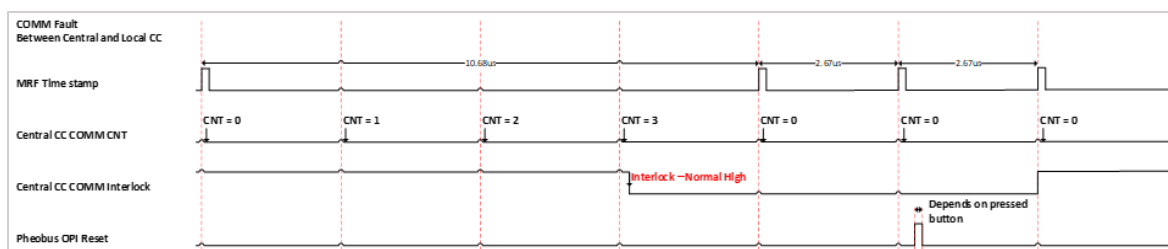
<Figure 2.1.13.42> Processing of turn-by-turn data.

The figure above shows the Local/Central Cell Controller's turn-by-turn data processing. The TBT data of 8 BPM units is continuously stored and updated in the local CC's internal buffer at 375 kHz. The data serves as a basis for determining whether the beam deviates from normal orbit during operation. The internal buffer of Local/Central CC saves 375,000 passage data at maximum. It will adopt the ring buffer method in which the oldest data is deleted and the latest data is saved. Among the saved 375,000 passage TBT data, the amount of data of about 1,000 ms (BPM TBT Data 375,000 passages) before and after the orbit interlock will be collected and transmitted to the data server. Another user will use the provided data to analyze the beam trajectory. The Local/Central CC should be developed to allow the internal programs downloaded by remote users. Unlike a Local CC, the Central CC is designed to store and collect the TBT data from each Local CC, transmit the interlock status from peripheral devices, and perform operation commands.



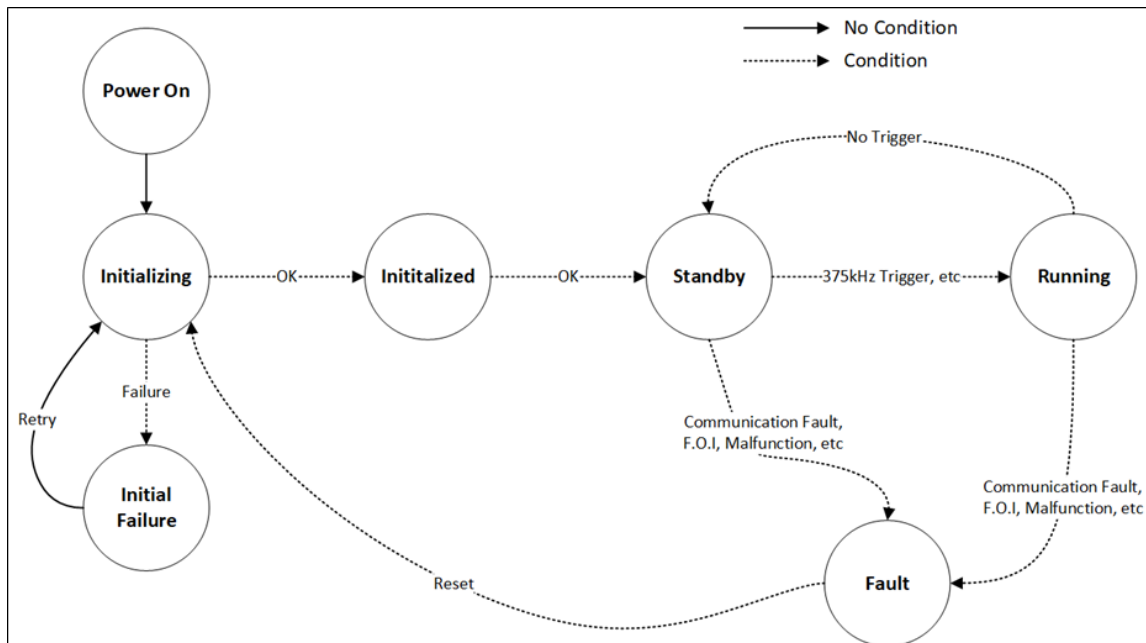
<Figure 2.1.13.43> FOI timing chart.

The figure above shows what the Central and Local CC should do in the event of FOI in the order of FOI occurrence, processing of the TBT data collected for 1,000ms, and orbit interlock processing in a timing chart. If the beam is out of normal orbit, the local CC in charge of the cell generates the orbit interlock signal via logic calculation, transmits the signal to the Central CC through communication, and transmits the FOI signal to peripheral devices. This figure illustrates the above processing, including the triggering, within the required 100 us and the time flow in which Local CC determines the orbit interlock and sends the 1,000ms TBT data before/after the orbit interlock judgment to the control network.



<Figure 2.1.13.44> Timing chart – communication fault.

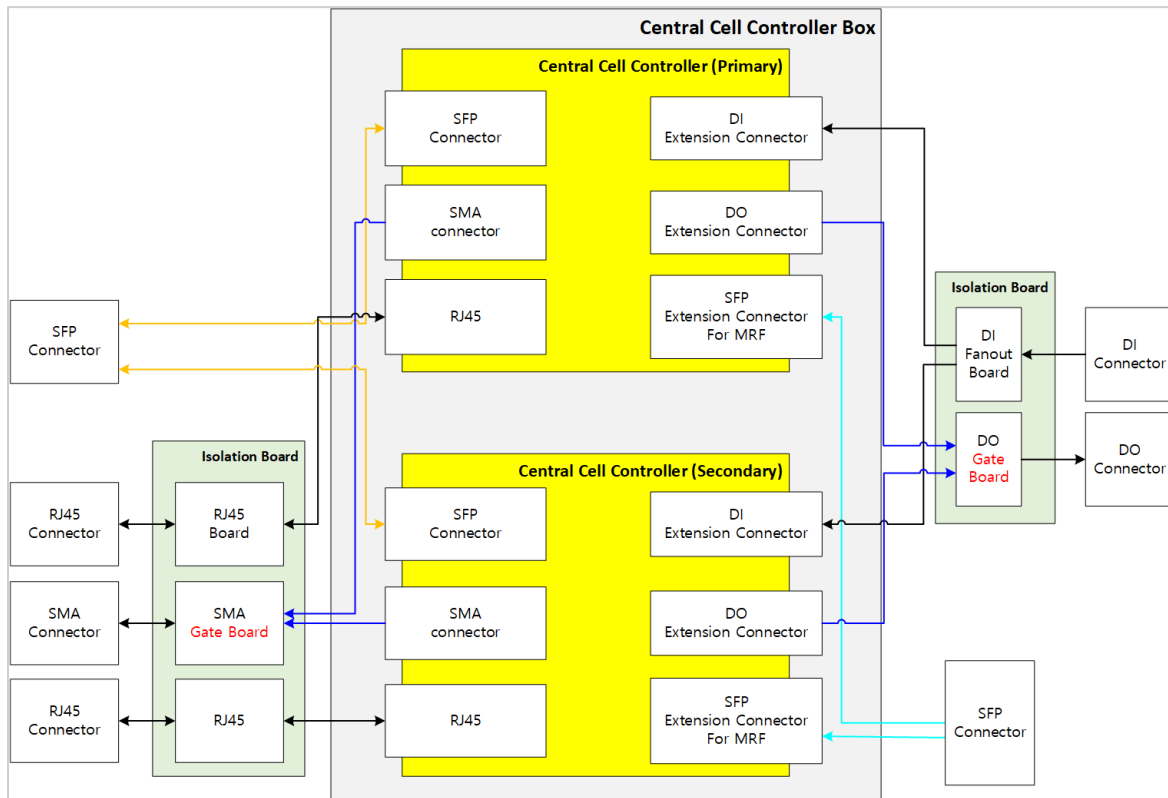
The figure above shows the timing chart of a communication fault. It is an example that illustrates a communication fault during operation between the Central CC and the Event Timing System. The communication period is 375khz. If the delivery of a communication packet from the Event Timing System to the Central CC is not confirmed for a specific time, the Central CC generates an interlock signal. It can be checked in the central operation room. If the cause of the interlock is checked and resolved, the operator should press the fault reset button on the OPI (Operator Interface) to normalize the system.



<Figure 2.1.13.45> FOI Sequence.

The figure above shows the FOI sequence. There are four broad steps: Initial, Standby, Running, and Fault. A more detailed sequence will be added depending on the conditions.

- Initial: It initializes the controller status and judges whether the controller is normal or not
- Standby: It is ready to receive timing events from the Event Timing System
- Running: It receives timing events from the Event Timing System and repeatedly processes TBT data.
- Fault: State of device failures or similar conditions. Latching fault status until the Reset command comes from the user.



<Figure 2.1.13.46> Local/Central Cell Controller's hardware architecture.

The figure above shows the hardware architecture of the Local and Central Cell Controllers. The Local and Central cell controllers will have the same hardware, but software function will be different. Ports of controllers should be isolated with peripheral devices to prevent electrical damage. In addition, 3.3V, 5V, 24V, and optical cables can be connected with peripheral devices, and the signal distribution function should be considered.

2.2 Girder system

2.2.1 Overview

The performance of the light obtained from a next-generation synchrotron radiation accelerator is determined by the beam stability in addition to the existing design goals of the synchrotron radiation accelerator. In order for synchrotron radiation accelerator users to obtain stable measurement results, properties such as light intensity, light position, polarization, and coherence must be kept constant. This is called beam stability, and efforts from all departments of the accelerator are needed to improve it.

Factors that affect beam stability include accelerator and beamline equipment, infrastructure such as water and electricity, mechanical vibration, temperature, electrical noise, and ground movement. If these factors differ from the ideal values, they affect beam stability, and this difference is collectively called error. These errors can be static or vary over time. In addition, errors can be random or systematic.

The electron beam size of the 4GSR storage ring is only 10% of the beam size of the existing 3GSR storage ring, and accordingly, the stability of the electron beam must also be increased accordingly. The stability of the electron beam can be largely divided into static stability and dynamic stability.

Dynamic stability can be divided into short-term stability and long-term stability. Short-term stability aims to reduce the amplitude of rapid movements from 0.1 to 1 kHz to 10% of the beam size. Long-term stability aims to keep changes in the electron beam position over several weeks below 1 μm .

Static stability is determined by the precision of device manufacturing and alignment, and dynamic stability is determined by the magnetic field strength stability of the electromagnet, mechanical vibration, and ground movement. Static stability determines beam positioning during the construction and commissioning stages, and beam positioning must be in a sufficiently stable region for a few turns after beam injection in the first commissioning stage to enable beam storage through orbit correction using correction magnets.

Static stability, in addition to commissioning, also affects the degree of necessity for accelerator and beamline alignment during restart after shutdown. The alignment state of the magnets is also important, and the electron beam must pass through the center of the magnet accurately to minimize the multi-pole effect, and this criterion is usually on the order of

several tens of μm . A stable girder system is essential to minimize the impact of mechanical vibration and ground movement on electromagnets and vacuum chambers.

The Korea 4GSR girder system was designed to meet the 800 m circumference of the storage ring based on the stable accelerator operation of the PLS-II girder system. As shown in <Table 2.2.1.1>, various alignment mechanisms are employed in circular synchrotron radiation accelerator girder systems worldwide, including motor-driven cam movers, manual wedge jacks, and motor-driven wedge jacks.

Currently, the PLS-II girder system uses an alignment mechanism through screw jacks, and it is designed and operated to enable a wide driving range and secure mechanical rigidity. The Korea 4GSR girder system was developed by utilizing a ball screw jack with improved transfer precision and durability from the existing power transmission TM screw jack. In addition, a girder system using a motor control driving unit and a displacement sensor for accelerator operation convenience was developed.

In this chapter, we will explain the basic research results on implementing the optimal girder system based on the self-weight and vibration analysis of the girder system applied to the Korea-4GSR project.

<Table 2.2.1.1> Adjustment method of magnet girder and supports for each photon source

Facility	Adjustment method	
Spring-8	Manual adjustment	6-Point Support
SOLEIL		4-Wedge jack
SSRF		3-Wedge jacks, 3-Assistant supports
NSLS-II		8-Point support
APS-U		3-Point support, 3-points adjustment
SIRIUS		4-Point wedge jacks
SLS	Automatic adjustment	5-cam mover mechanisms
Diamond		5-cam mover mechanisms
TPS		6-cam mover mechanisms
ESRF-EBS		4-Motorized wedges, 3-Manual sedges

A. Girder System Requirements for the Korea 4GSR

The girder system of 4GSR in Korea must meet specific design requirements different from conventional circular accelerators. While international upgrade projects from 3rd to 4th generation circular accelerators have focused on the characteristics of the existing accelerator building, ground conditions, and the dismantling and installation of accelerator equipment, the Korea 4GSR requires a girder system that can be stably operated in a new environment with different ground conditions and building characteristics. To meet these requirements, the development of the girder system must satisfy the following conditions:

- **Electron Beam Height:** The girder system must support the electron beam at a height of 1.4 meters.
- **Girder Top Surface Flatness and Low Deformation Rate:** The top surface of the girder must exhibit high flatness and a low deformation rate to ensure the accurate installation and operation of the accelerator equipment.
- **High First-Order Resonance Frequency:** The girder system must achieve a high first-order resonance frequency under constrained conditions to minimize vibrations and ensure stability.
- **Motor-Driven Alignment Mechanism:** The girder system must incorporate a motor-driven alignment mechanism to facilitate precise alignment of the accelerator components.
- **Optimized Girder Design for Storage Ring Tunnel Space:** The girder design must be optimized to maximize the available space within the storage ring tunnel.
- **Mounting Holes for Diverse Equipment Installation:** The girder system must include mounting holes to accommodate the installation of various accelerator components.
- **Thermal Stability:** The girder system must exhibit high thermal stability to minimize thermal deformations and maintain the alignment of the accelerator components.

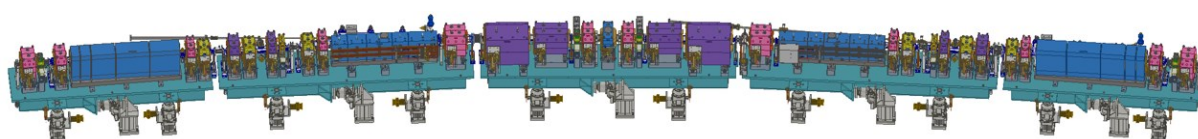
These requirements will ensure the stable and efficient operation of the Korea 4GSR and contribute to its successful utilization as a cutting-edge research facility. Key parameters for developing the Korea 4GSR girder system can be found in <Table 2.2.1.2>. The adjustment range, resonance frequency characteristics, adjustment mechanism, and adjustment accuracy of the girder system were determined through <Table 2.2.1.2>.

<Table 2.2.1.2> Key parameter for the girder system.

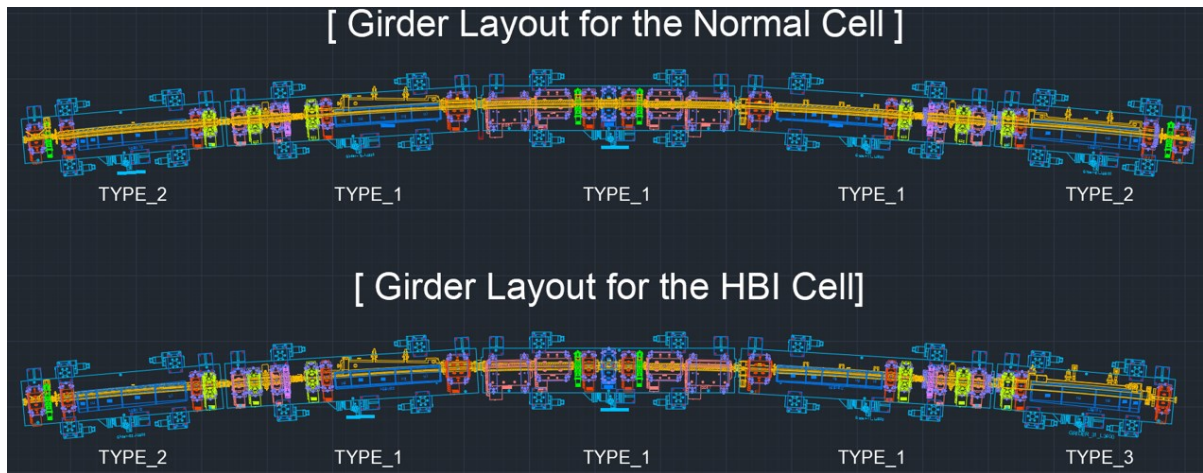
Parameter	Value			
	Korea 4GSR	ESRF-EBS	APS-U	HEPS
# of Cell	28 cells	32 cells	40 cells	48 cells
Circumference or SR	798.8 m	844 m	1100 m	1360.4 m
Beam height	1.4 m	1.2 m	1.4 m	1.2 m
Leveling range (Y-axis)	± 10 mm	± 5 mm	± 13 mm	± 9 mm
Lowest natural frequency	50 Hz	50 Hz	42 Hz	54 Hz
Maximum Girder length	<5 m	5.1 m	5.568 m	3.8 m
Girder to girder alignment	± 50 μm	50 μm	50 μm rms	± 50 μm
Adjustment method (Y-axis)	Motorized	Motorized	Manual	Manual
Adjustment method (X, Z-axis)	Manual	Manual	Manual	Manual
Positioning accuracy (Y, X-axis)	± 50 μm	50 μm	30 μm	± 50 μm
Positioning accuracy (Z-axis)	± 200 μm	1 mm	70 μm	± 200 μm

B. Storage Ring Girder System Layout

The design of the girder is significantly influenced by the beam physics design and device configuration. The storage ring has a circumference of approximately 800 m with a total of 28 cells, which are mainly classified into normal cells and High Beta Injection (HBI) cells. As shown in <Figure 2.2.1.1>, each cell consists of 5 girders. Normal cells are symmetrical in the upstream and downstream directions with respect to the central bending section, while HBI cells have girders connected to the injection section with a length of 3400 mm in the longitudinal direction, considering the overall structure of the storage ring, compared to normal cells. The two layouts of the girder system can be seen in <Figure 2.2.1.2>.



<Figure 2.2.1.1> Design of the girder in the achromat.



<Figure 2.2.1.2> Girder system layout in the storage ring.

The girders for installing the storage ring accelerator devices are composed of three types. All girders are supported at four points in the vertical direction and are designed to allow adjustment in the horizontal and beam directions. In the case of normal cells, three girders at the center of each cell are designed to be 4,800 mm in length along the beam direction, and the girders at both ends of the cell are designed to be 3,800 mm. Similar to the normal cells, the HBI cells have three 4,800 mm long girders at the center of each cell, 3,400 mm long girder connected to the injection section, and 3,800 mm long girder connected to the standard cell. The types of magnets installed in each girder are shown in the <Table 2.2.1.3>.

<Table 2.2.1.3> Magnet placement on each girder

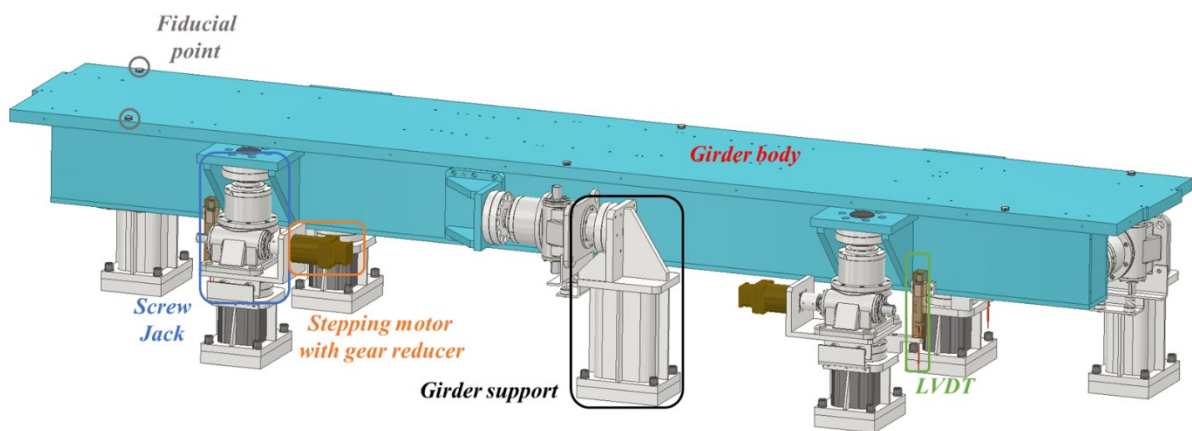
Girder			Magnet Placement	
Type	Length	Position	Normal cell	HBI cell
1	4.8 m	Upstream to Center	DQ31U, S32U, DQ32U, Q31U, S33U, Q32U, LGBM2U, Q51U	
		Center	DQ51U, DQ52U, CO2U, Q52U, CENT, Q52D, CO2D, DQ52D, DQ51D	
		Center to Downstream	Q51D, LGBM2D, Q32D, S33D, O31D, DQ32D, S32D, DQ31D	
2	3.8 m	Upstream	Q11U, CO1U, Q12U, LGBM1U, Q31U, S31U	-
		Downstream	S31D, Q31D, LGBM1D, Q12D, CO1D, Q11D	
3	3.4 m	-	-	QH4U, LGBM1U, Q31U, S31U

2.2.2 System Design

A. Structural Design and Consideration

The girder design is generally carried out in accordance with the requirements or constraints such as beam stability, alignment, and ease of installation. As shown in <Figure 2.2.2.1>, the Korea 4GSR girder system is mainly composed of a girder body, girder supports, and adjustment devices. The four vertical girder supports are designed to support a self-weight of 15 tons, including the weight of the girder itself (5 tons) and the maximum weight of the accelerator devices including magnets and chambers (10 tons).

The specifications for the storage ring girder design can be found in <Table 2.2.2.1>, which includes the total quantity of the three types of girder systems, the performance of the adjustment devices, and the characteristics of the girder monitoring system. In addition, in order to secure the mechanical rigidity and machinability of the designed girder system, it is planned to be manufactured using SS400 and S45C series materials with mechanical properties as shown in <Table 2.2.2.2>.



<Figure 2.2.2.1> Girder design.

<Table 2.2.2.1> Specification of girder system

Parameter		Type 1	Type 2	Type 3
Girder body	Quantity of Girder [set]	84	52	4
	Total length [m]	4.8	3.8	3.4
Adjustment System	Vertical adjusting method	Stepping Motor with Screw Jack		
	Transverse and longitudinal adjusting method	Manual with Screw jack		
	Quantity of screw jack [set]	588	364	28
	Quantity of stepping motor system [set]	336	208	16
	Quantity of LVDT [set]	336	208	16
	Loading capacity of screw jack [ton]	12		
	Max. Torque for the Stepping motor [N*m]	3.88		
	Gear ratio of gear reducer [ratio]	320 : 1		
	Working range of screw jack [mm]	±20 (40)		
	Measure range of LVDT [mm]	±10 (20)		

<Table 2.2.2.2> Mechanical properties of the girder material.

Mechanical Properties	Value	
	SS400	S45C
Density	7.85×10^{-6} [kg/mm ³]	7.85×10^{-6} [kg/mm ³]
Tensile strength	415 to 515 [MPa]	686 [MPa]
Young's Modulus	160 [GPa]	205 [GPa]

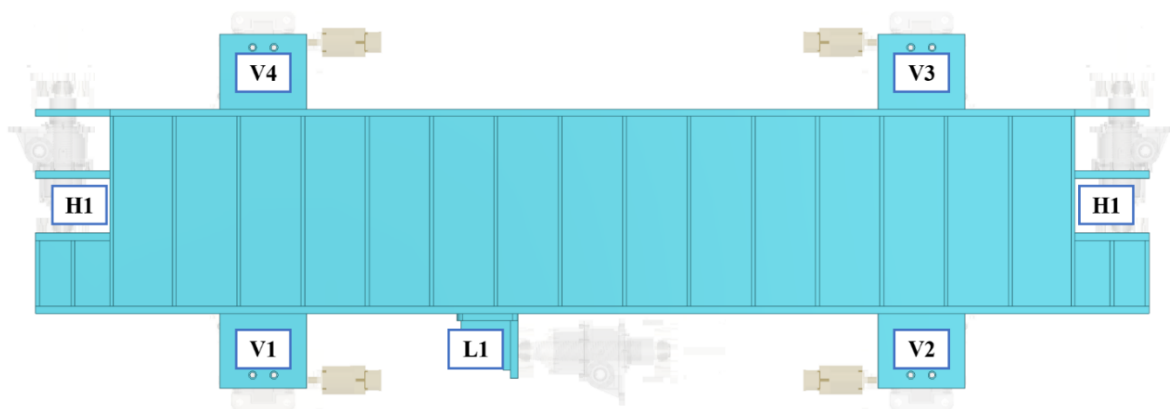
The adjustment device arrangement of the girder system, which consists of a total of 7 adjustment devices, is configured to be driven in the Vertical, Horizontal, and Beam lattice directions, as shown in <Figure 2.2.2.2>.

The adjustment device in the Vertical direction, which mainly bears the load for accelerator operation, is designed with a motor-driven method for ease of adjustment during alignment for the installation and maintenance of the accelerator devices. The adjustment devices in the horizontal and lattice directions are designed with a manual adjustment method so that adjustment is possible in cases where they have a significant impact on the initial installation and beam operation.

In order to support a weight of more than 15 tons, including the weight of the girder body, not only the selection of materials but also the reinforcement of the girder body is essential.

For the Korea 4GSR, the rigidity of the girder was increased by installing ribs and additional reinforcing bars inside the girder body, at the end of the girder upper plate, and at the installation part of the adjustment device.

As shown in <Table 2.2.2.3>, each allowable load of the Vertical support part is configured to withstand a load of more than 7 tons, for a total of more than 20 tons, and the Horizontal and Lattice directions are designed to withstand more than 450 kg and 900 kg, respectively.



<Figure 2.2.2.2> Structural reinforcement and Load point of the girder body.

<Table 2.2.2.3> Load distribution applied to the adjustment device

Screw Jack	Static load [kgf]	Seismic Load [kgf]	Total Load [kgf]
V1	3,691	3,928	7,619
V2	3,670	3,904	7,574
V3	3,620	3,844	7,464
V4	3,612	3,835	7,447
H1	0	460	460
H2	0	458	458
L1	0	918	918

To enhance the vibration characteristics, such as the natural frequency of the girder system, it should be developed in a direction that increases the rigidity of the system and reduces its weight, as can be seen in the equation below.

To reduce the weight while maintaining the rigidity of the girder system applied to the Korea 4GSR, the overall height of the girder body was configured to be 600 mm or less, and

the thickness of the plate material forming the body was configured to be around 20 mm.

In order to secure deformation and torsional rigidity due to self-weight, the configuration of internal reinforcing members was also shape-optimized to reduce the overall weight of the girder system.

$$f_n = \frac{1}{2\pi} \sqrt{\frac{k}{m}}$$

f_n : Natural frequency
 k : Stiffness of the system
 m : Effective mass

The components for driving the girder system are shown in <Figure 2.2.2.3>. The ball screw-based adjustment device can be assembled using a disk-shaped bearing case for the constraint of the girder body and the adjustment device, and it is designed to facilitate the installation and disassembly of the adjustment device during installation and maintenance by utilizing a spherical plain bearing between the bearing disks.

The fastening method using the bearing has the advantage that it can be installed in the vertical, horizontal, and beam lattice directions because rotational motion is possible in the state fixed with the lock nut when the fastening force of the disk is lowered. When the fastening force of the disk is increased, it plays a role of binding the structure while maintaining the angle desired by the user and maintaining mechanical rigidity.

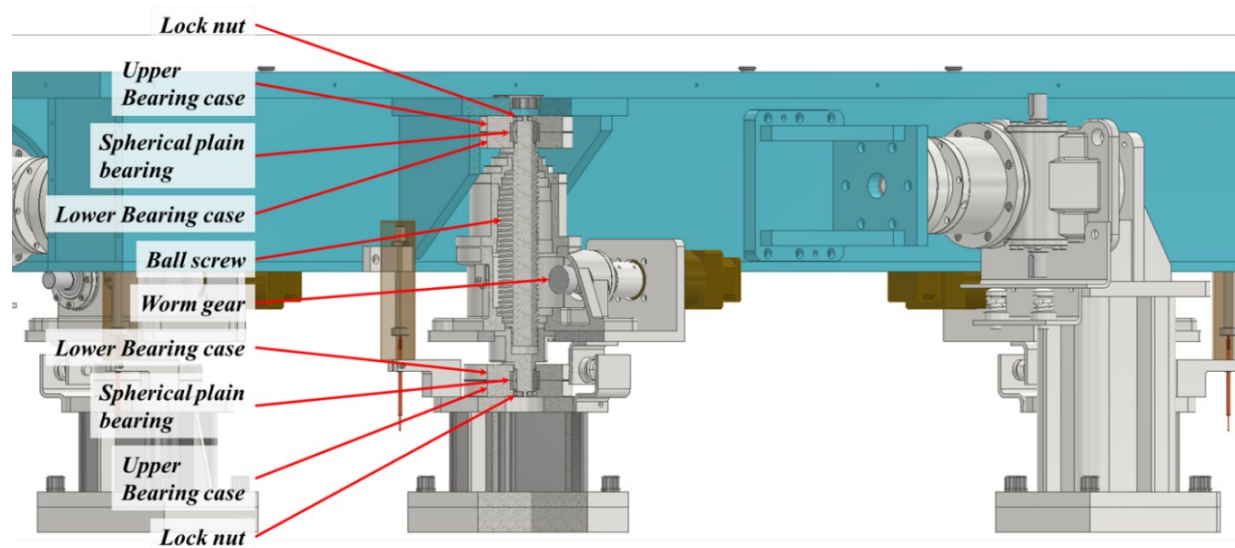
The part connecting the adjustment device is configured at both ends of the girder body and the lower support, securing process margin for securing the installation position during ball screw installation and maintenance. As the lower part of the adjustment device is fastened with a disk, unlike the form generally fastened to the body of the adjustment device, the rigidity reinforcement of the lower case of the adjustment device was necessarily considered.

In order to reinforce the rigidity of the lower case, the thickness of the parts was increased and the length was shortened in the existing case design, thereby reinforcing the rigidity through minimal measures without additional reinforcement measures. The S45C used for the ball screw has higher mechanical rigidity than ordinary carbon steel, so it was used in the girder system, and driving using a step motor in a limited space was made possible by using a worm gear that converts vertical motion and rotational motion.

The step motor connected to the worm gear performs two functions. The first function is the brake function of the ball screw jack. The screw jack that performs vertical motion

through the worm gear restricts displacement movement by using a mechanical stopper on the worm gear shaft after the adjustment is completed, but a dual safety method is applied by utilizing the brake function of the motor as an additional safety device.

In addition, a high-precision displacement sensor based on a Linear Variable Displacement Transducer (LVDT) was used for vertical displacement control. The signal from the displacement sensor is used as a monitoring system for the operation of the synchrotron radiation accelerator through the control system, and it is designed to enable motor control based on the acquired displacement data.



<Figure 2.2.2.3> Assembly of ball screw jack and girder support.

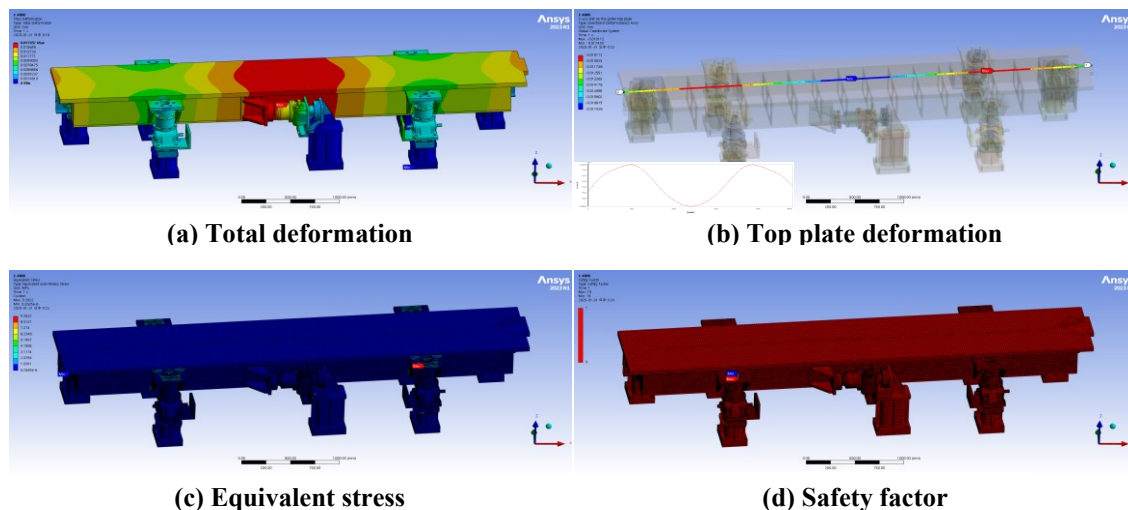
2.2.3 Analysis of Stiffness and Frequency Responsiveness

A. Static analysis

A structural stability analysis using static finite element analysis (FEA) was performed to confirm the deformation due to the self-weight of girder system. A mechanical analysis was performed on the entire structure constituting the girder system, including the designed girder and adjustment device. The deformation analysis due to self-weight was performed using Ansys. For the girder system for mechanical impact assessment, a girder with a length of 4,800 mm in the beam direction was selected as a representative model and conducted.

In <Figure 2.2.3.1>, the amount of displacement due to the gravity of the girder system itself can be confirmed, and the maximum displacement was confirmed to be 17.4 μm . It can be seen that the maximum displacement occurs at the center point in the beam length direction, which is the center of gravity of the girder body. The maximum stress of the girder system is 9.35 MPa, and it can be seen that concentrated load is distributed in the vertical adjustment device that actually supports the girder body.

Additionally, the structural safety factor can be confirmed, and it was confirmed that a very stable structure is secured by being evaluated as a safety factor of 15.



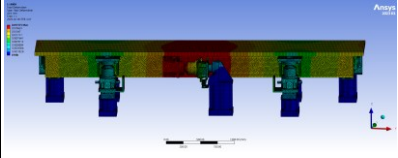
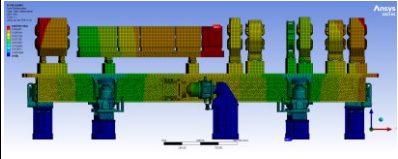
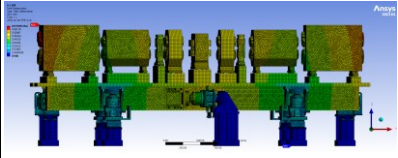
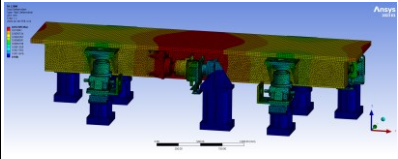
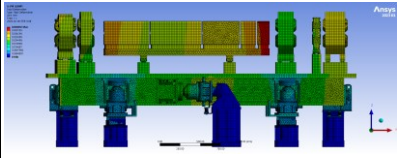
<Figure 2.2.3.1> Result of static analysis.

<Table 2.2.3.1> presents the displacement of the girder system, including the magnets that comprise it. The overall behavior of the 4GSR acceleration device within each girder configuration and magnet-integrated structure, along with the resulting displacement variations of the girder top plate, can be observed in detail.

The results presented were obtained using a simplified electromagnet model that considered the magnet's mass and center of gravity rather than its complete structure to calculate efficiency. The tabulated total deformation values correspond to the peak displacement magnitudes observed within each analyzed case.

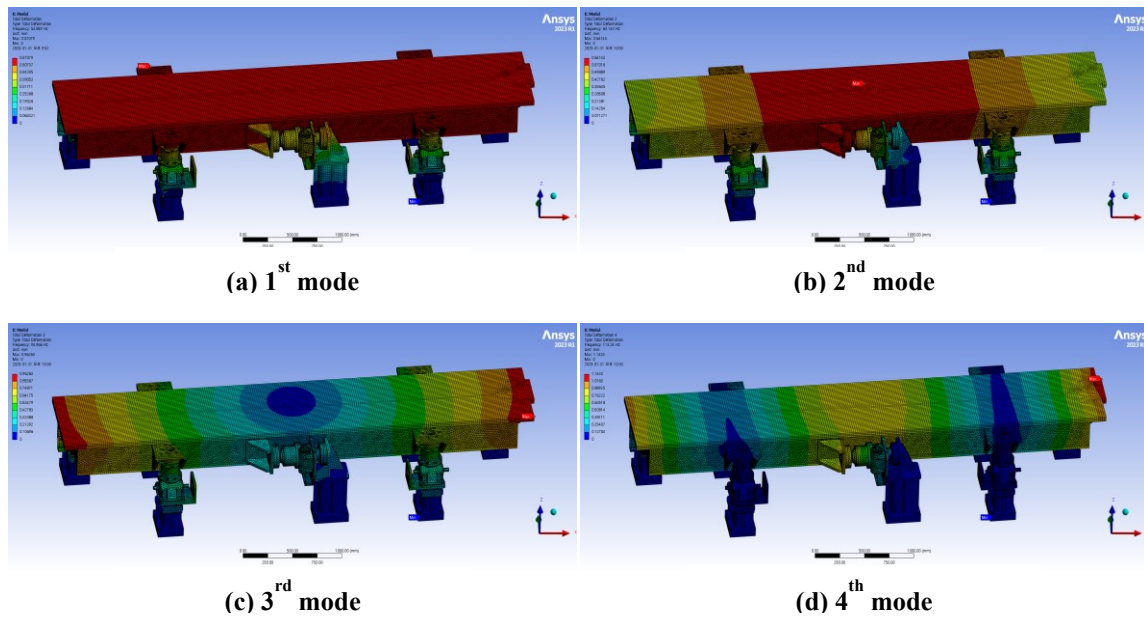
Furthermore, the girder top plate elevation deviations demonstrate a consistent trend, with the central girder region exhibiting maximal displacement and the vertical support interfaces displaying minimal displacement. This table provides a comprehensive summary of the girder top plate displacement differentials.

<Table 2.2.3.1> Displacement comparison by weight and type of girders

Type of girder	Displacement [μm]		Figure	Note
	Total	Top plate of girder (Dev. of flatness)		
Type_1	17.4	7.42		Own weight (4.5 ton)
	49.1	14.44		With LGBM #2 (9.6 ton)
	75.6	21.84		With CBM (13.5 ton)
Type_2	12	3.77		Own weight (3.9 ton)
	44	6.22		With LGBM #1 (7.8 ton)

B. Modal analysis

Considering the structural and material properties of the girder system, the design was carried out in the direction of increasing the natural frequency of the structure itself in consideration of the dynamic properties of the system. The design of the girder vibration part was carried out through modal analysis based on linear vibration theory and finite element method. Analyzing the dynamic characteristics of the girder plays an important role in avoiding resonance phenomena and reducing displacement due to vacuum. The 3D model for modal analysis includes the girder body, adjustment device, and supporter. <Figure 2.2.3.2> and <Table 2.2.3.2> show the FEA modal analysis results of the girder system of Type_1 (girder itself). The primary natural frequency of the girder system was confirmed to be 53.28 Hz or higher, which is a value that does not overlap with the commercial power supply frequency of 220V, 60 Hz.

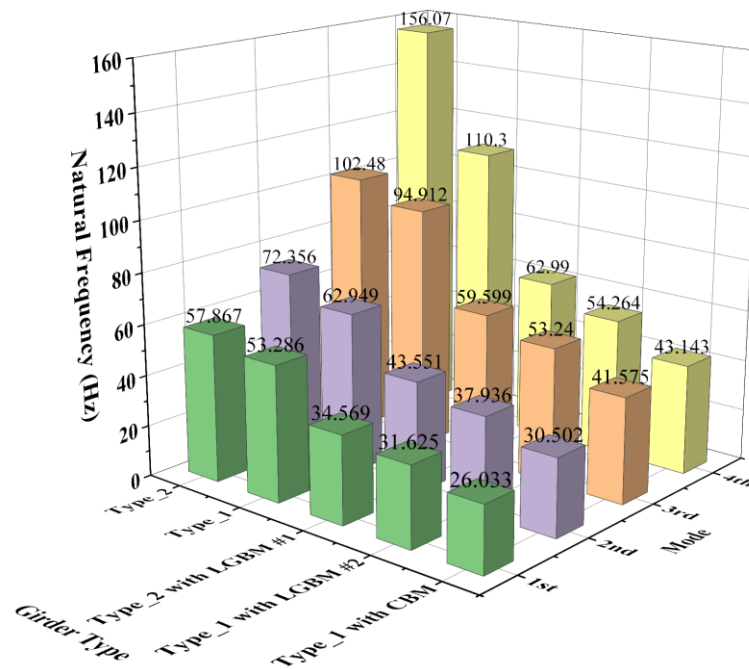


<Figure 2.2.3.2> Result of modal analysis.

<Table 2.2.3.2> Result of natural frequency with mode and mechanical properties for the Type_1

Mode	Frequency [Hz]	Type
1st	53.286	Transversal translation
2nd	62.949	Transversal translation + Roll
3rd	94.912	Translation along beam direction
4th	110.3	Torsional

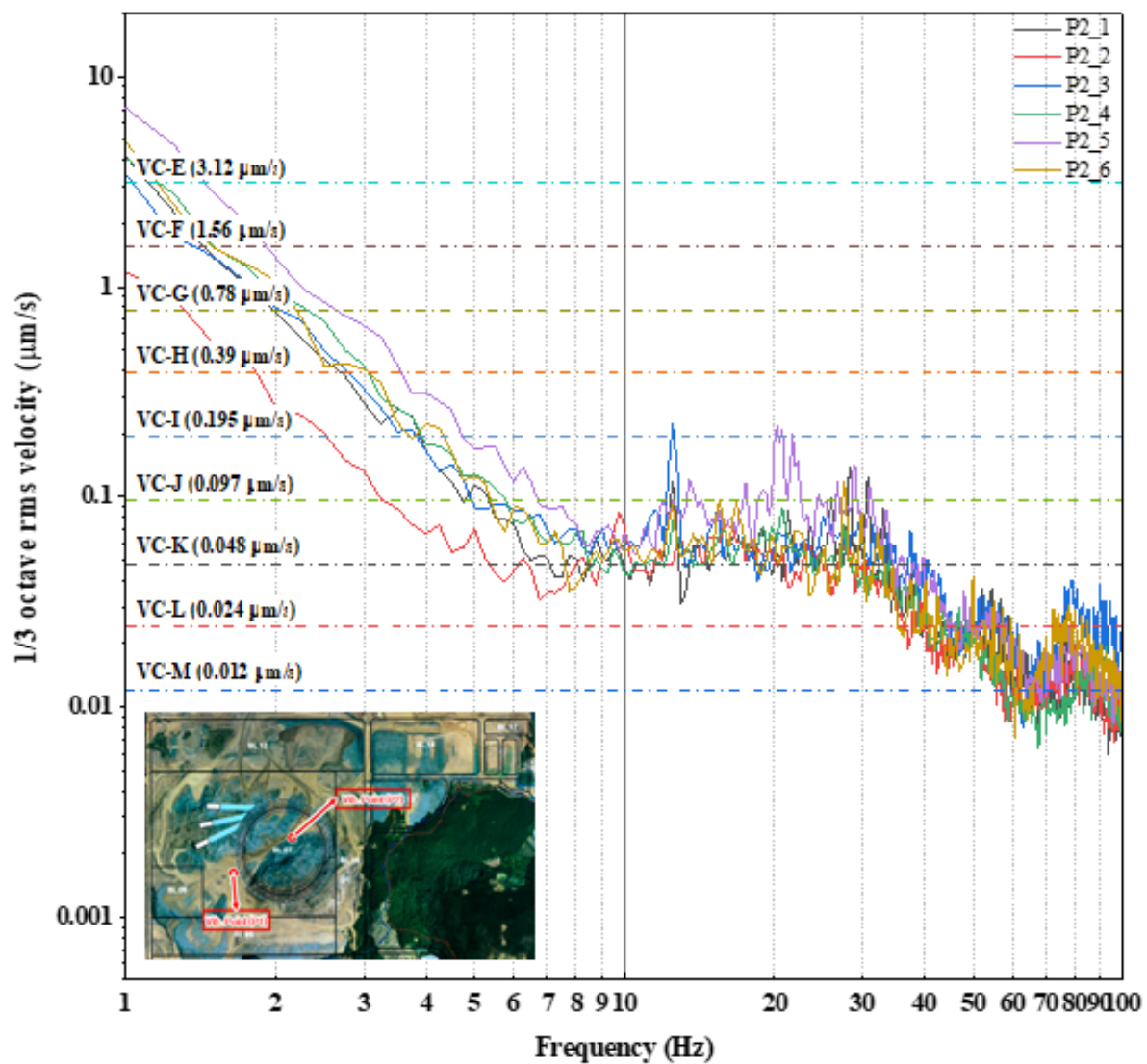
<Figure 2.2.3.3> is a detailed visualization of the natural frequency distribution from the first to fourth modes in all analytical cases in forms 1 and 2 of the girder type under development. The analysis of natural frequencies for each girder configuration reveals a trend of decreasing natural frequencies with increasing girder and upper magnet weight. This observation indicates a direct correlation between the system's mass and its inherent natural frequency characteristics. Based on these findings, the development of optimized girder designs for next-generation accelerator support structures can leverage this data to avoid resonance with superimposed frequencies, such as power supply frequencies, coolant flow frequencies, and operational frequencies.



<Figure 2.2.3.3> Natural frequency distribution of each girder system.

C. Random analysis

Securing mechanical stability is essential for stable accelerator operation and electron beam maintenance. In a synchrotron radiation accelerator, mechanical stability can be defined as securing suppression against external vibrations. External vibration factors that affect the accelerator devices can largely include natural factors, external vehicle traffic and abnormal impacts, and vibration factors generated from facilities to maintain the temperature stability of the accelerator devices. Natural factors include the vibration propagation characteristics of the accelerator ground itself, seasonal changes, and phenomena such as earthquakes. Here, the vibration characteristics of the ground itself can directly affect the accelerator devices through the accelerator building, so it is necessary to acquire and analyze ground vibration data to secure accelerator stability. In particular, since the girder system is a structure that primarily receives ground vibrations among the accelerator devices, research to appropriately suppress vibration factors generated from the ground must be conducted. To acquire ground vibration data, vibration data was measured using an accelerometer with an accuracy of 10 V/g. <Figure 2.2.3.4> shows the ground vibration data measured at the Korea-4GSR accelerator site, and random vibration evaluation affecting the girder system was performed using this data.



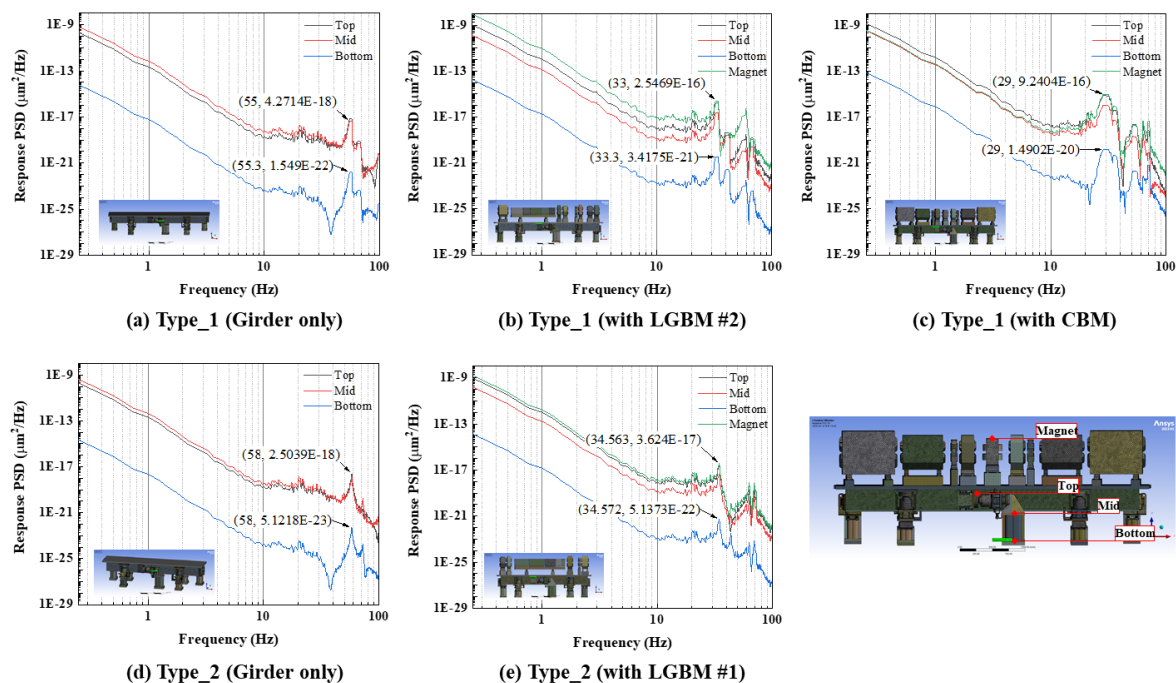
<Figure 2.2.3.4> Ground vibration value on the Korea 4GSR.

<Table 2.2.3.3> Random vibration data for the girder system

Contents		Value	Note
Deformation [mm]	Total	4.06×10^{-7}	Vertical axis
	Top plate	3.97×10^{-7}	Vertical axis
Stress [MPa]	1-Sigma	1.52×10^{-4}	Probability: 68.269%
	2-Sigma	3.04×10^{-4}	Probability: 95.45%
	3-Sigma	4.56×10^{-4}	Probability: 99.73%
PSD response with natural Freq. [$\mu\text{m}^2/\text{Hz}$]	1 st mode	1.56×10^{-17}	at 53.859 Hz
	2 nd mode	3.13×10^{-18}	at 63.143 Hz
	3 rd mode	2.79×10^{-19}	at 94.966 Hz

In the previously performed modal analysis, while the natural frequency of the girder

system itself was confirmed and information on deformation was included as part of the result data, it is not suitable for use as actual displacement data due to the characteristics of the modal analysis engine. In order to confirm the behavior of the mechanical system according to the actual external force, analysis for random motion is necessary. Through the results of <Table 2.2.3.3>, as a result of confirming the displacement characteristics of the girder system according to the ground vibration level, it was confirmed that the vertical displacement of the upper part of the girder had a low change of 39.7 μm , and the PSD values for the natural frequency derived through modal analysis were 1.56×10^{-17} , 3.13×10^{-18} , and 2.79×10^{-19} [$\mu\text{m}^2/\text{Hz}$] from the 1st to 3rd modes, respectively. This is a significantly low level compared to the beam size of Korea-4GSR, confirming that it is sufficiently valuable as a girder system. <Figure 2.2.3.5> presents the PSD response of the investigated girder configurations. The presented results are organized based on the measurement locations: the girder support base, the girder support mid-plane, the girder upper surface, and the magnet top surface. The analysis reveals that the induced ground vibration leads to amplified vibration at frequencies slightly shifted from the natural frequencies identified in the modal analysis. Furthermore, a progressive increase in vibration magnitude is observed as the vibration propagates from the ground to the electromagnet.

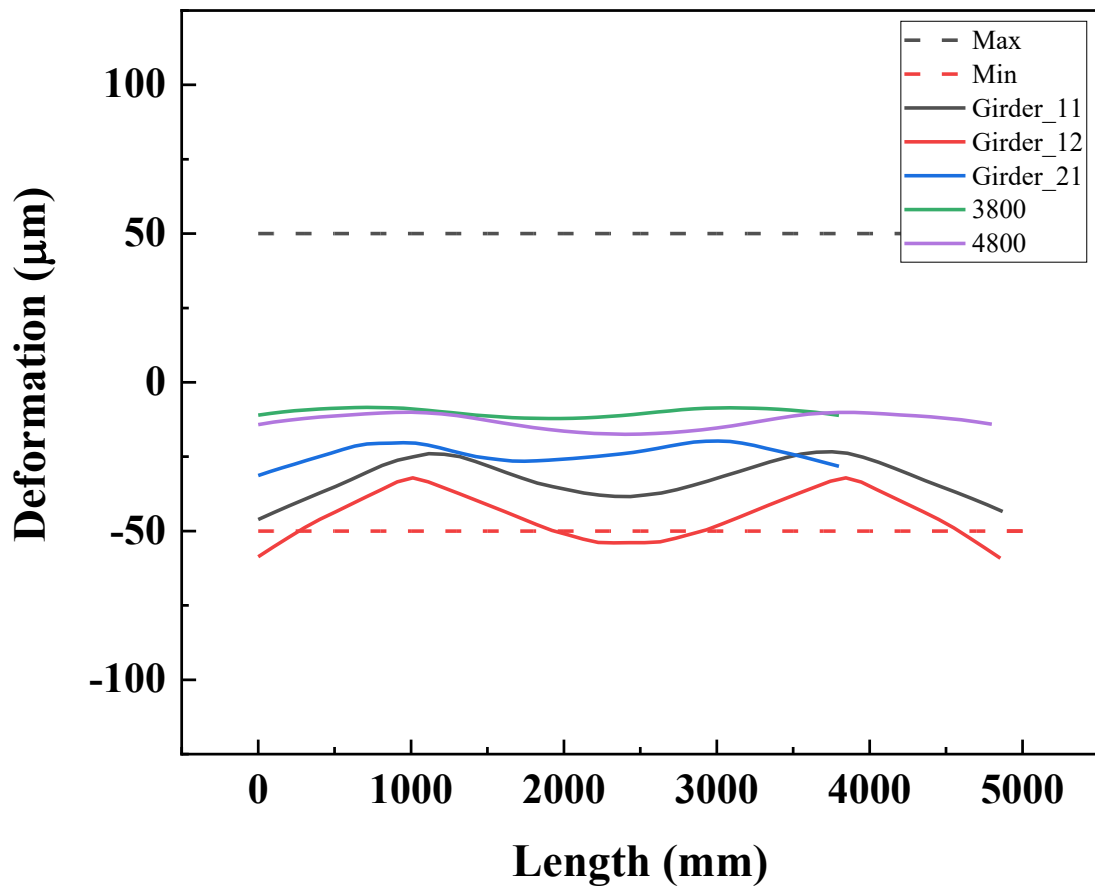


<Figure 2.2.3.5> Response for the PSD & Value position.

2.2.4. Mechanical Structural Analysis Results

In the field of mechanical structure of girder system development, a comprehensive mechanical stability evaluation of the girder system of Korea 4GSR, a next-generation synchrotron radiation facility, was conducted using finite element analysis. The investigation focuses on evaluating the structural response to gravitational loading and vibrational excitation prior to fabrication. Mechanical stability analysis necessitates a comprehensive evaluation of not only the girder structure itself, but also the combined configuration of the components mounted on its superstructure. Through this report, a finite element analysis was performed on the type_1 and type_2 configurations representing the system with the final superstructure specification to ensure a thorough evaluation of mechanical performance.

Under static gravitational loading, type_2, the lightest configuration, exhibited a maximum deflection of $12\mu\text{m}$, while type_1 with CBM, the heaviest, displayed a maximum deflection of $75.6\mu\text{m}$. As shown in <Figure 2.2.4.1>, the girder top plate deformation approaches the allowable misalignment tolerance of $50\mu\text{m}$. Deflections exceeding this limit can be compensated for through precision survey and alignment procedures. Modal analysis revealed first mode natural frequencies of 57.86 Hz for type_2 and 26 Hz for type_1 with CBM. Subsequent random vibration analysis, based on the modal results, demonstrated a vertical displacement of 39.7 pm at the girder top surface. This value is significantly below 450 nm, representing 10% of the $4.5\mu\text{m}$ beam size reported in previous studies, thereby ensuring minimal impact on beam operation. Based on these findings, it is anticipated that further refinement of the girder system can be achieved through field experiments involving measurements and prototype testing in a controlled environment.



<Figure 2.2.4.1> Comparisons of the girder deformation and misalignment value.

2.2.5. Girder Control System

The girder control system is designed to ensure beam stability by controlling the vertical movement of girder frames. Operation of the girder control system will be performed during maintenance periods when beam operation within the storage ring is suspended, and it consists of a total of four sets. These sets control the girders in 28 cells of the storage ring and three girders in the injector. Each set is located in a shed and tunnel, and each set is responsible for seven sectors of the storage ring. This configuration allows for independent operation of the five girder frames within each sector. To manage this extensive control area, all communication interfaces utilize EtherCAT, and all data is handled by EPICS IOCs in each IPC. The goal is to make all data communicated with the EPICS IOCs accessible to users through CSS Phoebus.

A. Control system requirements

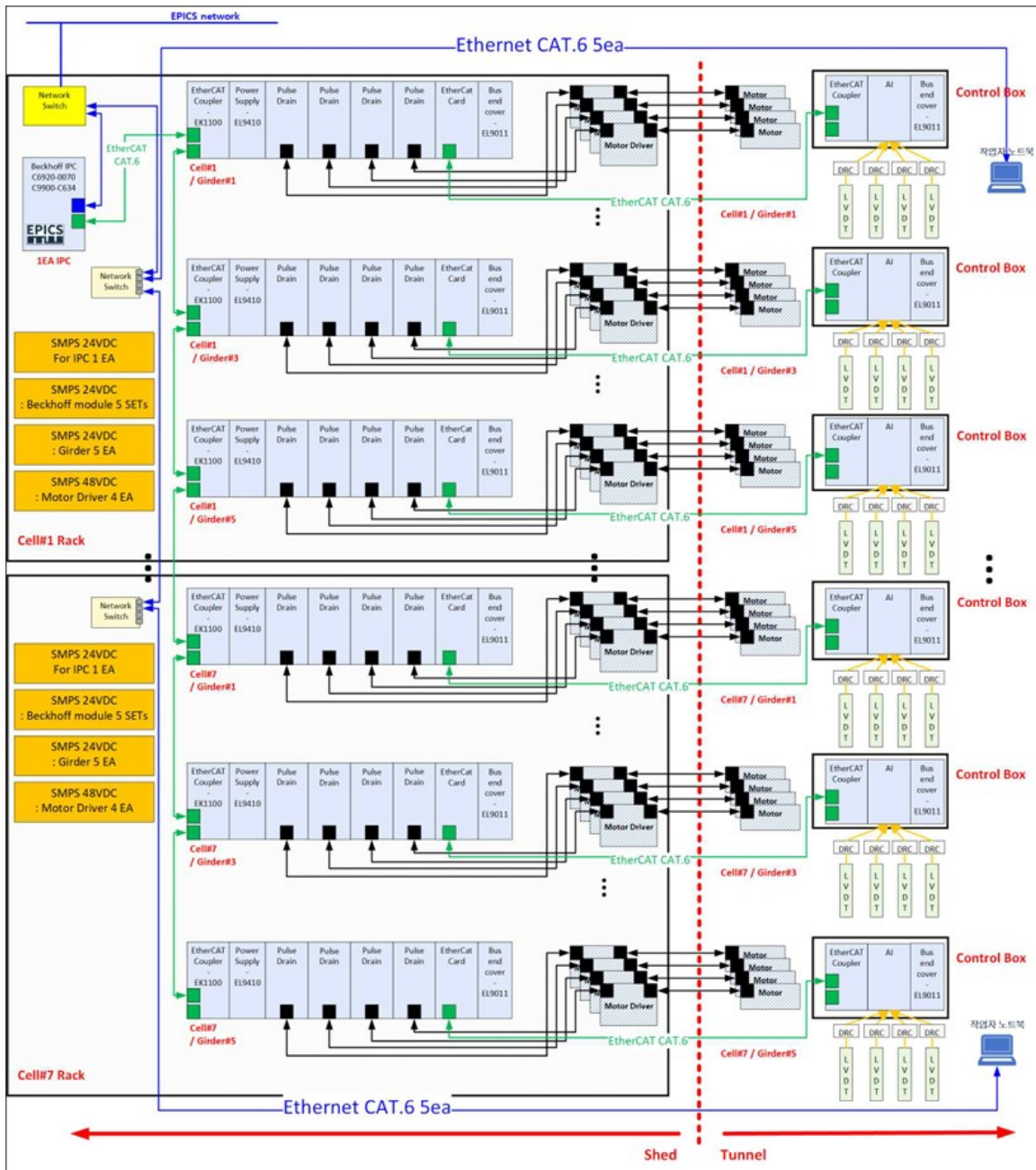
The 4GSR girder control system encompasses the control of 28 cells in the storage ring and three girders in the injector. Each set is located in a shed and tunnel, with each set responsible for controlling seven sectors of the storage ring. The system has the following functional requirements:

- EPICS integration via IPC and sensor and motor control through the EtherCAT interface.
- Girder upper/lower position verification using LVDTs.
- LVDT and motor control through EPICS.
- Precise control of girder frame upper/lower position using stepping motors.
- Position interlock using 4 LVDTs installed on the girder frame.
- Monitoring and control of the girder control system through CSS Phoebus.
- EtherCAT communication cycle time within 100ms.

B. Architecture

<Figure 2.2.5.1> illustrates the basic architecture of the girder control system, showing the interrelationship between devices responsible for seven sectors based on one set. The 4GSR girder control system is divided into four sets to control a total of 140 girder frames in the storage ring and three frames in the injector. Each set is equipped with an IPC that transmits and receives data from the girder frames it manages. It also verifies the position data of the LVDTs installed on each girder, controls the motors installed on the girder frames, and generates interlock signals when the position range is exceeded.

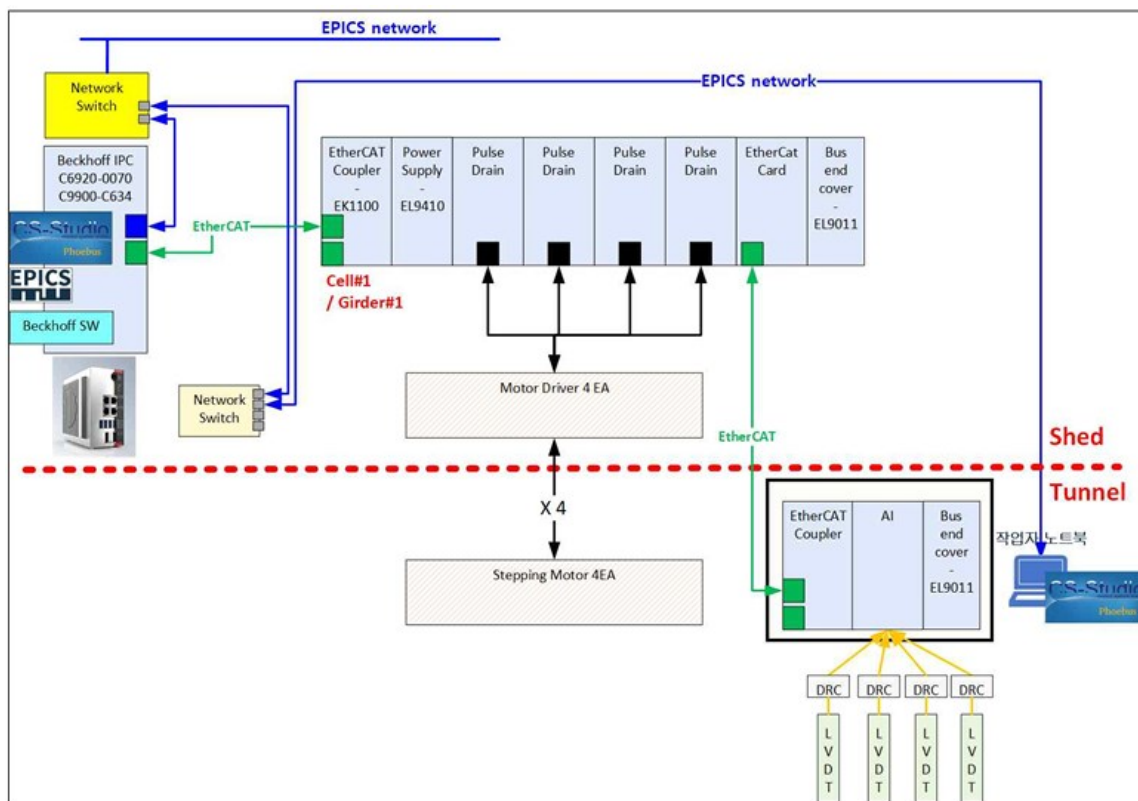
All data is transmitted and received through EPICS, and CSS Phoebebus allows operators to monitor and control the system. As shown in <Figure 2.2.5.1>, EtherCAT is used as the communication interface for controlling and monitoring LVDTs and stepping motors. The IPC controls and monitors information from all sensors and stepping motors through EtherCAT and includes an EPICS IOC internally to publish information from all sensors and stepping motors to the EPICS Network. This allows operators to access the girder control system at any time from any location with EPICS Network access. Access is restricted to authorized users through IP and MAC address management of operator computers.



<Figure 2.2.5.1> Architecture design for the girder control system.

C. Software configuration

The software configuration of the girder control system is structured as shown in <Figure 2.2.5.1> and <Table 2.2.5.2>. To meet the software functional requirements, communication utilizes the EPICS CA protocol and EtherCAT. As depicted in <Figure 2.2.5.2>, the EPICS CA protocol supports control and monitoring through CSS Phoebus from the control room and remote locations, while the EtherCAT protocol enables communication with all modules connected to the IPC. <Table 2.2.5.1> outlines the essential elements for the development of the girder control system and details the software configuration to be installed on the IPC and OPI server.



<Figure 2.2.5.2> Software configuration.

<Table 2.2.5.1> Detail of each software

S/W	Version	Description	Install Location	Note
Windows	10 or more	OS installed on IPC	IPC	
EPICS	7.0.7 or more	SW platform to use girder control system, need to install various libraries to be linked with Beckhoff SW, develop EPICS IOC	IPC	
Beckhoff S/W	-	EtherCAT and Analog Input, software for controlling Pulse Drains and PLC software	IPC	
CSS Phoebebus	V4.7.3	GUI for using the girder control system	For worker	

D. Status of parts for girder system control

<Table 2.2.5.2> summarizes the key hardware for controlling the girder system in the storage ring and injection section, allowing for detailed verification of component status and quantities. The actual development of the girder control system will be based on the components listed in <Table 2.2.5.2>.

<Table 2.2.5.2> Key components for girder system control

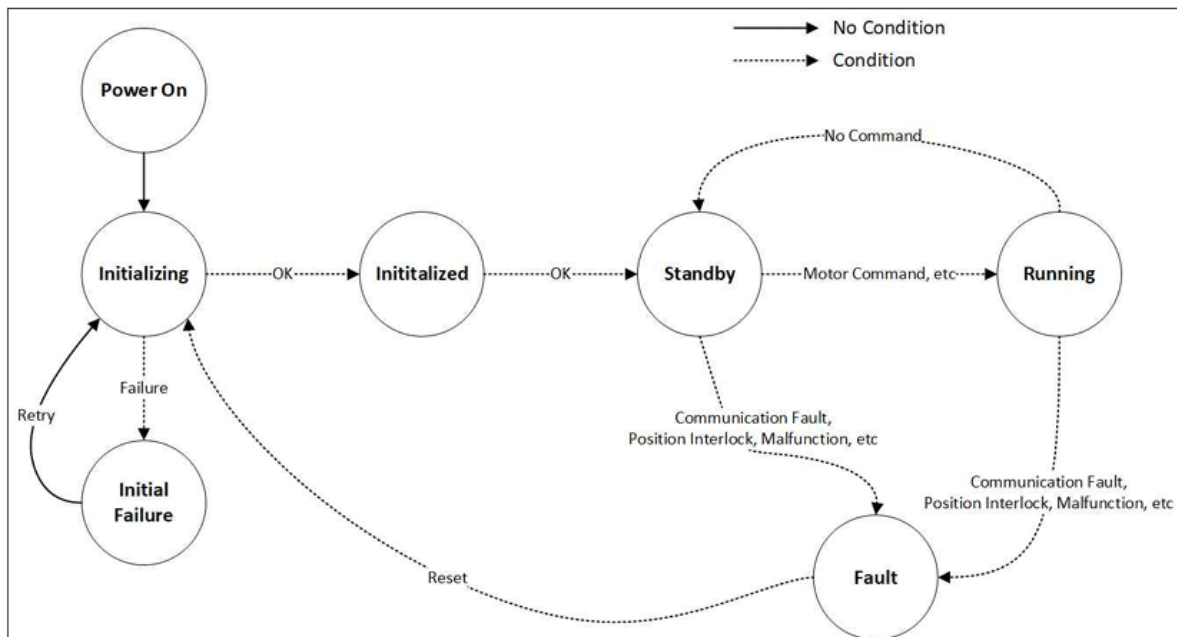
Location	Device	Quantity	Description
Shed	Network S/W #1	4	For EPICS communications, 8ch RJ45
	Network S/W #2	28	SA working between Shed and SR for laptop, 8ch RJ45
	IPC	4	Includes EPICS IOC, PLC SW, Windows 10 or more versions
	EtherCAT Coupler	143	For EtherCAT connectivity in IPC and Shed
	Power supply	143	Add IPC P.S. as needed
	Pulse drain module	572	For motor driver control
	EtherCAT module	143	For communication with the girder module
	End cover	143	For engagement of the control module
	Motor Driver	572	For step motor control
	Rack	28	SMPS, electrical equipment, terminal blocks, etc
	Etc.	-	-
Tunnel	Stepping motor	572	Motor reducer must be included
	EtherCAT coupler	143	For EtherCAT connectivity in IPC and Shed
	AI card	143	16 bit, 4ch, -10 to 10V analog input
	LVDT	572	20mm range measurement, -10 to 10V output, 5um accuracy, lead wire and transducer included
	End cover	143	For engagement of the control module
	Control box	143	Electrical equipment terminals and power supply fastening
	Etc.	-	SMPS, electrical equipment, terminal blocks, etc
Common	PLC SW	4	-

E. Controller sequence

The girder control system will be based on the sequence in <Figure 2.2.5.3>, which is divided into four stages: Initial, Idle, Running, and Fault. The following are descriptions of each stage:

- Initial: Initializes the controller and verifies its operational status.
- Idle (Standby): A waiting state where no commands are received from the IPC.
- Running: A state where commands are received from the IPC and the motor is continuously controlled.
- Fault: A state resulting from communication failures, position interlocks, controller malfunctions, interlocking device failures, etc. The Fault state is latched until a Reset command is issued through the OPI.

Sub-states such as -ing and -ed, which are conditions for transitioning from each state to the next, will be added during development. Detailed sequences will be further refined during development.



<Figure 2.2.5.3> Girder control system state transition diagram.

F. Signal list

The signals and types handled by the girder control system are as shown in <Table 2.2.5.3> below.

<Table 2.2.5.3> Random vibration data for the girder system

Protocol	From	To	Description	Note
EtherCAT	LVDT	IPC	LVDT status	
	Step motor	IPC	Motor status	
	IPC	Step motor	Step motor command	
EPICS CA	IPC	OPI Server	LVDT Status Step Motor Status Controller Fault Code Communication Stat	
	OPI Server	IPC	Step Motor Command Reset Command Run Command Etc.	

2.2.6. Girder Control System Results

The girder control system, which must interface with motors and LVDTs in the tunnel, requires empirical verification due to the critical importance of girder frame position. Key verification points include data processing speed, data transmission speed, and interlock triggering during girder frame position movement by motors. To achieve this, the EtherCAT interface was used, and EPICS integration was implemented to enable remote operation. In the current phase, the design of the girder control system's basic performance, connectivity with peripheral devices, and operational plan has been completed. Based on this report, the plan is to develop a prototype device and complete the verification of its actual performance.

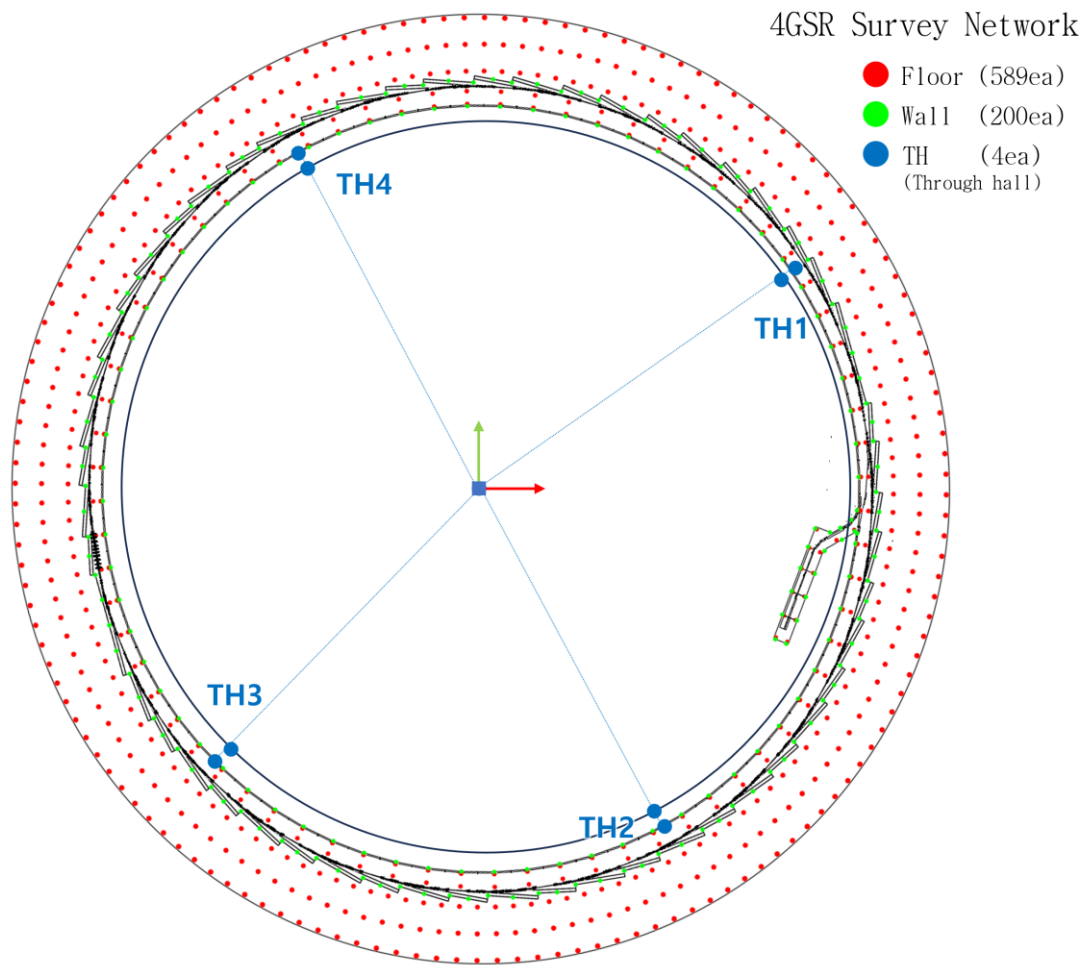
2.3 Precision Survey and Alignment

2.3.1 Precision Survey and Alignment

Surveying is the process of determining the spatial relationships between different points on the Earth's surface and representing them through numerical data or drawings. It involves collecting data and processing information about distance, direction, elevation, mass, time, and environmental factors. Surveying can be classified into various types based on its purpose, such as land surveying, topographic surveying, leveling, tunnel surveying, and astronomical surveying. In general surveying, the highest precision required is typically 1 mm, but accelerator surveying demands even higher precision. The main devices of the recently constructed 4GSR are state-of-the-art accelerators that can perform at their best only when installed and maintained with high alignment accuracy. To operate the accelerator continuously and stably, the installation plan for the devices must be reviewed based on surveying and alignment from the foundational design stage. This report describes the establishment of precision surveying and alignment equipment for the construction of the 4GSR, the installation of fiducials, the alignment of major devices, the survey network, monitoring devices, and the required manpower.

A. Survey Reference Coordinate

To position arbitrary devices at desired points within a specific space, it is necessary to define surveying coordinates for that space and establish physical coordinate axes. In the case of the synchrotron accelerator, a survey network is constructed by considering the spatial dimensions of each section, such as the gallery where the MPS, controller racks, modulators, and klystrons are installed; the linear accelerator tunnel where the accelerating structures are located; the storage ring where the electromagnets, insertion devices, and diagnostic devices are installed; and the beamline where experimental apparatus are set up, as shown below in <Figure 2.3.1.1>.

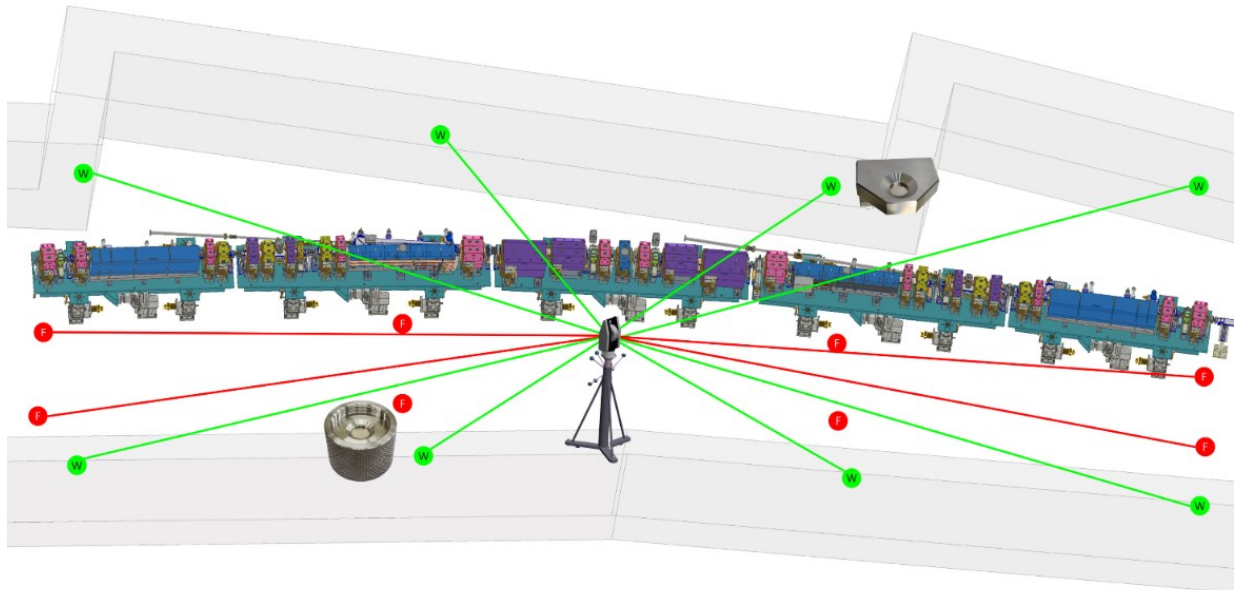


<Figure 2.3.1.1> 4GSR Survey Network.

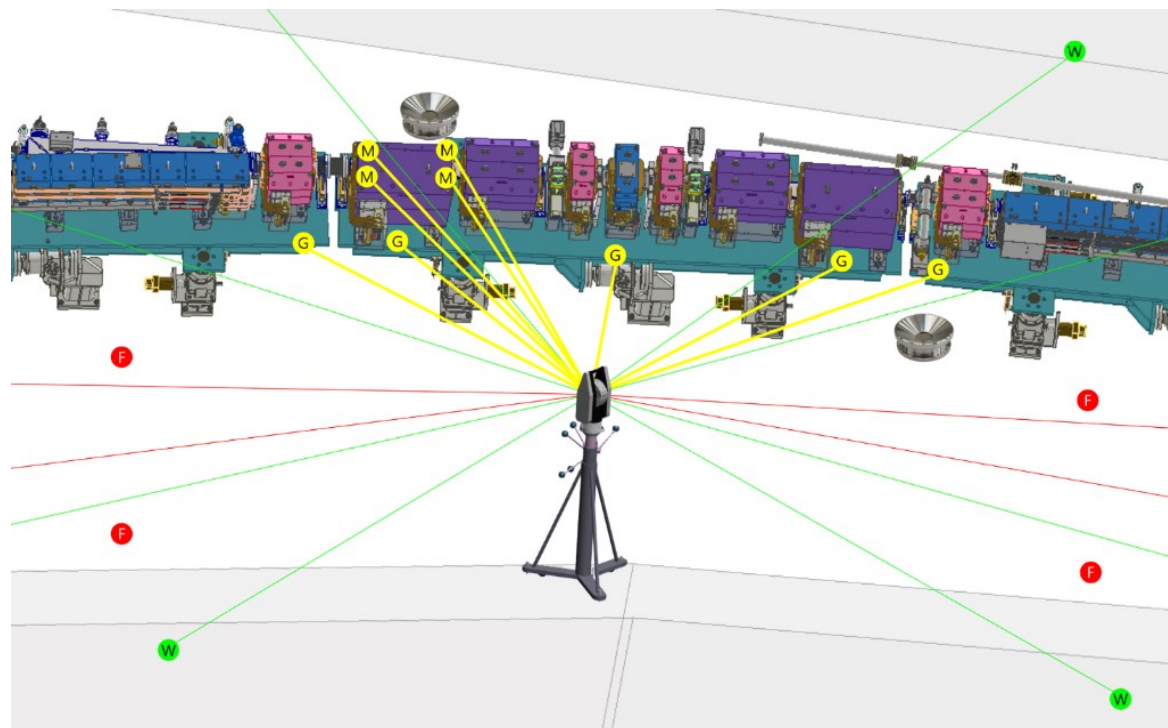
The survey network should be constructed broadly enough to sufficiently cover the measurement objects in order to minimize errors. 4GSR survey network has been established to ensure that the linear accelerator, storage ring, and beamline devices can all be measured accurately. The overall reference coordinate system is set as described above, with the origin of the storage ring at (0,0,0). For reference, the height of the 4GSR floor is GL (ground level) 156.3 m. By establishing a right-handed coordinate system that aligns with the mechanical CAD coordinate system, there is no confusion when exchanging coordinate information with the other device teams.

To establish a surveying reference frame, surveying points are installed on the walls and floor. <Figure 2.2.1.2> and <Figure 2.2.1.3> shows the details of the 4GSR surveying reference point network construction and the concept of device measurement. The survey network is set up considering the characteristics of the area, with the intervals, heights, and widths of each reference point established before installation across the entire section. On the floor of the storage ring, two rows of points are installed at 10 m intervals, while on the

walls, points are set at a height of 1.8 m and at intervals of approximately 10 m. The intervals can be adjusted based on the arrangement of the building and devices, with a center around 10 m. The device surveying reference points are mostly located at the upper edges of the devices for easy alignment. While three points are sufficient to express location information, four points are installed to prevent potential damage or errors at the reference points and to enhance precision. In the figure below, F denotes floor reference points, W denotes wall reference points, M denotes magnet reference points, and G denotes girder reference points.



<Figure 2.3.1.2> 4GSR Detailed conceptual drawing of the construction of the survey network.



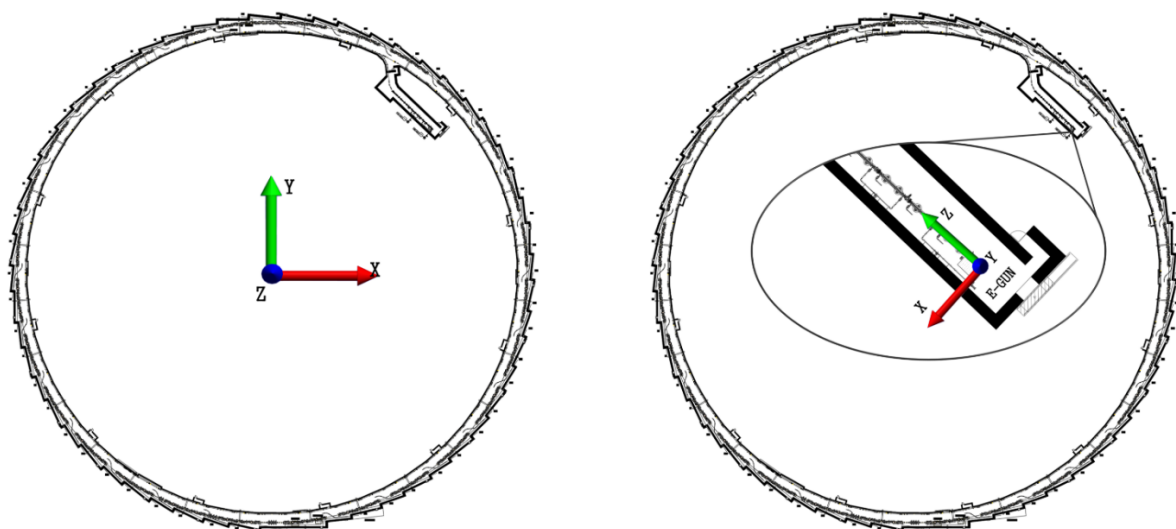
<Figure 2.3.1.3> Device measurement conceptual diagram.

B. Absolute Positioning

It generally refers to placing accelerator devices within a global reference grid, known as a global coordinate system. The absolute positions of the accelerator and beamline components serve as important database references for surveying and alignment, so it is crucial to carefully analyze the surveying data along with the relative positions.

C. Relative Positioning

The alignment technique discussed must be considered alongside absolute positioning when precisely aligning the components of a radiation accelerator. This technique involves relatively aligning the components by allowing local tolerances between adjacent devices. To enhance beam stabilization, it is necessary to define the relative positioning error for the devices in each section and then perform precise alignment accordingly. <Figure 2.3.1.4> illustrates the global coordinate system (left image) and the local coordinate system (right image). In the global coordinate system, the origin is located at the center of the storage ring, with X (+) pointing to the right, Z (+) directed opposite to gravity, and Y (+) in the remaining perpendicular direction. In local coordinate system, Z (+) follows the direction of beam travel, Y (+) points opposite to gravity, and X (+) is to the left relative to the beam travel direction. Both systems employ a right-handed coordinate system. One advantage of using the global coordinate system is that it facilitates understanding of how much a device deviates from alignment in the direction of beam travel. Additionally, it simplifies information exchange with other device teams. The local coordinate system, on the other hand, is useful for presenting final alignment data and results.



<Figure 2.3.1.4> Coordinating system of Global coordinate (left) and Local coordinate(right).

D. Layout Reference Frame

From the perspective of beam physics, synchrotron accelerators are designed using a lattice coordinate system, where the spatial positions of each device are defined within this framework. In this system, the spatial positions of the accelerator's components, combined with their center coordinates, form what is referred to as a layout reference frame. To position this layout reference frame within a specific space, processes such as coordinate rotation and transformation are performed relative to the surveying reference frame of that space.

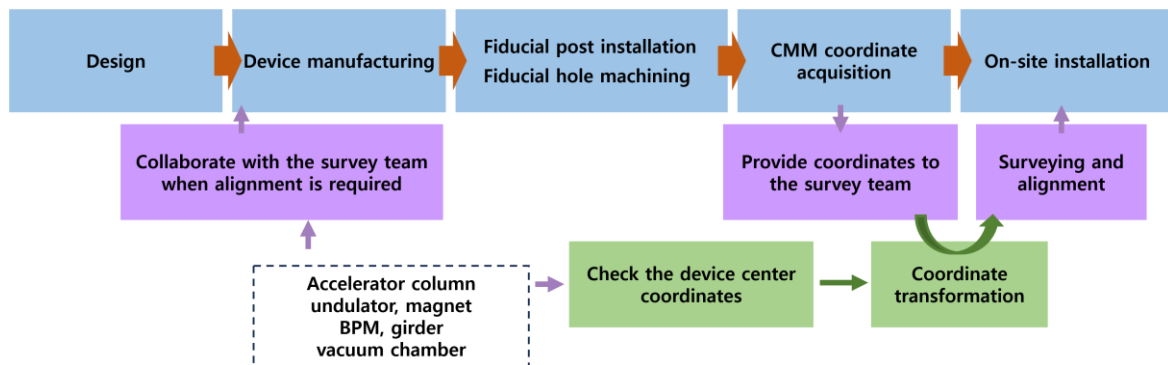
E. Fiducialization

Fiducialization is the process of determining the mechanical, electrical, or magnetic center points or centerlines of each device and transferring that coordinate information to fiducials installed externally on the devices. In other words, it links the measurement points of the devices to reference points, enabling the devices to be accurately positioned within the layout reference frame. Precision devices requiring high-accuracy measurement and alignment such as accelerator tubes, electromagnets, vacuum chambers, Beam Position Monitors (BPMs), and other optical components must undergo this process.

Fiducialization should be efficiently coordinated with the alignment team starting from the design phase. This collaboration encompasses determining the types and locations of fiducials, performing Coordinate Measurement Machine (CMM) measurements, managing on-site installation, and ensuring precise alignment. <Figure 2.3.1.5> illustrates the Fiducialization Workflow. For example, after establishing the coordinate center, height, and orientation of individual electromagnets, the coordinates obtained during the fiducialization process are used to position these devices within the overall coordinate system and define their individual positions. This coordinate information is shared between the device team and alignment experts and is continuously utilized throughout the equipment's installation and operational phases.

For electromagnets, the mechanical center is determined first, followed by the measurement of the magnetic center (magnetic field measurement) to obtain the final corrected coordinates used for measurement and alignment. Regarding the number of fiducials required for electromagnets, there are approximately 51 main electromagnets in the 4GSR LINAC and LTB sections, 465 in the Booster and BTS sections, and 1,125 in the Synchrotron section, totaling around 1,641 electromagnets. Since an average of four






fiducials is installed on each electromagnet, a total of approximately 6,812 fiducials are needed.



<Figure 2.3.1.5> Fiducialization flowchart.

<Table 2.3.1.1> categorizes the shapes, sizes, and installation devices used for fiducialization by type. For vacuum vessels, it is often challenging to install dish-type fiducials due to their low thickness and potential for magnetic interference. In such cases, a location with good measurement visibility is chosen, and a direct hole is drilled to serve as the fiducial.

<Table 2.3.1.1> Fiducial class according to the device

device	type		size	remarks
Magnet, girder		Dish type	ø34.0, H:12.3mm	
Magnet, girder, BPM chamber, strong back		1/4" hole	1/4" drilling hole	
Wall structure		Wall type	L:60.0mm, W:46.0mm H:41.0mm	
Building floor		Floor type	ø50.0 H:35.0mm	
Magnet, girder		Cone type	ø25.0, H:19.0mm	Installed in devices that are sensitive to magnetic influences

<Table 2.3.1.2> summarizes the types and detailed quantities of fiducials for electromagnets by area. All major devices requiring alignment must have fiducials installed.

<Table 2.3.1.2> Types and fiducial quantities of electromagnets by installation zone

Region	Magnet	Quantity	Fiducial Qty.
LINAC	Electron Gun	1	4
	Solenoid	1	4
	Accelerating Tube	4	24
	Quadrupole, Quadrupole + Corrector	10	40
	Steering	10	40
	Dipole	1	4
	Subtotal	27	116
LTB	Bending	4	16
	Quadrupole + Corrector	10	40
	Corrector	8	32
	Septum	1	4
	Kicker	1	4
	Subtotal	24	96
Booster Ring	Combined Bending	64	256
	Quadrupole	70	280
	Sextupole	64	256
	Corrector	240	960
	Subtotal	438	1,752
BTS	Kicker	1	4
	Combined Bending	1	4
	Bending	2	8
	Septum	5	20
	Quadrupole	10	40
	Corrector	8	32
	Subtotal	27	108
SR	Kicker	4	16
	Septum	1	4
	Center Bend	30	120
	Longitudinal Gradient Bending	120	720
	Quad-Bend and Reverse Bend	240	960
	Quadrupole	352	1,408
	Quadrupole	18	72
	Sextupole + Slow corrector	180	720
	Octupole	60	240
	Fast-Slow Corrector	120	480
	Subtotal	1,125	4,740
Total		1,641	6,812

2.3.2 Establishment of Precision Surveying Equipment

A. Measurement Equipment

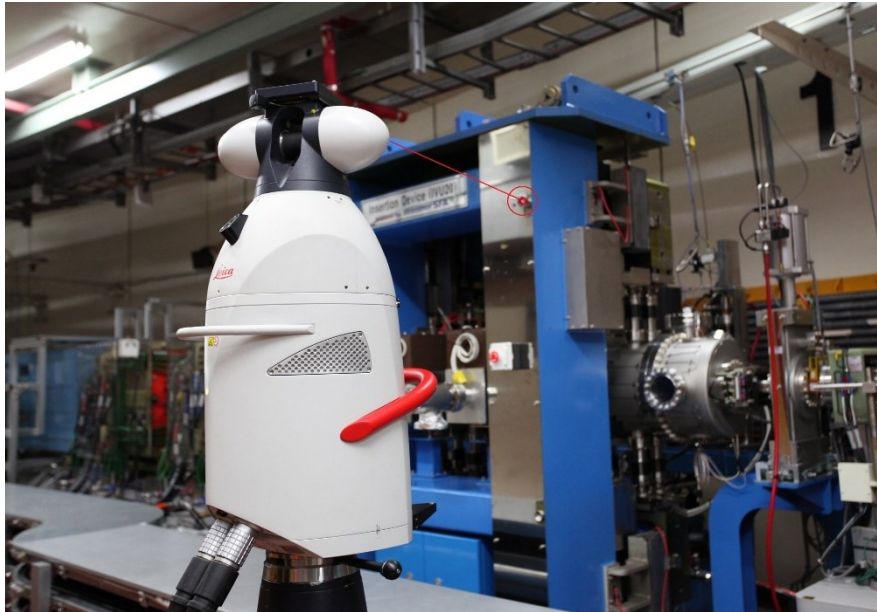
To install and align the 4GSR, various surveying tools, such as Laser Trackers, Total Stations, Optical Tooling, Digital Levels, and analysis software like SA, are utilized. <Table 2.3.2.1> provides a detailed list of the main equipment used in constructing the 4GSR. One of the most commonly used tools is the Laser Tracker system, a state-of-the-art non-contact 3D measurement device. It employs a laser interferometer to measure distances precisely and encoders to capture vertical and horizontal angles. The observed angle data is transmitted online to a computer, enabling tasks such as coordinating setting and transformation, shape analysis, error evaluation, and determining the position of objects in 3D space. The Laser Tracker is widely used for the alignment and geometric measurement of individual machinery during the assembly of the 4GSR device. It is also instrumental in measuring the positions of reference markers. <Figure 2.3.2.1> shows the equipment primarily used by an alignment team at a research institute operating a device similar to the 4GSR. <Figure 2.3.2.2> depicts the process of measuring an insertion device in the Pohang Accelerator's PLS-II storage ring using a Laser Tracker.

<Table 2.3.2.1> Survey & Measurement Main Equipment

Device	Measuring Range	Measure	Usage
Laser tracker A	0 m to 15 m (max.60 m)	$U_{x,y,z} = \pm 15 \mu\text{m} + 6 \mu\text{m/m}$	Network Measurement, Alignment
Laser tracker B	1.5 m to 15 m (max.80 m)	$U_{x,y,z} = \pm 15 \mu\text{m} + 6 \mu\text{m/m}$	Network Measurement, Alignment
Theodolite Total station	1.5 m to 100 m (max.600 m)	Angular: 0.15 mgon (0.5") \rightarrow 0.1mm/40m Distance: 0.2 mm + 2ppm \Rightarrow 0.3mm/40m	Network Measurement, Alignment
Theodolite	0.5 m to 20 m	Angular: 0.15 mgon (0.5") \Rightarrow 0.1mm/40m	Axis-Alignment, Auto-Collimation
Precision Level A	1.6 m to 10 m	$\pm 0.3 \text{ mm/km}$ (optical/analog)	Network Measurement, Height transfer
Precision Level B	5 m to 10 m	$\pm 0.3 \text{ mm/km}$ (Barcode/digital)	Network Measurement, Height transfer



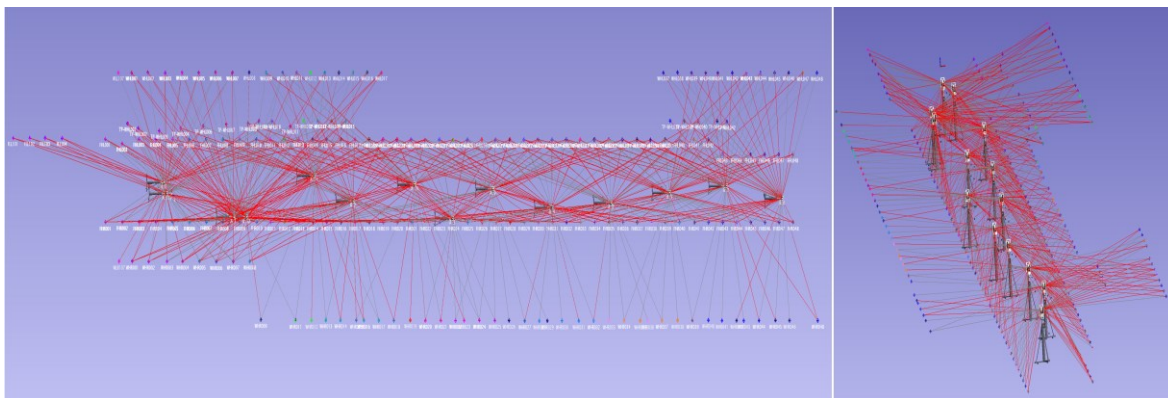
<Figure 2.3.2.1> Laser Tracker & Precision Level.



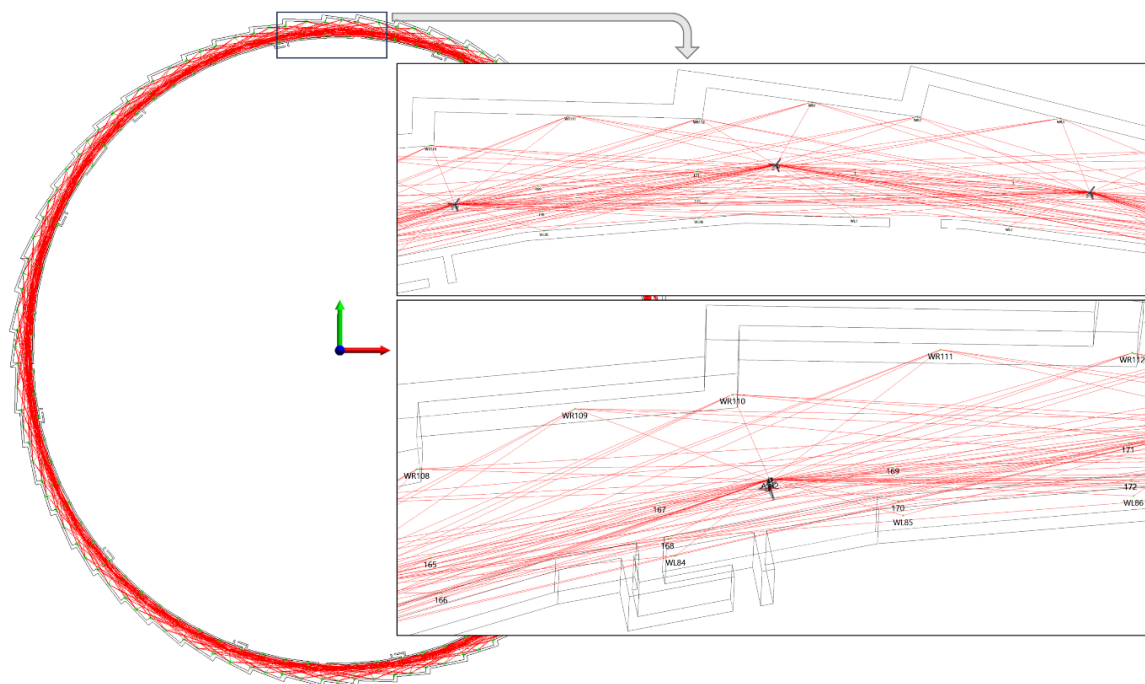
<Figure 2.3.2.2> ID Measurement picture through Laser Tracker (PLS-II).

B. Survey Network

In the accelerator storage ring tunnel, a survey network is typically established at intervals of 8 to 12 meters. However, as the alignment precision of the 4GSR device increases, closer spacing becomes necessary. <Figure 2.3.2.3> illustrates the survey network of the PAL-XFEL tunnel, which generally includes four measurement points per cross-section: two on the floor and two on the left and right walls. By overlapping measurement points as shown, measurement precision is significantly enhanced. The beamline survey network, in contrast, is installed at intervals approximately 2 to 3 times longer than those of the storage ring. This difference accounts for the space required for beamline device placement.

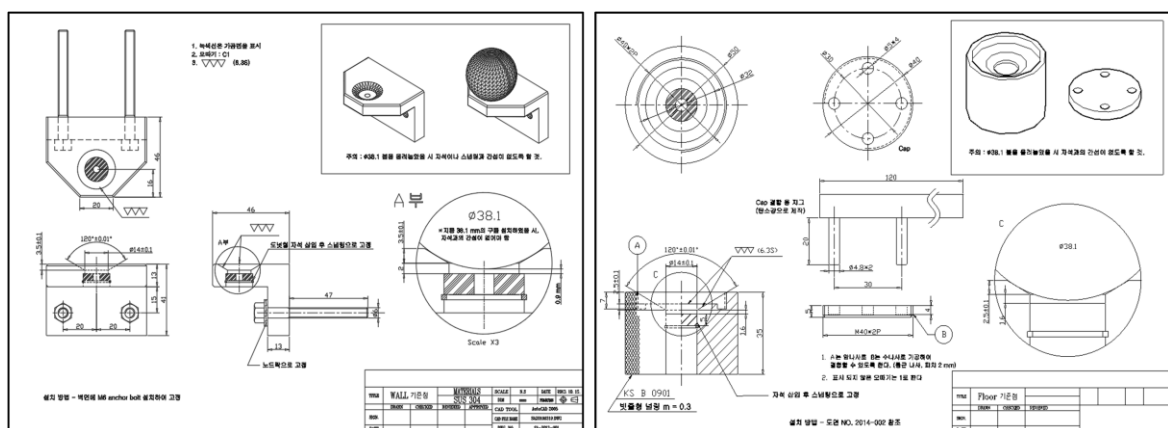


<Figure 2.3.2.3> Pohang Accelerator PAL-XFEL Survey Network.

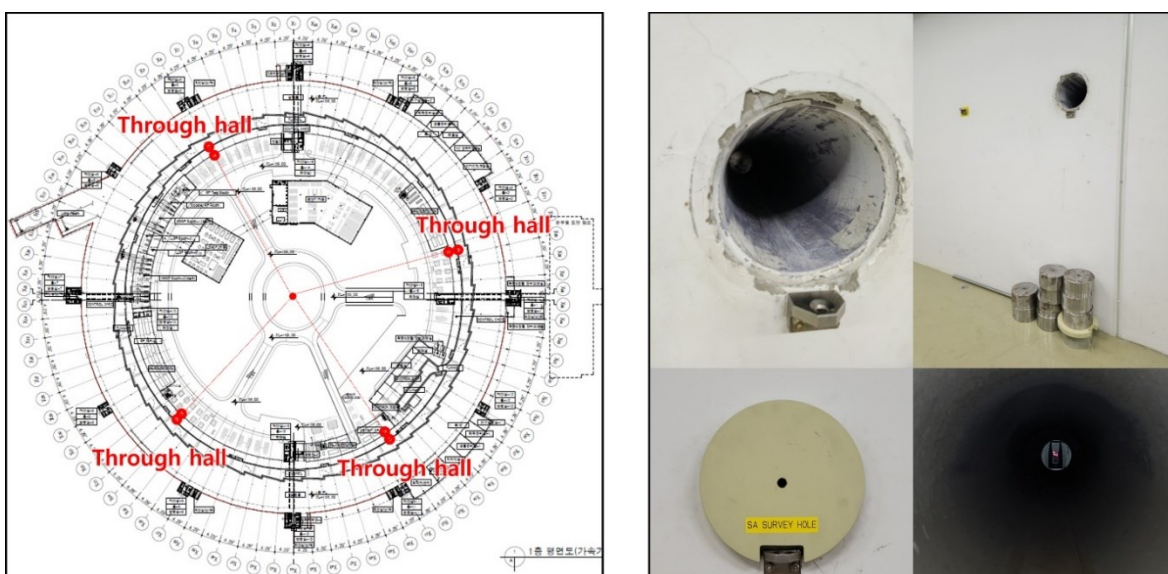


<Figure 2.3.2.4> A conceptual diagram of the survey network for 4GSR.

<Figure 2.3.2.5> shows the design plan for the survey network monuments installed on the tunnel floor and walls, while <Figure 2.3.2.6> illustrates the installation of through halls in the survey network. To reduce cumulative errors that can occur over long distances in the 800-meter-long 4GSR storage ring, four through halls were installed to maintain accurate alignment by allowing horizontal penetration through the building. The image on the right shows a photo of the through hall installed in the Pohang Accelerator XFEL tunnel. Instead of using the vertical centering method with an optical plummet to reduce errors, a horizontal through hall installation method utilizing laser tracker equipment offering significantly improved performance was adopted.



<Figure 2.3.2.5> Monument mounting on tunnel floor and wall.



<Figure 2.3.2.6> Through hall survey network and installation case.

2.3.3 Devices Alignment

A. Girder and main device anchor marking

In the installation phase of the storage ring, the first step is to mark the positions of the girders and major device anchors. The number and locations of the anchors to be marked are provided by the girder and device managers. <Figure 2.3.3.1> shows photos taken during the Pohang Accelerator Performance Improvement Project: on the left, marking the anchor positions of the storage ring girders, and on the right, marking the centerline of the beamline section. Given the large number of anchor markings for the storage ring girders, templates are prepared and tested to significantly reduce installation time, especially considering the short installation period. Using templates can reduce the work time by approximately 50% and effectively prevent errors that might occur during the process.

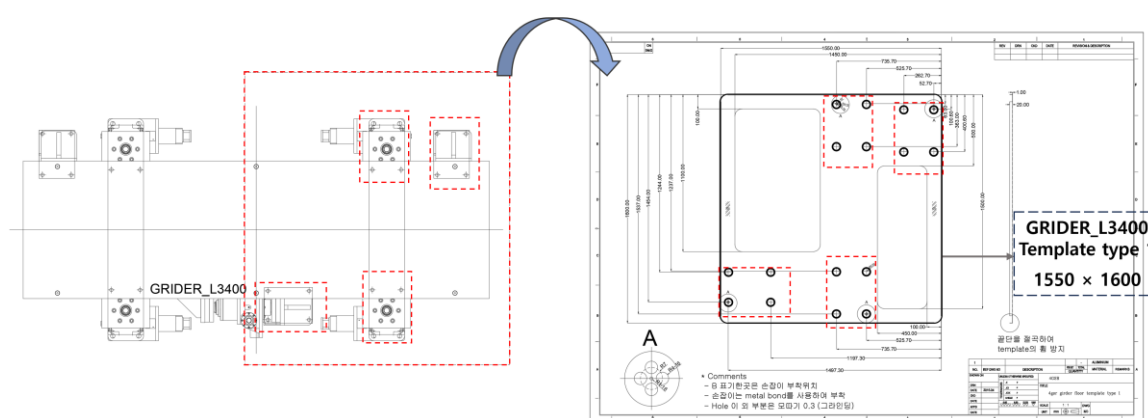


<Figure 2.3.3.1> Anchor marking (PLS-II storage ring and beamline section).

<Figure 2.3.3.2> is one of the fabrication drawings for the 4GSR storage ring girder anchor bolt marking templates. The templates are divided into lengths of less than 2 meters to account for transportation and deformation, with each divided into two sections. There is a total of six types, and assuming two teams are working, 12 templates are required. <Table 2.3.3.1> shows the types and quantities of storage ring girder templates.

<Table 2.3.3.1> Storage ring girder template type and quantity

Girder	Template Type	Total
GIRDER_L4800	L4800-1	2
	L4800-2	2
GIRDER_L3800	L3800-1	2
	L3800-2	2
GIRDER_L3400	L3400-1	2
	L3400-2	2
Total		12 ea



<Figure 2.3.3.2> 4GSR storage ring girder template for anchor bolt marking.

B. Collaboration between assignees

Surveying and alignment engineers must actively participate in the fieldwork in the following areas and establish strong collaborative relationships with domain experts:

Calculating the alignment error between a theoretically perfect device alignment and the practical alignment of the device.

Discussing the thermal stability and ground behavior around the device that affect its alignment stability.

Providing design consultation on the device's support and alignment mechanisms during the early stages of production.

In emergency situations such as earthquakes or fires, device experts assess the damage and discuss priorities to ensure the efficient and urgent restoration of the device.

C. Key devices alignment

Among the main devices, a representative example is the alignment of electromagnets. Electromagnets vary not only in function but also in shape, making the process of establishing measurement standard coordinates crucial. Therefore, before the actual installation of the device, it is essential to participate in the manufacturer's magnetic field measurement and device coordinate-setting process for verification. As a preliminary task for magnetic field measurement, the alignment of the magnetic field measurement device itself is also performed. Similarly, a verification process is required at this stage. Given the importance of this task, direct discussions with the manufacturer on technical issues can help ensure smoother progress. Other major devices follow a similar procedure to that of the electromagnets. All devices are pre-aligned by installing girders, electromagnets, and chambers sequentially in the beamline experimental area. They are then moved as one girder set to the storage ring. The sequence of installation and alignment tasks is as follows:

Align the base plate of the girder assembly building to be as flat as possible.

Perform grouting treatment if necessary.

Install the girder on the flat base plate.

Align the girder to the design height based on its average value.

Install and align magnets, containers, and other components.

Measure and store the positions, converting them to storage ring coordinates.

Align the base plate of the storage ring tunnel to be as flat as possible.

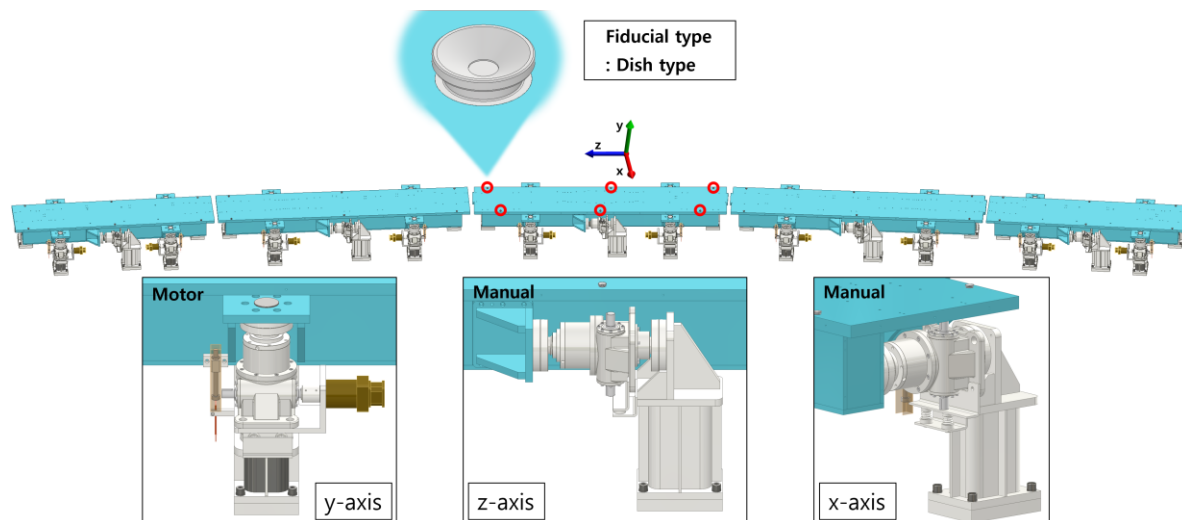
Transport the girder to the storage ring tunnel and install it using alignment mechanisms.

Adjust the girder by measuring and installing the device in the same manner as in the girder assembly building.

Upon first installation, measure all devices on top of the girder and align the girder.

(1) Girder alignment

On the girders of the storage ring, magnet devices are pre-aligned in a separate assembly area. These devices are aligned to a specified tolerance using individual adjustment devices based on the reference points of the girders, and then moved and installed as a complete girder unit. There are different types of girders, including the longest 4,800 mm type, and the 3,800 mm and 3,400 mm types. Most of the 28 cells are arranged in a specific order. After each girder is moved to its designated position and installed, it is realigned. To facilitate these operations, six reference points are installed on each girder. <Figure 2.3.3.3> shows a model of a normal cell girder to be installed in the storage ring. Each girder is equipped with a ball screw jack on each axis. The y-axis is aligned using a motor, while the x and z axes are aligned manually, as shown in the figure. <Table 2.3.3.2> shows the quantity and number of fiducials for each girder in the storage ring.



<Figure 2.3.3.3> Girder model of normal cell for storage ring.

<Table 2.3.3.2> Quantity and number of fiducial for each girder

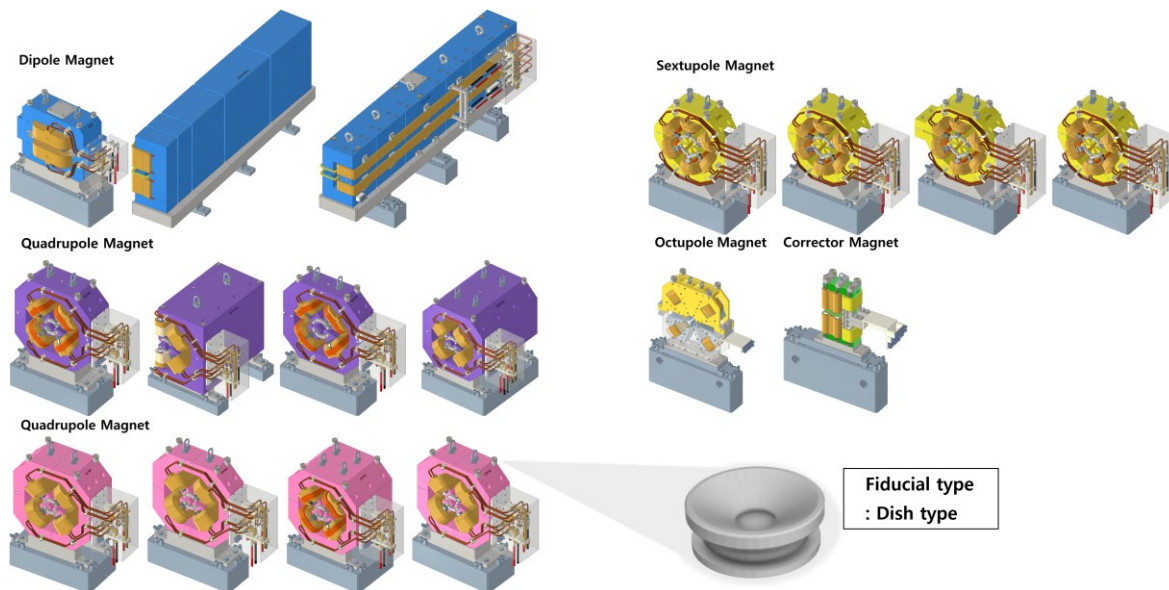
Girder type	Main equipment	Qty.	Fiducial Qty.	Fiducial type
4,800	CMB, LGBM	84	504	Dish
3,800	LGBM	52	312	Dish
3,400	LGBM	4	24	Dish
3,400	Kicker, Septum	3	18	Dish
Girder total Qty.		143		
Fiducial total Qty.			858	

(2) Electromagnet alignment

The approximately 1,641 electromagnets in the storage ring are divided into types based on their number of poles, including two-pole, four-pole, six-pole, and eight-pole configurations, each with various shapes. <Figure 2.3.3.4> and <Table 2.3.3.3> show the location and quantity of measurement reference points for each type of electromagnet. Normally, four reference points are selected and installed at the upper edge of the object to be measured. However, if the object is long, six or eight reference points may be used to improve accuracy. This process was determined in consultation with the electromagnet equipment team, and the fiducial point type was standardized to a saucer type.

<Table 2.3.3.3> Electromagnet fiducial point installation quantity

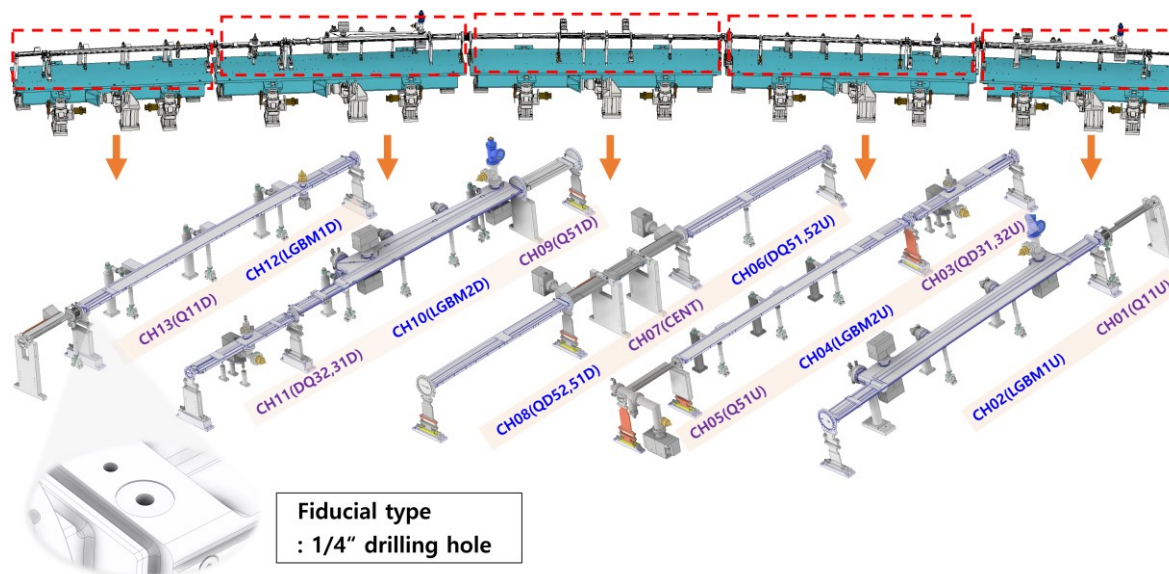
Magnet summary							
	Magnet Type	Qty.	Fiducial Qty.		Magnet Type	Qty.	Fiducial Qty.
LINAC	Electron Gun	1	4	BTS	Kicker	1	4
	Solenoid	1	4		Combined Bending	1	4
	Accelerating Tube	4	24		Bending	2	8
	Quadrupole, Quadrupole +Corrector	10	40		Septum	5	20
	Steering	10	40		Quadrupole	10	40
	Dipole	1	4		Corrector	8	32
	Subtotal	27	116		Subtotal	27	108
LTB	Magnet Type	Qty.	Fiducial Qty.	Storage	Magnet Type	Qty.	Fiducial Qty.
	Bending	4	16		Kicker	4	16
	Quadrupole + Corrector	10	40		Septum	1	4
	Corrector	8	32		Center Bend	30	120
	Septum	1	4		Longitudinal Gradient Bending	120	720
	Kicker	1	4		Quad-Bend and Reverse Bend	240	960
	Subtotal	24	96		Quadrupole	352	1,408
Booster	Magnet Type	Qty.	Fiducial Qty.	Ring	Quadrupole	18	72
	Combined Bending	64	256		Sextupole + Slow corrector	180	720
	Quadrupole	70	280		Octupole	60	240
	Sextupole	64	256		Fast-Slow Corrector	120	480
	Corrector	240	960		Subtotal	1,125	4,740
	Subtotal	438	1,752		Total	1,641	6,812
Ring							



<Figure 2.3.3.4> Electromagnet fiducial point installation location.

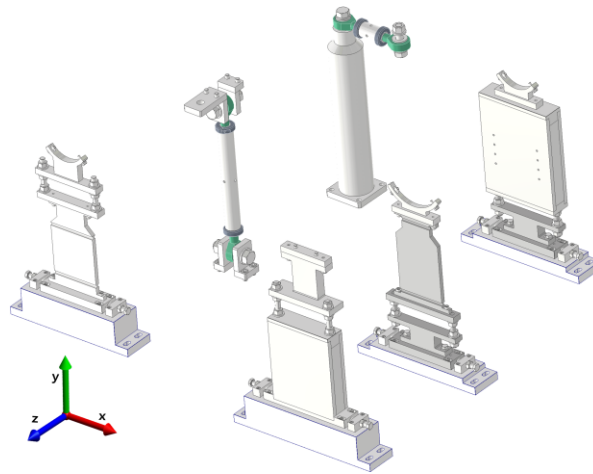
(3) Vacuum chamber alignment

The normal cell of the storage ring is equipped with 13 types of chambers, each with a unique shape. To align these chambers, at least three fiducials must be installed. <Figure 2.3.3.5> shows a model of the storage ring normal cell chambers and fiducials, with each chamber featuring a 1/4" drilled hole.



<Figure 2.3.3.5> Model of storage ring normal cell chambers and fiducials.

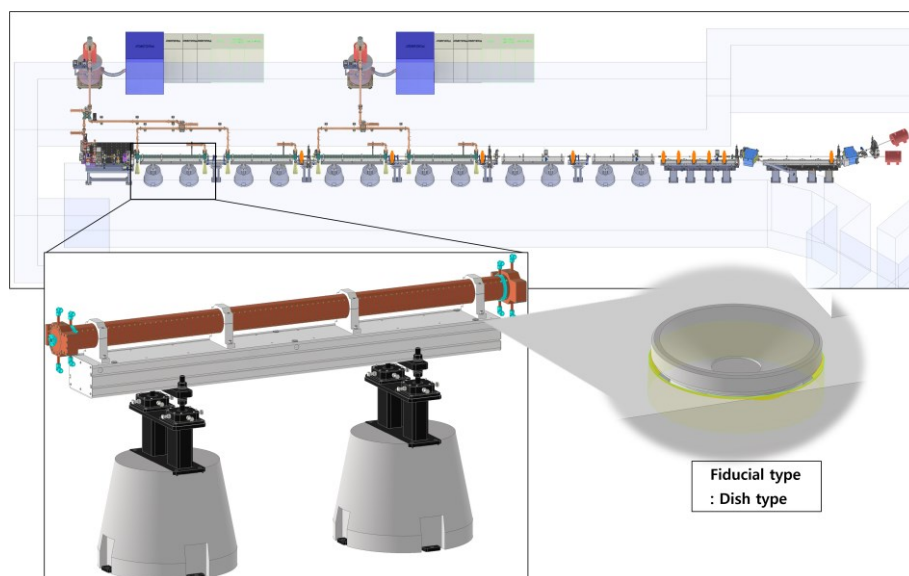
Each chamber is aligned using individual adjusting devices. <Figure 2.3.3.6> presents a model of the adjusting devices to be applied to the chamber.



<Figure 2.3.3.6> Model of adjusting devices for storage ring chambers.

(4) Alignment of linear accelerator tube

During the review process of the accelerator tube drawings, the types and locations of the surveying reference points were modified to ensure a smoother alignment line and improve precision. To secure a better alignment angle, it was decided to process six holes in the accelerator tube strongback, as shown in <Figure 2.3.3.7>, and insert fiducial posts for installation.



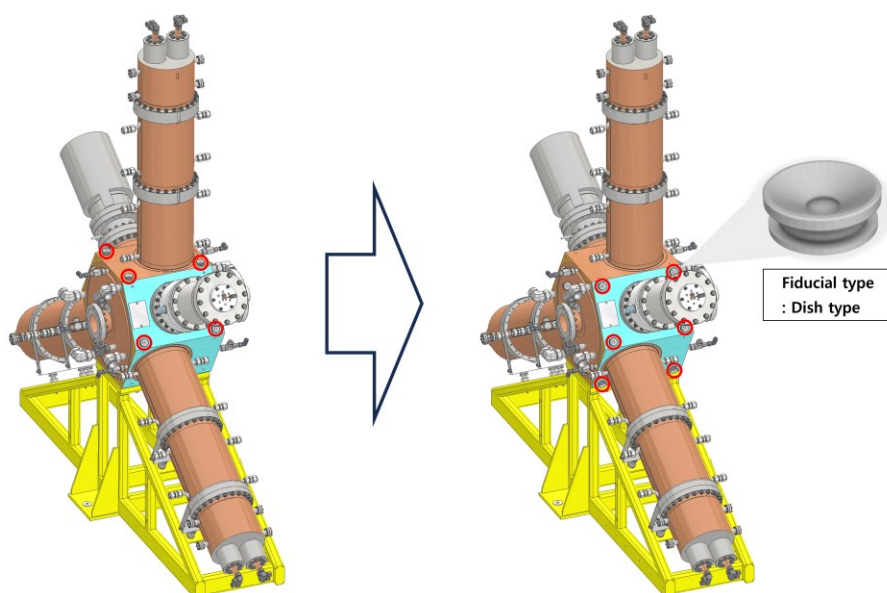
<Figure 2.3.3.7> After machining 6 holes in the acceleration tube strongback, install the fiducial post.

(5) RF Cavity alignment

Another important device in the alignment section, with a large quantity, is the RF Cavity. Due to its complex shape, it was decided in consultation with the RF device team to install a total of six fiducials: four on the top surface and two on the inclined surface inside the tunnel. After reviewing the installation model of the SR, HOM Damped NC Cavity requested by the RF group, the positions and quantities for alignment were determined, and modifications were made, as shown in <Figure 2.3.3.8>, for easier measurement. Similar to the electromagnet, the fiducial point type was standardized to a dish type, and an additional adjustment device was requested to be installed on the RF Cavity support to facilitate rapid alignment during the operational period. <Table 2.3.3.4> shows the positions and quantities of the main RF cavities in the storage ring.

<Table 2.3.3.4> Positions and quantities of main RF Cavities.

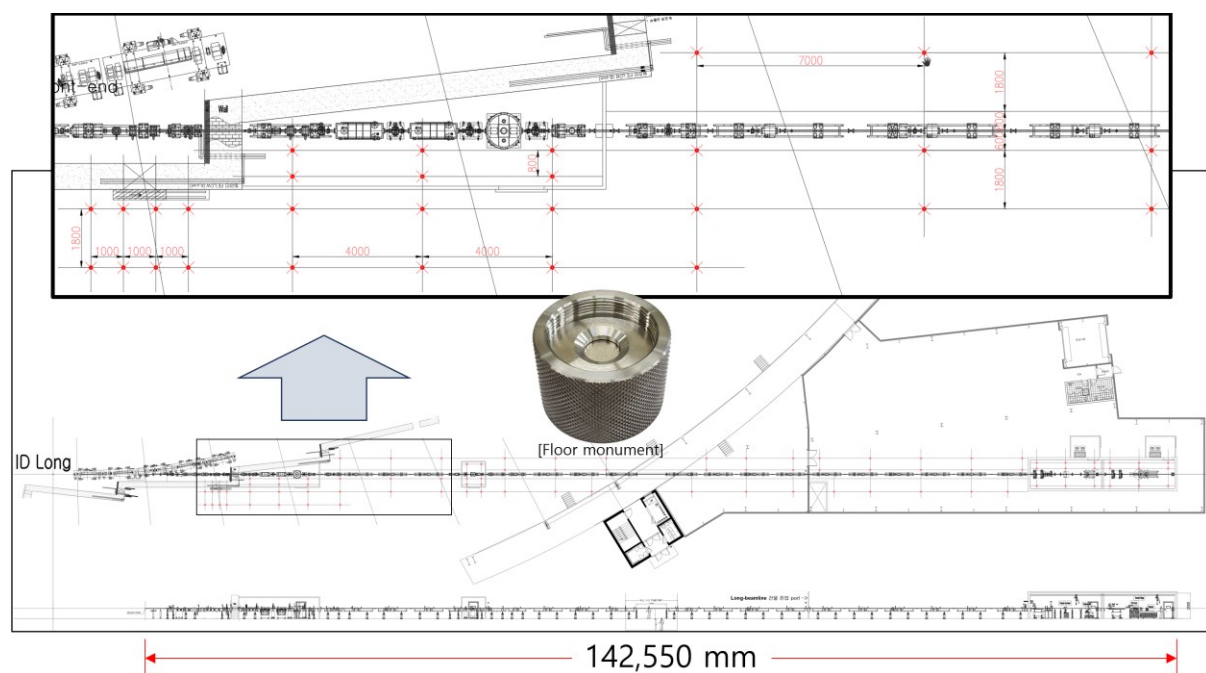
SR Main RF Cavity: 500_MHz_HOM_Damped_NC_Cavity			
Cell No.	Type	Qty.	Fiducial Qty.
#13 Cell	RF Cavity	2	12
#14 Cell	RF Cavity	4	24
#15 Cell	RF Cavity	4	24
Total		10	60



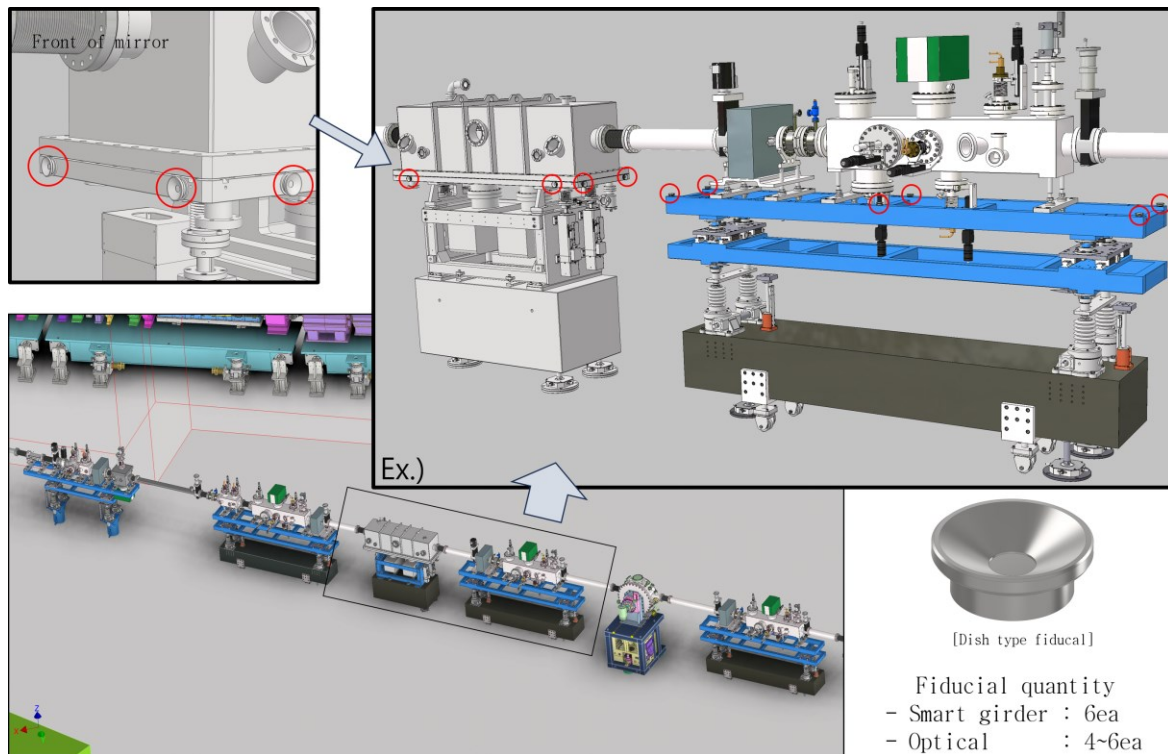
<Figure 2.3.3.8> Six fiducials on the measuring surface
(Left: Before change, Right: After change).

(6) Long Beam Line Survey Network Construction

Unlike PLS-II, the 4GSR will have a long beamline, exceeding 140 meters. A simple lattice structure surveying network, like those used for shorter beamlines (less than 30 to 40 meters), will be insufficient. Therefore, a separate survey network will be established to align devices along the beamline. Each beamline will require 89 monuments on the tunnel floor, and 276 fiducials will be installed on the girders for device measurement. Additionally, a small number of monuments will be installed on the nearby walls <Figure 2.3.3.9> and <Figure 2.3.3.10> show details of the floor monuments and fiducials for device measurement.



<Figure 2.3.3.9> Long beam line floor monument.



<Figure 2.3.3.10> Long beam line device measuring fiducials in detail.

As a result of test measurements to determine the position and number of fiducials for spectrometers and mirror devices used for localization of 4GSR beamline core devices, the quantity required for seven units of localized core devices in 2024 is 104 fiducials. The diameter of the lower plate type fiducial to be installed in the beamline optics was reduced from 32 mm to 26 mm due to the small area.

(7) Device misalignment

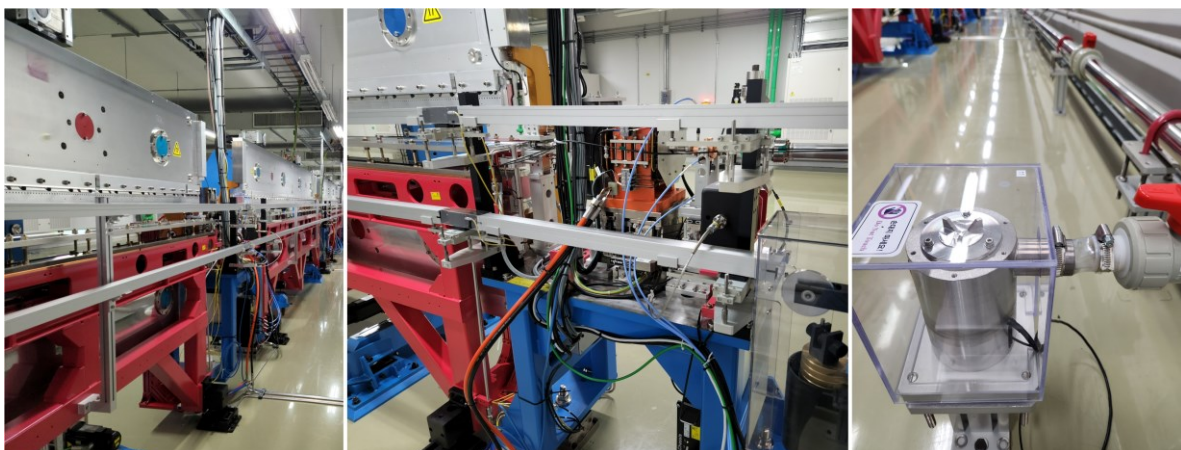
The alignment of accelerator devices is critical for beam operation. If the misalignment is large, collisions within the vacuum chamber can occur. Therefore, it is essential to minimize alignment errors to ensure efficient beam transport and reduce beam loss. The causes of alignment errors include survey network errors, measurement equipment errors, errors during the fiducialization process of the devices, and human errors in data acquisition and processing. In this context, we will discuss the device alignment errors, assuming that all other factors are controlled at their optimal state. <Table 2.3.3.5> shows the scale of the 4GSR and other accelerators around the world, along with the allowable alignment tolerances. The allowable tolerances between the 4GSR electromagnets and adjacent girders are 30 μm and 100 μm .

<Table 2.3.3.5> Accelerator Main Device Alignment Tolerance (RMS).

Machine	E(GeV)	C(m)	Magnet-to-Magnet(μm)	Cut-off($\pm\sigma$)	Girder-to-Girder(μm)	Cut-off($\pm\sigma$)
4GSR	4	798.84	30	2	100	2
ALS-U	2	196.5	10	2	50	2
APS-U	6	1103.6	30	2	100	1
Diamond-II	3.5	560.57	25	2	150	2
ESRF-EBS	6	843.97	60	2.5	NA+	NA+
NLS-II	3	792	30	1	100	1
SIRIUS	3	518.4	40	1	80	1
MAX-IV	3	528	20	1	NA*	NA*
SOLEIL-II	2.75	353.74	30	2	50	2

D. Ground monitoring system

The 4GSR ground is stable due to the underlying granite bedrock, so monitoring devices were not installed during the initial construction phase. However, after precisely measuring the ground behavior early in the construction process, monitoring devices can be installed later in areas with significant displacement if necessary. Ground monitoring sensors can be sourced globally from companies such as French F. Company and Russian B. Company. The primary operating software is provided by the manufacturer, but the software must be adapted to suit the site conditions. <Figure 2.3.3.11> shows the WPS and HLS devices currently installed and operating in the Pohang Accelerator PAL-XFEL tunnel.

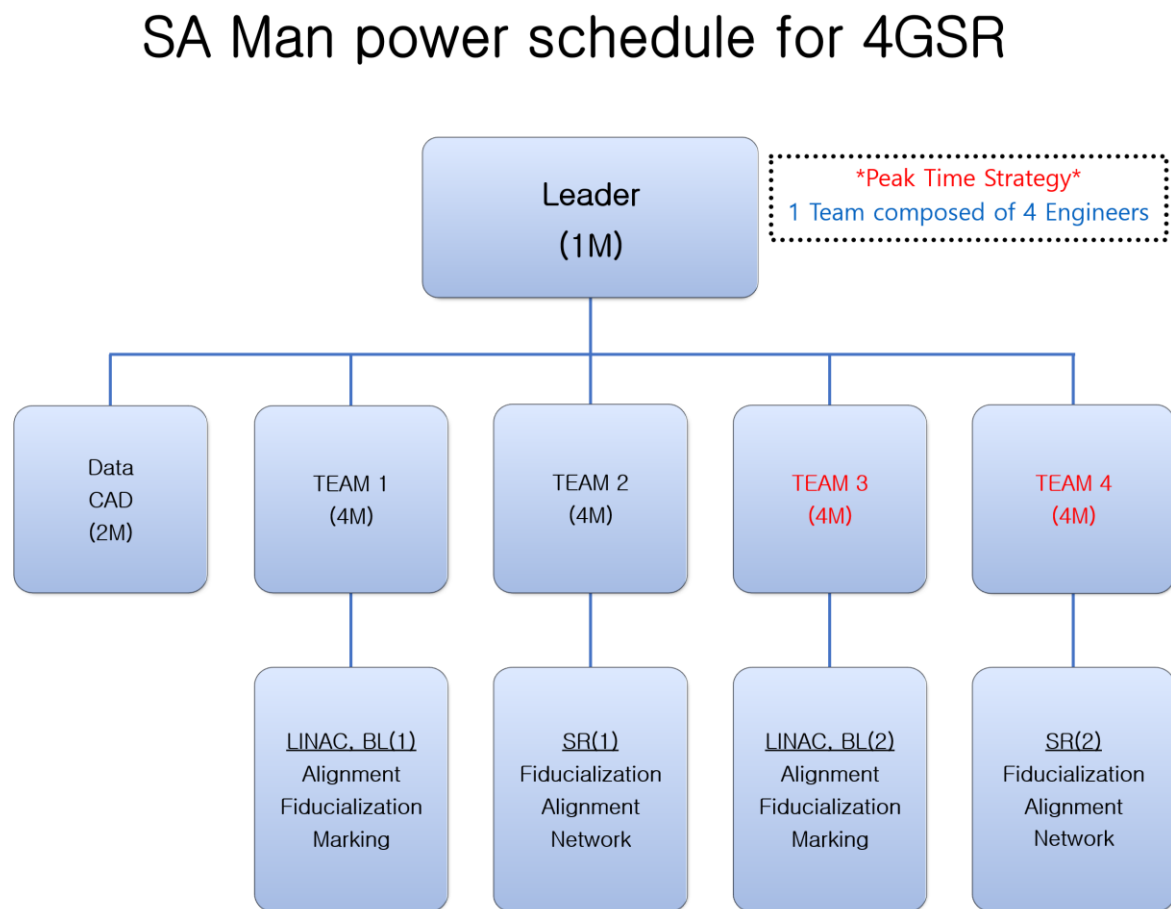


<Figure 2.3.3.11> WPS and HLS devices installed in the PAL-XFEL tunnel of Pohang Accelerator.

2.3.4 Alignment Team

The construction of the accelerator project presents challenges related to workforce composition, as the personnel required for installation and alignment must be concentrated over a short period. Experience in accelerator surveying and alignment is critical, particularly the expertise and leadership of the team leader in a group of four. Foreign research institutes typically require personnel to undergo specialized training in accelerator surveying and alignment for a certain period before being deployed. It is recommended to use technicians with at least 2 to 5 years of experience for precise alignment tasks during the assembly and installation phases (France ESRF, Design Report, 2019).

<Figure 2.3.4.1> shows the required workforce during peak installation and alignment activities. The surveying and alignment team is typically the first to begin and the last to finish their work during the construction phase. Therefore, it is essential to ensure sufficient personnel are available from the start of the project.



<Figure 2.3.4.1> SA Man power schedule.

2.3.5 Transportation and Installation

To ensure on-site installation stability and optimize the schedule for the 4GSR accelerator, the installation will proceed through the following steps. Prior to installation, electromagnets and vacuum devices must undergo pre-evaluation to ensure optimized conditions. Precise surveying of the installation site must be conducted rigorously. The main installation steps are as follows:

1. Precise surveying of the storage ring tunnel and coordinate definition of the accelerator.
2. Marking of girder installation locations based on precise survey data.
3. Girder assembly.
4. Precise surveying and alignment between girders.
5. Electromagnet assembly.
6. Precise survey and alignment of electromagnets.
7. Separation of the upper part of the electromagnets.
8. Assembly of supports and related components.
9. Vacuum chamber installation.
10. Precise surveying and alignment of the vacuum chamber.
11. Fastening of vacuum connections.
12. Reassembly of electromagnets.
13. Assembly of cables and LCW (Liquid Cooling Water).
14. Final precise surveying and alignment verification.
15. Vacuum pumping and leak evaluation.
16. Bake-out and NEG (Non-Evaporable Getter) activation.
17. Gate valve opening.